UNIVERSITAT DE BARCELONA

Carbon capture and storage in compressional basins: global to reservoir-scale assessments and integrated case study of the Puig-reig anticline (SE Pyrenees)

Xiaolong Sun

UNIVERSITAT DE BARCELONA

GRUP DE GEOLOGIA SEDIMENTÀRIA

Carbon capture and storage in compressional basins: global to reservoir-scale assessments and integrated case study of the Puig-reig anticline (SE Pyrenees)

PhD Thesis

Xiaolong Sun

Barcelona, 2021

Supervised by Dr. Enrique Gómez Rivas and Dr. Juan Alcalde

Tutored by Dr. Anna Travé

Department of Mineralogy, Petrology and Applied Geology

Doctoral Program of Earth Sciences HDK09

University of Barcelona (UB)

Department of Mineralogy, Petrology and Applied Geology

Faculty of Earth Sciences

University of Barcelona

Carbon capture and storage in compressional basins: global to reservoir-scale assessments and integrated case study of the Puig-reig anticline (SE Pyrenees)

Thesis presented by:

Xiaolong Sun

To obtain the degree of doctor from the University of Barcelona

Thesis conducted within the framework of the Doctoral Program in Earth Sciences supervised by **Dr. Enrique Gómez Rivas** and **Dr. Juan Alcalde** and tutored by **Dr. Anna Travé**

Barcelona, 2021

Xiaolong Sun

Dr. Enrique Gómez Rivas

Dr. Anna Travé

Dr. Juan Alcalde

Acknowledgments

This thesis was funded by the Ph.D. scholarship (201806450043) from the China Scholarship Council. This thesis was also funded by the Catalan Council to the Grup Consolidat de Recerca "Geologia Sedimentària" (2017SGR-824) and the DGICYT Spanish Project PGC2018-093903-B-C22 (Ministerio de Ciencia, Innovación y Universidades/Agencia Estatal de Investigación/Fondo Europeo de Desarrollo Regional, Unión Europea).

First and foremost, I would like to express my sincere gratitude to my supervisors, Dr. Anna Travé, Dr. Enrique Gomez-Rivas and Dr. Juan Alcalde for their invaluable guidance during my Ph.D. study. Their immense knowledge and plentiful experience helped me throughout this Ph.D. project. They also gave me constant support and encouragement in my daily life. I could not have imagined having better advisors and mentors for my Ph.D. study.

I would like to express my gratitude to Dr. Juan Diego Martín-Martín for his support and encouragement during my study in the Department of Mineralogy, Petrology and Applied Geology. I would like to thank Daniel Muñoz-López and Dr. David Cruset for their great contributions to this thesis and other publications, including field campaigns, data analyses, and reviewing papers. I would like to thank Dr. Albert Griera, Dr. Amanda Owen and Dr. Irene Cantarero for their great contributions to our peer-reviewed papers about fracture distribution, sedimentology and cementation, respectively. Besides, I would also like to thank Dr. Gareth Johnson, Dr. Lucía Struth, Mahdi Bakhtbidar, Dr. Javier Elío, Dr. Víctor Vilarrasa, Dr. Jacobo Canal, Dr. Julio Ballesteros, Dr. Niklas Heinemann, Dr. Stuart Haszeldine, Dr. Andrew Cavanagh, Dr. David Vega-Maza, Dr. Fernando Rubiera, Dr. Roberto Martínez-Orio, Dr. Ramon Carbonell and Dr. Ignacio Marzan for their contributions to our peer-reviewed paper about CO_2 capture and storage.

I would like to thank Dr. Dolors Barsó Romeu, Dr. Xavier Llovet Ximenes, Dr. Joaquin Perona Moreno, Dr. Leopoldo David Pena Gonzalez and Dr. Cedric John for their contributions to lab work, including thin section, element composition, carbon and oxygen isotope, strontium isotope, and clumped isotope thermometry, respectively. I would like to thank Patricia Cabello Lopez for

allowing me attending a Petrel software training course and for her useful suggestions on reservoir modelling. I would also like to thank Enric Sangrà and Francesc Baiget for their support during field campaigns.

I would like to thank my friends, colleagues and research team for a cherished time spent together in labs and in social settings, including Jun Wu, Kainan Xie, Congcong Zhang, Baoqin Hao, Jingyi Shu, Victoriano Pineda González, Telm Bover-Arnal, Ariana Carrazana, Gabriel Cofrade Rivas, Oriol Vilanova Pagès, etc. Thanks to them, I had a fulfilling and happy three years in Barcelona.

Last but not least, I would like to thank my family, including my parents, my younger sister, my girlfriend and her parents for their full support during my study abroad.

Agradecimientos

Esta tesis ha sido financiada por la beca de doctorado (201806450043) de la China Scholarship Council. Esta tesis también ha sido financiada por la Generalitat de Catalunya al Grup Consolidat de Recerca “Geologia Sedimentària” (2017SGR-824) y por el proyecto DGICYT PGC2018-093903-B-C22 del Ministerio de Ciencia, Innovación y Universidades/Agencia Estatal de Investigación/Fondo Europeo de Desarrollo Regional, Unión Europea.

En primer lugar, me gustaría expresar mi más sincera gratitud a mis supervisores, la Dr. Anna Travé, el Dr. Enrique Gomez-Rivas y el Dr. Juan Alcalde por su inestimable guía durante mis estudios de doctorado. Su inmenso conocimiento y experiencia me han ayudado a desarrollar mi proyecto. También me han dado un apoyo constante e insuflado ánimos a diario. No podría imaginar unos consejeros y mentores mejores que ellos.

También me gustaría expresar mi gratitud al Dr. Juan Diego Martín-Martín por su apoyo y estímulo durante mi estancia en el Departamento de Mineralogía, Petrología y Geología Aplicada. Quiero darles las gracias a Daniel Muñoz-López y al Dr. David Cruset por la gran contribución a esta tesis y a las publicaciones resultantes, incluyendo las campañas de campo, los análisis de datos y las revisiones de los artículos. Me gustaría agradecerle al Dr. Albert Griera y a las Drs. Amanda Owen e Irene Cantarero por sus magníficas contribuciones a los artículos sobre distribución de fracturas, sedimentología y cementación, respectivamente. Además, también quiero agradecerles al Dr. Gareth Johnson, Dr. Lucía Struth, Mahdi Bakhtbidar, Dr. Javier Elío, Dr. Víctor Vilarrasa, Dr. Jacobo Canal, Dr. Julio Ballesteros, Dr. Niklas Heinemann, Dr. Stuart Haszeldine, Dr. Andrew Cavanagh, Dr. David Vega-Maza, Dr. Fernando Rubiera, Dr. Roberto Martínez-Orio, Dr. Ramon Carbonell y Dr. Ignacio Marzan su contribución a los artículos sobre almacenamiento geológico de CO_2.

Me gustaría agradecerles también al Dr. Dolors Barsó Romeu, Dr. Xavier Llovet Ximenes, Dr. Joaquin Perona Moreno, Dr. Leopoldo David Pena Gonzalez y Dr. Cedric John sus contribuciones al trabajo de laboratorio en láminas delgadas, composición elemental, isótopos de carbono y oxígeno, isótopos de estroncio y termometría de isótopos clumped, respectivamente. Me gustaría

agradecerle a Patricia Cabello López que me haya permitido asistir a su curso sobre Petrel y también las valiosas sugerencias que me ha dado sobre modelización de reservorios. También quiero agradecerles a Enric Sangrà y a Francesc Baiget su ayuda durante las campañas de campo.

Me gustaría darles las gracias a mis amigos, colegas y grupo de investigación por el tiempo y los grandes momentos vividos en el laboratorio y en las veladas sociales, incluyendo a Jun Wu, Kainan Xie, Congcong Zhang, Baoqin Hao, Jingyi Shu, Victoriano Pineda González, Telm Bover-Arnal, Ariana Carrazana, Gabriel Cofrade Rivas, Oriol Vilanova Pagès, etc. Gracias a ellos he pasado tres años felices y edificantes en Barcelona.

Por ultimo, pero no por ello menos importante, me gustaría darle las gracias a mi familia, a mis padres, a mi hermana pequeña, a mi novia y sus padres por su apoyo durante mi etapa de estudios en el extranjero.

Agraïments

Aquesta tesi ha estat finançada per la beca de doctorat (201806450043) del China Scholarship Council. Aquesta tesi també va ser finançada pel Consell Català al Grup Consolidat de Recerca "Geologia Sedimentària" (2017SGR-824) i el DGICYT Spanish Project PGC2018-093903-B-C22 (Ministerio de Ciencia, Innovación y Universidades / Agencia Estatal de Investigación / Fons Europeu de Desenvolupament Regional, Unió Europea).

En primer lloc, vull expressar el meu sincer agraïment als meus supervisors, la doctora Anna Travé, el doctor Enrique Gómez-Rivas i el doctor Juan Alcalde per la seva inestimable orientació durant el meu doctorat. El seu immens coneixement i la seva abundant experiència m´han ajudat al llarg d'aquest projecte de doctorat. Ells també m'han donat suport i ànims constants en la meva vida diària. No m'hauria pogut imaginar tenir millors assessors i mentors per al meu doctorat.

Vull expressar el meu agraïment al doctor Juan Diego Martín-Martín pel seu suport i ànims durant el meu estudi al Departament de Mineralogia, Petrologia i Geologia Aplicada. Vull agrair a Daniel Muñoz-López i al doctor David Cruset les seves grans contribucions a aquesta tesi i a altres publicacions, incloses campanyes de camp, anàlisis de dades i revisió de treballs. Vull agrair al doctor Albert Griera, a la doctora Amanda Owen i a la doctora Irene Cantarero les seves grans contribucions als nostres treballs sobre distribució de fractures, sedimentologia i cimentació, respectivament. A més, també vull donar les gràcies al Dr. Gareth Johnson, a la Dra. Lucía Struth, a Mahdi Bakhtbidar, al Dr. Javier Elío, al Dr. Víctor Vilarrasa, al Dr. Jacobo Canal, al Dr. Julio Ballesteros, al Dr. Niklas Heinemann, al Dr. Stuart Haszeldine , al Dr. Andrew Cavanagh, al Dr. David Vega-Maza, al Dr. Fernando Rubiera, al Dr. Roberto Martínez-Orio, al Dr. Ramon Carbonell i al Dr. Ignacio Marzan per les seves contribucions al nostre article sobre captura i emmagatzematge de CO_2.

Vull agrair a la doctora Dolors Barsó i als doctors Xavier Llovet, Joaquin Perona, Leopoldo David Pena i Cedric John per les seves contribucions al treball de laboratori, incloses l'elaboració de les làmines primes, la composició d'elements amb la microsonda electrònica, l'anàlisi dels isòtops de carboni i oxigen, isòtop d'estronci i clumped isòtops, respectivament. M'agradaria

donar les gràcies a Patricia Cabello per haver-me permès assistir a un curs de formació en programari Petrel i pels seus útils suggeriments sobre la modelització de reservoris. També vull agrair a Enric Sangrà i Francesc Baiget el seu suport durant les campanyes de camp.

Vull agrair als meus amics, col·legues i equip d'investigació el temps estimat que passem junts en laboratoris i entorns socials, inclosos Jun Wu, Kainan Xie, Congcong Zhang, Baoqin Hao, Jingyi Shu, Victoriano Pineda, Telm Bover-Arnal, Ariana Carrazana, Gabriel Cofrade, Oriol Vilanova, etc. Gràcies a ells he tingut tres anys satisfactoris i feliços a Barcelona.

Per últim, però no menys important, voldria agrair a la meva família, inclosos els meus pares, la meva germana petita la meva xicota i els seus pares, el seu ple suport durant el meu estudi a l'estranger.

Table of contents

Abstract

Carbon capture and storage (CCS) has been proposed as a potential technology to mitigate climate change. However, there is currently a huge gap between the global CCS deployment and that which will be ultimately required. To date, CCS deployment has been restricted to the most favourable tectonic settings, such as extensional passive margin and post-rift basins and compressional foreland basins. In addition, CCS deployment has stalled in most countries, with only limited commercial projects realised mainly in hydrocarbon-rich countries for enhanced oil recovery. This Ph.D. thesis aims to assess the potential of CCS development in compressional basins and hydrocarbon-limited regions at different scales: from a global-scale assessment to a national-scale assessment in Spain and finally, to a reservoir-scale analogue case study, focusing on the Puig-reig anticline (SE Pyrenees).

Compressional settings host some of the most significant oil and gas resources in the world and will be key to the large-scale deployment of CCS. On the global scale, we present an integrated source-to-sink analysis tool that combines basin distribution, hydrocarbon resources and CO_2 emissions to assess the potential of compressional basins for CCS development. This methodology allows identifying five high-priority regions for prospective CCS development in compressional basins: North America, north-western South America, south-eastern Europe, the western Middle East and western China. The results indicate that compressional basins will have to play a critical role in the future of CCS if this technology is to be implemented worldwide.

Instead of developing CCS via CO_2 enhanced oil recovery (CO_2-EOR), hydrocarbon-limited countries need to devise alternative strategies if they intend to implement CCS in their decarbonisation strategies. On the national scale, we present a novel systematic source-to-sink assessment methodology based on a hubs and clusters approach to identify favourable regions for CCS deployment in hydrocarbon-limited countries. Throughout the evaluation of the Spanish case study, we identify 15 emission hubs from the power and the hard-to-abate sectors and priority source-to-sink clusters, based on screening and ranking processes using a multi-criteria decision-

making method. North-Western and North-Eastern Spain are recognised as priority regions due to resilience provided by different types of CO_2 sources and multiple geological storage structures. CCS, especially in the hard-to-abate sector, and in combination with other low-carbon energies, remains a significant contributor to the Paris Agreement's mid-century net-zero target. This methodology can attract renewed public and political interest in viable deployment pathways of CCS in hydrocarbon-limited countries.

The Ebro Foreland Basin, identified as one of the most potential areas for CCS development in Spain, is a typical hydrocarbon-limited compressional basin with low availability of geological and geophysical data required for the suitability assessment for CO_2 storage. In this work, we carry out an integrated study of the Puig-reig anticline (SE Pyrenees) to be used as an outcrop analogue to explore the reservoir potential of foreland basin margin sedimentary systems. This anticline exposes continuous outcrops deposited in a proximal to medial fluvial fan system with an overall southeast downstream trend. The proximal deposits, mainly spreading in the northwest portion of the anticline, are characterised by conglomerates with minor interbedded sandstones. These are interpreted as having been deposited from unconfined flash floods and wide-shallow channel streams. The medial deposits, covering the rest of the anticline, consist of interbedded beds of conglomerates, sandstones and claystones, deposited in braided channel streams and overbanks.

In order to understand the fracture distribution in the Puig-reig anticline and how it can potentially affect reservoir potential, fracture networks have been characterised using the linear scanline method, and four fracture sets (F1 to F4) have been identified in the target structure. The north limb shows low fracture intensity but large fracture length and aperture. The crest and the crest-limb transition zones present relatively high fracture intensity and variable fracture length and aperture. The south limb has low fracture intensity and small fracture length and aperture. Based on multiple linear regression analysis, we observe that fracture intensity is mainly controlled by the structural position, bedding thickness and lithological associations, with more intense fracturing in thin sandstone layers with multiple interlayers of fine deposits in the high

strain zones. The fracture length mainly depends on bedding thickness and is affected by lithological associations. The fracture apertures are mainly controlled by lithofacies.

An integrated analysis of structural, petrological and geochemical characteristics allows identifying five generations of calcite cements (Cc0 to Cc4) and fluid regimes in the Puig-reig anticline. Before intensive deformation, Cc0 precipitated in intergranular porosity from meteoric fluids in the phreatic zone. During the most intense phase of thrusting and folding, Cc1 precipitated in intergranular porosity, faults and F1 to F4 fracture sets from hydrothermal fluids migrated from the deep areas of the SE Pyrenees. During the late stage of fold growth, Cc2 mainly precipitated in normal and strike-slip faults in the anticline crest from the mixing between hydrothermal and meteoric fluids during the crestal collapse, or from hydrothermal fluids with shallower burial depth compared to that of Cc1. Cc3 mainly precipitated in faults and F1 and F4 fracture sets in the north-western zone of the anticline from formation fluids probably migrated through the frontal thrusts. During the continuous denudation, Cc4 precipitated in the reopened F1 to F4 fracture sets from meteoric fluids.

The comparison of the Puig-reig anticline with other similar depositional and tectonic settings worldwide allows exploring the reservoir potential for CO_2 storage at foreland basin margins. In the Puig-reig anticline, the proximal to medial deposits present low porosity of host rocks due to the prevailing presence of calcite cement, with limited high porosity concentrated in massive medium and coarse lithofacies in the medial fluvial fan. Sandstone lithofacies deposited from the medial fluvial fan and located in the high strain zones feature relatively high fracture intensity, which have relative high potential to be effective reservoirs. The study conducted in the Puig-reig anticline provides a conceptual model useful to understand the reservoir characteristics at the basin margins. According to this model, the reservoir potential is comprehensively controlled by sedimentology, diagenesis and deformation. The effective combination of both structure and facies can make basin margin locations potential areas for effective reservoirs, even in the presence of overall low porosity. Future work will focus on building a static reservoir model of the Puig-reig anticline based on the results obtained in the sedimentology, fracture and diagenesis

studies, and finally carrying out fluid flow simulations to determine the main controls on CO_2 injection and storage in such a geological setting.

Resumen

La captura y almacenamiento de CO_2 (CCS por sus siglas en inglés) es uno de las principales tecnologías propuestas para mitigar el cambio climático. Sin embargo, actualmente la diferencia entre el despliegue de esta tecnología y la necesidad imperiosa de descarbonización de nuestra sociedad es enorme. Hasta el momento el CCS solo se ha llevado a cabo en zonas geológicas más favorables, como los márgenes pasivos y post-rift en zonas extensionales y en las cuencas de antepaís de zonas compresivas. Además, el desarrollo del CCS se ha detenido en la mayoría de los países del mundo, existiendo únicamente una serie de proyectos comerciales principalmente en países con abundantes recursos petrolíferos y relacionados con la recuperación mejorada. Esta tesis de doctorado pretende evaluar el potencial de las cuencas compresivas y de los países con recursos petrolíferos limitados para el desarrollo de la tecnología de CCS en diferentes escalas: desde una perspectiva global a una nacional centrada en España y, finalmente centrándose en un caso de estudio a escala de reservorio, desarrollado en el anticlinal de Puig-reig (sudeste de los Pirineos).

A escala global, se presenta una herramienta para el análisis integrado de fuente-sumidero de CO_2, que combina la distribución de cuencas, recursos petrolíferos y emisiones de CO_2 globales para determinar el potencial de las cuencas compresivas para el desarrollo de CCS. Esta metodología ha permitido identificar cinco regiones con potencial para el desarrollo de CCS: Norte América, el noroeste de Sudamérica, el sudeste de Europa, el oeste de Oriente Próximo y el oeste de China. Los resultados de este análisis indican que las cuencas compresivas jugarán un papel determinante en el desarrollo del CCS si es que esta tecnología se implementa a la escala necesaria.

A escala nacional, se presenta una metodología para el análisis de fuente sumidero de CO_2 basado en una metodología de “hubs and clusters”, indicada para idenficar regiones con alta prospectividad para el desarrollo de CCS en regiones con recursos petrolíferos limitados. Esta herramienta se ha aplicado en un caso de estudio centrado en España, donde se han identificado 15 hubs de emisiones en sectores de producción de energía y de industrias de difícil abatimiento

y se han diseñado clústers de fuente-sumidero basados en procesos de filtrado y clasificación utilizando métodos de toma de decisiones multi-criterio. Se han identificado el noroeste y noreste de España como las zonas de desarrollo prioritario gracias a la resiliencia que les proporciona el diferentes fuentes de emisiones de CO_2 y acceso a múltiples estructuras geológicas para el almacenamiento. El CCS, especialmente para descarbonizar los sectores industriales de difícil abatimiento, y en combinación con otras energías de bajas emisiones, sigue siendo un elemento fundamental para alcanzar los objetivos firmados en los Acuerdos de Paris para alcanzar las emisiones netas nulas hacia la mitad de este siglo. La metodología presentada puede atraer un interés político y social renovado sobre esta tecnología, en especial en países con recursos petrolíferos limitados.

La cuenca de antepaís del Ebro, identificada como una de las áreas prioritarias para el desarrollo del CCS en España, es una cuenca compresiva típica con muy poco interés petrolífero y por tanto con una información geológica y geofísica disponible muy limitada. En esta tesis, se ha llevado a cabo un estudio integral del anticlinal de Puig-reig (sureste de los Pirineos), para su uso como análogo en superficie para explorar el potencial de las cuencas sedimentarias de antepaís para el almacenamiento geológico de CO_2. Este anticlinal ofrece afloramientos continuos de depósitos de sistemas abanicos fluviales proximal a medio con una trayectoria descendente orientada hacia el sudeste. Los depósitos proximales, que se extienden principalmente a lo largo de la porción noroeste del anticlinal, se caracterizan por tener conglomerados con capas menores de areniscas interestratificadas. Estos depósitos son interpretados como depósitos de inundación no restringidos y canales anchos y poco profundos. Los depósitos de la zona media que cubren el resto del anticlinal consisten en capas interestratificadas de conglomerados, arenas y arcillas, depositados en canales braided y desbordamiento de los canales.

Para tratar de entender la distribución de las fracturas en el anticlinal de Puig-reig y como éstas pueden afectar al potencial de reservorio de esta estructura se ha caracterizado la red de fracturación utilizando el método de escaneado lineal, mediante el cual se han identificado cuatro sets de fracturas diferentes (F1 a F4). El extremo norte del anticlinal está caracterizado por una baja densidad de fracturación pero con unas fracturas de gran longitud y grado de apertura. La

cresta y las zonas de transición entre la cresta y los extremos presentan una intensidad de fracturación relativamente elevada y fracturas de longitud y apertura variables. El extremo sur del anticlinal tiene una intensidad de fracturación baja y fracturas cortas y con baja apertura. Mediante un análisis de regresión lineal múltiple se ha podido determinar que la intensidad de fracturación está controlada principalmente por la posición estructural, el grosor de la estratificación y las asociaciones litológicas, observándose la fracturación más intensa en capas finas de areniscas con intercalaciones de depósitos más finos de las zonas de mayor deformación del anticlinal. Las aperturas de las fracturas están controladas principalmente por las litofacies.

El análisis integrado de las características estructurales, petrológicas y geoquímicas permiten identificar cinco generaciones distintas de cementos de calcita (de Cc0 a Cc4) y de regímenes de flujo en el anticlinal de Puig-reig. Antes de la deformación intensa, el cemento Cc0 precipitó en la porosidad intergranular a partir de fluidos meteóricos provenientes de la zona freática. Durante la fase más intensa de cabalgamiento y plegamiento, el Cc1 precipitó en los poros, fallas y en los sets F1 a F4 de fracturas a partir de fluidos hidrotermales migrados desde zonas profundas del sudeste de los Pirineos. Durante la última fase de crecimiento del pliegue, el Cc2 precipitó principalmente en fallas normales y strike-slip en la cresta del anticlinal. El origen de los fluidos podría provenir de una mezcla de fluidos hidrotermales y meteóricos ocurridos durante el colapso de la cresta, o bien a partir de fluidos hidrotermales pero con profundidades de enterramiento menores que las del Cc1. El Cc3 precipitó principalmente en las fallas y en las fracturas de los sets F1 y F4 en la zona noroeste del anticlinal, con fluidos probablemente migrados a través de los cabalgamientos frontales. Durante la denudación constante, el Cc4 precipitó en las fracturas reabiertas de los sets F1 a F4 a partir de fluidos meteóricos.

Mediante la comparativa del anticlinal de Puig-reig con otras zonas en el mundo con ambientes deposicionales y tectónicos similares se puede explorar el potencial de reservorio de este tipo de estructuras en cuencas de antepaís para el almacenamiento geológico de CO_2. En el anticlinal de Puig-reig, los depósitos de la zona proximal a media presentan una porosidad baja debido a la presencia de cemento de calcita, con ciertas zonas de porosidad más elevada concentradas en litofacies masivas de grano medio y grueso correspondientes a la zona media del abanico. Las

litofacies de areniscas depositadas en la zona media del abanico y localizadas en zonas de deformación elevada presentan una relativamente alta intensidad de fracturación, con cierto potencial para configurar reservorios efectivos. El estudio realizado en el anticlinal de Puig-reig puede proporcionar un modelo conceptual útil para comprender las características de los reservorios en los márgenes de cuenca. En concordancia con este modelo, el potencial de reservorio está considerablemente controlado por la sedimentología, la diagénesis y la deformación. La combinación efectiva de la estructura y las facies puede hacer de las zonas marginales de la cuenca zonas con potencial como reservorios, incluso en zonas con baja porosidad. La futura línea de trabajo se centrará en la construcción de un modelo estático del reservorio en el anticlinal de Puig-reig basado en los resultados obtenidos en los estudios sedimentológico, de fracturas y diagenético, para finalmente producir simulaciones de flujo de fluidos, con los que determinar los principales controles sobre la inyección y el almacenamiento de CO_2 en este tipo de áreas geológicas.

Resum

La captura i emmagatzematge de carboni (CCS) s'ha proposat com una tecnologia potencial per mitigar el canvi climàtic. No obstant això, actualment hi ha una enorme bretxa entre el desplegament global de CCS i el que finalment serà necessari. Fins ara, el desplegament de CCS s'ha restringit a les configuracions tectòniques més favorables, com ara marges passius extensius, conques post-rift i conques d'avantpaís compressives. A més, el desplegament de CCS s'ha estancat a la majoria de països, amb pocs projectes comercials realitzats principalment a països rics en hidrocarburs per millorar la recuperació del petroli. Aquesta tesi doctoral té com a objectiu avaluar el potencial de desenvolupament de CCS en conques de compressió i regions sense hidrocarburs a diferents escales: des d'una avaluació a escala mundial fins a una avaluació a escala nacional a Espanya i, finalment, a l'estudi d'un analeg a escala de dipòsit, l'anticlinal de Puig-reig (SE Pirineus).

Els entorns compressius contenen alguns dels reservoris de petroli i gas més importants del món i seran claus per al desplegament a gran escala de CCS. A escala mundial, presentem una eina d'anàlisi integrada que combina la distribució de la conca, els recursos d'hidrocarburs i les emissions de CO_2 per avaluar el potencial de les conques compressives per al desenvolupament de CCS. Aquesta metodologia ens ha permès identificar cinc regions d'alta prioritat per al desenvolupament potencial de CCS a les conques compressives: Amèrica del Nord, nord-oest d'Amèrica del Sud, sud-est d'Europa, l'Oest de l'Orient Mitjà i l'oest de la Xina. Els resultats indiquen que les conques compressives hauran de tenir un paper crític en el futur de la CCS si aquesta tecnologia s'implementa a tot el món.

En lloc de desenvolupar CCS mitjançant la recuperació del petroli (CO_2-EOR), els països que tenen pocs hidrocarburs han d'elaborar estratègies alternatives si tenen la intenció d'implementar CCS en les seves estratègies de descarbonització. A escala nacional, presentem una nova metodologia sistemàtica d'avaluació basada en "centres i clústers" per identificar les regions favorables al desplegament de CCS als països amb pocs hidrocarburs. Aquesta eina l'hem aplicat en un cas de l'estat espanyol, on identifiquem 15 centres d'emissions en sectors de producció

d'energia i d'indústries difícils d'abatre i s'han dissenyat els clústers prioritaris de font-embornal, basats en processos de selecció i classificació mitjançant un mètode de presa de decisions multicriteri. El nord-oest i el nord-est d'Espanya s'han identificat com les regions prioritàries degut a la resiliència que els hi proporciona diferents tipus de fonts de CO_2 i múltiples estructures d'emmagatzematge geològic. El CCS, especialment per descarbonitzar el sector difícil de reduir, i en combinació amb altres energies de baixes emissions en carboni, continua sent un contribuent significatiu a l'objectiu de emissions zero netes per mitjans d'aquest segle segons l'Acord de París. Aquesta metodologia que presentem pot atreure un interès públic i polític renovat sobre aquesta tecnologia, en especial en els països amb pocs hidrocarburs.

La conca d'avantpaís de l'Ebre, identificada com una de les àrees potencials per al desenvolupament de CCS a Espanya, és una conca compressiva típica amb poc interès pels hidrocarburs i, per tant, amb baixa disponibilitat de dades geològiques i geofísiques necessàries per a l'avaluació de la idoneïtat per a l'emmagatzematge de CO_2. En aquest treball, realitzem un estudi integrat de l'anticlinal de Puig-reig (SE Pirineus) per utilitzar-lo com un anàleg en superfície per explorar el potencial de les conques sedimentaries d'avantpaís per l'emmagatzemament de CO_2. Aquest anticlinal exposa afloraments continus dipositats en un sistema de ventalls fluvials proximals a intermedis amb una tendència general descendent cap el sud-est. Els dipòsits proximals, que s'estenen principalment a la part nord-oest de l'anticlinal, es caracteritzen per conglomerats amb gresos intercalats. S'interpreta com si s'haguessin dipositat a partir d'inundacions instantànies no confinades i canals amples i de poca fondària. Els dipòsits de la zona intermèdia, que cobreixen la resta de l'anticlinal, consisteixen en capes interestratificades de conglomerats, gresos i argiles, dipositats en canals trenats i sobreeiximent dels canals.

Per tal d'entendre la distribució de les fractures a l'anticlinal de Puig-reig i com aquestes poden afectar el potencial del reservori d'aquesta estructura, s'han caracteritzat les xarxes de fractures mitjançant el mètode de la línia d'escaneig lineal i s'han identificat quatre conjunts de fractures (F1 a F4). L'extrem nord de l'anticlinal presenta una intensitat de fractures baixa, però una gran longitud i obertura de les fractures. La cresta i les zones de transició entre la cresta i els flancs presenten una intensitat de fractures relativament alta i una longitud i una obertura de les fractures

variables. L'extrem sud té una intensitat de fractures baixa i una longitud i una obertura de les fractures petites. Basat en l'anàlisi de regressió lineal múltiple, observem que la intensitat de la fractura està controlada principalment per la posició estructural, el gruix de les capes i les associacions litològiques, amb una fracturació més intensa en les capes fines de arenites amb múltiples capes de dipòsits fins a les zones de més deformació de l'anticlinal. La longitud de la fractura depèn principalment del gruix de les capes i es veu afectada per les associacions litològiques. Les obertures de les fractures estan controlades principalment per les litofàcies.

Una anàlisi integrada de les característiques estructurals, petrològiques i geoquímiques permet identificar cinc generacions de ciments de calcita (Cc0 a Cc4) i de règim de fluids a l'anticlinal de Puig-reig. Abans de la deformació intensiva, Cc0 precipitava en la porositat intergranular a partir de fluids meteòrics a la zona freàtica. Durant la fase més intensa d'encavalcament i plegament, Cc1 va precipitar en porositat intergranular, falles i en els conjunts de fractures de F1 a F4 a partir de fluids calents migrats des de les zones profundes. Durant la fase tardana del creixement del plec, el Cc2 precipità principalment en falles normals i direccionals en la cresta de l´anticlinal a partir de la barreja entre fluids calents i meteòrics durant el col·lapse de la cresta o bé a partir de fluids calents però a una profunditat d'enterrament inferior a la de Cc1. Cc3 precipità principalment en falles i en els conjunts de fractures F1 i F4 a la zona nord-oest de l'anticlinal a partir de fluids de formació que probablement van migrar a través dels encavalcaments frontals. Durant la denudació contínua, Cc4 va precipitar en els conjunts de fractures reoberts de F1 a F4 a partir de fluids meteòrics.

La comparació de l'anticlinal de Puig-reig amb altres zones del mon amb ambients deposicional i tectònics similars permet explorar el potencial de d'emmagatzematge de CO_2 d'aquest tipus d'estructures en conques d'avantpaís. A l'anticlinal de Puig-reig, els dipòsits proximals a intermedis presenten una porositat baixa de les roques hostes a causa de la presència predominant de ciment de calcita, amb algunes zones de porositat més elevada concentrades en litofàcies massives de gra mig a groller de les zones intermèdies del ventall fluvial. Les litofàcies d'arenites dipositades en la zona intermèdia del ventall i situades a les zones major deformació presenten una intensitat de fractura relativament elevada, amb un potencial relativament elevat per ser

dipòsits efectius. L'estudi realitzat a l'anticlinal de Puig-reig proporciona un model conceptual útil per entendre les característiques dels reservoris en els marges d'una conca. Segons aquest model, el potencial del reservori està controlat de manera exhaustiva per la sedimentologia, la diagènesi i la deformació. La combinació efectiva tant de l'estructura com de la fàcies pot fer de les zones del marge de la conca que siguin zones potencials com reservoris efectius, fins i tot en presència d'una porositat baixa. Els treballs futurs es centraran en la construcció d'un model estàtic del dipòsit de l'anticlinal de Puig-reig basat en els resultats obtinguts en els estudis de sedimentologia, fractures i diagènesi i, finalment, la realització de simulacions de flux de fluids per determinar els principals controls d'injecció i emmagatzematge de CO_2 en aquests tipus de sistemes geològics sedimentaris.

1 Introduction

1.1 Current status of CCS deployment

Estimations indicate that massive greenhouse gas emissions from human activities have caused a global temperature increase of 0.8°C to 1.2°C above pre-industrial levels (Intergovernmental Panel on Climate Change, 2018). This global warming has numerous impacts on natural and human systems, *e.g.,* many land and ocean ecosystems have already changed (Hoegh-Guldberg et al., 2018) and will continue to do so in the future (Millington et al., 2019; Trisos et al., 2020). Limiting global warming to 2°C or even 1.5°C above pre-industrial levels will require a combination of different approaches to climate change mitigation that are compatible with sustainable development, including CO_2 emission reductions (Intergovernmental Panel on Climate Change, 2018). Carbon capture and storage (CCS) is widely considered an efficient and safe method for decarbonisation (MacDowell et al., 2010; Alcalde et al., 2018; Bui et al., 2018), and remains a core component of national and global emission reduction strategies to mitigate climate change (Scott et al., 2013; Global CCS Institute, 2017). For example, in an ambitious 1.5°C temperature raise scenario, CCS may contribute with 550 to 1017 gigatons (Gt) of global CO_2 emission reduction by year 2100 (Intergovernmental Panel on Climate Change, 2018). However, CCS deployment has been slow due to various barriers including the high-cost perception of CCS development, lack of market mechanisms and incentives, insufficient penalty mechanisms for major CO_2 emitters, an inadequate legal framework, low public acceptance, potential safety and environment issues (Leung et al., 2014; Budinis et al., 2018), and uncertainty in the characterisation of storage sites (Espie et al., 2018). This has resulted in a huge gap between the global CCS provision and that required to meet the anticipated contribution of CCS to global and regional carbon emission reduction targets. According to the latest CCS facility database (Global CCS Institute, 2020), there were only 28 commercial CCS facilities in operation worldwide in 2020, with a maximum capture capacity of around 40 million tonnes of CO_2 per annum (Mtpa). While there are multiple projects in advanced stages of planning and development,

if the current trend of CCS deployment continues, it would still be very far from the global decarbonisation targets (Koelbl et al., 2014; Bui et al., 2018; Intergovernmental Panel on Climate Change, 2018).

Global assessments of CO_2 storage indicate that most regions contain sufficient storage capacity (Consoli and Wildgust, 2017; Kearns et al., 2017; Ringrose and Meckel, 2019), supporting CCS as a feasible technology for emission reduction planning. However, apart from the storage capacity, other geological factors can have significant effects on a region's suitability for CCS. These include the tectonic setting, basin architecture, reservoir quality, caprock sealing capacity, depth, geothermal gradient, reservoir pressure and hydrogeology (Bachu, 2003; Wei et al., 2013; Edlmann et al., 2015). In particular, the tectonic setting under which a targeted basin was formed exerts a significant effect on the other factors listed above (Edlmann et al., 2015; McDermott et al., 2017).

To date, CCS deployment has been restricted to the most favourable tectonic settings, such as extensional passive margin and post-rift basins and compressional foreland basins. Compressional basins mainly include peripheral foreland basins, developed adjacent to mountain belts, and retro-arc foreland basins, developed adjacent to island volcanic arcs. Using geomechanical facies assessments, Edlmann et al. (2015) ranked peripheral foreland basins as the most suitable sites for CO_2 storage, followed by passive continental margins, rift and strike-slip basins. In addition, compressional basins host abundant hydrocarbon resources, *e.g.,* accounting for 28% of global giant fields Mann et al. 2003). Hydrocarbon-bearing provinces are the primary targets of CCS because of their proven sufficient capacity and suitable characteristics to trap and store fluids over long periods of time, and the availability of a substantial number of geological datasets and host industrial infrastructures with potential for re-use for CCS development (Godec et al., 2011; Kuuskraa et al., 2013; Alcalde et al., 2019). These aspects grant compressional basins, more especially foreland basins, a great potential for the development of CCS. To date, CCS development in compressional basins shows a heterogeneous distribution, with commercial CCS facilities mainly concentrating in North America and the Middle East. Europe and China account for significant proportions of global CO_2 emissions and host large compressional basins that could

be used for CO_2 storage, and yet there is only one commercial CCS facility (Karamay Dunhua Oil Technology CCUS EOR Project) with very limited capacity (0.1 Mtpa) in operation in these basins (Global CCS Institute, 2020). Despite their promising prospect, the potential for CCS development of compressional basins has not been yet assessed quantitatively according to the global and regional carbon emission distribution.

Global development of CCS has been historically closely bound to the production of oil and gas via CO_2-EOR (Liu et al., 2018). Commercial CCS facilities in operation are mainly concentrated in a few hydrocarbon-rich countries with effective government support for CCS deployment, such as the USA, Canada, and Norway. Hydrocarbon-limited countries such as many European Union (EU) countries, will need to devise alternative strategies if they intend to implement ambitious decarbonisation strategies via CCS development. As the third-largest greenhouse gas (GHG) emitter after China and the United States, the EU has proposed its updated ambitious reduction target of GHG emissions that aims to achieve a reduction of at least 55% by 2030 compared to 1990 and to achieve net-zero GHG emissions by 2050 (European Commission, 2020). The EU has confirmed the essential role of CCS as a technology able to significantly reduce CO_2 emissions, promoting CCS to become an integral part of the European energy policy (Lupion and Herzog, 2013). However, there are currently no commercial CCS facilities in operation within the EU (European Commission, 2020). Thus, there should be more scope for CCS development in the EU, especially in those countries that have massive emissions and bear high potential for CCS development.

As the fifth-largest CO_2 emitter in the EU, Spain needs to take a pro-active role in meeting the EU's emission reduction target. CCS is considered a feasible option for emission reduction in Spain (Ministerio para la Transición Ecológica y el Reto Demográfico, 2007) and has been endorsed by the Spanish Parliament (Boletín Oficial del Estado, 2010). Regional and national assessments of CO_2 storage capacity and storage suitability have revealed a relatively high potential for CCS development in Spain (Vangkilde-Pedersen et al., 2009; Instituto Geológico y Minero de España, 2010a; Martínez del Olmo, 2019). Spain had a head start on CCS in the late 2000s (Patel, 2010), with three pilot projects for CO_2 capture and one for CO_2 storage developed

between 2006 and 2014. However, this trend was not continued due to the economic crisis and uncertainty about the role of CCS in the energy transition, and no commercial or demonstration projects are planned in the near future (Global CCS Institute, 2020).

For countries that do not host operational commercial facilities and have to-date lacked consistent government support for CCS deployment, a hubs and clusters strategy is gaining momentum and even promotes the implementation of this important technology. For example, the UK and the Netherlands are developing CCS hub projects for dedicated geological storage in the North Sea (Alcalde et al., 2019; Hoffman et al., 2021). As a typical hydrocarbon limited country in the EU, Spain can be used as a case study to explore how the hubs and clusters strategy can be applied in these hydrocarbon-limited countries to attract renewed public and political interest in viable deployment pathways of CCS.

1.2 Case study of reservoir potential at foreland basin margins

Northern Spain is dominated by compressional tectonic settings due to the continental collision between the Iberian and European plates, which resulted in the formation of the Ebro and Duero foreland basins. The Ebro Foreland Basin has recently been selected as one of the most potential basins for the large-scale deployment of CCS in Southern and Eastern Europe (Strategy CCUS, 2020). The ALGECO2 project (2009-2010) conducted by the Spanish Geological and Mining Survey (IGME) to evaluate the potential structures for CO_2 storage in Spain (Instituto Geológico y Minero de España, 2010b) identified multiple favourable storage structures within the Ebro Foreland Basin . However, there is very limited geological and geophysical data available in the Ebro Foreland Basin compared to hydrocarbon-bearing basins due to the limited hydrocarbon exploration activities carried out in this area. This imposes significant uncertainty on the suitability assessment of storage sites. More subsurface data will be needed in such hydrocarbon-limited regions to reduce the uncertainty and thus advance the maturity of storage resources. However, in areas with limited well data and seismic resolution of subsurface reservoirs, outcrop analogues can play an important role in improving the accuracy of reservoir prediction in the subsurface (Howell et al., 2014), by providing reliable geological conceptual models and

quantitative attribute information (Dichiarante et al., 2020).

Alluvial and fluvial fans are the dominant deposits at the active margins of non-marine foreland basins (DeCelles and Cavazza, 1999; Horton and Decelles, 2001; Ventra and Clarke, 2018). The northern margin of the Ebro Foreland Basin and the adjacent South Pyrenean fold-and-thrust belt present multiple alluvial fans and distributive fluvial systems. For example, Upper Eocene to Oligocene alluvial and fluvial systems developed in the north-eastern margin of the Ebro Foreland Basin. An excellent example of these systems is the conglomerate-dominated Berga Group developing near the frontal thrust sheets that wedges out into the fluvial Solsona Formation deposits towards the foreland basin (Sáez, 1987; Ford et al., 1997; Williams et al., 1998; Sáez et al., 2007; de Gibert and Sáez, 2009; Barrier et al., 2010). Such alluvial-fluvial deposits in the subsurface show high potential to become effective storage sites. For example, the eastern, deeper part of the Puig-reig anticline in the SE Pyrenees was considered a suitable site for storage of natural gas (Instituto Geológico y Minero de España, 1995). Besides, such well-exposed outcrops provide excellent outcrop analogues of similar systems in the subsurface. In the study area, previous studies focused on the description and interpretation of the sedimentary environments, the interactions between sedimentation and tectonic activities (*e.g.*, Ford et al., 1997; Williams et al., 1998; Sáez et al., 2007; Barrier et al., 2010; Carrigan et al., 2016), the evolution of fluid regime, and the relationships between fluid flow and deformation (*e.g.*, Cruset et al., 2016, 2018). In this thesis, the Puig-reig anticline has been used as a reservoir analogue to explore the reservoir potential of similar sedimentary systems at foreland basin margins.

At foreland basin margins, these alluvial and fluvial coarse clastic belts tend to present a relatively restricted radial extent and show high architectural unpredictability due to the lack of viable conceptual models activities (Moscariello, 2018). Accordingly, resource exploration and development at these basin margins are generally considered high risk and low return activities (Moscariello, 2018). However, alluvial fan and fluvial fan successions at basin margins have good preservation potential if the subsidence rate creates sufficient space to accommodate the significant sediment supply (Moscariello, 2005). Apart from the depositional characteristics, other aspects such as the complex structural and diagenetic characteristics of foreland basin

margin rocks can produce a strong reservoir heterogeneity. Reservoir quality can be comprehensively controlled by the sedimentary systems of sediments and the fracturing and diagenesis processes that they experience (*e.g.,* Morad et al., 2010; Taylor et al., 2010; Zhang et al., 2011; Watkins et al., 2018).

Sedimentary rocks of foreland basin margins and fold-and-thrust belts typically undergo intensive fracturing as folds grow, resulting in the formation of complex fracture networks. Many studies have analysed factors controlling the distribution of fracture networks, particularly how the structural position and the characteristics of sedimentary rocks impact the resulting fracture networks (Underwood et al., 2003; Florez-Niño et al., 2005; Lorenz et al., 2006; Wennberg et al., 2006; Ortega et al., 2010; Ogata et al., 2017). Fracture attributes, including fracture intensity, orientation, length, aperture and connectivity have been described to be closely related to the structural position of a rock volume within a fold (Peacock, 2001; Bellahsen et al., 2006; Ghosh and Mitra, 2009; Watkins et al., 2015a). In addition, the characteristics of the hosting sedimentary rocks, including the lithofacies architecture, lithological assemblages, bedding thickness, depositional components, textures, grain size and presence of cements and other diagenetic products, determine the rock mechanical properties (Shackleton et al., 2005; Olson et al., 2007; Ferrill and Morris, 2008; Laubach et al., 2009) and thus control fracture attributes and distribution. Fracture networks control fracture permeability and thus play a key role in terms of storage capacity, injectivity and sealing properties (Iding and Ringrose, 2010; Bond et al., 2013; Wilson et al., 2015), all critical factors for the success of CO_2 storage operations. As important fluid migration pathways and potential source for reservoir space, fracture networks have been widely studied in thrust belts composed of carbonate deposits due to their abundant hydrocarbon resources, *e.g.,* in the Zagros fold-and-thrust belt (Stephenson et al., 2007), the Bighorn Basin (Bellahsen et al., 2006), the Apennines (Van Dijk et al., 2000) and the Oman Mountains (Gomez-Rivas et al., 2014). However, studies of fracturing of thrust belts composed of sandstone deposits are significantly less well documented (Watkins et al., 2015a). An example of understudied systems is alluvial-fluvial fans.

At foreland basin margins or fold-and-thrust belts, fracturing, thrusting and folding are

generally accompanied by flow of various external fluids within and/or across different hydrostratigraphic units through connected fracture networks and porosity of host rocks (Travé et al., 2007; Fischer et al., 2009; Evans and Fischer, 2012; Evans et al., 2012; Ogata et al., 2014; Muñoz-López et al., 2020). These external fluids can provide the material sources and physical-chemical conditions for cementation (Bons et al., 2012). Calcite cement is one of the predominant authigenic minerals in clastic rocks (Morad, 1998; Walderhaug and Bjørkum, 1998), such as in alluvial-fluvial settings (*e.g.,* Hall et al., 2004; Wanas, 2008; Taylor and Machent, 2011; Cruset et al., 2016). The presence and distribution of calcite cement can exert significant effects on reservoir properties and heterogeneity (Dutton et al., 2002; Davis et al., 2006; Xiong et al., 2016; Cui et al., 2017; Wang et al., 2017). On the macro scale, calcite cement distribution in host rocks is mainly controlled by the depositional characteristics and the stacking patterns of sequence stratigraphy. Another factor that controls cement distribution in rocks at multiple scales is the development of faults and fractures, which control fluid migration across different hydrostratigraphic units (Evans and Fischer, 2012; Evans et al., 2012). On the small scale, cement distribution is controlled by lithofacies and reservoir permeability, in a way that cementation tends to affect the more permeable deposits, *e.g.,* reservoirs with coarse grain size and high quartz content (Dutton et al., 2002; Hall et al., 2004; Van Den Bril and Swennen, 2009). Thus, calcite cements tend to be heterogeneously distributed and can exert key effects on reservoir quality. Previous studies in the SE Pyrenees have mainly focused on unravelling the relationships between the evolution of fluid regimes and the deformation history of related structures using the geological information obtained from calcite cements (*e.g.*, Cruset et al., 2016, 2018). However, these well-exposed structures have not been studied as reservoir analogues to explore cement distribution and how it controls reservoir potential.

In this Ph.D. thesis, the Puig-reig anticline is used as a reservoir analogue to explore the reservoir potential for CO_2 storage and its controlling factors of similar sedimentary systems at foreland basin margins, based on an integrated study of the depositional characteristics and diagenetic evolution of the alluvial-fluvial succession and the fracture networks that these rocks host.

1.3 Scientific questions addressed in this thesis

(1) CCS development potential in compressional basins

There is currently a huge gap between the global deployment of CCS and that which will be ultimately required to meet the emission reduction targets needed to mitigate climate change. CCS deployment has been restricted to favourable tectonic settings, such as extensional passive margin and post-rift basins and compressional foreland basins. To reach an adequate level of deployment, the CCS potential of regions in different tectonic settings needs to be explored and assessed worldwide. Despite being ubiquitous in all continents, the potential of compressional basins to safely store captured CO_2 has not been systematically studied, especially in terms of comparison between their storage capacity and the demand for storage, which is directly determined by the geographic distribution and volume of carbon emissions.

To what extent compressional basins represent the best CCS option in certain regions, and can they play an essential role in global CCS development?

(2) CCS development potential in hydrocarbon-limited regions

Historically, CCS development has been closely bound to oil and gas production. To date, most commercial CCS facilities in operation concentrate in a few hydrocarbon-rich countries and most are purposed for CO_2-EOR, while only a few projects are for dedicated CCS. In many hydrocarbon-limited countries (such as most EU countries), CCS deployment has stalled, and these countries need to devise alternative strategies for CCS development instead of CO_2-EOR. For countries that lack of consistent government support for CCS deployment, a strategy based on hubs and clusters is gaining momentum and promoting the implementation of CCS for dedicated geological storage.

Is the hubs and clusters approach a suitable strategy to attract renewed interest in viable deployment pathways of CCS in hydrocarbon-limited countries?

(3) Analogue study in a hydrocarbon-limited foreland basin

As a typical hydrocarbon-limited country in the EU, Spain hosts interesting geological assets

for potential CCS development, such as the Ebro Foreland Basin, that has been selected as a potential basin for large-scale deployment of CCS (Strategy CCUS, 2020). However, there is significant uncertainty on the suitability assessment of storage sites due to the very limited amount of geological and geophysical data available for the characterisation of the target sites. Under such circumstance, analogue studies can provide reliable geological conceptual models and help to reduce the uncertainty of reservoir performance in the subsurface. There are well-exposed alluvial-fluvial deposits at the northern margin of the Ebro Foreland Basin, which have been previously studied focusing on unravelling tectonic activities, sedimentary systems, fluid evolutions and their interactions.

As the dominant deposits at the active margins of non-marine foreland basins, can these excellent outcrops be used as analogues to explore the reservoir potential of similar sedimentary systems in the subsurface?

(4) Fracture distribution in folded detrital rocks at foreland basin margins

At foreland basin margins and their adjacent fold-and-thrust belts, fractures tend to develop due to intensive deformation. As important fluid migration pathways and potential reservoir space, fracture networks have a significant impact on reservoir performance. Fracture networks have been widely studied in foreland basin margins and thrust belts composed of carbonate deposits due to their abundant hydrocarbon resources. However, studies of fracturing of thrust belts composed of sandstone deposits are significantly less well documented. An example of these understudied systems are alluvial-fluvial fan systems. The alluvial-fluvial outcrops available in the north-eastern Ebro Foreland Basin have not been yet approached as outcrop analogues to determine the fracture networks of folded detrital rocks.

At foreland basin margins, how does the complex structural and depositional characteristics of the folded alluvial-fluvial deposits impact the resulting fracture networks?

(5) Calcite cementation and fluid evolution in the Puig-reig anticline

In the Southern Pyrenees, most previous studies of calcite cement focused on unravelling the relationships between fluid flow and deformation in the cover thrust sheets, whereas only a few

studies focus on the adjacent Ebro Foreland Basin. In the Puig-reig anticline, at the north-eastern margin of the Ebro Foreland Basin, previous studies have only addressed the fracture-filling calcite veins in the anticline crest, revealing cementation phases and fluid regimes related to the early fold growth and the crestal collapse. Besides, the well-exposed alluvial-fluvial outcrops have not been used as outcrop analogues to explore calcite cement distribution in folded detrital rocks at foreland basin margins.

What is the complete cementation history and fluid evolution during the evolution of the Puig-reig anticline? How is calcite cement distributed in different depositional and structural settings?

1.4 Objectives of this thesis

The overarching aim of this thesis is to assess the potential of CCS development in compressional basins and hydrocarbon-limited regions, from a global-scale assessment to a national-scale assessment in Spain and, finally, to a reservoir-scale case study, focusing on the Puig-reig anticline (SE Pyrenees).

(1) Global-scale assessment of CCS development potential in compressional basins

An integrated source-to-sink analysis tool combines open-access information on compressional basin distribution and characteristics, hydrocarbon resources and CO_2 emissions. This tool is used to evaluate the potential role of compressional basins in global CCS development and to what extent compressional basins represent the best CCS option in certain regions.

(2) National-scale assessment of CCS development potential in hydrocarbon-limited regions

Based on a hubs and clusters strategy, a new source-to-sink assessment methodology has been developed to evaluate the potential of CCS development in hydrocarbon-limited regions. As a case study, this methodology is applied in Spain to identify high-priority source-sink clusters for CCS development and to help to devise the important role of CCS in the decarbonization strategy of this country.

(3) Reservoir-scale case study of the storage potential at foreland basin margins: the Puig-reig Anticline (SE Pyrenees)

As one of the most potential basins for large-scale deployment of CCS in Southern and Eastern Europe, the Ebro Foreland Basin has very reduced amount of geological and geophysical data available due to the limited hydrocarbon resources existing in this area. In this thesis, the Puig-reig anticline is used as an outcrop analogue for the evaluation of the reservoir potential of similar sedimentary systems at foreland basin margins. The study of this analogue provides reliable geological conceptual models and thus reduce the uncertainty of reservoir prediction in the subsurface of this type of reservoirs. The analogue study consists of four parts:

- The sedimentology of the Puig-reig anticline has been studied based on the petrographic observations and the logging of cross-sections in field campaigns to reveal the reservoir distribution across the anticline.
- The fracture network in the Puig-reig anticline has been studied using the linear scanline method to reveal the fracture distribution and the related controlling factors. This study also aims to provide an outcrop analogue for the prediction of fractured clastic reservoirs in the subsurface, especially in the research context that fracturing in siliciclastic thrust belts is much less well documented than that in carbonate ones.
- The calcite cementation in the Puig-reig anticline has been studied based on petrographic and geochemical analyses. This study aims to build the cementation history and fluid evolution across the whole anticline and during the complete fold evolution. Furthermore, the comparison between the Puig-reig anticline and other studies worldwide aims to explore the distribution of calcite cement in different settings.
- The reservoir potential of the Puig-reig anticline has been studied based on the comprehensive analysis of sedimentology, fracture network and cement cementation. This work aims to evaluate the reservoir potential of folded fluvial settings at foreland basin margins and the related controlling factors.

1.5 Publications derived from this thesis

A total of five scientific articles have resulted from the work conducted during this thesis. Four of these articles have been published or are in different stages of review or revision in international peer-reviewed science citation index (SCI) journals with high impact at the time of submission of this thesis, and the fifth one is in preparation. These articles (Appendix 1 to 5), as well as other conference publications (Appendix 6), are included in the Appendix section of this thesis.

Article 1 (Appendix 1) includes the global-scale assessment of CCS development potential in compressional basins using an integrated source-to-sink assessment methodology:

[1] Sun, X., Alcalde, J., Gomez-Rivas, E., Struth, L., Johnson, G., Travé, A., 2020. Appraisal of CO_2 storage potential in compressional hydrocarbon-bearing basins: Global assessment and case study in the Sichuan Basin (China). Geoscience Frontiers, 11, 2309-2321. doi.org/10.1016/j.gsf.2020.02.008. IF: 6.853 (2020); Q1 (Geosciences, Multidisciplinary – 9/188).

Article 2 (Appendix 2) includes the national-scale assessment of CCS development potential in hydrocarbon-limited regions using a new source-to-sink assessment methodology based on a hubs and clusters strategy:

[2] Sun, X., Alcalde, J., Bakhtbidar, M., Elío, J., Vilarrasa, V., Canal, J., Ballesteros, J., Heinemann, N., Haszeldine, S., Cavanagh, A., Vega-Maza, D., Rubiera, F., Martínez-Orio, R., Johnson, G., Carbonell, R., Marzan, I., Travé, A., Gomez-Rivas, E., 2021. Hubs and clusters approach to unlock the development of Carbon Capture and Storage – case study in Spain. Applied Energy, in press. IF: 9.746 (2020); Q1 (Energy & Fuels – 9/144).

Articles 3, 4, 5 consist of the reservoir-scale study of storage potential for CO_2 storage at foreland basin margins, focusing on the Puig-reig anticline (SE Pyrenees), including the study of sedimentology and reservoir potential in Article 3 (Appendix 3), the study of fracture network in Article 4 (Appendix 4), and the study of cementation and fluid in Article 5 (Appendix 5):

[3] Sun, X., Alcalde, J., Gomez-Rivas, Owen, A., Griera, A., Martín-Martín, J.D., Cruset, D., Travé, A., 2021. Fluvial sedimentation and its reservoir potential at foreland basin margins: A case study of the Puig-reig anticline (South-eastern Pyrenees). Sedimentary Geology, in review.

IF: 3.397 (2020); Q1 (Geology – 7/48).

[4] Sun, X., Gomez-Rivas, E., Alcalde, J., Martín-Martín, J.D., Ma, C., Muñoz-López, D., Cruset, D., Cantarero, I., Griera, A., Travé, A., 2021. Fracture distribution in a folded fluvial succession: the Puig-reig anticline (South-eastern Pyrenees). Marine and Petroleum Geology, 132, 105169. doi.org/10.1016/j.marpetgeo.2021.105169. IF: 4.348 (2020); Q1 (Geosciences, Multidisciplinary – 35/199).

[5] Sun, X., Gomez-Rivas, E., Cruset, D., Alcalde, J., Muñoz-López, D., Cantarero, I., Martín-Martín, J.D., Travé, A., 2021. Fluid evolution and calcite cementation in a folded fluvial succession at an active basin margin: the Puig-reig anticline example (SE Pyrenees). In preparation for submission to Sedimentology. IF: 4.155 (2020); Q1 (Geology – 4/48).

2 Methodology

2.1 Source-to-sink assessment methodology for CCS potential in compressional basins

To appraise the potential of CCS development in compressional basins, we present an integrated source-to-sink assessment methodology that combines comprehensive and open-access information on basin distribution, hydrocarbon resources and CO_2 emissions based on geographical information systems (GIS).

The main input data used in this global-scale assessment were obtained from three different sources. (1) Based on the CGG Robertson Sedimentary Basins compilation (Robertson, 2014), we divided global hydrocarbon-bearing basins into five major tectonic settings: foreland basins, passive margin basins, intracratonic basins, rift and post-rift basins, and other basins (Fig. 1A). (2) From the National Petroleum Assessment and the World Petroleum Assessment of the United State Geological Survey (USGS) (USGS, 1995, 2000; Bird et al., 2008), we obtained global basin shapes and values for conventional hydrocarbon resources of more than 200 basins (Fig. 1B). (3) From the version v4.3.2 of the Emissions Database for Global Atmospheric Research (EDGAR) (EDGAR, 2018; Janssens-Maenhout et al., 2019), we extracted the stationary CO_2 emissions of each basin in 2012 (Fig. 1C).

Using a GIS-based software (QGIS Development Team, 2018), we input the basin polygon shapes and geo-referenced the hydrocarbon resources and CO_2 emissions. For the storage potential appraisal, we assume that compressional regions with high potential for developing CCS must encompass sufficient hydrocarbon resources (V_H) as a proxy for storage space, and CO_2 emissions (V_{CO_2}) as CO_2 source. We combined these two elements by creating an integrated evaluation parameter ($V_{CCS\text{-}P}$) that equals the product of normalised V_H and V_{CO_2}. Hydrocarbon resources are not quantitatively equivalent to storable CO_2 emissions, which involve different geological requirements (Goodman et al., 2011), but it is an accurate enough proxy to quantify and rank CO_2 storage potential of these hydrocarbon-bearing basins.

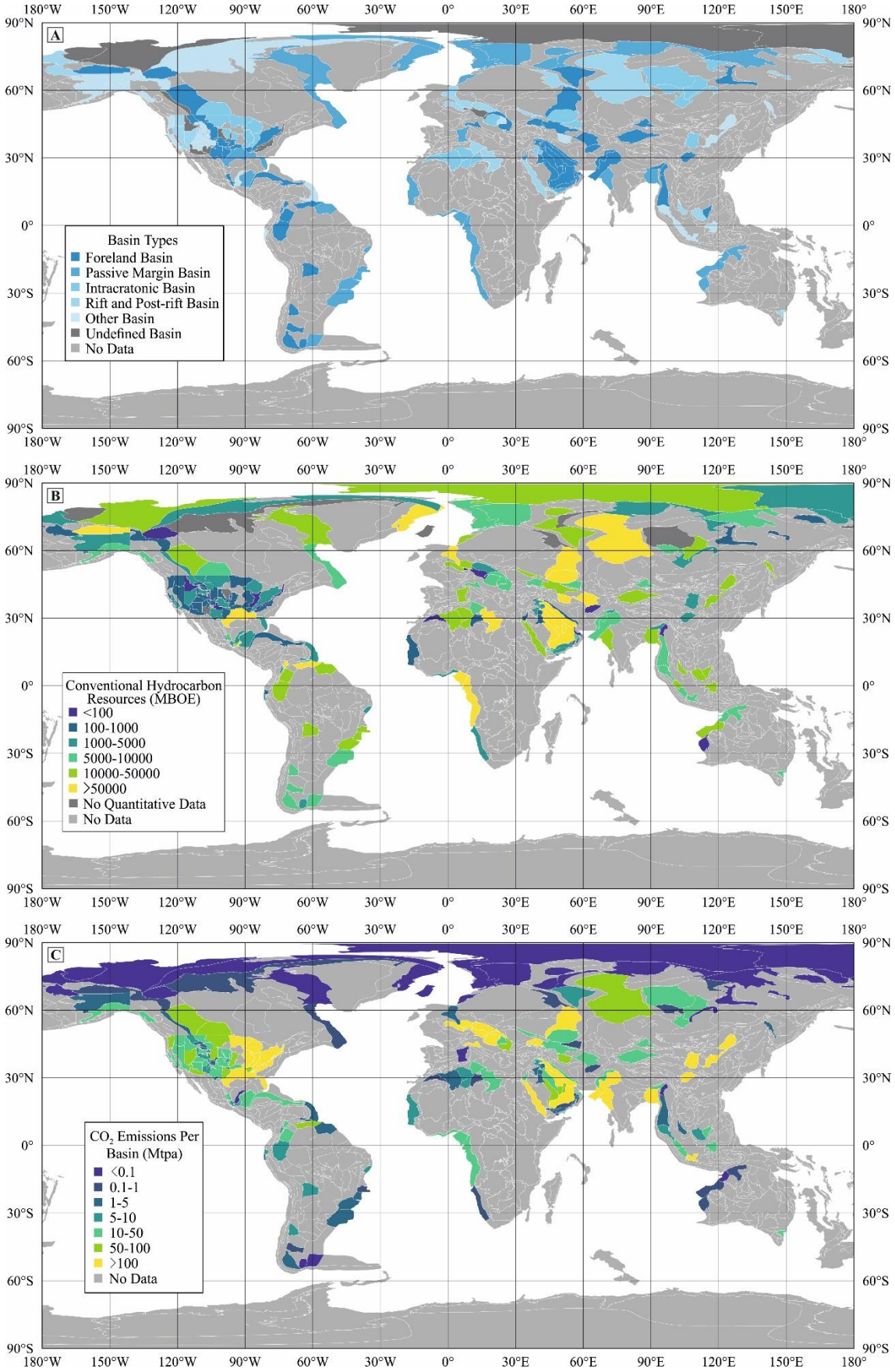
A
Basin Types
Foreland Basin
Passive Margin Basin
Intracratonic Basin
Rift and Post-rift Basin
Other Basin
Undefined Basin
No Data
B
Conventional Hydrocarbon Resources (MBOE)
<100
100-1000
1000-5000
5000-10000
10000-50000
>50000
No Quantitative Data
No Data
C
CO2 Emissions Per Basin (Mtpa)
<0.1
0.1-1
1-5
5-10
10-50
50-100
>100
No Data
180°W 150°W 120°W 90°W 60°W 30°W 0° 30°E 60°E 90°E 120°E 150°E 180°
90°N 60°N 30°N 0° 30°S 60°S 90°S

Figure 1. (A) Tectonic settings of main hydrocarbon-bearing basins (Robertson, 2014). (B) Distribution of major conventional hydrocarbon resources (given in million barrel of oil equivalent (MBOE)): basins in the United States (USGS, 1995), the Arctic Circle (Bird et al., 2008), and other regions (USGS, 2000). (C) Distribution of potential CO_2 emission sources (in Mtpa) within the main hydrocarbon-bearing basins.

2.2 Source-to-sink assessment methodology for CCS potential in hydrocarbon-limited regions

Instead of developing CCS via CO_2-EOR, hydrocarbon-limited regions need to devise alternative strategies if they intend to implement CCS in their decarbonisation strategies. To appraise the potential of CCS development in hydrocarbon-limited regions, we present a novel source-to-sink assessment methodology that not only considers the matching between CO_2 sources and storage resources but also adopts the hubs and clusters strategy. This methodology is derived and adapted from the one used for the site selection in the Acorn project of the UK North Sea (Alcalde et al., 2019). The workflow created and used in this study is summarized in Fig. 2 and comprises three main steps. First, we define the potential CO_2 emission hubs as CO_2 sources for CCS development and the potential CO_2 storage sites available. Emission hubs are divided into different sectors based on the industrial types of emissions because they can play different roles in different stages of CCS development. Subsequently, a preliminary screening process is to select potential storage sites for each emission hub, based on basic screening criteria, such as storage capacity and distance to the emission hub. A scoring process is to grade the suitability of each potential storage site, involving storage capacity, reservoir-caprock suitability, development cost, data availability, etc. Finally, the scored sites are ranked to select priority source-to-sink clusters using a Multi-Criteria Decision Making (MCDM) process that allows selection considering multiple factors at the same time.

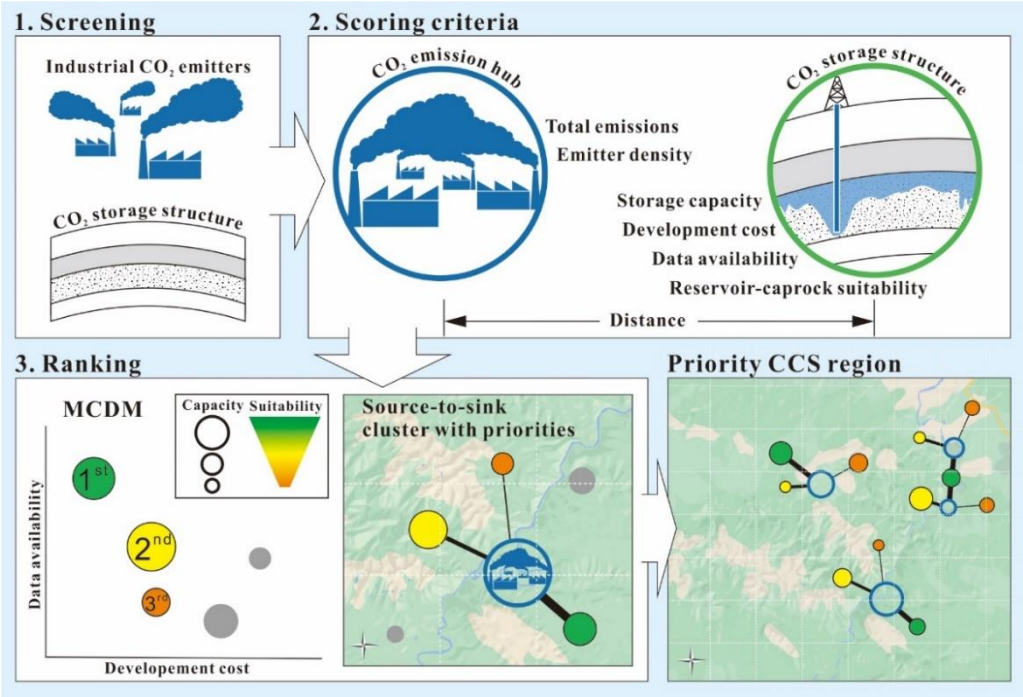

Figure 2. Workflow of the source-to-sink assessment based on a hubs and clusters strategy: Step 1, screening of the potential CO_2 sources and storage structures; Step 2, scoring criteria of potential emission hubs and storage structures; Step 3, the MCDM scheme for ranking source-to-sink cluster priorities. The ultimate goal is to identify favourable regions to deploy CCS most efficiently.

We apply this methodology in a case study in Spain to identify the priority CCS development regions in this country. Spain's industrial facilities with CO_2 emissions higher than 0.1 Mtpa are selected as CO_2 sources for CCS development (Fig. 3A). CO_2 emission hubs include CO_2 sources within a circular area with a diameter smaller than 60 km and annual CO_2 emissions higher than 2 Mtpa, trying to minimise the number of hubs and maximise the CO_2 emissions per hub without making hubs too large. Emission hubs are divided into two types of industrial sectors because CCS can play different roles at different stages of decarbonisation plans: the more immediate power sector (*i.e.*, CCS to decarbonise the power system) and the more sustained hard-to-abate sector (*i.e.*, CCS to decarbonise other industrial systems). The emissions of the so-called Hard-to-abate sector encompass those coming from basic industries, such as steel, cement, chemicals, plastic, paper, etc. (Rumayor et al., 2020).

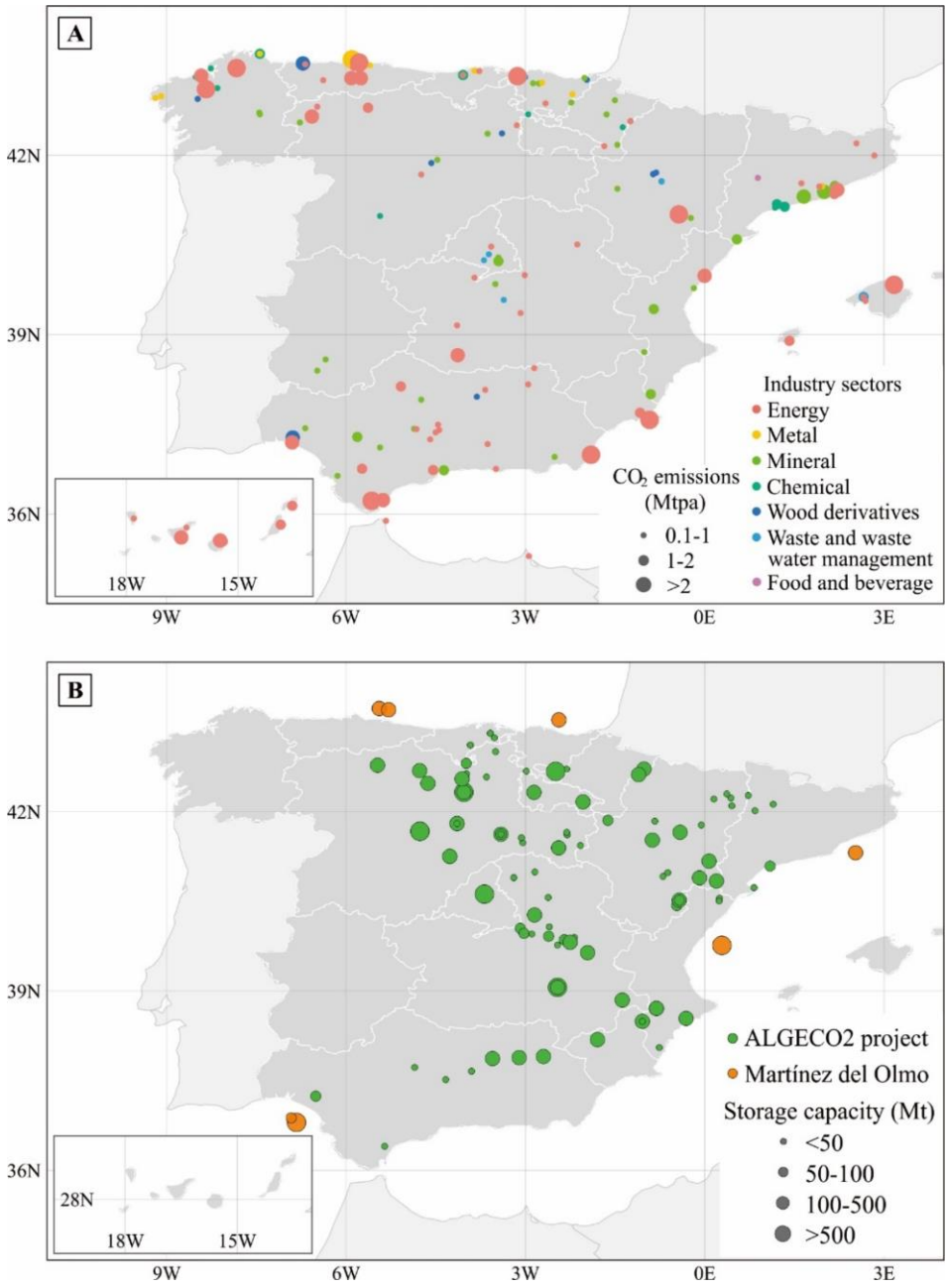

Figure 3. (A) Large industrial sources of CO_2 emissions (≥ 0.1 Mtpa) by industrial sectors in Spain in 2018. Data source: Basque Government (2019); MITECO (2020a). (B) CO_2 storage structures in Spain from the ALGECO2 project (Instituto Geológico y Minero de España, 2010b) and Martínez del Olmo (2019).

For each emission hub a preliminary screening process is applied to all storage structures (Fig. 3B; 103 onshore saline aquifers from the ALGECO2 project (Instituto Geológico y Minero de España, 2010b) and 7 offshore saline aquifers from Martínez del Olmo (2019)). This screening process determines whether storage structures are taken forward to the following assessment steps or disqualified, and is based on two criteria: theoretical storage capacity and source-to-sink

distance. In the following step, for each emission hub the filtered potential structures are scored based on four ranking criteria, including theoretical storage capacity, the suitability of reservoir-caprock systems, development cost, and the availability of seismic and well data for their assessment. After quantifying the four ranking criteria, the Technique for Order of Preference by Similarity to Ideal Solution (TOPSIS) method (Yoon and Hwang, 1995) is used to rank potential storage structures for each emission hub based on different weighting scenarios (geological, economic, and comprehensive scenarios), and finally to select the priority source-to-sink clusters.

2.3 Methods for reservoir-scale case study of the Puig-reig anticline

The Puig-reig anticline is used as an outcrop analogue for the evaluation of the reservoir potential of similar sedimentary systems at foreland basin margins. The analogue study combines the comprehensive analysis of sedimentology, fracture network and diagenesis of the Puig-reig anticline based on field and laboratory data.

2.3.1 Outcrops and samples

The Puig-reig anticline is located at the north-eastern margin of the Ebro Foreland Basin and adjacent to the South Pyrenean fold-and-thrust belt (Fig. 4A, B, C). This anticline presents excellent outcrops along roads that cut through the structure in a roughly north-south direction, between the towns of Sant Llorenç de Morunys in the north and Solsona in the south (Fig. 4B, D). To reveal the sedimentary characteristics and the distribution of lithofacies across the anticline, seven high-resolution (decimetre-scale) stratigraphic logs with a total thickness of about 3,000 m were built from seven cross-sections (Fig. 4D). The detailed sedimentary data acquired include bedding thickness, grain size, sedimentary structures and presence of bioturbation.

In this study, the Puig-reig anticline was divided into five structural positions from north to south, namely north limb, crest-north limb transition zone, crest, crest-south limb transition zone and south limb (Fig. 4E). Outcrops were selected for the systematic collection of fracture attributes in the field, representing different structural positions of the anticline and different lithofacies. Samples of host rocks and fracture-filling veins, representing different structural positions and lithofacies, were selected for petrographic and geochemical analyses in laboratories.

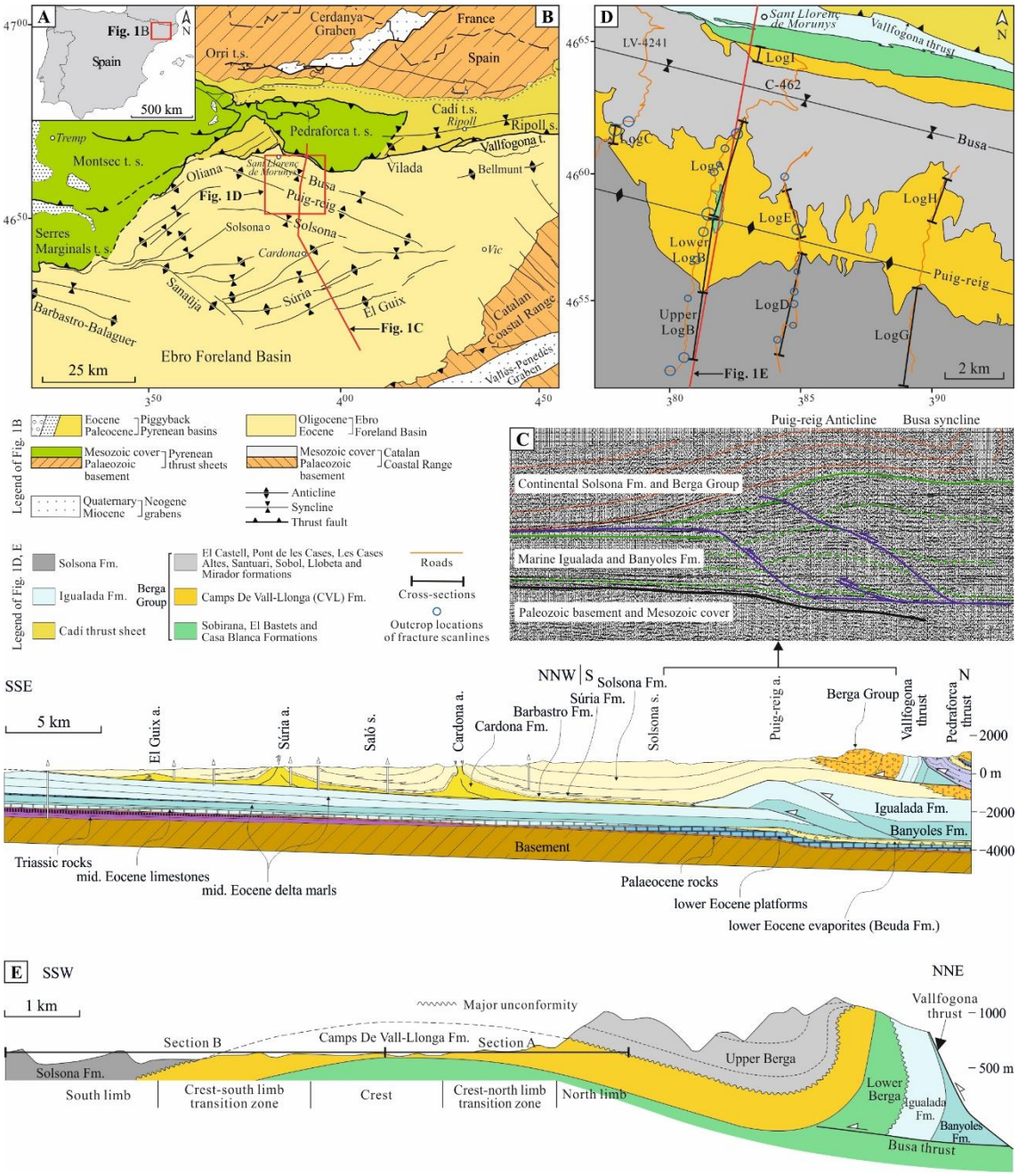

Figure 4. (A-B) Geographical location and main structural units of the SE Pyrenees (Vergés, 1993). (C) Cross-section of the frontal part of the SE Pyrenean fold-and-thrust belt and the Ebro Basin (Vergés, 1993). The seismic profile (Line S-2) is from the Spanish Geophysical Information System (SIGEOF) (Instituto Geológico y Minero de España, 1977). (D-E) Distribution of the Berga Group and the Solsona Formation and location of outcrops. The strata distribution is based on the regional geological map of Catalonia (Institut Cartogràfic i Geològic de Catalunya, 2006) and on Williams et al. (1998) and Barrier et al. (2010). The formation subdivision of the Berga Group follows the scheme of Williams et al. (1998).

2.3.2 Method for collecting fracture attributes

The linear scanline method was adopted in this study to collect fracture data because of the nearly vertical outcrops present in the Puig-reig anticline, which prevented the use of other fracture sampling methods. The linear scanline method has been widely used and discussed in the literature (Zeeb et al., 2013; Watkins et al., 2015a and references thereof). This method is a fast technique for recording a wide range of fracture attributes, including fracture orientation, length, spacing, intensity, aperture, and fracture filling. The fracture data was acquired in groups of at least two people, with the aim of reducing subjective acquisition biases (Andrews et al., 2019). We acquired data from 53 scanlines that add up to around 1,600 m in total scanline length, along the three western-most roads (Fig. 4D). Around 1,800 fractures with lengths greater than 20 cm intersecting the scanlines were measured. In this study, we did not include large faults with high offsets and obvious fault zones.

2.3.3 Petrography of host rocks and cements

To determine rock composition, porosity and diagenesis, 108 polished thin sections from host rocks and calcite veins were made from collected samples. Petrographic observations were taken using a Zeiss Axiophot optical microscope and a Technosyn Cold Cathodoluminescence microscope, model 8200 Mk5-1 operating 16 to 17 kV and 270 to 290 μA gun current. Among these, 30 sandstone thin sections were selected for rock composition analysis using the point-counting method (300-400 points) to reveal the compositional variations in different sedimentary lithofacies. Besides, 60 thin sections were analysed using NIS Elements and Image J software (Schneider et al., 2012) to quantitatively process microphotographs to determine cement contents and porosity. Based on the colour differences between different components, porosity was determined using microphotographs in parallel nicols, while cement contents were determined using microphotographs in cathodoluminescence.

2.3.4 Geochemistry of host rocks and cements

To determine the origin of cements and the evolution of fluid regime, samples of host rocks, intergranular porosity-filling cements and fracture-filling veins were selected for geochemical analyses. A total of 27 samples were selected for carbon- and oxygen-isotope analysis for different

generations of calcite cements using a 500 μm-diameter dental drill. 50-70 μg of calcite powders were reacted with 100% phosphoric acid for five minutes at 70°C. The resultant CO_2 was analysed using an automated Kiel Carbonate Device coupled to an isotope ratio mass spectrometer Thermo Finnigan MAT-252 following a modified McCrea's method (1950). The results were calibrated with secondary standards (RC-1 and CECC), traceable to NBS-18 and NBS-19 international standards. The standard deviation is ±0.01‰ for $\delta^{13}C$ and ±0.03‰ for $\delta^{18}O$ with respect to the VPDB standard (Vienna Pee Dee Belemnite).

Clumped isotope thermometry was applied to four samples of calcite cements to calculate the temperatures and $\delta^{18}O$ values of the fluids from which these calcite cements precipitated. Measurements were carried out in the Qatar Stable Isotope Laboratory at Imperial College London using a fully automated system, Imperial Batch Extraction (IBEX), and following the method of Adlan et al. (2020). Around 4 mg aliquots of calcite powders for each sample were individually dropped into 105% phosphoric acid at 90 °C and reacted for 10 min on an automated IBEX device. The resultant CO_2 was separated with a Porapak-Q trap and transferred into the bellows of a Thermo MAT 253 isotope ratio mass spectrometer (Thermo Instrument, Bremen, Germany). The characterisation of a replicate consisted of 8 acquisitions in dual inlet mode with 7 cycles per acquisition. The post-acquisition processing was completed using the free software Easotope (John and Bowen, 2016). We used the new Intercarb (I-CDES) approach to correcting our clumped isotope samples (Bernasconi et al., 2021) which relies on normalisation using 4 carbonate standards: ETH1 (0.205 ± 0016‰), ETH2 (0.209 ± 0.0015‰), ETH3 (0.613 ± 0.0014‰) and ETH4 (0.451 ± 0.0018‰). Values in the I-CDES are reported without acid correction factor at 90˚C. The raw Δ_{47} data were corrected for non-linearity using the pressure baseline correction (Bernasconi et al., 2013). Samples were measured three times (three replicate) and the average results were converted to temperatures using the interlaboratory calibration of Anderson et al. (2021). The calibration includes data from the Qatar Stable Isotope Laboratory, extends from 0-350˚C, and is measured using the new I-CDES scale: it is thus an ideal calibration for our study. Carbonate $\delta^{18}O$ values were corrected with the acid fractionation factors of Kim et al. (2015). The $\delta^{18}O_{fluid}$ was calculated using the equation of Kim et al. (2007) with the clumped

isotope temperatures and the carbonate $\delta^{18}O$ values, and are expressed in ‰ with respect to the Vienna Standard Mean Ocean Water (VSMOW).

Strontium isotopes ($^{87}Sr/^{86}Sr$) were measured for four samples of calcite cements. 10 to 20 mg of calcite powders for each sample were rinsed in ultrasonic MilliQ water to remove detrital contaminants. Each sample was treated individually to ensure that sufficient rinsing steps were applied. Cleaned fragments were dissolved in dilute nitric acid, and the resulting solution was centrifuged at medium speed for 20 minutes, and the supernatant was transferred to clean PFA beakers. Sr was separated from matrix and Rb using an extraction resin type Eichrom Sr-Spec in the ultra-clean laboratory LIRA (UB). Sr isotope ratios were determined by multicollector inductively coupled mass spectrometry on a Nu Instruments (Wrexham, UK) Plasma 3 MC-ICPMS at the University of Barcelona (CCiT-UB). $^{87}Sr/^{86}Sr$ ratios were normalized for instrumental mass bias with respect to the reference value of $^{86}Sr/^{88}Sr = 0.1194$. Instrumental drift was corrected by sample-standard bracketing (SSB) using NBS987 = 0.710230 as the primary standard with matching standard and sample Sr concentrations. External analytical reproducibility during the session is $^{87}Sr/^{86}Sr = 0.710339 \pm 0.000012$ (2σ, n=14).

Nine carbon-coated polished thin sections were selected to analyse major, minor and trace element concentrations on a CAMECA SX-50 electron microprobe. The microprobe was operated using 20 kV of excitation potential, 6 nA of current intensity and a beam diameter of 10 μm. In total, more than 400 probe points were selected, covering all generations of calcite cements recognized by petrographic observations. Detection limits are 107 ppm for Ca, 112 ppm for Mg, 119 ppm for Mn, 254 ppm for Sr, 77 ppm for Fe and 139 ppm for Na. Precision on major element analyses average 1.03% standard error at 3σ confidence levels.

3 Results

3.1 Global-scale source-to-sink assessment of CCS potential in compressional basins

The source-to-sink assessment methodology presented in Section 2.1 allows the exploration of the CCS potential in compressional hydrocarbon-bearing basins.

The hydrocarbon industry has abundant oil and gas resources stored in compressional basins, indicating their significant potential for CCS. Over 40% of hydrocarbon-bearing basins by area are located in foreland basins, which are mainly concentrated in North America, West South America, East Europe, West Middle East, Central Asia and China. Around 50% of global conventional hydrocarbon resources are hosted by compressional basins, which are mainly concentrated in the Middle East, North America, East Europe, Central Asia and China. Compressional basins contain significant CO_2 emission sources, with 3.8 Gt of annual emissions accounting for 34% of all hydrocarbon-bearing basins, mainly concentrating in North America, the Middle East, Europe and China.

Based on the distribution of the integrated evaluation parameter $V_{CCS\text{-}P}$, we have selected five high-priority regions for CCS development in compressional basins: North America, North-Western South America, South-Eastern Europe, Western Middle East, and Western China (Fig. 5A). These regions feature high hydrocarbon resources and CO_2 emissions and thus favourable source and sink matching. Besides, they are relatively isolated from other basin types for prospective CCS storage. Of the five high-priority regions, North America, Europe and China have explicit high-emission reduction targets in place (Fig. 5B), and therefore they are more likely to implement decarbonisation actions, like CCS.

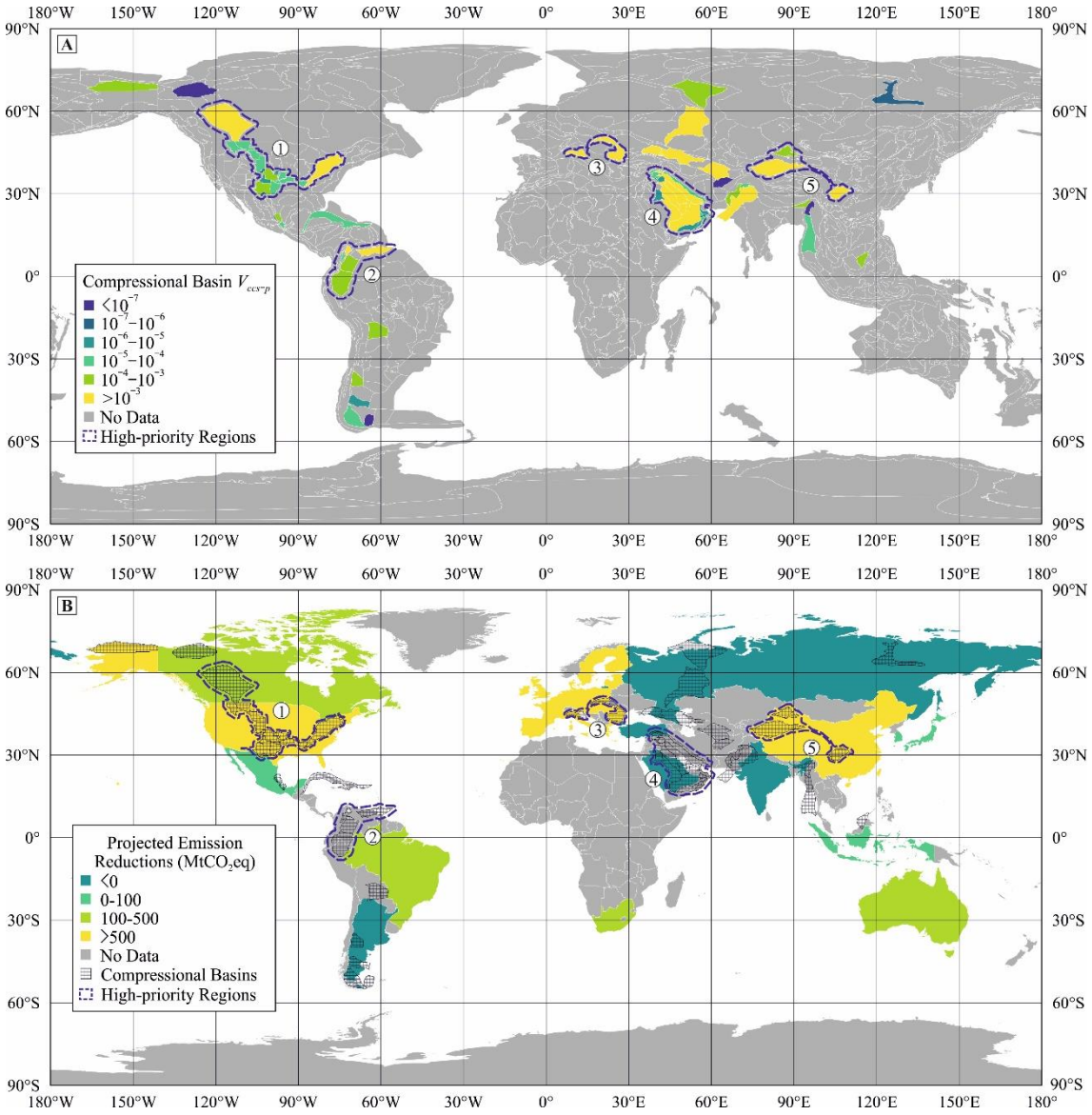

Figure 5. Five high-priority regions for CCS development in compressional basins: (1) North America; (2) North-Western South America; (3) South-Eastern Europe; (4) Western Middle East; (5) Western China. (A) Distribution of the integrated evaluation parameter ($V_{CCS\text{-}P}$) in compressional hydrocarbon-bearing basins. (B) The projected emission reductions of G20 economies (given in million tonnes of carbon dioxide equivalent ($MtCO_2eq$)) (data source den Elzen et al., 2016).

3.2 National-scale source-to-sink assessment of CCS potential in hydrocarbon-limited regions: A case study of Spain

The source-to-sink assessment methodology based on a hubs and clusters strategy presented in Section 2.2 allows the exploration of the CCS potential in spain, a hydrocarbon-limited country.

In 2018, there are 183 industrial facilities with CO_2 emissions larger than 0.1 Mtpa in Spain (Fig. 3A). These large CO_2 emitters release a total of 110.5 Mtpa (41% of Spain's total emissions), with 83 CO_2 emitters in the power industry accounting for 71.3 Mtpa, while 100 CO_2 emitters in other industries accounting for 39.2 Mtpa. In mainland Spain, 15 CO_2 emission hubs are identified as potential CO_2 sources for CCS development. These emission hubs emit 68.7 Mtpa of CO_2, representing 20.6% of Spain's GHG emissions in 2018. Among these, 11 emission hubs are in the power sector and have total CO_2 emissions of 52.8 Mtpa (Fig. 6A), which mainly come from thermal power plants and oil refineries. The remaining four emission hubs belong to the hard-to-abate sector and have total CO_2 emissions of 15.9 Mtpa (4.8% of Spain's GHG emissions in 2018) (Fig. 6B), which are mainly derived from iron and steel production, cement production and pulp production. The emission hubs are mainly distributed in coastal areas, *e.g.,* Galicia, Asturias, the Basque Country, and Catalonia in northern Spain, and Murcia and Andalusia in southern Spain (Fig. 6).

The priority and alternative storage structures most suitable to emission hubs are identified after the screening and ranking processes, leading to 15 priority source-to-sink clusters and their alternative structures (Fig. 7). Of these, 9 priority structures rather than 15 were selected because some adjacent emission hubs share the same potential storage locations. These priority and alternative structures are mainly distributed in Castilla and Leon, Asturias, and Aragon in northern Spain, and Murcia and Andalusia in southern Spain, with a few offshore storage structures (Fig. 7). Four regions that contain multiple emission hubs and potential storage structures are identified as potential CCS development regions in Spain, *i.e.,* North-Western Spain, North-Eastern Spain, South-Western Spain, South-Eastern Spain. Among these, the North-Western and North-Eastern regions host higher CO_2 emissions and more suitable storage structures dominated by

compressional settings, which deserve further analyses to assess and refine the potential of these structures as reservoirs for CO_2 storage.

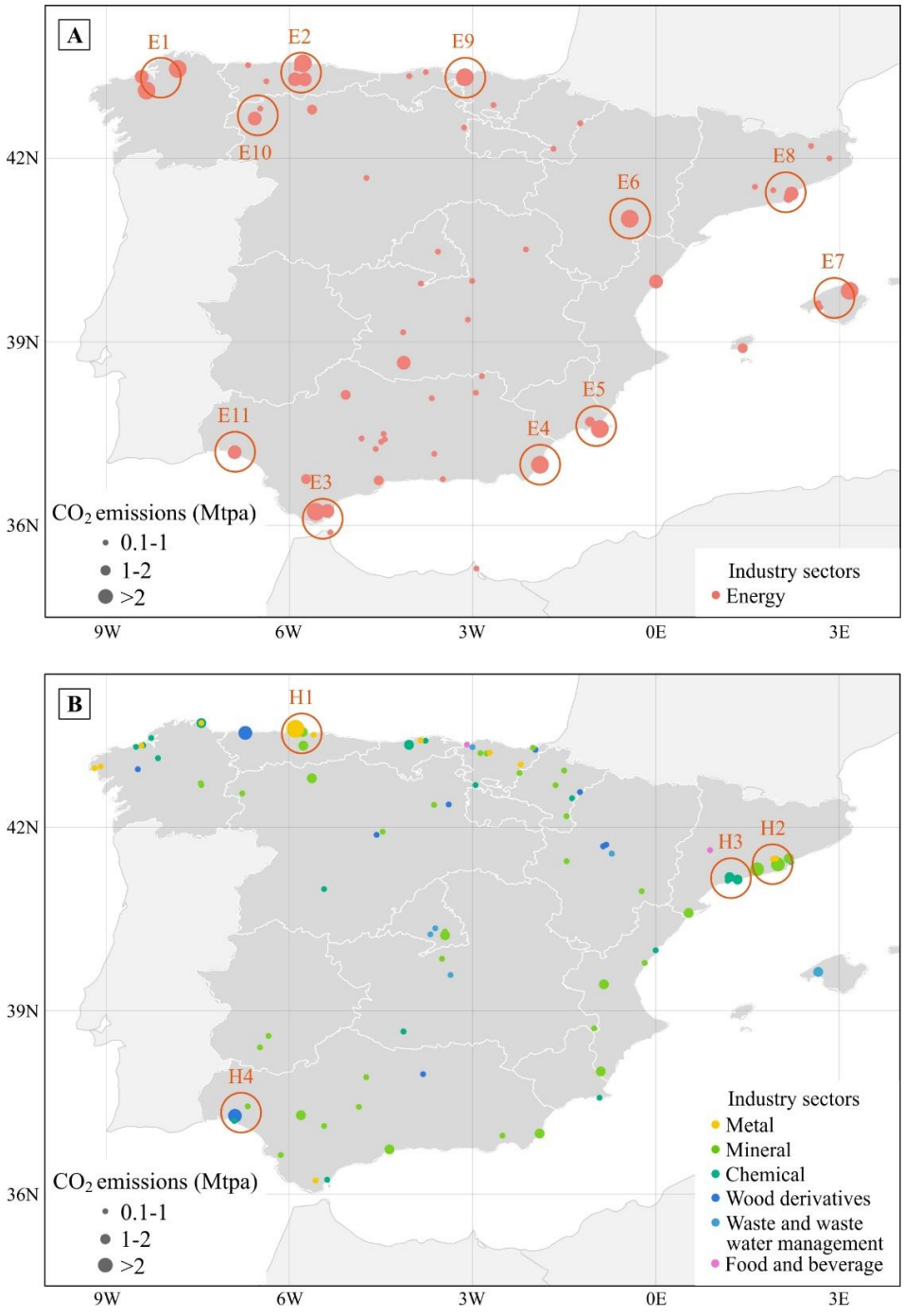

Figure 6. Distribution of identified CO_2 emission hubs: (A) 11 emission hubs in the power sector; (B) four emission hubs in the hard-to-abate sector.

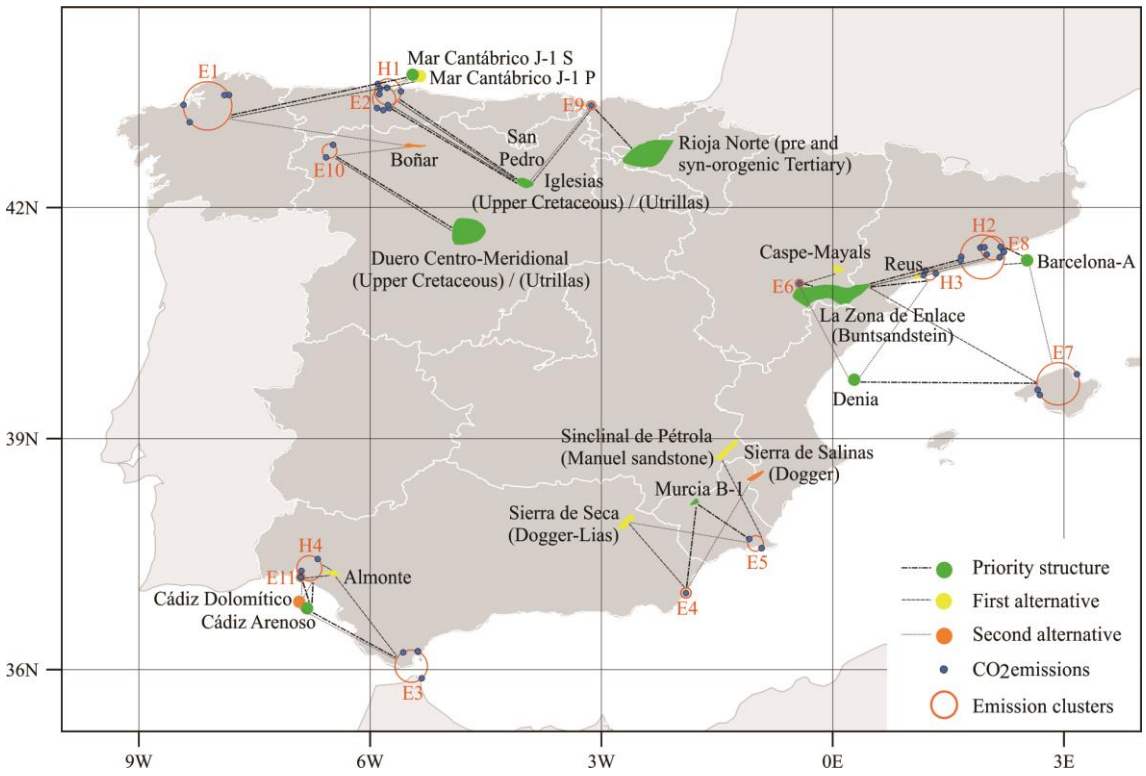

Figure 7. Distribution of 15 priority source-to-sink clusters and their alternative storage structures.

3.3 Reservoir-scale case study of the Puig-reig anticline (SE Pyrenees)

Using the methods presented in Section 2.3, we analyse the sedimentology, fracture network, diagenesis, and reservoir characteristics of the Puig-reig anticline.

3.3.1 Puig-reig anticline

The eastern part of the Ebro Basin displays an irregular shape bounded by the Pyrenees to the north and the Catalan Coastal Range to the southeast (Fig. 4A, B) (Vergés, 1993). The Vallfogona thrust represents the major frontal thrust between the SE Pyrenean thrust sheets and the Ebro Basin. The Busa syncline and the Puig-reig anticline developed along the footwall of the Vallfogona thrust during the Late Eocene and the Oligocene (Vergés, 1993). Based on the available seismic profiles across the Puig-reig anticline (Fig. 4C), the anticline was interpreted to have been formed as a consequence of a duplex stack in depth (Vergés, 1993). In the lower part, the Banyoles and Igualada Formations (Middle to Upper Eocene) mainly consist of marine marls. They were duplicated by thrusting and detached above the Lutetian Beuda gypsums and the Late

Priabonian Cardona salts (Vergés et al., 1992; Serra-Kiel et al., 2003a, 2003b). In the upper part, the Berga Group and the Solsona Formation (Upper Eocene to Oligocene) were deposited during the endorheic stage of the Ebro Basin (Puigdefàbregas et al., 1986, 1992), after a rapid transition from marine to continental environments of deposition at around 36 Ma during the Priabonian (Costa et al., 2010). During the Oligocene, the Vallfogona footwall was folded forming the km-scale, south-verging and gentle Puig-reig anticline. The fold-trend is ESE/WNW, slightly oblique to the main Pyrenean structures (Vergés, 1993).

To the north, at the footwall of the Vallfogona thrust ramp, the Berga Group consists of > 2000 m-thick alluvial and proximal fluvial conglomerates interbedded with minor sandstones and claystones, which display growth strata geometries (Ford et al., 1997; Suppe et al., 1997). To the south, the Berga deposits become progressively finer-grained and thinner bedded and wedge out into the fluvial conglomerates, sandstones and claystones of the Solsona Formation (Williams et al., 1998; Barrier et al., 2010), which evolved downstream to terminal deposits of a distal fluvial system (Sáez et al., 2007). Finally, these fluvial deposits graded into evaporites and calcareous lacustrine strata towards the centre of the Ebro Basin (Sáez, 1987; Del Santo et al., 2000; Sáez et al., 2007). In this study, the formation subdivision of the Berga Group follows the scheme of Williams et al. (1998). We focus on the Camps de Vall-Llonga Formation, a sub-unit of the Berga Group, that covers the northern zone of the Busa syncline and a large area of the Puig-reig anticline, and the Solsona Formation that is mainly observed in the south limb of the anticline (Fig. 4D, E).

3.3.2 Sedimentology

We quantitatively describe and interpret the lithofacies and sedimentary facies of the deposits as well as their distributions over the Puig-reig anticline. Based on lithological characteristics and sedimentary structures, eight lithofacies are identified and are listed in Table 1, including three conglomerate facies, four sandstone facies, and one fine-grained facies. These lithofacies are combined into six lithofacies associations, deposited in three sedimentary environments, *i.e.,* proximal fluvial fan, proximal-medial fluvial fan, and medial-distal fluvial fan (Fig. 8).

Table 1. Subdivision and description of typical lithofacies.

Lithofacies	Description
Gs1	Pebble to boulder, occasional outsize clasts, very poor sorting, clast- to reddish matrix-supported, mainly massive structure and minor rough-stratified structure, unscoured or slightly scoured basal surface, sheet-like geometry
Gs2	Pebble to cobble, poor sorting, clast-supported, grey to reddish sand matrix, mainly massive structure, slightly or deep scoured basal surface, sheet-like geometry
Gch	Pebble to cobble, moderate to poor sorting, clast-supported, massive structure, scoured basal surface, channelised geometry
Smi	Fine to coarse sandstone, mainly massive structure, tabular geometry or sandstone lens, limited burrows
Sm	Mainly medium and coarse sandstone, massive structure, tabular geometry, limited burrows
Sl	Mainly fine to very fine sandstone, mainly parallel bedding structure and minor cross bedding structure, tabular geometry, common burrows
Sch	Medium to coarse sandstone, scattered gravelly clasts or muddy rip-up clasts, massive structure, channelised geometry, limited burrows
F	Claystone to siltstone, tabular geometry, intensive weathering, erosion and pedogenesis, very common trace fossils

Unconfined flash flood deposits with no overbanks (LAp1): LAp1 association is dominated by lithofacies Gs1 with limited Smi interlayers that generally pinch out laterally as sandstone lenses, which combine into large and structureless sheet-like bodies of coarse deposits with unscoured or slightly scoured basal surfaces. This association is dominantly found in the northwest portion of the Puig-reig anticline, *i.e.,* the upper part of log C.

Unconfined flash flood deposits and wide-shallow channel deposits with limited overbanks (LAp2): LAp2 association is composed of lithofacies Gs2, Smi and limited F. Lithofacies Smi and F can occur as stable tabular layers or pinch-out lenses. This association presents large and structureless sheet-like geometries, with slightly or deeply scoured surfaces. This association is dominantly found in the north limb of the anticline, mainly in log C and the upper part of logs A and E.

Channel filling deposits with minor or stable overbanks (LAm1 and LAm2): LAm1 and LAm2 associations are composed of lithofacies Gch, Sm, Sl, and F. An overall fining-upward trend is observed in these two lithofacies associations, from channelised Gch to tabular and interbedded Sm, Sl and F lithofacies. LAm1 association is characterised by channel fill deposits with minor overbank deposits, showing vertical or lateral accretions of conglomerates and sandstones. LAm2 association is composed of channel fill conglomerates and sandstones and

stable overbank fine deposits. These lithofacies associations are distributed across the anticline except for the south limb of the anticline.

Sandy channel filling deposits with stable overbanks (LAm3): LAm3 association is composed of lithofacies Sch, Sm, Sl and F. Compared to LAm1 and LAm2 associations, LAm3 also presents an overall fining-upward trend and is deposited from braided channel streams and overbanks. However, lithofacies Sch with channelised geometries and scoured basal surfaces replaced Gch conglomerate bodies as channel lag deposits. This association is dominantly found in the south limb and slightly developed in the crest and crest-south limb transition zone of the anticline.

Stable overbanks incised by isolated channels (LAm4): LAm4 association is composed of lithofacies Sch, Sl and F, which is characterised by stable tabular F and Sl deposits incised by channelised Sch bodies. Compared to the LAm3 association, LAm4 also presents channel and overbank deposits, but it contains more overbank fine deposits and isolated channel deposits and does not display a clearly fining-upward trend. This association is occasionally found in the south limb of the anticline.

The characteristics of lithofacies and lithofacies associations in the Puig-reig anticline collectively represent deposits from a proximal to medial fluvial system. The proximal deposits are mainly composed of LAp1 and LAp2 lithofacies associations deposited from unconfined flash floods and wide-shallow channels, with minor LAm1 and LAm2 lithofacies associations. The medial deposits are composed of LAm1 to LAm4 lithofacies associations deposited from braided channel streams and overbanks. The proximal-medial fluvial fan is composed of LAm1, LAm2 and limited LAm3 associations, while the medial-distal fluvial fan is composed of LAm3 and limited LAm2 and LAm4 associations. LAp1 and LAp2 associations decrease significantly from log C to log H (WNW to ESE) and from log A to log B (north to south), which are replaced by LAm1 and LAm2 and finally translated into LAm3 and LAm4 south-eastward (Fig. 9). This is consistent with a fluvial system with an overall south-east downstream trend.

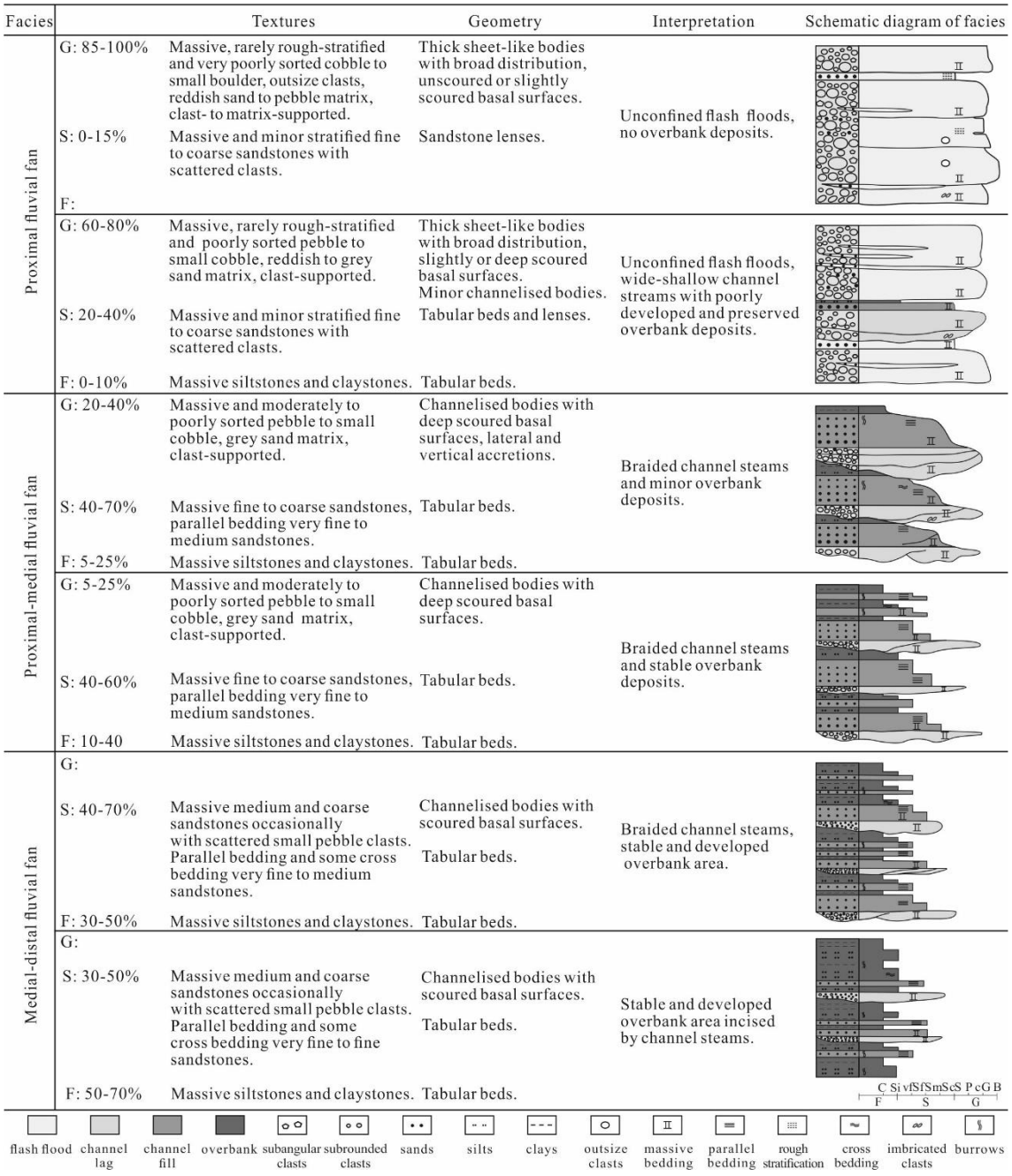

Figure 8. Summary of sedimentary characteristics of typical lithofacies associations in the Puig-reig anticline. G, S and F refer to the percentage contents of conglomerate, sandstone and fine-grained lithofacies, respectively. C: claystone; Si: siltstone; vfS: very fine sandstone; fS: fine sandstone; mS: medium sandstone; cS: coarse sandstone; P: pebble; cG: cobble; B: boulder.

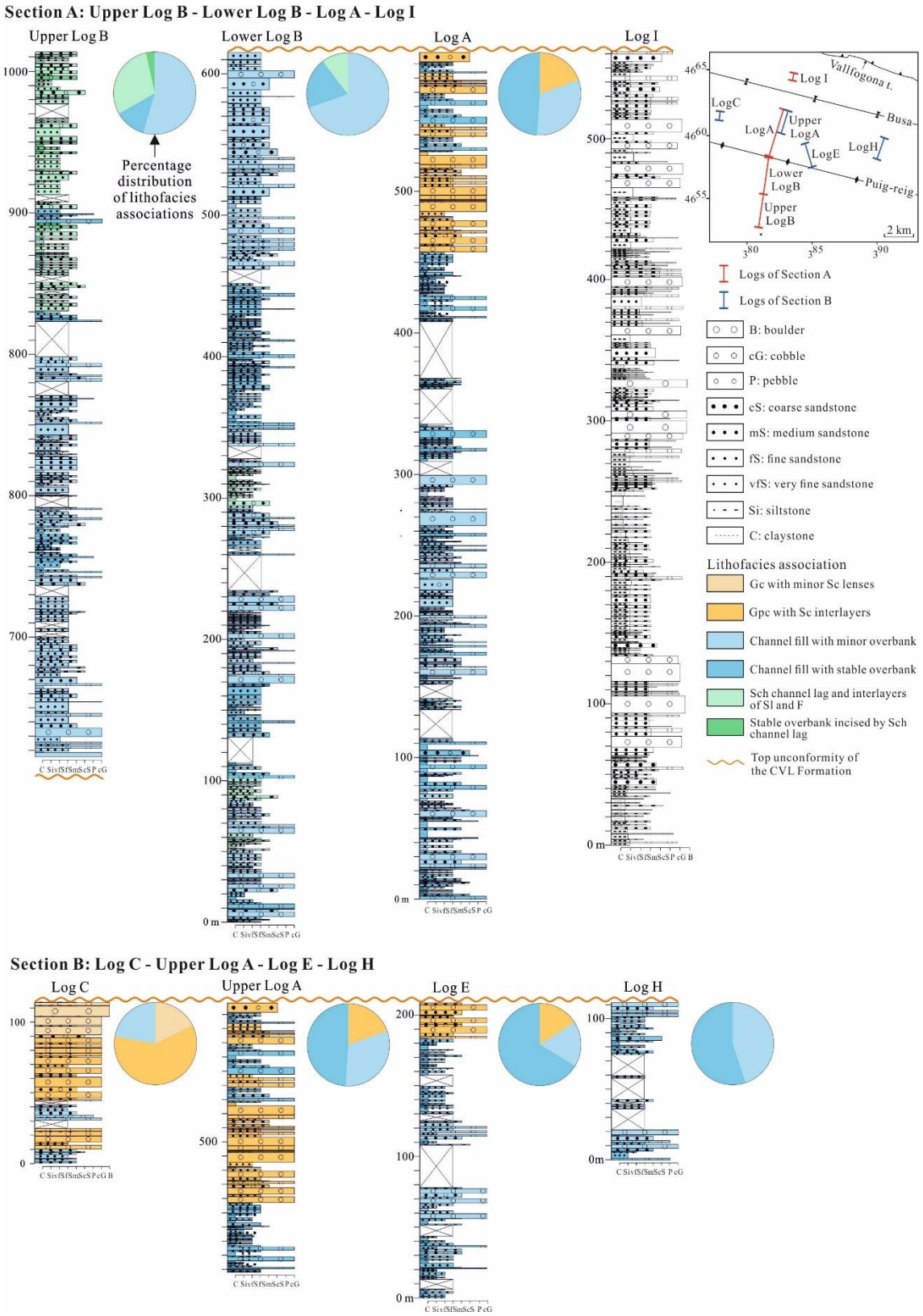

Figure 9. Correlation of stratigraphic logs and percentage distribution of lithofacies associations in the Puig-reig anticline. Log I is from Barrier et al. (2010).

3.3.3 Fracture network

To determine the fracture network and distribution in the Puig-reig anticline, the fracture attributes collected using the linear scanline method are systematically analysed in this section.

3.3.3.1 Fracture orientation

The orientation of the Puig-reig anticline hinge was estimated based on the distribution of bedding attitudes in the anticline crest, which features a strike of 105º. Four fracture sets (F1, F2, F3 and F4) were identified based on fracture orientation and their relationships with the fold hinge. The F1 and F2 sets with NNW-SSE and ENE-WSW orientations, respectively, are the predominant fracture sets observed, accounting for 44% and 28% of the total fractures analysed, respectively. The F3 set is characterised by a WNW-ESE orientation and strikes roughly parallel to the anticline hinge, accounting for 17% of the total fractures. The sampling of fractures from the F4 set, with NNE-SSW orientation, is very limited along the selected scanlines, because they are sub-parallel to the directions of most scanlines. All fractures present high dips, mainly ranging from 70º to 90º (92% of the fractures) and tend to be sub-perpendicular to the bedding surfaces.

3.3.3.2 Fracture spacing and intensity

We consider the apparent fracture spacing as the distance between two adjacent fractures independently of their orientations, which shows variation across the different structural positions (10A). The crest (0.5 m) features the smallest fracture spacing followed by the NTZ (0.6 m) and STZ (0.9 m), while the south and north limbs present lower fracture intensity (1.2 m and 1.5 m, respectively). Fracture spacing also varies significantly in different sedimentary facies and lithofacies (Fig. 11A). The proximal-medial fluvial fan in the NTZ, crest and STZ presents smaller fracture spacing, especially in tabular massive or bedding sandstone layers (0.6 m), while the proximal fluvial fan in the north limb and the medial-distal fluvial fan in the south limb have larger fracture spacing, especially for tabular conglomerate bodies and channelised (pebbly) sandstone bodies (3.0 m and 1.6 m, respectively).

The apparent fracture intensity is the reciprocal of the apparent fracture spacing. There can be an underestimation of the intensity of fracture sets intersecting scanlines at oblique angles (Zeeb et al., 2013a; Watkins et al., 2015b), which can be corrected with respect to the angle formed by

the fracture and the scanline (Terzaghi, 1965). The F4 set is sub-parallel to the directions of most scanlines, resulting in limited fractures intersecting scanlines and very small acute angles between fractures and scanlines. The corrected intensity is too sensitive to the number of fractures and the acute angles, leading to high uncertainty of the results. Thus, we only corrected the fracture intensity of the F1, F2 and F3 sets. The F1 set has high intensity in all structural positions, while the F2 and F3 sets mainly present high intensity in the crest and STZ of the anticline (Fig. 12A). The sum of the true fracture intensity of the three sets results in the highest intensity in the crest (2.38 m^{-1}) followed by the NTZ (1.68 m^{-1}) and STZ (1.56 m^{-1}), while the south limb and north limb correspond to the lowest intensity (1.02 m^{-1} and 0.85 m^{-1}, respectively) (Fig. 12A). Besides, the true fracture intensity varies significantly in different lithofacies (Fig. 12B). The massive or bedded sandstone layers of the proximal-medial fluvial fan in the NTZ, crest and STZ have the highest intensity values, with 2.49 m^{-1} and 1.92 m^{-1} on average, respectively. The tabular conglomerate bodies in the north limb and the channelised (pebbly) sandstone bodies in the south limb show the lowest values, with 0.31 m^{-1} and 0.69 m^{-1} on average, respectively.

3.3.3.3 Fracture length and aperture

Fracture length varies from several decimetres to up to ten meters, but mainly ranges between 0.5 m and 2.5 m (74% of the fractures) (Fig. 10B). Although there is no clear relationship between the fracture length and the structural position in which fractures are located, the north limb presents larger fracture length (1.52 m on average) compared to the other structural positions of the anticline, while the south limb features the smallest fracture length (1.27 m on average) (Fig. 10B). The proximal fluvial fan in the north limb and the medial-distal fluvial fan in the south limb present the largest and smallest fracture length, respectively (Fig. 11B). The fracture length of the proximal-medial fluvial fan in the NTZ, crest and STZ has values in between those of the other two facies (1.39 m on average). Furthermore, channelised conglomerate bodies tend to present longer fractures than sandstone layers (1.52 m and 1.30 m on average, respectively).

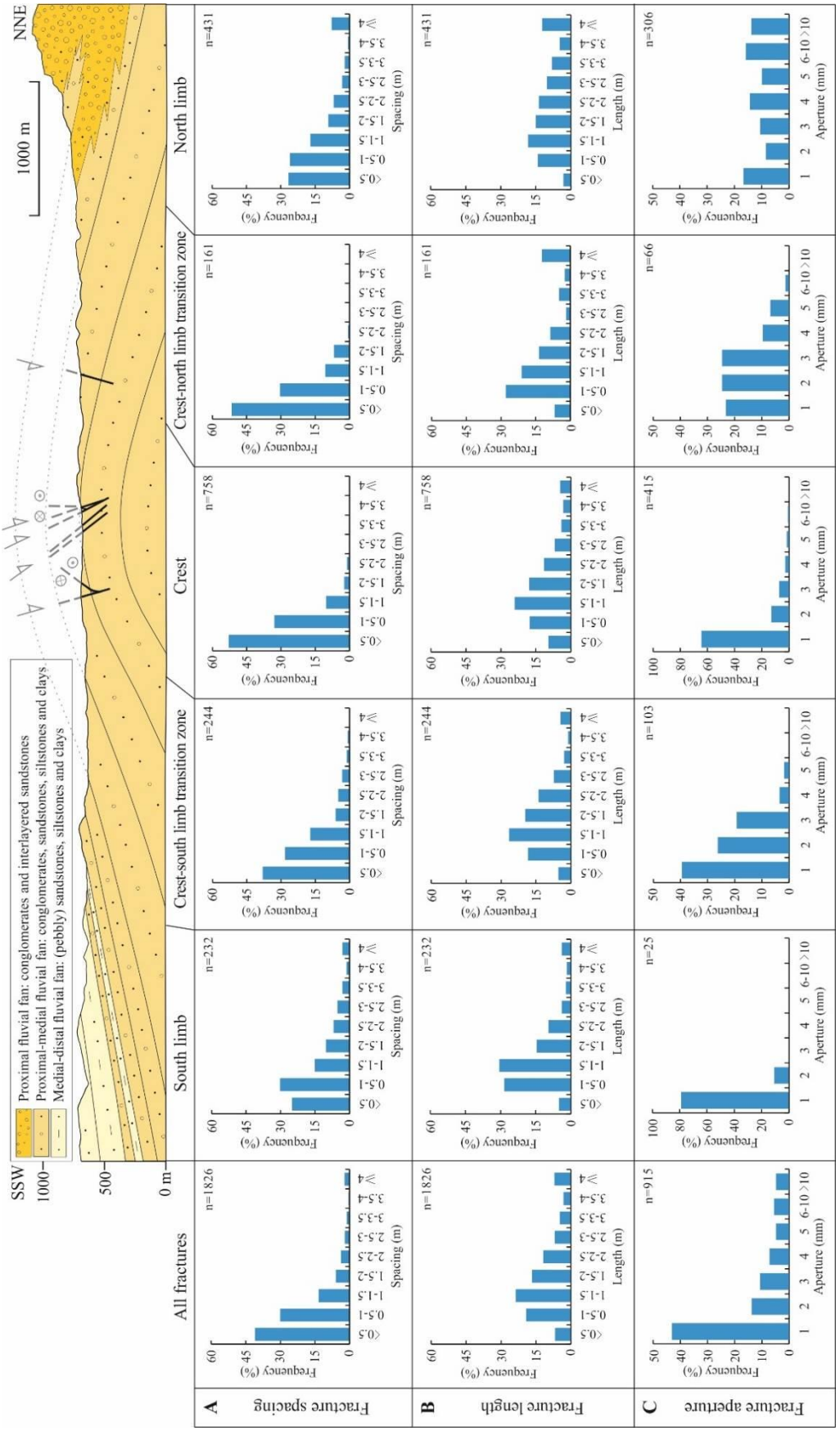

Figure 10. Distribution of (A) fracture spacing, (B) length and (C) aperture in different structural positions. The cross-section of the Puig-reig anticline is modified from Cruset et al. (2016).

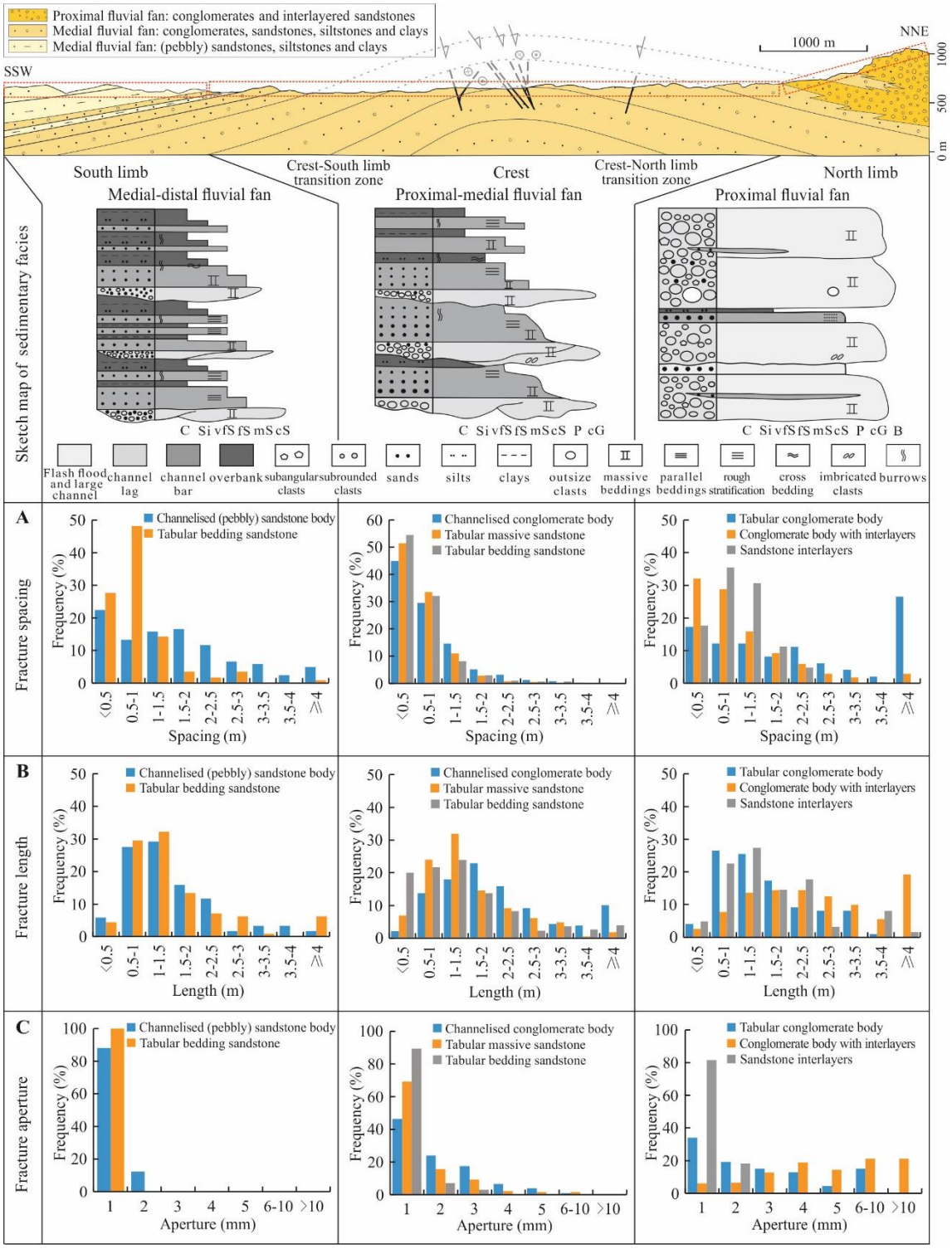

Figure 11. Distribution of fracture (A) spacing, (B) length and (C) aperture for typical lithofacies in different sedimentary facies (proximal to medial fluvial fan). The cross-section of the Puig-reig anticline is modified from Cruset et al. (2016).

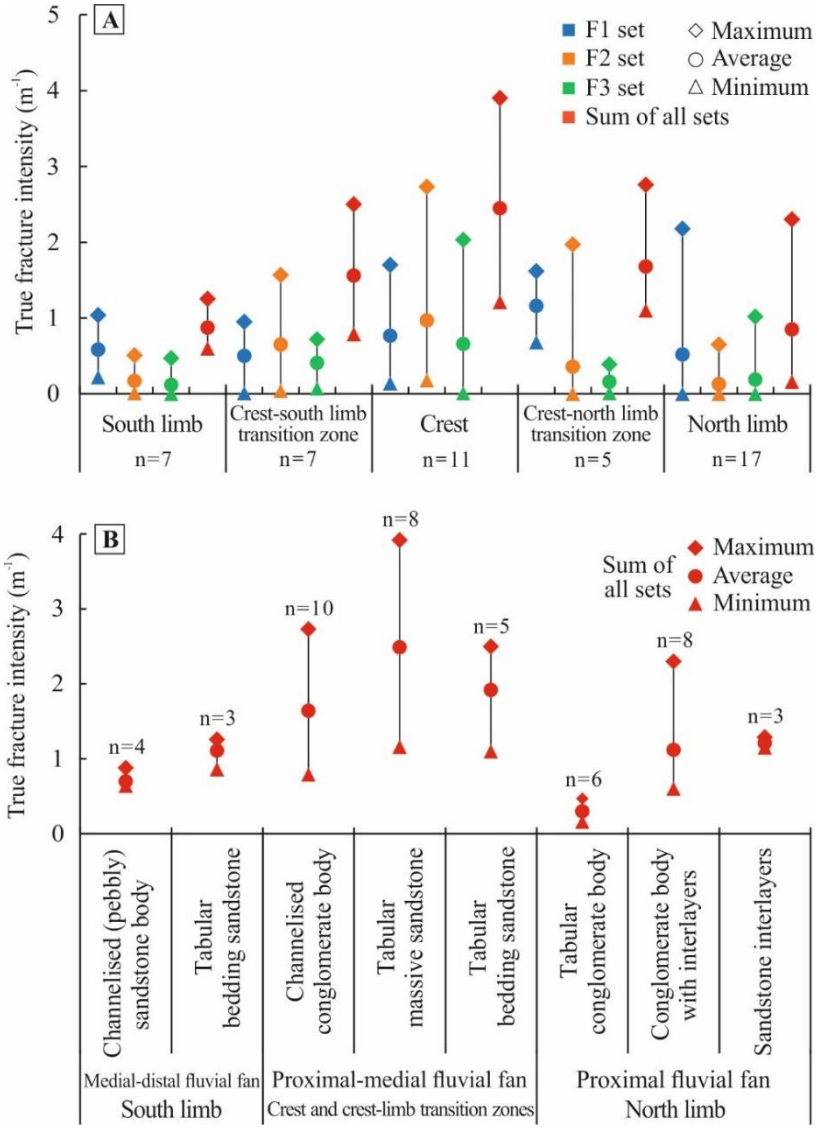

Figure 12. (A) True fracture intensity of the F1, F2, F3 fracture sets in different structural positions (B) True fracture intensity of typical lithofacies of different sedimentary facies (proximal to medial fluvial fan) in different structural positions. ('*n*' is the number of scanlines).

Fracture apertures resulting from stress related to the anticline growth could have potentially been affected by the subsequent stress release during the uplift and exhumation of the anticline. To avoid this uncertainty, in this study we only focus on fractures (now veins) filled with calcite cement precipitated during the anticline growth. Fracture apertures mainly range from 1 to 5 mm and present significant variation across the different structural positions (Fig. 10C). The north limb presents the largest fracture aperture, which mainly ranges between 1 mm and 5 mm but sometimes reaches up to several centimetres. The crest, NTZ and STZ present similar fracture aperture distributions that mainly range from 1 to 3 mm. The south limb has the smallest fracture

aperture with all aperture values below 2 mm. Moreover, fracture aperture also varies significantly across the different sedimentary facies and lithofacies (Fig. 11C). Fractures in the proximal fluvial fan, especially within the conglomerate bodies with interlayered sandstones, present distinctively large apertures, mainly ranging from a few millimetres to a few centimetres. In the crest, NTZ and STZ, channelised conglomerate bodies present wider fractures (1.99 mm on average) than sandstone layers (1.41 mm on average). In the south limb, fracture apertures of the medial-distal fluvial fan rocks are lower than 2 mm.

3.3.4 Calcite cementation

Based on the petrographic and geochemical analyses of calcite cements, we determine the complete history of calcite cementation during the evolution of the Puig-reig anticline.

3.3.4.1 Petrology of calcite cements

Field and microscope observations allow characterizing the distribution and petrographic characteristics of calcite cements (Fig. 13). Five calcite cement generations (Cc0 to Cc4) have been recognized in the Puig-reig anticline. Among these, Cc1 and Cc2 correspond to the two cementation phases identified by Cruset et al. (2016).

Cc0 calcite cement filled a small fraction of the host rock porosity, which can be found in different structural positions across the anticline and in different lithofacies. Cc0 consists of subhedral to euhedral blocky to slightly bladed crystals, with crystal sizes smaller than 0.5 mm (Fig. 13A1). Mechanical twins are rarely observed in this cement. Under cathodoluminescence, Cc0 crystals are non-luminescent with bright orange zonation (Fig. 13A2).

Cc1 calcite cement precipitated in the host rock porosity of all lithofacies and fractures in all structural positions, including reverse and strike-slip faults and F1 to F4 fracture sets (Fig. 13B1). In fractures Cc1 is characterised by subhedral to euhedral blocky to slightly elongated crystals with sizes mainly between 0.1 and 1 mm, and occasionally presents multi-episodic veins bounded by shear planes (Fig. 13B2, B3). This cement shows mechanical twins and homogeneously bright orange luminescence (Fig. 13B3, B4). Cc1 developed after Cc0 because Cc1 fills the residual intergranular pores where Cc0 precipitated along clast edges (Fig. 13A1, A2).

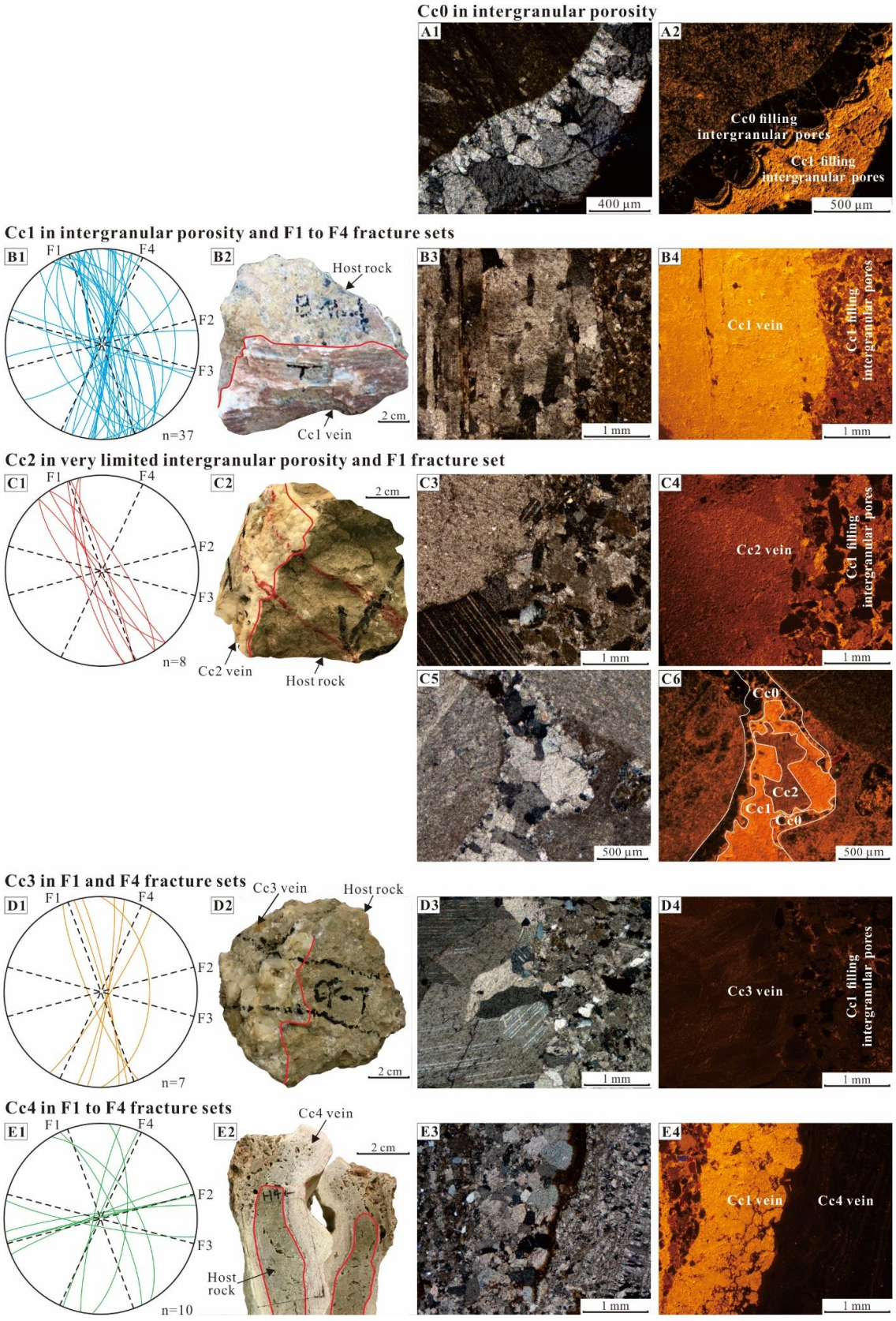

Figure 13. Lower hemisphere Schmidt stereoplots of fractures hosting calcite veins, as well as hand specimens and paired optical and CL microphotographs for different generations of calcite cements. '*n*'

represents the number of samples. (A1-A2) Cc0 calcite cement filled the intergranular porosity of host rocks and presents CL zonation characteristic; (B1-B4) Cc1 filled F1 to F4 fracture sets and intergranular porosity and presents homogeneous bright orange luminescence; (C1-C4) Cc2 veins developed in F1 fracture set and present duller luminescence than Cc1 filling intergranular porosity; (C5-C6) limited Cc2 cement filled residual pores after Cc0 and Cc1; (D1-D4) Cc3 veins precipitated in F1 and F4 fracture sets and present duller luminescence than Cc1 filling intergranular porosity; (E1-E4) Cc4 veins precipitated in F1 to F4 fracture sets and present non non-luminescent characteristic.

Cc2 calcite cement mainly precipitated in normal and strike-slip faults and fractures of the F1 set (Fig. 13C1). This cement concentrates in the anticline crest and occasionally in the NTZ and north limb. Cc2 is formed by euhedral blocky to slightly elongated crystals with sizes generally between 0.2 and 5 mm (Fig. 13C2, C3). Cc2 presents mechanical twins and duller luminescence compared to Cc1 (Fig. 13C3, C4). Cc2 developed after Cc1 because the intergranular porosity of all samples hosting Cc2 veins was cemented by Cc1. In one sample where intergranular pores were mainly filled by Cc1, limited Cc2 precipitated in the residual pores (Fig. 13C5, C6).

Cc3 calcite cement occasionally precipitated in F1 and F4 fracture sets at the western zone of the north limb of the anticline (Fig. 13D1). This cement consists of euhedral blocky crystals, with large crystal sizes generally between 1 and 20 mm (Fig. 13D2, D3). Cc3 presents abundant mechanical twins and very dull luminescence (Fig. 13D3, D4). Intergranular porosity was cemented by Cc1 in all samples hosting Cc3 veins, indicating that Cc3 developed after Cc1.

Cc4 calcite cement precipitated in F1 to F4 fracture sets (Fig. 13E1) in all the structural positions. Cc4 is commonly found in fracture coating as small as 1 mm-thick, characterised by anhedral to subhedral blocky and non-luminescent crystals, but occasionally as up to 10 mm-thick veins with a palisade structure (Fig. 13E2 to E4). Cc4 precipitated in reopened fractures filled by previous cements and does not present crystals with mechanical twins (Fig. 13E3, E4), indicating that Cc4 probably precipitated in relatively recent times after intensive compression.

3.3.4.2 Geochemistry of calcite cements

The geochemical features of host rocks and calcite cements are presented in Fig. 14, including carbon and oxygen isotopes, clumped isotope data, strontium isotopes, and elemental composition. The oxygen isotopes of carbonate clasts, clumped isotope data of Cc1 and Cc2, strontium isotopes

of host rocks, Cc1 and Cc2 are from Cruset et al. (2016). The elemental composition of Cc1 and Cc2 from Cruset et al. (2016) was also integrated into these results.

The carbonate clasts present $\delta^{13}C$ values ranging from -3.2 to +3.1‰ VPDB (Vienna Pee Dee Belemnite) and $\delta^{18}O$ values from -8.9 to -3.1‰ VPDB (Fig. 14A). Cc1 shows $\delta^{13}C$ values between -3.3 and +0.8‰ VPDB and $\delta^{18}O$ values between -8.0 and -4.9‰ VPDB. Cc2 shows $\delta^{13}C$ values between -1.6 and +0.1‰ VPDB and $\delta^{18}O$ values between -10.2 and -8.4‰ VPDB. Cc3 presents $\delta^{13}C$ values between -0.1 and +0.8‰ VPDB and $\delta^{18}O$ values between -4.6 and -3.4‰ VPDB. Cc4 has $\delta^{13}C$ values ranging from -10.2 to -4.2‰ VPDB and $\delta^{18}O$ values from -8.0 and -5.1‰ VPDB. The $\delta^{13}C$ values of Cc1 to Cc3 are within the $\delta^{13}C$ range of carbonate clasts of host rocks, whereas Cc4 has depleted $\delta^{13}C$ values with respect to host rocks. The $\delta^{18}O$ values of Cc1, Cc3 and Cc4 are within the $\delta^{18}O$ range of host rocks, whereas Cc2 has depleted $\delta^{18}O$ values with respect to host rocks.

The Δ_{47} values of Cc1 and Cc2 are modified from Cruset et al. (2016) by removing the acid correction factor (0.069‰ at 90˚C) to be able to compare to the values of Cc3 and Cc4 in the I-CDES that is expressed without correction factor at 90˚C. Cc1 has Δ_{47} values of 0.479 ± 0.009‰ and 0.425 ± 0.010‰, which translate to temperatures of 92 ± 5°C and 129 ± 8°C and in $\delta^{18}O_{fluid}$ values of +4.7 ± 0.6‰ and +9.2 ± 0.7‰ VSMOW (Vienna Standard Mean Ocean Water) (Fig. 14B). Cc2 has Δ_{47} values of 0.505 ± 0.010‰ and 0.482 ± 0.004‰, which indicate temperatures of 77 ± 5°C and 90 ± 3°C and $\delta^{18}O_{fluid}$ values of −1.7 ± 0.7‰ and −0.7 ± 0.3‰ VSMOW. For Cc3, Δ_{47} values are 0.527 ± 0.001‰ and 0.501 ± 0.007‰, which are converted to temperatures of 49 to 50°C and 59 to 65°C and $\delta^{18}O_{fluid}$ values of 3.9 to 4.3‰ VSMOW and 5.2 to 6.4‰ VSMOW. For Cc4, Δ_{47} values are 0.619 ± 0.014‰ and 0.609 ± 0.012‰, which indicate temperatures of 12 to 21°C and 16 to 23°C and $\delta^{18}O_{fluid}$ values of -5.7 to -3.6‰ VSMOW and -5 to -3.4‰ VSMOW.

Host rocks have $^{87}Sr/^{86}Sr$ ratios of 0.708865 and 0.708967 for mudstone and marly limestone, respectively (Fig. 14C). Cc1 shows higher $^{87}Sr/^{86}Sr$ ratios of 0.709138 and 0.709246. Cc2 has $^{87}Sr/^{86}Sr$ ratios of 0.708947 and 0.709002. Cc3 shows lower $^{87}Sr/^{86}Sr$ ratios of 0.708747 and 0.708813. Cc4 presents variable $^{87}Sr/^{86}Sr$ ratios ranging from 0.708757 to 0.710208.

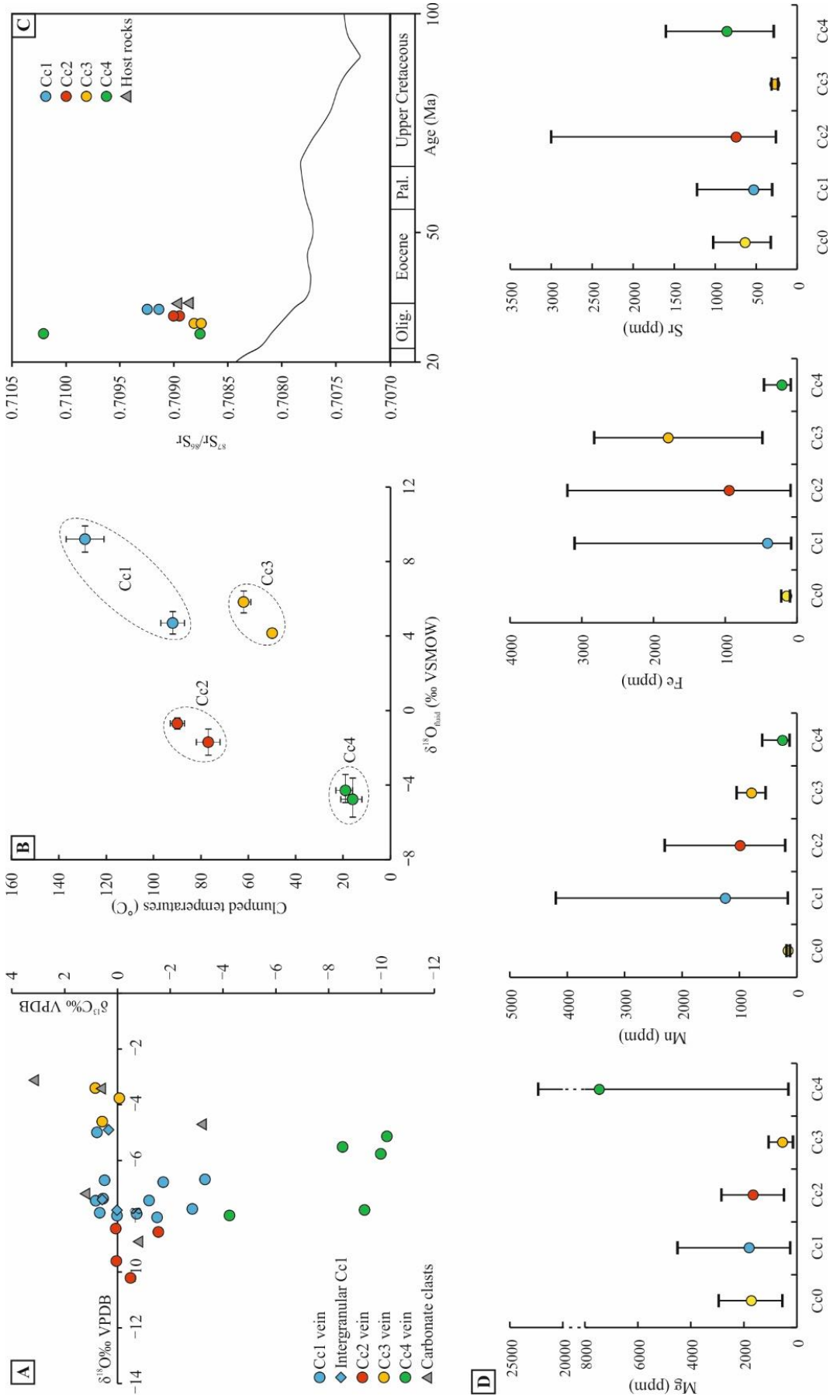
A
δ18O‰ VPDB
δ13C‰ VPDB
Cc1 vein
Intergranular Cc1
Cc2 vein
Cc3 vein
Cc4 vein
Carbonate clasts
B
Clumped temperatures (°C)
δ18Ofluid (‰ VSMOW)
Cc1
Cc2
Cc3
Cc4
C
87Sr/86Sr
Cc1
Cc2
Cc3
Cc4
Host rocks
Olig.
Eocene
Pal.
Upper Cretaceous
Age (Ma)
D
Mg (ppm)
Mn (ppm)
Fe (ppm)
Sr (ppm)
Cc0
Cc1
Cc2
Cc3
Cc4

Figure 14. (A) $\delta^{18}O$ vs. $\delta^{13}C$ cross plot of conglomerate carbonate clasts and Cc1 to Cc4 calcite cements. (B) Temperatures of precipitation in °C vs. $\delta^{18}O_{fluid}$ in ‰ VSMOW calculated from clumped isotope thermometry for Cc1 to Cc4 calcite cements. (C) $^{87}Sr/^{86}Sr$ ratios of host rocks and Cc1 to Cc4 calcite cements. The black line represents the $^{87}Sr/^{86}Sr$ ratios of seawater through time from the LOWESS curve (McArthur et al., 2012). (D) Mg, Mn, Fe and Sr composition of Cc0 to Cc4 calcite cements. The $\delta^{18}O$ and $\delta^{13}C$ values of carbonate clasts, clumped isotope data of Cc1 and Cc2, strontium isotope data of host rocks, Cc1 and Cc2 are from Cruset et al. (2016). The elemental composition data of Cc1 and Cc2 from Cruset et al. (2016) are integrated into these results.

Cc0 has elemental composition values ranging from 546 to 2950 ppm in Mg and ranging from below the detection limits to 1024, 221 and 178 ppm in Sr, Fe and Mn, respectively (Fig. 14D). Cc1 shows values ranging from 248 to 4500 ppm in Mg and from 158 to 4199 ppm in Mn, while values range from below the detection limits to 3100 and 1221 ppm in Fe and Sr, respectively. Cc2 has values ranging from 458 to 2846 ppm in Mg and from 202 to 2300 ppm in Mn, while values range from below the detection limits to 3200 and 3000 ppm in Fe and Sr, respectively. For Cc3, the Fe, Mg and Mn contents range from 483 to 2827 ppm, from 148 to 1062 ppm and from 545 to 1050 ppm, respectively, while the Sr content ranges from below the detection limit to 312 ppm. For Cc4, the Mg content ranges from 319 to 22340 ppm, while the Sr, Mn and Fe contents range from below the detection limits to 1601, 604 and 459 ppm respectively. Besides, Cc4 has a Ca content ranging from 368470 to 398507 ppm, which is lower than that of Cc1 to Cc3 ranging from 381100 to 399540 ppm.

3.3.5 Reservoir characteristics of host rocks

Based on Folk's (1980) sandstone classification scheme, all sandstone samples retrieved in the studied area plot in the litharenite field, with lithic content ranging from 60% to 90%, quartz content ranging from 5% to 30%, and limited feldspar content (Fig. 15A). Based on Zuffa's (1980) classification scheme of hybrid arenites, these samples mainly plot in the carbonate extrarenite field with minor in the non-carbonate extrarenite field (Fig. 15B). The content of carbonate extrabasinal grains mainly ranges from 40% to 70%. The content of non-carbonate extrabasinal grains, including non-carbonate lithic, quartz, feldspar, mainly ranges from 30% to 60%.

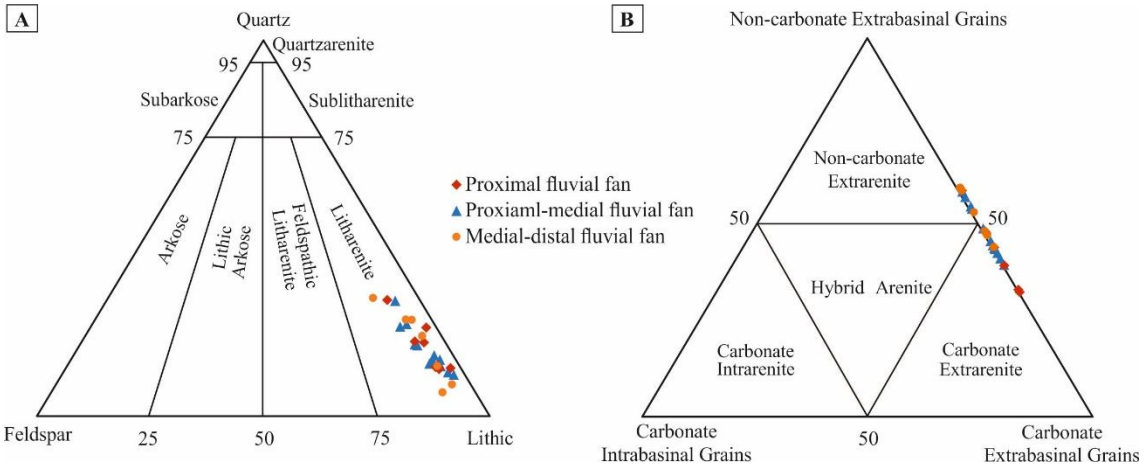

Figure 15. Classification of sandstones based on framework grain composition after (A) Folk's (1980) and (B) Zuffa's (1980) classification schemes.

The proximal to medial fluvial deposits of the the Camps de Vall-Llonga and Solsona Formations present very low intergranular porosity, which mainly ranges from 0% to 2% (Fig. 16A), with an average of 1.2%. Limited samples present relatively higher porosity concentrated in lithofacies Sch and Sm in the crest, crest-limb transition zones and southern limb of the anticline, mainly ranging from 2% to 8% (Fig. 16A). Calcite is the dominant cement in these fluvial deposits and mainly ranges from 5% to 15% (Fig. 16B), with an average value of 11.6%. Sandstone lithofacies has slightly higher cement content compared to conglomerate and fine-grained lithofacies, with an average value of 12.7% (Fig. 16B).

To quantitatively analyse the effect of diagenetic alteration on porosity loss, the original porosity (P_o) was calculated based on Scherer's empirical formula (Scherer, 1987), and the proportion of original porosity destroyed by cementation (PL_{cem}) and by compaction (PL_{com}) were calculated based on Houseknecht's formulas (Houseknecht, 1987):

$$P_o = 20.91 + 22.9/S_o \quad (1)$$

$$PL_{cem} = \frac{P_{cem}}{P_o} \times 100\% \quad (2)$$

$$PL_{com} = (P_o - P_{cem} - \mathrm{P}_r)/P_o \times 100\% \quad (3)$$

where S_o is the Trask sorting coefficient of grain size, whose values of different lithologies were acquired from grain size analysis data from Sun (2018); P_{cem} is cement content; and P_r is residual porosity. The sorting coefficient of siltstone and sandstone mainly ranges from 1.3 to 2.3, resulting in original porosity between 31% to 39% with an average of 35%, while the sorting coefficient of

conglomerate mainly ranges from 1.6 to 2.6, resulting in original porosity between 30% to 35% with an average of 32%. PL_{cem} mainly ranges from 20% to 50%, whereas PL_{com} mainly ranges from 40% to 80% (Fig. 17A, B). Limited samples with relatively high intergranular porosity have PL_{cem} and PL_{com} mainly ranging from 30% to 50% and from 40% to 60%, respectively (Fig. 17A).

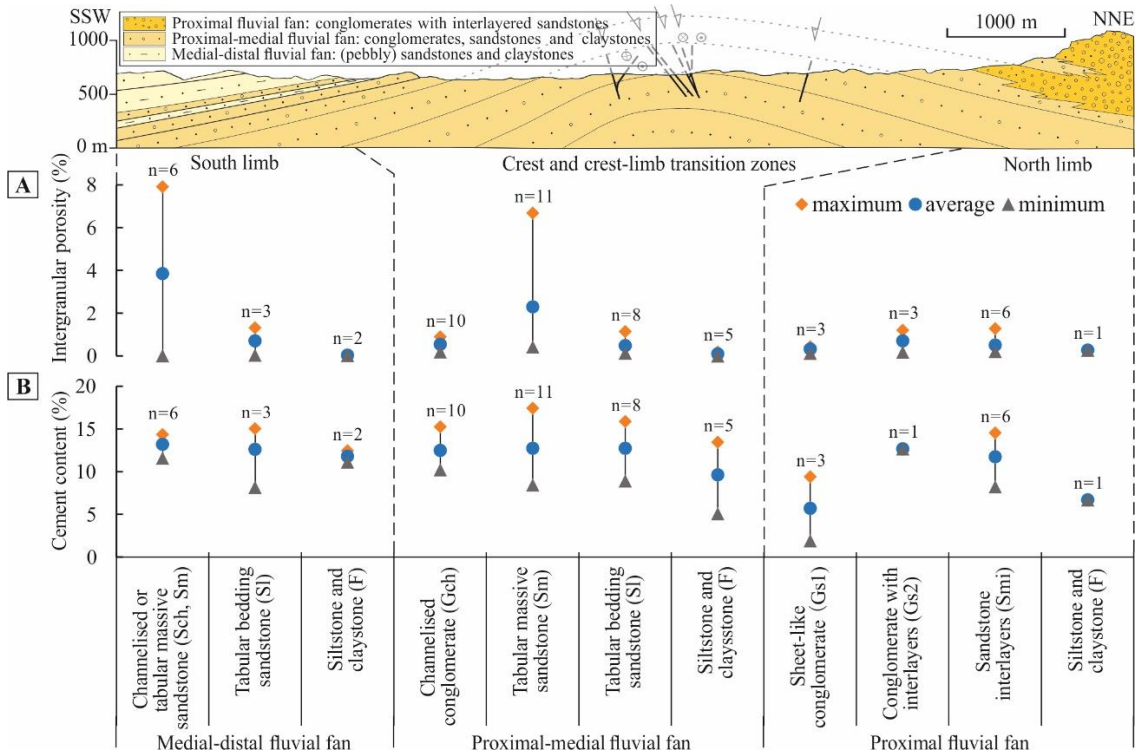

Figure 16. Distribution of intergranular porosity and cement content in different lithofacies and structural positions ('*n*' is the number of thin sections). The cross-section is modified from Cruset et al. (2016).

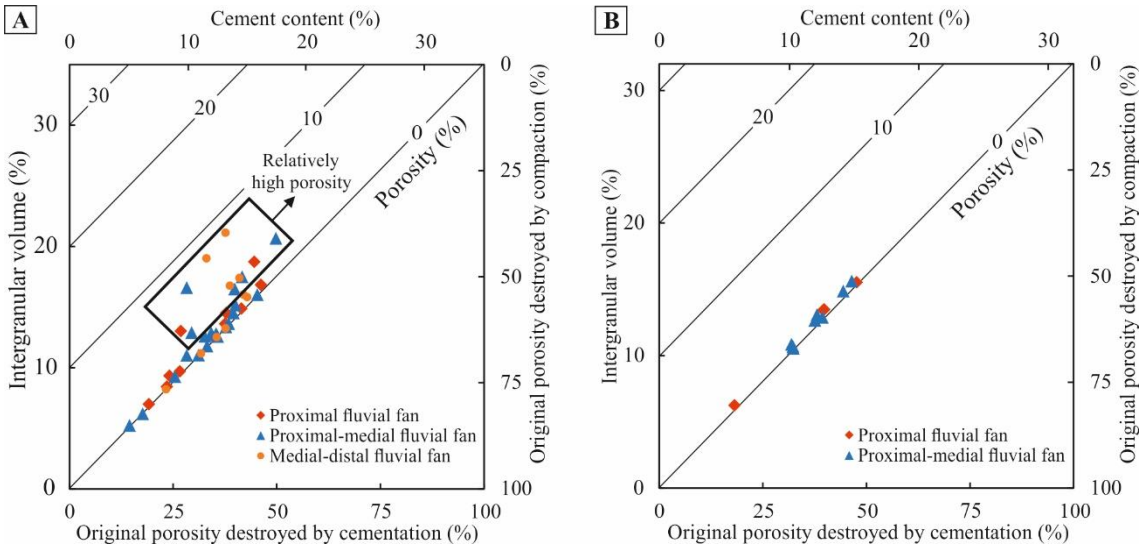

Figure 17. Cross plots of intergranular volume *vs.* cement content and porosity loss by compaction *vs.* cementation for (A) sandstone and fine-grained lithofacies and (B) conglomerate lithofacies.

4 Discussion

4.1 CCS potential in compressional basins and hydrocarbon-limited regions

CCS development has historically been closely bound to the production of oil and gas. Most of the CO_2 ever captured and injected in geological formations has been handled within the framework of CO_2-EOR projects (Liu et al., 2018). CO_2-EOR is considered a potential catalyst for large-scale CCS deployment (Kolster et al., 2017), as EOR activities can provide the revenue stream that makes profitable an otherwise too expensive CCS project (Kapetaki and Scowcroft, 2017). In addition, oil and gas fields are preferred targets for the storage of captured CO_2 because of their proven capacity to safely retain fluids over geological timescales. Substantial subsurface data, as well as infrastructure in place suitable for re-use, are usually available from exploration and production activities in these type of reservoirs (Alcalde et al., 2019). In Section 2.1, we use hydrocarbon volume as a proxy to quantify and rank CO_2 storage potential of hydrocarbon-bearing compressional basins, rather than using them as quantitatively equivalent to storable CO_2 emissions because of the property differences between hydrocarbons and CO_2. The source-to-sink assessment reveals the good matching between CO_2 emissions and potential storage capacity in the priority regions dominated by compressional settings. Thus, compressional basins can play a key role in CCS development if this technology is to be implemented worldwide, especially in North America, Europe and China, all regions with an urgent demand for emission reduction and explicit reduction targets in place.

CCS deployment has stalled in most countries, with only limited commercial projects realised mainly in hydrocarbon-rich countries for CO_2-EOR. To achieve the mid-century target of net-zero emissions this progress must be replicated widely, including CCS deployment in hydrocarbon-limited countries, where CCS will have to be developed only for dedicated geological storage instead of CO_2-EOR. Thus, hydrocarbon-limited countries need to devise alternative strategies if they intend to implement ambitious decarbonisation strategies via CCS. In these countries,

economies of scale can play a key role in reducing CCS costs, which in turn can incentivise investment and development in this important technology. In this sense, the implementation of CCS hubs and clusters can be an effective strategy to share the effort of developing full-chain CCS projects. CCS hubs and clusters connect multiple nearby CO_2 emitters and storage site locations to reach a critical mass for CCS development (Global CCS Institute, 2016). The different CCS activities such as planning, transport and storage infrastructure construction, government licensing, negotiations with property owners and so on can be shared amongst the cluster users, reducing the overall costs and risks compared with standalone projects (Global CCS Institute, 2016).

In Section 2.2, we present a new source-to-sink assessment methodology based on the hubs and clusters strategy, which is especially applicable for hydrocarbon-limited countries to attract renewed public and political interest in viable deployment pathways for CCS. We demonstrate this methodology by applying it to the Spain case study to identify favourable regions for CCS development. This assessment considers the spatial matching, *i.e.,* the distribution of emission hubs and the suitability of storage structures, the development cost, and the capacity matching (*i.e.,* the priority storage structure should have enough capacity to store the 30-year emissions of the emission hubs). The capacity matching can ensure the longevity of prospective CCS projects and respond to Spain's long-term emission reduction target by 2050. Emission hubs, rather than single emission facilities, are selected as CO_2 sources for the assessment. This is done to ensure the availability of CO_2 sources and thus the longevity of prospective CCS projects, in case some facilities within the emission hubs are shut down in the future (*e.g.*, the highly emitting coal thermal plants that are being decommissioned across the country (Ministerio Para La Transición Ecológica y El Reto Demográfico, 2020; Sanz-Hernández et al., 2020)). Emission hubs are divided into two sectors based on industrial emission types, *i.e.,* the power sector and the hard-to-abate sector. In the power industry, CCS is not the only option for decarbonisation because emissions can be mitigated by other methods, *e.g.,* switching to renewable resources and improving energy efficiency. In other industries, such as the cement or steel industries, emissions cannot be completely mitigated by using renewable energy or by improving energy efficiency due

to the existence of process-related emissions (Voldsund et al., 2019). The main advantage of the hubs and clusters strategy is that it can help to reduce the development costs of CCS deployment when multiple CO_2 emitters share infrastructure such as pipelines and storage complexes (Brownsort et al., 2016; Alcalde et al., 2019). For example, in the hard-to-abate sector, the CO_2 emissions of most industrial facilities range from 0.1 to 1 Mtpa in Spain, with only two facilities having emissions higher than 1.5 Mtpa. Compared to aiming for a single large project, a gradual development and build-out process may provide a more viable pathway in this sector. Previous research indicates smaller-scale industrial applications such as steel and cement works may benefit from CCS as much as power sector applications, but that sharing of infrastructure may be needed to make this economically viable (Mandova et al., 2019). Apart from being integrated into existing energy systems and emission-intensive industries, there is significant potential for combining CCS with blue hydrogen generation and bioenergy, other low-carbon energies that can greatly contribute to achieving the net-zero target.

Among the four potential regions for CCS development in Spain, NW and NE Spain can be considered the priority regions. In these regions, the emission hubs have high total CO_2 emissions of 48.6 Mtpa, accounting for 71% of all selected emission hubs. Furthermore, these emission hubs are from both the power sector and the hard-to-abate sector, ensuring the potential roles of these regions in different stages and scenarios of emission reduction. Even in a scenario where Spain completely relies on renewable resources and energy efficiency to reduce emissions in the power sector, CCS in the hard-to-abate sector would still be necessary to achieve net-zero emissions in this sector (Davis et al., 2018). In addition to multiple emission hubs, NW and NE Spain contain multiple storage structures. These structures are mainly located in the Ebro and Duero foreland basins and their adjacent mountains, which are dominated by compressional settings. Our analysis of the Ebro Foreland Basin is consistent with that of the STRATEGY CCUS project, which has recently selected this basin as one of the most poetential regions for large-scale deployment of CCS in Southern and Eastern Europe (Strategy CCUS, 2020). However, it should be noted that the availability of geological and geophysical data in most storage sites is very low, compared to other hydrocarbon-rich basins. In the Ebro Foreland Basin, the lack of exploration data,

particularly well data, imposes significant uncertainty on the suitability assessment of the storage sites, especially when trying to determine the injectivity in the reservoir formation. Unexpected low injectivity in a reservoir can dictate the fate of a CO_2 storage project, forcing its closure, examples being the In Salah project in Algeria (Stork et al., 2015) or the ZeroGen project in Australia (Garnett et al., 2014). Acquiring more geological data, particularly well data, to obtain better estimates of the injectivity is thus imperative in hydrocarbon-poor regions to reduce the uncertainty and thus advance the maturity of the storage sites. In addition, due to the limited well data and seismic resolution of subsurface reservoirs, outcrop analogues can play an important role in improving the accuracy of reservoir prediction in the subsurface (Howell et al., 2014), by providing reliable geological conceptual models and quantitative attribute information (Dichiarante et al., 2020), especially in these hydrocarbon-limited basins. Thus, in this thesis, the Puig-reig anticline is used as an outcrop analogue for the evaluation of the reservoir characteristics and the related controlling factors of similar sedimentary systems at foreland basin margins.

4.2 Case study of the Puig-reig anticline (SE Pyrenees)

The Puig-reig anticline constitutes an excellent case study of an analogue of a carbon storage site in compressional settings. This is because this anticline presents excellent outcrops consisted of fluvial fan deposits, which are the dominant deposits at non-marine foreland basin margins. Besides, this anticline features complex fracture networks, fluvial evolution and diagenetic history due to the complex sedimentary and structure characteristics at the active basin margin of the Ebro Foreland Basin. The case study of the Pugi-reig anticline aims to explore the reservoir potential of folded fluvial settings at foreland basin margins and the related controlling factors, based on the comprehensive analysis of sedimentologoy, fracture network and diagenesis.

4.2.1 Fluvial sedimentary environment

Previous studies interpreted the whole Berga Group as alluvial fan deposits that wedge out into fluvial fan deposits of the Solsona Formation (Williams et al., 1998; Barrier et al., 2010). However, here we focus on the analysis of the Camps de Vall-Llonga Formation of the Berga Group and the Solsona Formation in the Puig-reig anticline. They are interpreted as deposits of a proximal to

medial fluvial fan, based on the comprehensive analysis of the drainage basin, fan size and sedimentary characteristics, and their comparison to other similar sedimentary systems in the central Ebro Basin (Hirst and Nichols, 1986; Arenas, 1993; Nichols and Hirst, 1998; Arenas et al., 2001).

Alluvial fan deposits are sourced by areal-limited drainage basins, whereas fluvial fan deposits tend to have larger drainage basins with long-term expansion and integration of catchments (Moscariello, 2018). The Camps de Vall-Llonga and Solsona deposits are composed of polygenic clasts, including both carbonate and non-carbonate clasts (Fig. 15B). As noted by Riba (1976), the non-carbonate clasts of acid-intermediate plutonic rocks, Permo-Triassic red beds, Carboniferous micro-conglomerates, rare metasedimentary rocks and basic igneous rocks, all come from the basement of the Pyrenean Axial Zone. The varied composition of carbonate clasts reflects different source areas in the Mesozoic-Cenozoic series of the south Pyrenean thrust sheets and the Pyrenean Axial zone (Devonian carbonates). The polygenic clast compositions reveal the drainage basin of these deposits extending from the south Pyrenean thrust sheets to the Pyrenean Axial Zone, which is consistent with the large and regional-scale drainage basin of fluvial deposits.

Alluvial fans may range widely in radial length, rarely up to 10 km in exceptional circumstances favouring particularly long runout for sediment-water mixtures (*e.g.,* Blair, 2003), but the radial fans extent generally varies from several hundred metres to a few kilometres at most (Blair and McPheerson, 1994; Moscariello, 2018). The Camps de Vall-Llonga deposits are exposed from the Vallfogona thrust to the Puig-reig anticline, for around 9 km in the direction perpendicular to the Vallfogona thrust and for around 20 km in a direction roughly parallel to the thrust based on the studied outcrops and the regional geological map (Institut Cartogràfic i Geològic de Catalunya, 2006). Considering the folding of strata and the unexposed strata to the south, the actual extent of the Camps de Vall-Llonga deposits should be larger than the observable extent, which is larger than that of typical alluvial fans.

In the northwest portion of the study area, the Camps de Vall-Llonga Formation is dominated by proximal deposits from flash floods and wide-shallow channel streams (Fig. 9). The development of flash floods in the proximal fluvial fans is also documented in the northern margin

fans of the central Ebro Basin (Luzón, 2001, 2005). The rest of the Camps de Vall-Llonga Formation is dominated by the medial deposits from braided channel streams and overbanks. They tend to present an overall fining-upward trend from channel fill conglomerates and sandstones to overbank fine deposits, representing cyclic (avulsive) behaviour of the system as it developed through time. In the crest-south limb transition zone of the Puig-reig anticline, the Solsona Formation is still dominated by channel fill and overbank deposits. There are no perceptible differences of sedimentary environments in the transition area between the Camps de Vall-Llonga and Solsona formations, *i.e.,* the contact between the upper and lower log B (Fig. 9). In the south limb, conglomerate channel lags are gradually replaced by (pebbly) sandstone channel lags, *i.e.,* in the upper part of the upper log B. We interpret that these deposits still belong to the medial portion of the fluvial fan due to a lack of the terminal deposits of distal fluvial fan and the lacustrine sedimentary characteristics. The Camps de Vall-Llonga and Solsona formations therefore represent mappable units rather than distinct separate sedimentary systems. Based on observations from the whole Berga Group (Williams et al., 1998), paleocurrents are roughly directed towards the south or southeast (Barrier et al., 2010). The decrease of lithofacies associations dominated by conglomerates and the increase of lithofacies associations dominated by sandstones and fine deposits towards the south and southeast (Fig. 9) is consistent with the overall paleocurrent directions of the Berga Group, supporting the interpretation of fluvial fan deposits.

However, we do not discard the possibility of the presence of several alluvial fans developing during the deposition of the Berga Group, which are restricted at the northern basin margin with small fan size and local drainage basins, *e.g.,* the small stream-flow and gravity-flow-dominated alluvial fan identified by Barrier et al. (2010) at the top of Berga Group and located to the northwest in Fig. 2-9D. This has been observed to be the case in the northern margin of the central Ebro Basin, where two distributive fluvial systems (the Luna and Huesca systems) coincide and interfinger with a series of marginal alluvial fans (Hirst and Nichols, 1986; Nichols and Hirst, 1998; Arenas et al., 2001).

4.2.2 Fracture distribution pattern

This section discusses how fracture network attributes vary across the different structural positions and sedimentary facies within the Puig-reig anticline, and identifies the fracture distribution controlling factors. The study of fracture networks in an outcrop analogue allows gaining insights into the degree of damage and fracture permeability in equivalent subsurface systems.

Due to the lack of outcrops parallel to bedding, it is difficult to identify the terminations and relative cross-cutting relationships between the different fracture sets in the Puig-reig anticline. Thus, systematically establishing the chronology of the fracture sets and explaining the variation of fracture sets across the different structural positions are challenging tasks. Accordingly, here we focus on the exploration of the distribution of fracture spacing, intensity, length and aperture, and the related controlling factors.

Fig. 18A1 and A2 show a clear negative correlation between fracture intensity and distance to the anticline hinge for conglomerate and sandstone layers, respectively, with fracture intensity decreasing significantly away from the anticline hinge. For folds developed according to the Tangential Longitudinal Strain model (TLS) (*e.g.*, Hudleston and Treagus, 2010), the fold hinge and nearby structural positions tend to experience more intensive fracturing due to their greater curvature and finite strain with respect to the limbs (Bellahsen et al., 2006; Iñigo et al., 2012; Awdal et al., 2013).

Fig. 18B1 reveals a clear negative correlation between fracture intensity and bedding thickness for both conglomerate and sandstone layers in the anticline crest. Fig. 18B2 shows a similar negative correlation for sandstone layers in the south limb and conglomerate layers in the north limb. Fracture intensity has been described to be closely related to bedding thickness (Ladeira and Price, 1981), and many studies reported a negative correlation between these two factors (*e.g.,* Huang and Angelier, 1989; Florez-Niño et al., 2005; Wennberg et al., 2007).

Both physical experiments and numerical simulations have revealed that the strength of brittle rocks decreases with increasing grain size (Fredrich et al., 1990; Yu et al., 2018). Fracture intensity is generally higher within the stronger and more brittle rocks. Thus, coarse-grained rocks tend to

present higher fracture intensity than fine-grained rocks, especially in carbonates (Hugman and Friedman, 1979; Hanks et al., 1997). However, in the present case, there is not a clear relationship between fracture intensity and grain size (Fig. 18C1, C2), indicating that grain size is not a significant factor controlling fracture intensity in the Puig-reig anticline.

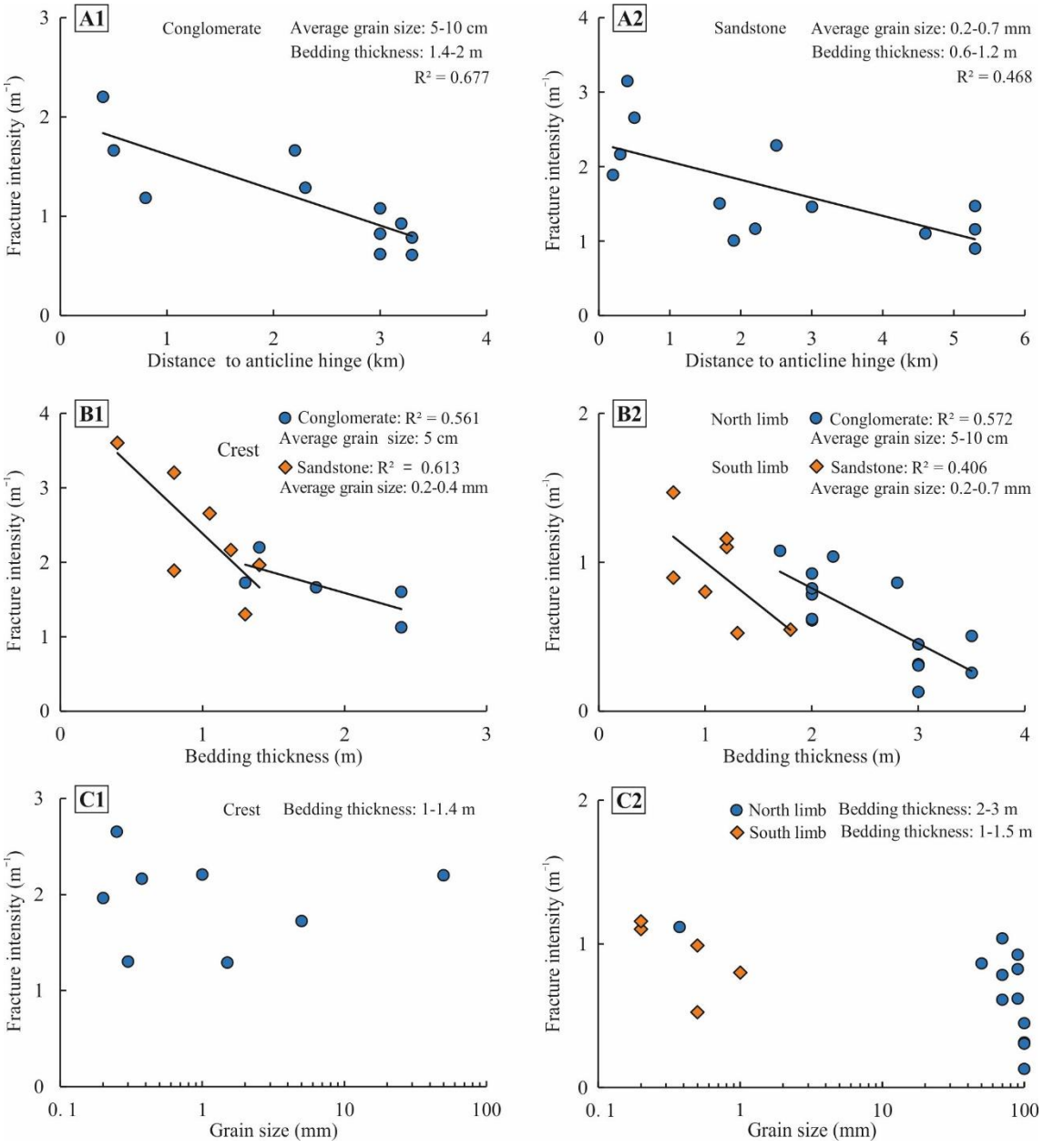

Figure 18. Cross plots between fracture intensity and structural position and sedimentary characteristics. (A) Fracture intensity *vs.* distance to anticline hinge. (B) Fracture intensity *vs.* bedding thickness. (C) Fracture intensity *vs.* grain size.

The high competence contrast at distinct mechanical stratigraphic positions (*e.g.,* at the interfaces between carbonate or sandstone layers and fine deposits) favours the development of joints or faults (Sibson, 1996; Wilkins et al., 2014). In this study, the interlayering between competent sandstone or conglomerate layers and thin incompetent fine deposits in the medial fluvial fan results in a high competence contrast, which favours the formation of fractures in the more competent layers. However, sandstone layers developed between thick incompetent fine deposits in the medial fluvial fan present relatively low fracture intensity compared to those with thin interlayers of fine deposits. This is probably because thick incompetent lithologies are capable of accommodating higher amount of pre-failure strain, *e.g.,* by means of inter-granular sliding, pressure solution, pore collapse and associated dewatering (Ferrill and Morris, 2008). Sandstone layers developed between thick conglomerate bodies in the proximal fluvial fan and the proximal-medial fluvial fan have relatively lower competence contrast and thus lower fracture intensity. Conglomerate layers with limited sandstone lenses in the proximal fluvial have the lowest fracture intensity due to very low competence contrast.

To quantitatively compare the relative importance of each factor for controlling fracture intensity, multiple linear regression analysis using SPSS software (IBM Corp, 2017) was employed in this study. First, lithological associations were classified and digitalised based on their effects on fracture intensity in three cathegories: (1) for lithological association of competent layers with multiple thin incompetent layers; (2) for lithological associations of competent layers between thick incompetent layers and interlayered competent conglomerate and sandstone layers; and (3) for competent conglomerate layers with limited sandstone lenses. Then, a multiple linear regression equation for fracture intensity can be used:

$$X_n = \frac{X - \bar{X}}{X_{max} - X_{min}} \quad (4)$$

$$I_n = c_1 \times P_1 + c_2 \times P_2 + c_3 \times P_3 + c_4 \times P_4 \quad (5)$$

where, X, X_n, $\bar{X}$, X_{max} and X_{min} are the actual, normalised, average, maximum and minimum values for each parameter, respectively; I_n is the normalised fracture intensity; P_1 to P_4 are the normalised influence factors on fracture intensity, of structural position (distance to the anticline hinge),

bedding thickness, lithological association, and lithology (grain size), respectively; and c_1 to c_4 are the standardised regression coefficients of the four influence factors, respectively. Finally, the relative importance of each factor for controlling fracture intensity can be determined based on the standardised regression coefficient of each factor:

$$I_n = -0.509 \times P_1 - 0.325 \times P_2 - 0.252 \times P_3 + 0.07 \times P_4 \ (R^2 = 0.636) \quad (6)$$

Thus, this analysis confirms the qualitative observations that fracture intensity is mainly controlled by the structural position and is also affected by bedding thickness and lithological associations, while the host rock's grain size has a very limited effect on fracture intensity.

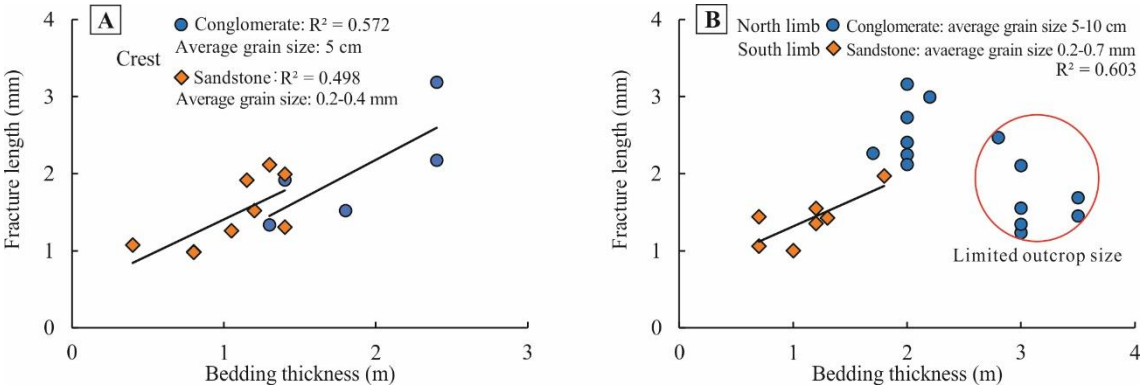

Figure 19. Cross plots between fracture length and bedding thickness of (A) the anticline crest and (B) the anticline limbs.

Fracture length shows positive correlations between bedding thickness for conglomerate and sandstone layers in the anticline crest (Fig. 19A) and sandstone layers in the south limb of the anticline (Fig. 19B). The limited outcrop size of some tabular conglomerate bodies in the northwest zone of the anticline resulted in anomalously small fracture lengths (Fig. 19B) due to the so-called 'censoring bias' (Zeeb et al., 2013). In addition, fracture length is also affected by lithological associations that determine the strength of bedding interfaces. Fracture terminations are more likely to occur at very weak bedding interfaces between competent and incompetent layers, whereas strong bedding interfaces that put in contact competent layers favour fracture propagation across the interfaces (Cooke and Underwood, 2001). In the medial fluvial fan, more fractures tend to abut at the weak bedding interfaces between conglomerates or sandstones and clays. In this case, the fracture length is limited by the bedding thickness when fractures are

stratabound (Wennberg et al., 2006). In the proximal fluvial fan, the common strong bedding interfaces between conglomerates and sandstones may promote the propagation of some long fractures but fewer fracture population.

Fracture apertures are generally smaller than 2 mm, while relatively larger values are mainly concentrated in conglomerate layers (Fig. 11C). Progressive stretching caused by folding can be accommodated by the propagation and/or re-opening and widening of previous fractures or by the formation of new ones (Watkins et al., 2015a), which can operate at the same time in all structural positions and lithofacies. However, we observe that it is difficult to form many new fractures to accommodate strain in large conglomerate bodies due to their high strength, especially in the north limb that has relatively lower strain. Moreover, the existing fractures and veins in these thick conglomerate bodies act as weak parts compared to the host rock with high strength. Thus, the propagation, re-opening and widening of the existing fractures can accommodate strain when it is not strong enough to form a significant number of new fractures.

Based on the above analysis, Fig. 20 shows a schematic diagram that summarises the main fracture patterns of the Puig-reig anticline. The crest of the anticline, which is dominated by proximal-medial fluvial deposits (conglomerates, sandstones and clays), presents relatively high fracture intensity and variable fracture length and aperture. The north limb, which is dominated by proximal fluvial deposits (conglomerates and sandstones) presents relatively low fracture intensity but large fracture length and aperture. The south limb, dominated by medial-distal fluvial deposits (sandstones and clays), presents relatively low fracture intensity and small length and aperture. The NTZ and STZ of the anticline feature variable fracture length and aperture and intermediate fracture intensity between the anticline crest and limbs. Fracture intensity is mainly controlled by the structural position, bedding thickness and lithological associations. Fracture length and aperture are mainly controlled by the host rock's sedimentary characteristics, while the structural position has a limited effect on them. Fracture length is mainly controlled by bedding thickness and affected by lithological associations. Fracture aperture is mainly controlled by lithology, with relatively larger values developed in conglomerate layers.

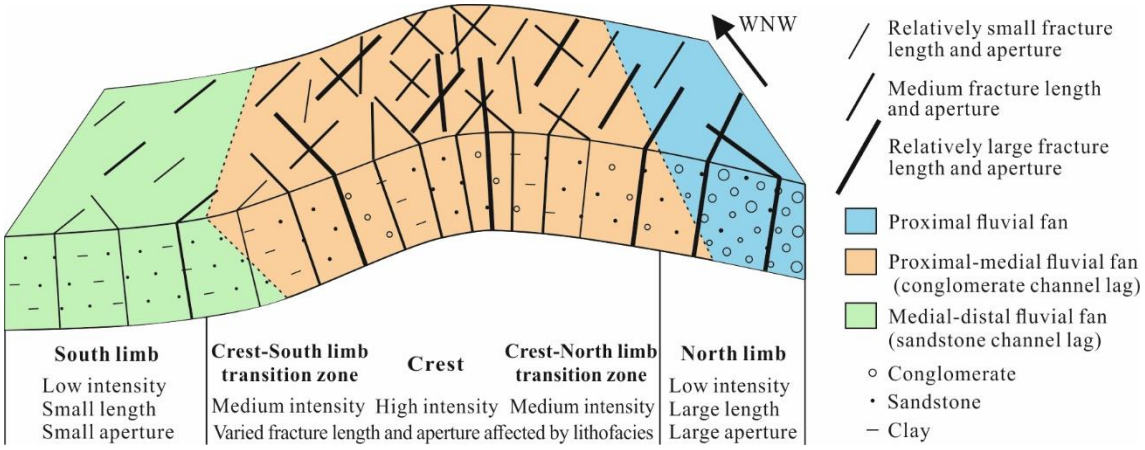

Figure 20. Schematic diagram of fracture distribution across different structural positions and sedimentary facies. Note: the diagram does not show the termination relations between different fracture sets due to the lack of outcrops parallel to bedding planes to determine them.

4.2.3 Changes in fluid regime during fold evolution

The petrographic characteristics of veins and host rocks and the geochemical data of calcite cements can be used to unravel the origin of the different fluids that precipitated such cements in the area. According to the results of this study, five calcite cement generations (Cc0 to Cc4) precipitated in the Puig-reig anticline rocks. Combining the fluid origin of calcite cement and the tectonic evolution of this anticline allows discussing the changes in fluid regimes during the complete fold evolution, to understand the permeability evolution during the diagenetic and tectonic history of this outcrop analogue. This is useful for predicting the behaviour of similar systems as storage sites in the subsurface.

Despite the lack of isotope data for Cc0, its petrologic characteristics and elemental composition hint at the fluid source. The concentric zonation of Cc0, varying from non-luminescent to bright luminescent zones (Fig. 13A1, A2), indicates fluctuations of the redox conditions probably in the meteoric phreatic environment (Muchez et al., 1998; Machel, 2000; Boggs and Krinsley, 2006; Vandeginste et al., 2012). The major non-luminescent zones represent oxidizing conditions during precipitation, whereas the minor bright luminescent zones are characteristic of more reducing conditions (Grover and Read, 1983). Cc0 has much lower Mn and Fe contents than the other cements (Fig. 14D), generally below the detection limits, which also supports the meteoric fluid origin. Cc0 developed in all structural positions and lithofacies,

indicating that the meteoric fluid from which Cc0 precipitated affected the whole anticline (Fig. 21A). As the earliest cement, Cc0 only precipitated in intergranular pores along clast edges and before the predominant Cc1 cement (Fig. 13A1, A2). Therefore, we interpret that Cc0 precipitated during early diagenetic stages before systematic fracturing and significant burial. Other studies documented similar calcite cements precipitated from meteoric fluids in a phreatic environment during early diagenetic stages (*e.g.,* Grover and Read, 1983; Emery and Dickson, 1989; Li et al., 2017).

Cc1 was previously interpreted as precipitated from hydrothermal fluids from the Palaeozoic basement (Cruset et al., 2016). The clumped isotope data reveals that Cc1 precipitated at temperatures between 92°C to 129°C (Fig. 14B), which are much higher than the maximum temperatures reached by the Berga Group and the Solsona Formation according to a maximum burial depth of 1.7 km (Cruset et al., 2016). This indicates an external hydrothermal fluid source from a depth of at least 4 km, or an even deeper source if we consider the cooling of the ascending fluids. The $\delta^{18}O_{fluid}$ of Cc1 ranges from +4.7 to +9.2‰ VSMOW (Fig. 14B), located within the range of formation, metamorphic and magmatic fluids (Taylor, 1987). Magmatic fluids are excluded because magmatism did not develop during the Pyrenean orogeny. The high $^{87}Sr/^{86}Sr$ ratios of Cc1, ranging from 0.709138 to 0.709246 (Fig. 14C), indicate that hydrothermal fluids interacted with highly radiogenic sources. The clumped isotope and strontium isotope data together indicate that fluids released from the Palaeozoic basement from a deep depth could have been the hydrothermal fluids responsible for the precipitation of Cc1. During thrusting and folding of the Puig-reig anticline, the damage zones of the blind thrust system at depth could have provided the paths for the hydrothermal fluids from the Palaeozoic basement to migrate upwards and reach the Berga Group and the Solsona Formation (Cruset et al., 2016). The connected fracture network and intergranular porosity of these alluvial-fluvial deposits would have allowed vertical and lateral migration of the hydrothermal fluids across different stratigraphic units. Cc1 filled most intergranular pores in different lithofacies and variable faults and fracture sets in different structural positions, indicating that the hydrothermal fluids from which Cc1 precipitated would have migrated along the whole anticline (Fig. 21B). Fluid flow could have been triggered

by horizontal or sub-horizontal compressive principal stress (*e.g.*, when the least principal stress is vertical), rather than by fluid pressure increase associated with decompression or fluid heating (such as in the model of Staude et al., 2009).

Cc2 was previously interpreted as precipitated from mixed fluids (Cruset et al., 2016). Clumped isotope data presented by these authors indicate that Cc2 precipitated at temperatures ranging between 77°C and 90°C (Fig 14B). These precipitation temperatures are lower than those of the precipitation of Cc1 but still higher than the maximum burial temperatures reached by the Berga Group and the Solsona Formation. Cc2 presents a more depleted $\delta^{18}O$ range than Cc1 and host rocks (Fig. 14A). Cc2 has lower $^{87}Sr/^{86}Sr$ ratios than Cc1 (Fig. 14C), indicating that the cement-forming fluids interacted with less radiogenic sources or mixed with fluids with lower $^{87}Sr/^{86}Sr$ ratios. The $\delta^{18}O_{fluid}$ composition of Cc2 ranges from -1.7 to -0.7‰ VSMOW (Fig. 14B), which is lower than that of Cc1 cement but higher than -6.4 to -4.6‰ VSMOW of modern rainwater (Travé and Calvet, 2001). Based on the available data, Cruset et al. (2016) interpreted that Cc2 precipitated in fractures from the mixing of meteoric waters with the hydrothermal fluids from which Cc1 precipitated. Accordingly, these authors proposed that small normal and strike-slip faults formed in the crest of the Puig-reig anticline during the crestal collapse, which provided connected paths for the percolation of low-temperature meteoric fluids from the surface to the bottom of the Berga and Solsona strata based on the fault-valve model (Sibson, 1981; Henderson and McCaig, 1996). These downward meteoric fluids would have then mixed with the upward hydrothermal fluids from the deeper basement from which Cc1 precipitated (Fig. 21C1). Then the mixed fluids would have migrated upwards through these connected faults due to the increasing fluid pressure related to the build-up stresses during compression (Henderson and McCaig, 1996) and finally would result in the precipitation of Cc2. As discussed by Bons et al. (2012) simultaneous downward and upward flow, such as that typically claim in conceptual models of mixing of surface-derived and deep fluids, would necessitate a geologically implausible fluid sink. Thus, such hydrological models need to involve asynchronous downward flow of meteoric fluids and upward flow of hydrothermal fluids to be hydrodynamically plausible.

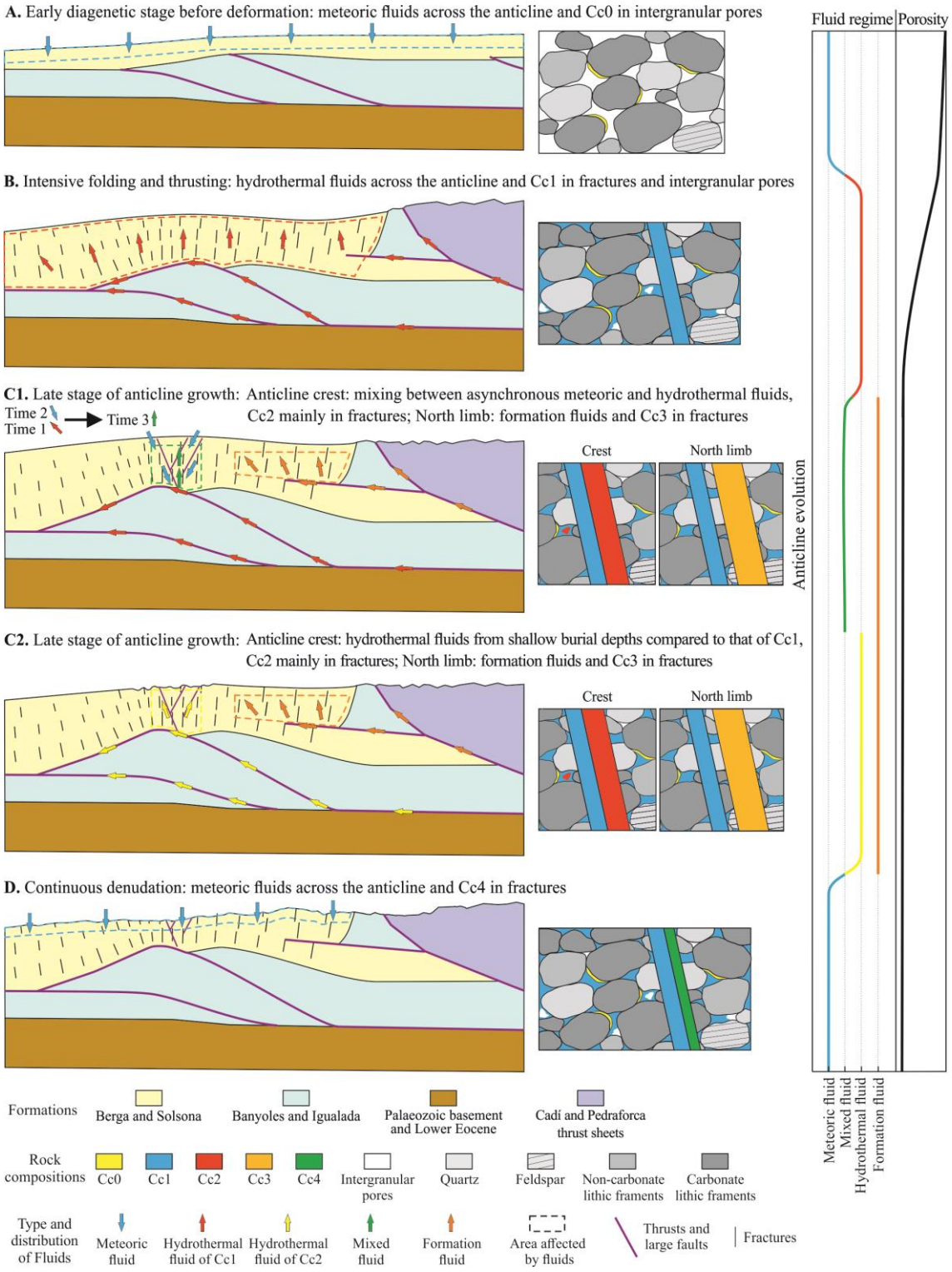

Figure 21. Schematic diagram of fluid regime evolution and related calcite cementation during the tectonic evolution of the Puig-reig anticline. (A) During early diagenetic stage before deformation, Cc0 precipitated in intergranular pores from meteoric fluids across the anticline. (B) During intensive folding and thrusting, Cc1 precipitated in intergranular pores and variable fractures from hydrothermal fluids across the anticline.

(C) During the late stage of anticline growth, Cc2 precipitated in fractures in the anticline crest from (C1) the mixing between asynchronous meteoric and hydrothermal fluids, modified from Cruset et al. (2016), or from (C2) hydrothermal fluids with meteoric signatures from shallower burial depth compared to that of Cc1, while Cc3 precipitated in fractures from formation fluids in the west zone of the north limb. (D) During the continuing denudation of the anticline, Cc4 precipitated in fractures from meteoric fluids across the anticline.

In this study, we propose an alternative model in which Cc2 could have precipitated from hydrothermal fluids from the basement but at shallower burial depths and at lower fluid temperatures compared to that of Cc1 (Fig. 21C2). Meteoric fluids could have migrated downwards from the erosional surface of the Pyrenees to the shallower basement driven by topography differences. The relatively low burial temperatures in such basement level would have resulted in a low degree of fluid-rock interaction, thus preserving part of the meteoric signature of the Cc2 fluid (Bons et al., 2014). In contrast, the Cc1 cement-forming fluids would have been sourced from deeper parts of the basement according to their geochemical signature and higher clumped isotope temperatures. Bons and Gomez-Rivas (2020) pointed out that meteoric fluids can infiltrate down from an erosional surface to be buried and then remobilised later, partly preserving their meteoric signature. Such signatures can be preserved for long periods of time if temperatures are relatively low. In the late stage of the fold growth of the Puig-reig anticline, the underneath thrusting could have mobilised the shallower hydrothermal fluids to the bottom of the anticline. In addition, the anticline crest could have raised and undergone partial exhumation, which could have caused an instantaneous decrease of the overburden pressure of underneath rocks and thus result in an overpressure of the trapped pore fluids. To maintain the original relative fluid pressure underneath fluids need to be expelled upwards (Staude et al., 2009), which could have resulted in the precipitation of Cc2 in the anticline crest.

Cc3 was only identified in section C, *i.e.*, the north-western part of the study area. This zone is dominated by proximal fluvial deposits, which have higher contents of marine carbonate clasts than medial and distal fluvial deposits. Cc3 has higher $\delta^{18}O$ and $\delta^{13}C$ values compared to other cements (Fig. 14A), and are closer to the isotopic compositional range of marine carbonates

(Veizer et al., 1999). This probably suggests interaction between the cement-forming fluids and marine carbonates. Based on the LOWESS curve (McArthur et al., 2012), the $^{87}Sr/^{86}Sr$ ratios of Cc3 between 0.708813 and 0.708747 are higher than those of seawater when the Mesozoic marine carbonates were deposited, but slightly lower than those of the host rocks of the Berga Group and Solsona Formation (Fig. 14C). This would suggest fluid-rock interaction between the cement-forming fluids and the radiogenic silicic clasts of the host rocks sourced from the Palaeozoic basement in the Axial Zone. Muñoz-López et al. (2020a) pointed that calcite cements precipitated from fluids that strongly interacted with basement rocks have significantly higher $^{87}Sr/^{86}Sr$ (>0.710) in nearby areas. The $^{87}Sr/^{86}Sr$ ratios of Cc3 in our study area are lower than those of this other case study probably because carbonate clasts dominate over silicic clasts in the zone where Cc3 precipitated. The $\delta^{18}O_{fluid}$ of Cc3 ranges from +4.1 to +5.8‰ VSMOW (Fig. 14B), which corresponds to the range of formation fluids (Taylor, 1987). Compared to Cc1 and Cc2, Cc3 precipitated at significantly lower temperatures, ranging between 50°C and 62°C (Fig. 14B). According to the current mean geothermal gradient of 26.7°C/km in the Ebro Foreland Basin (Fernàndez et al., 1998) and assuming a general surface temperature of 20°C, strata with burial depths around 1.5 km can reach the temperatures at which Cc3 precipitated. However, the depth could be slightly higher if we consider that fluids cool down while ascending. Compared to other generations of calcite cements, Cc3 presents higher Fe and low Mg and Sr concentrations (Fig. 14D). The high Fe concentration could result from the interaction between the cement-forming fluids and host rocks or be sourced from external fluids. Based on the available data, it is inferred that Cc3 precipitated from formation fluids that strongly interacted with the host rocks. Cc3 concentrates in the western zone of the north limb, indicating that the formation fluids locally migrated within the Berga Group (Fig. 21D). Based on the cross-sections (Fig. 4C, E), the frontal thrusts (such as the Vallfogona thrust) could have acted as the migration pathways for the formation fluids. For example, the blind branch of the Vallfogona thrust propagated into the lower and middle Berga Group in the north limb of the Puig-reig anticline, which could have facilitated the input of the formation waters into the Berga Group.

Cc4 occurs as thin coatings covering fracture surfaces or presents palisade structures of bladed

crystals (Fig. 13E3, E4). This cement is non-luminescent and has low Mn and Fe concentrations (Fig. 14D). Based on clumped isotope data, Cc4 precipitated from a fluid with temperatures ranging between 16°C and 19°C and with $\delta^{18}O_{fluid}$ ranging from -4.8 to -4.3‰ VSMOW (Fig. 14B). All these characteristics indicate a low-temperature meteoric fluid. In addition, Cc4 is characterised by highly depleted values of $\delta^{13}C$ with respect to host rocks, ranging from -10.2 to -4.2‰ VPDB (Fig. 14A), indicating a strong influence of organic-derived carbon (Irwin et al., 1977; Cerling, 1984; Vilasi et al., 2006). In the Puig-reig anticline, the exposed fine sediments, deposited from fluvial overbanks, have experienced intensive pedogenesis and can provide soil-derived carbon for calcite cement (Cerling and Quade, 1993). Other studies documented that similar calcite cements with palisade structure and depleted $\delta^{13}C$ precipitated from meteoric fluids with a strong influence of soil-derived carbon related to pedogenic processes (*e.g.*, Travé and Calvet, 2001; Cantarero et al., 2010, 2014). The significantly variable $^{87}Sr/^{86}Sr$ ratios of Cc4, with a low value of 0.708757 and a very high value of 0.710208 (Fig. 14C), could be related to variable interactions between fluids and the different compositions of host rocks. Besides, the high Sr isotope ratio could also be affected by the clayey or siliceous impurities existing between the multi-layer palisades of Cc4 (Fig. 13E3, E4). The presence of small percentages of clay minerals can significantly increase the measured $^{87}Sr/^{86}Sr$ ratios due to the decay of ^{87}Rb to ^{87}Sr (Banner, 1995). Owing to continuous denudation after fold growth of the whole Puig-reig anticline, the burial depths of the Berga and Solsona strata became shallower. Besides, some of the fractures sealed by previous calcite veins could have been reactivated during exhumation. Thus, some faults and fracture could have been reopened while new ones formed and allow the input of meteoric fluids from which Cc4 precipitated. Cc4 developed in different fracture sets and different structural positions of the anticline, indicating that the meteoric fluid affected the whole study area (Fig. 21E).

4.2.4 Distribution pattern of calcite cements

Based on the comparison between the calcite cement distribution in the Puig-reig anticline and other areas worldwide, this section discusses the distribution pattern of calcite cement in detrital reservoirs in different settings. In the Puig-reig anticline, abundant fractures were filled by Cc1

to Cc4 calcite veins. Cc1 and Cc4 veins precipitated across the whole anticline, whereas Cc2 and Cc3 precipitated locally in the anticline crest and north limb, respectively. The intergranular porosity of host rocks corresponding to proximal and medial fluvial deposits was cemented by Cc0 and Cc1 calcite cements. Although Cc0 is relatively scarce in intergranular porosity, it precipitated in different lithofacies. As the predominant cement, Cc1 occluded the remaining intergranular porosity of host rocks in all lithofacies and structural positions.

In the Puig-reig anticline, the external hydrothermal fluids migrated from relatively more internal and deeper parts of the SE Pyrenees along connected thrusts and their damage zones. Such fluids flowed coevally with the anticline growth during horizontal compression. This resulted in the predominant Cc1 cement in both intergranular porosity and fractures. At foreland basin margins or fold-and-thrust belts, fracturing, thrusting and folding are generally accompanied by the fluid flow of various external fluids. Connected fracture networks allow fluid migration across different hydrostratigraphic units (Evans and Fischer, 2012; Evans et al., 2012). The intensive deformation and sufficient external fluids result in changes of fluid conditions in host rocks and fractures, including temperature, pressure, pH, Eh, solute concentration, and thus provide the material sources and physical-chemical conditions for cementation (Bons et al., 2012). Thus, prevalent calcite cement can develop in detrital rocks and their hosting fracture networks at basin margins (Fig. 22A), such as the Berga Group and the Solsona Formation at the north-eastern margin of the Ebro Basin (Cruset et al., 2016), the Peraltilla and Sariñena Formations at the northern margin of the central Ebro Basin (Yuste et al., 2004), or the Siwalik Group near the frontal thrusts in the Himalayan Basin (Guilbaud et al., 2012), among many other examples.

Apart from the external sources, detrital carbonates can provide the internal sources for calcite cementation in detrital rocks by dissolution-reprecipitation (Morad, 1998). Carbonate grains are relatively rare in sandstones due to strong chemical weathering during sediment transport (Morad et al., 2010). However, tectonically active settings, such as those in foreland basin margins and fold-and-thrust belts, provide short time and distance for sediment exposure and transportation, thus resulting in relatively weak chemical weathering of these detrital carbonates (Zuffa, 1985). Extrabasinal carbonate grains can become an important component of sandstones in these settings,

such as in the northern Ebro Basin (Yuste et al., 2004), the northern Apennines (Valloni and Zuffa, 1984), and the Laramide Foreland of southwestern Montana (Ingersoll et al., 1987). Detrital carbonates, such as biogenic carbonates, can provide the material sources for calcite cement by dissolution and favour the growth of cement by providing favourable nucleation substrates (Walderhaug and Bjørkum, 1998).

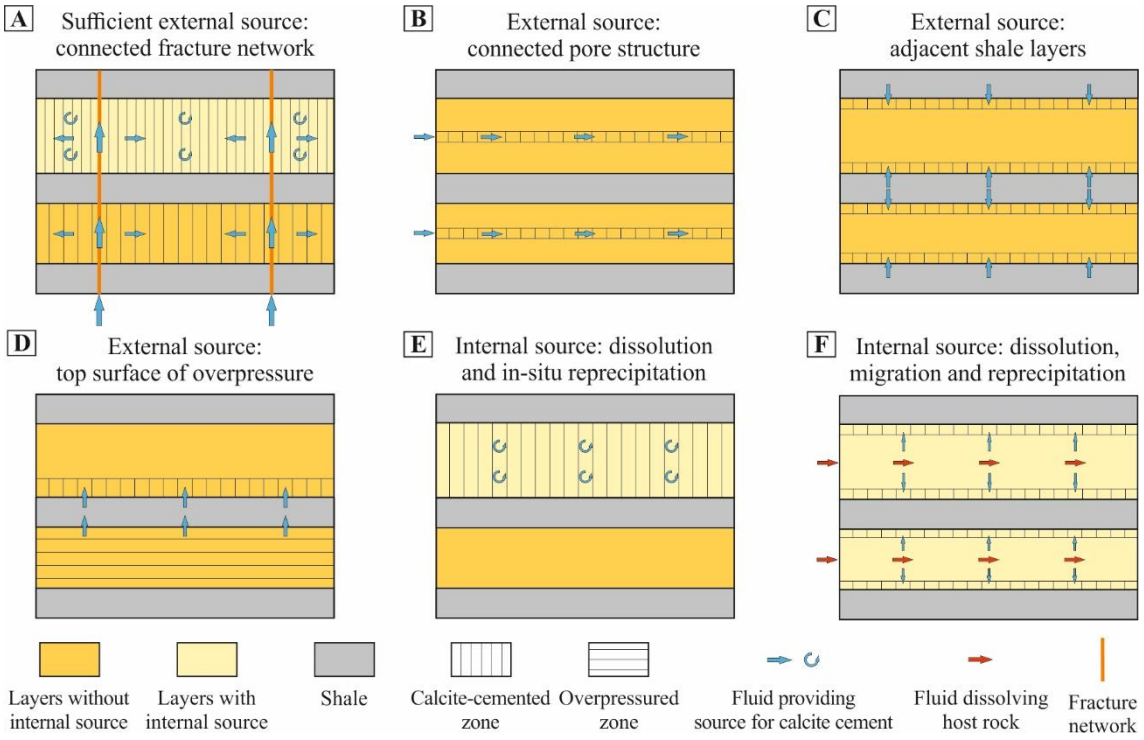

Figure 22. Schematic diagram of calcite cementation and distribution in detrital rocks in different settings. (A) Sufficient external sources migrate through connected fracture network; (B) External sources migrate through connected pore structure; (C) External sources migrate from adjacent shale layers; (D) External sources migrate from the top surface of an overpressured compartment; (E) Internal sources from host rocks: in-situ dissolution-reprecipitation; (F) Internal sources from host rocks: dissolution-migration-reprecipitation.

In settings not featuring intensive deformation and sufficient external fluids, calcite cement tends to show heterogeneous distributions in sandstones, including continuously cemented layers, stratabound or scattered concretions, and patchy cements (Walderhaug and Bjørkum, 1998). In settings relying on external sources migrated from their adjacent layers through the connected pore structures of host rocks, reservoir quality and lithofacies assemblages may exert a significant

effect on cement distribution. Some studies documented that calcite tends to precipitate in more permeable reservoirs because these reservoirs favour fluid flow from which cements can precipitate (Fig. 22B) (McBride et al., 1995; Dutton et al., 2002; Hall et al., 2004; Van Den Bril and Swennen, 2009). Other studies revealed that more intense calcite precipitation tends to occur along reservoir margins where sandstone reservoirs pinch out into fine deposits or are in contact with fine deposits (Fig. 22C), *e.g.,* the Lower Cretaceous Pendência Formation in the Potiguar basin (Dos Anjos et al., 2000) and the Upper Permian Bell Canyon Formation in the Delaware Basin (Dutton, 2008). Organic acids generated during the maturation of organic matter in these fine deposits could result in the dissolution of carbonate elements, which could be transported to adjacent sandstone reservoirs and provide external fluids for calcite cement (Dos Anjos et al., 2000; Dutton, 2008). In addition, other studies documented that calcite cementation also occurs at the top of overpressured reservoirs, where periodic changes of fluid pressure and formation hydrochemical conditions resulted in calcite cement (Fig. 22D), *e.g.,* the overpressured sandstone reservoirs in the central Junggar Basin (He et al., 2009; Yang et al., 2010) and in the Dongying Depression of the Bohai Bay Basin (Han et al., 2012; Zhang et al., 2019). In settings containing internal sources for carbonate cement, such as biogenic carbonates and carbonate rock fragments (Walderhaug and Bjørkum, 1998), cement distribution tends to be controlled by the distribution of these internal sources through in-situ dissolution and reprecipitation (Fig. 22E), *e.g.,* the Fensfjord Formation (Walderhaug et al., 1989) and the Rannoch Formation (Bjørkum and Walderhaug, 1990) in the North Sea. In addition, Liu et al. (2019) concluded a different fluid-rock interaction model of dissolution, migration and re-precipitation in the Xujiahe Formation of the Sichuan Basin. Hydrocarbon-related acidic fluids tend to flow along the more permeable reservoirs, resulting in intensive dissolution in coarse reservoirs, whereas intensive re-precipitation occurs in the marginal impermeable fine reservoirs (Fig. 22F).

4.2.5 Reservoir potential of the Puig-reig anticline

Based on the distribution of calcite cement, porosity, fracture intensity and lithofacies in the Puig-reig anticline, here we discuss the controlling factors of reservoir quality and the reservoir potential of the folded fluvial succession in the Puig-reig anticline in the SE Pyrenees.

Intergranular porosity of host rocks is mainly controlled by the sedimentary characteristics of deposits and the diagenetic processes they experience (Dos Anjos et al., 2000; Bjørlykke, 2014). In the Puig-reig anticline, the fluvial deposits present an overall low intergranular porosity due to compaction and cementation (Fig. 17), but which varies across the different lithofacies. Relatively higher porosity concentrates in lithofacies Sch and Sm in the medial fluvial fan, regardless of their relatively higher cement content with respect to other lithofacies (Fig. 16). Compared to lithofacies Sl and F, Sch and Sm show low contents of ductile matrix. Compared to conglomeratic facies, these medium to coarse sandstones present better grain sorting and lower matrix content. Based on the original porosity of sandstone and siltstone (35% on average), the porosity destroyed by compaction of lithofacies Sch and Sm mainly ranges from 40% to 70% with 57% on average, whereas that of lithofacies Sl and F mainly ranges from 55% to 75% with 63% on average and from 60% to 85% with 73% on average, respectively. Based on the original porosity of conglomerate (32% on average), the porosity destroyed by compaction of conglomerate lithofacies ranges mainly ranges from 60% to 72 with 67% on average. Lithofacies Sch and Sm experience relatively weaker compaction, resulting in more residual intergranular volume, which can provide more space for cementation and residual porosity. This is the main reason for the coexistence of relatively high residual porosity and calcite content in lithofacies Sch and Sm.

Fracture networks have a significant impact on reservoir performance. Based on the systematic analysis of the fracture network of the Puig-reig anticline, fracture intensity is mainly controlled by the structural position, bedding thickness and lithological associations. The crest and crest-limb transition zones present relatively higher fracture intensity due to the greater curvature and finite strain they experience compared to the limbs, if a Tangential Longitudinal Strain model (TLS) is assumed (Hudleston and Treagus, 2010). This observation is consistent with some previous studies of fracture distribution in folds (*e.g.,* Iñigo et al., 2012; Awdal et al., 2013; Watkins et al., 2015). Relatively thinner sandstone layers tend to present higher fracture intensity than thick conglomerate layers in all structural positions, which is also consistent with some previous fracture studies (*e.g.,* Florez-Niño et al., 2005; Wennberg et al., 2007). In addition, the lithological association of competent conglomerate or sandstone with interlayered fine deposits

in medial fluvial deposits favours the development of abundant fractures, compared to other lithological associations. Based on the analysis above, lithofacies Sl and Sm in the medial fluvial fan located in the crest and crest-limb transition zones of the anticline feature relatively higher fracture intensity than other structural positions and lithofacies.

Based on the distributions of calcite cement, porosity and fracture intensity in the Puig-reig anticline, the medial fluvial sandstones in the crest and crest-limb transition zones (35-55% of all lithofacies in these zones) present relatively greater potential to be effective reservoirs due to the high fracture intensity (1-3.5 m^{-1}). The northern limb presents relatively high percentages of sandstone and conglomerate reservoir deposits (65-100%) and lower percentages of fine deposits (0-35%), especially in the northwest zone of the anticline. However, the sandstone and conglomerate bodies have low potential to become effective reservoirs due to their low porosity (<1.5%) and fracture intensity (<1.2 m^{-1}). The southern limb presents relatively higher percentages of sandstones (50-65%) and very low percentages of conglomerates (0-15%). The sandstones have relatively low fracture intensity (<1.5 m^{-1}), but present some reservoir potential in Sch and Sm lithofacies due to relatively higher porosity (3.9% on average).

4.3 Reservoir potential of folded fluvial successions at foreland basin margins

As one of the dominant sedimentary systems at the active margins of non-marine foreland basins, alluvial and fluvial fans tend to present heterogeneous reservoir potential due to the interplay between complex sedimentary, diagenetic and deformation processes. Unravelling their reservoir characteristics is therefore key to the success of subsurface operations in these settings.

Compared to fluvial fans, alluvial fans present a radial-limited fan extent (Blair and McPheerson, 1994). Debris-flow alluvial fans tend to present poor primary reservoir quality due to texturally immature debris deposited from debris flows and hyperconcentrated flows (Sohn et al., 1999). These deposits have varied reservoir connectivity depending on their abundance in local sedimentary systems (Moscariello, 2018). On the other hand, water-lain alluvial fans,

generally dominated by sheet floods, have better reservoir potential due to the presence of relatively better sorted deposits and reservoir connectivity (Sohn et al., 1999; Moscariello, 2005). At basin margins, proximal fluvial deposits tend to consist of amalgamated channel belts with limited preservation of fine deposits (Weissmann et al., 2013). Thick conglomerate bodies can occur in proximal fluvial deposits (Vincent, 2002), which can be associated with channelised non-cohesive gravity or hyperconcentrated flows (Moscariello, 2018). Besides, flash floods can develop in these proximal fluvial environments, *e.g.,* in the Puig-reig anticline in the eastern Ebro Basin and other cases in the central Ebro Basin (Luzón, 2001, 2005), resulting in large and coarse sheet-like deposits. Compared to debris-flow alluvial fans, these proximal fluvial deposits can present higher reservoir potential due to their higher textural maturity and better reservoir connectivity. Apart from alluvial proximal fluvial fans, a large part of the basin marginal deposits comes from medial fluvial fans, dominated by channel belts with varied overbank fine deposits. Although medial fluvial deposits present a downstream reduction of the reservoir volume and a corresponding increase of overbank fine deposits, they are still dominated by conglomerate or sandstone reservoirs at basin margins and present higher textural maturity resulting in better primary reservoir quality. These proximal to medial fluvial fans present the highest potential in the Puig-reig structure to be effective reservoirs provided they do not undergo strong compaction and cementation processes.

Intensive diagenesis can result in low porosity and permeability, and thus reduce the reservoir potential in alluvial-fluvial deposits (Morad et al., 2010; Lai et al., 2018). Calcite cement is one of the prevailing authigenic minerals in these deposits (Hall et al., 2004; Taylor and Machent, 2011). As discussed in Section 3.2.4, the distribution pattern of calcite cement varies in different settings. At foreland basin margins or fold-and-thrust belts, fracturing, thrusting and folding are generally accompanied by the flow of various external fluids across different hydrostratigraphic units. Some of these external fluids can provide the material sources and physical-chemical conditions for calcite cementation (Bons et al., 2012). Besides, in tectonically active settings, such as foreland basin margins, carbonate extrabasinal grains can become an important source of sediment supply in alluvial-fluvial systems (Valloni and Zuffa, 1984; Morad et al., 2010). These

carbonates can provide the material sources for calcite cement by dissolution and favour the growth of cement by providing favourable nucleation substrates (Walderhaug and Bjørkum, 1998). Thus, calcite can develop as the prevalent cement in alluvial-fluvial deposits at foreland basin margins that experience intensive deformation accompanied by sufficient external fluids and/or host abundant detrital carbonates.

Calcite cementation is widely considered an important factor controlling reservoir quality because of its ability to reduce porosity and permeability (Davis et al., 2006; Xiong et al., 2016). As an example of this control, intensive calcite cementation filled most intergranular pores and resulted in the overall low porosity of host rocks in the Puig-reig anticline. However, calcite cements tend to precipitate in more permeable reservoirs (McBride et al., 1995; Dutton et al., 2002; Hall et al., 2004; Van Den Bril and Swennen, 2009). For example, in the Puig-reig anticline, medium-coarse sandstones in medial fluvial fan with higher porosity show higher calcite content (Fig. 16B). In addition, early calcite cement can affect the later evolution of reservoir quality (Hosa and Wood, 2017). For example, early cements can preserve intergranular space and improve reservoir quality by providing secondary porosity under the specific circumstance of intensive dissolution during later diagenetic stages, *e.g.,* the Upper Jurassic Ti-3 sandstones in the Flemish Pass Basin (Xiong et al., 2016), the Biyadh Formation in the western central Masila Basin (Hakimi et al., 2012), and the Lower Devonian Jauf Formation in Saudi Arabia (Al-Ramadan et al., 2004). Besides, mechanical contrasts between layers could be affected by the distribution of early calcite cement, which could have a significant effect on fracture development and thus reservoir potential, an effect observed for example in the Madison Formation in the Sheep Mountain of the Bighorn Basin (Barbier et al., 2012) and the Calcare Massiccio unit in the Umbria–Marche Apennines (Di Naccio et al., 2005). Thus, to determine the distribution of calcite cements and their real effects on reservoir potential, the specific geological backgrounds of host rocks should be fully considered.

At foreland basin margins, fracture networks are widely developed accompanied with intensive deformation in fold-and-thrust belts (Iñigo et al., 2012; Liu et al., 2017). These fracture networks can play a fundamental role both in fluid migration and the resulting reservoir quality, especially

in reservoirs with low porosity and permeability of host rocks (Casini et al., 2011; Watkins et al., 2018; Wang et al., 2020). However, systematic fracture assessment in subsurface rocks is limited by the inability of sampling subseismic-scale fractures and fractures with greater dimensions than that of the accessible rock volumes in boreholes (Ortega et al., 2006; Iñigo et al., 2012). Thus, a common strategy is to use outcrop analogues to extend sampling demonstrations, understand the controlling factors of fracture networks and reduce uncertainties in subsurface predictions (Sanderson, 2016; Miranda et al., 2018). Although many fractures are sealed by calcite cement in the Puig-reig anticline it can still be used as a reservoir analogue to explore the fracture distribution pattern and reservoir potential in folded clastic sediments, especially in the research context that fracturing in siliciclastic fold and thrust belts is much less documented than that in carbonate systems (Watkins et al., 2015a). Fracture intensity can be controlled by multiple factors in folded sedimentary successions, mainly including the sedimentary characteristics and the structural position. Fracture intensity and connectivity tend to be higher in high strain fold crests or forelimbs, such as in the cases of the Puig-reig anticline in the South-eastern Pyrenees, the Achnashellach Culmination in the Southern Moine Thrust Belt (Watkins et al., 2015b), or the Sub-Andean fold-thrust belt (Iñigo et al., 2012).

In alluvial-fluvial deposits, variable sedimentary characteristics can exert significant effects on fracture intensity. Proximal fluvial deposits, dominated by large and thick conglomerate and sandstone layers, tend to have lower fracture intensity than medial fluvial deposits that are defined by interlayered conglomerate or sandstone layers and fine deposits. This is because fracture intensity tends to present a negative correlation with bedding thickness (Huang and Angelier, 1989; Florez-Niño et al., 2005). Besides, the interlayered competent conglomerate or sandstone layers and incompetent fine deposits in medial fluvial deposits result in high competence contrast between these distinct mechanical stratigraphic layers, which favours the development of joints or faults (Sibson, 1996; Wilkins et al., 2014). For tight conglomerate and sandstone reservoirs at basin margins, fracture networks can significantly improve reservoir potential (Watkins et al., 2018).

In summary, compared to deposits in basin centre localities where reservoir quality is mainly

controlled by depositional and diagenetic characteristics, basin marginal reservoirs are most likely to be tectonically deformed and feature variable fracture networks. Intergranular porosity is mainly controlled by depositional facies and diagenetic alterations, while fracture networks are mainly controlled by structural position and depositional characteristics. In the right circumstances an effective combination of both structure and facies can make basin margin locations potential areas for effective reservoirs for carbon storage, even in the presence of low porosity.

4.4 Future work

The study conducted in the Puig-reig anticline provides a conceptual model useful to understand the reservoir (and storage site) characteristics at the basin margins. Based on the results obtained in the sedimentology, fracture and diagenesis studies, future work will focus on building static and dynamic reservoir models of the Puig-reig anticline, following the general workflow of reservoir modelling (Fig. 23) (King, 2011). The final aim is to determine whether such folded fluvial successions at foreland basin margins can become effective reservoirs for CO_2 storage, to understand the main controls on storage capacity and potential leakage, and thus to guide the subsurface operations of CO_2 storage in such a geological setting.

Static models show the three-dimensional geometric features and properties (such as porosity, permeability and fracture networks) of rocks and their spatial variations (Pranter et al., 2014; Soleimani and Jodeiri Shokri, 2015; Martinius et al., 2017), and thus provide a framework to characterise reservoir heterogeneities for CO_2 storage (Issautier et al., 2014). By compiling a range of geological data (distribution of sedimentary units and main structures, cements, porosities and permeabilities of host rocks, and upscaled permeability tensors of fracture networks), different sets of reservoir models will be built, in order to cover all the range of scenarios depending on the distribution of petrophysical properties of the different units. These models will be used to assess the distribution and static storage capacity of reservoirs in the fold system.

Dynamic models allow the assessments of effective storage capacity, injectivity and trapping

mechanisms, fluid migration and propagation of CO_2 plume, pressure buildup, potential leakage risks, etc. (Frykman et al., 2009; Hosseini et al., 2013; Soltanian et al., 2019). Issautier et al. (2013, 2016) carried out dynamic modelling in fluvial reservoirs, which revealed that the reservoir heterogeneities caused by sedimentary processes exert significant impacts on CO_2 storage capacity and performance. In the Puig-reig anticline, the static models generated will be finally used as frameworks for the modelling of CO_2 injection in the fluvial reservoirs with not only heterogeneous sedimentary characteristics but also heterogeneous fracture and cement distribution. A series of fluid flow simulations will be carried out to test the total capacity of the target structure, as well as to characterise fluid migration and storage efficiency of supercritical CO_2 during and after injection.

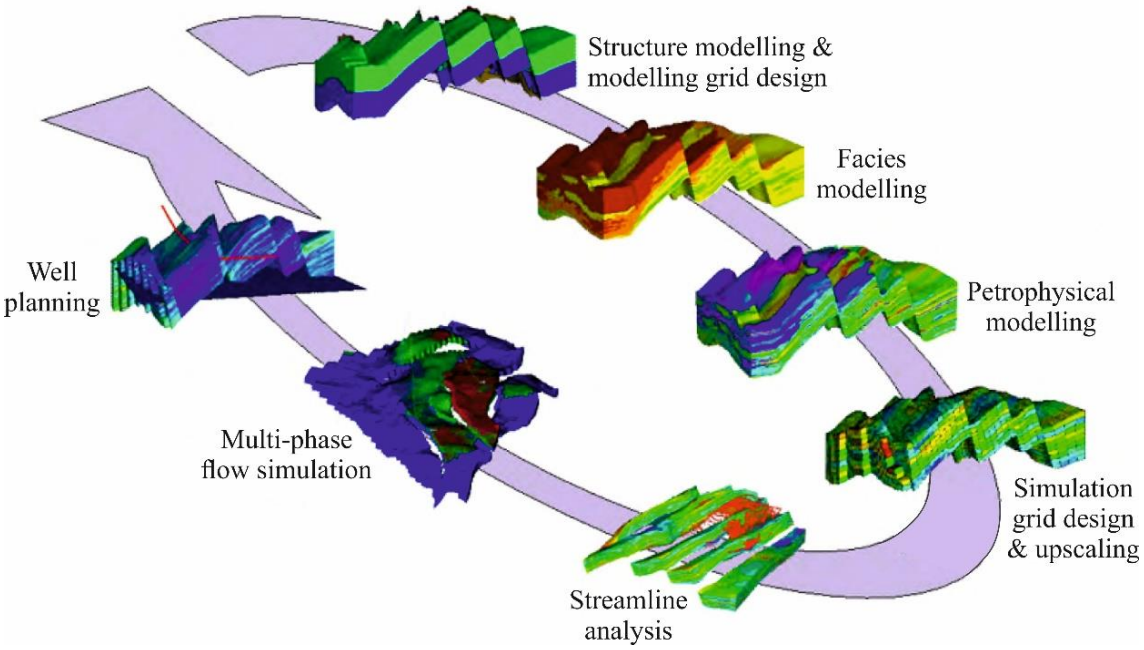

Figure 23. Integrated workflow of reservoir modelling (King, 2011).

5 Conclusions

This doctoral thesis was conceived to assess the potential of CCS development in compressional basins and hydrocarbon-limited countries. These assessments ranged from a global-scale assessment to a national-scale evaluation in Spain to a reservoir-scale assessment using the Puig-reig anticline (SE Pyrenees) as an outcrop analogue. The following main conclusions from this Ph.D. thesis can be highlighted:

- A source-to-sink assessment methodology has been employed to evaluate the potential of compressional basins for CCS development based on basin distribution, hydrocarbon resources and CO_2 emissions. Compressional settings host some of the most significant hydrocarbon-bearing basins and 36% of inland CO_2 emissions worldwide. Five high-priority regions have been selected for CCS development: North America, north-western South America, south-eastern Europe, western Middle East, and western China. In these regions, hydrocarbon-bearing basins have large proven capacity to safely retain fluids over geological timescales, substantial subsurface data and infrastructure in place suitable for re-use, as well as sufficient emission sources. These aspects make them priority targets for the development of CCS projects in compressional basins.
- An integrated source-sink assessment methodology based on a hubs and clusters strategy has been applied to the case of Spain to identify favourable regions for CCS deployment and to develop strategies to integrate CCS into the decarbonisation strategy in this hydrocarbon-limited country. 15 priority source-to-sink clusters and four high-potential CCS development regions have been identified in Spain. NW and NE Spain can be considered the two priority regions for CCS development due to resilience provided by different types of CO_2 sources and multiple geological structures. CCS, especially in the hard-to-abate sector, and in combination with other low-carbon energies (*e.g.,* blue hydrogen and bioenergy), remains a significant contributor to the Paris Agreement's mid-century net-zero target.
- In hydrocarbon-limited compressional basins, there is very low availability of geological

and geophysical data to assess the suitability of geological structures for CO_2 storage, such as the Ebro Foreland Basin in Spain. The Puig-reig anticline (SE Pyrenees) has been selected as an outcrop analogue to explore the reservoir potential of similar subsurface sedimentary systems at foreland basin margins. In this anticline, the exposed outcrops belong to the Camps de Vall-Llonga and Solsona Formations, which were deposited from a proximal to medial fluvial fan system with an overall south-east downstream trend. The proximal deposits were deposited from unconfined flash floods and wide-shallow channel streams. They are dominated by thick and large sheet-like conglomerate bodies with minor interlayered sandstones, and mainly spread in the northwest portion of the anticline. The medial deposits were deposited from braided channel streams and overbanks, dominated by the interbedded conglomerates, sandstones and claystones, which finally transferred to terminal deposits in the distal portion close to the basin centre.

- The linear scanline method has been used to systematically collect fracture data in different zones of the Puig-reig anticline, allowing to unravel the main depositional and structural controls on the distribution of fracture networks. Four main sets of fractures (F1 to F4) have been identified, *i.e.,* the NNW-SSE, ENE-WSW, WNW-ESE and NNE-SSW sets. Based on multiple linear regression analysis, we have observed that fracture intensity is mainly controlled by the structural position, the bedding thickness and lithological associations. Sandstone layers with multiple interlayers of fine deposits from the medial fluvial and located in the anticline crest feature relatively more intense fracturing. Fracture length is mainly controlled by bedding thickness and is affected by lithological associations. Fracture aperture is mainly controlled by lithology, with relatively larger values developed in conglomerate layers.
- An integrated analysis of structural, petrological and geochemical characteristics has allowed the identification of five generations of calcite cements (Cc0 to Cc4) in veins and host rocks, and with them unravel the volution of fluid regimes in the Puig-reig anticline. Predating the most intensive deformation stages, Cc0 precipitated in intergranular pores from meteoric fluids in the phreatic zone. During the most intense

phase of thrusting and folding, the predominant Cc1 cement precipitated in intergranular pores, faults and F1 to F4 fracture sets from hydrothermal fluids migrated from the internal and deeper parts of the SE Pyrenees. In the late stage of the anticline growth, Cc2 mainly developed in normal and strike-slip faults in the anticline crest. Cc2 could precipitate from the mixing between hydrothermal and meteoric fluids during the crest collapse or from hydrothermal fluids that kept their meteoric signatures and were buried shallower than those that formed Cc1. Cc3 developed in F1 and F4 fracture sets in the western zone of the north limb from formation fluids with temperatures between 50°C and 62°C and migrated through the frontal thrusts. During the continuous denudation, Cc4 precipitated in reopened F1 to F4 fracture sets across the anticline from meteoric fluids with temperatures between 16°C and 19°C.

- In the Puig-reig anticline, the predominant calcite cement resulted from external fluids accompanied by compressional deformation and/or from substantial detrital carbonates of host rocks, resulting in the low porosity of host rocks. Limited high porosity concentrated in massive medium and coarse lithofacies in the medial fluvial fan. In the context of overall low porosity, sandstone lithofacies deposited from the medial fluvial fan and located in the high strain zones present relatively higher potential to be effective reservoirs due to their high fracture intensity. At basin margins, reservoir potential is comprehensively controlled by sedimentology, diagenesis and deformation. An effective combination of both structure and facies can make basin margin locations potential areas for effective reservoirs, even in the case of low porosity.

In summary, the source-to-sink assessment reveals that compressional basins can play an essential role in global CCS development, especially in certain regions with high CO_2 emissions and dominated by compressional settings. The source-to-sink assessment methodology based on a hubs and clusters strategy is suitable for hydrocarbon-limited countries to attract renewed public and political interest in viable deployment pathways of CCS. In hydrocarbon-limited compressional basins, outcrop studies can play an important role in improving the accuracy of reservoir prediction in the subsurface by providing reliable geological conceptual models in

complex areas, such as the case of the Puig-reig anticline. Based on the results obtained in the sedimentology, fracture and diagenesis studies, future work will focus on building static and dynamic models of the Puig-reig anticline to understand the main controls on storage capacity, storage efficiency and fluid migration, and thus to guide the subsurface operations of CO_2 storage in such a geological setting.

Bibliography

Adlan, Q., Davies, A.J., John, C.M., 2020. Effects of oxygen plasma ashing treatment on carbonate clumped isotopes. Rapid Communications in Mass Spectrometry 34, e8802. https://doi.org/10.1002/rcm.8802

Al-Ramadan, K.A., Hussain, M., Imam, B., Saner, S., 2004. Lithologic characteristics and diagenesis of the Devonian Jauf sandstone at Ghawar Field, Eastern Saudi Arabia. Marine and Petroleum Geology 21, 1221–1234. https://doi.org/10.1016/j.marpetgeo.2004.09.002

Alcalde, J., Flude, S., Wilkinson, M., Johnson, G., Edlmann, K., Bond, C.E., Scott, V., Gilfillan, S.M.V., Ogaya, X., Haszeldine, R.S., 2018. Estimating geological CO2 storage security to deliver on climate mitigation. Nature Communications 9, 2201. https://doi.org/10.1038/s41467-018-04423-1

Alcalde, J., Heinemann, N., Mabon, L., Worden, R.H., de Coninck, H., Robertson, H., Maver, M., Ghanbari, S., Swennenhuis, F., Mann, I., Walker, T., Gomersal, S., Bond, C.E., Allen, M.J., Haszeldine, R.S., James, A., Mackay, E.J., Brownsort, P.A., Faulkner, D.R., Murphy, S., 2019. Acorn: Developing full-chain industrial carbon capture and storage in a resource- and infrastructure-rich hydrocarbon province. Journal of Cleaner Production 233, 963–971. https://doi.org/10.1016/j.jclepro.2019.06.087

Anderson, N.T., Kelson, J.R., Kele, S., Daëron, M., Bonifacie, M., Horita, J., Mackey, T.J., John, C.M., Kluge, T., Petschnig, P., Jost, A.B., Huntington, K.W., Bernasconi, S.M., Bergmann, K.D., 2021. A unified clumped isotope thermometer calibration (0.5–1,100°C) using carbonate-based standardization. Geophysical Research Letters 48, e2020GL092069. https://doi.org/10.1029/2020GL092069

Andrews, B.J., Roberts, J.J., Shipton, Z.K., Bigi, S., Tartarello, M.C., Johnson, G., 2019. How do we see fractures? Quantifying subjective bias in fracture data collection. Solid Earth 10, 487–516. https://doi.org/10.5194/se-10-487-2019

Arenas, C., 1993. Sedimentología y paleogeografía del Terciario del margen pirenaico y sector central de la cuenca del Ebro (zona aragonesa occidental). PhD thesis, University of Zaragoza, Zaragoza.

Arenas, C., Millán, H., Pardo, G., Pocoví, A., 2001. Ebro Basin continetal sedimentation associated with late compressional Pyrenean tectonics (North-Eastern lberia): Controls on basin margin fans and fluvial systems. Basin Research 13, 65–89. https://doi.org/10.1046/j.1365-2117.2001.00141.x

Awdal, A.H., Braathen, A., Wennberg, O.P., Sherwani, G.H., 2013. The characteristics of fracture

networks in the Shiranish Formation of the Bina Bawi Anticline; comparison with the Taq Taq Field, Zagros, Kurdistan, NE Iraq. Petroleum Geoscience 19, 139–155. https://doi.org/10.1144/petgeo2012-036

Bachu, S., 2003. Screening and ranking of sedimentary basins for sequestration of CO2 in geological media in response to climate change. Environmental Geology 44, 277–289. https://doi.org/10.1007/s00254-003-0762-9

Banner, J.L., 1995. Application of the trace element and isotope geochemistry of strontium to studies of carbonate diagenesis. Sedimentology 42, 805–824. https://doi.org/10.1111/j.1365-3091.1995.tb00410.x

Barbier, M., Hamon, Y., Callot, J.P., Floquet, M., Daniel, J.M., 2012. Sedimentary and diagenetic controls on the multiscale fracturing pattern of a carbonate reservoir: The Madison Formation (Sheep Mountain, Wyoming, USA). Marine and Petroleum Geology 29, 50–67. https://doi.org/10.1016/j.marpetgeo.2011.08.009

Barrier, L., Proust, J.N., Nalpas, T., Robin, C., Guillocheau, F., 2010. Control of alluvial sedimentation at foreland-basin active margins: A case study from the northeastern Ebro Basin (southeastern Pyrenees, Spain). Journal of Sedimentary Research 80, 728–749. https://doi.org/10.2110/jsr.2010.069

Basque Government, 2019. Registro vasco de emisiones y fuentes contaminantes del 2018 (EPER Euskadi / E-PRTR) [WWW Document]. URL https://www.euskadi.eus/registro-vasco-de-emisiones-y-fuentes-contaminantes-del-2018-eper-euskadi-e-prtr/web01-a2inginf/es/ (accessed 10.1.20).

Bellahsen, N., Fiore, P., Pollard, D.D., 2006. From spatial variation of fracture patterns to fold kinematics: A geomechanical approach. Geophysical Research Letters 33, 1–4. https://doi.org/10.1029/2005GL024189

Bernasconi, S.M., Daëron, M., Bergmann, K.D., Bonifacie, M., Meckler, A.N., Affek, H.P., Anderson, N., Bajnai, D., Barkan, E., Beverly, E., Blamart, D., Burgener, L., Calmels, D., Chaduteau, C., Clog, M., Davidheiser-Kroll, B., Davies, A., Dux, F., Eiler, J., Elliott, B., Fetrow, A.C., Fiebig, J., Goldberg, S., Hermoso, M., Huntington, K.W., Hyland, E., Ingalls, M., Jaggi, M., John, C.M., Jost, A.B., Katz, S., Kelson, J., Kluge, T., Kocken, I.J., Laskar, A., Leutert, T.J., Liang, D., Lucarelli, J., Mackey, T.J., Mangenot, X., Meinicke, N., Modestou, S.E., Müller, I.A., Murray, S., Neary, A., Packard, N., Passey, B.H., Pelletier, E., Petersen, S., Piasecki, A., Schauer, A., Snell, K.E., Swart, P.K., Tripati, A., Upadhyay, D., Vennemann, T., Winkelstern, I., Yarian, D., Yoshida, N., Zhang, N., Ziegler, M., 2021. InterCarb: A community effort to improve interlaboratory standardization of the carbonate clumped isotope thermometer

using carbonate standards. Geochemistry, Geophysics, Geosystems 22, e2020GC009588. https://doi.org/10.1029/2020GC009588

Bernasconi, S.M., Hu, B., Wacker, U., Fiebig, J., Breitenbach, S.F.M., Rutz, T., 2013. Background effects on Faraday collectors in gas-source mass spectrometry and implications for clumped isotope measurements. Rapid Communications in Mass Spectrometry 27, 603–612. https://doi.org/10.1002/rcm.6490

Bird, K.J., Charpentier, R.R., Gautier, D.L., Houseknecht, D.W., Klett, T.R., Pitman, J.K., Moore, T.E., , Schenk, C J, Tennyson, M E, Wandrey, C.R., 2008. Circum-Arctic resource appraisal : Estimates of undiscovered oil and gas north of the Arctic Circle. United States Geological Survey. https://doi.org/10.3133/fs20083049

Bjørkum, P.A., Walderhaug, O., 1990. Lateral extent of calcite-cemented zones in shallow marine sandstones. In: Buller, A.T., Berg, E., Hjelmeland, O., Kleppe, J., Torsæter, O., Aasen, J.O. (Eds.), North Sea Oil and Gas Reservoirs—II. Springer, Dordrecht, 331–336. https://doi.org/10.1007/978-94-009-0791-1_28

Bjørlykke, K., 2014. Relationships between depositional environments, burial history and rock properties. Some principal aspects of diagenetic process in sedimentary basins. Sedimentary Geology 301, 1–14. https://doi.org/10.1016/j.sedgeo.2013.12.002

Blair, T.C., 2003. Features and origin of the giant Cucomungo Canyon alluvial fan, Eureka Valley, California. In: Chan, M.A., Archer, A.. (Eds.), Extreme Depositional Environments: Mega End Members in Geologic Time. Geological Society of America Special Papers, 105–126. https://doi.org/10.1130/0-8137-2370-1.105

Blair, T.C., McPheerson, J.G., 1994. Alluvial fans and their natural distinction from rivers based on morphology, hydraulic processes, sedimentary processes, and facies assemblages. Journal of Sedimentary Research 64, 450–489. https://doi.org/10.1306/D4267DDE-2B26-11D7-8648000102C1865D

Boggs, S., Krinsley, D., 2006. Application of Cathodoluminescence Imaging to the Study of Sedimentary Rocks. Cambridge University Press, Cambridge. https://doi.org/10.1017/cbo9780511535475

Boletín Oficial del Estado, 2010. Ley 40/2010, de 29 de diciembre, de almacenamiento geológico de dióxido de carbono [WWW Document], BOE. URL https://www.boe.es/eli/es/l/2010/12/29/40/con (accessed 2.17.21).

Bond, C.E., Wightman, R., Ringrose, P.S., 2013. The influence of fracture anisotropy on CO2 flow. Geophysical Research Letters 40, 1284–1289. https://doi.org/10.1002/grl.50313

Bons, P.D., Elburg, M.A., Gomez-Rivas, E., 2012. A review of the formation of tectonic veins

and their microstructures. Journal of Structural Geology 43, 33–62. https://doi.org/10.1016/j.jsg.2012.07.005

Bons, P.D., Fusswinkel, T., Gomez-Rivas, E., Markl, G., Wagner, T., Walter, B., 2014. Fluid mixing from below in unconformity-related hydrothermal ore deposits. Geology 42, 1035–1038. https://doi.org/10.1130/G35708.1

Bons, P.D., Gomez-Rivas, E., 2020. Origin of meteoric fluids in extensional detachments. Geofluids 2020, 1–8. https://doi.org/10.1155/2020/7201545

Brownsort, P.A., Scott, V., Haszeldine, R.S., 2016. Reducing costs of carbon capture and storage by shared reuse of existing pipeline-Case study of a CO2 capture cluster for industry and power in Scotland. International Journal of Greenhouse Gas Control 52, 130–138. https://doi.org/10.1016/j.ijggc.2016.06.004

Budinis, S., Krevor, S., Dowell, N. Mac, Brandon, N., Hawkes, A., 2018. An assessment of CCS costs, barriers and potential. Energy Strategy Reviews 22, 61–81. https://doi.org/10.1016/j.esr.2018.08.003

Bui, M., Adjiman, C.S., Bardow, A., Anthony, E.J., Boston, A., Brown, S., Fennell, P.S., Fuss, S., Galindo, A., Hackett, L.A., Hallett, J.P., Herzog, H.J., Jackson, G., Kemper, J., Krevor, S., Maitland, G.C., Matuszewski, M., Metcalfe, I.S., Petit, C., Puxty, G., Reimer, J., Reiner, D.M., Rubin, E.S., Scott, S.A., Shah, N., Smit, B., Trusler, J.P.M., Webley, P., Wilcox, J., Mac Dowell, N., 2018. Carbon capture and storage (CCS): the way forward. Energy & Environmental Science 11, 1062–1176. https://doi.org/10.1039/C7EE02342A

Cantarero, I., Travé, A., Alías, G., Baqués, V., 2014. Polyphasic hydrothermal and meteoric fluid regimes during the growth of a segmented fault involving crystalline and carbonate rocks (Barcelona Plain, NE Spain). Geofluids 14, 20–44. https://doi.org/10.1111/gfl.12021

Cantarero, I., Travé, A., Alías, G., Baqués, V., 2010. Pedogenic products sealing normal faults (Barcelona Plain, NE Spain). Journal of Geochemical Exploration 106, 44–52. https://doi.org/10.1016/j.gexplo.2010.02.004

Carrigan, J.H., Anastasio, D.J., Kodama, K.P., Parés, J.M., 2016. Fault-related fold kinematics recorded by terrestrial growth strata, Sant Llorenç de Morunys, Pyrenees Mountains, NE Spain. Journal of Structural Geology 91, 161–176. https://doi.org/10.1016/j.jsg.2016.09.003

Casini, G., Gillespie, P.A., Vergés, J., Romaire, I., Fernández, N., Casciello, E., Saura, E., Mehl, C., Homke, S., Embry, J.C., Aghajari, L., Hunt, D.W., 2011. Sub-seismic fractures in foreland fold and thrust belts: Insight from the Lurestan Province, Zagros Mountains, Iran. Petroleum Geoscience 17, 363–282. https://doi.org/10.1144/1354-079310-043

Cerling, T.E., 1984. The stable isotopic composition of modern soil carbonate and its relationship

to climate. Earth and Planetary Science Letters 71, 229–240. https://doi.org/10.1016/0012-821X(84)90089-X

Cerling, T.E., Quade, J., 1993. Stable carbon and oxygen isotopes in soil carbonates. In: Swart, P.K., Lohmann, K.C., McKenzie, J., Savin, S. (Eds.), Climate Change in Continental Isotopic Records. Geophysical Monograph. American Geophysical Union, Washington, DC, 217–231. https://doi.org/10.1029/GM078p0217

Consoli, C.P., Wildgust, N., 2017. Current status of global storage resources. Energy Procedia 114, 4623–4628. https://doi.org/10.1016/j.egypro.2017.03.1866

Cooke, M.L., Underwood, C.A., 2001. Fracture termination and step-over at bedding interfaces due to frictional slip and interface opening. Journal of Structural Geology 23, 223–238. https://doi.org/10.1016/S0191-8141(00)00092-4

Costa, E., Garcés, M., López-Blanco, M., Beamud, E., Gómez-Paccard, M., Larrasoaña, J.C., 2010. Closing and continentalization of the South Pyrenean foreland basin (NE Spain): Magnetochronological constraints. Basin Research 22, 904–917. https://doi.org/10.1111/j.1365-2117.2009.00452.x

Cruset, D., Cantarero, I., Travé, A., Vergés, J., John, C.M., 2016. Crestal graben fluid evolution during growth of the Puig-reig anticline (South Pyrenean fold and thrust belt). Journal of Geodynamics 101, 30–50. https://doi.org/10.1016/j.jog.2016.05.004

Cruset, D., Cantarero, I., Vergés, J., John, C.M., Muñoz-López, D., Travé, A., 2018. Changes in fluid regime in syn-orogenic sediments during the growth of the south Pyrenean fold and thrust belt. Global and Planetary Change 171, 207–224. https://doi.org/10.1016/j.gloplacha.2017.11.001

Cui, Y., Jones, S.J., Saville, C., Stricker, S., Wang, G., Tang, L., Fan, X., Chen, J., 2017. The role played by carbonate cementation in controlling reservoir quality of the Triassic Skagerrak Formation, Norway. Marine and Petroleum Geology 85, 316–331. https://doi.org/10.1016/j.marpetgeo.2017.05.020

Davis, J.M., Roy, N.D., Mozley, P.S., Hall, J.S., 2006. The effect of carbonate cementation on permeability heterogeneity in fluvial aquifers: An outcrop analog study. Sedimentary Geology 184, 267–280. https://doi.org/10.1016/j.sedgeo.2005.11.005

Davis, S.J., Lewis, N.S., Shaner, M., Aggarwal, S., Arent, D., Azevedo, I.L., Benson, S.M., Bradley, T., Brouwer, J., Chiang, Y.-M., Clack, C.T.M., Cohen, A., Doig, S., Edmonds, J., Fennell, P., Field, C.B., Hannegan, B., Hodge, B.-M., Hoffert, M.I., Ingersoll, E., Jaramillo, P., Lackner, K.S., Mach, K.J., Mastrandrea, M., Ogden, J., Peterson, P.F., Sanchez, D.L., Sperling, D., Stagner, J., Trancik, J.E., Yang, C.-J., Caldeira, K., 2018. Net-zero emissions energy

systems. Science 360, eaas9793. https://doi.org/10.1126/science.aas9793

de Gibert, J.M., Sáez, A., 2009. Paleohydrological significance of trace fossil distribution in Oligocene fluvial-fan-to-lacustrine systems of the Ebro Basin, Spain. Palaeogeography, Palaeoclimatology, Palaeoecology 272, 162–175. https://doi.org/10.1016/j.palaeo.2008.10.030

DeCelles, P.G., Cavazza, W., 1999. A comparison of fluvial megafans in the Cordilleran (Upper Cretaceous) and modern Himalayan foreland basin systems. Geological Society of America Bulletin 111, 1315–1334. https://doi.org/10.1130/0016-7606(1999)111<1315:ACOFMI>2.3.CO;2

Del Santo, G., Garcia-Sansegundo, J., Sarasa, L., Torrebadella, J., 2000. Estratigrafía y estructura del Terciario en el sector oriental de la cuenca del Ebro entre Solsona y Manresa (NE de España). Revista de La Sociedad Geológica de España 13, 265–278.

den Elzen, M., Admiraal, A., Roelfsema, M., van Soest, H., Hof, A.F., Forsell, N., 2016. Contribution of the G20 economies to the global impact of the Paris agreement climate proposals. Climatic Change 137, 655–665. https://doi.org/10.1007/s10584-016-1700-7

Di Naccio, D., Boncio, P., Cirilli, S., Casaglia, F., Morettini, E., Lavecchia, G., Brozzetti, F., 2005. Role of mechanical stratigraphy on fracture development in carbonate reservoirs: Insights from outcropping shallow water carbonates in the Umbria-Marche Apennines, Italy. Journal of Volcanology and Geothermal Research 148, 98–115. https://doi.org/10.1016/j.jvolgeores.2005.03.016

Dichiarante, A.M., McCaffrey, K.J.W., Holdsworth, R.E., Bjørnarå, T.I., Dempsey, E.D., 2020. Fracture attribute scaling and connectivity in the Devonian Orcadian Basin with implications for geologically equivalent sub-surface fractured reservoirs. Solid Earth 11, 2221–2244. https://doi.org/10.5194/se-11-2221-2020

Dos Anjos, S.M.C., De Ros, L.F., De Souza, R.S., De Assis Silva, C.M., Sombra, C.L., 2000. Depositional and diagenetic controls on the reservoir quality of Lower Cretaceous Pendencia sandstones, Potiguar rift basin, Brazil. AAPG Bulletin 84, 1719–1742. https://doi.org/10.1306/8626c375-173b-11d7-8645000102c1865d

Dutton, S.P., 2008. Calcite cement in Permian deep-water sandstones, Delaware Basin, west Texas: Origin, distribution, and effect on reservoir properties. AAPG Bulletin 92, 765–787. https://doi.org/10.1306/01280807107

Dutton, S.P., White, C.D., Willis, B.J., Novakovic, D., 2002. Calcite cement distribution and its effect on fluid flow in a deltaic sandstone, Frontier Formation, Wyoming. AAPG Bulletin 86, 2007–2021. https://doi.org/10.1306/c9ebd5f3-1735-11d7-8645000102c1865d

EDGAR, 2018. Emissions Database for Global Atmospheric Research [WWW Document]. URL

http://edgar.jrc.ec.europa.eu/overview.php?v=432&SECURE=123 https://data.europa.eu/doi/10.2904/JRC_DATASET_EDGAR (accessed 12.12.18).

Edlmann, K., Edwards, M.A., Qiao, X.J., Haszeldine, R.S., McDermott, C.I., 2015. Appraisal of global CO2 storage opportunities using the geomechanical facies approach. Environmental Earth Sciences 73, 8075–8096. https://doi.org/10.1007/s12665-014-3965-3

Emery, D., Dickson, J.A.D., 1989. A syndepositional meteoric phreatic lens in the Middle Jurassic Lincolnshire Limestone, England, U.K. Sedimentary Geology 65, 273–284. https://doi.org/10.1016/0037-0738(89)90029-8

Espie, T., Canal-Vila, J., Tucker, O., Zweigel, P., 2018. The role of technology in enabling the expansion to gigatonne scale storage of CO2. 14th Greenhouse Gas Control Technologies Conference Melbourne. 21–26.

European Commission, 2020. Climate strategies & targets [WWW Document]. URL https://ec.europa.eu/clima/policies/strategies_en (accessed 2.17.21).

Evans, M.A., Bebout, G.E., Brown, C.H., 2012. Changing fluid conditions during folding: An example from the central Appalachians. Tectonophysics 576–577, 99–115. https://doi.org/10.1016/j.tecto.2012.03.002

Evans, M.A., Fischer, M.P., 2012. On the distribution of fluids in folds: A review of controlling factors and processes. Journal of Structural Geology 44, 2–24. https://doi.org/10.1016/j.jsg.2012.08.003

Fernàndez, M., Marzán, I., Correia, A., Ramalho, E., 1998. Heat flow, heat production, and lithospheric thermal regime in the Iberian Peninsula. Tectonophysics 291, 29–53. https://doi.org/10.1016/S0040-1951(98)00029-8

Ferrill, D.A., Morris, A.P., 2008. Fault zone deformation controlled by carbonate mechanical stratigraphy, Balcones fault system, Texas. AAPG Bulletin 92, 359–380. https://doi.org/10.1306/10290707066

Fischer, M.P., Higuera-Díaz, I.C., Evans, M.A., Perry, E.C., Lefticariu, L., 2009. Fracture-controlled paleohydrology in a map-scale detachment fold: Insights from the analysis of fluid inclusions in calcite and quartz veins. Journal of Structural Geology 31, 1490–1510. https://doi.org/10.1016/j.jsg.2009.09.004

Florez-Niño, J.M., Aydin, A., Mavko, G., Antonellini, M., Ayaviri, A., 2005. Fault and fracture systems in a fold and thrust belt: An example from Bolivia. AAPG Bulletin 89, 471–493. https://doi.org/10.1306/11120404032

Folk, R.L., 1980. Petrology of Sedimentary Rocks. Hemphill Publishing Company, Austin.

Ford, M., Williams, E.A., Artoni, A., Vergés, J., Hardy, S., 1997. Progressive evolution of a fault-

related fold pair from growth strata geometries, Sant Llorenç de Morunys, SE Pyrenees. Journal of Structural Geology 19, 413–441. https://doi.org/10.1016/s0191-8141(96)00116-2

Fredrich, J.T., Evans, B., Teng-Fong Wong, 1990. Effect of grain size on brittle and semibrittle strength: implications for micromechanical modelling of failure in compression. Journal of Geophysical Research 95, 10907–10920. https://doi.org/10.1029/jb095ib07p10907

Frykman, P., Bech, N., Sørensen, A.T., Nielsen, L.H., Nielsen, C.M., Kristensen, L., Bidstrup, T., 2009. Geological modeling and dynamic flow analysis as initial site investigation for large-scale CO2 injection at the Vedsted structure, NW Denmark. Energy Procedia 1, 2975–2982. https://doi.org/10.1016/j.egypro.2009.02.074

Garnett, A.J., Greig, C.R., Oettinger, M., 2014. ZeroGen IGCC with CCS - A Case History. University of Queensland, Brisbane.

Ghosh, K., Mitra, S., 2009. Structural controls of fracture orientations, intensity, and connectivity, Teton anticline, Sawtooth Range, Montana. AAPG Bulletin 93, 995–1014. https://doi.org/10.1306/04020908115

Global CCS Institute, 2020. CCS Facilities Database [WWW Document]. URL https://co2re.co/FacilityData (accessed 1.15.21).

Global CCS Institute, 2017. The global status of CCS: 2017 [WWW Document]. URL https://www.globalccsinstitute.com/wp-content/uploads/2018/12/2017-Global-Status-Report.pdf (accessed 2.17.21).

Global CCS Institute, 2016. Understanding Industrial CCS Hubs and Clusters [WWW Document]. URL https://www.globalccsinstitute.com/wp-content/uploads/2019/08/Understanding-Industrial-CCS-hubs-and-clusters.pdf (accessed 2.17.21).

Godec, M., Kuuskraa, V., Van Leeuwen, T., Stephen Melzer, L., Wildgust, N., 2011. CO2 storage in depleted oil fields: The worldwide potential for carbon dioxide enhanced oil recovery. Energy Procedia 4, 2162–2169. https://doi.org/10.1016/j.egypro.2011.02.102

Gomez-Rivas, E., Bons, P.D., Koehn, D., Urai, J.L., Arndt, M., Virgo, S., Laurich, B., Zeeb, C., Stark, L., Blum, P., 2014. The Jabal Akhdar Dome in the Oman mountains: Evolution of a dynamic fracture system. American Journal of Science 314, 1104–1139. https://doi.org/10.2475/07.2014.02

Goodman, A., Hakala, A., Bromhal, G., Deel, D., Rodosta, T., Frailey, S., Small, M., Allen, D., Romanov, V., Fazio, J., Huerta, N., Mcintyre, D., Kutchko, B., Guthrie, G., 2011. International Journal of Greenhouse Gas Control U.S. DOE methodology for the development of geologic storage potential for carbon dioxide at the national and regional scale. International Journal of Greenhouse Gas Control 5, 952–965. https://doi.org/10.1016/j.ijggc.2011.03.010

Grover, G., Read, J.F., 1983. Paleoaquifer and deep burial related cements defined by regional cathodoluminescent patterns, Middle Ordovician Carbonates, Virginia. AAPG Bulletin 67, 1275–1303. https://doi.org/10.1306/03B5B73B-16D1-11D7-8645000102C1865D

Guilbaud, R., Bernet, M., Huyghe, P., Erens, V., Chirouze, F., Dupont-Nivet, G., 2012. On the influence of diagenesis on the original petrographic composition of Miocene–Pliocene fluvial sandstone in the Himalayan foreland basin of western-central Nepal. Journal of Asian Earth Sciences 44, 107–116. https://doi.org/10.1016/j.jseaes.2011.04.025

Hakimi, M.H., Shalaby, M.R., Abdullah, W.H., 2012. Diagenetic characteristics and reservoir quality of the Lower Cretaceous Biyadh sandstones at Kharir oilfield in the western central Masila Basin, Yemen. Journal of Asian Earth Sciences 51, 109–120. https://doi.org/10.1016/j.jseaes.2012.03.004

Hall, J.S., Mozley, P., Davis, J.M., Roy, N.D., 2004. Environments of formation and controls on spatial distribution of calcite cementation in Plio-Pleistocene fluvial deposits, New Mexico, U.S.A. Journal of Sedimentary Research 74, 643–653. https://doi.org/10.1306/020904740643

Han, Y., He, S., Song, G., Wang, Y., Hao, X., Wang, B., Luo, S., 2012. Origin of carbonate cements in the overpressured top seal and adjacent sandstones in Dongying depression. Acta Petrolei Sinica 33, 385.

Hanks, C.L., Lorenz, J., Teufel, L., Krumhardt, A.P., 1997. Lithologic and structural controls on natural fracture distribution and behavior within the Lisburne Group, northeastern Brooks Range and North Slope subsurface, Alaska. AAPG Bulletin 81, 1700–1720. https://doi.org/10.1306/3b05c424-172a-11d7-8645000102c1865d

He, S., Yang, Z., He, Z., Wu, H., Wang, F., Meng, X., 2009. Mechanism of carbonate cementation and secondary dissolution porosity formation in deep-burial sandstones near the top overpressured surface in central part of Junggar basin. Earth Science - Journal of China University of Geosciences 34, 759–768. https://doi.org/10.3799/dqkx.2009.084

Henderson, I.H.C., McCaig, A.M., 1996. Fluid pressure and salinity variations in shear zone-related veins, central Pyrenees, France: Implications for the fault-valve model. Tectonophysics 262, 321–348. https://doi.org/10.1016/0040-1951(96)00018-2

Hirst, J.P.P., Nichols, G.J., 1986. Thrust tectonic controls on Miocene alluvial distribution patterns, southern Pyrenees. In: Allen, P.A., Homewood, P. (Eds.), Foreland Basins. International Association of Sedimentologists Special Publication, 153–164. https://doi.org/10.1002/9781444303810.ch13

Hoegh-Guldberg, O., Jacob, D., Taylor, M., Bindi, M., Brown, S., Camilloni, I., Diedhiou, A., Djalante, R., Ebi, K., Engelbrecht, F., Guiot, J., Hijioka, Y., Mehrotra, S., Payne, A.,

Seneviratne, S.I., Thomas, A., Warren, R., Zhou, G., 2018. Impacts of 1.5 C global warming on natural and human systems. In: Masson-Delmotte, V., Zhai, P., Pörtner, H.O., Roberts, D., Skea, J., Shukla, P.R., Pirani, A., Moufouma-Okia, W., Péan, C., Pidcock, R., Connors, S., Matthews, J.B.R., Chen, Y., Zhou, X., Gomis, M.I., Lonnoy, E., Maycock, T., Tignor, M., Waterfield, T. (Eds.), Global Warming of 1.5° C: An IPCC Special Report.

Hoffman, N., Marshall, S., Horan, S., 2021. Successful appraisal of the CarbonNet Pelican CO2 offshore storage site. 15th Greenhouse Gas Control Technologies Conference. SSRN, 1–7. https://doi.org/10.2139/ssrn.3811988

Horton, B.K., Decelles, P.G., 2001. Modern and ancient fluvial megafans in the foreland basin system of the Central Andes, Southern Bolivia: Implications for drainage network evolution if foldthrust belts. Basin Research 13, 43–63. https://doi.org/10.1046/j.1365-2117.2001.00137.x

Hosa, A., Wood, R., 2017. Quantifying the impact of early calcite cementation on the reservoir quality of carbonate rocks: A 3D process-based model. Advances in Water Resources 104, 89–104. https://doi.org/10.1016/j.advwatres.2017.02.019

Hosseini, S.A., Lashgari, H., Choi, J.W., Nicot, J.-P., Lu, J., Hovorka, S.D., 2013. Static and dynamic reservoir modeling for geological CO2 sequestration at Cranfield, Mississippi, U.S.A. International Journal of Greenhouse Gas Control 18, 449–462. https://doi.org/10.1016/j.ijggc.2012.11.009

Houseknecht, D.W., 1987. Assessing the relative importance of compaction processes and cementation to reduction of porosity in sandstones. AAPG Bulletin 71, 633–642. https://doi.org/10.1306/9488787F-1704-11D7-8645000102C1865D

Howell, J.A., Martinius, A.W., Good, T.R., 2014. The application of outcrop analogues in geological modelling: a review, present status and future outlook. Geological Society, London, Special Publications 387, 1–25. https://doi.org/10.1144/SP387.12

Huang, Q., Angelier, J., 1989. Fracture spacing and its relation to bed thickness. Geological Magazine 126, 355–362. https://doi.org/10.1017/S0016756800006555

Hudleston, P.J., Treagus, S.H., 2010. Information from folds: A review. Journal of Structural Geology 32, 2042–2071. https://doi.org/10.1016/j.jsg.2010.08.011

Hugman, R.H.H., Friedman, M., 1979. Effects of texture and composition on mechanical behavior of experimentally deformed carbonate rocks. AAPG Bulletin 63, 1478–1489. https://doi.org/10.1306/2f9185c7-16ce-11d7-8645000102c1865d

IBM Corp, 2017. IBM SPSS Statistics for Windows (Version 25.0) [WWW Document]. https://doi.org/https://www.ibm.com/support/pages/downloading-ibm-spss-statistics-25

Iding, M., Ringrose, P., 2010. Evaluating the impact of fractures on the performance of the In

Salah CO2 storage site. International Journal of Greenhouse Gas Control 4, 242–248. https://doi.org/10.1016/j.ijggc.2009.10.016

Ingersoll, R. V., Cavazza, W., Graham, S.A., 1987. Provenance of impure calclithites in the Laramide foreland of southwestern Montana. Journal of Sedimentary Research 57, 995–1003. https://doi.org/10.1306/212F8CC9-2B24-11D7-8648000102C1865D

Iñigo, J.F., Laubach, S.E., Hooker, J.N., 2012. Fracture abundance and patterns in the Subandean fold and thrust belt, Devonian Huamampampa Formation petroleum reservoirs and outcrops, Argentina and Bolivia. Marine and Petroleum Geology 35, 201–218. https://doi.org/10.1016/j.marpetgeo.2012.01.010

Institut Cartogràfic i Geològic de Catalunya, 2006. Regional geological map of Catalonia [WWW Document]. URL https://www.icgc.cat/en/Public-Administration-and-Enterprises/Downloads/Geological-and-geothematic-cartography/Geological-cartography/Geological-map-1-50-000/Regional-geological-map-of-Catalonia-1-50-000 (accessed 2.1.21).

Instituto Geológico y Minero de España, 2010a. Plan de selección y caracterización de áreas y estructuras favorables para el almacenamiento geológico de CO2 en España: Resumen ejecutivo [WWW Document]. URL http://info.igme.es/SidPDF/149000/047/149047_0000001.pdf (accessed 2.17.21).

Instituto Geológico y Minero de España, 2010b. The ALGECO2 Project [WWW Document]. URL http://info.igme.es/algeco2/ (accessed 10.1.20).

Instituto Geológico y Minero de España, 1995. Almacenamiento subterraneo de gas: previabilidad en formaciones detriticas y salinas [WWW Document]. URL http://info.igme.es/ConsultaSID/r.asp?IdDESCRIPTOR=2681 (accessed 3.20.21).

Instituto Geológico y Minero de España, 1977. Geophysical Information System [WWW Document]. URL http://info.igme.es/SIGEOF/# (accessed 2.1.21).

Intergovernmental Panel on Climate Change, 2018. Global Warming of 1.5°C: An IPCC special report [WWW Document]. URL https://www.ipcc.ch/sr15/ (accessed 6.1.19).

Irwin, H., Curtis, C., Coleman, M., 1977. Isotopic evidence for source of diagenetic carbonates formed during burial of organic-rich sediments. Nature 269, 209–213. https://doi.org/10.1038/269209a0

Issautier, B., Fillacier, S., Le Gallo, Y., Audigane, P., Chiaberge, C., Viseur, S., 2013. Modelling of CO2 injection in fluvial sedimentary heterogeneous reservoirs to assess the impact of geological heterogeneities on CO2 storage capacity and performance. Energy Procedia 37, 5181–5190. https://doi.org/10.1016/j.egypro.2013.06.434

Issautier, B., Viseur, S., Audigane, P., Chiaberge, C., Le Nindre, Y.-M., 2016. A new approach for evaluating the impact of fluvial type heterogeneity in CO2 storage reservoir modeling. Comptes Rendus Geoscience 348, 531–539. https://doi.org/10.1016/j.crte.2015.06.006

Issautier, B., Viseur, S., Audigane, P., le Nindre, Y.-M., 2014. Impacts of fluvial reservoir heterogeneity on connectivity: Implications in estimating geological storage capacity for CO2. International Journal of Greenhouse Gas Control 20, 333–349. https://doi.org/10.1016/j.ijggc.2013.11.009

Janssens-Maenhout, G., Crippa, M., Guizzardi, D., Muntean, M., Schaaf, E., Dentener, F., Bergamaschi, P., Pagliari, V., Olivier, J.G.J., Peters, J.A.H.W., van Aardenne, J.A., Monni, S., Doering, U., Petrescu, A.M.R., Solazzo, E., Oreggioni, G.D., 2019. EDGAR v4.3.2 Global Atlas of the three major greenhouse gas emissions for the period 1970–2012. Earth System Science Data 11, 959–1002. https://doi.org/10.5194/essd-11-959-2019

John, C.M., Bowen, D., 2016. Community software for challenging isotope analysis: First applications of 'Easotope' to clumped isotopes. Rapid Communications in Mass Spectrometry 30, 2285–2300. https://doi.org/10.1002/rcm.7720

Kapetaki, Z., Scowcroft, J., 2017. Overview of carbon capture and storage (CCS) demonstration project business models: risks and enablers on the two sides of the Atlantic. Energy Procedia 114, 6623–6630. https://doi.org/10.1016/j.egypro.2017.03.1816

Kearns, J., Teletzke, G., Palmer, J., Thomann, H., Kheshgi, H., Chen, Y.H., Paltsev, S., Herzog, H., 2017. Developing a consistent database for regional geologic CO2 storage capacity worldwide. Energy Procedia 114, 4697–4709. https://doi.org/10.1016/j.egypro.2017.03.1603

Kim, S.-T., Coplen, T.B., Horita, J., 2015. Normalization of stable isotope data for carbonate minerals: Implementation of IUPAC guidelines. Geochimica et Cosmochimica Acta 158, 276–289. https://doi.org/10.1016/j.gca.2015.02.011

Kim, S.-T., Mucci, A., Taylor, B.E., 2007. Phosphoric acid fractionation factors for calcite and aragonite between 25 and 75 °C: Revisited. Chemical Geology 246, 135–146. https://doi.org/10.1016/j.chemgeo.2007.08.005

King, M.J., 2011. On The Tyranny Of Corner Point Grids. SIAM Conference on Mathematical & Computational Issues in the Geosciences. Long Beach, 114.

Koelbl, B.S., van den Broek, M.A., Faaij, A.P.C., van Vuuren, D.P., 2014. Uncertainty in Carbon Capture and Storage (CCS) deployment projections: a cross-model comparison exercise. Climatic Change 123, 461–476. https://doi.org/10.1007/s10584-013-1050-7

Kolster, C., Masnadi, M.S., Krevor, S., Mac Dowell, N., Brandt, A.R., 2017. CO2 enhanced oil recovery: a catalyst for gigatonne-scale carbon capture and storage deployment? Energy &

Environmental Science 10, 2594–2608. https://doi.org/10.1039/C7EE02102J

Kuuskraa, V.A., Godec, M.L., Dipietro, P., 2013. CO2 utilization from "next generation " CO2 enhanced oil recovery technology. Energy Procedia 37, 6854–6866. https://doi.org/10.1016/j.egypro.2013.06.618

Ladeira, F.L., Price, N.J., 1981. Relationship between fracture spacing and bed thickness. Journal of Structural Geology 3, 179–183. https://doi.org/10.1016/0191-8141(81)90013-4

Lai, J., Wang, G., Wang, S., Cao, J., Li, M., Pang, X., Zhou, Z., Fan, X., Dai, Q., Yang, L., He, Z., Qin, Z., 2018. Review of diagenetic facies in tight sandstones: Diagenesis, diagenetic minerals, and prediction via well logs. Earth-Science Reviews 185, 234–258. https://doi.org/10.1016/j.earscirev.2018.06.009

Laubach, S.E., Olson, J.E., Cross, M.R., 2009. Mechanical and fracture stratigraphy. AAPG Bulletin 93, 1413–1426. https://doi.org/10.1306/07270909094

Leung, D.Y.C., Caramanna, G., Maroto-Valer, M.M., 2014. An overview of current status of carbon dioxide capture and storage technologies. Renewable and Sustainable Energy Reviews 39, 426–443. https://doi.org/10.1016/j.rser.2014.07.093

Li, Z., Goldstein, R.H., Franseen, E.K., 2017. Meteoric calcite cementation: diagenetic response to relative fall in sea-level and effect on porosity and permeability, Las Negras area, southeastern Spain. Sedimentary Geology 348, 1–18. https://doi.org/10.1016/j.sedgeo.2016.12.002

Liu, C., Zhang, R., Zhang, H., Wang, J., Mo, T., Wang, K., Zhou, L., 2017. Genesis and reservoir significance of multi-scale natural fractures in Kuqa foreland thrust belt, Tarim Basin, NW China. Petroleum Exploration and Development 44, 495–504. https://doi.org/10.1016/S1876-3804(17)30057-5

Liu, H., Consoli, C., Zapantis, A., 2018. Overview of carbon capture and storage (CCS) facilities globally. 14th Greenhouse Gas Control Technologies Conference Melbourne. 1–10. https://doi.org/10.2139/ssrn.3366353

Liu, Y., Hu, W., Cao, J., Wang, X., Zhu, F., Tang, Q., Gao, W., 2019. Fluid–rock interaction and its effects on the Upper Triassic tight sandstones in the Sichuan Basin, China: Insights from petrographic and geochemical study of carbonate cements. Sedimentary Geology 383, 121–135. https://doi.org/10.1016/j.sedgeo.2019.01.012

Lorenz, J.C., Cooper, S.P., Olsson, W.A., 2006. Natural fracture distributions in sinuous, channel-fill sandstones of the Cedar Mountain Formation, Utah. AAPG Bulletin 90, 1293–1308. https://doi.org/10.1306/03300605137

Lupion, M., Herzog, H.J., 2013. NER300: Lessons learnt in attempting to secure CCS projects in

Europe. International Journal of Greenhouse Gas Control 19, 19–25. https://doi.org/10.1016/j.ijggc.2013.08.009

Luzón, A., 2005. Oligocene–Miocene alluvial sedimentation in the northern Ebro Basin, NE Spain: Tectonic control and palaeogeographical evolution. Sedimentary Geology 177, 19–39. https://doi.org/https://doi.org/10.1016/j.sedgeo.2005.01.013

Luzón, A., 2001. Análisis tectosedimentario de los materiales terciarios continentales del sector central de la cuenca del Ebro (provincias de Huesca y Zaragoza). PhD thesis, Zaragoza University, Zaragoza.

MacDowell, N., Florin, N., Buchard, A., Hallett, J., Galindo, A., Jackson, G., Adjiman, C.S., Williams, C.K., Shah, N., Fennell, P., 2010. An overview of CO2 capture technologies. Energy and Environmental Science 3, 1645–1669. https://doi.org/10.1039/c004106h

Machel, H.G., 2000. Application of cathodoluminescence to carbonate diagenesis. In: Page, M., Barbin, V., Blanc, P., Ohnenstetter, D. (Eds.), Cathodoluminescence in Geosciences. Springer Berlin Heidelberg, Berlin, Heidelberg, 271–301. https://doi.org/10.1007/978-3-662-04086-7_11

Mandova, H., Patrizio, P., Leduc, S., Kjärstad, J., Wang, C., Wetterlund, E., Kraxner, F., Gale, W., 2019. Achieving carbon-neutral iron and steelmaking in Europe through the deployment of bioenergy with carbon capture and storage. Journal of Cleaner Production 218, 118–129. https://doi.org/10.1016/j.jclepro.2019.01.247

Mann, P., Gahagan, L., Gordon, M.B., 2003. Tectonic setting of the world's giant oil fields. In: Halbouty, M.. (Ed.), Giant Oil and Gas Fields of the Decade 1990–1999. AAPG Memoir, 15–105.

Martínez del Olmo, W., 2019. Cambio climático, acuerdos de Paris y trampas geológicas donde secuestrar el CO2 en España. Revista de La Sociedad Geológica de España 32, 87–106.

Martinius, A.W., Fustic, M., Garner, D.L., Jablonski, B.V.J., Strobl, R.S., MacEachern, J.A., Dashtgard, S.E., 2017. Reservoir characterization and multiscale heterogeneity modeling of inclined heterolithic strata for bitumen-production forecasting, McMurray Formation, Corner, Alberta, Canada. Marine and Petroleum Geology 82, 336–361. https://doi.org/10.1016/j.marpetgeo.2017.02.003

McArthur, J.M., Howarth, R.J., Shields, G.A., 2012. Strontium Isotope Stratigraphy. In: Gradstein, F.M., Ogg, J.G., Schmotz, M.D., Ogg, G.M. (Eds.), The Geologic Time Scale. Elsevier, 211–238. https://doi.org/10.1016/B978-0-444-59425-9.00007-X

McBride, E.F., Milliken, K.L., Cavazza, W., Cibin, U., Fontana, D., Picard, M.D., Zuffa, G.G., 1995. Heterogeneous distribution of calcite cement at the outcrop scale in Tertiary sandstones,

Northern Apennines, Italy. AAPG Bulletin 79, 1044–1062. https://doi.org/10.1306/8D2B21C3-171E-11D7-8645000102C1865D

Mccrea, J.M., 1950. On the isotopic chemistry of carbonates and a paleotemperature scale. The Journal of Chemical Physics 18, 849–857. https://doi.org/10.1063/1.1747785

McDermott, C.I., Miocic, J.M., Edlmann, K., Gilfillan, S.M. V., 2017. Natural analogue studies. In: Niemi, A., Bear, J., Bensabat, J. (Eds.), Geological Storage of CO2 in Deep Saline Formations. Springer, Dordrecht. https://doi.org/10.1007/978-94-024-0996-3_9

Millington, R., Cox, P.M., Moore, J.R., Yvon-Durocher, G., 2019. Modelling ecosystem adaptation and dangerous rates of global warming. In: Osborn, D. (Ed.), Emerging Topics in Life Sciences 3, 221–231. https://doi.org/10.1042/ETLS20180113

Ministerio para la Transición Ecológica y el Reto Demográfico, 2020. Inventario de instalaciones [WWW Document], Ministerio para la Transición Ecológica y el Reto Demográfico. URL https://www.miteco.gob.es/es/calidad-y-evaluacion-ambiental/temas/sistema-espanol-de-inventario-sei-/es-2020-nir_tcm30-508122.pdf (accessed 10.1.20).

Ministerio para la Transición Ecológica y el Reto Demográfico, 2007. Estrategia Española de Cambio Climático y Energía Limpia Horizonte 2007–2012–2020 [WWW Document]. URL https://www.miteco.gob.es/es/cambio-climatico/legislacion/documentacion/est_cc_energ_limp_tcm30-178762.pdf (accessed 2.17.21).

Ministerio Para La Transición Ecológica y El Reto Demográfico, 2020. Acuerdo por una transición energética justa para centrales térmicas en cierre: el empleo, la industria y los territorio [WWW Document], Ministerio Para La Transición Ecológica y El Reto Demográfico. URL https://www.transicionjusta.gob.es/common/acuerdoporunatransicionenergeticajustaparacentralestermicasencierrees.pdf (accessed 2.17.21).

Miranda, T.S., Santos, R.F., Barbosa, J.A., Gomes, I.F., Alencar, M.L., Correia, O.J., Falcão, T.C., Gale, J.F.W., Neumann, V.H., 2018. Quantifying aperture, spacing and fracture intensity in a carbonate reservoir analogue: Crato Formation, NE Brazil. Marine and Petroleum Geology 97, 556–567. https://doi.org/10.1016/j.marpetgeo.2018.07.019

Morad, S., 1998. Carbonate Cementation in Sandstones: Distribution Patterns and Geochemical Evolution. In: Morad, S. (Ed.), Carbonate Cementation in Sandstones. Blackwell Publishing Ltd., Oxford, 1–26. https://doi.org/10.1002/9781444304893.ch1

Morad, S., Al-Ramadan, K., Ketzer, J.M., De Ros, L.F., 2010. The impact of diagenesis on the heterogeneity of sandstone reservoirs: A review of the role of depositional fades and sequence

stratigraphy. AAPG Bulletin 94, 1267–1309. https://doi.org/10.1306/04211009178

Moscariello, A., 2018. Alluvial fans and fluvial fans at the margins of continental sedimentary basins: geomorphic and sedimentological distinction for geo-energy exploration and development. Geological Society, London, Special Publications 440, 215–243. https://doi.org/10.1144/SP440.11

Moscariello, A., 2005. Exploration potential of the mature Southern North Sea basin margins: some unconventional plays based on alluvial and fluvial fan sedimentation models. Geological Society, London, Petroleum Geology Conference Series 6, 595–605. https://doi.org/10.1144/0060595

Muchez, P., Nielsen, P., Sintubin, M., Lagrou, D., 1998. Conditions of meteoric calcite formation along a Variscan fault and their possible relation to climatic evolution during the Jurassic–Cretaceous. Sedimentology 45, 845–854. https://doi.org/10.1046/j.1365-3091.1998.00182.x

Muñoz-López, D., Alías, G., Cruset, D., Cantarero, I., John, C.M., Travé, A., 2020. Influence of basement rocks on fluid evolution during multiphase deformation: the example of the Estamariu thrust in the Pyrenean Axial Zone. Solid Earth 11, 2257–2281. https://doi.org/10.5194/se-11-2257-2020

Nichols, G.J., Hirst, J.P., 1998. Alluvial fans and fluvial distributary systems, Oligo-Miocene, northern Spain; contrasting processes and products. Journal of Sedimentary Research 68, 879–889. https://doi.org/10.2110/jsr.68.879

Ogata, K., Senger, K., Braathen, A., Tveranger, J., 2014. Fracture corridors as seal-bypass systems in siliciclastic reservoir-cap rock successions: Field-based insights from the Jurassic Entrada Formation (SE Utah, USA). Journal of Structural Geology 66, 162–187. https://doi.org/10.1016/j.jsg.2014.05.005

Ogata, K., Storti, F., Balsamo, F., Tinterri, R., Bedogni, E., Fetter, M., Gomes, L., Hatushika, R., 2017. Sedimentary facies control on mechanical and fracture stratigraphy in turbidites. Geological Society of America Bulletin 129, 76–92. https://doi.org/10.1130/B31517.1

Olson, J.E., Laubach, S.E., Lander, R.H., 2007. Combining diagenesis and mechanics to quantity fracture aperture distributions an fracture pattern permeability. Geological Society Special Publication 270, 101–116. https://doi.org/10.1144/GSL.SP.2007.270.01.08

Ortega, O.J., Gale, J.F.W., Marrett, R., 2010. Quantifying diagenetic and stratigraphic controls on fracture intensity in platform carbonates: An example from the Sierra Madre Oriental, northeast Mexico. Journal of Structural Geology 32, 1943–1959. https://doi.org/10.1016/j.jsg.2010.07.004

Ortega, O.J., Marrett, R.A., Laubach, S.E., 2006. A scale-independent approach to fracture

intensity and average spacing measurement. AAPG Bulletin 90, 193–208. https://doi.org/10.1306/08250505059

Patel, S., 2010. Spain makes headway in CCS efforts [WWW Document], Power. URL https://www.powermag.com/spain-makes-headway-in-ccs-efforts/ (accessed 1.15.21).

Peacock, D.C.P., 2001. The temporal relationship between joints and faults. Journal of Structural Geology 23, 329–341. https://doi.org/10.1016/S0191-8141(00)00099-7

Pranter, M.J., Hewlett, A.C., Cole, R.D., Wang, H., Gilman, J., 2014. Fluvial architecture and connectivity of the Williams Fork Formation: use of outcrop analogues for stratigraphic characterization and reservoir modelling. Geological Society, London, Special Publications 387, 57–83. https://doi.org/10.1144/SP387.1

Puigdefàbregas, C., Munñz, J.A., Marzo, M., 1986. Thrust belt development in the eastern Pyrenees and related depositional sequences in the southern foreland basin. In: Allen, P.A., Homewood, P. (Eds.), Foreland Basins. International Association of Sedimentologists Special Publication, 229–246. https://doi.org/10.1002/9781444303810.ch12

Puigdefàbregas, C., Muñoz, J.A., Vergés, J., 1992. Thrusting and foreland basin evolution in the Southern Pyrenees. In: McClay, K.R. (Ed.), Thrust Tectonics. Springer, Dordrecht, 247–254. https://doi.org/10.1007/978-94-011-3066-0_22

QGIS Development Team, 2018. QGIS Geographic Information System. Open Source Geospatial Foundation Project [WWW Document]. URL http://qgis.osgeo.org (accessed 12.12.18).

Riba, O., 1976. Syntectonic unconformities of the Alto Cardener, Spanish Pyrenees: a genetic interpretation. Sedimentary Geology 15, 213–233. https://doi.org/10.1016/0037-0738(76)90017-8

Ringrose, P.S., Meckel, T.A., 2019. Maturing global CO2 storage resources on offshore continental margins to achieve 2DS emissions reductions. Scientific Reports 9, 17944. https://doi.org/10.1038/s41598-019-54363-z

Robertson, C.G.G., 2014. Sedimentary Basins of the World [WWW Document]. URL https://www.cgg.com/en/What-We-Do/GeoConsulting/Robertson (accessed 12.12.18).

Rumayor, M., Dominguez-Ramos, A., Irabien, A., 2020. Toward the decarbonization of hard-to-abate sectors: A case study of the soda ash production. ACS Sustainable Chemistry & Engineering 8, 11956–11966. https://doi.org/10.1021/acssuschemeng.0c01598

Sáez, A., 1987. Estratigrafía y sedimentología de las formaciones lacustres del tránsito Eoceno-Oligoceno del NE de la Cuenca del Ebro. PhD thesis, University of Barcelona, Barcelona.

Sáez, A., Anadón, P., Herrero, M.J., Moscariello, A., 2007. Variable style of transition between Palaeogene fluvial fan and lacustrine systems, southern Pyrenean foreland, NE Spain.

Sedimentology 54, 367–390. https://doi.org/10.1111/j.1365-3091.2006.00840.x

Sanderson, D.J., 2016. Field-based structural studies as analogues to sub-surface reservoirs. Geological Society Special Publication 431, 207–217. https://doi.org/10.1144/SP436.5

Sanz-Hernández, A., Ferrer, C., López-Rodríguez, M.E., Marco-Fondevila, M., 2020. Visions, innovations, and justice? Transition contracts in Spain as policy mix instruments. Energy Research & Social Science 70, 101762. https://doi.org/10.1016/j.erss.2020.101762

Scherer, M., 1987. Parameters influencing porosity in sandstones: A model for sandstone porosity prediction. AAPG Bulletin 71, 485–491. https://doi.org/10.1306/94886ED9-1704-11D7-8645000102C1865D

Schneider, C.A., Rasband, W.S., Eliceiri, K.W., 2012. NIH Image to ImageJ: 25 years of image analysis. Nature Methods 9, 671–675. https://doi.org/10.1038/nmeth.2089

Scott, V., Gilfillan, S., Markusson, N., Chalmers, H., Haszeldine, R.S., 2013. Last chance for carbon capture and storage. Nature Climate Change 3, 105–111. https://doi.org/10.1038/nclimate1695

Serra-Kiel, J., Mató, E., Saula, E., Travé, A., Ferràndez-Canadell, C., Busquets, P., Samsó, J.M., Tosquella, J., Barnolas, A., Àlvarez-Pérez, G., Franquès, J., Romero, J., 2003a. An inventory of the marine and transitional Middle/Upper Eocene deposits of the Southeastern Pyrenean Foreland Basin (NE Spain). Geologica Acta 1, 201–229. https://doi.org/10.1344/105.000001610

Serra-Kiel, J., Travé, A., Mató, E., Saula, E., Ferràndez-Canadell, C., Busquets, P., Tosquella, J., Vergés, J., 2003b. Marine and transitional Middle/Upper Eocene units of the southeastern pyrenean foreland basin (NE Spain). Geologica Acta 1, 177–200. https://doi.org/10.1344/105.000001609

Shackleton, J.R., Cooke, M.L., Sussman, A.J., 2005. Evidence for temporally changing mechanical stratigraphy and effects on joint-network architecture. Geology 33, 101–104. https://doi.org/10.1130/G20930.1

Sibson, R.H., 1996. Structural permeability of fluid-driven fault-fracture meshes. Journal of Structural Geology 18, 1031–1042. https://doi.org/10.1016/0191-8141(96)00032-6

Sibson, R.H., 1981. Fluid flow accompanying faulting: field evidence and models. In: Simpson, D.W., Richards, P.G. (Eds.), Earthquake Prediction: An International Review. American Geophysical Union, 593–603. https://doi.org/10.1029/ME004p0593

Sohn, Y.K., Rhee, C.W., Kim, B.C., 1999. Debris flow and hyperconcentrated flood-flow deposits in an alluvial fan, northwestern part of the Cretaceous Yongdong Basin, Central Korea. The Journal of Geology 107, 111–132. https://doi.org/10.1086/314334

Soleimani, M., Jodeiri Shokri, B., 2015. 3D static reservoir modeling by geostatistical techniques used for reservoir characterization and data integration. Environmental Earth Sciences 74, 1403–1414. https://doi.org/10.1007/s12665-015-4130-3

Soltanian, M.R., Hajirezaie, S., Hosseini, S.A., Dashtian, H., Amooie, M.A., Meyal, A., Ershadnia, R., Ampomah, W., Islam, A., Zhang, X., 2019. Multicomponent reactive transport of carbon dioxide in fluvial heterogeneous aquifers. Journal of Natural Gas Science and Engineering 65, 212–223. https://doi.org/10.1016/j.jngse.2019.03.011

Staude, S., Bons, P.D., Markl, G., 2009. Hydrothermal vein formation by extension-driven dewatering of the middle crust: An example from SW Germany. Earth and Planetary Science Letters 286, 387–395. https://doi.org/10.1016/j.epsl.2009.07.012

Stephenson, B.J., Koopman, A., Hillgartner, H., McQuillan, H., Bourne, S., Noad, J.J., Rawnsley, K., 2007. Structural and stratigraphic controls on fold-related fracturing in the Zagros Mountain, Iran: Implications for reservoir development. Geological Society Special Publication 270, 1–21. https://doi.org/10.1144/GSL.SP.2007.270.01.01

Stork, A.L., Verdon, J.P., Kendall, J.M., 2015. The microseismic response at the In Salah Carbon Capture and Storage (CCS) site. International Journal of Greenhouse Gas Control 32, 159–171. https://doi.org/10.1016/j.ijggc.2014.11.014

Strategy CCUS, 2020. Milestone vote on CCUS roadmaps for Southern and Eastern Europe [WWW Document]. URL https://www.strategyccus.eu/news-and-events/news/milestone-vote-ccus-roadmaps-southern-and-eastern-europe (accessed 2.17.21).

Sun, X., 2018. Pore structure characterization of low permeability and tight sandstone reservoirs of Huagang Formation in Xihu Depression. Master thesis, China University of Petroleum (East China), Qingdao.

Suppe, J., Sàbat, F., Anton Muñoz, J., Poblet, J., Roca, E., Vergés, J., 1997. Bed-by-bed fold growth by kink-band migration: Sant llorenç de Morunys, eastern Pyrenees. Journal of Structural Geology 19, 443–461. https://doi.org/10.1016/S0191-8141(96)00103-4

Taylor, B.E., 1987. Stable isotope geochemistry of ore-forming fluids. In: Kyser, T.K. (Ed.), Short Course in Stable Isotope Geochemistry of Low Temperature Fluids. Mineralogical Association of Canada, 337–445.

Taylor, K.G., Machent, P.G., 2011. Extensive carbonate cementation of fluvial sandstones: An integrated outcrop and petrographic analysis from the Upper Cretaceous, Book Cliffs, Utah. Marine and Petroleum Geology 28, 1461–1474. https://doi.org/10.1016/j.marpetgeo.2011.06.003

Taylor, T.R., Giles, M.R., Hathon, L.A., Diggs, T.N., Braunsdorf, N.R., Birbiglia, G. V., Kittridge,

M.G., MacAulay, C.I., Espejo, I.S., 2010. Sandstone diagenesis and reservoir quality prediction: Models, myths, and reality. AAPG Bulletin 94, 1093–1132. https://doi.org/10.1306/04211009123

Terzaghi, R.D., 1965. Sources of error in joint surveys. Géotechnique 15, 287–304. https://doi.org/10.1680/geot.1965.15.3.287

Travé, A., Calvet, F., 2001. Syn-rift geofluids in fractures related to the early-middle Miocene evolution of the Vallès-Penedès half-graben (NE Spain). Tectonophysics 336, 101–120. https://doi.org/10.1016/S0040-1951(01)00096-8

Travé, A., Labaume, P., Vergés, J., 2007. Fluid systems in foreland fold-and-thrust belts: An overview from the southern Pyrenees. In: Lacombe, O., Lavé, J., Roure, F., Vergés, J. (Eds.), Thrust Belts and Foreland Basins. Springer, Berlin, Heidelberg, 93–115. https://doi.org/10.1007/978-3-540-69426-7

Trisos, C.H., Merow, C., Pigot, A.L., 2020. The projected timing of abrupt ecological disruption from climate change. Nature 580, 496–501. https://doi.org/10.1038/s41586-020-2189-9

Underwood, C.A., Cooke, M.L., Simo, J.A., Muldoon, M.A., 2003. Stratigraphic controls on vertical fracture patterns in Silurian dolomite, northeastern Wisconsin. AAPG Bulletin 87, 121–142. https://doi.org/10.1306/072902870121

USGS, 2000. World Petroleum Assessment [WWW Document]. URL https://energy.usgs.gov (accessed 12.12.18).

USGS, 1995. National Assessment of Oil and Gas Resources [WWW Document]. URL https://energy.usgs.gov (accessed 12.12.18).

Valloni, R., Zuffa, G.G., 1984. Provenance changes for arenaceous formations of the northern Apennines, Italy. Geological Society of America Bulletin 95, 1035–1039. https://doi.org/10.1130/0016-7606(1984)95<1035:PCFAFO>2.0.CO;2

Van Den Bril, K., Swennen, R., 2009. Sedimentological control on carbonate cementation in the Luxembourg Sandstone Formation. Geologica Belgica 12, 3–23.

Van Dijk, J.P., Bello, M., Toscano, C., Bersani, A., Nardon, S., 2000. Tectonic model and three-dimensional fracture network analysis of Monte Alpi (southern Apennines). Tectonophysics 324, 203–237. https://doi.org/10.1016/S0040-1951(00)00138-4

Vandeginste, V., Swennen, R., Allaeys, M., Ellam, R.M., Osadetz, K., Roure, F., 2012. Challenges of structural diagenesis in foreland fold-and-thrust belts: A case study on paleofluid flow in the Canadian Rocky Mountains West of Calgary. Marine and Petroleum Geology 35, 235–251. https://doi.org/10.1016/j.marpetgeo.2012.02.014

Vangkilde-Pedersen, T., Anthonsen, K.L., Smith, N., Kirk, K., neele, F., van der Meer, B., Le

Gallo, Y., Bossie-Codreanu, D., Wojcicki, A., Le Nindre, Y.M., Hendriks, C., Dalhoff, F., Peter Christensen, N., 2009. Assessing European capacity for geological storage of carbon dioxide-the EU GeoCapacity project. Energy Procedia 1, 2663–2670. https://doi.org/10.1016/j.egypro.2009.02.034

Veizer, J., Ala, D., Azmy, K., Bruckschen, P., Buhl, D., Bruhn, F., Carden, G.A.F., Diener, A., Ebneth, S., Godderis, Y., Jasper, T., Korte, C., Pawellek, F., Podlaha, O.G., Strauss, H., 1999. 87Sr/86Sr, δ13C and δ18O evolution of Phanerozoic seawater. Chemical Geology 161, 59–88. https://doi.org/10.1016/S0009-2541(99)00081-9

Ventra, D., Clarke, L.E., 2018. Geology and geomorphology of alluvial and fluvial fans: current progress and research perspectives. Geological Society, London, Special Publications 440, 1–21. https://doi.org/10.1144/SP440.16

Vergés, J., 1993. Estudi geològic del vessant sud del Pirineu oriental i central. Evolució cinemàtica en 3D. PhD thesis, University of Barcelona, Barcelona.

Vergés, J., Muñoz, J.A., Martínez, A., 1992. South Pyrenean fold and thrust belt: The role of foreland evaporitic levels in thrust geometry. In: McClay, K.R. (Ed.), Thrust Tectonics. Springer, Dordrecht, 255–264. https://doi.org/10.1007/978-94-011-3066-0_23

Vilasi, N., Swennen, R., Roure, F., 2006. Diagenesis and fracturing of Paleocene–Eocene carbonate turbidite systems in the Ionian Basin: The example of the Kelçyra area (Albania). Journal of Geochemical Exploration 89, 409–413. https://doi.org/10.1016/j.gexplo.2005.11.018

Vincent, S.J., 2002. The Sis palaeovalley: a record of proximal fluvial sedimentation and drainage basin development in response to Pyrenean mountain building. Sedimentology 48, 1235–1276. https://doi.org/10.1046/j.1365-3091.2001.00421.x

Voldsund, M., Gardarsdottir, S., De Lena, E., Pérez-Calvo, J.-F., Jamali, A., Berstad, D., Fu, C., Romano, M., Roussanaly, S., Anantharaman, R., Hoppe, H., Sutter, D., Mazzotti, M., Gazzani, M., Cinti, G., Jordal, K., 2019. Comparison of Technologies for CO2 Capture from Cement Production—Part 1: Technical Evaluation. Energies 12, 559. https://doi.org/10.3390/en12030559

Walderhaug, O., Bjørkum, P.A., 1998. Calcite Cement in Shallow Marine Sandstones: Growth Mechanisms and Geometry. In: Morad, S. (Ed.), Carbonate Cementation in Sandstones. International Association of Sedimentologists Special Publication, 179–192. https://doi.org/10.1002/9781444304893.ch8

Walderhaug, O., Bjørkum, P.A., Bolås, H.M.N., 1989. Correlation of calcite-cemented layers in shallow-marine sandstones of the Fensfjord Formation in the Brage Field. In: Collinson, J.D.

(Ed.), Correlation in Hydrocarbon Exploration. Springer, Dordrecht, 367–375. https://doi.org/10.1007/978-94-009-1149-9_28

Wanas, H.A., 2008. Calcite-cemented concretions in shallow marine and fluvial sandstones of the Birket Qarun Formation (Late Eocene), El-Faiyum depression, Egypt: Field, petrographic and geochemical studies: Implications for formation conditions. Sedimentary Geology 212, 40–48. https://doi.org/10.1016/j.sedgeo.2008.09.003

Wang, A., Liang, T., Li, L., Wang, Z., Fan, C., Wang, Y., Zhang, Y., Kong, H., 2017. Origin of diagenetic calcite cements in the continental Qaidam Basin, NW China: Implication for fluid flow and hydrocarbon migration. Journal of Geochemical Exploration 182, 94–109. https://doi.org/10.1016/j.gexplo.2017.09.002

Wang, Z., Lü, X., Wang, S., Li, Y., Zhou, X., Quan, H., Li, R., 2020. Fracture systems and petrophysical properties of tight sandstone undergoing regional folding: A case study of the Cretaceous reservoirs in the Kuqa foreland thrust belt, Tarim Basin., Marine and Petroleum Geology 111, 104055. https://doi.org/https://doi.org/10.1016/j.marpetgeo.2019.104055

Watkins, H., Bond, C.E., Healy, D., Butler, R.W.H., 2015a. Appraisal of fracture sampling methods and a new workflow tocharacterise heterogeneous fracture networks at outcrop. Journal of Structural Geology 72, 67–82. https://doi.org/10.1016/j.jsg.2015.02.001

Watkins, H., Butler, R.W.H., Bond, C.E., Healy, D., 2015b. Influence of structural position on fracture networks in the Torridon Group, Achnashellach fold and thrust belt, NW Scotland. Journal of Structural Geology 74, 64–80. https://doi.org/10.1016/j.jsg.2015.03.001

Watkins, H., Healy, D., Bond, C.E., Butler, R.W.H., 2018. Implications of heterogeneous fracture distribution on reservoir quality: an analogue from the Torridon Group sandstone, Moine Thrust Belt, NW Scotland. Journal of Structural Geology 108, 180–197. https://doi.org/10.1016/j.jsg.2017.06.002

Wei, N., Li, X., Wang, Y., Dahowski, R.T., Davidson, C.L., Bromhal, G.S., 2013. A preliminary sub-basin scale evaluation framework of site suitability for onshore aquifer-based CO2 storage in China. International Journal of Greenhouse Gas Control 12, 231–246. https://doi.org/10.1016/j.ijggc.2012.10.012

Weissmann, G.S., Hartley, A.J., Scuderi, L.A., Nichols, G.J., Davidson, S.K., Owen, A., Atchley, S.C., Bhattacharyya, P., Chakraborty, T., Ghosh, P., Nordt, L.C., Michel, L., Tabor, N.J., 2013. Prograding distributive fluvial systems—geomorphic models and ancient examples. In: Driese, S.G., Nordt, Lee C. (Eds.), New Frontiers in Paleopedology and Terrestrial Paleoclimatology: Paleosols and Soil Surface Analog Systems. SEPM Special Publication, 131–147. https://doi.org/10.2110/sepmsp.104.16

Wennberg, O.P., Azizzadeh, M., Aqrawi, A.A.M., Blanc, E., Brockbank, P., Lyslo, K.B., Pickard, N., Salem, L.D., Svånå, T., 2007. The Khaviz Anticline: an outcrop analogue to giant fractured Asmari Formation reservoirs in SW Iran. Geological Society, London, Special Publications 270, 23–42. https://doi.org/10.1144/gsl.sp.2007.270.01.02

Wennberg, O.P., Svånå, T., Azizzadeh, M., Aqrawi, A.M.M., Brockbank, P., Lyslo, K.B., Ogilvie, S., 2006. Fracture intensity vs. mechanical stratigraphy in platform top carbonates: the Aquitanian of the Asmari Formation, Khaviz Anticline, Zagros, SW Iran. Petroleum Geoscience 12, 235–246. https://doi.org/10.1144/1354-079305-675

Wilkins, S., Mount, V., Mahon, K., Perry, A., Koenig, J., 2014. Characterization and development of subsurface fractures observed in the Marcellus Formation, Appalachian Plateau, north-central Pennsylvania. AAPG Bulletin 98, 2301–2345. https://doi.org/10.1306/08191414024

Williams, E.A., Ford, M., Vergés, J., Artoni, A., 1998. Alluvial gravel sedimentation in a contractional growth fold setting, Sant Llorenç de Morunys, southeastern Pyrenees. Geological Society, London, Special Publications 134, 69–106. https://doi.org/10.1144/GSL.SP.1998.134.01.05

Wilson, T.H., Smith, V., Brown, A., 2015. Developing a model discrete fracture network, drilling, and enhanced oil recovery strategy in an unconventional naturally fractured reservoir using integrated field, image log, and three-dimensional seismic data. AAPG Bulletin 99, 735–762. https://doi.org/10.1306/10031414015

Xiong, D., Azmy, K., Blamey, N.J.F., 2016. Diagenesis and origin of calcite cement in the Flemish Pass Basin sandstone reservoir (Upper Jurassic): Implications for porosity development. Marine and Petroleum Geology 70, 93–118. https://doi.org/10.1016/j.marpetgeo.2015.11.013

Yang, Z., Zou, C., He, S., Li, Q., He, Z., Wu, H., Cao, F., Meng, X., Wang, F., Xiao, Q., 2010. Formation mechanism of carbonate cemented zones adjacent to the top overpressured surface in the central Junggar Basin, NW China. Science China Earth Sciences 53, 529–540. https://doi.org/10.1007/s11430-010-0037-8

Yoon, K.P., Hwang, C.L., 1995. Multiple Attribute Decision Making: An Introduction. Sage Publications, Thousand Oaks, CA.

Yu, Q., Zhu, W., Ranjith, P.G., Shao, S., 2018. Numerical simulation and interpretation of the grain size effect on rock strength. Geomechanics and Geophysics for Geo-Energy and Geo-Resources 4, 157–173. https://doi.org/10.1007/s40948-018-0080-z

Yuste, A., Luzón, A., Bauluz, B., 2004. Provenance of Oligocene-Miocene alluvial and fluvial fans of the northern Ebro Basin (NE Spain): An XRD, petrographic and SEM study.

Sedimentary Geology 172, 251–268. https://doi.org/10.1016/j.sedgeo.2004.10.001

Zeeb, C., Gomez-Rivas, E., Bons, P.D., Blum, P., 2013. Evaluation of sampling methods for fracture network characterization using outcrops. AAPG Bulletin 97, 1545–1566. https://doi.org/10.1306/02131312042

Zhang, R., Yao, G., Shou, J., Zhang, H., Tian, J., 2011. An integration porosity forecast model of deposition, diagenesis and structure. Petroleum Exploration and Development 38, 145–151.

Zhang, T., Zhang, S., Meng, W., Feng, Y., An, T., 2019. Characteristics and genetic mechanism of carbonate cements in sandstones near the overpressure top surface: A case study of the Niuzhuang Depression in Bohai Bay Basin. Journal of Petroleum Science and Engineering 181, 106172. https://doi.org/10.1016/j.petrol.2019.06.036

Zuffa, G.G., 1985. Optical analyses of arenites: Influence of methodology on compositional results. In: Zuffa, G.G. (Ed.), Provenance of Arenites: NATO-Advanced Study Institute Series C. Reidel Publishing Company, Dordrecht, 165–189.

Zuffa, G.G., 1980. Hybrid arenites: their composition and classification. Journal of Sedimentary Petrology 50, 21–29. https://doi.org/10.1306/212F7950-2B24-11D7-8648000102C1865D

Appendix 1 Appraisal of CO_2 storage potential in compressional hydrocarbon-bearing basins: Global assessment and case study in the Sichuan Basin (China)

Sun, X., Alcalde, J., Gomez-Rivas, E., Struth, L., Johnson, G., Travé, A., 2020. Appraisal of CO_2 storage potential in compressional hydrocarbon-bearing basins: Global assessment and case study in the Sichuan Basin (China). *Geoscience Frontiers,* 11, 2309-2321. doi.org/10.1016/j.gsf.2020.02.008.

Geoscience Frontiers 11 (2020) 2309–2321

Contents lists available at ScienceDirect

Geoscience Frontiers

journal homepage: www.elsevier.com/locate/gsf

Research Paper

Appraisal of CO_2 storage potential in compressional hydrocarbon-bearing basins: Global assessment and case study in the Sichuan Basin (China)

Xiaolong Sun [a,*], Juan Alcalde [b], Enrique Gomez-Rivas [a], Lucía Struth [b], Gareth Johnson [c], Anna Travé [a]

[a] Department of Mineralogy, Petrology and Applied Geology, University of Barcelona, Martí i Franquès s/n, Barcelona, 08028, Spain
[b] Department of Structure and Dynamics of the Earth, Institute of Earth Sciences Jaume Almera, ICTJA-CSIC, Lluis Sole i Sabaris s/n, Barcelona, 08028, Spain
[c] Department of Civil and Environmental Engineering, University of Strathclyde, Glasgow, G1 1XZ, United Kingdom

ARTICLE INFO

Handling Editor: Vinod Oommen Samuel

Keywords:
CO_2 storage
Compressional basins
CO_2 emissions
Sichuan Basin

ABSTRACT

Carbon capture and storage (CCS) has been proposed as a potential technology to mitigate climate change. However, there is currently a huge gap between the current global deployment of this technology and that which will be ultimately required. Whilst CO_2 can be captured at any geographic location, storage of CO_2 will be constrained by the geological storage potential in the area the CO_2 is captured. The geological storage potential can be evaluated at a very high level according to the tectonic setting of the target area. To date, CCS deployment has been restricted to more favourable tectonic settings, such as extensional passive margin and post-rift basins and compressional foreland basins. However, to reach the adequate level of deployment, the potential for CCS of regions in different tectonic settings needs to be explored and assessed worldwide. Surprisingly, the potential of compressional basins for carbon storage has not been universally evaluated according to the global and regional carbon emission distribution. Here, we present an integrated source-to-sink analysis tool that combines comprehensive, open-access information on basin distribution, hydrocarbon resources and CO_2 emissions based on geographical information systems (GIS). Compressional settings host some of the most significant hydrocarbon-bearing basins and 36% of inland CO_2 emissions but, to date, large-scale CCS facilities in compressional basins are concentrated in North America and the Middle East only. Our source-to-sink tool allows identifying five high-priority regions for prospective CCS development in compressional basins: North America, north-western South America, south-eastern Europe, the western Middle East and western China. We present a study of the characteristics of these areas in terms of CO_2 emissions and CO_2 storage potential. Additionally, we conduct a detailed case-study analysis of the Sichuan Basin (China), one of the compressional basins with the greatest CO_2 storage potential. Our results indicate that compressional basins will have to play a critical role in the future of CCS if this technology is to be implemented worldwide.

1. Introduction

The cumulative anthropogenic CO_2 emissions to the atmosphere have produced an approximate 1 °C increase in global average temperature above pre-industrial levels (Peters et al., 2012; Masson-Delmotte et al., 2018). Serious concerns about global warming have recently been raised in the latest Intergovernmental Panel on Climate Change (IPCC) Report, which warns of the need to limit global warming to 1.5 °C to avoid catastrophic environmental damage (Masson-Delmotte et al., 2018). Achieving this target will require the combination of different approaches to climate change mitigation compatible with sustainable development, including CO_2 emission reductions. Carbon Capture and Storage (CCS) can be an efficient and safe method to meet these reductions (Metz et al., 2005; Scott et al., 2013; Alcalde et al., 2018; Bui et al., 2018; Global CCS Institute, 2018). However, there are only 44 large-scale CCS facilities under different development and operation status globally, with a combined CO_2 removal capacity of 83.41 Megatons of CO_2 per annum (Mtpa) (Global CCS Institute, 2019). Note that the current CCS development also includes CO_2 enhanced oil recovery (CO_2-EOR) projects, which can catalyse the implementation of CCS from

* Corresponding author.
E-mail address: upc_sxl@126.com (X. Sun).
Peer-review under responsibility of China University of Geosciences (Beijing).

https://doi.org/10.1016/j.gsf.2020.02.008
Received 29 July 2019; Received in revised form 28 November 2019; Accepted 22 February 2020
Available online 4 March 2020

economic aspects (Stewart and Haszeldine, 2014), but whose effect in the decarbonisation significance is unclear (e.g., Ettehadtavakkol et al., 2014; Armstrong and Styring, 2015; Hornafius and Hornafius, 2015). If the trend of CCS development continued, even considering CO_2-EOR projects, it would still be very far from the global decarbonisation targets (Koelbl et al., 2014; Bui et al., 2018; Global CCS Institute, 2018; Masson-Delmotte et al., 2018; Fig. 1), e.g., 348 Gigatons (Gt) based on a scenario with a broad focus on sustainability (Masson-Delmotte et al., 2018).

Kearns et al. (2017) estimated the global practically accessible geological storage capacity for CO_2 to be between 8000 Gt and 55,000 Gt, indicating that the storage capacity seems not to be a limiting factor for CCS deployment for the rest of this century for most regions. However, storage capacity is not the only parameter that determines a region's suitability for CCS. Other factors include the tectonic setting, basin architecture, reservoir quality, caprock sealing capacity, depth, geothermal gradient, reservoir pressure, hydrogeology, and other environmental and economic factors (Bachu, 2003; Wei et al., 2013; Edlmann et al., 2015).

In particular, the tectonic settings under which a targeted basin was formed exert a significant effect on the other factors listed above (Edlmann et al., 2015; McDermott et al., 2017). Tectonic settings are broadly split into compressional, extensional and strike-slip categories that reflect the relative plate motions that determine their past and present stress state. Despite being ubiquitous in all continents, the potential of compressional basins to safely store captured CO_2 has not been systematically studied, especially in terms of comparison between their storage capacity and the demand for storage, which is directly determined by the geographic distribution and volume of carbon emissions. The present study aims to critically close this knowledge gap by providing a global assessment on the role of compressional basins in the future of global CCS.

Compressional basins are generally formed by the collision and subduction of tectonic plates and can also form within plates, and are characterized by shortening and deformation of the lithosphere. We consider here the two most common types of compressional basins: peripheral foreland basins, developed adjacent to mountain belts, and retro-arc foreland basins, developed adjacent to island volcanic arcs. Compressional basins tend to develop in tectonically active areas and experience faulting and folding, raising the risk of CO_2 leakage (Bachu, 2003). Compared to other basin types, such as those developed under extensional or strike-slip tectonic regimes, compressional basins present in some cases lower geothermal gradients because of the cooling effect of the relatively cold subducting plate (Edlmann et al., 2015). This results in lower reservoir temperature and higher CO_2 density, and further leads to high storage capacity and low buoyancy force due to lower density contrast between CO_2 and formation fluids (Bachu, 2003; Miocic et al., 2016; Iglauer, 2018). Moreover, compressional basins also typically present higher fluid pressure and lower risk of CO_2 leakage owing to their much higher minimum principal stress (Wei et al., 2013), compared with other basin types. Using geomechanical facies assessments, Edlmann et al. (2015) ranked peripheral foreland basins as the most suitable sites for CO_2 storage, followed by passive continental margins, rift and strike-slip basins. These results indicate that compressional basins, and more especially foreland basins, have great potential for CCS development.

Mann et al. (2003) studied 877 giant fields worldwide, observing that 27.83% of them are located in compressional settings. Tian et al. (2014) pointed out that 20.46% of globally undiscovered conventional hydrocarbon resources are stored in foreland basins. Abundant hydrocarbon resources are stored in compressional basins, especially concentrating in the Middle East, North America, South America, Central Asia, and China (Tian et al., 2014; Wang et al., 2016; Tong et al., 2018). Hydrocarbon-bearing provinces are the primary targets of CCS because of proven sufficient capacity and suitable characteristics to trap and store fluids over long periods of time and a substantial number of geological datasets and host industrial infrastructures with potential for re-use for CCS development (Godec et al., 2011; Kuuskraa et al., 2013; Alcalde et al., 2019).

However, it should be noted that the properties of hydrocarbons are different than those of CO_2, such as the physical-chemical processes (e.g., interfacial tension, wettability, density), their flow dynamics and the associated risks when these fluids are in the subsurface (Chiquet et al., 2007; Naylor et al., 2011; Alcalde et al., 2018; Miocic et al., 2019). Therefore, it must take care when using hydrocarbon reserves as a proxy for CO_2 storage potential. In this sense, we use hydrocarbon volume only as a proxy to quantify and rank CO_2 storage potential of these hydrocarbon-bearing basins, rather than using them as a quantitatively equivalent to storable CO_2 emissions. A detailed site characterisation is still needed to assess the storable CO_2 emissions and the potential security of a chosen hydrocarbon reservoir, case by case.

To date, large-scale CCS facilities in compressional basins are concentrated in North America and the Middle East. China and Europe account for significant proportions of global CO_2 emissions and host large compressional basins that could be used for CO_2 storage. However, there are currently no large-scale CCS facilities in operation or even under consideration in these basins, indicating that the potential of these regions still needs to be explored. Despite their promising prospect, the potential of compressional basins has not been assessed quantitatively and in detail to date. Global and regional assessments of CO_2 storage potential are critical to identify short- to middle-term prospects, which can become primary targets for the development of a CCS industry in high priority/high need regions. The overarching aim of this study is to reveal the role of compressional basins and evaluate how appropriate storage regions that developed in compressional settings are for CCS

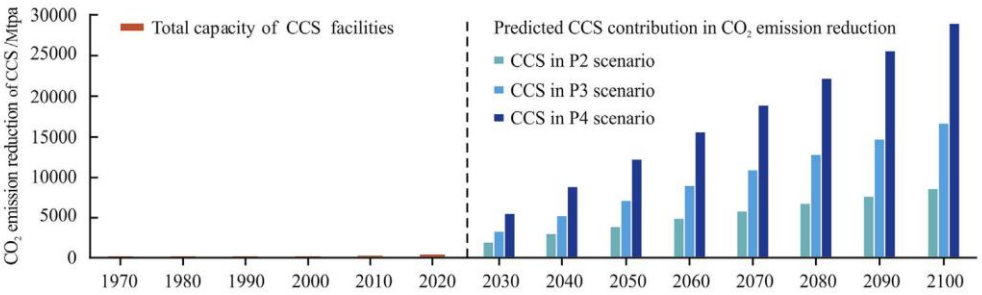

Fig. 1. Total capacity of CCS facilities (data source Global CCS Institute, 2019) and predicted CCS contribution in CO_2 emission reduction (in Mtpa) according to different IPCC Special Report on Global Warming of 1.5 °C scenarios (namely P2, P3 and P4). P2 is a sustainability-oriented scenario where emission reductions are mainly achieved by high human and low-carbon technology development, and low demand in energy and products; P3 is a middle-of-the-road scenario where emission reductions are mainly achieved by changing the ways energy is produced and products are manufactured, and to a lesser degree by demand reductions; P4 is a resource- and energy-intensive scenario where emission reductions are mainly achieved through technological means, making strong use of carbon dioxide removal through the deployment of bioenergy with CCS) (Global CCS Institute, 2018; Masson-Delmotte et al., 2018).

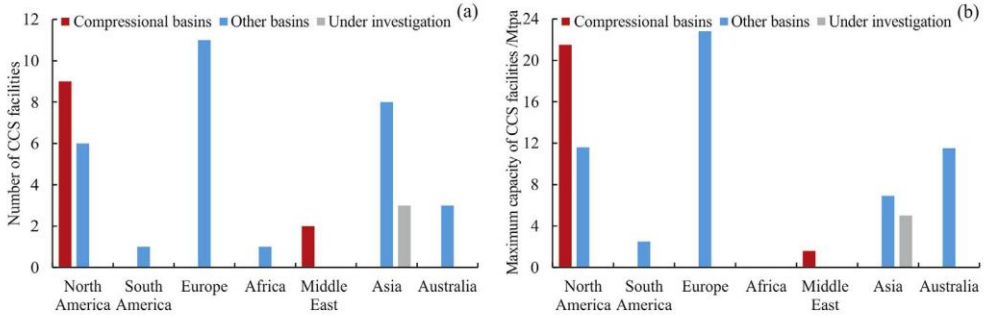

Fig. 2. (a) Number of large-scale CCS facilities and (b) capture and injection capacity (in Mtpa) in different regions of the world (data source Global CCS Institute, 2019). Grey bars represent CCS facilities whose storage sites and transportation methods are still under investigation.

development.

In this contribution, we analyse the spatial distribution of the main hydrocarbon-bearing basins in the world and compare their potential reservoir capacity with global CO_2 emissions using GIS methods. Based on previous source-to-sink appraisals (e.g., UNIDO, 2011; Edlmann et al., 2015), we adopt updated CO_2 emissions, comprehensively consider tectonic settings of basins and projected emission reductions of countries and, finally, create an integrated parameter to identify regions with high CO_2 storage potential in compressional basins. This detailed analysis allows us to evaluate to what extent compressional basins represent the best CCS option in certain regions, and whether they can play an essential role in global CCS development.

2. Current status of CCS in compressional basins

According to the latest data from the CCS Facilities Database (Global CCS Institute, 2019), there are 44 large-scale CCS facilities under different development and operation status, able to capture and inject at most 83.41 Mtpa of CO_2, once they are all fully functional (Fig. 2a and b). By number of facilities, most CCS activity is located in North America, Europe and Asia, with 15, 11 and 11 facilities, respectively. If measured by the capacity for CO_2 capture and injection, activity concentrates in North America, Europe, Asia and Australia, with 33.1, 22.8, 11.91 and 11.5 Mtpa, respectively. Global CCS development is hence far from achieving the CO_2 emission reduction targets set for 1.5 °C above pre-industrial levels (Masson-Delmotte et al., 2018).

CCS development in compressional basins shows a heterogeneous distribution to date (Fig. 2). There are currently eleven large-scale CCS facilities located in compressional basins, while there are 30 facilities in other basin types. The large-scale CCS facilities in compressional basins can capture and inject 23.1 Mpta of CO_2, accounting for 27.7% of all large-scale facilities globally. However, they are nearly all in North America with nine facilities that can capture and inject 21.5 Mpta of CO_2, with another two facilities and storing 1.6 Mpta of CO_2 in the Middle East. Furthermore, 90% of these facilities are enhanced oil recovery projects (CO_2-EOR), and therefore not fully dedicated to storage. Most regions do not host any large-scale CCS facilities either in operation or even under consideration. In the following sections, we investigate the characteristics of global compressional basins to identify areas with potential for CCS development.

3. Data and methods

3.1. Basin resources and CO_2 emission data

Suitable storage options include oil and gas fields, unconventional reservoirs, basaltic rocks and deep saline aquifers (Metz et al., 2005; Bachu, 2007; Matter et al., 2009). Oil and gas fields are likely targets for CCS because of their proven capacity to safely retain fluids over geological timescales. Furthermore, substantial subsurface data, as well as infrastructure in place suitable for re-use, are usually available from exploration and production activities (Alcalde et al., 2019). Although unconventional reservoirs show potential for CCS development and even resulted in recent CCS project evaluation and implementation, especially in coal seams and shales (Bachu, 2007; Kang et al., 2011; Liu et al., 2013), there are still noticeable uncertainties and risks due to their heterogeneous and tight characteristics. Basaltic rocks facilitate the transformation of CO_2 to carbonate minerals, referred to as mineral trapping, owing to their high reactivity and abundant metal ions, but this option is only very recent and it is still being investigated (Gislason and Oelkers, 2014). Saline aquifers and oil and gas fields are the most developed storage types because of the large potential capacity and the data availability respectively. However, the subsurface data that characterise global saline aquifers is more sparse and incomplete than in oil and gas fields, so we restrict our assessment to hydrocarbon-bearing basins.

Based on data from the National Petroleum Assessment and the World Petroleum Assessment of the United State Geological Survey (USGS) (USGS, 1995–2013, 2000; Bird et al., 2008), we obtained global basin shapes and values for conventional hydrocarbon resources of more than 200 basins (Fig. 3a). The total hydrocarbon resources utilized here consist of the cumulative hydrocarbon production, remaining recoverable hydrocarbon and undiscovered recoverable hydrocarbon estimated to exist based on geological knowledge and theory (USGS, 2000). Since the USGS only provides data on undiscovered resources for the United States (USGS, 1995–2013), we deduced their total resources using the ratio of undiscovered vs total resources of global basins (USGS, 2000). For most basins in the Arctic Circle, which have not experienced extensive exploration and development, undiscovered resource estimates are assumed to match their total resource estimates (Bird et al., 2008).

Based on the CGG Robertson Sedimentary Basins compilation (Robertson, 2014), we have divided global hydrocarbon-bearing basins into five major tectonic settings: foreland basins, passive margin basins, intracratonic basins, rift and post-rift basins, and other basins (Fig. 3b). Over 40% of hydrocarbon-bearing basins by area are located in foreland basins, which mainly concentrate in six regions (Fig. 3a and b): North America, West South America, East Europe, West Middle East, central Asia and China.

The global stationary CO_2 emissions in 2012 were extracted from the version v4.3.2 of the Emissions Database for Global Atmospheric Research (EDGAR) (EDGAR, 2018; Janssens-Maenhout et al., 2019) (Fig. 4). We use emission sources in 2012 to identify areas of high stationary emissions, assuming that these areas will require greater mitigation efforts. The dataset includes CO_2 emissions from various resources, including population, energy, fossil fuel consumption and production, agriculture, industry, and solid and liquid waste. Our current technological level does not allow us to capture small and dispersed CO_2 emissions, such as those associated with transport or agricultural activities. Thus, we have only considered emission points above 10,000 tons of CO_2 per annum (tpa), which add up to 32.72 Gt globally, constituting the 97% of the global total emissions (34.87 Gt; EDGAR, 2018).

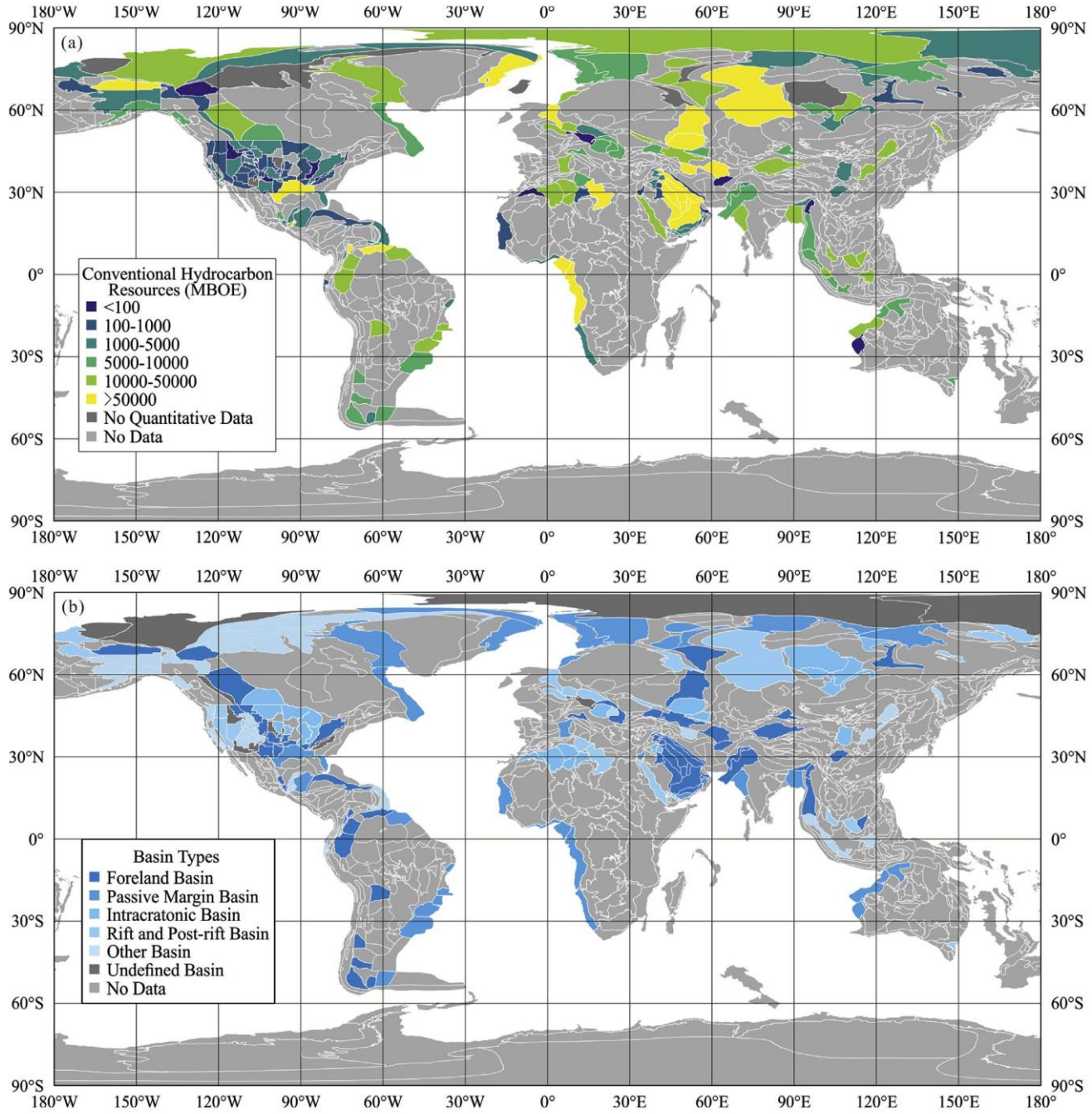

Fig. 3. Distribution of (a) major conventional hydrocarbon resources (given in million barrel of oil equivalent (MBOE)): basins in the United States (USGS, 1995–2013), the Arctic Circle (Bird et al., 2008) and other regions (USGS, 2000) and (b) the tectonic settings of main hydrocarbon-bearing basins (Robertson, 2014).

Finally, we have used the Projected Emission Reductions (PER) plans by 2030 that different G20 economies signed according to the unconditional Intended Nationally Determined Contributions (INDCs) scenario (Fig. 5) (Den Elzen et al., 2016). We assume that countries with high PER have greater urgency for addressing climate change mitigation, and thus CCS will be more likely to be implemented in them. These unconditional INDCs are not directly comparable, since different economies submitted their INDCs in various forms. For example, some countries provided baseline emission projections in INDCs while others did not. Moreover, China and India have proposed a combination of targets, which need to be calculated using their respective energy models (Den Elzen et al., 2016). Den Elzen et al. (2016) compiled these datasets and produced a unified and comparable dataset. However, since 2016, some of the G20 countries considered have changed their emission reduction plans. For example, the USA announced that they withdraw from the Paris Agreement, and its Nationally Determined Contribution was rated "Critically Insufficient" by the Climate Action Tracker (Climate Action Tracker, 2018). Furthermore, our focus on G20 countries does not imply that other countries do not have their own emission reduction plans. Thus, the data from Den Elzen et al. (2016) is not necessarily in line with the current climate policies, but offer a unified framework for comparison across countries.

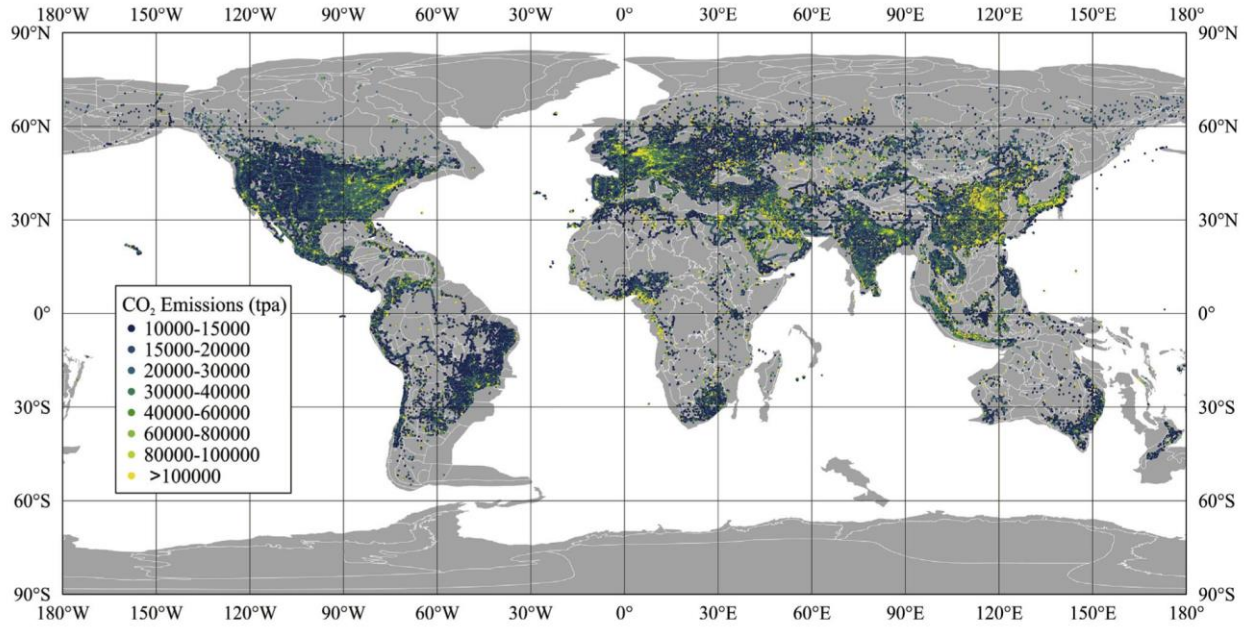

Fig. 4. Distribution of CO_2 emissions (tons per annum (tpa)) (data source EDGAR, 2018).

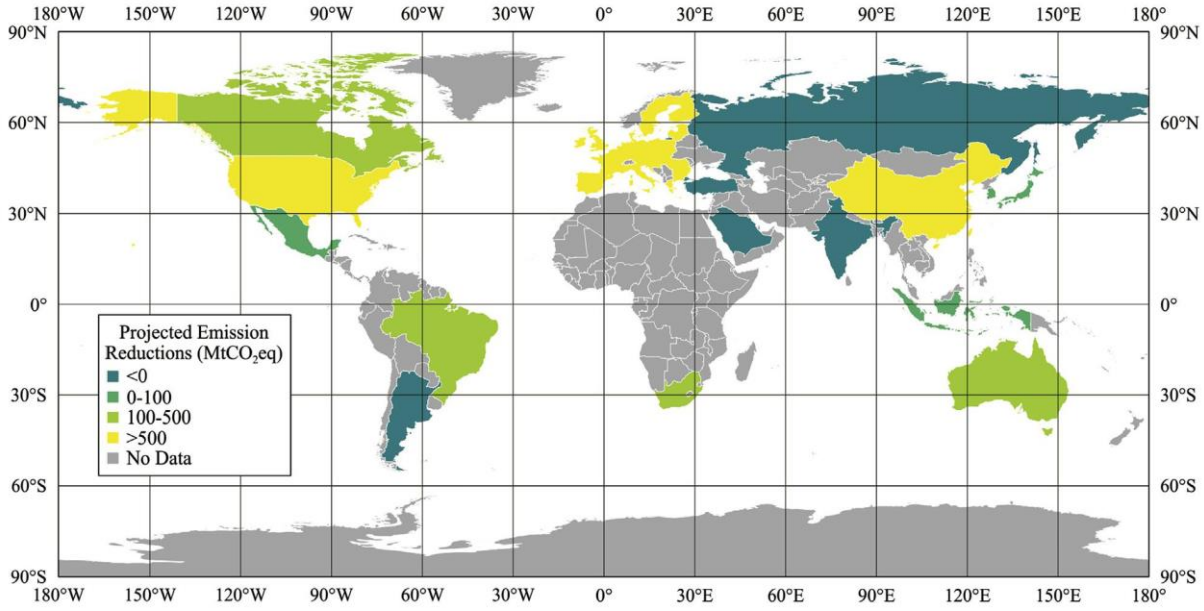

Fig. 5. Projected emission reductions in 2030 of G20 economies (Million tonnes CO_2 equivalent ($MtCO_2eq$)) (data source Den Elzen et al., 2016).

3.2. Data processing in GIS software

We have combined the three datasets (i.e., basin distribution, basin hydrocarbon resources and CO_2 emissions) to develop a source-to-sink matching approach. This process allows us to correlate the distribution of CO_2 emissions with the available storage space in compressional basins, using hydrocarbon resources as a proxy.

First, we input the basin polygon shapes and localised the CO_2 emission points into a GIS-based software (QGIS version 3.4.2, 2018). To delimit and calculate the combined CO_2 emissions in each basin, we summed all the CO_2 emissions lying within each basin (Fig. 6). As long distances between CO_2 sources and sinks (i.e., emission points and basins) can increase the transport and monitoring costs, making CCS financially unattractive, we only considered CO_2 emission points lying within the target basins and disregarded all other emission sources.

For the storage potential appraisal, we assume that compressional regions with high potential for developing CCS must encompass sufficient hydrocarbon resources and CO_2 emissions. Due to the difference in magnitude between hydrocarbon resources (V_H) and CO_2 emissions (V_{CO_2}), data processing is necessary before the selection of potential regions. We applied a data normalization based on a function of their minimum and maximum values:

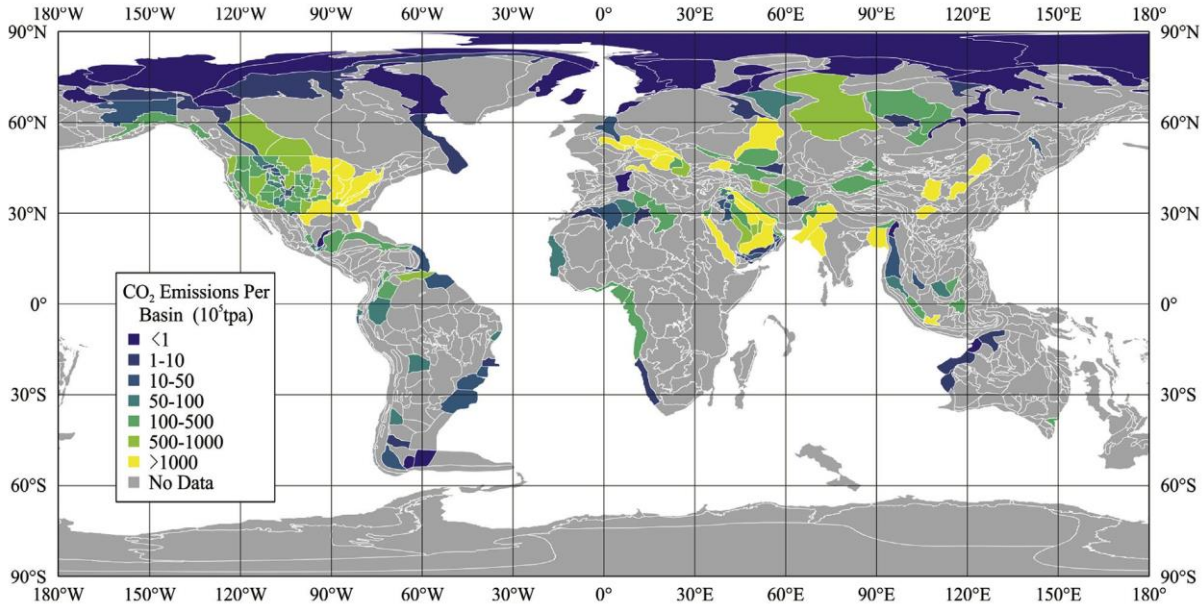

Fig. 6. Distribution of potential CO_2 emissions (in 10^5 tpa) within the main hydrocarbon-bearing basins. Only emission points above 10^4 tpa are considered in this study.

$$V_n = \frac{V - V_{\min}}{V_{\max} - V_{\min}} \quad (1)$$

where V_n, V, $V_{\min}$ and $V_{\max}$ are the normalized value, the actual value, the minimum value and the maximum value, respectively.

We created an integrated evaluation parameter ($V_{CCS\text{-}P}$) to evaluate basin potential for CO_2 storage:

$$V_{CCS-P} = V_{nH} \times V_{nCO_2} \quad (2)$$

where V_{nH} and V_{nCO_2} are the normalized values of V_H and V_{CO_2}, respectively.

Hydrocarbon resources are not quantitatively equivalent to storable CO_2 emissions, which require more geological parameters to be calculated (Goodman et al., 2011). Hence, we use hydrocarbon resources only as a proxy to quantify and rank CO_2 storage potential of these hydrocarbon-bearing basins. Finally, we obtained the distribution of $V_{CCS\text{-}P}$ that highlights basins with high (yellow) and low (blue) potential for CCS (Fig. 7a) and identified five high-priority regions that have high $V_{CCS\text{-}P}$ and are dominated by compressional basins (Fig. 7b).

4. Results and discussion

4.1. CO_2 storage potential in compressional basins

The hydrocarbon industry has abundant oil and gas resources stored in compressional basins, indicating their significant potential for CCS. Our GIS analysis relates the storage capacity of basins with the potential demand for carbon storage, according to the geographic distribution and volume of CO_2 emissions.

The total hydrocarbon resources in global compressional basins reach over 2184 billion barrels of oil equivalent (BBOE), accounting for around 50% of the total resources in all hydrocarbon-bearing basins. Compressional basins also contain significant CO_2 emission sources, with 3.8 Gt of CO_2 annual emissions accounting for 34% of all hydrocarbon-bearing basins. Compressional basins with high CO_2 emissions are mainly located in Western Canada, America, the Middle East, Europe and China (Fig. 6).

To select the target areas with the greatest CO_2 storage potential in compressional basins, which will be taken forward for detailed assessment, we favoured the areas with high $V_{CCS\text{-}P}$ compressional basins that are also relatively isolated from other basin types for prospective CCS storage. Based on the distribution of $V_{CCS\text{-}P}$, we have selected five high-priority regions for detailed assessment (Figs. 7 and 8): (1) North America, (2) north-western South America, (3) south-eastern Europe, (4) western Middle East, and (5) western China. Of the five high-priority regions, only North America, Europe and China have explicit high-emission reduction targets in place (Den Elzen et al., 2016) (Fig. 7c), and therefore they are more likely to implement decarbonisation actions, like CCS.

4.2. High-priority regions

4.2.1. North America

The area spreads across the USA and western Canada and is composed of 17 compressional basins adjacent to the Rocky Mountain, Marathon-Ouachita and Appalachian fold-and-thrust belts (Fig. 7b), which formed owing to the closing of ocean between Laurasia and Gondwana in the Late Paleozoic and the collision between the North American and Pacific plates during the Meso–Cenozoic (Ma et al., 2014).

These basins have 11 BBOE of undiscovered conventional hydrocarbon resources and 26.5 BBOE of estimated total hydrocarbon resources, mainly distributed in the Western Canadian Sedimentary Basin (WCSB), the Permian Basin, the Appalachian Basin and the Montana Thrust Belt. In this area, the major CO_2 sources relate to electricity generation in Canada and electricity, refinery, chemical and other hydrocarbon industries in the USA (U.S. Department of Energy Office of Fossil Energy, 2015). Around 1180 Mtpa of CO_2 emissions are distributed in compressional basins, mainly in the Appalachian Basin, the Bend Arch-Fort Worth Basin and the WCSB.

The USA and Canada account for 11.85% and 1.92% of global greenhouse gas emissions in 2012, respectively (Den Elzen et al., 2016). Their high emission reduction targets (Den Elzen et al., 2016) (Fig. 8) and high suitability for CCS development (Mitrovic et al., 2011; Blondes et al., 2013) have made this region the most active area of CCS development worldwide (Global CCS Institute, 2018). There are nine large-scale CCS facilities in operation or under advanced development in the target compressional basins that can capture and inject at most 21.5 Mtpa of CO_2, dominating the global CCS development in compressional

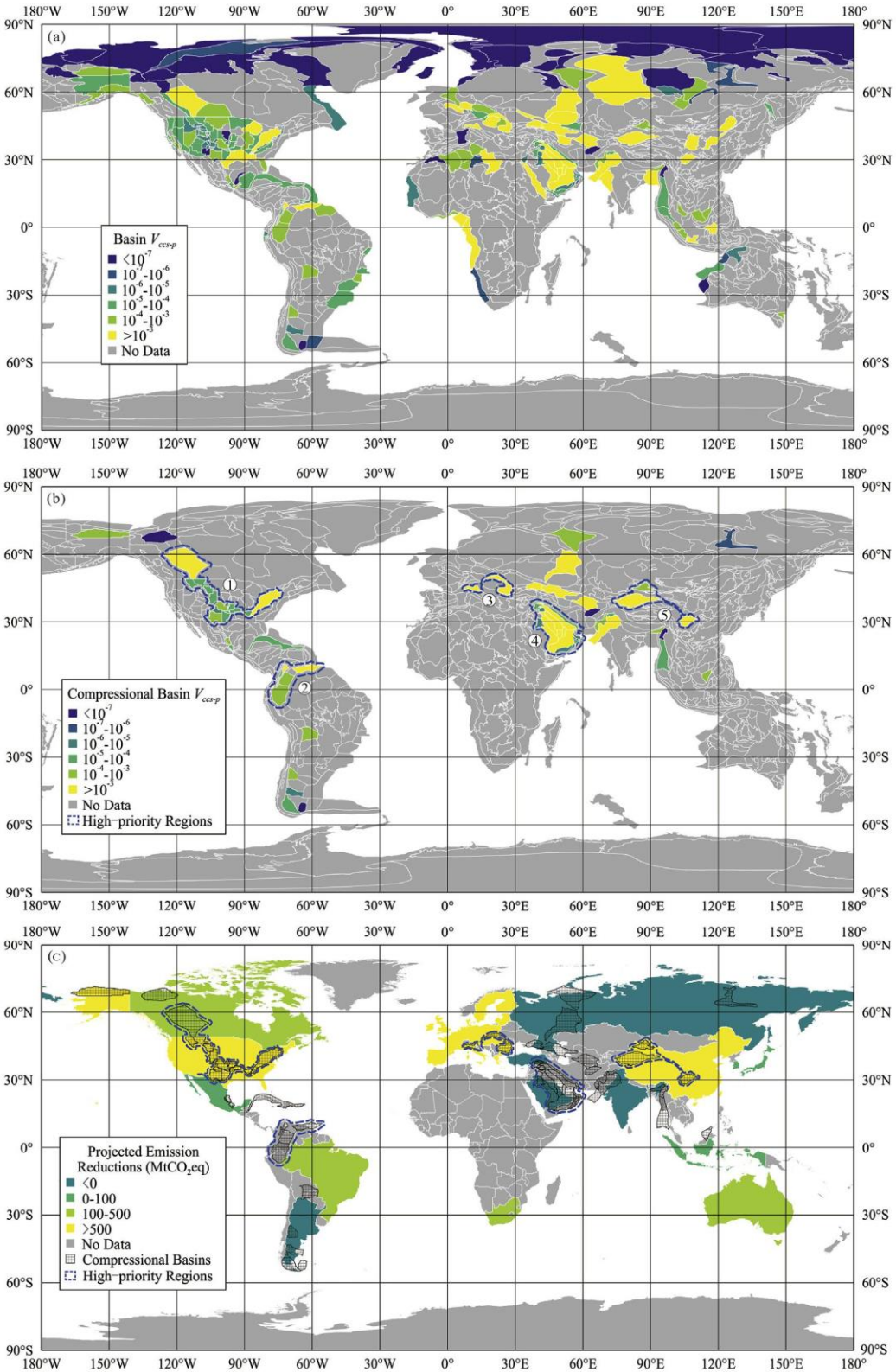

Fig. 7. Distribution of the integrated evaluation parameter (V_{CCS-P}) in (a) the main hydrocarbon-bearing basins in the world; (b) V_{CCS-P} in compressional hydrocarbon-bearing basins; and (c) distribution of the high-priority regions and the projected emission reductions of G20 economies (data source Den Elzen et al., 2016). The numbers in (b) and (c) mark the high-priority regions selected for detailed analyses: (1) North America; (2) north-western South America; (3) south-eastern Europe; (4) western Middle East; (5) western China.

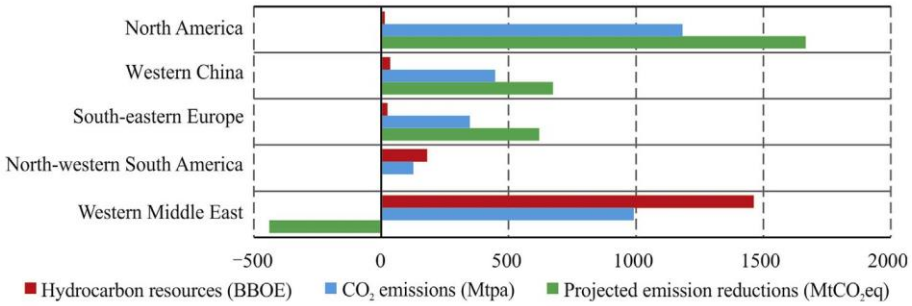

Fig. 8. Comparison of hydrocarbon resources (BBOE) (only the undiscovered resources are attainable for North America), CO_2 emissions (Mtpa) and projected emission reductions ($MtCO_2eq$) of the selected high-priority regions (Only the PER of the western Middle East is negative).

settings. According to the distribution of $V_{CCS\text{-}P}$ value, the compressional basins with the highest potential are the WCSB and the Appalachian Basin. The CO_2 emissions from the large-scale facilities in the WCSB (the Alberta Carbon Trunk Line and the Quest) derive mainly from fertiliser production, oil refining and hydrogen production (Global CCS Institute, 2019). Only two pilot and demonstration CCS facilities have been developed in the Appalachian Basin, the Marshall County ECBM Project (Wilson et al., 2012) and the Mountaineer Validation Facility (Mishra et al., 2014), both closed in the 2010's with around 40,000 t CO_2 stored in the subsurface.

4.2.2. North-western South America

Owing to the subduction of the Pacific and Caribbean plates under the South American Plate after the Late Cretaceous, fore-arc basins, the Andes and retro-arc foreland basins developed from offshore to inland in western and northern South America (Xie et al., 2009; Yang et al., 2009). Retro-arc foreland basins dominate hydrocarbon resources in north-western South America (Yang et al., 2009), which are regarded as the main CCS targets located in Peru, Ecuador, Colombia and Venezuela (Fig. 7b).

North-western South America has 178 BBOE of hydrocarbon resources, mainly distributed in Venezuela. On the other hand, CO_2 emissions are mainly outcomes from power generation, cement and refinery industries in west South America, accounting for 46%, 24% and 18% of the emissions, respectively (UNIDO, 2011). These compressional hydrocarbon-bearing basins in North-western South America contain 123 Mtpa of CO_2 emissions.

Colombia and Venezuela are the main CO_2 emitters in the region, accounting for around 0.5% of global greenhouse gas emissions in 2012, which aim to achieve emission reduction targets of 20% below business as usual level by 2030 (Den Elzen et al., 2016). Although there are no large-scale CCS facilities under operation or construction, other decarbonisation measures (e.g., enhancing energy efficiency, substituting energy-intense appliances with more efficient models) have been effectively applied in the region (Pereira et al., 1997; Román et al., 2018). The high potential for CCS of the region, marked by its $V_{CCS\text{-}P}$, may facilitate CCS development in the future. In particular, the East Venezuela Basin contains some of the largest oil accumulations in the world (Erlich and Barrett, 1992), a long history of production and suitability for CO_2-EOR (Manrique et al., 2003), which can open the door to a CCS industry in the area.

4.2.3. Southeastern Europe

The compressional setting in this region is closely related to the Alpine Orogeny, originated by the convergence of the African and European plates after the closing of the interposed Tethys Ocean (Castellarin, 2001). Three compressional basins with high CO_2 storage potential are located in southern and eastern Europe, the North Carpathian, Carpathian-Balkanian and Po basins (Fig. 7b), which mainly belong to Romania, Bulgaria, Poland, Ukraine and Italy. These three basins contain 21 BBOE of hydrocarbon resources and host activities emitting 344 Mtpa of CO_2 per year. CO_2 emissions are mostly produced from power generation, cement and refinery industries, accounting for 71%, 14% and 10% of the total emissions in these industries in south-eastern Europe, respectively (UNIDO, 2011).

The European Union countries are the third largest CO_2 emitter globally (www.globalcarbonatlas.org), and therefore have been urged to assume important emission reductions (e.g., 20% reduction by 2020) (da Graça Carvalho, 2012) and 40% by 2030 compared to 1990 (deLlano-Paz et al., 2016), which equal to more than 600 $MtCO_2eq$ (Den Elzen et al., 2016). Within these scenarios, CCS must be invoked in order to meet their CO_2 reduction targets (Vangkilde-Pedersen et al., 2009). Despite new initiatives are mainly concentrated in Norway, the UK and the Netherlands (Neele et al., 2017), the Carpathian region shows great storage potential and has drawn some attention for CCS development, particularly in Poland (Uliasz-Misiak, 2007; Radoslaw et al., 2009), which is a major coal producer in Europe. CCS could help in the transition to cleaner energy production systems while reducing the economic impact of this transformation (Odenberger et al., 2013).

4.2.4. Western Middle East

In this region, the foreland basins formed from the Cretaceous to the Miocene because of the subduction of the Arabian Plate under the Eurasian Plate (Mohajjel et al., 2003; Wang, 2012). These basins experienced transpression during the Pliocene, which superposed on previous passive margin and faulted basins (Wang, 2012). This area contains the greatest enrichment of hydrocarbon resources in the world. All these resources (1458 BBOE) are hosted in compressional basins, mainly distributed across the Zagros Fold Belt, the Rub Al Khali Basin, the Greater Ghawar Uplift and the Mesopotamian Foredeep Basin. The CO_2 emissions in this area (988 Mtpa) mainly result from power generation and refinery activities, which take up 64% and 16% of all CO_2 emissions of the Middle East (UNIDO, 2011).

The Middle Eastern INDCs are generally quite low. For example, CO_2 emission reductions in Iran, Iraq and Oman are 4%, 1% and 2% respectively, and countries such as the United Arab Emirates and Qatar have not committed to quantitative targets (Den Elzen et al., 2016). Saudi Arabia even has negative projected emission reductions relative to the current policy scenario in 2030 (Den Elzen et al., 2016) (Fig. 8). However, the availability of giant hydrocarbon fields in the area offers significant potential for CCS development, especially for CO_2-EOR projects (Algharaib, 2009). There are two large-scale CCS facilities operating for enhanced oil recovery, the Uthmaniyah CO_2-EOR Demonstration in Saudi Arabia and the Abu Dhabi CCS, whose capture capacities are both 0.8 Mtpa with CO_2 emissions resulting from natural gas and steel industries (Global CCS Institute, 2019).

4.2.5. Western China

Compressional settings in western China are controlled by the collision of the Indian and Eurasian plates and are closely related to the

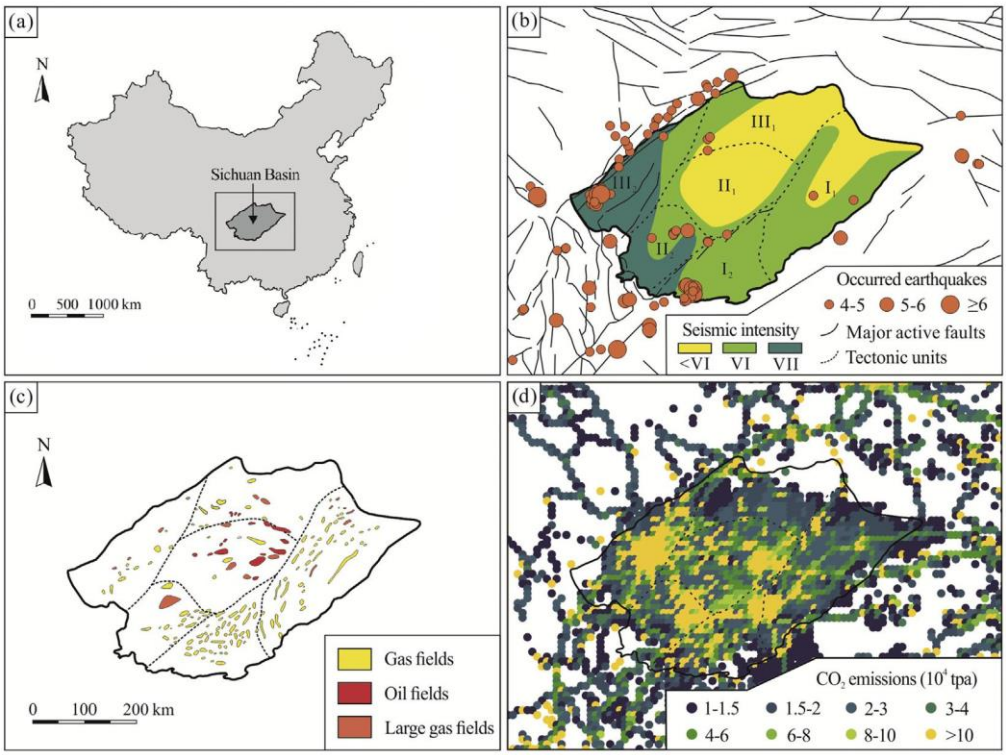

Fig. 9. (a) Geographical location, (b) tectonic units (the Eastern High-steep Fold Belt (I_1), the Southern Low-steep Fold Belt (I_2), the Central Gentle Fold Belt (II_1), the South-western Low-steep Fold Belt (II_2), the North-western Low-flat Fold Belt (III_1) and the Western Low-steep Fold Belt (III_2)) (Diao et al., 2017b), major active faults, seismic intensity (Wei et al., 2013), occurred earthquake from 2012 (≥4 magnitude) (data source China Earthquake Networks Centre, 2019), (c) oil and gas fields (Ma et al., 2010) and (d) CO_2 emissions (≥10,000 tpa) (data source EDGAR, 2018) of the Sichuan Basin.

evolution of the Tethys Ocean (Jia et al., 2003; Song et al., 2015). The main hydrocarbon-bearing basins include the Sichuan, Tarim and Junggar basins, which store 33.6 BBOE of conventional hydrocarbon resources. CO_2 emissions mainly result from cement, power plants, ammonia and steel industries (Li et al., 2009; Wei et al., 2013). Furthermore, compressional basins have 445 Mtpa of CO_2 emissions, dominated by the Sichuan Basin accounting for 87% of the total emissions.

As the second largest energy consumer and the largest carbon emitter, there is an urgent need for carbon emission reductions in China, with 671 Mt of CO_2 emissions to be reduced by 2030 compared to the current policy scenario (Den Elzen et al., 2016). CCS has been regarded as one of the essential actions for climate change mitigation (Li and Huang, 2010; Zhang et al., 2013). It has been evaluated that the Tarim, Junggar and Sichuan basins have high suitability for CCS (Wei et al., 2013; Guo et al., 2015). However, the nine large-scale CCS facilities that are in operation or in construction in China to date are located outside these basins, as most western basins (e.g., the Tarim and Junggar basins) are located relatively far away from the main industrial areas than eastern basins in China. The Sichuan Basin, on the other hand, with its relatively high hydrocarbon reserves and high CO_2 emissions, deserves more attention for CCS in China. Accordingly, we present here a more detailed analysis of the Sichuan basin and evaluate the opportunity that it represents for the future development of CCS in this region.

4.3. Case study: Sichuan Basin

Regions must satisfy several requirements to be considered suitable for CCS. These requirements are related to the characteristics of the storage site (i.e., tectonic activity, geo-temperature, pressure), the reservoir (i.e., volume, porosity, permeability), the caprock (sealing capability), and other economic and social aspects (e.g., source of CO_2, industrial infrastructures, policy support) (Bachu, 2003; Wei et al., 2013; Leung et al., 2014). In this respect, the Sichuan Basin presents a high $V_{CCS\text{-}P}$ and is located in China, a country with a high PER and therefore prospective decarbonisation plans. This basin is used here to illustrate the potential of compressional basins for CCS development from the above aspects.

The Sichuan Basin, located in SW China (Fig. 9a), is a typical superimposed basin (Ma, 2017a) that was developed during the Middle and Late Proterozoic, with the Yangtze Platform forming its basement. The Sichuan Basin developed in extensional settings before the Early Triassic, and was inverted into compressional settings due to the closing of the Paleo-Tethys Ocean and the collision between the oceanic crust and the Yangtze Platform, and accordingly formed a foreland basin in the Late Triassic and Jurassic. Since then, intense folding and erosion have constantly shaped the Sichuan Basin (Mao et al., 2006), currently surrounded by peripheral orogenic belts and a series of fold-and-thrust belts. The geothermal gradient in the Sichuan Basin generally ranges of 20–25 °C/km (Wang et al., 2011), resulting in higher storage capacity and lower buoyancy force than warmer basins (Bachu, 2003; Wei et al., 2013). The Sichuan Basin can be divided into six secondary tectonic units, among which, the Southern Low-steep Fold Belt (region I_2), the South-western Low-steep Fold Belt (II_2) and the Western Low-steep Fold Belt (III_2) have complicated tectonic background, with relatively high seismic intensity and more developed active faults, which may be responsible for the large number of earthquakes occurred (China Earthquake Networks Centre, 2019; Fig. 9b). On the other hand, the Central Gentle Fold Belt (II_1) has a relatively stable crust with low seismicity, making it is suitable for CO_2 storage (Fan et al., 2014) (Fig. 9b). It has an area of 37,000 km^2, which corresponds to a large basin according to the CCS evaluation criteria of Wei et al. (2013). Finally, the Eastern High-steep Fold Belt (I_1)

and the North-western Low-flat Fold Belt (III_1) have moderate tectonic environments.

The Sichuan Basin has the largest reserves and the second largest production of natural gas in China (Ma, 2017a). The latest data indicate that there are 12.5 trillion cubic meters of conventional natural gas resources (Ma, 2017b) and 81.2 million tons of oil (Luo et al., 2013). Hydrocarbon resources are mainly distributed in the Permian and Triassic units, and oil is mainly lying in the central Sichuan Basin, while natural gas is mainly stored in the eastern Sichuan Basin (Ma et al., 2010; Ma, 2017b) (Fig. 9c). All these hydrocarbon resources and fields indicate the significant potential of the Sichuan Basin for CCS. First, it has qualified reservoirs and caprocks which provide significant capacity to store and seal fluids over long periods of time. It is estimated that the Sichuan Basin can store 5.45 Gt or 3.41 Gt of CO_2 in hydrocarbon fields based on the methods of depleted hydrocarbon fields or enhanced hydrocarbon recovery, respectively (Diao et al., 2017a). Since oil and gas exploration and production in the Sichuan Basin started in 1953 (Zhang and Zhang, 2002), abundant boreholes, seismic data and other geological data provide prerequisites for CCS development. Finally, the Sichuan Basin has the most advanced and mature technology of the natural gas industry in China, including equipment, infrastructure, technology and research systems (Ma, 2017b). For instance, the total length of gas pipeline exceeds 4000 km with more than 50×10^9 m^3 of gas transportation capacity in total (Ma, 2017a, b), which will also benefit the construction of CO_2 pipelines or can even be directly utilized as CO_2 pipelines. Considering their hydrocarbon resources, I_1, I_2 and II_1 secondary tectonic units have high potential for CCS development.

Due to the relatively underdeveloped industry in western China, CO_2 emissions in most compressional basins are lower than in the eastern basins (Li et al., 2009; Wei et al., 2013), except for the Sichuan Basin where two of the most developed cities in China are located, Chongqing and Chengdu. The CO_2 emissions in the Sichuan Basin are mainly produced from cement manufacturing and power generation (Li et al., 2009). It is estimated that at least 0.39 Gt of utilizable CO_2 were emitted to the atmosphere in the Sichuan Basin in 2012, exceeding the sum of all other compressional basins in western China, and indicating the existence of sufficient CO_2 emissions in the Sichuan Basin to justify CCS development. Except for the northern part and southern edge of the Sichuan Basin, most regions have large CO_2 emission concentrations (Fig. 9d).

As the largest carbon emitter worldwide (Li and Huang, 2010), China accounts for 23.27% of global greenhouse emissions in 2012, whose emissions will peak around 2030 with between 14.7 and 14.0 $MtCO_2eq$ based on the current policy scenario and the Unconditional INDC scenario, respectively (Ma et al., 2014). CCS has been regarded as an essential technology for climate change mitigation in a series of released reports, e.g., the China's National Climate Change Programme, the China's Policies and Actions for Addressing Climate and the China's Intended Nationally Determined Contributions (Li and Huang, 2010; UNFCCC, 2015). At a smaller scale, the regions of Sichuan and Chongqing have proposed to explore and promote pilot and demonstration CCS projects within their Work Programme for "Control Greenhouse Gas Emissions During the Thirteenth Five-Year Plan", providing policy support for CCS development in the Sichuan Basin (Chongqing Municipal People's government, 2017; The People's Government of Sichuan Province, 2017). It is thus expected that the Sichuan Basin will draw the attention of different CCS stakeholders in the near future.

Based on the analysis of tectonic environments, hydrocarbon resources, CO_2 emissions and political support, the Central Gentle Fold Belt of the Sichuan Basin represents an optimal area to develop a CCS industry. Here, we present a preliminary discussion to identify the storage sites with greatest potential within this sector. From the Ediacaran (Sinian) to the Triassic, the Sichuan Basin was dominated by marine carbonate deposits with localized clastic sedimentation in stable sedimentary environments (Yang et al., 2016). Subsequently, after the marine-to-continental transition in the Late Triassic, the Sichuan Basin experienced continental sedimentation, mainly controlled by an alluvial fan-fluvial-delta-lacustrine depositional system. A series of source-reservoir-cap assemblages developed during the Ediacaran (Sinian), Cambrian, Silurian, Permian, Triassic and Jurassic (Luo et al., 2013; Wang et al., 2015), whose depths (generally more than 3500 m) meet the carbon storage requirements (Bachu, 2003; Wei et al., 2013). However, these reservoirs present two problems that should be taken into consideration. First, they tend to have low porosity and tight characteristics due to their deep burial with an average porosity of 3.24% and permeability of 1.45 mD for carbonate and 5.3% and 0.19 mD for clastic reservoirs (Wang, 2004; Yang et al., 2016). Second, caprocks deeper than around 2400 m cannot immobilize CO_2 permanently by structural trapping as efficiently as shallower reservoirs due to wettability reversal (Iglauer, 2018). Thus, it is priority to find shallower high-quality reservoir-caprock assemblages, which are mainly located in Jurassic and Triassic Xujiahe Formation (Fig. 10). In this sense, the Central Gentle Fold Belt contains the Guang'an, Hechuan and Bajiaochang large sized gas fields (around 300×10^9 m^3 of proved reserve in these gas fields (Ma et al., 2010)), whose reservoirs are dominated by Jurassic and Triassic Xujiahe Formation with reservoir and caprock burial generally ranging from 1500 m to 3500 m. Therefore, this area should be considered a priority for CCS implementation.

5. Conclusions

CCS will have an essential and challenging role in achieving the global target to limit the warming of global average temperature to 1.5 °C above pre-industrial levels. However, there is still a huge gap between the current CCS development and the ultimate objective, which is set to capture and store more than 300 Gt CO_2 by 2100 globally. CCS needs to develop fast, and for that purpose, it is crucial to consider the different potential storage options globally. Sedimentary basins in compressional tectonic settings are abundant and cover large areas on the Earth's surface. However, their potential for storing captured carbon has not been systematically evaluated against the geographic distribution of CO_2 emissions. To fill this knowledge gap, we employ a source-to-sink approach to evaluate the potential of compressional basins for CCS development based on basin distribution, hydrocarbon resources and CO_2 emissions. These inputs have been combined into an integrated evaluation parameter that allows the selection of five regions for potential CCS development in compressional basins: North America, north-western South America, south-eastern Europe, western Middle East, and western China. The most promising regions are located in the foreland basins of mountain chains, except in north-western South America, where the subduction of the Pacific and Caribbean plates under the South American plate resulted in the formation of hydrocarbon-rich retro-arc basins in Peru, Ecuador, Colombia and Venezuela. Among these potential regions, only North America and the Middle East currently have large-scale CCS facilities in operation, construction or development. The north-western South America and western Middle East regions present particularly high potential for CO_2-EOR and, in fact, there are two ongoing projects currently carrying out CO_2-EOR in the Middle East. Although CO_2-EOR is not a long-term solution for CO_2 emission reduction, because the overall emissions will increase due to the extra oil produced, it can initiate the development of a CCS industry in a suitable region while mitigating the upfront and operational costs with revenues from the enhanced production.

Being the largest coal user and CO_2 emitter in the world, China needs to decarbonise its energy and industrial sectors to promote a sustainable development. The most active and planned CCS facilities are located in the heavily industrialised east of the country, but our appraisal tool has identified the Sichuan Basin as a promising region for CCS development, according to the match between the existing carbon emissions and its potential storage capacity. The vast gas resources accumulated in the Sichuan Basin ensure the capacity and containment of the reservoirs. At the same time, the existing hydrocarbon infrastructure could be re-used

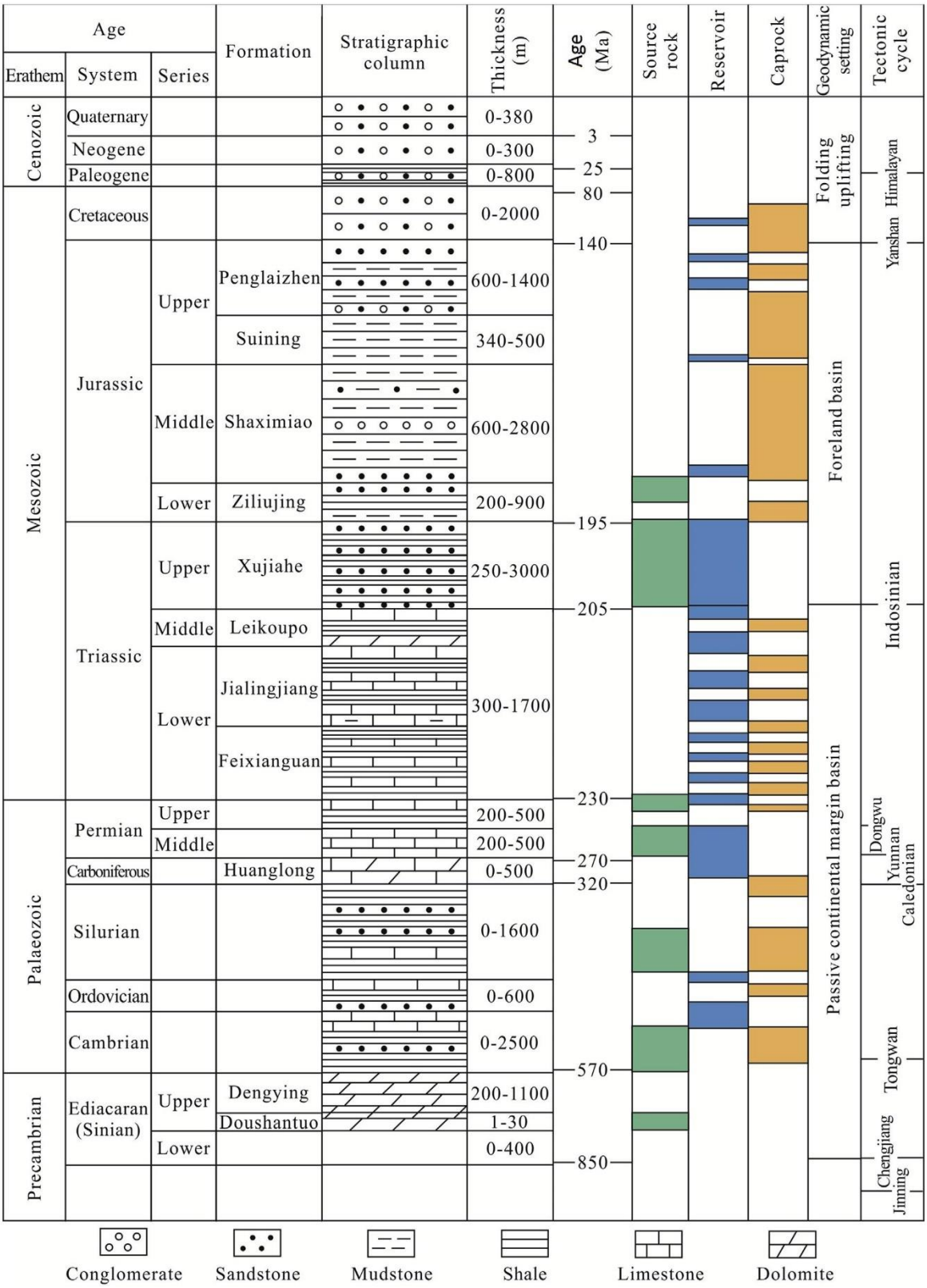

Fig. 10. Stratigraphic column, source-reservoir-caprock assemblages and tectonic evolution of the Sichuan Basin (after Luo et al., 2013).

for CCS, reducing the cost of implementation and hence increasing the prospects of this much needed industry in the region.

Declaration of competing interest

The authors declare that they have no known competing financial interests or personal relationships that could have appeared to influence the work reported in this paper.

Acknowledgements

This research was performed within the framework of DGICYT Spanish Projects CGL2015-66335-C2-1-R and PGC2018-093903-B-C22, Grup Consolidat de Recerca "Geologia Sedimentària" (2017-SGR-824), and was also funded by the China Scholarship Council (CSC) (201806450043). JA received funding by EIT Raw Materials – SIT4ME Project (17024) and is now funded by MICINN (Juan de la Cierva fellowship - IJC2018-036074-I). EGR acknowledges funding by the AGAUR (Agència de Gestió d'Ajuts Universitaris i de Recerca) of the Generalitat de Catalunya ("Beatriu de Pinós" fellowship 2017SGR-824) and the Spanish Ministry of Science, Innovation and Universities ("Ramón y Cajal" fellowship RYC2018-026335-I). GJ is funded by the University of Strathclyde Faculty of Engineering. The authors would like to thank the United States Geological Survey, the CGG Robertson Sedimentary Basins, and the Emissions Database for Global Atmospheric Research for allowing access to their databases.

References

Alcalde, J., Flude, S., Wilkinson, M., Johnson, G., Edlmann, K., Bond, C.E., Scott, V., Gilfillan, S.M., Ogaya, X., Haszeldine, R.S., 2018. Estimating geological CO_2 storage security to deliver on climate mitigation. Nat. Commun. 9 (1), 2201. https://doi.org/10.1038/s41467-018-04423-1.

Alcalde, J., Heinemann, N., Mabon, L., Worden, R.H., de Coninck, H., Robertson, H., Maver, M., Ghanbari, S., Swennenhuis, F., Mann, I., Walker, T., 2019. Acorn: developing full-chain industrial carbon capture and storage in a resource-and infrastructure-rich hydrocarbon province. J. Clean. Prod. 233, 963–971. https://doi.org/10.1016/j.jclepro.2019.06.087.

Algharaib, M.K., 2009. Potential applications of CO_2-EOR in the Middle East. In: Proc. SPE Middle East Oil and Gas Show and Conference. Society of Petroleum Engineers. https://doi.org/10.2118/120231-ms.

Armstrong, K., Styring, P., 2015. Assessing the potential of utilization and storage strategies for post-combustion CO_2 emissions reduction. Front. Energy Res. 3, 8.

Bachu, S., 2003. Screening and ranking of sedimentary basins for sequestration of CO_2 in geological media in response to climate change. Environ. Geol. 44 (3), 277–289. https://doi.org/10.1007/s00254-003-0762-9.

Bachu, S., 2007. Carbon dioxide storage capacity in uneconomic coal beds in Alberta, Canada: methodology, potential and site identification. Int. J. Greenh. Gas Contr. 1 (3), 374–385. https://doi.org/10.1016/S1750-5836(07)00070-9.

Bird, K.J., Charpentier, R.R., Gautier, D.L., Houseknecht, D.W., Klett, T.R., Pitman, J.K., Moore, T.E., Schenk, C.J., Tennyson, M.E., Wandrey, C.R., 2008. Circum-Arctic Resource Appraisal: Estimates of Undiscovered Oil and Gas North of the Arctic Circle (No. 2008-3049). U.S. Geological Survey, p. 4. https://doi.org/10.3133/fs20083049.

Blondes, M.S., Brennan, S.T., Merrill, M.D., Buursink, M.L., Warwick, P.D., Cahan, S.M., Cook, T.A., Corum, M.D., Craddock, W.H., DeVera, C.A., Drake II, R.M., Drew, L.J., Freeman, P.A., Lohr, C.D., Olea, R.A., Roberts-Ashby, T.L., Slucher, E.R., Varela, B.A., 2013. National assessment of geologic carbon dioxide storage resources: methodology implementation. In: U.S. Geological Survey Open-File Report 2013-1055, p. 26. https://doi.org/10.3133/ofr20131055.

Bui, M., Adjiman, C.S., Bardow, A., Anthony, E.J., Boston, A., Brown, S., Fennell, P.S., Fuss, S., Galindo, A., Hackett, L.A., Hallett, J.P., 2018. Carbon capture and storage (CCS): the way forward. Energy Environ. Sci. 11 (5), 1062–1176. https://doi.org/10.1039/C7EE02342A.

Castellarin, A., 2001. Alps-apennines and Po plain-frontal apennines relations. In: Vai, G.B., Martini, I.P. (Eds.), Anatomy of an Orogen: the Apennines and Adjacent Mediterranean Basins. Springer, Dordrecht, pp. 177–195. https://doi.org/10.1007/978-94-015-9829-3_13.

China Earthquake Networks Centre, 2019. http://news.ceic.ac.cn/index.html?time=1571215898 (accessed 14 November 2019).

Chiquet, P., Daridon, J.L., Broseta, D., Thibeau, S., 2007. CO_2/water interfacial tensions under pressure and temperature conditions of CO_2 geological storage. Energy Convers. Manag. 48 (3), 736–744.

Chongqing Municipal People's government, 2017. Chongqing's Work Programme for Control Greenhouse Gas Emissions during the Thirteenth Five-Year Plan. http://www.cq.gov.cn/publicity/cxjshjbh/jnyzyzhly/588919 (in Chinese).

Climate Action Tracker, 2018. U.S. Climate Policy: One Year on from Announcement of Paris Agreement Withdrawal. https://climateactiontracker.org/press/us-climate-policy-one-year-announcement-paris-agreement-withdrawal (accessed 12 November 2018).

da Graça Carvalho, M., 2012. EU energy and climate change strategy. Energy 40 (1), 19–22. https://doi.org/10.1016/j.energy.2012.01.012.

deLlano-Paz, F., Fernandez, P.M., Soares, I., 2016. Addressing 2030 EU policy framework for energy and climate: cost, risk and energy security issues. Energy 115, 1347–1360. https://doi.org/10.1016/j.energy.2016.01.068.

Den Elzen, M., Admiraal, A., Roelfsema, M., van Soest, H., Hof, A.F., Forsell, N., 2016. Contribution of the G20 economies to the global impact of the Paris agreement climate proposals. Climatic Change 137 (3–4), 655–665. https://doi.org/10.1007/s10584-016-1700-7.

Diao, Y.J., Zhu, G.W., Jin, X.L., Zhang, C., Li, X.F., 2017a. Theoretical potential assessment of CO_2 geological utilization and storage in the Sichuan Basin. Geol. Bull. China 36 (6), 1088–1095 (in Chinese with English abstract).

Diao, Y.J., Zhu, G.W., Cao, H., Zhang, C., Li, X.F., Jin, X.L., 2017b. Mesoscale assessment of CO_2 storage potential and geological suitability for target area selection in the Sichuan Basin. Geofluids 2017, 1–17. https://doi.org/10.1155/2017/9587872.

EDGAR, 2018. Emissions Database for Global Atmospheric Research. http://edgar.jrc.ec.europa.eu/overview.php?v=432&SECURE=123 https://data.europa.eu/doi/10.2904/JRC_DATASET_EDGAR (accessed 12 November 2018).

Edlmann, K., Edwards, M.A., Qiao, X.J., Haszeldine, R.S., McDermott, C.I., 2015. Appraisal of global CO_2 storage opportunities using the geomechanical facies approach. Environ. Earth Sci. 73 (12), 8075–8096. https://doi.org/10.1007/s12665-014-3965-3.

Erlich, R.N., Barrett, S.F., 1992. Petroleum geology of the eastern Venezuela Foreland Basin. In: Macqueen, R.W., Leckie, D.A. (Eds.), Foreland Basins and Fold Belts, vol. 55. AAPG Memoir, pp. 341–362.

Ettehadtavakkol, A., Lake, L.W., Bryant, S.L., 2014. CO_2-EOR and storage design optimization. Int. J. Greenh. Gas Contr. 25, 79–92. https://doi.org/10.1016/j.ijggc.2014.04.006.

Fan, J.J., Jia, X.F., Hu, Q.Y., Pan, J.Y., Zhang, S.Q., Zhang, C., 2014. Potential and suitable conditions evaluation of CO_2 storage in the salt water aquifer in the depth of Sichuan basin. Ground Water 36 (6), 59–64.

Gislason, S.R., Oelkers, E.H., 2014. Carbon storage in basalt. Science 344 (6182), 373–374. https://doi.org/10.1126/science.1250828.

Global CCS Institute, 2018. The Global Status of CCS: 2018. Australia. https://www.globalccsinstitute.com/resources/global-status-report/.

Global CCS Institute, 2019. CCS Facilities Database. https://co2re.co/StorageData. (Accessed 15 May 2019).

Godec, M., Kuuskraa, V., Van Leeuwen, T., Melzer, L.S., Wildgust, N., 2011. CO_2 storage in depleted oil fields: the worldwide potential for carbon dioxide enhanced oil recovery. Energy Procedia 4, 2162–2169. https://doi.org/10.1016/j.egypro.2011.02.102.

Goodman, A., Hakala, A., Bromhal, G., Deel, D., Rodosta, T., Frailey, S., Small, M., Allen, D., Romanov, V., Fazio, J., Huerta, N., 2011. U.S. DOE methodology for the development of geologic storage potential for carbon dioxide at the national and regional scale. Int. J. Greenh. Gas Contr. 5 (4), 952–965. https://doi.org/10.1016/j.ijggc.2011.03.010.

Guo, J.Q., Wen, D.G., Zhang, S.Q., Xu, T.F., Li, X.F., Diao, Y.J., Jia, X.F., 2015. Potential and suitability evaluation of CO_2 geological storage in major sedimentary basins of China and the demonstration project in Ordos Basin. Acta Geol. Sin.-Engl. Ed. 89 (4), 1319–1332. https://doi.org/10.1111/1755-6724.12531.

Hornafius, K.Y., Hornafius, J.S., 2015. Carbon negative oil: a pathway for CO_2 emission reduction goals. Int. J. Greenh. Gas Contr. 37, 492–503. https://doi.org/10.1016/j.ijggc.2015.04.007.

Iglauer, S., 2018. Optimum storage depths for structural CO_2 trapping. Int. J. Greenh. Gas Contr. 77, 82–87. https://doi.org/10.1016/j.ijggc.2018.07.009.

Janssens-Maenhout, G., Crippa, M., Guizzardi, D., Muntean, M., Schaaf, E., Dentener, F., Bergamaschi, P., Pagliari, V., Olivier, J.G., Peters, J.A., Aardenne, J.A.V., 2019. EDGAR v4.3.2 Global atlas of the three major greenhouse gas emissions for the period 1970–2012. Earth Syst. Sci. Data 11 (3), 959–1002. https://doi.org/10.5194/essd-2018-164.

Jia, C.Z., Wei, G.Q., Li, B.L., Xiao, A.C., Ran, Q.G., 2003. Tectonic evolution of two-epoch foreland basins and its control for natural gas accumulation in China's mid-western areas. Acta Pet. Sin. 24 (2), 13–17 (in Chinese with English abstract).

Kang, S.M., Fathi, E., Ambrose, R.J., Akkutlu, I.Y., Sigal, R.F., 2011. Carbon dioxide storage capacity of organic-rich shales. SPE J. 16 (4), 842–855. https://doi.org/10.2118/134583-pa.

Kearns, J., Teletzke, G., Palmer, J., Thomann, H., Kheshgi, H., Chen, Y.H.H., Paltsev, S., Herzog, H., 2017. Developing a consistent database for regional geologic CO_2 storage capacity worldwide. Energy Procedia 114, 4697–4709. https://doi.org/10.1016/j.egypro.2017.03.1603.

Koelbl, B.S., van den Broek, M.A., Faaij, A.P., van Vuuren, D.P., 2014. Uncertainty in Carbon Capture and Storage (CCS) deployment projections: a cross-model comparison exercise. Climatic Change 123 (3–4), 461–476. https://doi.org/10.1007/s10584-013-1050-7.

Kuuskraa, V.A., Godec, M.L., Dipietro, P., 2013. CO_2 utilization from "next generation" CO_2 enhanced oil recovery technology. Energy Procedia 37, 6854–6866. https://doi.org/10.1016/j.egypro.2013.06.618.

Leung, D.Y., Caramanna, G., Maroto-Valer, M.M., 2014. An overview of current status of carbon dioxide capture and storage technologies. Renew. Sustain. Energy Rev. 39, 426–443. https://doi.org/10.1016/j.rser.2014.07.093.

Li, H.J., Huang, S.C., 2010. China's development potential & latest actions on CCS. China Coal 36 (1), 13–17 (in Chinese with English abstract).

Li, X., Wei, N., Liu, Y., Fang, Z., Dahowski, R.T., Davidson, C.L., 2009. CO_2 point emission and geological storage capacity in China. Energy Procedia 1 (1), 2793–2800. https://doi.org/10.1016/j.egypro.2009.02.051.

Liu, F., Ellett, K., Xiao, Y., Rupp, J.A., 2013. Assessing the feasibility of CO_2 storage in the New Albany Shale (Devonian–Mississippian) with potential enhanced gas recovery using reservoir simulation. Int. J. Greenh. Gas Contr. 17, 111–126. https://doi.org/10.1016/j.ijggc.2013.04.018.

Luo, Z.L., Han, J.H., Luo, C., Luo, Q.H., Han, K.Y., 2013. The discovery characteristics and prospects of commercial oil and gas layers/reservoirs in Sichuan basin. Xinjiang Pet. Geol. 34 (5), 504–514 (in Chinese with English abstract).

Ma, F., Zhang, G.Y., Tian, Z.J., Yang, L.Y., Liu, Z.D., Li, F., 2014. The enrichment characteristics and undiscovered resources evaluation of the conventional oil and gas in North America. Earth Sci. Front. 21 (3), 91–100 (in Chinese with English abstract).

Ma, X.H., 2017a. A golden era for natural gas development in the Sichuan Basin. Nat. Gas. Ind. B 4 (3), 163–173 (in Chinese with English abstract).

Ma, X.H., 2017b. Natural gas and energy revolution: a case study of Sichuan-Chongqing gas province. Nat. Gas. Ind. B 4 (2), 91–99 (in Chinese with English abstract).

Ma, Y.S., Cai, X.Y., Zhao, P.R., Luo, Y., Zhang, X.F., 2010. Distribution and further exploration of the large-medium sized gas fields in Sichuan Basin. Acta Pet. Sin. 31 (3), 347–354 (in Chinese with English abstract).

Mann, P., Gahagan, L., Gordon, M.B., 2003. Tectonic setting of the world's giant oil and gas fields. AAPG Memoir 78, 15–105.

Manrique, E., Ranson, A., Alvarado, V., 2003. Perspectives of CO_2 injection in Venezuela. In: 24th Annual Workshop and Symposium for the IEA Collaborative Project on Enhanced Oil Recovery, Canada, pp. 7–10.

Mao, Q., Zou, G.F., Zhang, H.M., Jin, H., Huang, H.B., 2006. Discussion on geodynamic evolution and oil/gas prospect of the Sichuan Basin. Nat. Gas. Ind. 26 (11), 7–10 (in Chinese with English abstract).

Masson-Delmotte, T.W., Zhai, P., Pörtner, H.O., Roberts, D., Skea, J., Shukla, P.R., Pirani, A., Moufouma-Okia, W., Péan, C., Pidcock, R., Connors, S., 2018. IPCC, 2018: Summary for Policymakers. Global Warming of 1.5 °C. Geneva, Switzerland. https://report.ipcc.ch/sr15/pdf/sr15_spm_final.pdf.

Matter, J.M., Broecker, W.S., Stute, M., Gislason, S.R., Oelkers, E.H., Stefánsson, A., Wolff-Boenisch, D., Gunnlaugsson, E., Axelsson, G., Björnsson, G., 2009. Permanent carbon dioxide storage into basalt: the CarbFix pilot project, Iceland. Energy Procedia 1 (1), 3641–3646. https://doi.org/10.1016/j.egypro.2009.02.160.

McDermott, C.I., Miocic, J.M., Edlmann, K., Gilfillan, S.M.V., 2017. Natural analogue studies. In: Niemi, A., Bear, J., Bensabat, J. (Eds.), Geological Storage of CO_2 in Deep Saline Formations. Springer, Dordrecht, pp. 473–520.

Metz, B., Davidson, O., de Coninck, H., Loos, M., Meyer, L., 2005. IPCC Special Report on Carbon dioxide Capture and Storage. Intergovernmental Panel on Climate Change, United States. https://www.osti.gov/biblio/20740954.

Miocic, J.M., Johnson, G., Bond, C.E., 2019. Uncertainty in fault seal parameters: implications for CO_2 column height retention and storage capacity in geological CO_2 storage projects. Solid Earth 10, 951–967. https://doi.org/10.5194/se-10-951-2019.

Miocic, J.M., Gilfillan, S.M., Roberts, J.J., Edlmann, K., McDermott, C.I., Haszeldine, R.S., 2016. Controls on CO_2 storage security in natural reservoirs and implications for CO_2 storage site selection. Int. J. Greenh. Gas Contr. 51, 118–125. https://doi.org/10.1016/j.ijggc.2016.05.019.

Mishra, S., Oruganti, Y.D., Gupta, N., Ganesh, P.R., McNeil, C., Bhattacharya, I., Spitznogle, G., 2014. Modeling CO_2 plume migration based on calibration of injection and post-injection pressure response at the AEP Mountaineer Project. Greenhouse Gases: Sci. Technol. 4 (3), 331–356. https://doi.org/10.1002/ghg.1434.

Mitrović, M., Malone, A., 2011. Carbon capture and storage (CCS) demonstration projects in Canada. Energy Procedia 4, 5685–5691. https://doi.org/10.1016/j.egypro.2011.02.562.

Mohajjel, M., Fergusson, C.L., Sahandi, M.R., 2003. Cretaceous–Tertiary convergence and continental collision, Sanandaj–Sirjan zone, western Iran. J. Asian Earth Sci. 21 (4), 397–412. https://doi.org/10.1016/S1367-9120(02)00035-4.

Naylor, M., Wilkinson, M., Haszeldine, R.S., 2011. Calculation of CO_2 column heights in depleted gas fields from known pre-production gas column heights. Mar. Petrol. Geol. 28 (5), 1083–1093. https://doi.org/10.1016/j.marpetgeo.2010.10.005.

Neele, F., Sinayuc, C., Nermoen, A., Burlacu, A., 2017. Status of CCS and CCU in South Eastern Europe. ECO-BASE, D1.1, p. 73.

Odenberger, M., Kjärstad, J., Johnsson, F., 2013. Prospects for CCS in the EU energy roadmap to 2050. Energy Procedia 37, 7573–7581. https://doi.org/10.1016/j.egypro.2013.06.701.

Pereira, N., Bonduki, Y., Perdomo, M., 1997. Potential options to reduce GHG emissions in Venezuela. Appl. Energy 56 (3–4), 265–286. https://doi.org/10.1016/S0306-2619(97)00010-X.

Peters, G.P., Andrew, R.M., Boden, T., Canadell, J.G., Ciais, P., Le Quéré, C., Marland, G., Raupach, M.R., Wilson, C., 2012. The challenge to keep global warming below 2 °C. Nat. Clim. Change 3 (1), 2–4. https://doi.org/10.1038/nclimate1783.

Quantum GIS (QGIS) version 3.4.2, 2018. QGIS Development Team. http://qgis.org.

Radoslaw, T., Barbara, U.M., Adam, W., 2009. CO_2 storage capacity of deep aquifers and hydrocarbon fields in Poland–EU GeoCapacity Project results. Energy Procedia 1 (1), 2671–2677. https://doi.org/10.1016/j.egypro.2009.02.035.

Robertson, C.G.G., 2014. Sedimentary Basins of the World. https://www.cgg.com/en/What-We-Do/GeoConsulting/Robertson.

Román, R., Cansino, J.M., Rodas, J.A., 2018. Analysis of the main drivers of CO_2 emissions changes in Colombia (1990–2012) and its political implications. Renew. Energy 116, 402–411. https://doi.org/10.1016/j.renene.2017.09.016.

Scott, V., Gilfillan, S., Markusson, N., Chalmers, H., Haszeldine, R.S., 2013. Last chance for carbon capture and storage. Nat. Clim. Change 3 (2), 105–111. https://doi.org/10.1038/nclimate1695.

Song, X.D., Li, J.T., Bao, Z.W., Li, S.T., Wang, L.S., Ren, J.Y., 2015. Deep structure of major basins in Western China and implications for basin formation and evolution. Earth Sci. Front. 22 (1), 126–136. https://doi.org/10.13745/j.esf.2015.01.011 (in Chinese with English abstract).

Stewart, J.R., Haszeldine, R.S., 2014. Carbon Accounting for Carbon Dioxide Enhanced Oil Recovery. Scottish Carbon Capture and Storage (SCCS), p. 62.

The People's Government of Sichuan Province, 2017. Sichuan Province's Work Programme for Control Greenhouse Gas Emissions during the Thirteenth Five-Year Plan. http://www.sc.gov.cn/zcwj/xxgk/NewT.aspx?i=20170518084142-766800-00-000 (in Chinese).

Tian, Z.J., Wu, Y.P., Wang, Z.M., 2014. Global conventional oil and gas resource assessment and its potential. Earth Sci. Front. 21 (3), 10–17 (in Chinese with English abstract).

Tong, X.G., Zhang, G.Y., Wang, Z.M., Wen, Z.X., Tian, Z.J., Wang, H.J., Ma, F., Wu, Y.P., 2018. Distribution and potential of global oil and gas resources. Petrol. Explor. Dev. 45 (4), 727–736.

Uliasz-Misiak, B., 2007. Polish hydrocarbon deposits usable for underground CO_2 storage. Gospod. Surowcami Miner. 23 (4), 111–120.

UNFCCC, 2017. Intended nationally determined contributions (INDCs). https://www4.unfccc.int/sites/submissions/indc/Submission%20Pages/submissions.aspx (accessed 12 December 2018).

(UNIDO) United Nations Industrial Development Organization, 2011. Global Technology Roadmap for CCS in Industry-Sectoral Assessment: Sources and Sinks Matching Report, p. 180.

(USGS) United States Geological Survey, 1995-2013. National Assessment of Oil and Gas Resources. https://energy.usgs.gov.

(USGS) United States Geological Survey, 2000. World Petroleum Assessment. https://energy.usgs.gov.

U.S. Department of Energy Office of Fossil Energy, 2015. Carbon Storage Atlas, fifth ed. https://www.netl.doe.gov/node/5841.

Vangkilde-Pedersen, T., Kirk, K., Smith, N., Maurand, N., Wojcicki, A., Neele, F., Hendriks, C., Le Nindre, Y., Lyng Anthonsen, K., 2009. EU Geocapacity–Assessing European Capacity for Geological Storage of Carbon dioxide. Project no. SES6-518318. http://www.geology.cz/geocapacity.

Wang, H.J., Ma, F., Tong, X.G., Liu, Z.D., Zhang, X.S., Wu, Z.Z., Li, D.H., Wang, B., Xie, Y.F., Yang, L.Y., 2016. Assessment of global unconventional oil and gas resources. Petrol. Explor. Dev. 43 (6), 925–940. https://doi.org/10.1016/S1876-3804(16)30111-2 (in Chinese with English abstract).

Wang, J.Q., 2004. Characteristics of petroleum geology in the Sichuan basin–commemorating Mr. Huang Jiqing's 100th birthday. Petrol. Geol. Exp. 26 (2), 115–120 (in Chinese).

Wang, W., Zhou, Z.Y., Guo, T.L., Xu, C.H., 2011. Early Cretaceous-Paleocene geothermal gradients and Cenozoic tectono-thermal history of Sichuan basin. J. Tongji Univ. Nat. Sci. 39 (4), 606–613 (in Chinese with English abstract).

Wang, X.J., 2012. Superposed evolution of Persian Gulf Basin and its petroleum distribution. Chin. J. Geol. 47 (4), 1223–1227 (in Chinese with English abstract).

Wang, X.J., Yang, Z.R., Han, B., 2015. Superposed evolution of Sichuan Basin and its petroleum accumulation. Earth Sci. Front. 22 (3), 161–173 (in Chinese with English abstract).

Wei, N., Li, X., Wang, Y., Dahowski, R.T., Davidson, C.L., Bromhal, G.S., 2013. A preliminary sub-basin scale evaluation framework of site suitability for onshore aquifer-based CO_2 storage in China. Int. J. Greenh. Gas Contr. 12, 231–246. https://doi.org/10.1016/j.ijggc.2012.10.012.

Wilson, T.H., Siriwardane, H., Zhu, L., Bajura, R.A., Winschel, R.A., Locke, J.E., Bennett, J., 2012. Fracture model of the Upper Freeport coal: Marshall County West Virginia pilot ECBMR and CO_2 sequestration site. Int. J. Coal Geol. 104, 70–82. https://doi.org/10.1016/j.coal.2012.05.005.

Xie, Y.F., Zhao, M.Z., Yang, F.Z., Wei, C.G., 2009. Primary Types of sedimentary basins and petroleum geological characteristics of typical basins in Latin America. China Petrol. Explor. 14 (1), 65–73 (in Chinese with English abstract).

Yang, F.Z., Wei, C.G., Yin, J.Q., Zhang, C.L., Xie, Y.F., 2009. Structural characteristics of typical oil-bearing basins in northwest of South America. Geotect. Metallogenia 33 (2), 230–235.

Yang, G., Li, G.H., Li, N., Chen, S.L., Wang, H., Xu, L., 2016. Hydrocarbon accumulation characteristics and enrichment laws of multi-layered reservoirs in the Sichuan Basin. Nat. Gas. Ind. 36 (11), 1–11 (in Chinese with English abstract).

Zhang, J., Zhang, Q., 2002. History and prospects of oil and gas exploration in Sichuan Basin. Nat. Gas. Ind. 22 (Z1), 3–7 (in Chinese).

Zhang, X., Fan, J.L., Wei, Y.M., 2013. Technology roadmap study on carbon capture, utilization and storage in China. Energy Pol. 59, 536–550. https://doi.org/10.1016/j.enpol.2013.04.005.

Appendix 2 Hubs and clusters approach to unlock the development of Carbon Capture and Storage - case study in Spain

Sun, X., Alcalde, J., Bakhtbidar, M., Elío, J., Vilarrasa, V., Canal, J., Ballesteros, J., Heinemann, N., Haszeldine, S., Cavanagh, A., Vega-Maza, D., Rubiera, F., Martínez-Orio, R., Johnson, G., Carbonell, R., Marzan, I., Travé, A., Gomez-Rivas, E., 2021. Hubs and clusters approach to unlock the development of Carbon Capture and Storage – case study in Spain. *Applied Energy,* in press.

Applied Energy xxx (xxxx) 117418

Contents lists available at ScienceDirect

Applied Energy

journal homepage: www.elsevier.com/locate/apenergy

Hubs and clusters approach to unlock the development of carbon capture and storage – Case study in Spain

Xiaolong Sun [a], Juan Alcalde [b,*], Mahdi Bakhtbidar [a,b], Javier Elío [c], Víctor Vilarrasa [d,e], Jacobo Canal [f], Julio Ballesteros [g], Niklas Heinemann [h], Stuart Haszeldine [h], Andrew Cavanagh [h], David Vega-Maza [i], Fernando Rubiera [j], Roberto Martínez-Orio [k], Gareth Johnson [l], Ramon Carbonell [b], Ignacio Marzan [b], Anna Travé [a], Enrique Gomez-Rivas [a]

[a] Department of Mineralogy, Petrology and Applied Geology, University of Barcelona, c/ Martí i Franques s/n, Barcelona 08028, Spain
[b] Geosciences Barcelona (GEO3BCN-CSIC), Lluís Solé i Sabarís s/n, Barcelona 08028, Spain
[c] Department of Planning, Aalborg University, Copenhagen, Denmark
[d] Institute of Environmental Assessment and Water Research (IDAEA), Spanish National Research Council (CSIC), c/ Jordi Girona 18-26, Barcelona 08034, Spain
[e] Mediterranean Institute for Advanced Studies (IMEDEA), Spanish National Research Council (CSIC), c/ Miquel Marquès 21, Esporles, Spain
[f] Repsol Technology Lab, Calle Agustín de Betancourt s/n, Móstoles 28935, Spain
[g] Facultad de Derecho, University of Salamanca, Paseo Francisco Tomás y Valiente s/n, Salamanca 37007, Spain
[h] School of GeoSciences, University of Edinburgh, Edinburgh EH9 3FE, Scotland, United Kingdom
[i] TermoCal. School of Engineering, University of Valladolid. Paseo del Cauce 59, Valladolid 47011, Spain
[j] Instituto de Ciencia y Tecnología del Carbono, INCAR-CSIC, c/Francisco Pintado Fe, 26, Oviedo 33011, Spain
[k] IGME – Instituto Geológico y Minero de España – Geological Survey of Spain. C/Ríos Rosas 23, Madrid 28003, Spain
[l] Department of Civil and Environmental Engineering, University of Strathclyde, Glasgow, G1 1XZ Scotland, United Kingdom

ARTICLE INFO

Keywords:
CO_2 emission hubs
Hubs and clusters
Source-to-sink
CCS site selection
Spain

ABSTRACT

Many countries have assigned an indispensable role for carbon capture and storage (CCS) in their national climate change mitigation pathways. However, CCS deployment has stalled in most countries with only limited commercial projects realised mainly in hydrocarbon-rich countries for enhanced oil recovery. If the Paris Agreement is to be met, then this progress must be replicated widely, including hydrocarbon-limited countries. In this study, we present a novel source-to-sink assessment methodology based on a hubs and clusters approach to identify favourable regions for CCS deployment and attract renewed public and political interest in viable deployment pathways. Here, we apply this methodology to Spain, where fifteen emission hubs from both the power and the hard-to-abate industrial sectors are identified as potential CO_2 sources. A priority storage structure and two reserves for each hub are selected based on screening and ranking processes using a multi-criteria decision-making method. The priority source-to-sink clusters are identified indicating four potential development regions, with the North-Western and North-Eastern Spain recognised as priority regions due to resilience provided by different types of CO_2 sources and geological structures. Up to 68.7 Mt CO_2 per year, comprising around 21% of Spanish emissions can be connected to clusters linked to feasible storage. CCS, especially in the hard-to-abate sector, and in combination with other low-carbon energies (e.g., blue hydrogen and bioenergy), remains a significant and unavoidable contributor to the Paris Agreement's mid-century net-zero target. This study shows that the hubs and clusters approach can facilitate CCS deployment in Spain and other hydrocarbon-limited countries.

1. Introduction

Human activities are estimated to have caused a global temperature increase of 0.8–1.2 °C above pre-industrial levels [1]. Global warming has numerous impacts on natural and human systems, e.g., many land and ocean ecosystems and some of the services the ecosystems provide have already changed [2]. Limiting global warming to 2 °C or even 1.5 °C above pre-industrial levels will require a combination of different approaches to climate change mitigation that are compatible with sustainable development. Among the technically feasible options, CCS is widely considered an efficient and safe method for decarbonisation [3–5], and remains a core component of national and global emission

* Corresponding author.
E-mail address: jalcalde@geo3bcn.csic.es (J. Alcalde).

https://doi.org/10.1016/j.apenergy.2021.117418
Received 5 April 2021; Received in revised form 28 June 2021; Accepted 7 July 2021
0306-2619/

reduction strategies to mitigate climate change [6–7]. For example, CCS may contribute in 14% of global CO_2 emission reduction by 2060 according to the Energy Technology Perspectives 2 °C scenario, equivalent to accumulated storage of 140 gigatons (Gt) of CO_2 [7]. In the more ambitious 1.5 °C scenario, the IPCC calculates a cumulative CCS of 550–1017 Gt by 2100 [1]. Importantly, CCS is also a key component of two technologies that could help to achieve net-zero emissions. First, CCS can be combined with hydrogen manufacture from hydrocarbons to produce "blue hydrogen", which can help to reduce emissions as a substitution of fossil fuels during the transition toward low-carbon industry [8–9]. Blue hydrogen can play an important transitional role while the entire energy system switches into full renewables [10–11]. Second, the combination of bio-energy production together with CCS (BECCS) is regarded as a core Negative Emission Technology (NET), crucial for meeting ambitious climate change mitigation scenarios [12–13]. Both technologies can help alleviate the costs related to ambitious climate targets [11,14] while promoting to the creation of a CCS industry, and thus the potential contribution of these promising technologies into decarbonisation strategies must be considered.

To date, 191 parties have submitted their "Nationally Determined Contributions" (NDC) to the Paris Agreement. Among these, more than forty countries mentioned CCS as a potential greenhouse gas (GHG) reduction method [15]. However, CCS deployment has been slow due to various barriers including: the high-cost perception of CCS development, a lack of market mechanisms and incentives, insufficient penalty mechanisms for major CO_2 emitters, an inadequate legal framework, low public acceptance, potential safety and environment issues [16–17], and uncertainty in the characterisation of storage sites [18]. According to the latest CCS database [19], there are currently 68 commercial CCS facilities and 6 CCS hubs under different development and operation status worldwide. Among these, only 28 commercial CCS facilities are in operation so far, with a maximum capacity of around 40 million tonnes of CO_2 per annum (Mtpa). A reasonable projection of the current CCS rate into the future will result in 700 Mtpa, far from the minimum 6000 Mtpa needed to achieve the 2 °C target [13]. Therefore, there is still a huge gap between the current global CCS provision and that required to meet the anticipated contribution of CCS to global and regional reduction targets. On the other hand, most commercial CCS facilities in operation are concentrated in a few hydrocarbon-rich countries with effective government support for CCS deployment, such as the USA, Canada, and Norway [19]. Most CCS projects are purposed for CO_2 enhanced oil recovery (CO_2-EOR), whereas only a few projects are for dedicated geological storage in these countries. For other countries that do not host operational commercial facilities and have to date lacked consistent government support for CCS deployment, a hubs and clusters strategy is gaining momentum and even promotes the implementation of this important technology. For example, the UK and the Netherlands are developing CCS hub projects for dedicated geological storage in the North Sea [20–21]. The hubs and clusters strategy could also be applied to other countries for dedicated geological storage, especially in hydrocarbon-limited countries.

The European Union (EU) is the third-largest greenhouse gas emitter after China and the United States, which emitted 3.89 Gt of GHG in 2018 with 3.45Gt from CO_2 emissions, accounting for around 10% of global CO_2 emissions [22]. In 2020, the EU proposed its updated GHG emission reduction target that aims to achieve a reduction of at least 55% by 2030 compared to 1990 and to achieve net-zero GHG emissions by 2050 [23]. The EU has confirmed the essential role of CCS as a technology able to significantly reduce CO_2 emissions, promoting CCS to become an integral part of the European energy policy [24], and encouraging research in it via Horizon 2020 [25] and Horizon Europe [26], the main EU Research and Innovation programmes. However, there are currently no commercial CCS facilities in operation in the EU, with only a few facilities under development in the Netherlands and Ireland [19]. There should be more scope for CCS development in the EU to achieve the ambitious net-zero target. Although the EU has sufficient storage capacity [27], the storage resource remains at a very early and immature stage with a huge gap between the requirements for a matched capacity reserve and its current inventory of large theoretical capacity resource (Fig. 1) [28]. Further assessments are needed to advance the maturity of the storage resource and thus to attract renewed interest for CCS. In addition, hydrocarbon resources are limited in many EU countries, and thus CO_2-EOR is not an option for facilitating large-scale CCS deployment.

In this study, we present a new source-to-sink assessment methodology for hydrocarbon-limited countries based on a hubs and clusters strategy and apply it in a case study in Spain. We analyse the status of Spain's CCS development, examine its potential, aim to attract renewed interest for the deployment of this important technology in Spain and show that the approach proposed in Spain can be replicated internationally. We first present the general methodology. Then, we review the current GHG emissions and the history of CCS developments in Spain to critically identify the strengths and deficiencies of CCS deployment to date. Subsequently, we carry out a detailed and systematic source-to-sink assessment. Emission hubs in different industrial sectors are identified as CO_2 sources for CCS deployment. The priority storage structure and alternative back-up structures for each emission hub are selected based on systematically screening and ranking processes using a multi-criteria decision-making (MCDM) method. Potential and priority regions are identified based on the distribution of the source-to-sink clusters. Finally, in our discussion we analyse the barriers and challenges of CCS development in Spain and explore its potential and opportunities with respect to different aspects of the CCS chain. Of particular importance is the integration of this technology with other low-carbon (e.g., blue hydrogen) or even negative emission technologies, chiefly BECCS. These technologies will likely have a key role in most countries' aims, including Spain, to meet its CO_2 reduction commitments.

2. The hubs & clusters strategy

The development of CCS has been historically closely bound to the production of oil and gas via CO_2 enhanced oil recovery (CO_2-EOR). Most of the CO_2 ever captured and injected in geological formations has been handled within the framework of CO_2-EOR projects, and the majority of the CCS projects in operation and under construction are purposed for CO_2-EOR [29]. Among the 28 commercial CCS facilities in operation, 22 facilities are for CO_2-EOR, while only a few facilities are for dedicated geological storage, located in Norway, Australia, the USA, and Canada [19]. EOR activities can provide the revenue stream that makes profitable an otherwise too expensive CCS project [30]. However, CCS can be only developed for dedicated geological storage rather

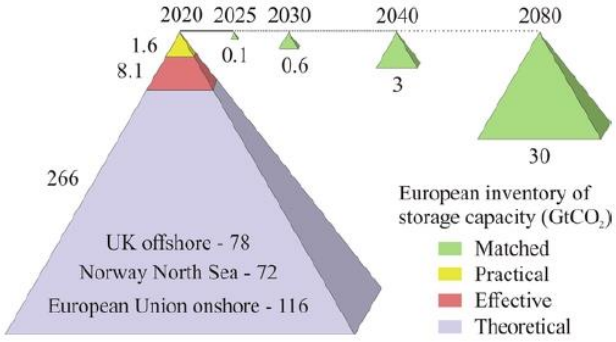

Fig. 1. Four-tier resource pyramid of European CO_2 storage capacity (in Gt) with forecasted requirements of matched capacity, framed by Carbon Sequestration Leadership Forum (CSLF) terminology: Theoretical (a regional first approximation), Effective (sum of identified prospects and exploration targets), Practical (matured prospects and candidate sites) and Matched (storage sites with bankable capacity available for injection). From Cavanagh et al. [28].

than CO_2-EOR in hydrocarbon-limited countries. These countries need to devise alternative strategies if they intend to implement ambitious decarbonisation strategies via CCS development.

In hydrocarbon-limited countries, economies of scale can play a key role in reducing the costs of CCS, which in turn can incentivise investment and development in this important technology. In this sense, the implementation of CCS hubs and clusters can be an effective strategy to share the effort of developing full-chain CCS projects. CCS hubs and clusters connect multiple nearby CO_2 emitters and storage site locations to reach a critical mass for CCS development [31]. The different CCS activities such as planning, transport and storage infrastructure construction, government licensing, negotiations with property owners and so on can be shared amongst the cluster users, reducing the overall costs and risks compared with standalone projects [31]. This strategy is gaining momentum and different CCS hubs and clusters are currently being developed around the world (e.g., the Rotterdam CCUS Porthos hub in the Netherlands, the Net Zero Teeside project in the UK, or the CarbonNet project in Australia [19]). While these countries already have important hydrocarbon industries in place, we argue that this strategy can be implemented successfully in other hydrocarbon-limited countries.

In global or regional evaluations of CCS potential, multiple studies have employed source-to-sink assessments as a first-order approach, which geographically match large CO_2 emitters with basins or reservoirs, such as for global basins [32–33] or a single country [32–34,160, 161]. In this study, we present a novel source-to-sink assessment methodology that not only considers the matching between CO_2 sources and storage resources but also adopts the hubs and clusters strategy. This methodology is derived and adapted from the one used for the site selection in the Acorn project of the UK North Sea [20]. The workflow created and used in this study is summarized in Fig. 2 and comprises three main steps. First, we define the potential CO_2 emission hubs as CO_2 sources for CCS development and the potential CO_2 storage sites available. Emission hubs are divided into different sectors based on the industrial types of emissions because they can play different roles in different stages of CCS development. The second step is to identify the priority source-to-sink clusters. A preliminary screening process is to select potential storage structures for each emission hub, based on basic screening criteria, such as storage capacity and distance to the emission hub. Subsequently, a scoring process is to grade the suitability of each potential storage site, involving storage capacity, reservoir-caprock suitability, development cost, data availability, etc. Finally, the scored sites are ranked and the preferred source-sink clusters are selected using a Multi-Criteria Decision Making (MCDM) process that allows selection considering multiple factors at the same time. This methodology is especially applicable for hydrocarbon-limited countries because the hubs and clusters strategy can reduce costs and hence attract interest in this decarbonisation technology. In the implementation of the methodology in different regions, specific parameters and values can be selected according to the actual conditions of evaluated objects. In the next section, we apply this methodology and present a case study of Spain, a hydrocarbon-limited country but with pressing decarbonisation needs.

3. Case study: Spain

As the fifth-largest CO_2 emitter in the EU, Spain needs to take a proactive role in meeting the EU's emission reduction target. CCS is considered a feasible option for emission reduction in Spain [35] and has been approved by the Spanish Parliament [36]. National assessments of CO_2 storage capacity and storage suitability have revealed a high potential for CCS development in Spain [37–38]. Spain had a head start on CCS in the late 2000 s [39], with three pilot projects for CO_2 capture and one for CO_2 storage developed between 2006 and 2014. However, this trend was not continued. The economic crisis and uncertainty about the role of CCS in the energy transition slowed that momentum, and no commercial or demonstration projects are planned in the near future [19].

3.1. Review of CCS development in Spain

3.1.1. Deployment of capture and storage projects

Different Spanish institutions have been involved in multiple research projects related to all aspects of the CCS chain (Appendix A). Al-

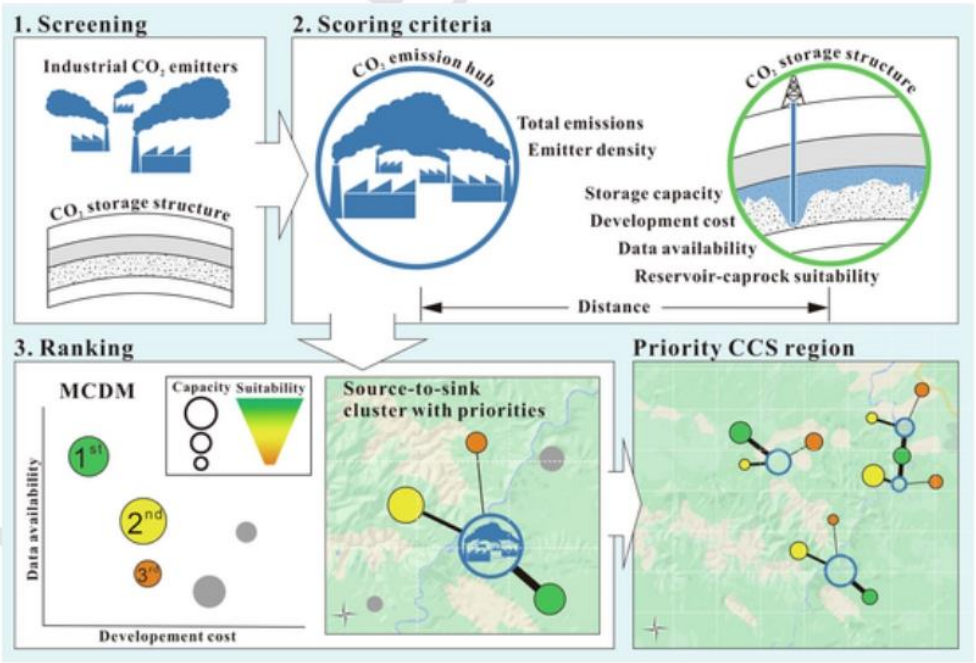

Fig. 2. Workflow of the source-to-sink assessment based on hubs and clusters strategy: Step 1, screening of the potential CO_2 sources and storage sites; Step 2, scoring criteria of potential emission hubs and storage structures; Step 3, The MCDM scheme for ranking source-to-sink cluster priorities. The ultimate goal is to identify favourable regions to deploy CCS most efficiently.

though there are currently no commercial CCS facilities active or planned, these research activities resulted in three major CCS pilot facilities developed in Spain [19].

3.1.1.1. Compostilla OXYCFB300. The Spanish Government created the CIUDEN Foundation (www.ciuden.es) in 2006, which led the public sector development of CCS in Spain. This includes the development of the Compostilla OXYCFB300 project, co-funded by the European Energy Programme for Recovery (EEPR) and the Spanish Government, and developed by a consortium of three partners: Endesa Generación, CIUDEN, and Foster Wheeler Energia Oy [40]. The Compostilla OXYCFB300 project involved the construction of a CO_2 capture and transport plant, located in the village of Cubillos del Sil (NW Spain), and a pilot project for CO_2 storage, located near the village of Hontomín (N Spain) [41]. The CIUDEN's capture technology development plant included a 20 MWth pulverised coal boiler provided with horizontal and vertical burners capable of burning from subbituminous to anthracitic type coals, and a 30 MWth circulating fluidised bed (CFB) boiler, which was the first of its kind globally for executing test runs at a large pilot scale under both air-combustion and oxy-combustion conditions [40,42]. The results of the CFB were expected to contribute to the development of the OXYCFB300 project. The storage pilot plant of Hontomín included an injection well and a monitoring well at a depth of 1.5 km, targeting CO_2 injection in a dome-shaped Jurassic carbonate formation sealed by marls [43], with an estimated capacity of 14 Mt of CO_2. The project included an ambitious site characterisation program, including the acquisition of baseline geophysical [44–48] and geochemical [49–51] datasets. CO_2 injection tests at laboratory and field scales were carried out in the fractured carbonate reservoir, one of the first in this type of reservoir, which guided the subsequent larger injection of 2300 tonnes of CO_2 [52–53]. CIUDEN also promoted a comprehensive public outreach strategy that was implemented in the Compostilla OXYCFB300 project, in parallel with the technological development activities [41]. The strategy was designed and implemented by an outreach team that concentrated on achieving interaction with the public at different levels, from local and regional to national and international. Special activities were tailored to different stakeholders, and the socioeconomic characteristics of local areas were also considered to develop an integrated communication plan. The capture project peaked in the mid-2010 s and is currently in a decommissioning stage, but the storage project is still active [54].

3.1.1.2. Elcogas. The company ELCOGAS S.A. developed a pre-combustion CO_2 capture and H_2 production pilot plant with a 335 MW Integrated Gasification Combined Cycle (IGCC), in Puertollano, an old industry centre for hydrocarbon refinery and processing located in Central-SW Spain [55–56]. The ELCOGAS CO_2 capture plant was built as part of the PSE-CO_2 project in 2010 [57], the world's first pre-combustion capture pilot in a power plant [58], setting Spain at the forefront of CO_2 capture technology [39]. The 14 MW pilot plant was capable of treating up to 2% of the total syngas generated in the IGCC plant, capturing 100 tonnes of CO_2 per day with a capture efficiency > 90% on average and producing 2 tonnes of H_2 per day [59]. By 2014, the plant had captured 3,500 tonnes of CO_2 [59]. However, the power plant had accumulated a large debt by 2014. A Spanish government rescue package proposed on the basis that the ELCOGAS plant was environmentally beneficial was rejected by the European Commission. The power plant was shut down together with the CO_2 capture and H_2 production plant in 2016 [58].

3.1.1.3. La Pereda. The La Pereda pilot, located in NW Spain on the site of the coal-fired La Pereda power plant, was developed by a consortium of national and international partners including Endesa Generación, Hunosa, Foster Wheeler, and CSIC (the Spanish National Research Council), commencing in 2009 [60]. This project received EU funding through three projects: CaOling (2009–2013), ReCaL (2012–2015), and CaO2 (2014–2017) [61]. La Pereda became operational in 2012, with an aim to demonstrate the viability of post-combustion capture of CO_2 using calcium looping under conditions comparable to those expected in a large-scale plant [61]. The system included two interconnected circulating fluidised bed reactors, an absorber able to treat up to 2400 kg/h and a circulating fluid bed (CFB) calciner with a firing power up to 3 MWth [60], fed by the 50 MW power plant [62]. The plant reached capture efficiencies of over 90% for CO_2 and over 95% for SO_2 [63]. The operating company, Hunosa, is currently converting the La Pereda power plant to biomass-fuelled, but there is no news about the reuse of the capture pilot facility.

A 300 kWth plant based on the same concept of carbonation/calcination was installed in La Robla, Spain [64]. The plant was connected to a 655 MWe coal power plant, property of Gas Natural Fenosa (currently Naturgy). This plant developed the "negative emissions" concept using carbonation/calcination cycles for capture of CO_2 produced from the combustion on a fluidised bed of biomass. The pilot plant of 300 kWth in the carbonator reached capture efficiency rates of over 70% and was built in the frame of the project CENIT CO_2, as part of a collaboration between Gas Natural Fenosa and CSIC.

3.1.2. Previous evaluations of CCS potential in Spain

The EU-based GeoCapacity project (2006–2009) focused on mapping large CO_2 point sources, infrastructure, and potential for geological storage in 25 European countries [27]. The main objective of this project was to compile a European capacity assessment for CO_2 storage in deep saline aquifers and hydrocarbon reservoirs. The assessment revealed a potential for CCS development in Spain, with a total storage capacity of 14 Gt, almost entirely from deep saline aquifers. Spain was ranked as the fourth largest theoretical resource in Europe after Norway, Germany, and the United Kingdom [65].

Subsequently, the Spanish Geological and Mining Survey (IGME) conducted the ALGECO2 project (2009–2010) to mature the characterisation of potential storage structures in Spain [66]. The main objectives of this project included the identification of suitable reservoir-caprock systems, the preliminary 3D characterisation of these target structures, the preliminary estimate of storage capacities, and establishing the scientific and technical criteria to rank potential structures [67]. The total storage capacity of the 103 evaluated onshore deep saline aquifers is up to 44 Gt, with 15 highly favourable and feasible structures identified by the project [37]. This database was incorporated in the European Commission's CO2Stop database [68]. Martínez del Olmo [38] rechecked the characteristics of these favourable structures and improved the results by complementing the inventory for all of Spain with depleted hydrocarbon fields and offshore saline aquifers.

The COMET project (2010–2013) aimed to identify and assess the most cost-effective CO_2 transport and storage infrastructure able to serve the West Mediterranean area, namely Portugal, Spain and Morocco [69]. The overall strategy of COMET comprised four fundamental tasks, including the harmonized inventory of present and future CO_2 sources and sinks in the region, the least cost modelling of national and regional energy systems, the in-depth assessment of selected transport networks, and the dissemination of the information [69]. Joint large-scale transnational infrastructures were suggested and joined on to more nationwide focused alternatives to achieve better financial performance [70]. Based on the results of the COMET project, Carneiro et al. [71] conducted a cost assessment for CCS development in the West Mediterranean area, and concluded that about 11–15 clusters of 43 storage prospects defined in the study area are cost-effective, depending on the emission mitigation scenario.

3.1.3. CCS legislation in Spain

In December 2010, the Spanish Head of State signed the country's first law on Geological Storage of CO_2, the 40/2010 Law [36], a transposition of the European Directive 2009/31/CE [72]. This law was envisaged to incorporate the regulations of the European Directive into the Spanish legal system and to adapt their use to Spain's geological, industrial and energy characteristics. This law is limited to the regulation of storage activities, and not to capture and transport activities, which are regulated under other pollution and environmental laws. 18 amendments were proposed but most of them were refused mainly due to issues relating to the jurisdiction of regional governments for the implementation of this law [73]. After the law's approval, the conflict that arose from the refused amendments between three litigating regions (Aragon, Galicia, and Catalonia) and the Central State Administration [74] was concluded with the judgement of the Spanish Constitutional Court (165/2016), which ruled in favour of the central government [75]. However, the ruling itself was not free of controversy and included a strongly-argued dissenting vote in favour of the regions [76–77].

Alenza-García [73] developed a comprehensive assessment of the 40/2010 Law, finding a strong similarity with the provisions reflected in the European Directive 2009/31/CE, hence lacking original content (as in "self-developed"). This is particularly obvious in the more immature sections of the 2009/31/CE Directive, which were not developed in the transposed 40/2010 Law. The 40/2010 Law presents a limited legal framework, which refers to future regulatory developments that have not been addressed yet. A positive aspect is the substantial technical content within the articles of the law, particularly in those referring to site characterisation and the monitoring requirements of prospective storage sites. Finally, Alenza-García [73] highlighted the presence of a penalty system, including sanctions ranging from 0.2 million euros (M€) for minor infringements and up to 5 M€ for serious infringements (e.g., leakage back to the atmosphere or the ocean).

Spain has not yet developed a regulatory framework to govern the permitting process of CCS activities. However, the case of the Hontomín Technology Development Plant can be used as a reference to support the development of industrial-scale projects [78]. Firstly, the lack of a regulatory framework for CCS deployment compelled the exploration permit to be granted within the Mining Regulation. Thus, the Mining Authority considered the Hontomín geological formations as a resource of Section B "Underground Structures" (22/1973 Law). The exploration permit allowed the assessment of site feasibility for CO_2 storage. Subsequently, the storage permit requirements were established by a Task Force built by the Mining Authority, i.e., IGME and CIUDEN. The requirements established in the 40/2010 Law were used where the existing mining regulation was not sufficient. The Task Force identified the information needed to grant the Hontomín storage permit, including dynamic modelling, surveillance and monitoring, and mitigation tools, amongst others. The storage permit was finally granted in July 2018, which may serve as a good practice guideline for regulators, operators, and administrations.

3.1.4. Cost assessments

Multiple studies identify cost as the principal barrier for the development of CCS [17,79]. Based on the analysis of Gouveia et al. [80], the adoption of CCS in the Iberian Peninsula greatly depends on the cost evolution of both renewable resources and CCS: CCS becomes cost-effective after mature renewables, namely onshore wind and hydropower, are fully exploited up to their technical–economic potential. According to the Global CCS Institute, the cost of CO_2 capture is falling because of various reasons, including improvements in solvents, newer non-solvent based capture technologies, improved CO_2 compression strategies, economies of scale, and modularisation [81]. However, the high cost of CO_2 capture is still one of the major barriers to CCS development. In the power sector, the pathway to lower costs involves a combination of advances in power generation technology and advances in CO_2 capture technologies [82]. In the remaining industrial sectors, a severe cut in CO_2 emissions within reasonable cost does not seem possible without CCS deployment, since a significant share of the emissions is process-embedded and cannot be avoided by applying measures such as a transition from fossil fuel to renewable resources [83]. In countries like Spain that have a framework of emission reduction favourable to renewables resources and energy efficiency, CCS in sectors hard to be abated via renewables (e.g., cement or steel factories) may play an important role to achieve a long-term and ambitious emission reduction target [84]. Based on a techno-economic analysis and systematic review of CCS in some industries [85], the cost per tonne of CO_2 avoided varies significantly in different industries. Spain's large CO_2 emitters (≥1 Mtpa) in the hard-to-abate sector are from cement, iron and steel, and pulp and paper industries. Among these, CCS in the cement industry using calcium looping technology presents a much lower overall cost than that in the other two industries [85], and could therefore become priority sources for CCS development in Spain.

Achieving significant cost reductions of CCS deployment will require not only a vigorous and sustained level of technical research and CCS development, but also a substantial level of commercial deployment [86], which in turn will require a significant market for CO_2 capture technologies that can only be established by government actions. In Spain, a new law on "Asignación de Derechos de Emisiones Gratuitos" (i.e., Free Emission Trading), transposed from the EU's Directive 2003/87/CE [87], plans to progressively reduce the free emission rights [88]. This could lead to an increasing cost of emitting CO_2, which may promote the CO_2 capture market and make CCS economically more feasible [89]. Furthermore, the combination of CCS with other low-carbon technologies, such as bioenergy and blue hydrogen generation could help reducing the upfront costs related to CCS, via clustering and infrastructure sharing [11,13–14]. This could create an incentive to develop these technologies synergically. Developing the clean hydrogen infrastructure at the scale demanded in the clean energy strategies is unlikely to happen without blue hydrogen [90], and this is aligned with the mature renewable scenario where CCS can become cost-effective [80]. The CCS portion of BECCS strongly influences the cost of the operations [91], and therefore it is important to identify priority CCS areas for early development.

3.2. GHG emissions and reduction target in Spain

The national GHG emissions for Spain in 2018 were estimated to be 334.3 million tonnes of CO_2 equivalents ($MtCO_2eq$) [92], the fifth largest emitter in the EU after Germany, France, Italy and Poland. These emissions represent an increase of 15.5% with respect to the emissions in 1990 (289.4 $MtCO_2eq$) and a reduction of 24.7% of the emissions with respect to 2005 (428.9 $MtCO_2eq$). The GHG emissions derived from the four sectors (as defined by the Intergovernmental Panel on Climate Change - IPCC) are: energy industries (75.8%), industrial processes and product use (8.3%), agriculture (11.9%) and waste (4.0%). The CO_2 reduction achieved in 2018 due to land use, land-use change and forestry (LULUCF) activities was 38.5 $MtCO_2eq$. Detailed discussions of GHG emission trends in Spain are discussed elsewhere [92–94].

CO_2 emissions are the main GHG source in Spain, accounting for 269.7 Mt in 2018 (80.7% of the total GHG emissions). The energy industries (including fuel combustion activities, such as electricity generation, heating and transport) with 245 Mt and the industrial processes and product use sector with 20 Mt are the most intense CO_2 emitters, representing 92.3% and 7.5% of the CO_2 emissions, respectively, while the waste and agriculture sectors mainly emit non-CO_2 GHGs (Fig. 3A). Spain has traditionally been a fossil fuel importing country, which currently accounts for 75% of its energy production: coal (10%), natural gas (21%), and fuel–oil (44%) [95]. In the energy

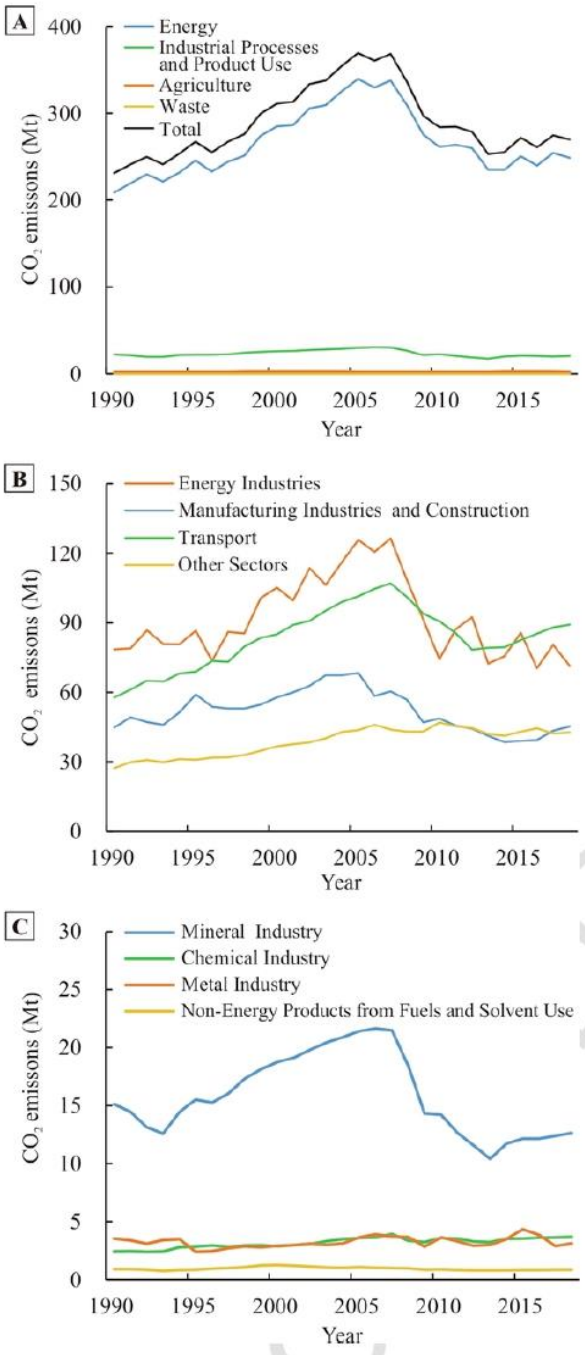

Fig. 3. National inventory of annual CO_2 emissions in Spain from 1990 to 2018: (A) CO_2 sources by sectors (as defined by the IPCC); (B) energy-related activities; (C) the industrial processes and product use sector. Data source: MITECO [92].

sector, CO_2 emissions mainly come from fuel combustion activities, including transport (89.2 Mt), power generation (71.5 Mt), manufacturing industries and construction (45.3 Mt), and others (42.9 Mt) (Fig. 3B). In the industrial processes and product use sector, CO_2 emissions are mainly derived from mineral (12.7 Mt), chemical (3.7 Mt) and metal (3.1 Mt) industries (Fig. 3C).

The Spanish Government has approved the National Long-Term Decarbonisation Strategy in response to the EU's target [96]. Spain aims to achieve a GHG emission reduction of 90% by 2050 compared to 1990, equivalent to a reduction from 334.3 $MtCO_2eq$ in 2018 to 28.9 $MtCO_2eq$ in 2050. The remaining 10% of emissions will be solved by nature-based carbon sinks, e.g., LULUCF. This long-term decarbonisation strategy also aims for 100% renewable electricity generation by 2050 [84]. Spain's decarbonisation target is technologically neutral, i.e., all decarbonisation technologies should have equal opportunities to develop cost-efficient solutions in different economic sectors. This strategy is consistent with the Spanish Integrated National Energy and Climate Plan 2021–2030, published in January 2020 [97].

Both these two major decarbonisation plans released by the government highlight the importance of CCS, but are not explicit about the mechanisms, costs, benefits or dates of its implementation. Although CCS has been considered a feasible option for emission reduction in Spain [35] and approved by the Spanish Parliament [36], the explicit support to CCS development given by the Spanish government has been limited to the creation of the CIUDEN Foundation, a public sector CCS delivery (see Section 3.1 for the specific actions taken by the foundation). Given the large tonnage scale and geographic focus as point sources, CCS could be an effective tool to decarbonise the power and industry sectors.

3.3. Priority CCS region selection methodology

To identify and characterise the priority CCS development regions in Spain (i.e., target CO_2 emission hubs and their most suitable storage sites), we carry out a detailed and systematic source-to-sink assessment using the methodology presented in Section 2 and Fig. 2. The methodology is suited to the decarbonisation needs and storage opportunities of Spain, but the values chosen for the different evaluation parameters can be adapted to different emission and storage scenarios, so it can be easily adapted to other countries and contexts.

3.3.1. Screening of emission sources and storage sites

Industrial facilities with large CO_2 emissions are seen as primary sources to implement CO_2 capture in their industrial processes [98], because it is more efficient to address their emissions than from small and dispersed CO_2 emissions. In 2018, there were 183 industrial facilities with CO_2 emissions large than 0.1 Mtpa in Spain, which are classified by industrial sectors in Fig. 4A [99–100]. These large CO_2 emitters have total emissions of 110.5 Mtpa (41% of Spain's total emissions), with 83 CO_2 emitters in the power industry accounting for 71.3 Mtpa, while 100 CO_2 emitters in other industries accounting for 39.2 Mtpa. In the power industry, CCS is not the only option for decarbonisation. Indeed, emissions can be mitigated by other methods in the future, e.g., switching to renewable resources and improving energy efficiency. Coal-fired power plants are some of the largest single CO_2 emitters in Spain, and the government has established a plan for the closure of these plants [101–103]. However, an early penetration of CCS in the power sector is needed to achieve ambitious mitigation targets in Spain [80].

On the other hand, emissions from other industries, including metal, mineral, chemical, wood derivatives, waste and waste-water management, and food and beverage industries (hereby called "hard-to-abate sector") cannot be mitigated by using renewable energy or by improving energy efficiency due to the existence of process-related emissions. Thus, we separate these two sectors to allow the exploration of CCS deployment at two development stages, one more immediate (to decarbonise the power system) and one more sustained (to decarbonise other industrial systems).

For economies of scale, transport networks would need to serve multiple facilities and/or storage sites [4,104–105]. In this study, CO_2 emission hubs include potential CO_2 sources for CCS development within a circular area with a diameter smaller than 60 km and annual CO_2 emissions higher than 2 Mtpa. The values of 60 km and 2 Mtpa were chosen based on the distribution of these large CO_2 emitters, trying to minimise the number of clusters and maximise the CO_2 emissions per cluster without making clusters too large.

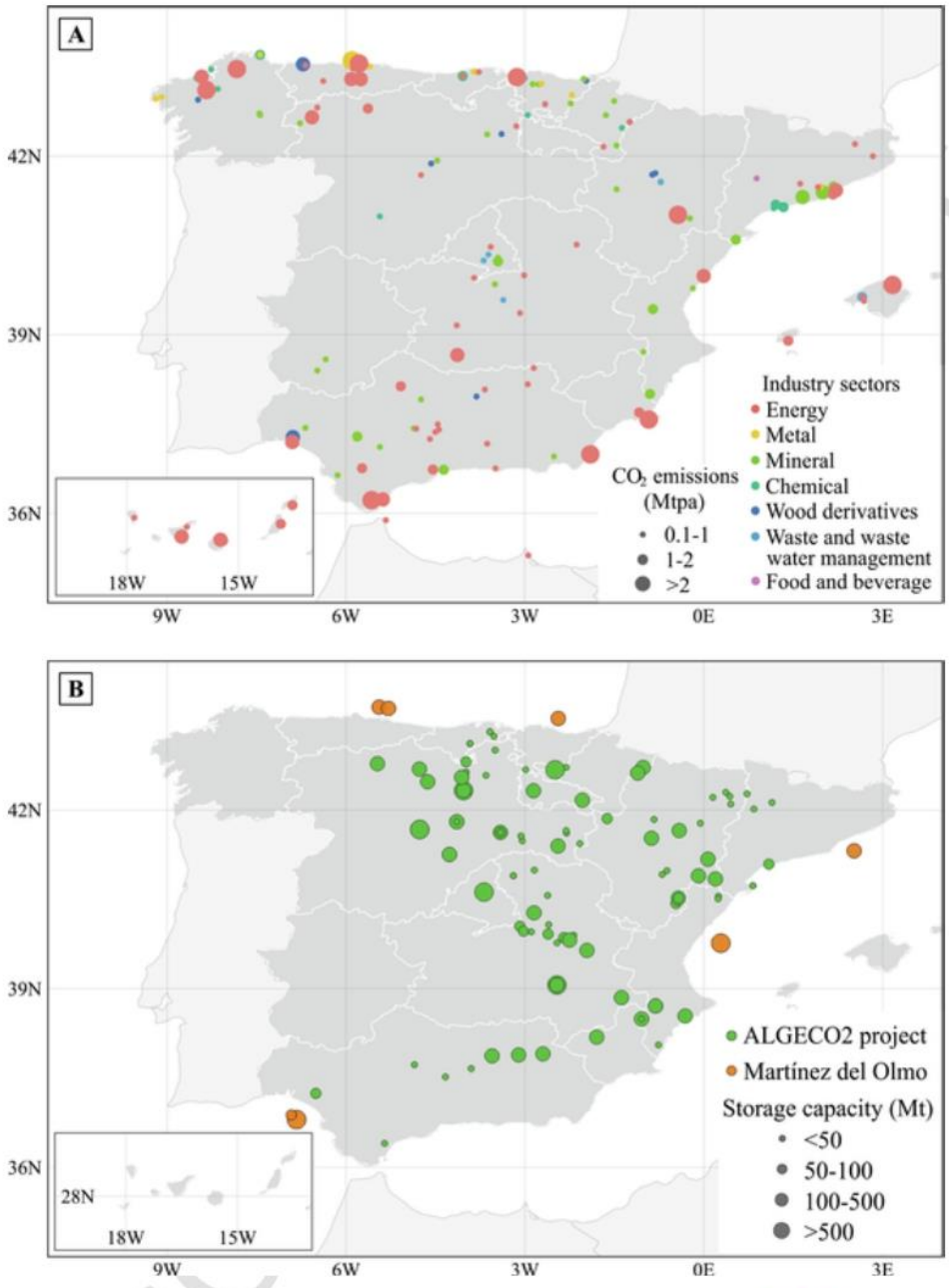

Fig. 4. (A) Large industrial sources of CO_2 emissions (≥0.1 Mtpa) by industrial sectors in Spain in 2018. Data source: [99–100]. (B) CO_2 storage structures in Spain from the ALGECO2 project [66] and Martínez del Olmo [38].

Finally, the CO_2 emissions in the Canary Islands present relatively high emissions derived from their heavy dependence on external energy sources, chiefly oil [106–107]. However, none of the storage portfolios have identified any suitable geological structures onshore of any the islands. Due to its distinct geographical location and remoteness from mainland Spain, the implementation of CCS in the Canary Islands was not included in this work. A specific study addressing the specificities of this archipelago is nevertheless strongly advised.

For the screening of the storage structures, geological data from 110 storage sites were extracted from previous studies, including 103 onshore saline aquifers from the ALGECO2 project [66] and 7 offshore saline aquifers [38] (Fig. 4B). For each emission hub identified in the previous step, a preliminary screening process is applied to all storage sites to determine whether they are taken forward or disqualified. This preliminary screening is based on two basic criteria: theoretical storage capacity and source-to-sink distance. This screening process reduces the input structures to a more manageable number and allows the selection of potential structures for each emission hub for the following ranking process. We assume that potential storage structures must have a capacity large enough so that they can store 90% of the thirty-year CO_2 emissions of the respective emission hub based on the capture efficiency, generally assumed as 90% [108]. The maximum source-to-sink distance has been set to 200 km to limit transport and monitoring costs. The distance limitation is extended to 300 km if fewer than five structures pass the screening process for an emission hub.

3.3.2. Scoring

For each emission hub, the filtered potential structures are scored based on four criteria including theoretical storage capacity, the suitability of reservoir-caprock systems, development cost, and the availability of seismic and well data for their assessment.

3.3.2.1. Storage capacity. Storage capacity is positively correlated with the ranking of the storage structures. High storage capacity is required to guarantee the selected storage structures are economically suitable and capable of storing all CO_2 from the emission hub. Storage capacity, even in the form of static volume, can also have an influence on the unit cost of CO_2 stored: assuming a similar capital expenditure of prospective CCS projects, the larger the storage capacity, the lower the unit cost of CO_2 stored because of the economy of scale [20].

3.3.2.2. Reservoir-caprock suitability. To evaluate the suitability of reservoir-caprock systems, five parameters are adopted from the ALGECO2 database and Martínez del Olmo [38]: the effective thickness, porosity and permeability of reservoirs, and the effective thickness of caprocks and the presence of fractures within caprocks. For reservoirs, porosity is here used as a proxy for effective capacity, and effective thickness and permeability are used as proxies for injectivity. Due to the lack of permeability data in the offshore storage structures from Martínez del Olmo [38], an indirect permeability value was inferred from porosity based on the correlation (trend line) between permeability and porosity of onshore storage structures. Whilst not a perfect predictor, porosity and permeability are correlated and so permeability is estimated from known porosity. For caprocks, high effective thickness and low presence of fractures are used as a proxy for high-sealing capacity [109]. The presence of fractures in caprocks was estimated in an expert elicitation carried out in the framework of the ALGECO2 project [66]. To quantitatively evaluate the suitability of reservoir-caprock systems, the presence of fractures in caprocks is assigned a value: 1 for high, 2 for medium and 3 for low presence level of fractures. Then, we applied a data normalisation to all five parameters based on a function of their minimum and maximum values to achieve non-dimensionalisation of these parameters:

$$V_n = \frac{V - V_{\min}}{V_{\max} - V_{\min}} \tag{1}$$

Where V_n, V, V_{min} and V_{max} are the normalised, actual, minimum and maximum values, respectively. The five normalised parameters add up to the total suitability score of each storage structure.

3.3.2.3. Development cost. To provide a proxy for the development cost, we consider both the pipeline construction for CO_2 transportation and well drilling for CO_2 injection. The development cost of onshore and offshore structures is calculated based on a 5-well storage system [20]:

$$Cost_{onshore} = l \cdot P_{onshore} + 5 \cdot d \cdot D_{onshore} \tag{2}$$

$$Cost_{offshore} = l_{onshore} \cdot P_{onshore} + l_{offshore} \cdot P_{offshore} + 5 \cdot d \cdot D_{offshore} \tag{3}$$

where l is the distance from onshore structures to the emission hubs, $l_{onshore}$ and $l_{offshore}$ are the onshore and offshore distances from offshore structures to the emission hubs, d is the middle depth of the storage reservoir, $P_{onshore}$ and $P_{offshore}$ are the cost of onshore and offshore pipeline construction per kilometre, and $D_{onshore}$ and $D_{offshore}$ are the cost of onshore and offshore borehole drilling per kilometre. All costs in this section are in 2020€. $P_{onshore}$ is assigned a value of 0.88 M€ per kilometre based on the onshore pipeline capital cost in a scenario with a pipeline diameter of 24 in. [110]. $D_{onshore}$ is assigned 1.56 M€ per kilometre based on data collected from the report of oil and gas upstream costs in the U.S. [111]. $P_{offshore}$ is assigned 1.47 M€ per kilometre based on the offshore pipeline costs in the Gulf of Mexico in a scenario with a pipeline diameter of 14 to 24 in. [112]. $D_{offshore}$ is assigned 7.78 M€ per kilometre based on the offshore well drilling cost per kilometre reported by Hinton [113] and the average well cost breakout reported by the U.S. Energy Information Administration [111].

3.3.2.4. Data availability. The availability of seismic and well data is crucial to guarantee the certainty of storage capacity and the suitability of reservoir-caprock systems. Existing data can also be used in CCS deployment and thus reduce the development cost. To determine the data availability factors, we only considered datasets included in the Spanish Geological Survey's repositories, in both ALGECO2 [66] and the Spanish Geophysical Information System [114]. The availability of seismic data is graded into four levels (Table 1). 3D seismic data is assigned a value of 3 representing the highest data availability, which only covers a few of the offshore structures. 2D seismic data is subdivided into "high 2D" and "low 2D" and assigned values of 2 and 1, respectively, based on the density of survey lines. A value of 0 is assigned to structures that are not crossed by any seismic line. Similarly, the availability of well data is also divided into four levels based on the number of wells (Table 1). The final data availability value is the sum of the availability of seismic data and well data.

3.3.3. Ranking

After defining and quantifying the four ranking criteria, the MCDM method is used to rank potential storage structures for each emission hub. MCDM is a branch of operational research dealing with finding optimal results in complex scenarios including various indicators, conflicting objectives and criteria [115]. MCDM methods have been applied in many aspects of the CCS chain, e.g., barrier analysis [79] and the selection of storage sites [116]. It has been proven as an effective method in the assessment of CCS in Spain [117–119]. The Technique for Order of Preference by Similarity to Ideal Solution (TOPSIS) method [120] is adopted in this study. This method is a compensatory process, i.e., a poor result in one criterion can be negated by a good result in another criterion, thus no alternatives are excluded due to a single poor result in one criterion. TOPSIS is very suitable to explicitly evaluate multiple conflicting criteria in decision-making. For one emission hub, the values of each criterion for all potential structures are normalised and weighted based on the following method:

$$Y_{ij} = \frac{X_{ij}}{\sqrt{\sum_{i=1}^{n} X_{ij}^2}} \cdot W_i \tag{4}$$

where Y is the normalised and weighted value, X is the actual value, W is the weighting of the criterion, i is the number of potential structures for the emission hub and j is the number of the criteria (four criteria in this study). Once the values of all criteria for all potential structures are normalised and weighted, a pair of positive and negative ideal solutions are hypothesised based on the best and worst values for each criterion; i.e., the positive ideal solution is the one that maximises the positive criteria and minimises the negative criteria, and vice versa (Fig. 5). The distance (i.e., differences) between each structure to the positive and negative ideal solutions are calculated. Finally, the TOPSIS score (T_s) of each structure is calculated as:

Table 1
Criteria to evaluate the availability of seismic and well data (0 for low availability, to 3 for high availability).

Data availability	Seismic density	Well number
3	High (3D)	≥5
2	High (2D)	3–4
1	Low (2D)	1–2
0	None	None

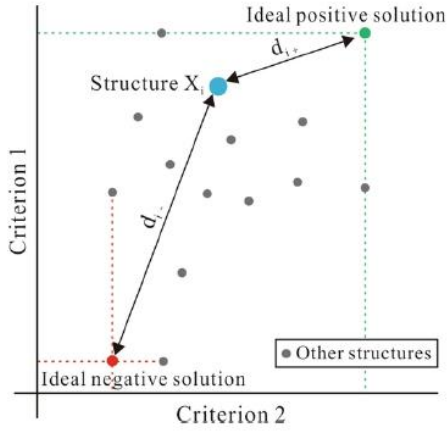

Fig. 5. Scheme of the ranking methodology adapted from the Technique for Order Preference by Similarity to Ideal Solution (TOPSIS) [120]. The structures are defined in a multidimensional space determined by their values in each of the four ranking criteria. The best and worst values of the structures in each criterion determine the ideal positive and negative solutions, respectively. The distances to these ideal positive (d_{j+}) and negative (d_{j-}) solutions are combined into a TOPSIS score (Ts), which is therefore dependent on all criteria at the same time.

$$T_s = \frac{d_+}{d_+ + d_-} \tag{5}$$

where d_+ and d_- are the separation from the ideal positive and negative solutions, respectively.

The criteria are not equally considered when assessing the suitability of a storage site. Hence, a relative weighting is applied to the different criteria values to reflect this variability. The weighting of each criterion has been chosen subjectively, based on the authors' best knowledge and is listed as a percentage in Table 2. Three weighting scenarios are applied: geological, economic and a combined scenario. The geological scenario assigns higher weightings to storage capacity and the suitability of reservoir-caprock systems and lower weightings to development cost and the availability of seismic and well data compared to the economic scenario. When the two scenarios result in different priority structures for one emission hub, the final result is determined by the third scenario which uses averages of the two scenarios weightings, here defined as "comprehensive scenario".

The MCDM method has been implemented using Microsoft Excel. The specific assessment process and result for each emission hub can be found in the Supplement. After the ranking of potential storage structures for each emission hub, the priority structure is identified, and the second- and third-best structures are listed as alternatives.

Table 2
Weighting scenarios of four ranking criteria in the Technique for Order Preference by Similarity to Ideal Solution (TOPSIS) method.

Criteria Scenarios	Storage capacity	Suitability of reservoir-caprock systems	Development cost	Data availability
Geological scenario	25%	40%	25%	10%
Economic scenario	15%	30%	35%	20%
Comprehensive scenario	20%	35%	30%	15%

4. Results

4.1. CO_2 emission hubs and priority source-to-sink clusters

The application of the methodology presented to the Spain case resulted in the selection of 15 CO_2 emission hubs as potential CO_2 sources for CCS development. These emission hubs emit 68.7 Mtpa of CO_2, representing 20.6% of Spain's GHG emissions in 2018, so the contribution of CCS in decarbonizing Spain could be significant. Among these, 11 emission hubs are in the power sector and have total CO_2 emissions of 52.8 Mtpa (Fig. 6A, Table 3), which mainly come from thermal power plants and oil refineries. The remaining four emission hubs belong to the hard-to-abate sector and have total CO_2 emissions of 15.9 Mtpa (4.8% of Spain's GHG emissions in 2018) (Fig. 6B, Table 3), which are mainly derived from iron and steel production, cement production and pulp production. The emission hubs are mainly distributed in coastal areas, e.g., Galicia, Asturias, the Basque Country, and Catalonia in northern Spain, and Murcia and Andalusia in southern Spain (Fig. 6).

The priority and alternative storage structures most suitable to the 15 emission hubs were identified after the screening and ranking stages, leading to 15 priority source-to-sink clusters and their alternative structures, whose detailed features are listed in Table 4. Of these, 9 priority structures rather than 15 were selected because some adjacent emission hubs share the same potential storage locations. These priority and alternative structures are mainly distributed in Castilla and Leon, Asturias, and Aragon in northern Spain, and Murcia and Andalusia in southern Spain, with a few offshore storage structures (Fig. 7).

4.2. Potential development regions outline

Four potential CCS development regions in Spain are identified based on the distribution of priority source-to-sink clusters and their alternative storage structures (Fig. 7). The development regions need to meet two requirements:

- They should contain multiple emission hubs. Three of the four identified regions have emission hubs from both the power sector and the hard-to-abate sector, and one region only contains power emission hubs. The emission hubs from different sectors are necessary to ensure that the identified regions can play potential roles in different development stages of emissions reduction, as explained in Section 4.1.
- They should also contain multiple potential storage structures, especially the structures shared by multiple emission hubs, which are beneficial to the development of large CCS regions in the future.

4.2.1. North-Western Spain region

North-Western Spain region has five emission hubs with total CO_2 emissions of 33.4 Mtpa, accounting for almost half of the emissions of all emission hubs. E1, E2 and H1 are the three largest emission hubs in Spain, with CO_2 emissions of 11.6, 10.3 and 7.1 Mtpa, respectively. The E1 and E2 hubs include the two largest emitters in the power sector in 2018, Unidad de Producción Térmica As Pontes (closed in 2020) and Central Térmica de Aboño, which are two thermal power plants emitting 7.9 and 7.1 Mtpa, respectively. The H1 hub has the largest emitter in the hard-to-abate sector, ArcelorMittal Asturias, an iron and steel enterprise with emissions of 5.7 Mtpa. The E1 hub is located in the northwestern corner and far from potential structures. Although the source-to-sink distance was extended to 300 km, the priority structures of other emission hubs were not placed within this radius. Its priority structure is an offshore structure, Mar Cantábrico J-1 S. The E2 and H1 hubs share the same priority and alternative structures due to their proximity. The priority structure, Iglesias (Utrillas), has a high capacity, a good reservoir-seal system and reliable seismic and well data. The priority structure of the E9 hub, Rioja Norte (pre and *syn*-orogenic Ter-

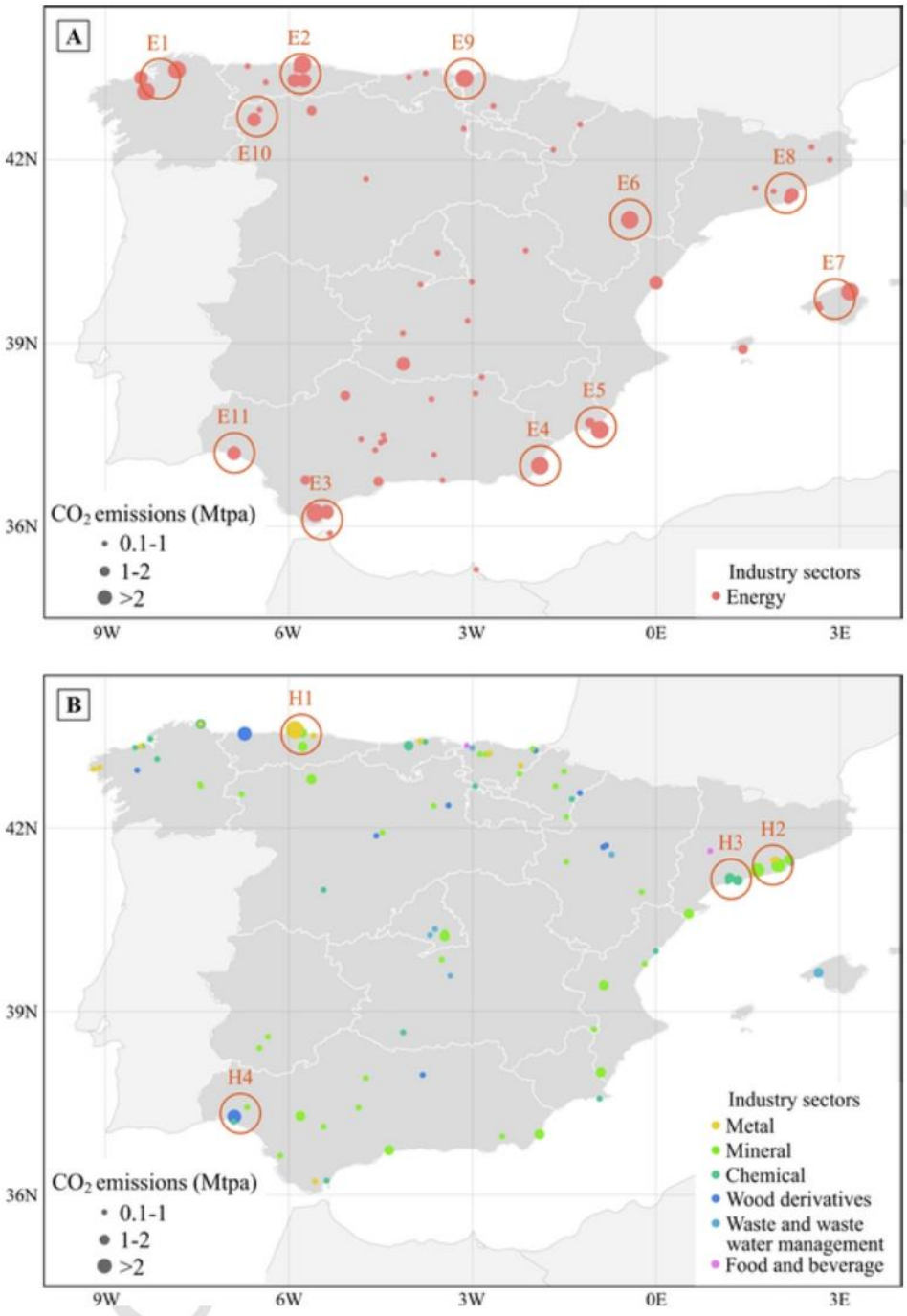

Fig. 6. Distribution of identified CO_2 emission hubs: (A) 11 emission hubs in the power sector; (B) four emission hubs in the hard-to-abate sector.

tiary), has a very large storage capacity (>500 Mt). However, it is located in pre-orogenic sediments and at depths > 3,500 m (reaching up to 5,000 m depth), which is far from the optimal storage depth [121] and could significantly increase the drilling cost. Thus, Iglesias (Utrillas) could be regarded as a good alternative structure for the E9 hub. The priority structure of the E10 hub, Duero Centro-Meridional (Upper Cretaceous), has also suitable features for CO_2 storage but lacks sufficient seismic data, resulting in high uncertainty.

4.2.2. North-Eastern Spain region

Five emission hubs are located in North-Eastern Spain region: E6, E7, E8, H2 and H3, with CO_2 emissions between 2.3 and 4.2 Mtpa, which together account for 22% of the emissions of all hubs. The main emitters include two thermal power plants, Central Térmica de Andorra (closed in June 2020) with emissions of 3.1 Mtpa and Central Térmica de Cicle Combinat with 1.4 Mtpa, as well as two cement enterprises with emissions of around 1 Mtpa (Cementos Molins and Cementos Portland Valderrivas). The E6, H2 and H3 hubs share the same priority structure, the Área de La Zona de Enlace (Buntsandstein), which has very good reservoir quality, but a relatively high uncertainty in the effective thickness of caprock due to the lack of seismic data coverage. Thus, other structures, e.g., Barcelona-A, Reus and Caspe-Mayals, can be seen as good alternative structures for these emission hubs. The priority structure of the E8 hub is Barcelona-A due to their proximity. The

Table 3
Annual CO_2 emissions for identified emission hubs, divided into the power sector and the hard-to-abate sector, and location of the hub centroid in latitude and longitude (WGS84).

Power sector					Hard-to-abate sector				
Hubs	No. Sites	Emission (Mtpa)	Latitude	Longitude	Hubs	No. Sites	Emission (Mtpa)	Latitude	Longitude
E1	4	11.6	43.34	−8.12	H1	5	7.1	43.51	−5.8
E2	6	10.3	43.4	−5.84	H2	9	4.2	41.43	1.91
E3	9	6.3	36.19	−5.39	H3	4	2.3	41.16	1.24
E4	1	6.3	36.99	−1.9	H4	5	2.3	37.26	−6.85
E5	3	3.2	37.62	−0.98					
E6	1	3.1	41.01	−0.43					
E7	3	2.8	39.68	2.84					
E8	5	2.8	41.44	2.03					
E9	1	2.3	43.32	−3.11					
E10	2	2.1	42.73	−6.53					
E11	3	2	37.2	−6.9					
Total	38	52.8			Total	23	15.9		

E7 hub is located in the Balearic Islands, which is relatively far from potential structures (only a few onshore and offshore structures are located within a distance of 300 km). Its priority structure is Denia, needing long offshore transport that could significantly increase development costs.

4.2.3. South-Western Spain region

Three emission hubs are located in South-Western Spain region: E3, E11 and H4, with CO_2 emissions of 6.3, 2.3 and 2.3 Mtpa, respectively, accounting for 16% of the total emissions of all hubs. The main emitters with emissions higher than 1 Mtpa include a thermal power plant (Central Térmica Los Barrios – in decommissioning), two refinery enterprises (Refinería Gibraltar and Refinería La Rábida), and a pulp and paper enterprise (Complejo Industrial de Huelva). Very limited potential storage structures are found in this region. No more than five structures passed the screening process for these emission hubs, even when the source-to-sink distance was extended to 300 km. These three emission hubs share the same priority structure (Cádiz Arenoso). This structure has a high storage capacity and good reservoir-seal quality, which makes it suitable for CCS development. As alternative structures, Almonte has a relatively smaller storage capacity of less than 100 Mt compared to other potential structures. Moreover, its reservoir depth mainly ranges from 580 m to 850 m, and its suitability would need to be verified given a low CO_2 storage density in the gas phase, making the storage much less efficient than a supercritical setting.

4.2.4. South-Eastern Spain region

South-Eastern Spain region has two emission hubs in the power sector, E4 and E5, with CO_2 emissions of 6.3 and 3.2 Mtpa, accounting for 14% of the emissions of all hubs. The main emissions come from a thermal power plant emitting 6.3 Mtpa (Central Térmica Litoral de Almería – expected closure in 2021), which represents the third-largest emitter in Spain, and a refinery with emissions of 2.5 Mtpa (Repsol Petróleo Cartagena). There are also relatively limited potential storage structures in this region compared to NW and NE Spain. The E4 and E5 hubs share the same priority structure, Murcia B-1, which has high storage capacity and available seismic and well data that reduce the uncertainty of its storage suitability. In this region, the priority and alternative structures present relatively low porosity and permeability.

5. Discussion

5.1. Priority CCS clusters and regions

In this work, we have presented a general methodology and have applied it to show the feasibility and potential of CCS clusters in Spain. In the ALGECO2 project, 15 highly favourable and feasible structures were identified based on the suitability of storage structures and the quality of usable data [122] (Fig. 8A). In this study, we employed a source-to-sink assessment based on a hubs and clusters strategy to identify the prospective regions in Spain with the greatest CCS development potential, as a step forward from the available storage structure portfolio (Fig. 8B). This assessment takes into account three further factors: the spatial matching, i.e., the distribution of emission hubs and storage structures, the development cost, and the capacity matching, i.e., the priority storage should have enough capacity to store the 30-year emissions of the emission hub. This allows the identification of priority regions that ensure the longevity of prospective CCS projects and respond to Spain's long-term emission reduction target by 2050.

Emission hubs, rather than single emission facilities, were selected as CO_2 sources for the assessment. The adoption of emission hubs can ensure the availability of CO_2 sources and thus the longevity of prospective CCS projects necessary to achieve Spain's long-term target, in case some facilities within the emission hubs are shut down in the future. The assessment presented in this work could also serve to plan for the conversion or the creation of new clusters dedicated to blue hydrogen and BECCS, which rely on an early and extensive penetration of CCS (these options are explored in detail in section 5.2.2).

The main advantage of the hubs and clusters strategy is that it can help reduce the development cost of CCS deployment when multiple CO_2 emitters share infrastructure such as pipelines and storage complexes [20,105]. For example, in the hard-to-abate sector, only two industrial facilities have CO_2 emissions higher than 1.5 Mtpa in Spain, with the emissions of the rest ranging from 0.1 to 1 Mtpa. Compared to aiming for a single large project, a gradual development and build-out process may provide a more viable pathway in this sector. Note that small hard-to-abate emitters are distributed throughout the territory and could benefit from CCS infrastructure built for the identified clusters (see Fig. 6B). Previous research indicates smaller-scale industrial applications such as steel and cement works may benefit from CCS as much as power sector applications, but that sharing of infrastructure may be needed to make this economically viable [123].

Priority source-to-sink clusters were identified using the methodology presented in Section 4. However, it should be noted that the availability of geological/geophysical data in most storage sites is very low, compared to other potential storage regions in Europe. For instance, there is a limited number of exploration wells in Spain (710 in total), compared to the 9,200 in France, 8,500 in Italy and 26,000 in the United Kingdom [38]. This is a result of the lack of hydrocarbon resources in Spain in comparison to similar sized countries. The lack of exploration data in Spain, particularly well data, imposes significant uncertainty on the suitability assessment of the storage sites, especially when trying to determine the injectivity (or maximum rate of injection) in the reservoir formation. Injectivity is a key parameter that determines the suitability of a storage site [124]. Unexpected low injectivity in a reservoir can dictate the fate of a CO_2 storage project, forcing its

Table 4
Detailed features of the priority and alternative storage structures for emission hubs. Data of priority structures obtained from ALGECO2 Database [66], Martínez del Olmo [38] and the Spanish Geophysical Information System [114].

Emission hubs				Priority storage structures											Alternative storage structures	
Sectors	Name	Emission (Mtpa)	90% of emission in 30 years (Mtpa)	Name	Capacity (Mt)	Reservoir effective thickness (m)	Reservoir porosity (%)	Reservoir permeability (mD)	Seal effective thickness (m)	Presence of natural fractures in seal	Reservoir middle depth (m)	Onshore distance to emission hub (offshore distance) (km)	Seismic	Well	First alternative structures	Second alternative structures
Power sector	E1	11.6	313.2	Mar Cantábrico J-1 S	270	140	12	n/a	1,000	n/a	1,320	217(3.5)	High 3D	0	Mar Cantábrico J-1P	Boñar
	E2	10.3	278.1	Iglesias (Utrillas)	678	135	14	10–100	1,344	low	1,845	190	High 2D	>5	Iglesias (Cretaceous)	Mar Cantábrico J-1 S
	E3	6.3	170.1	Cádiz Arenoso	>700	40–50	25	n/a	1,200	n/a	1,523	147 (10)	High 3D	3	Almonte	Cádiz Dolomítico
	E4	6.3	170.1	Murcia B-1	366	1,235	9	1–10	720	low	1,500	134	High 2D	2	Sierra Seca (Dogger-Lias)	Sierra de Salinas (Dogger)
	E5	3.2	86.4	Murcia B-1	366	1,235	9	1–10	720	low	1,500	95	High 2D	2	Sinclinal de Pétrola (Manuel sandstone)	Sierra Seca (Dogger-Lias)
	E6	3.1	83.7	La Zona de Enlace (Buntsandstein)	>500	162	13	100–1000	81	low	2,165	32	Low 2D	>5	Denia	Caspe-Mayals
	E7	2.8	75.6	Denia	>700	80	22	n/a	350	n/a	2,128	28 (1 9 2)	High 3D	0	La Zona de Enlace (Buntsandstein)	Barcelona-A
	E8	2.8	75.6	Barcelona-A	>500	150	8	n/a	600	n/a	2,432	29 (15)	High 3D	0	La Zona de Enlace (Buntsandstein)	Reus
	E9	2.3	62.1	Rioja Norte (pre- and *syn*-orogenic Tertiary)	>500	1,190	10	10–100	2,832	low	4,390	87	High 2D	>5	Iglesias (Utrillas)	San Pedro
	E10	2.1	56.7	Duero Centro-Meridional (Upper Cretaceous)	1,229	97	6.5	10–100	756	low	1,110	187	Low 2D	>5	Duero Centro-Meridional (Utrillas)	Boñar
	E11	2.0	54	Cádiz Arenoso	>700	40–50	25	n/a	1,200	n/a	1,523	21 (10)	High 3D	3	Almonte	Cádiz Dolomítico
Hard-to-abate sector	H1	7.1	191.7	Iglesias (Utrillas)	678	135	14	10–100	1,344	low	1,845	195	High 2D	>5	Iglesias (Cretaceous)	Mar Cantábrico J-1 S
	H2	4.2	113.4	La Zona de Enlace (Buntsandstein)	>500	162	13	100–1000	81	low	2,165	178	Low 2D	>5	Barcelona-A	Reus
	H3	2.3	62.1	La Zona de Enlace (Buntsandstein)	>500	162	13	100–1000	81	low	2,165	115	Low 2D	>5	Reus	Denia
	H4	2.3	62.1	Cádiz Arenoso	>700	40–50	25	n/a	1,200	n/a	1,523	23(10)	High 3D	3	Almonte	Cádiz Dolomítico

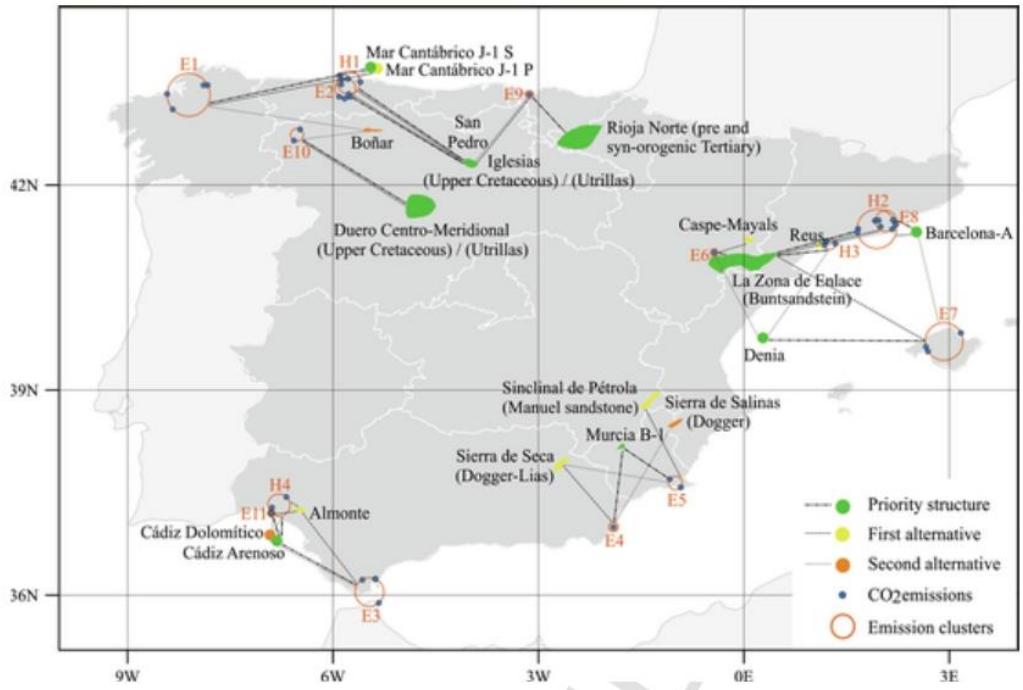

Fig. 7. The priority source-to-sink clusters and their alternative storage structures.

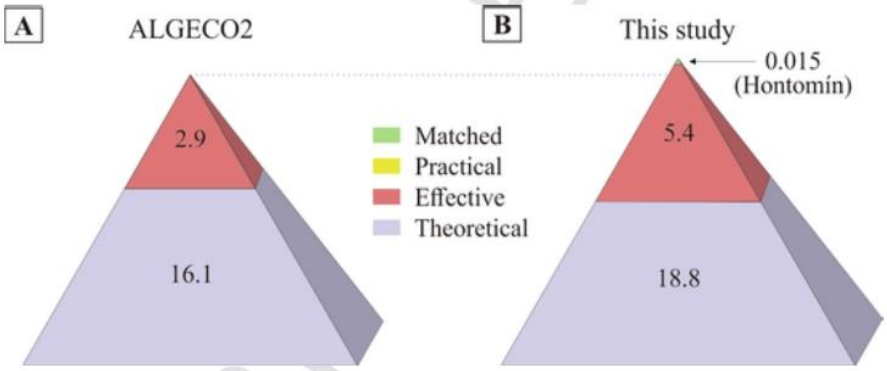

Fig. 8. Four-tier resource pyramid of Spain's CO_2 storage capacity (in Gt) framed by Carbon Sequestration Leadership Forum (CSLF) terminology after Cavanagh et al. [28] (see Fig. 1 for the description of the tiers). (A) Resource capacity outlined in the ALGECO2 project [66]. (B) Resulting from the source-sink matching process described in this study. The 5.4 Gt of effective capacity in (B) corresponds to the priority structures in Table 4 which have been assessed and assigned to priority emission hubs.

closure, examples being the In Salah project in Algeria [125] or the ZeroGen project in Australia [126]. Acquiring more geological data, particularly well data, to obtain better estimates of the injectivity is thus imperative in hydrocarbon-poor regions to reduce the uncertainty and thus increase the maturity of the storage sites.

Among the four potential CCS development regions, NW and NE Spain can be considered the priority regions in Spain. The emission hubs in the two regions have high total CO_2 emissions of 48.6 Mtpa, accounting for 71% of all selected emission hubs in Spain. Furthermore, they include emission hubs in both the power sector and the hard-to-abate sector, which can ensure the regions can play potential roles in different stages and scenarios of emission reduction. In this study, emission hubs are calculated from Spain's inventory of CO_2 emissions in 2018 [92]. Spain has a framework of emission reduction favourable to renewables resources and energy efficiency, and has established a plan to close coal-fired power plants. For example, three coal-based power plants included in this assessment (Central Térmica de Andorra in E6 hub and UPT Compostilla and Central Térmica de Anllares in E10 hub) have been recently closed, but they are included in our assessment because they were still included in the 2018 Spanish government inventory used as input for the emission data [92]. This is indicative of the rapid adaptation of the power sector to the use of sustainable energy sources. In contrast, in the hard-to-abate sector, the process-related emissions cannot be mitigated by other emission reduction approaches, and thus the potential of the source-to-sink clusters can be considered more predictable in the long term. Even in a scenario where Spain completely relies on renewable resources and energy efficiency to reduce emissions in the power sector, CCS in the hard-to-abate sector would still be necessary to achieve net-zero emissions in this sector [127].

In NW and NE Spain, the main CO_2 emitters (≥1 Mtpa) in the hard-to-abate sector are an iron and steel enterprise in the H1 hub and two cement enterprises in the H2 and H3 hubs. These could mean long lasting, reliable emissions locations. Another two large CO_2 emitters of the hard-to-abate sector are in pulp and paper industry. In the cement industry, between 50% and two-thirds of the CO_2 emissions are process related, i.e., originating from the calcination of limestone where $CaCO_3$

is converted to CaO and CO_2 [128–129]. CCS is considered the method with the most potential for the overall reduction of the process-related emissions in the cement industry [129–130]. Cement plants possess several features favourable for CO_2 capture, e.g., high CO_2 concentration, few emission points and stable operation [131]. Based on a techno-economic analysis and systematic review of CCS in some industries [85], the cost of CCS in the cement industry is relatively lower than that in iron and steel industry and pulp and paper industry. Worldwide, there are two commercial CCS facilities in construction (Langskip CCS - Brevik in Norway) or development stages (LafargeHolcim CCS in the United States) and two pilot and demonstration facilities in operation or in construction in cement industry [19], indicating the feasibility of and interest in CCS deployment in this industry.

In addition to multiple emission hubs, NW and NE Spain contain more potential storage structures compared to SW and SE Spain (Fig. 4B and 7). The potential structures in NW Spain are mainly located in the Duero Basin and the Cantabrian Mountains. In NE Spain, the four priority and alternative onshore structures are Área de La Zona de Enlace (Buntsandstein), Reus and Caspe-Mayals, also identified as structures with high favourability in the ALGECO2 project [122]. In addition, two offshore potential structures, Barcelona-A and Denia, were also assessed as structures with very high suitability and very low risk by Martínez del Olmo [38]. The onshore structures are mainly distributed in the Ebro Basin and the Iberian Chain. Our analysis of the Ebro Basin is consistent with that of the STRATEGY CCUS project, which has recently selected the Ebro Basin as one of the three priority regions for large-scale deployment of CCS in Southern and Eastern Europe [132]. The Área de La Zona de Enlace (Buntsandstein) structure is shared by all emission hubs in NE Spain, and the Reus structure is shared by three emission hubs. These two structures present suitable reservoir-caprock systems and relatively low development cost since they are close to the emission hubs. They can be selected as potential candidates for further assessment to verify their suitability for CCS deployment. Our assessment results can be regarded as a reference for the selection of the most optimal storage sites for future CCS projects.

5.2. CCS development strategy

After establishing the feasibility and potential of CCS to decarbonise the power and industrial sectors in Spain, we now discuss the future of this technology in a broader, *trans*-national context. Although exercises to explore potential decarbonisation pathways envisage a significant role for CCS in different countries [6,80], most countries are yet to develop coherent strategies for its deployment due to various barriers, as discussed in the introduction section. Despite being the fifth highest GHG emitter in the EU, Spain is ranked eighth in the CCS Readiness Index database [133], which monitors the progress of CCS deployment by comprehensively considering a country's policy, law and storage resource development. There are no demonstration or commercial CCS projects planned in the near future in Spain, despite the great potential illustrated in this work. This is a clear indication that Spain's CCS development has stalled like in many other countries.

The CCS strategy proposed in this work involves a system of CCS hubs and clusters that could help to resolve this stagnation. This strategy is being progressively adopted in the North Sea region countries (e.g., Acorn in the UK [20] or Rotterdam in the Netherlands [134]) as well as other regions in the world [135]. Our approach has identified suitable priority options that can serve as First of a Kind CCS options in the different priority regions, as well as suitable alternatives that can be used for upscaling the CCS hubs. This can help to reduce costs via economy of scale and attract investment for build-out options [20,105,136]. Spain should explore this incremental strategy to promote the development of a CCS industry. In alignment with this incremental philosophy, two other factors must be considered to produce a holistic CCS-based strategy, the trans-national context and the integration with other clean energy technologies.

5.2.1. Trans-national context

The hubs and clusters identified in this work have been optimised for the decarbonisation of the Spanish industrial sectors. However, the battle against Climate Change is global, and the Spanish efforts are aligned with international directives and targets. Some of the source-to-sink clusters proposed in our case study lie close to border regions and could be of interest for industrial clusters in nearby countries. Thus, the strategy proposed needs to be put into a trans-national context.

Pipelines are considered to be the most viable method for onshore transport of high volumes of CO_2 over long distances [137], especially when the CO_2 source comes from a power or industrial plant with a long lifetime [16]. The challenge is to develop long-term strategies for CO_2 pipeline networks that optimise source-to-sink transmission [70]. For commercial-scale CCS projects, an extensive network of CO_2 pipelines needs to be developed, involving multiple CO_2 sources and storage sites. Due to an uneven distribution of CO_2 sources and potential storage structures, the construction of European pipeline infrastructures may become trans-national [138]. For the Iberian Peninsula, when Spain and Portugal are considered together in building a pipeline network, fewer hubs would be required, as well as less pipeline infrastructure and equipment, which would reduce costs for construction and installation [139]. Moreover, the existing natural gas pipeline network that connects Spain and Portugal can be used as a proxy when installing a future CO_2 pipeline network. Similarly, joint large-scale trans-national infrastructures have also been suggested in the western Mediterranean, including Spain, Portugal and Morocco [70]. In the western Mediterranean, most of the storage capacity is located in Spain [71,139–140] and, accordingly, Portugal and Morocco can benefit from gaining access to Spain's storage capacity by a trans-national pipeline network. Furthermore, Spain's pipeline network can also connect with a European network, as an EU-wide coordination of CO_2 transport planning, as well as the resolution of legal issues surrounding trans-boundary transport and liability, are essential to enable CCS in support of the EU targets [141]. The Connecting Europe Facility for Energy (CEF Energy), for example, is able to fund trans-national pipelines for CO_2 via Projects of Common Interest (e.g., this tool has already funded the CO2-SAPLING Transport and Infrastructure Project with this aim [142]). Vessel transport may complement pipeline networks in the western Mediterranean in some cases, achieving the transport of small CO_2 volumes over long distances, e.g., accessing the large CO_2 storage capacity in the North Sea [143].

5.2.2. Integration with clean energy technologies: Blue hydrogen and BECCS

This study shows that CCS has the potential to contribute significantly to the decarbonisation of Spain by storing CO_2 emissions from both the power sector and the hard-to-abate sector. Additionally, CCS can also be combined with low-carbon or carbon–neutral technologies to generate net-zero or even negative emissions [4], e.g., the implementation of blue hydrogen production as well as BECCS, two technologies with the potential to push forward the energy transition towards a zero-carbon society and with potential for alleviating the related costs [144].

Hydrogen can be adopted as a key energy carrier [145–147], which is an energy vector that tackles security of energy supply, ideally with net-zero emissions, and hence can decarbonise energy sectors such as energy intensive industries, heating and transport [148–149]. Renewable production of hydrogen ('green hydrogen') relies on either biomass processing or water splitting, the latter divided into electrolysis, thermolysis and photoelectrolysis technologies [150]. Machhammer et al. [151] compared the cost and carbon footprint related to hydrogen production technologies and identified several Pareto-efficient technologies: water electrolysis using wind power (zero carbon footprint for

operation; high cost), methane pyrolysis (medium carbon footprint; medium cost) and conventional methane steam reforming (SMR) (high carbon footprint; low cost). Hydrogen from methane steam reforming in combination with CCS ('blue hydrogen') can provide a low-cost route with low carbon footprint to the decarbonisation of heating as well as support the development of other aspects of the hydrogen economy including the use of fuel cells [4]. The large-scale generation of hydrogen using steam methane reformation is only sustainable if supported by CCS, because CO_2 is a by-product of the methane reforming process and needs to be stored permanently in large quantities. The abundance of CO_2 storage potential close to industry hubs could make hydrogen production using SMR a suitable low-carbon energy option for Spain. The deployment of blue hydrogen will be a part of a transitional phase during which the installation of a fully sustainable hydrogen infrastructure, such as large-scale electrolysers, is implemented, in line with the EU hydrogen strategy [152]. Therefore, the application of CCS will support Spain's transition to meet the targets of the Spanish Green Hydrogen Roadmap [153], which envisages ambitious targets, i.e., 4 GW electrolysers installed capacity by 2030 and at least 25% with green hydrogen, in response to the EU hydrogen strategy [152]. Blue hydrogen could be a bridging technology to reach these targets in the medium term [10].

Achieving global net zero CO_2 emission targets will also likely require NET to offset the unavoidable release of anthropogenic greenhouse gases [154]. BECCS is a NET that combines bioenergy applications with CCS. Biomass binds CO_2 from the atmosphere as it grows and, if captured and stored in geological formations after conversion, results in a net removal of CO_2 from the atmosphere [4]. Despite important criticisms towards its deployment at the scale needed, BECCS is regarded as a key tool for achieving decarbonisation targets [12–13,155]. BECCS could be not only a zero carbon power source, but help to counteract the effect of dispersed or fugitive emissions [156], such as those from the transport sector, which is the major source of CO_2 emissions in Spain (Fig. 3). A relevant issue in the feasibility of large-scale deployment of BECCS is the availability of biomass feedstocks and land for production. Competition between different sectors for feedstocks and competition with other ecosystem services are limiting factors for BECCS as a large-scale NET, since land demand for BECCS is relatively high and largely depends on the selected feedstocks [154,157]. Coupling land-use-energy of different technologies in integrated assessment models (IAMs) indicates a competition for resources, in particular a need to address land used challenges, i.e., mitigation and adaptation to climate change, desertification and land degradation, and food security [158]. Further work should focus on evaluating how much sustainable BECCS can be produced in Spain, considering all these issues.

Spain's long-term decarbonisation strategy neither explicitly dismisses nor endorses BECCS, echoing the debate around assessing and supporting best practices that would strike a right balance between competing agents such as food and energy security, climate change, land challenges, and water stresses. However, Spain's CO_2 storage potential makes BECCS a realistic opportunity to meet future emission targets. BECCS also has the potential of enabling a just transition of the power sector and the creation of new technology-based jobs, that help to ease the evolution into a more sustainable industry model [156,159].

6. Conclusions

To achieve the Paris Agreement's long-term emission reduction target, i.e., achieving net-zero CO_2 emissions by 2050, all countries need to take serious decarbonisation actions, and CCS is an integral technology to achieve this. CCS clusters with their associated hubs will be essential to decarbonise intensive industries and enable sustainable economic development. Selecting the most suitable hubs and clusters is therefore key to identify opportunities for investment and development.

We presented an integrated source-to-sink analysis tool based on a comprehensive analysis of CO_2 emission hubs, the suitability of storage structures, and the matching of sources and sinks, including Multi-Criteria Decision Analysis tools, which reveals the potential of CCS development in our case study in Spain. This workflow identified 15 priority source-to-sink clusters and four high-potential CCS development regions were identified, located in the four corners of the country. To ensure the reliability of prospective CCS projects, development areas should be selected in the regions with multiple storage structures and emissions, which will persist into decades ahead, preferably from both the power and the hard-to-abate sectors. NW and NE Spain can be considered the two priority regions for CCS development, followed by the SW and SE regions. The source-to-sink clusters in the priority regions, especially where storage structures are shared by multiple emission hubs, deserve further research and could become the prioritised options for future pilot and demonstration projects.

Many countries (e.g., Spain, UK, Germany, Japan or Korea) made promising starts on CCS in the late 2000 s, but its deployment has been stagnant partly due to a lack of political and financial support. The proposed hubs and clusters strategy could attract renewed public and political interest in this technology. The current global energy decarbonisation strategy is favourable to the switch towards renewable energy resources, where CCS can have a secondary (and short-to-middle term) decarbonisation role. However, CCS in the hard-to-abate sector will still be necessary to deal with the process-related emissions. CO_2 emitters in this sector with relatively low development cost can be priority sources for CCS development, e.g., in the cement industry. Apart from being integrated into existing energy systems and emission-intensive industries, there is significant potential for combining CCS with blue hydrogen generation and bioenergy, other low-carbon energies that can greatly contribute to achieving the Paris Agreement's net-zero target.

Uncited references

[160,161].

CRediT authorship contribution statement

Xiaolong Sun: Data curation, Formal analysis, Methodology, Writing. **Juan Alcalde:** Conceptualization, Methodology, Validation, Writing, Supervision. **Mahdi Bakhtbidar:** Data curation, Formal analysis. **Javier Elío:** Data curation, Formal analysis. Victor Vilarrasa: Writing. Jacobo Canal: Writing. Julio Ballesteros: Writing. Niklas Heinemann: Writing. Stuart Haszeldine: Writing. Andrew Cavanagh: Writing. David Vega-Maza: Writing. Fernando Rubiera: Writing. Roberto Martínez-Orio: Writing. Gareth Johnson: Conceptualization, Writing. Ramon Carbonell: Writing. . **Ignacio Marzan:** Writing, ValidationAnna Travé: Writing. . **Enrique Gomez-Rivas:** Validation, Writing, Supervision.

Declaration of Competing Interest

The authors declare that they have no known competing financial interests or personal relationships that could have appeared to influence the work reported in this paper.

Acknowledgements

Funding was provided by the Grup Consolidat de Recerca "Geologia Sedimentària" (2017SGR-824) and the DGICYT Spanish Project PGC2018-093903-B-C22. XS acknowledges funding by the China Scholarship Council for a PhD scholarship (201806450043). JA is funded by MICINN (Juan de la Cierva fellowship - IJC2018-036074-I). EGR acknowledges funding provided by MICINN ("Ramón y Cajal" fellowship RYC2018-026335-I). VV acknowledges funding from the European Re-

search Council (ERC) under the European Union's Horizon 2020 Research and Innovation Program through the Starting Grant GEoREST (www.georest.eu) (Grant agreement No. 801809). IDAEA-CSIC is a Centre of Excellence Severo Ochoa (Spanish Ministry of Science and Innovation, Project CEX2018-000794-S). NH is funded by the Engineering and Physical Sciences Research Council (EPSRC) funded research project "HyStorPor" (EP/S027815/1). SH and AC are funded by EPSRC EP/P026214/1 UKCCSRC 2017, and EU project 837754 - STRATEGY CCUS. DVM is funded by the Spanish Ministry of Science, Innovation and Universities ("Beatriz Galindo Senior" fellowship BEAGAL18/00259). GJ is funded by the University of Strathclyde Faculty of Engineering.

Appendix A

Table A1.

Appendix B. Supplementary data

Supplementary data to this article can be found online at https://doi.org/10.1016/j.apenergy.2021.117418.

Table A1
Non-exhaustive list of projects related to CCS lead or participated by Spanish institutions

Topic	Acronym	Full name	Funding body	Date (start–end years)	References or Links
Capture	ECO-Scrub	Enhanced capture with oxygen for scrubbing of CO_2	RFCS	2007–2010	https://op.europa.eu/en/publication-detail/-/publication/293a59ae-700a-475b-83ad-2f98514278ad
Capture	ECLAIR	Emission free chemical looping coal combustion process	RFCS	2008–2012	https://op.europa.eu/en/publication-detail/-/publication/c971f36e-fa56-4c0a-9053-b8fd9100a06e
Capture	CaOling	Development of postcombustion CO_2 capture with CaO in a large testing facility	FP7	2009–2013	https://cordis.europa.eu/project/id/241302
Capture	FECUNDUS	Advanced concepts and process schemes for CO_2 free fluidised and entrained bed co-gasification of coals	RFCS	2010–2013	https://op.europa.eu/en/publication-detail/-/publication/5683e484-ef5d-11e6-8a35-01aa75ed71a1
Capture	ReCal	Novel calcium looping CO_2 capture process incorporating sorbent reactivation by recarbonation	RFCS	2012–2015	https://op.europa.eu/en/publication-detail/-/publication/f24545b2-9c46-11e8-a408-01aa75ed71a1
Capture	ASC2	Amine-impregnated solid sorbent for CO_2 capture	RFCS	2013–2017	https://op.europa.eu/en/publication-detail/-/publication/7d2d8212-9c72-11e9-9d01-01aa75ed71a1
Capture	SUCCESS	Scale-up of oxygen carrier for Chemical Looping Combustion using environmentally sustainable materials	FP7	2013–2017	https://clc-success.project.tuwien.ac.at/home/
Capture	CaO2	Calcium looping CO_2 capture technology with extreme oxy-coal combustion conditions in the calciner	RFCS	2014–2017	https://op.europa.eu/en/publication-detail/-/publication/08a126e1-9d3f-11e9-9d01-01aa75ed71a1
Capture	HiPerCap	High Performance Capture	FP7	2014–2017	https://cordis.europa.eu/project/id/608555
Capture	ASCENT	Advanced Solid Cycles with Efficient Novel Technologies	FP7	2014–2018	https://cordis.europa.eu/project/id/608512
Capture	CEMCAP	CO2 capture from cement production	H2020	2015–2018	https://www.sintef.no/projectweb/cemcap/
Capture	FlexiCaL	Development of flexible coal power plants with CO2 capture by Calcium Looping	RFCS	2016–2019	https://www.flexical.eu/
Capture	GRAMOFON	New process for efficient CO_2 capture by innovative adsorbents based on modified graphene aerogels and MOF materials	H2020	2016–2020	http://www.gramofonproject.eu/
Capture	FLEDGED	FLExible Dimethyl ether production from biomass Gasification with sorption-enhancED processes	H2020	2016–2020	https://cordis.europa.eu/project/id/727600/es
Capture	Cleanker	CLEAN clinKER production by calcium looping process	H2020	2017–2021	http://www.cleanker.eu/
Capture	CLARA	Chemical looping gasification for sustainable production of biofuels	H2020	2018–2022	https://cordis.europa.eu/project/id/817841/es
Capture	C4U	Advanced Carbon Capture for steel industries integrated in CCUS Clusters	H2020	2020–2024	https://c4u-project.eu/
Capture	GLAMOUR	GLycerol to Aviation and Marine prOducts with sUstainable Recycling	H2020	2020–2024	https://cordis.europa.eu/project/id/884197/es
Capture and usage	CENIT SOST CO_2	Nuevas Utilizaciones industriales Sostenibles del CO_2	Spanish Government – Private funding	2008–2011	https://www.ecestaticos.com/file/6292f8da3aec91e6df801b68eaf14be2/1394023865.pdf
Storage	CARBOLAB	Improving the knowledge of carbon storage and coal bed methane production by "in situ" underground tests	RFCS	2009–2013	https://op.europa.eu/en/publication-detail/-/publication/1ce238a4-f1dd-4b52-987f-005ef562f173
Storage	MUSTANG	A multiple space and time scale approach for the quantification of deep saline formations for CO2 storage	FP7	2009–2014	https://cordis.europa.eu/project/id/227286
Storage	PANACEA	Predicting and monitoring the long-term behavior of CO_2 injected in deep geological formations	FP7	2012–2014	http://www.panacea-co2.org/
Storage	TRUST	High resolution monitoring, real time visualization and reliable modeling of highly controlled, intermediate and up-scalable size pilot injection tests of underground storage of CO2	FP7	2012–2017	http://www.trust-co2.org/
Storage	ENOS	ENabling Onshore CO2 Storage in Europe	H2020	2016–2020	http://www.enos-project.eu/
Storage	PCROCKSS	Interacción cemento Portland – roca en medios ácidos: secuestro geológico del CO2 y gestión de residuos de minas de sulfuros	Spanish Government	2018–2020	https://www.idaea.csic.es/project/pcrockss/
Storage	GEoREST	Predicting earthquakes induced by fluid injection	H2020ERC-STG	2019–2024	https://www.georest.eu/
Storage	HydroPore	A new upscaling approach for multiphase flow, mechanical deformation, and hydrodynamic transport in permeable media	Spanish Government	2020–2023	http://hydropore.es/
Full CCS chain	OXYCFB300 Compostilla	OXYCFB300 Compostilla Carbon Capture and Storage Demonstration Project	EEPR	2009–2012	https://www.globalccsinstitute.com/archive/hub/publications/137158/Compostilla-project-OXYCFB300-carbon-capture-storage-demonstration-project-knowledge-sharing-FEED-report.pdf
Full CCS chain	ECCSEL	European Carbon Dioxide Capture and Storage Laboratory Infrastructure	H2020	2015–2017	http://www.eccsel.org/
Full CCS chain	ACT	Accelerating CCS technologies as a new low-carbon energy vector	H2020	2016–2021	http://www.act-ccs.eu/

References

[1] Intergovernmental Panel on Climate Change. Global Warming of 1.5°C: An IPCC special report; 2018.

[2] Hoegh-Guldberg O, Jacob D, Taylor M, Bindi M, Brown S, Camilloni I, et al. Impacts of 1.5 C global warming on natural and human systems. Global warming of 1.5° C. An IPCC Special. Report. 2018. https://doi.org/10.1093/aje/kwp410.

[3] Alcalde J, Flude S, Wilkinson M, Johnson G, Edlmann K, Bond CE, et al. Estimating geological CO2 storage security to deliver on climate mitigation. Nat Commun 2018;9(1). https://doi.org/10.1038/s41467-018-04423-1.

[4] Bui M, Adjiman CS, Bardow A, Anthony EJ, Boston A, Brown S, et al. Carbon capture and storage (CCS): the way forward. Energy Environ Sci 2018;11(5): 1062–176. https://doi.org/10.1039/C7EE02342A.

[5] MacDowell N, Florin N, Buchard A, Hallett J, Galindo A, Jackson G, et al. An overview of CO2 capture technologies. Energy Environ Sci 2010;3(11):1645. https://doi.org/10.1039/c004106h.

[6] Scott V, Gilfillan S, Markusson N, Chalmers H, Haszeldine RS. Last chance for carbon capture and storage. Nat Clim Chang 2013;3(2):105–11. https://doi.org/10.1038/nclimate1695.

[7] Global CCS Institute. The global status of CCS 2017;2017.

[8] Dawood F, Anda M, Shafiullah GM. Hydrogen production for energy: An overview. Int J Hydrogen Energy 2020;45(7):3847–69. https://doi.org/10.1016/j.ijhydene.2019.12.059.

[9] Heinemann N, Alcalde J, Miocic JM, Hangx SJT, Kallmeyer J, Ostertag-Henning C, et al. Enabling large-scale hydrogen storage in porous media - the scientific challenges. Energy Environ Sci 2021;14(2):853–64. https://doi.org/10.1039/D0EE03536J.

[10] van Renssen S. The hydrogen solution?. Nat Clim Chang 2020;10(9):799–801. https://doi.org/10.1038/s41558-020-0891-0.

[11] Noussan M, Raimondi PP, Scita R, Hafner M. The role of green and blue hydrogen in the energy transition—a technological and geopolitical perspective. Sustain 2021;13:1–26. https://doi.org/10.3390/su13010298.

[12] Fajardy M, Mac Dowell N. Can BECCS deliver sustainable and resource efficient negative emissions?. Energy Environ Sci 2017;10(6):1389–426. https://doi.org/10.1039/C7EE00465F.

[13] Haszeldine RS, Flude S, Johnson G, Scott V. Negative emissions technologies and carbon capture and storage to achieve the Paris Agreement commitments. Philos Trans R Soc A Math Phys Eng Sci 2018;376(2119):20160447. https://doi.org/10.1098/rsta.2016.0447.

[14] Selosse S, Ricci O. Achieving negative emissions with BECCS (bioenergy with carbon capture and storage) in the power sector: New insights from the TIAM-FR (TIMES Integrated Assessment Model France) model. Energy 2014;76:967–75. https://doi.org/10.1016/j.energy.2014.09.014.

[15] Nationally UNFCCC. Determined Contributions (NDCs) 2020.

[16] Leung DYC, Caramanna G, Maroto-Valer MM. An overview of current status of carbon dioxide capture and storage technologies. Renew Sustain Energy Rev 2014; 39:426–43. https://doi.org/10.1016/j.rser.2014.07.093.

[17] Budinis S, Krevor S, Mac DN, Brandon N, Hawkes A. An assessment of CCS costs, barriers and potential. Energy Strateg Rev 2018;22:61–81. https://doi.org/10.1016/j.esr.2018.08.003.

[18] Espie T, Canal-Vila J, Tucker O, Zweigel P. The Role of Technology in Enabling the Expansion to Gigatonne Scale Storage of Co2." In 14th Greenhouse Gas Control Technologies Conference Melbourne, pp. 21-26. 2018. 14th Greenhouse Gas Control Technologies Conference Melbourne, 2018, p. 21–6.

[19] Global CCS Institute. CCS Facilities Database; 2020.

[20] Alcalde J, Heinemann N, Mabon L, Worden RH, de Coninck H, Robertson H, et al. Acorn: Developing full-chain industrial carbon capture and storage in a resource- and infrastructure-rich hydrocarbon province. J Clean Prod 2019;233:963–71. https://doi.org/10.1016/j.jclepro.2019.06.087.

[21] Hoffman N, Marshall S, Horan S. Successful appraisal of the CarbonNet Pelican CO2 offshore storage site. In: SSRN, editor. 15th International Conference on Greenhouse Gas Control Technologies, GHGT-15, Abu Dhabi: 2021, p. 1–7. https://doi.org/10.2139/ssrn.3811988.

[22] Le Quéré C, Andrew RM, Friedlingstein P, Sitch S, Hauck J, Pongratz J, et al. Global Carbon Budget 2018. Earth Syst Sci Data 2018;10(4):2141–94. https://doi.org/10.5194/essd-10-2141-2018.

[23] European Commission. Climate strategies & targets; 2020. https://ec.europa.eu/clima/policies/strategies_en.

[24] Lupion M, Herzog HJ. NER300: Lessons learnt in attempting to secure CCS projects in Europe. Int J Greenh Gas Control 2013;19:19–25. https://doi.org/10.1016/j.ijggc.2013.08.009.

[25] European Commission. Horizon 2020: Climate action, environment, resource efficiency and raw materials; 2020.

[26] European Commission. Orientations towards the first Strategic Plan for Horizon Europe. 2019.

[27] Vangkilde-Pedersen T, Anthonsen KL, Smith N, Kirk K, neele F, van der Meer B, et al. Assessing European capacity for geological storage of carbon dioxide-the EU GeoCapacity project. Energy Procedia 2009;1(1):2663–70. https://doi.org/10.1016/j.egypro.2009.02.034.

[28] Cavanagh A, Wilkinson M, Haszeldine S. DELIVERABLE D2.1 REPORT Methodologies for cluster development and best practices for data collection in the promising regions. Part 2 Bridging the Gap Storage Resource Assessment Methodologies; 2020.

[29] Liu H, Consoli C, Zapantis A. Overview of Carbon Capture and Storage (CCS) Facilities Globally. 14th Greenhouse Gas Control Technologies Conference Melbourne 21-26 October 2018 (GHGT-14), 2018, p. 1–10. https://doi.org/10.2139/ssrn.3366353.

[30] Kapetaki Z, Scowcroft J. Overview of Carbon Capture and Storage (CCS) Demonstration Project Business Models: Risks and Enablers on the Two Sides of the Atlantic. Energy Procedia 2017;114:6623–30. https://doi.org/10.1016/j.egypro.2017.03.1816.

[31] Global CCS Institute. Understanding Industrial CCS Hubs and Clusters. vol. 1. 2016.

[32] BRADSHAW J, DANCE T. Greenhouse Gas Control Technologies 7. Elsevier; 2005. p. 583–91.

[33] Sun X, Alcalde J, Gomez-Rivas E, Struth L, Johnson G, Travé A. Appraisal of CO2 storage potential in compressional hydrocarbon-bearing basins: Global assessment and case study in the Sichuan Basin (China). Geosci Front 2020;11(6):2309–21. https://doi.org/10.1016/j.gsf.2020.02.008.

[34] Wei N, Li X, Wang Y, Dahowski RT, Davidson CL, Bromhal GS. A preliminary sub-basin scale evaluation framework of site suitability for onshore aquifer-based CO2 storage in China. Int J Greenh Gas Control 2013;12:231–46. https://doi.org/10.1016/j.ijggc.2012.10.012.

[35] Estrategia Española de Cambio Climático y Energía Limpia Horizonte 2007–2012–2020; 2007..

[36] Boletín Oficial del Estado. Ley 40/2010, de 29 de diciembre, de almacenamiento geológico de dióxido de carbono. Madrid, Spain: 2010.

[37] Spanish Geological Survey. Selección y caracterización de áreas y estructuras favorables para el almacenamiento geológico de CO2 en España. 2010.

[38] Martínez Del Olmo W. Cambio Climático, acuerdos de paris y trampas geológicas donde secuestrar el CO2 en españa. Rev La Soc Geológica España 2019;32:87–106.

[39] Patel S. Spain makes headway in CCS efforts. Power 2010;154.

[40] Lupion M, Diego R, Loubeau L, Navarrete B. CIUDEN CCS project: Status of the CO2 capture technology development plant in power generation. Energy Procedia 2011;4:5639–46. https://doi.org/10.1016/j.egypro.2011.02.555.

[41] Lupion M, Pérez A, Torrecilla F, Merino B. Lessons learned from the public perception and engagement strategy - Experiences in CIUDEN's CCS facilities in Spain. Energy Procedia 2013;37:7369–79. https://doi.org/10.1016/j.egypro.2013.06.678.

[42] Gómez M, Fernández A, Llavona I, Kuivalainen R. Experiences in sulphur capture in a 30 MWth Circulating Fluidized Bed boiler under oxy-combustion conditions. Appl Therm Eng 2014;65:617–22. https://doi.org/10.1016/j.applthermaleng.2014.05.025.

[43] Alcalde J, Marzán I, Saura E, Martí D, Ayarza P, Juhlin C, et al. 3D geological characterization of the Hontomín CO2 storage site, Spain: Multidisciplinary approach from seismic, well-log and regional data. Tectonophysics 2014;627: 6–25. https://doi.org/10.1016/j.tecto.2014.04.025.

[44] Alcalde J, Martí D, Calahorrano A, Marzan I, Ayarza P, Carbonell R, et al. Active seismic characterization experiments of the Hontomín research facility for geological storage of CO2. Spain. Int J Greenh Gas Control 2013;19:785–95. https://doi.org/10.1016/j.ijggc.2013.01.039.

[45] Alcalde J, Martí D, Juhlin C, Malehmir A, Sopher D, Saura E, et al. 3-D reflection seismic imaging of the hontomín structure in the basque-cantabrian Basin (Spain). Solid Earth 2013;4(2):481–96. https://doi.org/10.5194/se-4-481-2013.

[46] Ogaya X, Queralt P, Ledo J, Marcuello Á, Jones AG. Geoelectrical baseline model of the subsurface of the Hontomín site (Spain) for CO2 geological storage in a deep saline aquifer: A 3D magnetotelluric characterisation. Int J Greenh Gas Control 2014;27:120–38. https://doi.org/10.1016/j.ijggc.2014.04.030.

[47] Ogaya X, Alcalde J, Marzán I, Ledo J, Queralt P, Marcuello A, et al. Joint interpretation of magnetotelluric, seismic and well-log data in Hontomín (Spain). Solid Earth Discuss 2016;7:1–27. https://doi.org/10.5194/se-2016-24.

[48] Andrés J, Alcalde J, Ayarza P, Saura E, Marzán I, Martí D, et al. Basement structure of the Hontomín CO2storage site (Spain) determined by integration of microgravity and 3-D seismic data. Solid Earth 2016;7:827–41. https://doi.org/10.5194/se-7-827-2016.

[49] Nisi B, Vaselli O, Tassi F, de Elio J, Huertas AD, Mazadiego LF, et al. Hydrogeochemistry of surface and spring waters in the surroundings of the CO2 injection site at Hontomín-Huermeces (Burgos, Spain). Int J Greenh Gas Control 2013;14:151–68. https://doi.org/10.1016/j.ijggc.2013.01.012.

[50] Metcalf A, Granados A, Delgado HA. Determining seasonal natural effects over isotopic baselines for CO 2 storage monitoring. Energy Procedia 2014;51:48–55. https://doi.org/10.1016/j.egypro.2014.07.006.

[51] Elío J, Nisi B, Ortega MF, Mazadiego LF, Vaselli O, Grandia F. CO2 soil flux baseline at the technological development plant for CO2 injection at Hontomin (Burgos, Spain). Int J Greenh Gas Control 2013;18:224–36. https://doi.org/10.1016/j.ijggc.2013.07.013.

[52] de Dios JC, Delgado MA, Martínez C, Ramos A, Álvarez I, Marín JA, et al. Hydraulic characterization of fractured carbonates for CO2 geological storage: Experiences and lessons learned in Hontomín Technology Development Plant. Int J Greenh Gas Control 2017;58:185–200. https://doi.org/10.1016/j.ijggc.2017.01.008.

[53] de Dios JC, Martínez C, Ramos A, Marín JA, Artieda J. On-Site Hydraulic Characterization Tests. In: de Dios JC, Mishra S, Poletto F, Ramos A, editors. CO2 Injection in the Network of Carbonate Fractures. Cham: Springer International Publishing; 2021. p. 103–36. https://doi.org/10.1007/978-3-030-62986-1.

[54] ENOS Project. The Hontomin Technology Development Plant; 2020. http://www.enos-project.eu/sites/operational-storage-field-site/hontomin/ [accessed March 7, 2021].

[55] Casero P, García-Peña F, Coca P. Elcogas pre-combustion carbon capture pilot, Real experience of commercial technology. Energy Procedia 2013;37:6374–82. https://doi.org/10.1016/j.egypro.2013.06.567.

[56] Casero P, Peña FG, Coca P, Trujillo J. ELCOGAS 14 MWth pre-combustion carbon dioxide capture pilot. Technical & economical achievements. Fuel 2014;116:804–11. https://doi.org/10.1016/j.fuel.2013.07.027.

[57] Casero P, Coca P, Garcia G, Hervás N. Captura de CO2 en procesos pre-combustión. Experiencia real de ELCOGAS en GICC Puertollano. Bol Del Grup Español Del Carbón 2015;35:2–7.

[58] Plaza MG, Pevida C. Current status of CO2 capture from coal facilities. New Trends Coal Convers Combust Gasification, Emiss Coking 2018;31–58. https://doi.org/10.1016/B978-0-08-102201-6.00002-9.

[59] Casero P, Coca P, García-Peña F, Hervás N. Integrated Gasification Combined Cycle (IGCC) Technologies. Elsevier; 2017. p. 753–75. https://doi.org/10.1016/B978-0-08-100167-7.00019-6.

[60] Sánchez-Biezma A, Paniagua J, Diaz L, Lorenzo M, Alvarez J, Martínez D, et al. Testing postcombustion CO2 capture with CaO in a 1.7 MW t pilot facility. Energy Procedia 2013;37:1–8. https://doi.org/10.1016/j.egypro.2013.05.078.

[61] Arias B, Diego ME, Méndez A, Abanades JC, Díaz L, Lorenzo M, et al. Operating Experience in la Pereda 1.7 MWth Calcium Looping Pilot. Energy Procedia 2017;114:149–57. https://doi.org/10.1016/j.egypro.2017.03.1157.

[62] Arias B, Diego ME, Méndez A, Alonso M, Abanades JC. Calcium looping performance under extreme oxy-fuel combustion conditions in the calciner. Fuel 2018;222:711–7. https://doi.org/10.1016/j.fuel.2018.02.163.

[63] Arias B, Diego ME, Abanades JC, Lorenzo M, Diaz L, Martínez D, et al. Demonstration of steady state CO2 capture in a 1.7MWth calcium looping pilot. Int J Greenh Gas. Control 2013;18:237–45. https://doi.org/10.1016/j.ijggc.2013.07.014.

[64] Diego ME, Alonso M. Operational feasibility of biomass combustion with in situ CO2 capture by CaO during 360 h in a 300 kWth calcium looping facility. Fuel 2016;181:325–9. https://doi.org/10.1016/j.fuel.2016.04.128.

[65] GeoCapacity E.U. Assessing European capacity for geological storage of carbon dioxide. D16, WP2 report, storage capacity. 2009.

[66] IGME. The ALGECO2 project - Plan de selección y caracterización de áreas y estructuras favorables para el almacenamiento geológico de CO2 en España; 2010. http://info.igme.es/algeco2/ [accessed February 15, 2021].

[67] Pueyo EL, Calvin P, Casas AM, Oliva-Urcia B, Klimowitz J, García-Lobón JL, et al. A research plan for a large potential CO2 reservoir in the Southern Pyrenees. Geotemas 2012;13:1970–3.

[68] European Commission. CO2StoP - CO2 Storage Potential in Europe - Project No. ENER/C1/154-2011-SI2.611598; 2012. https://setis.ec.europa.eu/co2storageatlas [accessed February 15, 2021].

[69] Boavida D, Carneiro JF, Ramírez A, Martinez R, Czernichowski-Lauriol I, Tosato G, et al. Integrated infrastructure for CO2 transport and storage in the west Mediterranean. Energy Procedia 2011;4:2440–7. https://doi.org/10.1016/j.egypro.2011.02.138.

[70] Boavida D, Carneiro J, Martinez R, van den Broek M, Ramirez A, Rimi A, et al. Planning CCS development in the west Mediterranean. Energy Procedia 2013;37:3212–20. https://doi.org/10.1016/j.egypro.2013.06.208.

[71] Carneiro J, Martinez R, Suaréz I, Zarhloule Y, Rimi A. Injection rates and cost estimates for CO2 storage in the west Mediterranean region. Environ Earth Sci 2015;73(6):2951–62. https://doi.org/10.1007/s12665-015-4029-z.

[72] European Parliament. Directive 2009/31/EC of the European Parliament and of the Council of 23 April 2009 on the geological storage of carbon dioxide; 2009.

[73] Alenza-García JF. El nuevo régimen legal del almacenamiento geológico del dióxido de carbono. Rev Adm Pública 2011;185:289–322.

[74] Carmona ICP. Problemas competenciales derivados de la Ley 40/2010 de almacenamiento geológico de dióxido de carbono. Rev Catalana Dret Ambient 2013;4:1–29.

[75] Boletín Oficial del Estado. Sentencia 165/2016 de 6 de octubre de 2016 del Tribunal Constitucional. Madrid, Spain: 2016.

[76] i Manzano JJ. Jurisprudencia constitucional en materia de protección del medio ambiente. Rev Catalana Dret Ambient 2017;8:1–21.

[77] Sancho JP. La controversia competencial sobre las concesiones de almacenamiento geológico de dióxido de carbono. Rev Aragon Adm Pública 2019;53:437–79.

[78] de Dios JC, Martínez R. The permitting procedure for CO2 geological storage for research purposes in a deep saline aquifer in Spain. Int J Greenh Gas Control 2019;91:102822. https://doi.org/10.1016/j.ijggc.2019.102822.

[79] Sara J, Stikkelman RM, Herder PM. Assessing relative importance and mutual influence of barriers for CCS deployment of the ROAD project using AHP and DEMATEL methods. Int J Greenh Gas Control 2015;41:336–57. https://doi.org/10.1016/j.ijggc.2015.07.008.

[80] Gouveia JP, Seixas J, Labriet M, Fortes P, Gargiulo M. Prospective scenarios for the adoption of CCS technologies in the Iberian Peninsula. Sustain Energy Technol Assessments 2013;2:31–41. https://doi.org/10.1016/j.seta.2013.02.002.

[81] Kearns D. CCS talks: The technology cost curve. 2020.

[82] Rubin ES, Davison JE, Herzog HJ. The cost of CO2 capture and storage. Int J Greenh Gas Control 2015;40:378–400. https://doi.org/10.1016/j.ijggc.2015.05.018.

[83] Viebahn P, Daniel V, Samuel H. Integrated assessment of carbon capture and storage (CCS) in the German power sector and comparison with the deployment of renewable energies. Appl Energy 2012;97:238–48. https://doi.org/10.1016/j.apenergy.2011.12.053.

[84] MITECO. Estrategia de descarbonización a largo plazo 2050; 2020. https://www.miteco.gob.es/es/prensa/documentoelp_tcm30-516109.pdf [accessed February 15, 2021].

[85] Leeson D, Mac Dowell N, Shah N, Petit C, Fennell PS. A Techno-economic analysis and systematic review of carbon capture and storage (CCS) applied to the iron and steel, cement, oil refining and pulp and paper industries, as well as other high purity sources. Int J Greenh Gas Control 2017;61:71–84. https://doi.org/10.1016/j.ijggc.2017.03.020.

[86] Rubin ES. Understanding the pitfalls of CCS cost estimates. Int J Greenh Gas Control 2012;10:181–90. https://doi.org/10.1016/j.ijggc.2012.06.004.

[87] European Commission. Directive 2003/87/EC of the European Parliament and of the Council. 2003.

[88] Boletín Oficial del Estado. Real Decreto 18/2019, de 25 de enero, por el que se desarrollan aspectos relativos a la aplicación del régimen de comercio de derechos de emisión de gases de efecto invernadero en el periodo 2021–2030. BOE 2019;23:7143–53.

[89] Duan H-B, Fan Y, Zhu L. What's the most cost-effective policy of CO2 targeted reduction: An application of aggregated economic technological model with CCS?. Appl Energy 2013;112:866–75. https://doi.org/10.1016/j.apenergy.2013.01.047.

[90] Van de Graaf T, Overland I, Scholten D, Westphal K. The new oil? The geopolitics and international governance of hydrogen. Energy Res. Soc Sci 2020;70:101667. https://doi.org/10.1016/j.erss.2020.101667.

[91] Singh U, Loudermilk EM, Colosi LM. Accounting for the role of transport and storage infrastructure costs in carbon negative bioenergy deployment. Greenh Gases Sci Technol 2021;11(1):144–64. https://doi.org/10.1002/ghg3.v11.110.1002/ghg.2041.

[92] Ministerio para la Transición Ecológica y el Reto Demográfico. Inventario nacional de gases de efecto invernadero (GEI). Serie 1998-2018; 2020.

[93] European Environment Agency. Trends and projections in Europe 2017;2017.

[94] Dreblow E, Duwe M, Wawer T, Donat L, Zelljadt E, Ayres A. Assessment of climate change policies in the context of the European Semester. Spain: Country Report; 2013.

[95] MITECO. La Energía en España 2017. Ministerio para la Transición Energética; 2018. https://energia.gob.es/balances/Balances/LibrosEnergia/Libro-Energia-2017.pdf [accessed March 7, 2021].

[96] Ministerio para la Transición Ecológica y el Reto Demográfico. Estrategia de descarbonización a largo plazo 2050; 2020.

[97] MITECO. Plan nacional integrado de energía y clima 2021-2030; 2020. https://www.miteco.gob.es/images/es/pnieccompleto_tcm30-508410.pdf [accessed February 15, 2021].

[98] IOGP. The potential for CCS and CCU in Europe. Report to the thirty second meeting of the European Gas Regulatory. Forum. 2019.

[99] MITECO. Inventario de instalaciones; 2020. https://www.miteco.gob.es/es/calidad-y-evaluacion-ambiental/temas/sistema-espanol-de-inventario-sei-/es-2020-nir_tcm30-508122.pdf [accessed March 7, 2021].

[100] Basque Government. Registro vasco de emisiones y fuentes contaminantes del 2018 (EPER Euskadi / E-PRTR); 2019.

[101] MITECO. Acuerdo por una transición energética justa para centrales térmicas en cierre: el empleo, la industria y los territorio; 2020. https://www.miteco.gob.es/images/es/acuerdoporunatransicionenergeticajustaparacentralestermicasencierres_tcm30-509582.pdf [accessed February 15, 2021].

[102] Ministerio para la Transición Ecológica y el Reto Demográfico. Plan nacional integrado de energía y clima 2021-2030; 2020.

[103] Sanz-Hernández A, Ferrer C, López-Rodríguez ME, Marco-Fondevila M. Visions, innovations, and justice? Transition contracts in Spain as policy mix instruments. Energy Res. Soc Sci 2020;70:101762. https://doi.org/10.1016/j.erss.2020.101762.

[104] Global CCS Institute. The global status of CCS. Special report: understanding industrial CCS hubs and clusters. Melbourne, Australia: 2016.

[105] Brownsort PA, Scott V, Haszeldine RS. Reducing costs of carbon capture and storage by shared reuse of existing pipeline—Case study of a CO2 capture cluster for industry and power in Scotland. Int J Greenh Gas Control 2016;52:130–8. https://doi.org/10.1016/j.ijggc.2016.06.004.

[106] Uche-Soria M, Rodríguez-Monroy C. Energy planning and its relationship to energy poverty in decision making. A first approach for the Canary Islands. Energy Policy 2020;140:111423. https://doi.org/10.1016/j.enpol.2020.111423.

[107] Gils HC, Simon S. Carbon neutral archipelago–100% renewable energy supply for the Canary Islands. Appl Energy 2017;188:342–55. https://doi.org/10.1016/j.apenergy.2016.12.023.

[108] Rao AB, Rubin ES. Identifying cost-effective CO2 control levels for amine-based CO2 capture systems. Ind Eng Chem Res 2006;45(8):2421–9. https://doi.org/10.1021/ie050603p.

[109] Worden RH, Allen MJ, Faulkner DR, Utley JEP, Bond CE, Alcalde J, et al. Lower Cretaceous Rodby and Palaeocene Lista Shales: Characterisation and comparison of top-seal mudstones at two planned CCS sites, Offshore UK. Minerals 2020;10:691. https://doi.org/10.3390/min10080691.

[110] Parker NC. Using natural gas transmission pipeline costs to estimate hydrogen pipeline costs. 2003.

[111] U.S. Energy Information Administration. Trends in U.S. oil and gas upstream costs. 2016.

[112] Kaiser MJ. Offshore pipeline construction cost in the U.S. Gulf of Mexico. Mar. Policy 2017;82:147–66. https://doi.org/10.1016/j.marpol.2017.05.003.

[113] Hinton D, Masterson N, Lippert A, King R. Petroleum: An energy profile. Pittsburgh, PA, USA: EIA Publication DOE/EIA-0545; 1999.

[114] Instituto Geológico y Minero de España. Geophysical Information System. 2020.

[115] Kumar A, Sah B, Singh AR, Deng Y, He X, Kumar P, et al. A review of multi criteria decision making (MCDM) towards sustainable renewable energy development. Renew Sustain Energy Rev 2017;69:596–609. https://doi.org/10.1016/j.rser.2016.11.191.

[116] Deveci M, Demirel NÇ, John R, Özcan E. Fuzzy multi-criteria decision making for carbon dioxide geological storage in Turkey. J Nat Gas Sci Eng 2015;27:692–705. https://doi.org/10.1016/j.jngse.2015.09.004.

[117] Llamas B, Castañeda M de la C, Laín C, Pous J. Multi-criteria algorithm-based methodology used to select suitable domes for compressed air energy storage. Int J Energy Res 2017;41(14):2108–20. https://doi.org/10.1002/er.v41.1410.1002/er.3771.
[118] Llamas B, Cienfuegos P. Multicriteria decision methodology to select suitable areas for storing CO2. Energy Environ 2012;23(2–3):249–64. https://doi.org/10.1260/0958-305X.23.2-3.249.
[119] Llamas B, Cámara A. Application of multicriteria algorithm to select suitable areas for storing CO2: CO2SiteAssess software. Energy Procedia 2014;63:4977–86. https://doi.org/10.1016/j.egypro.2014.11.527.
[120] Yoon PK, Hwang CL. Multiple Attribute Decision Making: An Introduction. Thousand Oaks, CA: Sage Publications Inc.; 1995.
[121] Iglauer S. Optimum storage depths for structural CO2 trapping. Int J Greenh Gas Control 2018;77:82–7. https://doi.org/10.1016/j.ijggc.2018.07.009.
[122] Instituto Geológico y Minero de España. Plan de selección y caracterización de áreas y estructuras favorables para el almacenamiento geológico de CO2 en España: Resumen ejecutivo; 2010.
[123] Mandova H, Patrizio P, Leduc S, Kjärstad J, Wang C, Wetterlund E, et al. Achieving carbon-neutral iron and steelmaking in Europe through the deployment of bioenergy with carbon capture and storage. J Clean Prod 2019;218:118–29. https://doi.org/10.1016/j.jclepro.2019.01.247.
[124] Grataloup S, Bonijoly D, Brosse E, Dreux R, Garcia D, Hasanov V, et al. A site selection methodology for CO2 underground storage in deep saline aquifers: case of the Paris Basin. Energy Procedia 2009;1(1):2929–36. https://doi.org/10.1016/j.egypro.2009.02.068.
[125] Stork AL, Verdon JP, Kendall JM. The microseismic response at the In Salah Carbon Capture and Storage (CCS) site. Int J Greenh Gas Control 2015;32:159–71. https://doi.org/10.1016/j.ijggc.2014.11.014.
[126] Garnett AJ, Greig CR, Oettinger M. ZeroGen IGCC with CCS - A Case. History. 2014.
[127] Davis SJ, Lewis NS, Shaner M, Aggarwal S, Arent D, Azevedo IL, et al. Net-zero emissions energy systems. Science (80-) 2018;360:eaas9793. https://doi.org/10.1126/science.aas9793.
[128] Flude S, Johnson G, Gilfillan SM V., Haszeldine RS. Inherent Tracers for Carbon Capture and Storage in Sedimentary Formations: Composition and Applications. Environ Sci Technol 2016;50:7939–55. https://doi.org/10.1021/acs.est.6b01548.
[129] Voldsund M, Gardarsdottir S, De Lena E, Pérez-Calvo J-F, Jamali A, Berstad D, et al. Comparison of Technologies for CO2 Capture from Cement Production—Part 1: Technical Evaluation. Energies 2019;12(3):559. https://doi.org/10.3390/en12030559.
[130] International Energy Agency. Technology Roadmap: Low-Carbon Transition in the Cement Industry. 2018.
[131] Gardarsdottir S, De Lena E, Romano M, Roussanaly S, Voldsund M, Pérez-Calvo J-F, et al. Comparison of Technologies for CO2 Capture from Cement Production—Part 2: Cost Analysis. Energies 2019;12(3):542. https://doi.org/10.3390/en12030542.
[132] Strategy CCUS Project. Milestone vote on CCUS roadmaps for Southern and Eastern Europe; 2020.
[133] CCS Readiness Index 2019.
[134] Ros M, Read A, Uilenreef J, Limbeek J. Start of a CO2 hub in Rotterdam: Connecting CCS and CCU. Energy Procedia 2014;63:2691–701. https://doi.org/10.1016/j.egypro.2014.11.291.
[135] Singh P, Haines M. A review of existing carbon capture and storage cluster projects and future opportunities. Energy Procedia 2014;63:7247–60. https://doi.org/10.1016/j.egypro.2014.11.761.
[136] Berly T, Garnett A. Scaling Up CO2 Transport and Storage Infrastructure. 14th Greenhouse Gas Control Technologies Conference Melbourne 2018. https://doi.org/10.2139/ssrn.3366352.
[137] Svensson R, Odenberger M, Johnsson F, Strömberg L. Transportation systems for CO2 - Application to carbon capture and storage. Energy Convers Manag 2004;45(15–16):2343–53. https://doi.org/10.1016/j.enconman.2003.11.022.
[138] Energy European Commission. Infrastructure - priorities for 2020 and beyond a blueprint for an integrated european energy network. 2011.
[139] Costa I, Rochedo P, Costa D, Ferreira P, Araújo M, Schaeffer R, et al. Placing hubs in CO2 pipelines: An application to industrial co2 emissions in the Iberian Peninsula. Appl Energy 2019;236:22–31. https://doi.org/10.1016/j.apenergy.2018.11.050.
[140] Martinez R, Suárez I, Carneiro J, Zarhloule Y, Le Nindre YM, Boavida D. Storage capacity evaluation for development of CO2 infrastructure in the west mediterranean. Energy Procedia 2013;37:5209–19. https://doi.org/10.1016/j.egypro.2013.06.437.
[141] Stewart RJ, Scott V, Haszeldine RS, Ainger D, Argent S. The feasibility of a European-wide integrated CO2 transport network. Greenh Gases Sci Technol 2014;4:481–94. https://doi.org/10.1002/ghg.1410.
[142] Mackinnon D, Gomersall S. ACORN - A North East Response to Evolve and Thrive Through Decarbonisation. Day 2 Wed, September 04, 2019, SPE; 2019. https://doi.org/10.2118/195715-MS.
[143] Geske J, Berghout N, van den Broek M. Cost-effective balance between CO2 vessel and pipeline transport: Part II - Design of multimodal CO2 transport: The case of the West Mediterranean region. Int J Greenh Gas Control 2015;33:122–34. https://doi.org/10.1016/j.ijggc.2014.12.005.
[144] Quarton CJ, Samsatli S. The value of hydrogen and carbon capture, storage and utilisation in decarbonising energy : Insights from integrated value chain optimisation. Appl Energy 2020;257:113936. https://doi.org/10.1016/j.apenergy.2019.113936.
[145] Mazloomi K, Gomes C. Hydrogen as an energy carrier: Prospects and challenges. Renew Sustain Energy Rev 2012;16(5):3024–33. https://doi.org/10.1016/j.rser.2012.02.028.
[146] Scafidi J, Gilfillan SMV. Offsetting Carbon Capture and Storage costs with methane and geothermal energy production through reuse of a depleted hydrocarbon field coupled with a saline aquifer. Int J Greenh Gas Control 2019;90:102788. https://doi.org/10.1016/j.ijggc.2019.102788.
[147] Heinemann N, Booth MG, Haszeldine RS, Wilkinson M, Scafidi J, Edlmann K. Hydrogen storage in porous geological formations – onshore play opportunities in the midland valley (Scotland, UK). Int J Hydrogen Energy 2018;43(45):20861–74. https://doi.org/10.1016/j.ijhydene.2018.09.149.
[148] Ball M, Wietschel M. The Hydrogen Economy: Opportunities and Challenges. Cambridge University Press; 2009. https://doi.org/10.1016/j.ijhydene.2008.11.014.
[149] Mouli-Castillo J, Heinemann N, Edlmann K. Mapping geological hydrogen storage capacity and regional heating demands: An applied UK case study. Appl Energy 2021;283:116348. https://doi.org/10.1016/j.apenergy.2020.116348.
[150] Nikolaidis P, Poullikkas A. A comparative overview of hydrogen production processes. Renew Sustain Energy Rev 2017;67:597–611. https://doi.org/10.1016/j.rser.2016.09.044.
[151] Machhammer O, Bode A, Hormuth W. Financial and Ecological Evaluation of Hydrogen Production Processes on Large Scale. Chem Eng Technol 2016;39(6):1185–93. https://doi.org/10.1002/ceat.201600023.
[152] European Commission. A hydrogen strategy for a climate-neutral Europe; 2020.
[153] MITECO. Hoja de Ruta del Hidrógeno: una apuesta por el hidrógeno renovable; 2020. https://www.miteco.gob.es/es/ministerio/h2executivesummary_tcm30-513831.pdf [accessed March 7, 2021].
[154] Smith P, Davis SJ, Creutzig F, Fuss S, Minx J, Gabrielle B, et al. Biophysical and economic limits to negative CO2 emissions. Nat Clim Chang 2016;6(1):42–50. https://doi.org/10.1038/nclimate2870.
[155] Muratori M, Calvin K, Wise M, Kyle P, Edmonds J. Global economic consequences of deploying bioenergy with carbon capture and storage (BECCS). Environ Res Lett 2016;11(9):95004. https://doi.org/10.1088/1748-9326/11/9/095004.
[156] Cabral RP, Bui M, Mac DN. A synergistic approach for the simultaneous decarbonisation of power and industry via bioenergy with carbon capture and storage (BECCS). Int J Greenh Gas Control 2019;87:221–37. https://doi.org/10.1016/j.ijggc.2019.05.020.
[157] Alcalde J, Smith P, Haszeldine RS, Bond CE. The potential for implementation of Negative Emission Technologies in Scotland. Int J Greenh Gas Control 2018;76:85–91. https://doi.org/10.1016/j.ijggc.2018.06.021.
[158] Smith P, Calvin K, Nkem J, Campbell D, Cherubini F, Grassi G, et al. Which practices co-deliver food security, climate change mitigation and adaptation, and combat land degradation and desertification?. Glob Chang Biol 2020;26(3):1532–75. https://doi.org/10.1111/gcb.v26.310.1111/gcb.14878.
[159] Patrizio P, Leduc S, Kraxner F, Fuss S, Kindermann G, Mesfun S, et al. Reducing US Coal Emissions Can Boost Employment. Joule 2018;2(12):2633–48. https://doi.org/10.1016/j.joule.2018.10.004.
[160] Viebahn P, Vallentin D, Höller S. Prospects of carbon capture and storage (CCS) in India's power sector - An integrated assessment. Appl Energy 2014;117:62–75. https://doi.org/10.1016/j.apenergy.2013.11.054.
[161] Wang PT, Wei YM, Yang B, Li JQ, Kang JN, Liu LC, et al. Carbon capture and storage in China's power sector: Optimal planning under the 2 °C constraint. Appl Energy 2020;263. https://doi.org/10.1016/j.apenergy.2020.114694.

Supplement of

Hubs and clusters approach to unlock the development of Carbon Capture and Storage – case study in Spain

Xiaolong Sun[a], Juan Alcalde[b*], Mahdi Bakhtbidar[a,b], Javier Elío[c], Víctor Vilarrasa[d,e], Jacobo Canal[f], Julio Ballesteros[g], Niklas Heinemann[h], Stuart Haszeldine[h], Andrew Cavanagh[h], David Vega-Maza[i], Fernando Rubiera[j], Roberto Martínez-Orio[k], Gareth Johnson[l], Ramon Carbonell[b], Ignacio Marzan[b], Anna Travé[a] and Enrique Gomez-Rivas[a]

[a] Department of Mineralogy, Petrology and Applied Geology, University of Barcelona, c/ Martí i Franques s/n, Barcelona, 08028, Spain

[b] Geosciences Barcelona (GEO3BCN-CSIC), Lluís Solé i Sabarís s/n, Barcelona, 08028, Spain

[c] Department of Planning, Aalborg University, Copenhagen, Denmark

[d] Institute of Environmental Assessment and Water Research (IDAEA), Spanish National Research Council (CSIC), Calle de Jordi Girona 18-26, Barcelona, 08034, Spain

[e] Mediterranean Institute for Advanced Studies (IMEDEA), Spanish National Research Council (CSIC), Esporles, Spain

[f] Repsol Technology Lab, Calle Agustín de Betancourt s/n, Móstoles, 28935, Spain

[g] Facultad de Derecho, University of Salamanca, Paseo Francisco Tomás y Valiente s/n, Salamanca, 37007, Spain.

[h] School of GeoSciences, University of Edinburgh, Edinburgh, EH9 3FE, Scotland, United Kingdom

[i] TermoCal. School of Engineering, University of Valladolid. Paseo del Cauce 59, Valladolid, 47011, Spain

[j] Instituto de Ciencia y Tecnología del Carbono, INCAR-CSIC, c/Francisco Pintado Fe, 26, Oviedo, 33011, Spain

[k] IGME – Instituto Geológico y Minero de España – Geological Survey of Spain. C/Ríos Rosas 23, Madrid, 28003, Spain

[l] Department of Civil and Environmental Engineering, University of Strathclyde, Glasgow, G1 1XZ, Scotland, United Kingdom

* Corresponding author: jalcalde@geo3bcn.csic.es

Assessment processes

The assessment processes of the 15 CO_2 emission hubs are listed in Tables 1-15 of this supplement. The assessment of each emission hub includes the scoring of data, the normalization and weighting of data, and the Technique for Order of Preference by Similarity to Ideal Solution (TOPSIS) ranking, allowing to the identification of priority source-to-sink clusters for each emission hub. The assessment has been implemented using Microsoft Excel, resulting in 15 tables showing the specific processes (Table 1 to 15). Data of storage structures are obtained from ALGECO2 Database [1], Martínez del Olmo [2] and the Spanish Geophysical Information System [3].

References

[1] Instituto Geológico y Minero de España. The ALGECO2 project 2010. http://info.igme.es/algeco2/ (accessed October 1, 2020).

[2] Martínez del Olmo W. Cambio climático, acuerdos de Paris y trampas geológicas donde secuestrar el CO2 en España. Rev La Soc Geológica España 2019;32:87–106.

[3] Instituto Geológico y Minero de España. Geophysical Information System 2020. http://info.igme.es/SIGEOF/# (accessed October 1, 2020).

Table 1. Assessment process of E1 emission hub.

Storage structure	Storage capacity (Mt)	Scoring of reservoir-caprock suitability					Development cost		Scoring of data availability	
		Effective thickness of reservoirs	Porosity of reservoirs	Permeability of reservoirs	Effective thickness of caprocks	Presence of fractures in caprocks	Well cost (M€)	Pipeline cost (M€)	Seismic	Well
Boñar	169	0.07	0.50	0.50	0.01	0.50	7	198	2	3
Mar Cantábrico J-1 P	250	1.00	0.08	0.00	0.34	1.00	81	207	3	0
Mar Cantábrico J-1 S	270	0.09	0.35	0.50	0.34	1.00	51	196	3	0
Campillo	132	0.08	0.50	0.50	0.00	1.00	22	249	2	2
Villameriel	119	0.05	0.42	0.50	0.02	1.00	19	264	1	2

Storage structure	Scoring of ranking criteria								Normalisation and weighting of ranking criteria				TOPSIS ranking					
	Storage capacity (Mt)	Rank of criterion	Reservoir-caprock suitability	Rank of criterion	Development cost (M€)	Rank of criterion	Data availability	Rank of criterion	Storage capacity	Reservoir-caprock suitability	Development cost	Data availability	Distance to ideal positive solution (d-)	Distance to ideal negative solution (d-)	TOPSIS score (T_S)	Ranking (Comprehensive scenario)	Ranking (Geological scenario)	Ranking (Economic scenario)
Boñar	169	3	1.57	5	205	1	5	1	0.0763	0.1177	0.1056	0.0910	0.0784	0.0605	0.5642	3	3	2
Mar Cantábrico J-1 P	250	2	2.42	1	288	5	3	3	0.1131	0.1813	0.1483	0.0546	0.0568	0.0871	0.3950	2	2	3
Mar Cantábrico J-1 S	270	1	2.28	2	247	2	3	3	0.1222	0.1708	0.1273	0.0546	0.0437	0.0892	0.3287	1	1	1
Campillo	132	4	2.08	3	271	3	4	2	0.0598	0.1558	0.1395	0.0728	0.0776	0.0435	0.6406	4	4	4
Villameriel	119	5	1.99	4	283	4	3	3	0.0536	0.1494	0.1456	0.0546	0.0930	0.0318	0.7451	5	5	5
Weighting (Comprehensive scenario)	20%		35%		30%		15%		0.1222	0.1813	0.1056	0.0910	Ideal positive solution					
									0.0536	0.1177	0.1483	0.0546	Ideal negative solution					

Table 2. Assessment process of E2 emission hub.

Storage structure	Storage capacity (Mt)	Scoring of reservoir-caprock suitability					Development cost		Scoring of data availability	
		Effective thickness of reservoirs	Porosity of reservoirs	Permeability of reservoirs	Effective thickness of caprocks	Presence of fractures in caprocks	Well cost (M€)	Pipeline cost (M€)	Seismic	Well
Oeste de Polientes (Bunt)	82	0.14	0.04	0.00	0.01	1.00	23	144	2	1
San Pedro	198	0.12	0.65	0.50	0.01	1.00	12	152	2	3
Campillo	132	0.08	0.50	0.50	0.00	1.00	22	104	2	2
Boñar	169	0.07	0.50	0.50	0.01	0.50	7	66	2	3
Villameriel	119	0.05	0.42	0.50	0.02	1.00	19	125	1	3
Mar Cantábrico J-1 P	250	1.00	0.08	0.00	0.34	1.00	81	46	3	0
Mar Cantábrico J-1 S	270	0.09	0.35	0.50	0.34	1.00	51	37	3	0
Iglesias (Cretaceous)	448.05	0.12	0.13	0.50	0.46	1.00	13	167	2	3
Iglesias (Utrillas)	678.2	0.09	0.42	0.50	0.47	1.00	14	167	2	3
Iglesias (Buntsandstein)	154.15	0.10	0.00	0.00	0.03	1.00	16	167	2	3

Storage structure	Scoring of ranking criteria								Normalisation and weighting of ranking criteria				TOPSIS ranking					
	Storage capacity (Mt)	Rank of criterion	Reservoir-caprock suitability	Rank of criterion	Development cost (M€)	Rank of criterion	Data availability	Rank of criterion	Storage capacity	Reservoir-caprock suitability	Development cost	Data availability	Distance to ideal positive solution (d-)	Distance to ideal negative solution (d-)	TOPSIS score (Ts)	Ranking (Comprehensive scenario)	Ranking (Geological scenario)	Ranking (Economic scenario)
Oeste de Polientes (Bunt)	82	10	1.18	9	167	7	3	8	0.0171	0.0649	0.1069	0.0332	0.1563	0.0110	0.9345	10	10	10
San Pedro	198	5	2.28	3	163	6	5	1	0.0412	0.1252	0.1047	0.0553	0.1157	0.0723	0.6154	6	5	7
Campillo	132	8	2.08	6	126	3	4	6	0.0275	0.1140	0.0807	0.0442	0.1209	0.0655	0.6487	7	7	6
Boñar	169	6	1.57	8	74	1	5	1	0.0351	0.0861	0.0471	0.0553	0.1169	0.0796	0.5949	5	6	3
Villameriel	119	9	1.99	7	144	5	4	6	0.0246	0.1093	0.0922	0.0442	0.1280	0.0553	0.6983	8	8	8
Mar Cantábrico J-1 P	250	4	2.42	2	127	4	3	8	0.0520	0.1326	0.0814	0.0332	0.0980	0.0867	0.5305	4	4	4
Mar Cantábrico J-1 S	270	3	2.28	4	88	2	3	8	0.0561	0.1249	0.0567	0.0332	0.0889	0.0958	0.4811	3	3	2
Iglesias (Cretaceous)	448	2	2.22	5	180	8	5	1	0.0931	0.1217	0.1152	0.0553	0.0844	0.0993	0.4594	2	2	5
Iglesias (Utrillas)	678	1	2.48	1	182	9	5	1	0.1410	0.1357	0.1163	0.0553	0.0692	0.1459	0.3216	1	1	1
Iglesias (Buntsandstein)	154	7	1.13	10	183	10	5	1	0.0320	0.0620	0.1174	0.0553	0.1492	0.0267	0.8481	9	9	9
Weighting (Comprehensive scenario)	20%		35%		30%		15%		0.1410	0.1357	0.0471	0.0553	Ideal positive solution					
									0.0171	0.0620	0.1174	0.0332	Ideal negative solution					

Table 3. Assessment process of E3 emission hub.

Storage structure	Storage capacity (Mt)	Scoring of reservoir-caprock suitability					Development cost		Scoring of data availability	
		Effective thickness of reservoirs	Porosity of reservoirs	Permeability of reservoirs	Effective thickness of caprocks	Presence of fractures in caprocks	Well cost (M€)	Pipeline cost (M€)	Seismic	Well
Alto Guadalquivir (Mesozoic)	239	1.00	0.24	0.00	0.27	0.50	12	218	1	0
Guadiana Menor (Mesozoic)	171	0.71	0.15	0.00	0.56	0.00	16	244	1	0
Almonte	73	0.09	1.00	0.50	0.02	1.00	6	135	2	3
Cádiz Arenoso	700	0.03	0.83	1.00	0.41	1.00	59	144	3	2
Cádiz Dolomitico	60	0.10	0.15	0.50	0.09	1.00	99	163	3	2

Storage structure	Scoring of ranking criteria								Normalisation and weighting of ranking criteria				TOPSIS ranking					
	Storage capacity (Mt)	Rank of criterion	Reservoir-caprock suitability	Rank of criterion	Development cost (M€)	Rank of criterion	Data availability	Rank of criterion	Storage capacity	Reservoir-caprock suitability	Development cost	Data availability	Distance to ideal positive solution (d-)	Distance to ideal negative solution (d-)	TOPSIS score (Ts)	Ranking (Comprehensive scenario)	Ranking (Geological scenario)	Ranking (Economic scenario)
Alto Guadalquivir (Mesozoic)	239	2	2.01	3	230	3	1	4	0.0625	0.1332	0.1379	0.0171	0.1722	0.0628	0.7327	4	3	4
Guadiana Menor (Mesozoic)	171	3	1.42	5	260	4	1	4	0.0447	0.0959	0.1559	0.0171	0.2107	0.0290	0.8790	5	5	5
Almonte	73	4	2.61	2	141	1	5	1	0.0192	0.1760	0.0843	0.0855	0.1697	0.1280	0.5700	2	2	2
Cádiz Arenoso	700	1	3.27	1	203	2	5	1	0.1830	0.2202	0.1219	0.0855	0.0376	0.2222	0.1449	1	1	1
Cádiz Dolomitico	60	5	1.84	4	262	5	5	1	0.0157	0.1267	0.1571	0.0855	0.2051	0.0750	0.7323	3	4	3
Weighting (Comprehensive scenario)	20%		35%		30%		15%		0.1830	0.2202	0.0843	0.0855	Ideal positive solution					
									0.0157	0.0959	0.1571	0.0171	Ideal negative solution					

Table 4. Assessment process of E4 emission hub.

Storage structure	Storage capacity (Mt)	Scoring of reservoir-caprock suitability					Development cost		Scoring of data availability	
		Effective thickness of reservoirs	Porosity of reservoirs	Permeability of reservoirs	Effective thickness of caprocks	Presence of fractures in caprocks	Well cost (M€)	Pipeline cost (M€)	Seismic	Well
Alto Guadalquivir (Mesozoic)	239	1.00	0.24	0.00	0.27	0.50	12	155	1	0
Guadiana Menor (Mesozoic)	171	0.71	0.15	0.00	0.56	0.00	16	128	1	0
Murcia B-1	366	0.88	0.23	0.00	0.24	1.00	12	118	2	1
Sierra Seca (Dogger-Lias)	487	0.28	0.15	0.00	0.13	1.00	9	108	1	0
Sierra de Salinas (Dogger)	179	0.17	0.15	0.00	0.08	1.00	13	160	1	2

Storage structure	Scoring of ranking criteria								Normalisation and weighting of ranking criteria				TOPSIS ranking					
	Storage capacity (Mt)	Rank of criterion	Reservoir-caprock suitability	Rank of criterion	Development cost (M€)	Rank of criterion	Data availability	Rank of criterion	Storage capacity	Reservoir-caprock suitability	Development cost	Data availability	Distance to ideal positive solution (d-)	Distance to ideal negative solution (d-)	TOPSIS score (Ts)	Ranking (Comprehensive scenario)	Ranking (Geological scenario)	Ranking (Economic scenario)
Alto Guadalquivir (Mesozoic)	239	3	2.00	2	167	4	1	3	0.0683	0.1751	0.1516	0.0327	0.1109	0.0555	0.6666	4	3	4
Guadiana Menor (Mesozoic)	171	5	1.42	4	144	3	1	3	0.0488	0.1246	0.1309	0.0327	0.1403	0.0262	0.8427	5	5	5
Murcia B-1	366	2	2.35	1	129	2	3	1	0.1047	0.2061	0.1175	0.0982	0.0362	0.1257	0.2235	1	1	1
Sierra Seca (Dogger-Lias)	487	1	1.56	3	118	1	1	3	0.1392	0.1365	0.1067	0.0327	0.0955	0.1043	0.4781	2	2	2
Sierra de Salinas (Dogger)	179	4	1.41	5	173	5	3	1	0.0510	0.1234	0.1571	0.0982	0.1309	0.0655	0.6666	3	4	3
Weighting (Comprehensive scenario)	20%		35%		30%		15%		0.1392	0.2061	0.1067	0.0982	Ideal positive solution					
									0.0488	0.1234	0.1571	0.0327	Ideal negative solution					

Table 5. Assessment process of E5 emission hub.

Storage structure	Storage capacity (Mt)	Scoring of reservoir-caprock suitability					Development cost		Scoring of data availability	
		Effective thickness of reservoirs	Porosity of reservoirs	Permeability of reservoirs	Effective thickness of caprocks	Presence of fractures in caprocks	Well cost (M€)	Pipeline cost (M€)	Seismic	Well
Sinclinal de Pétrola (Manuel sandstone)	264	0.02	0.58	0.50	0.16	0.50	15	124	1	1
Sierra de Benejama (Manuel sandstone)	107	0.01	0.42	0.50	0.16	1.00	12	107	1	0
Sierra de Benejama (Dogger)	255	0.13	0.15	0.00	0.01	0.50	10	107	1	0
Sierra de Salinas (Dogger)	179	0.17	0.15	0.00	0.08	1.00	13	84	1	2
Macaroba (Jurassic)	450	0.28	0.15	0.00	0.24	0.00	13	103	1	0
Murcia B-1	366	0.88	0.23	0.00	0.24	1.00	12	84	2	1
Sierra Seca (Dogger-Lias)	487	0.28	0.15	0.00	0.13	1.00	9	136	1	0

Storage structure	Scoring of ranking criteria								Normalisation and weighting of ranking criteria				TOPSIS ranking					
	Storage capacity (Mt)	Rank of criterion	Reservoir-caprock suitability	Rank of criterion	Development cost (M€)	Rank of criterion	Data availability	Rank of criterion	Storage capacity	Reservoir-caprock suitability	Development cost	Data availability	Distance to ideal positive solution (d-)	Distance to ideal negative solution (d-)	TOPSIS score (Ts)	Ranking (Comprehensive scenario)	Ranking (Geological scenario)	Ranking (Economic scenario)
Sinclinal de Pétrola (Manuel sandstone)	264	4	1.76	3	139	6	2	3	0.0610	0.1428	0.1314	0.0588	0.0869	0.0998	0.4653	2	3	3
Sierra de Benejama (Manuel sandstone)	107	7	2.10	2	119	5	1	4	0.0246	0.1706	0.1130	0.0294	0.1100	0.1183	0.4819	4	4	4
Sierra de Benejama (Dogger)	255	5	0.79	6	117	4	1	4	0.0588	0.0646	0.1107	0.0294	0.1511	0.0445	0.7726	7	7	7
Sierra de Salinas (Dogger)	179	6	1.41	5	97	2	3	1	0.0412	0.1145	0.0920	0.0883	0.1048	0.0967	0.5201	5	5	2
Macaroba (Jurassic)	450	2	0.67	7	116	3	1	4	0.1038	0.0548	0.1102	0.0294	0.1503	0.0838	0.6420	6	6	6
Murcia B-1	366	3	2.35	1	96	1	3	1	0.0845	0.1914	0.0906	0.0883	0.0279	0.1671	0.1429	1	1	1
Sierra Seca (Dogger-Lias)	487	1	1.56	4	145	7	1	4	0.1123	0.1268	0.1374	0.0294	0.0992	0.1135	0.4662	3	2	5
Weighting (Comprehensive scenario)	20%		35%		30%		15%		0.1123	0.1914	0.0906	0.0883	Ideal positive solution					
									0.0246	0.0548	0.1374	0.0294	Ideal negative solution					

Table 6. Assessment process of E6 emission hub.

Storage structure	Storage capacity (Mt)	Scoring of reservoir-caprock suitability					Development cost		Scoring of data availability	
		Effective thickness of reservoirs	Porosity of reservoirs	Permeability of reservoirs	Effective thickness of caprocks	Presence of fractures in caprocks	Well cost (M€)	Pipeline cost (M€)	Seismic	Well
Maestrazgo 1	57	0.01	0.19	0.50	0.04	0.50	11	57	2	3
Maestrazgo 2	123	0.06	0.15	0.50	0.06	1.00	12	47	2	3
Maestrazgo 3	83	0.08	0.31	1.00	0.22	1.00	18	47	2	3
Arnedo	114	0.11	0.27	1.00	0.01	1.00	9	164	1	1
Magallón	100	0.05	0.19	1.00	0.01	1.00	8	121	1	3
La Zona de Enlace (Muschelkalk-III)	134	0.04	0.17	0.50	0.05	1.00	10	49	1	3
La Zona de Enlace (Buntsandstein)	500	0.11	0.38	1.00	0.01	1.00	17	28	1	3
Roncal-Illón	348	0.05	0.04	0.50	0.03	1.00	14	172	1	1
Leyre-Berdun	137	0.05	0.17	0.00	0.15	1.00	11	165	1	1
Lopín	109	0.06	0.12	1.00	0.07	1.00	8	61	1	2
Monegrillo	112.54	0.03	0.38	1.00	0.02	0.50	9	63	1	2
Caspe-Mayals	105.98	0.14	0.69	1.00	0.02	1.00	6	40	1	2
Reus	82.99	0.06	0.35	1.00	0.06	1.00	11	113	1	3
Denia	700	0.05	0.73	1.00	0.11	1.00	83	123	3	0
Almazán Meridional	129.93	0.01	0.16	0.00	0.02	1.00	8	154	2	3
Gabaldón	177	0.14	0.15	0.50	0.04	1.00	26	176	2	2

Storage structure	Scoring of ranking criteria								Normalisation and weighting of ranking criteria				TOPSIS ranking					
	Storage capacity (Mt)	Rank of criterion	Reservoir-caprock suitability	Rank of criterion	Development cost (M€)	Rank of criterion	Data availability	Rank of criterion	Storage capacity	Reservoir-caprock suitability	Development cost	Data availability	Distance to ideal positive solution (d-)	Distance to ideal negative solution (d-)	TOPSIS score (Ts)	Ranking (Comprehensive scenario)	Ranking (Geological scenario)	Ranking (Economic scenario)
Maestrazgo 1	57	16	1.24	15	68	6	5	1	0.0112	0.0509	0.0396	0.0497	0.1441	0.0854	0.6277	9	12	9
Maestrazgo 2	123	8	1.77	11	60	4	5	1	0.0242	0.0731	0.0346	0.0497	0.1224	0.0942	0.5653	5	8	4
Maestrazgo 3	83	14	2.60	3	66	5	5	1	0.0164	0.1072	0.0382	0.0497	0.1223	0.1046	0.5390	4	4	3
Arnedo	114	9	2.39	6	173	12	2	14	0.0224	0.0986	0.1004	0.0199	0.1416	0.0543	0.7228	13	13	14
Magallón	100	13	2.26	7	129	10	4	5	0.0196	0.0931	0.0751	0.0397	0.1306	0.0663	0.6635	11	11	11
La Zona de Enlace (Muschelkalk-III)	134	6	1.75	12	58	3	4	5	0.0264	0.0722	0.0338	0.0397	0.1212	0.0923	0.5675	6	7	5
La Zona de Enlace (Buntsandstein)	500	2	2.50	4	45	1	4	5	0.0982	0.1031	0.0261	0.0397	0.0435	0.1401	0.2368	1	1	1
Roncal-Illón	348	3	1.62	13	186	14	2	14	0.0683	0.0666	0.1080	0.0199	0.1229	0.0609	0.6687	12	5	13
Leyre-Berdun	137	5	1.37	14	175	13	2	14	0.0269	0.0563	0.1018	0.0199	0.1508	0.0249	0.8583	16	16	16
Lopín	109	11	2.25	8	69	7	3	10	0.0215	0.0928	0.0401	0.0298	0.1213	0.0920	0.5689	7	6	6
Monegrillo	113	10	1.93	9	72	8	3	10	0.0221	0.0793	0.0417	0.0298	0.1245	0.0849	0.5945	8	9	8
Caspe-Mayals	106	12	2.85	2	46	2	3	10	0.0208	0.1175	0.0269	0.0298	0.1183	0.1161	0.5047	3	3	2
Reus	83	15	2.47	5	125	9	4	5	0.0163	0.1016	0.0723	0.0397	0.1312	0.0737	0.6403	10	10	10
Denia	700	1	2.89	1	206	16	3	10	0.1375	0.1189	0.1197	0.0298	0.0956	0.1447	0.3979	2	2	7
Almazán Meridional	130	7	1.19	16	162	11	5	1	0.0255	0.0490	0.0939	0.0497	0.1484	0.0419	0.7797	14	15	12
Gabaldón	177	4	1.83	10	202	15	4	5	0.0348	0.0752	0.1173	0.0397	0.1444	0.0405	0.7809	15	14	15
Weighting (Comprehensive scenario)	20%		35%		30%		15%		0.1375	0.1189	0.0261	0.0497	Ideal positive solution					
									0.0112	0.0490	0.1197	0.0199	Ideal negative solution					

Table 7. Assessment process of E7 emission hub.

Storage structure	Storage capacity (Mt)	Scoring of reservoir-caprock suitability					Development cost		Scoring of data availability	
		Effective thickness of reservoirs	Porosity of reservoirs	Permeability of reservoirs	Effective thickness of caprocks	Presence of fractures in caprocks	Well cost (M€)	Pipeline cost (M€)	Seismic	Well
Barcelona-A	500	0.10	0.19	0.50	0.20	1.00	95	257	3	0
Denia	700	0.05	0.73	1.00	0.11	1.00	83	307	3	0
La Zona de Enlace (Muschelkalk-III)	134	0.04	0.17	0.50	0.05	1.00	10	344	1	3
Reus	83	0.06	0.35	1.00	0.06	1.00	11	308	1	3
La Zona de Enlace (Buntsandstein)	500	0.11	0.38	1.00	0.01	1.00	17	367	1	3
Caspe-Mayals	106	0.14	0.69	1.00	0.02	1.00	6	372	1	2
Maestrazgo 3	83	0.08	0.31	1.00	0.22	1.00	18	378	2	3
La Zona de Enlace (Muschelkalk-III)	57	0.01	0.19	0.50	0.04	0.50	10	381	2	3
Maestrazgo 2	123	0.06	0.15	0.50	0.06	1.00	11	378	2	3

Storage structure	Scoring of ranking criteria								Normalisation and weighting of ranking criteria				TOPSIS ranking					
	Storage capacity (Mt)	Rank of criterion	Reservoir-caprock suitability	Rank of criterion	Development cost (M€)	Rank of criterion	Data availability	Rank of criterion	Storage capacity	Reservoir-caprock suitability	Development cost	Data availability	Distance to ideal positive solution (d-)	Distance to ideal negative solution (d-)	TOPSIS score (Ts)	Ranking (Comprehensive scenario)	Ranking (Geological scenario)	Ranking (Economic scenario)
Barcelona-A	500	2	1.99	6	352	2	3	7	0.0975	0.1012	0.0942	0.0367	0.0655	0.0953	0.4073	3	3	3
Denia	700	1	2.89	1	390	7	3	7	0.1365	0.1469	0.1044	0.0367	0.0309	0.1510	0.1701	1	1	1
La Zona de Enlace (Muschelkalk-III)	134	4	1.75	8	354	3	4	4	0.0262	0.0892	0.0948	0.0490	0.1255	0.0346	0.7837	8	8	8
Reus	83	8	2.47	5	319	1	4	4	0.0162	0.1256	0.0855	0.0490	0.1228	0.0673	0.6461	6	6	6
La Zona de Enlace (Buntsandstein)	500	2	2.50	4	384	5	4	4	0.0975	0.1274	0.1028	0.0490	0.0485	0.1086	0.3088	2	2	2
Caspe-Mayals	106	6	2.85	2	378	4	3	7	0.0207	0.1452	0.1014	0.0367	0.1195	0.0830	0.5902	4	4	4
Maestrazgo 3	83	7	2.60	3	396	9	5	1	0.0163	0.1324	0.1062	0.0612	0.1229	0.0738	0.6247	5	5	5
La Zona de Enlace (Muschelkalk-III)	57	9	1.24	9	390	8	5	1	0.0111	0.0629	0.1046	0.0612	0.1522	0.0245	0.8611	9	9	9
Maestrazgo 2	123	5	1.77	7	390	6	5	1	0.0241	0.0903	0.1044	0.0612	0.1273	0.0390	0.7656	7	7	7
Weighting (Comprehensive scenario)	20%		35%		30%		15%		0.1365	0.1469	0.0855	0.0612	Ideal positive solution					
									0.0111	0.0629	0.1062	0.0367	Ideal negative solution					

Table 8. Assessment process of E8 emission hub.

Storage structure	Storage capacity (Mt)	Scoring of reservoir-caprock suitability					Development cost		Scoring of data availability	
		Effective thickness of reservoirs	Porosity of reservoirs	Permeability of reservoirs	Effective thickness of caprocks	Presence of fractures in caprocks	Well cost (M€)	Pipeline cost (M€)	Seismic	Well
Barcelona-A	500	0.10	0.19	0.50	0.20	1.00	95	47	3	0
La Zona de Enlace (Muschelkalk-III)	134	0.04	0.17	0.50	0.05	1.00	10	148	1	3
La Zona de Enlace (Buntsandstein)	500	0.11	0.38	1.00	0.01	1.00	17	165	1	3
Caspe-Mayals	106	0.14	0.69	1.00	0.02	1.00	6	147	1	2
Reus	83	0.06	0.35	1.00	0.06	1.00	11	77	1	3

Storage structure	Scoring of ranking criteria								Normalisation and weighting of ranking criteria				TOPSIS ranking					
	Storage capacity (Mt)	Rank of criterion	Reservoir-caprock suitability	Rank of criterion	Development cost (M€)	Rank of criterion	Data availability	Rank of criterion	Storage capacity	Reservoir-caprock suitability	Development cost	Data availability	Distance to ideal positive solution (d-)	Distance to ideal negative solution (d-)	TOPSIS score (Ts)	Ranking (Comprehensive scenario)	Ranking (Geological scenario)	Ranking (Economic scenario)
Barcelona-A	500	1	1.99	4	142	2	3	4	0.1848	0.1393	0.1244	0.0554	0.0787	0.1589	0.3313	1	2	1
La Zona de Enlace (Muschelkalk-III)	134	3	1.75	5	158	4	4	1	0.0496	0.1228	0.1382	0.0739	0.1670	0.0340	0.8307	5	5	5
La Zona de Enlace (Buntsandstein)	500	1	2.50	2	182	5	4	1	0.1848	0.1753	0.1596	0.0739	0.0856	0.1638	0.3431	2	1	2
Caspe-Mayals	106	4	2.85	1	153	3	3	4	0.0392	0.1998	0.1344	0.0554	0.1574	0.0815	0.6589	4	3	4
Reus	83	5	2.47	3	89	1	4	1	0.0307	0.1728	0.0775	0.0739	0.1565	0.0978	0.6154	3	4	3
Weighting (Comprehensive scenario)	20%		35%		30%		15%		0.1848	0.1998	0.0775	0.0739	Ideal positive solution					
									0.0307	0.1228	0.1596	0.0554	Ideal negative solution					

Table 9. Assessment process of E9 emission hub.

Storage structure	Storage capacity (Mt)	Scoring of reservoir-caprock suitability					Development cost		Scoring of data availability	
		Effective thickness of reservoirs	Porosity of reservoirs	Permeability of reservoirs	Effective thickness of caprocks	Presence of fractures in caprocks	Well cost (M€)	Pipeline cost (M€)	Seismic	Well
Oeste de Polientes (Bunt)	82	0.14	0.04	0.00	0.01	1.00	23	80	2	1
Rioja Norte (pre and syn-orogenic Tertiary)	28482	0.85	0.27	0.50	1.00	1.00	34	76	2	3
Rioja Sur (Upper Cretaceous)	240	0.03	0.15	0.50	0.63	1.00	24	99	1	2
Iglesias (Cretaceous)	448	0.12	0.13	0.50	0.46	1.00	13	118	2	3
Iglesias (Utrillas)	678	0.09	0.42	0.50	0.47	1.00	14	118	2	3
Iglesias (Buntsandstein)	154	0.10	0.00	0.00	0.03	1.00	16	118	2	3
Don Juan Este (Upper Cretaceous)	79	0.20	0.13	0.50	0.27	1.00	8	168	1	1
Don Juan Este (Utrillas)	132	0.08	0.50	0.50	0.28	1.00	10	168	1	1
Don Juan Este (Jurassic carbonate)	77	0.17	0.08	0.50	0.28	1.00	12	168	1	1
Don Juan Oeste (Upper Cretaceous)	230	0.17	0.13	0.50	0.32	1.00	9	166	1	1
Don Juan Oeste (Utrillas)	219.76	0.07	0.42	0.50	0.32	1.00	11	166	1	1
San Pedro	197.97	0.12	0.65	0.50	0.01	1.00	12	101	2	3
Campillo	132.13	0.08	0.50	0.50	0.00	1.00	22	134	2	2
Villameriel	118.55	0.05	0.42	0.50	0.02	1.00	19	137	1	3
Arnedo	113.94	0.11	0.27	1.00	0.01	1.00	9	137	1	1
Roncal-Illón	348	0.05	0.04	0.50	0.03	1.00	14	162	1	1
Leyre-Berdun	137	0.05	0.17	0.00	0.15	1.00	11	159	1	1
Vizcaya-C2	250	0.08	0.19	0.50	0.70	1.00	90	52	3	0

Storage structure	Scoring of ranking criteria								Normalisation and weighting of ranking criteria				TOPSIS ranking					
	Storage capacity (Mt)	Rank of criterion	Reservoir-caprock suitability	Rank of criterion	Development cost (M€)	Rank of criterion	Data availability	Rank of criterion	Storage capacity	Reservoir-caprock suitability	Development cost	Data availability	Distance to ideal positive solution (d-)	Distance to ideal negative solution (d-)	TOPSIS score (Ts)	Ranking (Comprehensive scenario)	Ranking (Geological scenario)	Ranking (Economic scenario)
Oeste de Polientes (Bunt)	82	16	1.18	17	103	1	3	8	0.0006	0.0447	0.0483	0.0306	0.2204	0.0376	0.8543	14	15	10
Rioja Norte (pre and syn-orogenic Tertiary)	28482	1	3.62	1	111	2	5	1	0.1999	0.1365	0.0518	0.0510	0.0036	0.2248	0.0157	1	1	1
Rioja Sur (Upper Cretaceous)	240	6	2.31	7	123	4	3	8	0.0017	0.0872	0.0574	0.0306	0.2055	0.0530	0.7949	6	5	5
Iglesias (Cretaceous)	448	3	2.22	9	131	5	5	1	0.0031	0.0838	0.0613	0.0510	0.2041	0.0563	0.7838	4	7	4
Iglesias (Utrillas)	678	2	2.48	3	133	6	5	1	0.0048	0.0934	0.0621	0.0510	0.2003	0.0635	0.7594	2	2	2
Iglesias (Buntsandstein)	154	10	1.13	18	134	7	5	1	0.0011	0.0427	0.0630	0.0510	0.2203	0.0374	0.8550	15	16	7
Don Juan Este (Upper Cretaceous)	79	17	2.11	11	176	15	2	11	0.0006	0.0797	0.0826	0.0204	0.2123	0.0371	0.8511	13	12	15
Don Juan Este (Utrillas)	132	13	2.36	5	178	17	2	11	0.0009	0.0891	0.0835	0.0204	0.2098	0.0465	0.8187	8	8	12
Don Juan Este (Jurassic carbonate)	77	18	2.03	13	180	18	2	11	0.0005	0.0764	0.0844	0.0204	0.2135	0.0338	0.8633	16	14	16
Don Juan Oeste (Upper Cretaceous)	230	7	2.12	10	175	13	2	11	0.0016	0.0800	0.0821	0.0204	0.2111	0.0375	0.8492	12	11	14
Don Juan Oeste (Utrillas)	220	8	2.31	6	177	16	2	11	0.0015	0.0873	0.0829	0.0204	0.2095	0.0447	0.8242	9	9	13
San Pedro	198	9	2.28	8	113	3	5	1	0.0014	0.0862	0.0528	0.0510	0.2048	0.0619	0.7680	3	4	3
Campillo	132	12	2.08	12	156	11	4	6	0.0009	0.0785	0.0730	0.0408	0.2090	0.0427	0.8302	10	10	9
Villameriel	119	14	1.99	14	156	10	4	6	0.0008	0.0752	0.0729	0.0408	0.2099	0.0401	0.8396	11	13	11
Arnedo	114	15	2.39	4	146	9	2	11	0.0008	0.0903	0.0685	0.0204	0.2076	0.0502	0.8051	7	6	8
Roncal-Illón	348	4	1.62	15	175	14	2	11	0.0024	0.0610	0.0822	0.0204	0.2163	0.0186	0.9210	17	17	17
Leyre-Berdun	137	11	1.37	16	170	12	2	11	0.0010	0.0516	0.0795	0.0204	0.2206	0.0102	0.9556	18	18	18
Vizcaya-C2	250	5	2.48	2	141	8	3	8	0.0018	0.0935	0.0662	0.0306	0.2045	0.0549	0.7883	5	3	6
Weighting (Comprehensive scenario)	20%		35%		30%		15%		0.1999	0.1365	0.0483	0.0510	Ideal positive solution					
									0.0005	0.0427	0.0844	0.0204	Ideal negative solution					

Table 10. Assessment process of E10 emission hub.

Storage structure	Storage capacity (Mt)	Scoring of reservoir-caprock suitability					Development cost		Scoring of data availability	
		Effective thickness of reservoirs	Porosity of reservoirs	Permeability of reservoirs	Effective thickness of caprocks	Presence of fractures in caprocks	Well cost (M€)	Pipeline cost (M€)	Seismic	Well
Duero Centro-Meridional (Upper Cretaceous)	1229	0.06	0.13	0.50	0.26	1.00	9	164	1	3
Duero Centro-Meridional (Utrillas)	813	0.01	0.42	0.50	0.26	1.00	9	164	1	3
Campillo	132	0.08	0.50	0.50	0.00	1.00	22	127	2	2
Boñar	169	0.07	0.50	0.50	0.01	0.50	7	76	2	3
Villameriel	119	0.05	0.42	0.50	0.02	1.00	19	139	1	3
Mar Cantábrico J-1 P	250	1.00	0.08	0.00	0.34	1.00	81	122	3	0
Mar Cantábrico J-1 S	270	0.09	0.35	0.50	0.34	1.00	51	116	3	0

Storage structure	Scoring of ranking criteria								Normalisation and weighting of ranking criteria				TOPSIS ranking					
	Storage capacity (Mt)	Rank of criterion	Reservoir-caprock suitability	Rank of criterion	Development cost (M€)	Rank of criterion	Data availability	Rank of criterion	Storage capacity	Reservoir-caprock suitability	Development cost	Data availability	Distance to ideal positive solution (d+)	Distance to ideal negative solution (d-)	TOPSIS score (Ts)	Ranking (Comprehensive scenario)	Ranking (Geological scenario)	Ranking (Economic scenario)
Duero Centro-Meridional (Upper Cretaceous)	1229	1	1.95	6	173	5	4	2	0.1598	0.1237	0.1211	0.0580	0.0710	0.1486	0.3232	1	1	1
Duero Centro-Meridional (Utrillas)	813	2	2.19	3	174	6	4	2	0.1057	0.1391	0.1215	0.0580	0.0856	0.1018	0.4569	2	2	2
Campillo	132	6	2.08	4	149	2	4	2	0.0172	0.1319	0.1044	0.0580	0.1521	0.0520	0.7450	6	6	4
Boñar	169	5	1.57	7	83	1	5	1	0.0219	0.0997	0.0584	0.0725	0.1480	0.0892	0.6238	3	3	3
Villameriel	119	7	1.99	5	158	3	4	2	0.0154	0.1265	0.1104	0.0580	0.1565	0.0443	0.7794	7	7	6
Mar Cantábrico J-1 P	250	4	2.42	1	204	7	3	6	0.0325	0.1536	0.1425	0.0435	0.1553	0.0565	0.7332	5	4	7
Mar Cantábrico J-1 S	270	3	2.28	2	168	4	3	6	0.0351	0.1446	0.1173	0.0435	0.1412	0.0552	0.7190	4	5	5
Weighting (Comprehensive scenario)	20%		35%		30%		15%		0.1598	0.1536	0.0584	0.0725	Ideal positive solution					
									0.0154	0.0997	0.1425	0.0435	Ideal negative solution					

Table 11. Assessment process of E11 emission hub.

Storage structure	Storage capacity (Mt)	Scoring of reservoir-caprock suitability					Development cost		Scoring of data availability	
		Effective thickness of reservoirs	Porosity of reservoirs	Permeability of reservoirs	Effective thickness of caprocks	Presence of fractures in caprocks	Well cost (M€)	Pipeline cost (M€)	Seismic	Well
Almonte	73	0.09	1.00	0.50	0.02	1.00	6	31	2	3
Cádiz Arenoso	700	0.03	0.83	1.00	0.41	1.00	59	33	3	2
Cádiz Dolomítico	60	0.10	0.15	0.50	0.09	1.00	99	25	3	2

Storage structure	Scoring of ranking criteria								Normalisation and weighting of ranking criteria				TOPSIS ranking					
	Storage capacity (Mt)	Rank of criterion	Reservoir-caprock suitability	Rank of criterion	Development cost (M€)	Rank of criterion	Data availability	Rank of criterion	Storage capacity	Reservoir-caprock suitability	Development cost	Data availability	Distance to ideal positive solution (d-)	Distance to ideal negative solution (d-)	TOPSIS score (Ts)	Ranking (Comprehensive scenario)	Ranking (Geological scenario)	Ranking (Economic scenario)
Almonte	73	2	2.61	2	37	1	5	1	0.0208	0.1999	0.0690	0.0866	0.1844	0.1558	0.5420	2	2	2
Cádiz Arenoso	700	1	3.27	1	92	2	5	1	0.1982	0.2502	0.1737	0.0866	0.1048	0.2725	0.2778	1	1	1
Cádiz Dolomítico	60	3	1.84	3	125	3	5	1	0.0170	0.1412	0.2347	0.0866	0.2687	0.1509	0.6403	3	3	3
Weighting (Comprehensive scenario)	20%		35%		30%		15%		0.1982	0.2502	0.0690	0.0866	Ideal positive solution					
									0.0170	0.1412	0.2347	0.0866	Ideal negative solution					

Table 12. Assessment process of H1 emission hub.

Storage structure	Storage capacity (Mt)	Scoring of reservoir-caprock suitability					Development cost		Scoring of data availability	
		Effective thickness of reservoirs	Porosity of reservoirs	Permeability of reservoirs	Effective thickness of caprocks	Presence of fractures in caprocks	Well cost (M€)	Pipeline cost (M€)	Seismic	Well
Oeste de Polientes (Bunt)	82	0.14	0.04	0.00	0.01	1.00	23	147	2	1
San Pedro	198	0.12	0.65	0.50	0.01	1.00	12	156	2	3
Campillo	132	0.08	0.50	0.50	0.00	1.00	22	109	2	2
Boñar	169	0.07	0.50	0.50	0.01	0.50	7	75	2	3
Villameriel	119	0.05	0.42	0.50	0.02	1.00	19	132	1	3
Mar Cantábrico J-1 P	250	1.00	0.08	0.00	0.34	1.00	81	42	3	0
Mar Cantábrico J-1 S	270	0.09	0.35	0.50	0.34	1.00	51	30	3	0
Iglesias (Cretaceous)	448	0.12	0.13	0.50	0.46	1.00	13	172	2	3
Iglesias (Utrillas)	678	0.09	0.42	0.50	0.47	1.00	14	172	2	3
Iglesias (Buntsandstein)	154	0.10	0.00	0.00	0.03	1.00	16	172	2	3

Storage structure	Scoring of ranking criteria								Normalisation and weighting of ranking criteria				TOPSIS ranking					
	Storage capacity (Mt)	Rank of criterion	Reservoir-caprock suitability	Rank of criterion	Development cost (M€)	Rank of criterion	Data availability	Rank of criterion	Storage capacity	Reservoir-caprock suitability	Development cost	Data availability	Distance to ideal positive solution (d-)	Distance to ideal negative solution (d-)	TOPSIS score (Ts)	Ranking (Comprehensive scenario)	Ranking (Geological scenario)	Ranking (Economic scenario)
Oeste de Polientes (Bunt)	82	10	1.18	9	170	7	3	8	0.0171	0.0649	0.1062	0.0332	0.1545	0.0119	0.9283	10	10	10
San Pedro	198	5	2.28	3	168	6	5	1	0.0412	0.1252	0.1049	0.0553	0.1139	0.0723	0.6116	6	5	6
Campillo	132	8	2.08	6	131	4	4	6	0.0275	0.1140	0.0823	0.0442	0.1202	0.0648	0.6498	7	7	7
Boñar	169	6	1.57	8	83	2	5	1	0.0351	0.0861	0.0517	0.0553	0.1169	0.0760	0.6062	5	6	5
Villameriel	119	9	1.99	7	151	5	4	6	0.0246	0.1093	0.0944	0.0442	0.1274	0.0545	0.7005	8	8	8
Mar Cantábrico J-1 P	250	4	2.42	2	123	3	3	8	0.0520	0.1326	0.0768	0.0332	0.0953	0.0888	0.5176	4	4	3
Mar Cantábrico J-1 S	270	3	2.28	4	82	1	3	8	0.0561	0.1249	0.0511	0.0332	0.0883	0.0997	0.4699	3	3	2
Iglesias (Cretaceous)	448	2	2.22	5	185	8	5	1	0.0931	0.1217	0.1156	0.0553	0.0815	0.0992	0.4508	2	2	4
Iglesias (Utrillas)	678	1	2.48	1	186	9	5	1	0.1410	0.1357	0.1166	0.0553	0.0655	0.1459	0.3099	1	1	1
Iglesias (Buntsandstein)	154	7	1.13	10	188	10	5	1	0.0320	0.0620	0.1178	0.0553	0.1475	0.0267	0.8466	9	9	9
Weighting (Comprehensive scenario)	20%		35%		30%		15%		0.1410	0.1357	0.0511	0.0553	Ideal positive solution					
									0.0171	0.0620	0.1178	0.0332	Ideal negative solution					

Table 13. Assessment process of H2 emission hub.

Storage structure	Storage capacity (Mt)	Scoring of reservoir-caprock suitability					Development cost		Scoring of data availability	
		Effective thickness of reservoirs	Porosity of reservoirs	Permeability of reservoirs	Effective thickness of caprocks	Presence of fractures in caprocks	Well cost (M€)	Pipeline cost (M€)	Seismic	Well
Barcelona-A	500	0.10	0.19	0.50	0.20	1.00	95	57	3	0
La Zona de Enlace (Muschelkalk-III)	134	0.04	0.17	0.50	0.05	1.00	10	139	1	3
La Zona de Enlace (Buntsandstein)	500	0.11	0.38	1.00	0.01	1.00	17	157	1	3
Monegrillo	113	0.03	0.38	1.00	0.02	0.50	9	172	1	2
Caspe-Mayals	106	0.14	0.69	1.00	0.02	1.00	6	138	1	2
Reus	83	0.06	0.35	1.00	0.06	1.00	11	69	1	3

Storage structure	Scoring of ranking criteria								Normalisation and weighting of ranking criteria				TOPSIS ranking					
	Storage capacity (Mt)	Rank of criterion	Reservoir-caprock suitability	Rank of criterion	Development cost (M€)	Rank of criterion	Data availability	Rank of criterion	Storage capacity	Reservoir-caprock suitability	Development cost	Data availability	Distance to ideal positive solution (d-)	Distance to ideal negative solution (d-)	TOPSIS score (Ts)	Ranking (Comprehensive scenario)	Ranking (Geological scenario)	Ranking (Economic scenario)
Barcelona-A	500	1	1.99	4	152	4	3	4	0.1350	0.1245	0.1238	0.0520	0.0815	0.1160	0.4127	2	2	3
La Zona de Enlace (Muschelkalk-III)	134	3	1.75	6	149	3	4	1	0.0362	0.1098	0.1215	0.0693	0.1328	0.0342	0.7954	5	5	5
La Zona de Enlace (Buntsandstein)	500	1	2.50	2	173	5	4	1	0.1350	0.1568	0.1416	0.0693	0.0793	0.1233	0.3913	1	1	2
Monegrillo	113	4	1.93	5	181	6	3	4	0.0304	0.1206	0.1475	0.0520	0.1461	0.0134	0.9157	6	6	6
Caspe-Mayals	106	5	2.85	1	144	2	3	4	0.0286	0.1787	0.1175	0.0520	0.1197	0.0753	0.6137	4	4	4
Reus	83	6	2.47	3	80	1	4	1	0.0224	0.1545	0.0654	0.0693	0.1151	0.0951	0.5478	3	3	1
Weighting (Comprehensive scenario)	20%		35%		30%		15%		0.1350	0.1787	0.0654	0.0693	Ideal positive solution					
									0.0224	0.1098	0.1475	0.0520	Ideal negative solution					

Table 14. Assessment process of H3 emission hub.

Storage structure	Storage capacity (Mt)	Scoring of reservoir-caprock suitability					Development cost		Scoring of data availability	
		Effective thickness of reservoirs	Porosity of reservoirs	Permeability of reservoirs	Effective thickness of caprocks	Presence of fractures in caprocks	Well cost (M€)	Pipeline cost (M€)	Seismic	Well
Barcelona-A	500	0.10	0.19	0.50	0.20	1.00	95	112	3	0
Maestrazgo 1	57	0.01	0.19	0.50	0.04	0.50	11	145	2	3
Maestrazgo 2	123	0.06	0.15	0.50	0.06	1.00	12	138	2	3
Maestrazgo 3	83	0.08	0.31	1.00	0.22	1.00	18	138	2	3
La Zona de Enlace (Muschelkalk-III)	134	0.04	0.17	0.50	0.05	1.00	10	83	1	3
La Zona de Enlace (Buntsandstein)	500	0.11	0.38	1.00	0.01	1.00	17	102	1	3
Monegrillo	113	0.03	0.38	1.00	0.02	0.50	9	131	1	2
Caspe-Mayals	106	0.14	0.69	1.00	0.02	1.00	6	86	1	2
Reus	83	0.06	0.35	1.00	0.06	1.00	11	13	1	3
Denia	700	0.05	0.73	1.00	0.11	1.00	83	170	3	0
Lopin	109.33	0.06	0.12	1.00	0.07	1.00	8	160	1	2

Storage structure	Scoring of ranking criteria								Normalisation and weighting of ranking criteria				TOPSIS ranking					
	Storage capacity (Mt)	Rank of criterion	Reservoir-caprock suitability	Rank of criterion	Development cost (M€)	Rank of criterion	Data availability	Rank of criterion	Storage capacity	Reservoir-caprock suitability	Development cost	Data availability	Distance to ideal positive solution (d-)	Distance to ideal negative solution (d-)	TOPSIS score (Ts)	Ranking (Comprehensive scenario)	Ranking (Geological scenario)	Ranking (Economic scenario)
Barcelona-A	500	3	1.99	7	206	10	3	7	0.0718	0.0929	0.1218	0.0347	0.1421	0.0778	0.6461	7	5	11
Maestrazgo 1	57	11	1.24	11	157	7	5	1	0.0082	0.0578	0.0925	0.0579	0.1805	0.0615	0.7460	11	11	10
Maestrazgo 2	123	5	1.77	9	150	6	5	1	0.0177	0.0829	0.0889	0.0579	0.1617	0.0702	0.6973	9	10	8
Maestrazgo 3	83	9	2.60	3	157	8	5	1	0.0120	0.1216	0.0926	0.0579	0.1605	0.0887	0.6441	6	7	5
La Zona de Enlace (Muschelkalk-III)	134	4	1.75	10	93	3	4	4	0.0193	0.0820	0.0549	0.0463	0.1485	0.0990	0.6000	5	6	4
La Zona de Enlace (Buntsandstein)	1054	1	2.50	4	118	4	4	4	0.1515	0.1170	0.0700	0.0463	0.0596	0.1746	0.2546	1	1	1
Monegrillo	113	6	1.93	8	140	5	3	7	0.0162	0.0900	0.0825	0.0347	0.1597	0.0748	0.6809	8	9	6
Caspe-Mayals	106	8	2.85	2	92	2	3	7	0.0152	0.1333	0.0546	0.0347	0.1439	0.1215	0.5422	3	4	3
Reus	83	10	2.47	5	24	1	4	4	0.0119	0.1153	0.0143	0.0463	0.1414	0.1474	0.4896	2	3	2
Denia	700	2	2.89	1	253	11	3	7	0.1006	0.1349	0.1495	0.0347	0.1463	0.1204	0.5485	4	2	7
Lopin	109	7	2.25	6	168	9	3	7	0.0157	0.1053	0.0994	0.0347	0.1645	0.0695	0.7030	10	8	9
Weighting (Comprehensive scenario)	20%		35%		30%		15%		0.1515	0.1349	0.0143	0.0579	Ideal positive solution					
									0.0082	0.0578	0.1495	0.0347	Ideal negative solution					

Table 15. Assessment process of H4 emission hub.

Storage structure	Storage capacity (Mt)	Scoring of reservoir-caprock suitability					Development cost		Scoring of data availability	
		Effective thickness of reservoirs	Porosity of reservoirs	Permeability of reservoirs	Effective thickness of caprocks	Presence of fractures in caprocks	Well cost (M€)	Pipeline cost (M€)	Seismic	Well
Almonte	73	0.09	1.00	0.50	0.02	1.00	6	27	2	3
Cádiz Arenoso	700	0.03	0.83	1.00	0.41	1.00	59	35	3	2
Cádiz Dolomítico	60	0.10	0.15	0.50	0.09	1.00	99	29	3	2
Alto Guadalquivir (Mesozoic)	239	1.00	0.24	0.00	0.27	0.50	12	263	1	0

Storage structure	Scoring of ranking criteria								Normalisation and weighting of ranking criteria				TOPSIS ranking					
	Storage capacity (Mt)	Rank of criterion	Reservoir-caprock suitability	Rank of criterion	Development cost (M€)	Rank of criterion	Data availability	Rank of criterion	Storage capacity	Reservoir-caprock suitability	Development cost	Data availability	Distance to ideal positive solution (d-)	Distance to ideal negative solution (d-)	TOPSIS score (Ts)	Ranking (Comprehensive scenario)	Ranking (Geological scenario)	Ranking (Economic scenario)
Almonte	73	3	2.61	2	33	1	5	1	0.0197	0.1830	0.0305	0.0860	0.1743	0.2439	0.4167	2	2	2
Cádiz Arenoso	700	1	3.27	1	95	2	5	1	0.1877	0.2290	0.0887	0.0860	0.0582	0.2700	0.1772	1	1	1
Cádiz Dolomítico	60	4	1.84	4	128	3	5	1	0.0161	0.1292	0.1205	0.0860	0.2180	0.1540	0.5860	3	3	3
Alto Guadalquivir (Mesozoic)	239	2	2.01	3	275	4	1	4	0.0641	0.1409	0.2582	0.0172	0.2822	0.0494	0.8510	4	4	4
Weighting (Comprehensive scenario)	20%		35%		30%		15%		0.1877	0.2290	0.0305	0.0860	Ideal positive solution					
									0.0161	0.1292	0.2582	0.0172	Ideal negative solution					

Appendix 3 Fluvial sedimentation and its reservoir potential at foreland basin margins: A case study of the Puig-reig anticline (South-eastern Pyrenees)

Sun, X., Alcalde, J., Gomez-Rivas, Owen, A., Griera, A., Martín-Martín, J.D., Cruset, D., Travé, A., 2021. Fluvial sedimentation and its reservoir potential at foreland basin margins: A case study of the Puig-reig anticline (South-eastern Pyrenees). *Sedimentary Geology,* in review.

Fluvial sedimentation and its reservoir potential at foreland basin margins: A case study of the Puig-reig anticline (South-eastern Pyrenees)

Xiaolong Sun[a*], Juan Alcalde[b], Enrique Gomez-Rivas[a], Amanda Owen[c], Albert Griera[d], Juan Diego Martín-Martín[a], David Cruset[b], Anna Travé[a]

[a] Departament de Mineralogia, Petrologia i Geologia Aplicada, Facultat de Ciències de la Terra, Universitat de Barcelona (UB), c/ Martí i Franquès s/n, Barcelona, 08028, Spain

[b] Geosciences Barcelona (GEO3BCN-CSIC), Lluís Solé i Sabarís s/n, Barcelona, 08028, Spain

[c] School of Geographical and Earth Sciences, University of Glasgow, University Avenue, Glasgow, 8NN, UK

[d] Departament de Geologia, Universitat Autònoma de Barcelona, Bellaterra (Cerdanyola del Vallès), 08193, Spain

Abstract: Fluvial fans represent one of the dominant sedimentary systems at the active margins of non-marine foreland basins. The Puig-reig anticline at the north-eastern margin of the Ebro Foreland Basin (SE Pyrenees, Spain) exposes continuous outcrops of late Eocene-early Oligocene fluvial deposits, from proximal to medial fluvial fan environments. The proximal deposits, located in the northern limb of the anticline, especially in the northwest zone, are characterised by conglomerates with minor interbedded sandstones, which present thick and wide sheet-like geometries with unscoured or scoured basal surfaces. These are interpreted to be the deposits of unconfined flash floods and wide-shallow channel streams. The medial deposits, covering the rest of the anticline, consist of interbedded beds of conglomerates, sandstones and claystones, deposited from braided channel streams and overbanks. Distal deposits are found towards the south, beyond the anticline, and are characterised by sandstone and clay deposits of terminal lobes or lacustrine deltas and interdistributary bays. This study assesses the impact of the primary depositional characteristics, diagenesis and deformation of the most heterolithic portion of the system, with implications for the understanding of folded fluvial reservoirs. Diagenetic processes, mainly mechanical compaction and calcite cementation, resulted in overall low matrix porosity, with limited relatively higher porosity developed in sandstone lithofacies in the medial deposits. Deformation associated with thrusting and fold growth resulted in the formation of abundant fractures, with relatively higher fracture intensities observed in sandstone lithofacies in the anticline crest. This study shows that post depositional processes can both improve and diminish the reservoir potential of basin proximal fluvial deposits, by the development of open fracture networks and by compaction-cementation, respectively. The comparison of the Puig-reig anticline with other similar settings worldwide shows that foreland basin margin locations can be potential areas for effective reservoirs, even in the case of low matrix porosity.

Keywords: fluvial fans, braided-stream flows, reservoir potential, Ebro Foreland Basin, Pyrenees.

1 Introduction

Reservoirs in foreland basins and adjacent fold-and-thrust belts host some of the most significant hydrocarbon resources in the world , e.g., the Zagros fold-and-thrust belt, the Persian Gulf, the Amu-Darya Basin, the Tarim Basin, the Permian Basin (Mann et al., 2003; Wang et al., 2016), which are also one of the primary targets for low-carbon technologies such as carbon capture and storage (CCS) (Sun et al., 2020). Alluvial and fluvial fans are the main deposits at active margins of non-marine foreland basins (DeCelles and Cavazza, 1999; Horton and Decelles, 2001; Ventra and Clarke, 2018). Alluvial fans are often dominated by conglomeratic facies, and can be concurrent with flow deposits of larger distributive fluvial systems, which transfer large volumes of coarse and fine sediments across basins (Williams et al., 1998; Weissmann et al., 2013, 2015). These coarse clastic belts tend to present relatively restricted radial extent and show high architectural unpredictability due to the lack of viable conceptual models. Thus, hydrocarbon exploration and development at continental basin margins are generally considered to have high risk and low return (Moscariello, 2018). However, alluvial fan and fluvial fan successions at basin margins have good preservation potential if the subsidence rate creates sufficient space to accommodate the significant sediment thickness (Moscariello, 2005). Complex sedimentary and structural characteristics at the basin margins can result in strong reservoir heterogeneity. Reservoir quality in such settings is mainly controlled by their sedimentary characteristics, e.g., petrographic characteristics and stratigraphic sequence, as well as the diagenesis and fracturing processes that they experience (e.g., Morad et al., 2010; Taylor et al., 2010; Zhang et al., 2011; Watkins et al., 2018). Due to the limited well data and seismic resolution of subsurface reservoirs, outcrop analogues play an important role in improving the accuracy of reservoir prediction in the subsurface (e.g., Howell et al., 2014), by providing reliable geological conceptual models and quantitative attribute information (Dichiarante et al., 2020). It is therefore essential to systematically study outcropping reservoir analogues to fully understand and predict the distribution and reservoir potential of alluvial-fluvial deposits in the subsurface.

The northern margin of the Ebro Basin and the adjacent South Pyrenean fold-and-thrust belt present multiple alluvial fans and distributive fluvial systems. For example, the Huesca and Luna systems (Upper Eocene to Oligocene) and series of marginal alluvial fans in the northern margin of the central Ebro Basin have been appraised and well documented (Hirst and Nichols, 1986; Nichols and Hirst, 1998; Arenas et al., 2001; Yuste et al., 2004; Luzón, 2005; Nichols, 2005; Donselaar and Overeem, 2008; Martin et al., 2021). Similar Upper Eocene to Oligocene alluvial and fluvial systems develop in the north-eastern margin of the Ebro Basin, such as the conglomerate-dominated Berga Group developing near frontal thrust sheets that translates into the fluvial Solsona Formation deposits towards the foreland basin (Sáez, 1987; Ford et al., 1997; Williams et al., 1998; Sáez et al., 2007; de Gibert and Sáez, 2009; Barrier et al., 2010). Based on the study of outcrops near the thrust sheets, Williams et al. (1998)

interpreted the Berga Group as a type II alluvial fan setting, using the terminology of Blair and McPherson (1994a, 1994b), due to repeated subaerial sheetflood events and mass movements. More recently, combining new outcrops across the Puig-reig anticline, Barrier et al. (2010) identified two distinct alluvial fans in the Berga Group. The first one is a large braided-stream-flow-dominated alluvial fan, which is related to the majority of the Berga Group deposits. The large alluvial fan was fed by a regional drainage basin including the south Pyrenean cover thrust sheets and the Pyrenean Axial Zone (Vergés, 2007). The second one is a small and local alluvial fan, which developed after the first large fan at the top of the Berga Group and is dominated by stream flows and gravity flows. This small alluvial fan was fed by a local drainage basin, extending only on the outermost cover thrust sheets.

The alluvial-fluvial strata show high potential to become effective reservoirs, e.g., the Puig-reig anticline, which was assessed as a potential site for gas storage (Instituto Geológico y Minero de España, 1995). Besides, the well-exposed outcrops can provide excellent reservoir analogues to determine the reservoir potential of folded alluvial-fluvial successions at basin margins. Previous studies of the alluvial-fluvial deposits in the north-eastern Ebro Basin were focused on the description and interpretation of the sedimentary environments and the interactions between sedimentation and tectonic activities (Williams et al., 1998; Sáez et al., 2007; Barrier et al., 2010; Carrigan et al., 2016), whereas these well-exposed outcrops have not been used as analogues to explore the reservoir potential of similar sedimentary systems in the subsurface. In this study, we focus on the Puig-reig anticline, which continuously exposes high-quality outcrops that present variations of sedimentary facies across the structure. We quantitatively describe and interpret the lithofacies and sedimentary facies of the deposits as well as their distribution over the Puig-reig anticline. In addition, we determine the reservoir quality of different lithofacies and their structural positions along the anticline based on a comprehensive analysis of lithology, cement, porosity, fracture distribution to explore the reservoir potential of the studied anticline and other similar systems at basin margins. This allows an assessment of how primary depositional characteristics as well as subsequent diagenetic and tectonic processes may influence the resource and storage potential of basin proximal deposits.

2 Geological setting

The Pyrenees is a doubly verging orogenic belt that formed during the continental collision between the Iberian and European plates from Late Cretaceous to Miocene (Muñoz, 1992; Vergés et al., 2002). This orogenic belt is characterised by an antiformal stack of basement-involved thrusts (the Axial Zone) surrounded by two fold-and-thrust belts that were transported to the north and south over the Aquitanian (France) and Ebro (Spain) foreland basins, respectively (Choukroune, 1989; Roure et al., 1989; Muñoz, 1992). The eastern part of the Ebro Basin displays an irregular shape bounded by the Pyrenees to the north and the Catalan Coastal Range to the southeast (Fig. 1A, B) (Vergés, 1993). The Vallfogona thrust represents the major frontal thrust between the SE Pyrenean thrust sheets and the Ebro Basin (Vergés et

al., 1998). The Busa syncline and the Puig-reig anticline developed along the footwall of the Vallfogona thrust during Late Eocene and Oligocene (Fig. 1B, C) (Vergés, 1993). The Busa syncline developed over a blind thrust flat (Busa thrust) connected to the Vallfogona floor thrust. A geometric reconstruction allowed an interpretation of the Puig-reig anticline as the consequence of a duplex stack in deep (Vergés, 1993). The Puig-reig is a km-scale south-verging gentle anticline with a flat hinge. The fold-trend is ESE/WNW, slightly oblique to the main Pyrenean structures (Vergés, 1993).

The Ebro Basin sediment fill includes synorogenic Paleocene to Oligocene marine to non-marine deposits lying on top of the Paleozoic basement and Mesozoic sediments (Fig. 1C). The lower part of the Puig-reig anticline is mainly composed of deltaic sandstones and marine marls of the Banyoles and Igualada formations (Middle-to-Upper Eocene), which deposited between the Beuda and Cardona evaporitic formations (Vergés et al., 1992; Serra-Kiel et al., 2003a, 2003b). These deposits were followed by alluvial-fluvial sediments of the Berga Group and the Solsona Formation (Upper Eocene to Oligocene), which were deposited during the endorheic stage of the Ebro basin (Puigdefàbregas et al., 1986, 1992) after a rapid transition from marine to continental environments of deposition (Costa et al., 2010). To the north, at the footwall of the Vallfogona thrust, the Berga Group consists of > 2000 m-thick alluvial and proximal fluvial conglomerates interbedded with minor sandstones and claystones, which displays growth strata (Ford et al., 1997; Suppe et al., 1997). To the south, the Berga deposits became progressively finer-grained and thinner-bedded fluvial conglomerates, sandstones and claystones of the Solsona Formation (Williams et al., 1998; Barrier et al., 2010), which translated downstream to distal terminal deposits of the Súria Formation (Sáez et al., 2007). These fluvial deposits graded into evaporites and calcareous lacustrine strata towards the centre of the Ebro Basin, e.g., the Torà, Barbastro, Castelltallat and Calaf formations (Sáez, 1987; Del Santo et al., 2000; Sáez et al., 2007). These formations collectively represent the basin proximal to basin centre facies within an internally drained continent basin. The formation subdivision of the Berga Group used in this study follows the scheme of Williams et al. (1998). In the study area, we focus on the Camps de Vall-Llonga Formation, a sub-unit of the Berga Group, that covers the northern zone of the Busa syncline and a large area of the Puig-reig anticline, and the Solsona Formation that is mainly observed in the southern limb of the anticline (Fig. 1D, E).

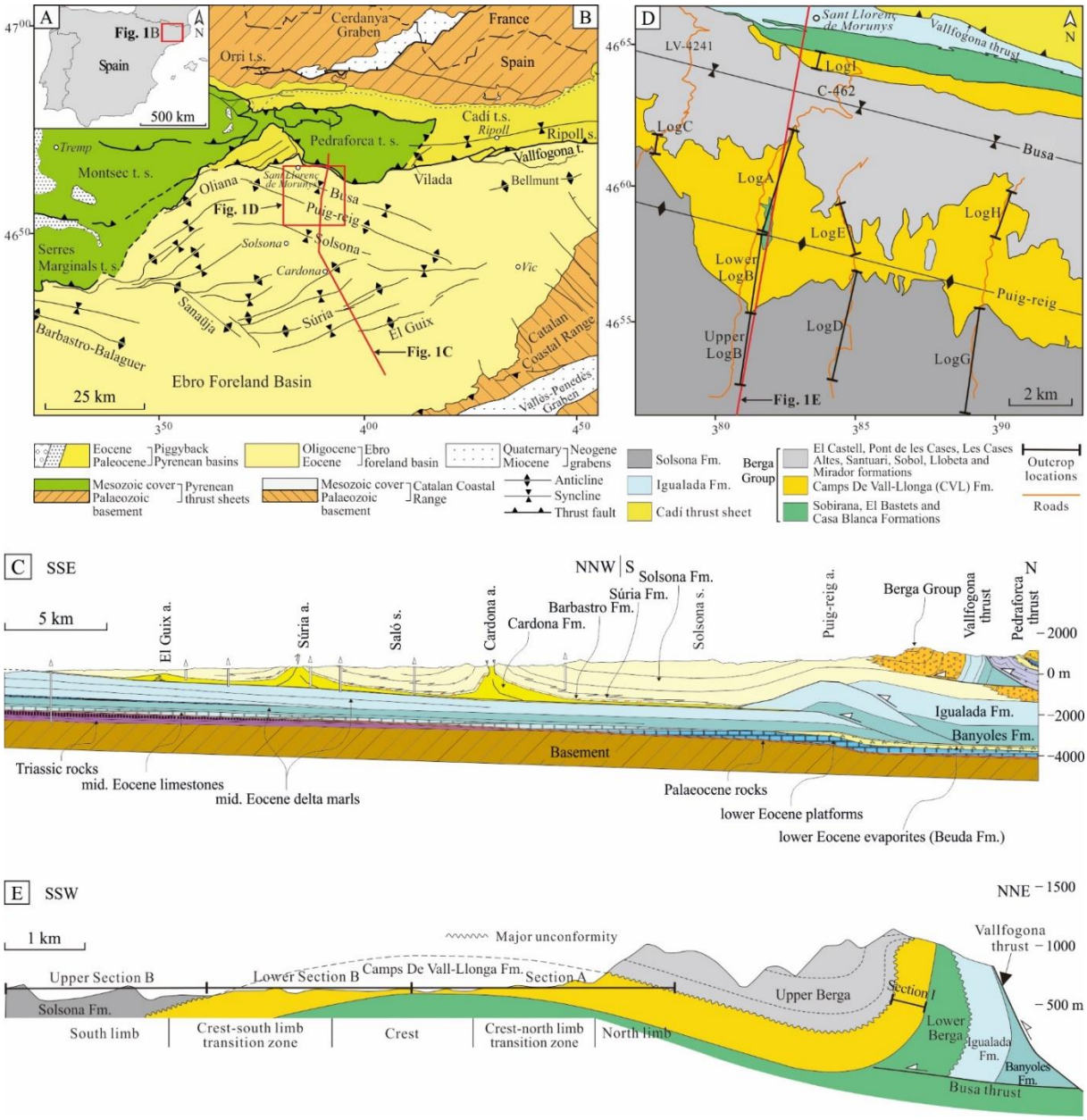

Fig. 1. (A-B) Geographical location and main structural units of the SE Pyrenean fold-and-thrust belt (Vergés, 1993). (C) Geological cross section of the frontal part of the SE Pyrenean fold-and-thrust belt and the Ebro Basin (Vergés, 1993). (D-E) Distribution of the Berga Group and the Solsona Formation and location of outcrops. The strata distribution in Fig. 1D is based on the regional geological map of Catalonia (Institut Cartogràfic i Geològic de Catalunya, 2006). The formation subdivision of the Berga Group follows the scheme of Williams et al. (1998). Fig. 1E is modified from Williams et al. (1998) and Barrier et al. (2010).

3 Outcrops and methods

The Puig-reig anticline presents excellent outcrops along roads that cut through the structure in a roughly north-south direction, between the towns of Sant Llorenç de Morunys in the north and Solsona in the south (Fig. 1B, D). Seven high-resolution (decimetre-scale) stratigraphic logs with a total thickness exceeding 3,000 m were built (Fig. 1D). Among these, logs A, C, E and H and the lower

portion of log B represent the strata of the Camps de Vall-Llonga Formation, while logs D and G and the upper portion of log B correspond to the Solsona Formation. The ca. 9 km-long geological cross-section of the Puig-reig anticline (sections A and B, Fig. 1E) is roughly parallel to the N-S shortening direction of the South-eastern Pyrenees and displays the continuous transition from proximal to relatively distal deposits. Moreover, log I of the Camps de Vall-Llonga Formation in the northern zone of the Busa syncline from Barrier et al. (2010) was utilised in this study for comparison. The detailed sedimentary data acquired include bedding thickness, grain size, sedimentary structures and presence of bioturbation, which collectively allow the identification of sedimentary facies and facies associations. The Puig-reig anticline was divided into five structural positions from north to south (i.e., north limb, crest-north limb transition zone, crest, crest-south limb transition zone and south limb; Fig. 1E). The terms 'proximal' and 'distal' were not used to name the structural positions as in other studies (e.g., Ge et al., 1997; Martínez-Martínez et al., 2002) to avoid potential confusions with sedimentary system terms used to divide facies and environments of deposition (i.e., proximal, medial and distal).

To determine rock composition, diagenetic alteration and porosity, 108 polished thin sections from host rocks and calcite veins were made from collected samples. These samples are representative of the different sedimentary lithofacies that can be defined in the area and different structural positions of the anticline. Petrographic observations were taken using a Zeiss Axiophot optical microscope and a Technosyn Cold Cathodoluminescence microscope, model 8200 Mk5-1 operating 16 to 17 kV and 270 to 290 μA gun current. Among these, 30 sandstone thin sections were selected for rock composition analysis using the point-counting method (300-400 points) to reveal potential compositional variations in different sedimentary lithofacies. In total, 60 thin sections were analysed using NIS Elements and Image J software (Schneider et al., 2012) to quantitatively process microphotographs to determine cement contents and matrix porosity. Based on the colour differences between different components, matrix porosity was determined using microphotographs in parallel nicols, while cement contents were determined using microphotographs in cathodoluminescence. To quantitatively analyse the effect of diagenetic alteration on porosity loss, the original porosity (P_o) of different lithologies was calculated based on Scherer's empirical formula (Scherer, 1987), and the proportion of original porosity destroyed by cementation (PL_{cem}) and by compaction (PL_{com}) of different lithologies were calculated based on Houseknecht's formulas (Houseknecht, 1987):

$$P_o = 20.91 + 22.9/S_o \quad (1)$$

$$PL_{cem} = \frac{P_{cem}}{P_o} \times 100\% \quad (2)$$

$$PL_{com} = (P_o - P_{cem} - \mathrm{P}_r)/P_o \times 100\% \quad (3)$$

where S_o is the Trask sorting coefficient of grain size, whose values of different lithologies were acquired from grain size analysis data from Sun (2018); P_{cem} is cement content; and P_r is residual porosity.

Abundant fractures were observed in the folded sediments of the Puig-reig anticline due to intensive

tectonic deformation, which could exert a significant effect on their reservoir potential as important fluid migration pathways and storage space. The data and analysis of the fracture networks in the Puig-reig anticline from (Sun et al., 2021) were incorporated into this study to comprehensively analyse the reservoir potential in the anticline.

4 Results

4.1 Sedimentology

Eight lithofacies were identified based on lithological characteristics and sedimentary structures, including three conglomerate facies, four sandstone facies, and one fine-grained facies (Table 1), which can combine into six lithofacies associations.

Table 1. Subdivision and description of typical lithofacies.

Lithofacies	Description
Gs1	pebble to boulder, occasional outsize clasts, very poor sorting, clast- to reddish matrix-supported, mainly massive structure and minor rough-stratified structure, unscoured or slightly scoured basal surface, sheet-like geometry
Gs2	pebble to cobble, poor sorting, clast-supported, grey to reddish sand matrix, mainly massive structure, slightly or deep scoured basal surface, sheet-like geometry
Gch	pebble to cobble, moderate to poor sorting, clast-supported, massive structure, scoured basal surface, channelised geometry
Smi	fine to coarse sandstone, mainly massive structure, tabular geometry or sandstone lens, limited burrows
Sm	mainly medium and coarse sandstone, massive structure, tabular geometry, limited burrows
Sl	mainly fine to very fine sandstone, mainly parallel bedding structure and minor cross bedding structure, tabular geometry, common burrows
Sch	medium to coarse sandstone, scattered gravelly clasts or muddy rip-up clasts, massive structure, channelised geometry
F	claystone to siltstone, tabular geometry, intensive weathering, erosion and pedogenesis, very common trace fossils

4.1.1 Lithofacies

Conglomerate lithofacies (Gs1, Gs2 and Gch)

The conglomerate lithofacies is subdivided into three subfacies (Gs1, Gs2 and Gch), based on subtle internal lithological differences. All subfacies have polygenic clasts composed of carbonate, siliciclastic, igneous and metamorphic lithologies. In subfacies Gs1, the clasts consist of very poorly sorted and subrounded pebbles to small boulders, with occasional outsize carbonate clasts. This lithofacies is clast- to matrix-supported. The matrix consists of reddish sands to small pebbles and lacks clays (Fig. 2A). Gs1 conglomerate bodies tend to present a massive structure and minor rough-stratified layers, unscoured or slightly scoured basal surfaces, and a sheet-like geometry. The thickness of a single bed can range from 1 to 6 m, while bed associations can be up to around 50 m. Horizons can be traced over several kilometres using satellite imagery. Gs1 is only found in the upper part of log C, in the northwest zone of the Puig-reig anticline.

Subfacies Gs2 has relatively smaller grain size and lower matrix content compared to subfacies Gs1,

and stratified structure and unscoured basal surfaces are rarely observed. This lithofacies is composed of poorly sorted and subrounded pebbles to cobbles. It is mainly clast-supported and contains grey to reddish matrix of fine to coarse sands (Fig. 2B). Gs2 conglomerate bodies are massive, and have a slightly or deep scoured basal surface, and a sheet-like geometry. The thickness of a single bed generally ranges between 1 and 5 m, while bed associations can be up to around 50 m. Gs2 develops in the northern limb, mainly in log C and the upper part of logs A and E.

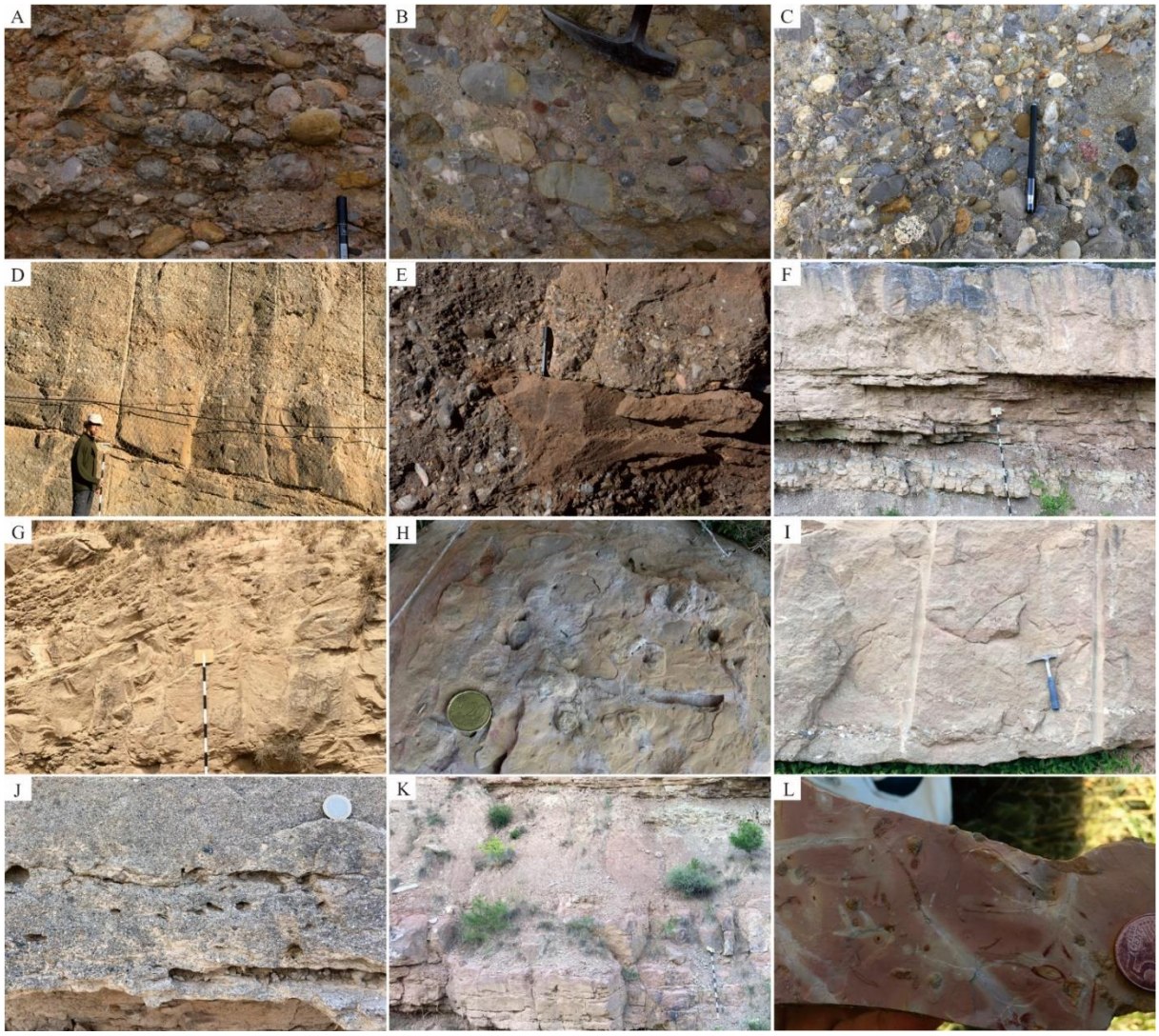

Fig. 2. Field images illustrating typical lithofacies and sedimentary characteristics. (A) Gs1: clast- to reddish matrix-supported pebble to small boulder conglomerate. (B) Gs2: clast-supported pebble to cobble conglomerate with reddish to grey matrix. (C) Gch: clast-supported pebble to small cobble conglomerate with grey sand matrix. (D-E) Smi: reddish to grey massive medium to coarse sandstone extending laterally or pinching out as sandstone lenses. (F) Sm: massive coarse or medium sandstone; Sl: parallel bedding fine sandstone. (G) Sl: cross-bedding fine sandstone. (H) Burrows in fine sandstone. (I) Sch: channelised pebbly coarse sandstone body. (J) Sch: muddy rip-up clasts in the bottom of channelised pebbly coarse sandstone. (K) F: reddish fine deposits with pedogenic characteristics. (L) Abundant trace fossils in fine-grained deposits.

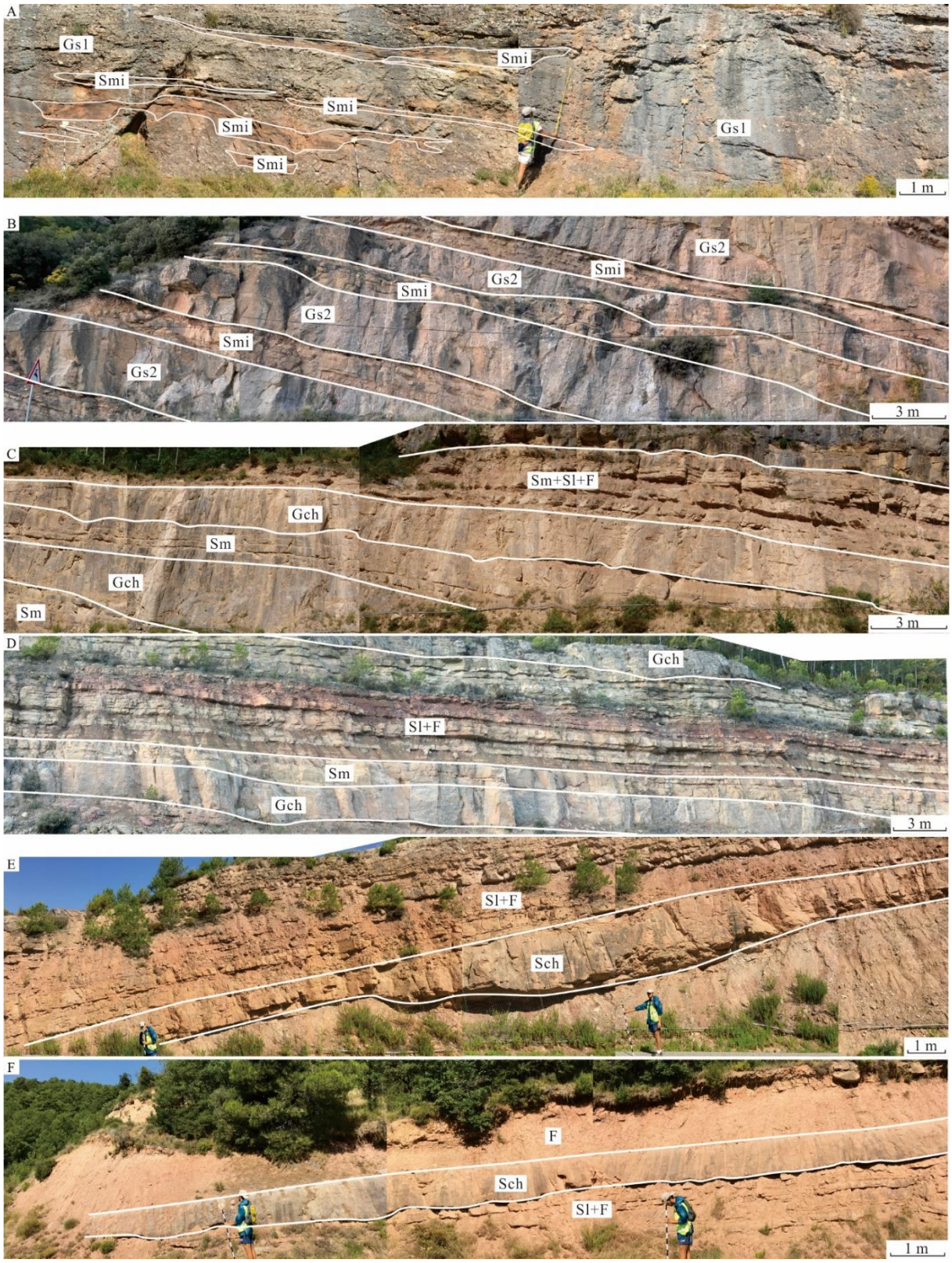

Fig. 3. Field images of typical sedimentary lithofacies associations. (A) LAp1: Gs1 with limited Smi lenses; (B) LAp2: Gs2 with Smi interlayers; (C) LAm1: channel fill Gch, Sm and Sl and minor overbank F; (D) LAm2: Gch channel lag and interlayers of Sm, Sl and overbank F; (E) LAm3: Sch channel lag and interlayers of Sl and overbank F; (F) LAm4: Sl and stable overbank F incised by Sch channel.

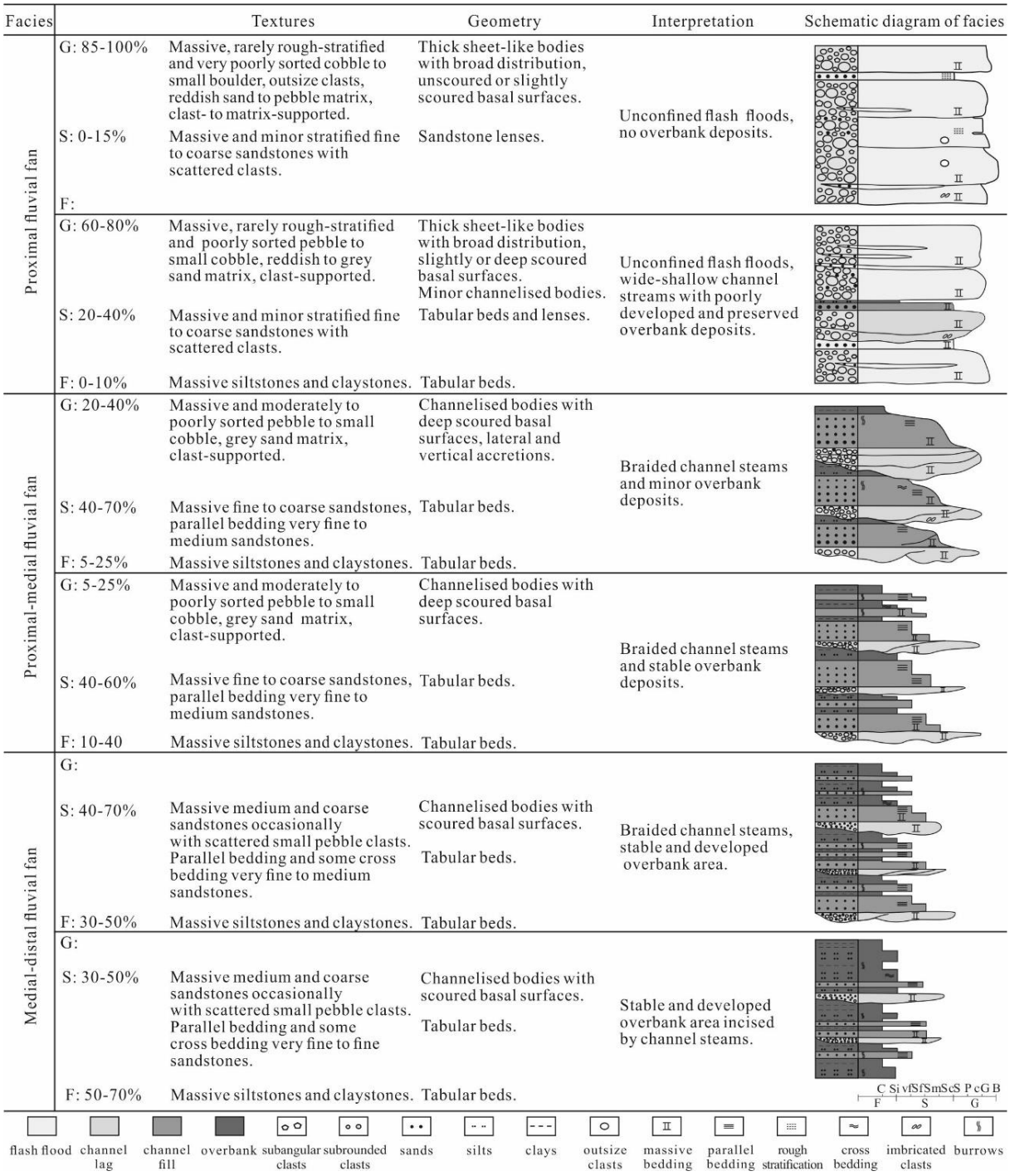

Fig. 4. Summary of sedimentary characteristics of typical lithofacies associations in the Puig-reig anticline. G, S and F refer to the percentage contents of conglomerate, sandstone and fine-grained lithofacies, respectively. C: claystone; Si: siltstone; vfS: very fine sandstone; fS: fine sandstone; mS: medium sandstone; cS: coarse sandstone; P: pebble; cG: cobble; B: boulder.

Subfacies Gch consists of moderately to poorly sorted and subrounded pebble to small cobble size clasts, which tend to be clast-supported with grey, fine to coarse sand matrix (Fig. 2C). Gch conglomerate bodies generally present a channelised geometry and deep scoured basal surfaces, which differ from Gs1 and Gs2 conglomerate bodies. Gch presents lateral wedge-out and changes laterally and

vertically to sandstones and claystones. The thickness of a single bed generally ranges from 0.5 to 4 m. Gch is the most widespread conglomerate lithofacies, which develops in most areas of the anticline except for the southern limb.

Sandstone lithofacies (Smi, Sm, Sl and Sch)

Subfacies Smi includes reddish to grey, medium and coarse sandstones and minor fine sandstones. These sandstone layers tend to present a massive structure with locally scattered gravel clasts of a few millimetres in size, and in some minor cases parallel-bedding can be observed. The thickness of Smi ranges from 0.2 to 2 m. They can present a tabular geometry interbedded with Gs2 (Fig. 2D) or occur as sandstone lenses within Gs1 and Gs2 conglomerate bodies that rapidly pinch out laterally (Fig. 2E). Very limited large (with diameter up to 1.5 cm) vertical or oblique burrows are observed in these coarse sand deposits. Smi mainly develops in the northern limb of the anticline.

Subfacies Sm is mainly composed of grey, medium and coarse sandstones. Sm sandstone layers tend to present a massive structure with bedding thickness ranging from 0.5 to 1.5 m (Fig. 2F). They show a tabular geometry with sharp and unscoured basal surfaces. They are commonly found above Gch layers or interbedded with laminated fine sandstones. Burrows are uncommon in these coarse sandstone layers, similarly to Smi layers. Sm is one of the dominant lithofacies and is widely observed across the anticline.

Subfacies Sl is composed of grey, fine to very fine sandstones and minor medium sandstones. Parallel-bedding is the most common structure (Fig. 2F), while cross-bedding is occasionally observed (Fig. 2F). Sl tends to be interbedded with Sm and fine deposits. Vertical, oblique or horizontal burrows are more commonly present in these fine sandstones (Fig. 2H). Sl is another dominant lithofacies and widely developed across the anticline.

Sch is composed of grey, medium to coarse sandstones, with scattered gravelly clasts (Fig. 2I, J). It has a similar massive structure as Sm layers, but has a channelised geometry with scoured surfaces and generally develops at the bottom of lithofacies association. Muddy rip-up clasts are sometimes present at the bottom of Sch due to the scour and re-deposition of fine deposits (Fig. 2J). Sch mainly develops in the southern limb of the anticline.

Fine-grained lithofacies (F)

Lithofacies F includes reddish to grey siltstones and claystones. They occur as tabular bodies and are commonly interbedded with Sm and Sl (Fig. 2K). Small burrows and other trace fossils, e.g., *Taenidium barretti* and *Helminthoidichnites* (de Gibert and Sáez, 2009) are very common in these fine deposits (Fig. 2L). These deposits tend to be affected by intensive weathering, erosion and pedogenesis. Lithofacies F is widely developed across the anticline.

4.1.2 Lithofacies associations and sedimentary environments

Unconfined flash flood deposits with no overbanks (LAp1)

LAp1 association is dominated by lithofacies Gs1 with limited Smi interlayers that generally pinch out laterally as sandstone lenses (Figs. 3A, 4), which combine into large and structureless sheet-like bodies of coarse deposits with unscoured or slightly scoured basal surfaces. These characteristics collectively represent unconfined flow of a flashy nature (Blair and McPheerson, 1994; Nichols and Hirst, 1998; Williams et al., 1998). This association is dominantly found in the northwest portion of the Puig-reig anticline, i.e., the upper part of log C.

Unconfined flash flood deposits and wide-shallow channel deposits with limited overbanks (LAp2)

LAp2 association is composed of lithofacies Gs2, Smi and limited F. Lithofacies Smi and F can occur as stable tabular layers or pinch-out lenses (Figs. 3B, 4). This association presents large and structureless sheet-like geometries, slightly or deep scoured surfaces. These features can collectively represent unconfined flow of a flashy nature or wide-shallow channel flow (Arenas et al., 2001; Yuste et al., 2004; Luzón, 2005). This association is dominantly found in the northern limb of the anticline, mainly in log C and the upper part of logs A and E.

Channel filling deposits with minor or stable overbanks (LAm1 and LAm2)

LAm1 and LAm2 associations are composed of lithofacies Gch, Sm, Sl, and F. An overall fining-upward trend is observed in these two lithofacies associations, from channelised Gch to tabular and interbedded Sm, Sl and F lithofacies, which collectively represent braided channel streams and overbanks (Nichols and Hirst, 1998; Arenas et al., 2001). LAm1 association is characterised by channel fill deposits with minor overbank deposits, showing vertical or lateral accretions of conglomerates and sandstones (Figs. 3C, 4). LAm2 association is composed of channel fill conglomerates and sandstones and stable overbank fine deposits (Figs. 3D, 4). These lithofacies associations are distributed across the anticline except for the southern limb of the anticline.

Sandy channel filling deposits with stable overbanks (LAm3)

LAm3 association is composed of lithofacies Sch, Sm, Sl and F (Figs. 3E, 4). Compared to LAm1 and LAm2 associations, LAm3 also presents an overall fining-upward trend and is deposited from braided channel streams and overbanks. However, lithofacies Sch with channelised geometries and scoured basal surfaces replaced Gch conglomerate bodies as channel lag deposits. This association is dominantly found in the southern limb and slightly developed in the crest and crest-south limb transition zone of the anticline.

Stable overbanks incised by isolated channels (LAm4)

LAm4 association is composed of lithofacies Sch, Sl and F, which is characterised by stable tabular F and Sl deposits incised by channelised Sch bodies (Figs. 3F, 4). Compared to the LAm3 association, LAm4 also represents channel and overbank deposits, but it contains more overbank fine deposits and isolated channel deposits and does not present a clearly fining-upward trend. This association is occasionally found in the southern limb of the anticline.

The characteristics of the described lithofacies associations (Fig. 4) can collectively represent deposits from a fluvial fan system. The proximal deposits are mainly composed of LAp1 and LAp2 lithofacies associations deposited from unconfined flash floods and wide-shallow channels, with minor LAm1 and LAm2 lithofacies associations. The medial deposits are composed of LAm1 to LAm4 lithofacies associations deposited from braided channel streams and overbanks. The proximal-medial fluvial fan is mainly composed of LAm1, LAm2 and limited LAm1 associations, while the medial-distal fluvial fan is mainly composed of LAm3 and limited LAm2 and LAm4 associations. Based on the distribution of lithofacies (Fig. 5), the conglomerate lithofacies decreases from log C to log H and from log A to log B, log E to log D and log H to log G, respectively. Furthermore, the lithofacies associations present a similar distribution pattern (Fig. 6). LAp1 and LAp2 associations decrease significantly from log C to log H (WNW to ESE) and from log A to log B (north to south), which are replaced by LAm1 and LAm2 and finally translated into LAm3 and LAm4 south-eastward. The distributions of lithofacies and lithofacies associations are consistent with a fluvial system with an overall south-east downstream trend.

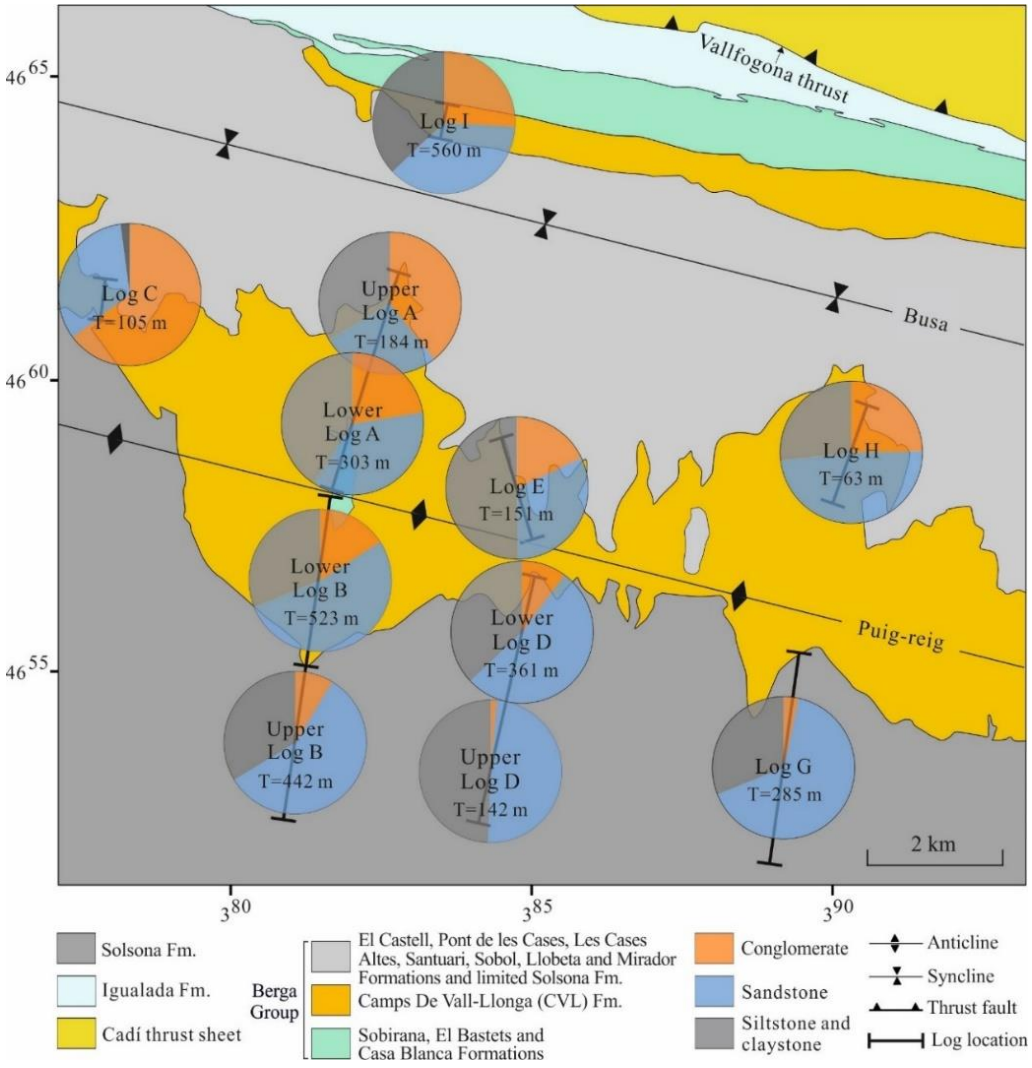

Fig. 5. Percentage distribution of lithofacies (conglomerate, sandstone and fine-grained facies) in the Puig-reig anticline. *T* is the cumulative thickness of deposit layers. Log I is from Barrier et al. (2010).

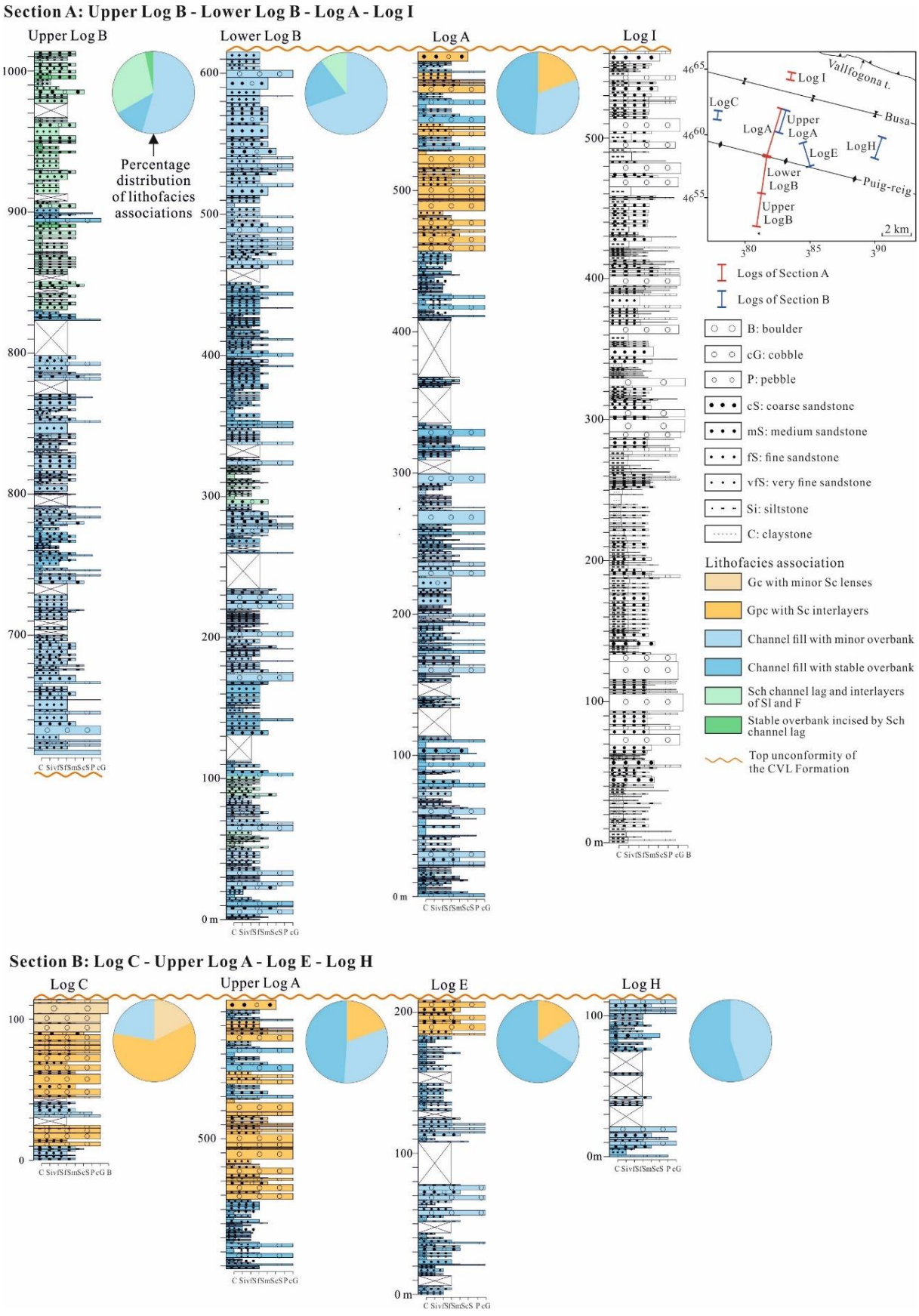

Fig. 6. Correlation of stratigraphic logs and percentage distribution of lithofacies associations in the Puig-reig anticline. Log I is from Barrier et al. (2010).

4.2 Reservoir characteristics

Based on Folk's (1980) sandstone classification scheme, all sandstone samples of the studied area plot within the litharenite field, with lithic content ranging from 60% to 90%, quartz content ranging from 5% to 30%, and very limited feldspar content (Fig. 7A). Based on Zuffa's (1980) classification scheme of hybrid arenites, these samples mainly plot in the carbonate extrarenite field with minor in the non-carbonate extrarenite field (Fig. 7B). The content of carbonate extrabasinal grains mainly ranges from 40% to 70%, while the content of non-carbonate extrabasinal grains, including non-carbonate lithic, quartz, feldspar, mainly ranges from 30% to 60%. The proximal fluvial fan has a slightly higher content of carbonate extrabasinal grains, compared to the medial fluvial fan. However, as can be seen in Fig. 7, no portion of the fan has a distinctive compositional signature with overlap between the different samples.

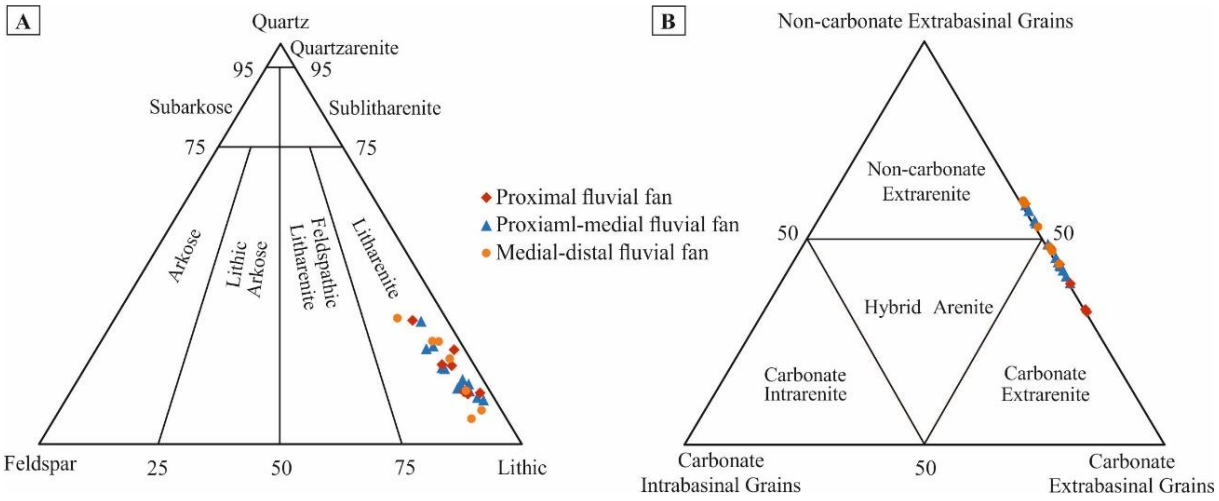

Fig. 7. Classification of sandstones based on framework grain composition after (A) Folk's (1980) and (B) Zuffa's (1980) classification schemes.

Most deposits present very low matrix porosity. Matrix porosity mainly ranges from 0% to 2% (Fig. 8), with an average of 1.2%. It varies across different lithofacies and presents an overall increasing and then decreasing trend with increasing grain size (Fig. 9A). Limited samples present relatively higher matrix porosity concentrated in lithofacies Sch and Sm in the crest, crest-limb transition zones and southern limb of the anticline, mainly ranging from 2% to 8% (Fig. 8). Calcite is the dominant cement mainly ranging from 5% to 15% (Fig. 8), with an average value of 11.6%, which also presents an overall increasing and then decreasing trend with increasing grain size (Fig. 9B). Sandstone lithofacies has slightly higher cement content compared to conglomerate and fine-grained lithofacies, with an average value of 12.7%. There is no clear correlation between cement content and matrix porosity (Fig. 10).

Original porosity was calculated based on the Trask sorting coefficient of different lithologies from Sun (2018). Sorting coefficient of siltstone and sandstone mainly ranges from 1.3 to 2.3, resulting in original porosity between 31% to 39% with an average of 35%, while sorting coefficient of

conglomerate mainly ranges from 1.6 to 2.6, resulting in original porosity between 30% to 35% with an average of 32%. Cementation and compaction are the most significant diagenetic processes in the Puig-reig anticline. Original porosity destroyed by cementation mainly ranges from 20% to 50%, whereas that destroyed by compaction mainly ranges from 40% to 80% (Fig. 11A, B). Limited samples with relatively high matrix porosity have porosity destroyed by cementation and compaction mainly ranging from 30% to 50% and from 40% to 60%, respectively (Fig. 11A).

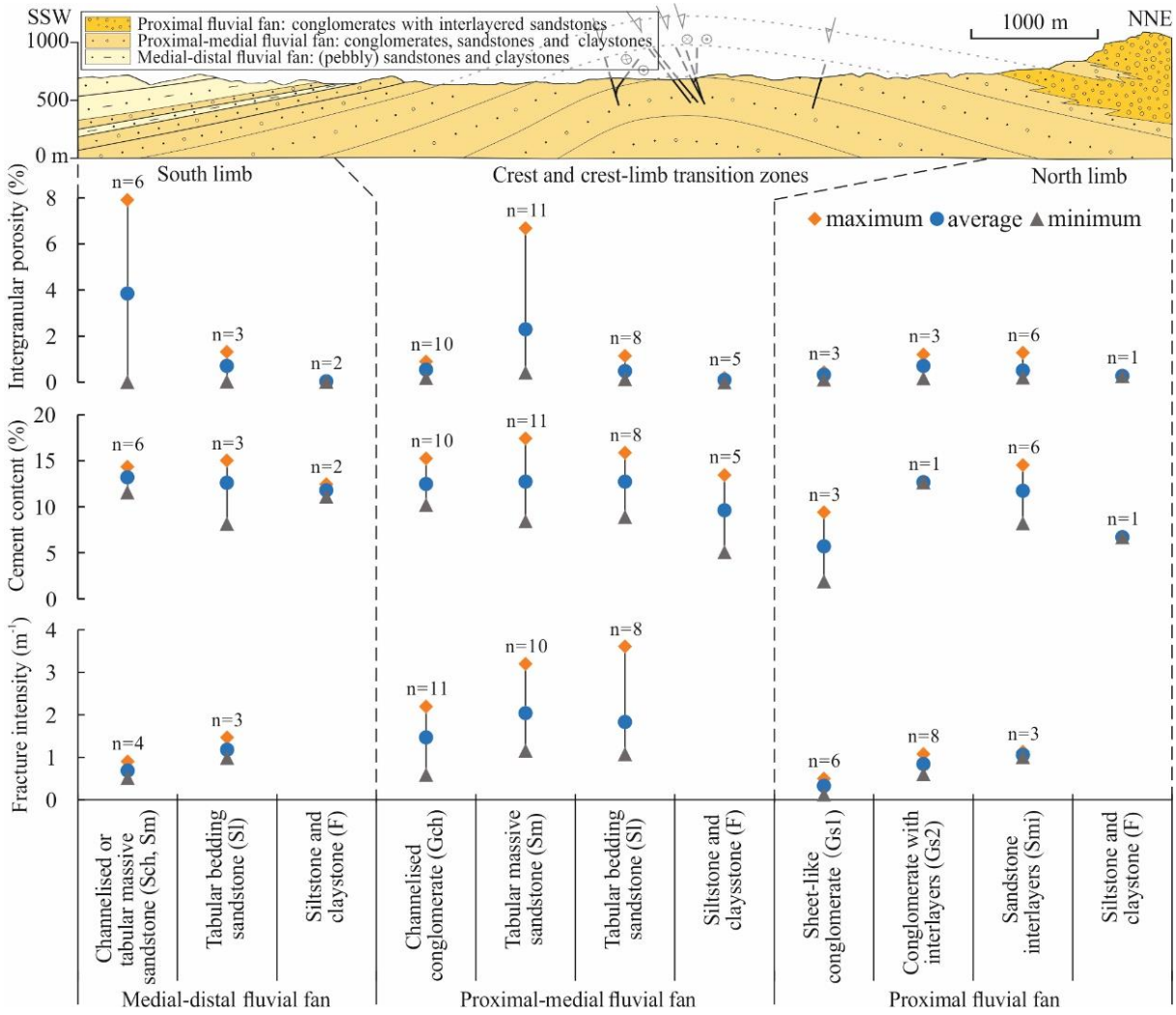

Fig. 8. Distribution of matrix porosity, cement content and fracture intensity in different lithofacies, sedimentary facies and structural positions (*n* is the number of thin sections or fracture scanlines sampling each lithofacies). The cross section is modified from Cruset et al. (2016). Fracture intensity data is from Sun et al. (2021).

Fracture intensity data were obtained from previous research in the Puig-reig anticline (Sun et al., 2021). Fine-grained lithofacies tend to experience intensive weathering, erosion and pedogenesis and thus impede the identification of fracture attributes in these layers. Thus, fracture attributes were only measured in conglomerate and sandstone lithofacies using the linear scanline method. Fracture intensity mainly ranges from 0.5 m^{-1} to 2.5 m^{-1}, with relatively higher values developed in the crest and crest-limb transition zones of the anticline, especially in sandstone lithofacies with values larger than 1 m^{-1}

(Fig. 8). Fracture intensity decreases with increasing distance to anticline hinge and with increasing bedding thickness (Fig. 9C, D).

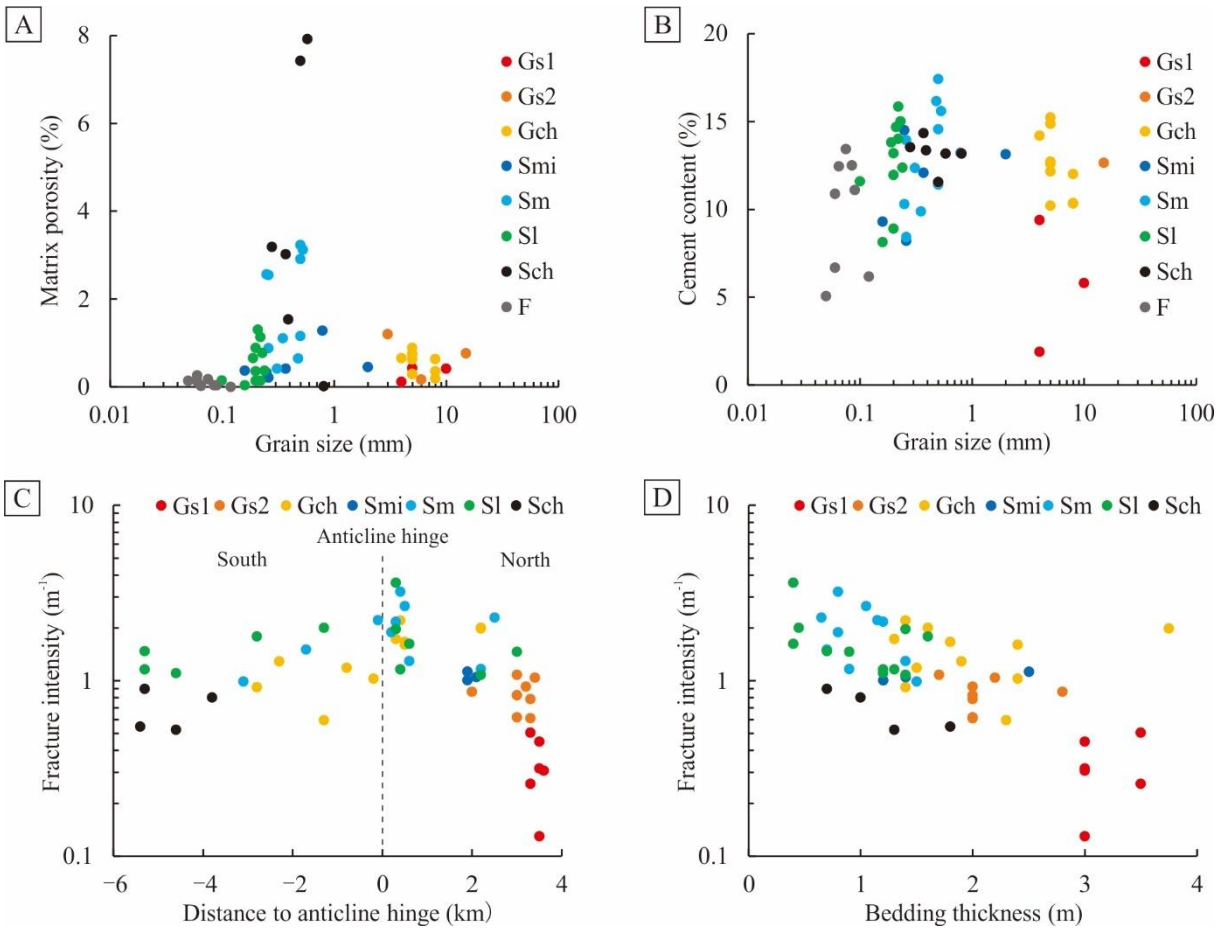

Fig. 9. Crossplots between reservoir characteristics and sedimentary characteristics and structural position. (A) Matrix porosity *vs.* grain size. (B) Cement content *vs.* grain size. (C) Fracture intensity *vs.* distance to anticline hinge. (D) Fracture intensity vs. bedding thickness. Fracture intensity data is from Sun et al. (2021).

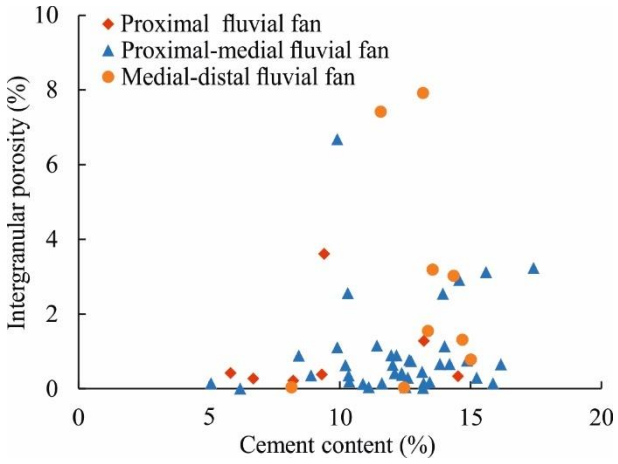

Fig. 10. Crossplot of cement content *vs.* matrix porosity.

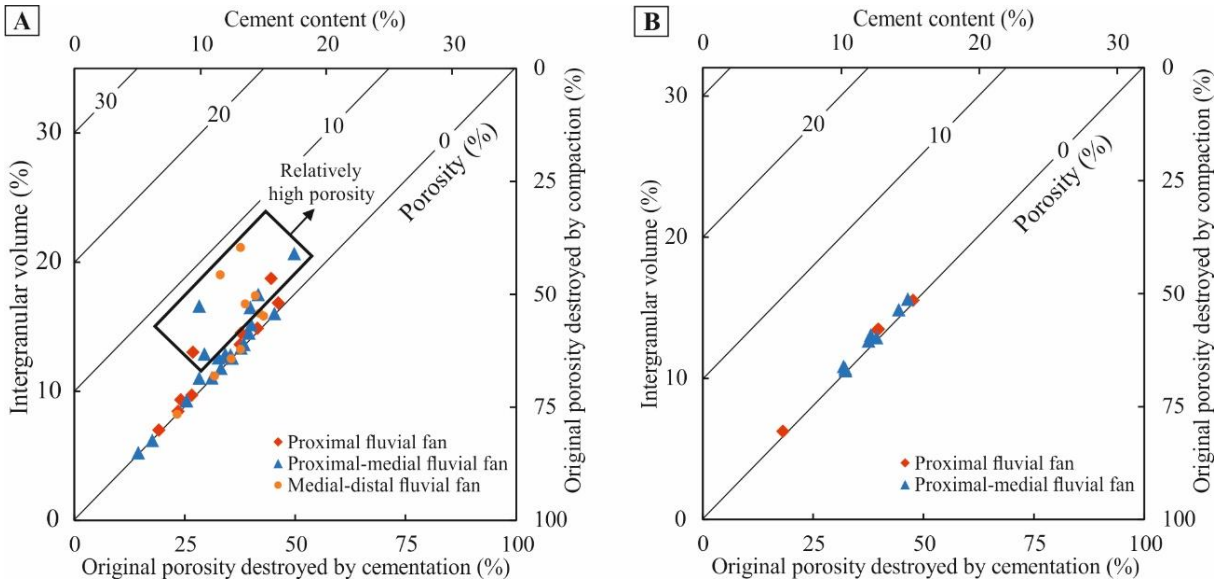

Fig. 11. Crossplots of intergranular volume *vs.* cement content and porosity loss by compaction *vs.* cementation for (A) sandstone and fine-grained lithofacies and (B) conglomerate lithofacies.

5 Discussion

5.1 Fluvial fan sedimentary environments

Previous studies interpreted the whole Berga Group as alluvial fan deposits that wedge out into fluvial fan deposits of the Solsona Formation (Williams et al., 1998; Barrier et al., 2010). However, here we focus on the analysis of the Camps de Vall-Llonga Formation of the Berga Group and the Solsona Formation in the Puig-reig anticline. They are interpreted as deposits of a proximal to medial fluvial fan, based on the comprehensive analyses of the drainage basin, fan size and sedimentary characteristics and the comparison to other similar sedimentary systems in the central Ebro Basin (Hirst and Nichols, 1986; Arenas, 1993; Nichols and Hirst, 1998; Arenas et al., 2001).

Alluvial fan deposits are sourced by areal-limited drainage basins, whereas fluvial fan deposits tend to have larger drainage basins with long-term expansion and integration of catchments (Moscariello, 2018). The Camps de Vall-Llonga and Solsona deposits are composed of polygenic clasts, including both carbonate and non-carbonate clasts (Fig. 7B). As noted by Riba (1976), the non-carbonate clasts of acid-intermediate plutonic rocks, Permo-Triassic red beds, Carboniferous micro-conglomerates, rare metasedimentary rocks and basic igneous rocks, all come from the basement of the Pyrenean Axial Zone. The varied carbonate clasts reflect source areas in the Mesozoic-Cenozoic series of the south Pyrenean thrust sheets and the Pyrenean Axial zone (Devonian carbonates). The polygenic compositions reveal the drainage basin of the Camps de Vall-Llonga and Solsona deposits extending from the south Pyrenean thrust sheets to the Pyrenean Axial Zone, which is consistent with the large and regional-scale drainage basin of fluvial deposits.

Alluvial fans may range widely in radial length, rarely up to 10 km in exceptional circumstances

favouring particularly long runout for sediment-water mixtures (e.g., Blair, 2003), but the radial fans extent generally varies from several hundred metres to a few kilometres at most (Blair and McPheerson, 1994; Moscariello, 2018). The Camps de Vall-Llonga deposits spread over a large area from the Vallfogona thrust to the Puig-reig anticline. The Camps de Vall-Llonga formation is exposed for around 9 km in the direction perpendicular to the Vallfogona thrust and for around 20 km in a direction roughly parallel to the thrust based on the studied outcrops and the regional geological map of the study area (Institut Cartogràfic i Geològic de Catalunya, 2006). Considering the folding of strata and the unexposed strata to the south, the actual extent of the Camps de Vall-Llonga deposits should be larger than the observable extent, which is larger than that of typical alluvial fans. There has been much debate regarding how alluvial fans are distinguished from distributive (fluvial) fan systems (Ventra and Clarke, 2018). In reality, there is likely a continuum between the two systems that the Camps de Vall-Llonga Formation sits close to. However, its size and prevalence of channelised facies indicate that they are the deposits of a distributive fluvial system (fluvial fan).

In the northwest portion of the study area, the Camps de Vall-Llonga Formation is dominated by the proximal deposits from flash floods and wide-shallow channel streams. The development of flash floods in the proximal fluvial fans is also documented in the northern margin fans of the central Ebro Basin (Luzón, 2001, 2005). The channel fill deposits within flash flood conglomerates may have formed during the waning stages of flood events or developed on fan surfaces by later confined flow events (Blair and McPheerson, 1994; Nichols and Hirst, 1998). The rest of the Camps de Vall-Llonga Formation is dominated by the medial deposits from braided channel streams and overbanks. They tend to present an overall fining-upward trend from channel fill conglomerates and sandstones to overbank fine deposits, representing cyclic (avulsive) behaviour of the system as it developed through time. In the crest-south limb transition zone of the Puig-reig anticline, the Solsona Formation is still dominated by channel fill and overbank deposits. There are no perceptible differences of sedimentary environments in the transition area between the Camps de Vall-Llonga and Solsona formations, i.e., the contact between the upper and lower log B (Fig. 6). In the southern limb, conglomerate channel lags are gradually replaced by (pebbly) sandstone channel lags, i.e., in the upper part of upper log B. We interpret that these deposits still belong to the medial portion of the fluvial fan due to a lack of the terminal deposits of distal fluvial fan and the lacustrine sedimentary characteristics. The Camps de Vall-Llonga and Solsona formations therefore represent mappable units rather than distinct separate sedimentary systems. The distal fluvial deposits can be found 20 km south of our study area. Deposits here are composed of terminal lobes during low lake-level stages and fluvial-dominated deltas and interdistributary bays during high lake level stages, which grades into evaporites and calcareous lacustrine strata near the basin centre (Del Santo et al., 2000; Sáez et al., 2007). Based on observations from the whole Berga Group (Williams et al., 1998), paleocurrents are roughly directed towards the south or southeast, but they also comprise a large component subparallel to the mountain-front structures (Barrier et al., 2010). The decrease of

lithofacies associations dominated by conglomerates and the increase of lithofacies associations dominated by sandstones and fine deposits towards the south and southeast (Figs. 5, 6) is consistent with the overall paleocurrents of the Berga Group, supporting the interpretation of fluvial fan deposits.

However, we do not discard the possibility of several alluvial fans developing during the deposition of the Berga Group, which are restricted at the northern basin margin with small fan size and local drainage basins, e.g., the small stream-flow and gravity-flow-dominated alluvial fan identified by Barrier et al. (2010) at the top of Berga Group and located to the northwest in Fig. 1D. This has been observed to be the case in the northern margin of the central Ebro Basin where two distributive systems (the Luna and Huesca fluvial systems) coincide and interfinger with a series of marginal alluvial fans (Hirst and Nichols, 1986; Nichols and Hirst, 1998; Arenas et al., 2001).

5.2 Reservoir potential of the folded fluvial succession in the Puig-reig anticline

Based on the distribution of calcite cement, porosity, fracture intensity and lithology in the Puig-reig anticline, here we discuss the controlling factors of reservoir quality and the reservoir potential of the folded fluvial succession in the Puig-reig anticline in the SE Pyrenees.

Reservoir matrix porosity is mainly controlled by the sedimentary characteristics of deposits and the diagenetic processes they experience (Dos Anjos et al., 2000; Bjørlykke, 2014). In the Puig-reig anticline, the fluvial deposits present an overall low matrix porosity due to intensive compaction and cementation (Fig. 10), but which varies across the different lithofacies. Relatively high matrix porosity concentrates in lithofacies Sch and Sm in the medial fluvial fan, regardless their relatively higher cement contents with respect to other lithofacies (Fig. 9A, B). Compared to lithofacies Sl and F, Sch and Sm have low contents of ductile matrix. Compared to conglomeratic facies, these medium to coarse sandstones present better grain sorting and lower matrix contents, thus resulting in relatively higher original and residual porosity. Based on the original porosity of sandstone and siltstone (35% on average), the porosity destroyed by compaction of lithofacies Sch and Sm mainly ranges from 40% to 70% with 57% on average, whereas that of lithofacies Sl and F mainly ranges from 55% to 75% with 63% on average and from 60% to 85% with 73% on average, respectively. Lithofacies Sch and Sm experience relatively weaker compaction, resulting in more residual intergranular volume which can provide more space for cementation and residual porosity. This is the main reason for the coexistence of relatively higher residual porosity and calcite content in lithofacies Sch and Sm.

Fracture networks have a significant impact on reservoir performance. According to the systematic analysis of fracture networks in the Puig-reig anticline (Sun et al., 2021), fracture intensity is mainly affected by structural position, bedding thickness (Fig. 9C, D) and lithological association. The crest and crest-limb transition zones present relatively higher fracture intensity due to the greater curvature and finite strain they experience compared to the limbs (Figs. 8, 9C), if a Tangential Longitudinal Strain model (TLS) is assumed (Hudleston and Treagus, 2010). This observation is consistent with some

previous studies of fracture distribution in folds (e.g., Iñigo et al., 2012; Awdal et al., 2013; Watkins et al., 2015). If flexural slip was the dominant folding mechanism, then thin and soft layers in limbs would be ones subjected to the highest strain. However, our field data better matches the first option because the anticline crest features more intensive fracturing than the limbs. Relatively thinner sandstone layers tend to present higher fracture intensity than thick conglomerate layers in all structural positions (Figs. 8, 9D), which is also consistent with some previous fracture studies (e.g., Florez-Niño et al., 2005; Wennberg et al., 2007). In addition, the lithological association of competent conglomerate or sandstone and incompetent fine deposits in medial fluvial deposits favour the development of abundant fractures, compared to the lithological association of competent conglomerate and sandstone in proximal fluvial. Based on the analysis above, lithofacies Sl and Sm in the medial fluvial fan located in the crest and crest-limb transition zones of the anticline feature relatively higher fracture intensity than other structural positions and lithofacies.

Based on the distribution of calcite cement, porosity and fracture intensity, the medial fluvial sandstones in the crest and crest-limb transition zones (35-55% of all lithofacies in these zones) present relatively greater potential to be effective reservoirs due to the high fracture intensity (1-3.5 m^{-1}). The northern limb presents relatively high percentages of sandstone and conglomerate deposits (65-100%) and lower percentages of fine deposits (0-35%), especially in the northwest zone (Fig. 5). However, the sandstone and conglomerate bodies have low potential to become effective reservoirs due to their low matrix porosity (<1.5%) and fracture intensity (<1.2 m^{-1}). The southern limb presents relatively higher percentages of sandstones (50-65%) and very low percentages of conglomerates (0-15%) (Fig. 5). The sandstones have relatively low fracture intensity (<1.5 m^{-1}), but present some reservoir potential in Sch and Sm lithofacies due to relatively higher matrix porosity (3.9% on average).

5.3 Reservoir potential of folded alluvial-fluvial successions at foreland basin margins

As one of the dominant sedimentary systems at the active margins of non-marine foreland basins, alluvial and proximal fluvial fans tend to present heterogeneous reservoir potential due to the interplay between complex sedimentary, diagenetic and deformation processes. Unravelling their reservoir characteristics is therefore key to the success of subsurface operations.

Compared to fluvial fans, alluvial fans present radial-limited fan extent (Blair and McPheerson, 1994). Debris-flow alluvial fans tend to present poor primary reservoir quality due to texturally immature debris deposited from debris flows and hyperconcentrated flows. These deposits have varied reservoir connectivity depending on their abundance in local sedimentary systems (Moscariello, 2018). On the other hand, water-lain alluvial fans, generally dominated by sheet floods, have better reservoir potential due to the presence of relatively better sorted deposits and reservoir connectivity (Moscariello, 2005). At basin margins, proximal fluvial deposits tend to consist of amalgamated channel belts with limited preservation of fine deposits (Weissmann et al., 2013). Thick conglomerate bodies can occur in proximal

fluvial deposits (Vincent, 2002), which can be associated with channelised non-cohesive gravity or hyperconcentrated flows (Moscariello, 2018). Besides, flash floods can develop in these proximal fluvial environments, e.g., in the Puig-reig anticline (Fig. 6) and other cases (Luzón, 2001, 2005), resulting in large and coarse sheet-like deposits. Compared to debris-flow alluvial fans, these proximal fluvial deposits can present higher reservoir potential due to their higher textural maturity and better reservoir connectivity. In addition, fluvial deposits at basin margins mainly result from medial fluvial fans, dominated by channel belts with varied overbank fine deposits. Although medial fluvial deposits present a downstream reduction of the reservoir volume and a corresponding increase of overbank fine deposits, they are still dominated by conglomerate or sandstone reservoirs at basin margins and present higher textural maturity resulting in better primary reservoir quality. These water-lain alluvial fans and proximal to medial fluvial fans present high potential to be effective reservoirs without undergoing strong compaction and cementation.

Intensive diagenesis can result in low matrix porosity and permeability, and thus reduce the reservoir potential in alluvial-fluvial deposits (Morad et al., 2010; Lai et al., 2018). Carbonate cement is one of the prevailing authigenic minerals in these deposits (Hall et al., 2004; Taylor and Machent, 2011). In tectonically active settings, such as foreland basin margins, carbonate extrabasinal grains can become important sediments in alluvial-fluvial systems (Valloni and Zuffa, 1984; Morad et al., 2010). This is because such settings provide short time and distance for sediment transportation and exposure, thus resulting in relatively weak chemical weathering of these carbonate compositions (Zuffa, 1985). These extrabasinal carbonate grains favour the nucleation and growth of carbonate cement in these alluvial-fluvial deposits. In addition, at foreland basin margins, intensive fracturing, thrusting and folding are accompanied with fluid flow of various geological fluids including hydrothermal, meteoric and formation fluids, from which carbonate cement precipitates (Travé et al., 1997, 2000, 2007; Cruset et al., 2018, 2020). Thus, intensive carbonate cementation can result in an overall or localised low matrix porosity of alluvial-fluvial deposits at basin margins, e.g., the Peraltilla and Sariñena formations in the central Ebro Basin (Yuste et al., 2004), the Berga Group and the Solsona Formation in the eastern Ebro Basin (Cruset et al., 2016), the Siwalik Group in the Himalayan Basin (Guilbaud et al., 2012), and the Wuqia Group and the Artux Formation in the south-western Tarim Basin (Zheng et al., 2006). On the other hand, the prevailing carbonate cement can preserve intergranular space and improve reservoir quality by providing secondary porosity under the specific circumstance of intensive dissolution (Al-Ramadan et al., 2004; Hakimi et al., 2012).

At foreland basin margins, fracture networks are widely developed accompanied with intensive deformation in fold-and-thrust belts (Iñigo et al., 2012; Liu et al., 2017). These fracture networks can play a fundamental role both in fluid migration and the resulting reservoir quality, especially in reservoirs with low matrix porosity and permeability (Casini et al., 2011; Watkins et al., 2018; Wang et

al., 2020). Fracture intensity can be controlled by multiple factors in folded sedimentary successions, mainly including the sedimentary characteristics and the structural position. Fracture intensity and connectivity tend to be higher in high strain fold crests or forelimbs, such as in the cases of the Puig-reig anticline in the South-eastern Pyrenees (Sun et al., 2021), the Achnashellach Culmination in the Southern Moine Thrust Belt (Watkins et al., 2015), or the Sub-Andean fold-thrust belt (Iñigo et al., 2012). In alluvial-fluvial deposits, variable sedimentary characteristics can exert significant effects on fracture intensity. Proximal fluvial deposits, dominated by large and thick conglomerate and sandstone layers, tend to have lower fracture intensity than medial fluvial deposits, which are defined by interlayered conglomerate or sandstone layers and fine deposits (Sun et al., 2021). This is because fracture intensity tends to present a negative correlation with bedding thickness (Huang and Angelier, 1989; Florez-Niño et al., 2005). Besides, the interlayered competent conglomerate and sandstone layers and incompetent fine deposits in medial fluvial deposits result in high competence contrast between these distinct mechanical stratigraphic layers, which favours the development of joints or faults (Sibson, 1996; Wilkins et al., 2014). For tight conglomerate and sandstone reservoirs at basin margins, fracture networks can significantly improve reservoir potential (Watkins et al., 2018; Sun et al., 2021).

In summary, compared to deposits in basin centre localities where reservoir quality is mainly controlled by depositional and diagenetic characteristics, basin proximal reservoirs are most likely to be tectonically deformed and feature variable fracture networks. Matrix porosity is mainly controlled by depositional facies and diagenetic, while fracture networks are mainly controlled by depositional characteristics and structural position, e.g., in the Puig-reig anticline (Figs. 8, 9). In the right circumstances an effective combination of both structure and facies can make basin margin locations potential areas for effective reservoirs, even in the case of low matrix porosity.

6 Conclusions

The lithofacies and sedimentary facies of the folded fluvial succession in the Puig-reig anticline, located at the north-eastern margin of the Ebro Foreland Basin (SE Pyrenees), have been analysed to explore the reservoir potential in the studied anticline and other similar systems at basin margins. Based on a comprehensive analysis of lithofacies, porosity, cement and fracture intensity distribution, the following conclusions can be highlighted:

(1) The Camps de Vall-Llonga and Solsona formations in the Puig-reig anticline were deposited as part of proximal to medial deposits of a fluvial fan system. The proximal deposits in the study area are characterised by unconfined flash floods and wide-shallow channel streams. They are dominated by thick and large sheet-like conglomerate bodies with minor interlayered sandstones, and mainly spread in the northern limb of the anticline. The medial deposits are characterised by braided channel streams and overbanks, dominated by the interbedded conglomerates, sandstones and claystones,

which finally change to terminal deposits in the distal portion close to the basin centre.

(2) The fluvial deposits present overall low matrix porosity due to intensive compaction and calcite cementation, with relatively high porosity developed in Sm and Sch lithofacies in the medial fluvial fan. Fracture intensity is mainly affected by structural position, bedding thickness and lithological association, with relatively higher values developed in sandstone lithofacies in the high strain zones of the anticline. Sandstone lithofacies deposited in the medial fluvial fan and located in the crest and crest-limb transition zones presents relatively higher potential to be effective reservoirs.

(3) The comprehensive analysis of the Puig-reig anticline can provide an effective analogue for the exploration of subsurface reservoirs. The comparison with other similar settings worldwide shows reservoir potential is comprehensively controlled by sedimentology, diagenesis and deformation at basin margins. An effective combination of both structure and facies can make basin margin locations potential areas for effective reservoirs, even in the case of low matrix porosity.

Acknowledgements

Funding was provided by the Catalan Council to the Grup Consolidat de Recerca “Geologia Sedimentària” (2017SGR-824) and the DGICYT Spanish Project PGC2018-093903-B-C22. XS acknowledges funding by the China Scholarship Council for a PhD scholarship (201806450043). JA is funded by MICINN (Juan de la Cierva fellowship - IJC2018-036074-I). EGR acknowledges funding provided by the Spanish Ministry of Science, Innovation and Universities (“Ramón y Cajal” fellowship RYC2018-026335-I). We thank Enric Sangrà and Francesc Baiget for their support during field campaigns.

References

Al-Ramadan, K.A., Hussain, M., Imam, B., Saner, S., 2004. Lithologic characteristics and diagenesis of the Devonian Jauf sandstone at Ghawar Field, Eastern Saudi Arabia. Mar. Pet. Geol. 21, 1221–1234.

Arenas, C., 1993. Sedimentología y paleogeografía del Terciario del margen pirenaico y sector central de la cuenca del Ebro (zona aragonesa occidental) (Ph.D. thesis). University of Zaragoza, Zaragoza.(in Spanish).

Arenas, C., Millán, H., Pardo, G., Pocoví, A., 2001. Ebro Basin continetal sedimentation associated with late compressional Pyrenean tectonics (North-Eastern lberia): Controls on basin margin fans and fluvial systems. Basin Res. 13, 65–89.

Awdal, A.H., Braathen, A., Wennberg, O.P., Sherwani, G.H., 2013. The characteristics of fracture networks in the Shiranish Formation of the Bina Bawi Anticline; comparison with the Taq Taq Field, Zagros, Kurdistan, NE Iraq. Pet. Geosci. 19, 139–155.

Barrier, L., Proust, J.N., Nalpas, T., Robin, C., Guillocheau, F., 2010. Control of alluvial sedimentation

at foreland-basin active margins: A case study from the northeastern Ebro Basin (southeastern Pyrenees, Spain). J. Sediment. Res. 80, 728–749.

Bjørlykke, K., 2014. Relationships between depositional environments, burial history and rock properties. Some principal aspects of diagenetic process in sedimentary basins. Sediment. Geol. 301, 1–14.

Blair, T.C., 2003. Features and origin of the giant Cucomungo Canyon alluvial fan, Eureka Valley, California, in: Chan, M.A., Archer, A.. (Eds.), Extreme Depositional Environments: Mega End Members in Geologic Time. Geological Society of America Special Papers, 370, pp. 105–126.

Blair, T.C., McPheerson, J.G., 1994. Alluvial fans and their natural distinction from rivers based on morphology, hydraulic processes, sedimentary processes, and facies assemblages. J. Sediment. Res. 64, 450–489.

Blair, T.C., McPherson, J.G., 1994. Alluvial fan processes and forms, in: Abrahams, A.D., Parsons, A.J. (Eds.), Geomorphology of Desert Environments. Springer, Dordrecht, pp. 354–402.

Carrigan, J.H., Anastasio, D.J., Kodama, K.P., Parés, J.M., 2016. Fault-related fold kinematics recorded by terrestrial growth strata, Sant Llorenç de Morunys, Pyrenees Mountains, NE Spain. J. Struct. Geol. 91, 161–176.

Casini, G., Gillespie, P.A., Vergés, J., Romaire, I., Fernández, N., Casciello, E., Saura, E., Mehl, C., Homke, S., Embry, J.C., Aghajari, L., Hunt, D.W., 2011. Sub-seismic fractures in foreland fold and thrust belts: Insight from the Lurestan Province, Zagros Mountains, Iran. Pet. Geosci. 17, 363–282.

Choukroune, P., 1989. The Ecors Pyrenean deep seismic profile reflection data and the overall structure of an orogenic belt. Tectonics 8, 23–39.

Costa, E., Garcés, M., López-Blanco, M., Beamud, E., Gómez-Paccard, M., Larrasoaña, J.C., 2010. Closing and continentalization of the South Pyrenean foreland basin (NE Spain): Magnetochronological constraints. Basin Res. 22, 904–917.

Cruset, D., Cantarero, I., Benedicto, A., John, C.M., Vergés, J., Albert, R., Gerdes, A., Travé, A., 2020. From hydroplastic to brittle deformation: Controls on fluid flow in fold and thrust belts. Insights from the Lower Pedraforca thrust sheet (SE Pyrenees). Mar. Pet. Geol. 120, 104517. https://doi.org/10.1016/j.marpetgeo.2020.104517

Cruset, D., Cantarero, I., Travé, A., Vergés, J., John, C.M., 2016. Crestal graben fluid evolution during growth of the Puig-reig anticline (South Pyrenean fold and thrust belt). J. Geodyn. 101, 30–50.

Cruset, D., Cantarero, I., Vergés, J., John, C.M., Muñoz-López, D., Travé, A., 2018. Changes in fluid regime in syn-orogenic sediments during the growth of the south Pyrenean fold and thrust belt. Glob. Planet. Change 171, 207–224.

de Gibert, J.M., Sáez, A., 2009. Paleohydrological significance of trace fossil distribution in Oligocene fluvial-fan-to-lacustrine systems of the Ebro Basin, Spain. Palaeogeogr. Palaeoclimatol. Palaeoecol.

272, 162–175.

DeCelles, P.G., Cavazza, W., 1999. A comparison of fluvial megafans in the Cordilleran (Upper Cretaceous) and modern Himalayan foreland basin systems. Bull. Geol. Soc. Am. 111, 1315–1334.

Del Santo, G., Garcia-Sansegundo, J., Sarasa, L., Torrebadella, J., 2000. Estratigrafía y estructura del Terciario en el sector oriental de la cuenca del Ebro entre Solsona y Manresa (NE de España). Rev. la Soc. Geológica España 13, 265–278.(in Spanish with English abstract).

Dichiarante, A.M., McCaffrey, K.J.W., Holdsworth, R.E., Bjørnarå, T.I., Dempsey, E.D., 2020. Fracture attribute scaling and connectivity in the Devonian Orcadian Basin with implications for geologically equivalent sub-surface fractured reservoirs. Solid Earth 11, 2221–2244.

Donselaar, M.E., Overeem, I., 2008. Connectivity of fluvial point-bar deposits: An example from the Miocene Huesca fluvial fan, Ebro Basin, Spain. Am. Assoc. Pet. Geol. Bull. 92, 1109–1129.

Dos Anjos, S.M.C., De Ros, L.F., De Souza, R.S., De Assis Silva, C.M., Sombra, C.L., 2000. Depositional and diagenetic controls on the reservoir quality of Lower Cretaceous Pendencia sandstones, Potiguar rift basin, Brazil. Am. Assoc. Pet. Geol. Bull. 84, 1719–1742.

Florez-Niño, J.M., Aydin, A., Mavko, G., Antonellini, M., Ayaviri, A., 2005. Fault and fracture systems in a fold and thrust belt: An example from Bolivia. Am. Assoc. Pet. Geol. Bull. 89, 471–493.

Folk, R.L., 1980. Petrology of Sedimentary Rocks. Hemphill Publishing Company, Austin .

Ford, M., Williams, E.A., Artoni, A., Vergés, J., Hardy, S., 1997. Progressive evolution of a fault-related fold pair from growth strata geometries, Sant Llorenç de Morunys, SE Pyrenees. J. Struct. Geol. 19, 413–441.

Ge, H., Jackson, M.P.A., Vendeville, B.C., 1997. Kinematics and dynamics of salt tectonics driven by progradation. Am. Assoc. Pet. Geol. Bull. 81, 398–423.

Guilbaud, R., Bernet, M., Huyghe, P., Erens, V., Chirouze, F., Dupont-Nivet, G., 2012. On the influence of diagenesis on the original petrographic composition of Miocene–Pliocene fluvial sandstone in the Himalayan foreland basin of western-central Nepal. J. Asian Earth Sci. 44, 107–116.

Hakimi, M.H., Shalaby, M.R., Abdullah, W.H., 2012. Diagenetic characteristics and reservoir quality of the Lower Cretaceous Biyadh sandstones at Kharir oilfield in the western central Masila Basin, Yemen. J. Asian Earth Sci. 51, 109–120.

Hall, J.S., Mozley, P., Davis, J.M., Roy, N.D., 2004. Environments of Formation and Controls on Spatial Distribution of Calcite Cementation in Plio-Pleistocene Fluvial Deposits, New Mexico, U.S.A. J. Sediment. Res. 74, 643–653.

Hirst, J.P.P., Nichols, G.J., 1986. Thrust tectonic controls on Miocene alluvial distribution patterns, southern Pyrenees., in: Allen, P.A., Homewood, P. (Eds.), Foreland Basins. International Association of Sedimentologists Special Publication, pp. 153–164.

Horton, B.K., Decelles, P.G., 2001. Modern and ancient fluvial megafans in the foreland basin system

of the Central Andes, Southern Bolivia: Implications for drainage network evolution if foldthrust belts. Basin Res. 13, 43–63.

Houseknecht, D.W., 1987. Assessing the relative importance of compaction processes and cementation to reduction of porosity in sandstones. Am. Assoc. Pet. Geol. Bull. 71, 633–642.

Howell, J.A., Martinius, A.W., Good, T.R., 2014. The application of outcrop analogues in geological modelling: a review, present status and future outlook. Geol. Soc. London, Spec. Publ. 387, 1–25.

Huang, Q., Angelier, J., 1989. Fracture spacing and its relation to bed thickness. Geol. Mag. 126, 355–362.

Hudleston, P.J., Treagus, S.H., 2010. Information from folds: A review. J. Struct. Geol. 32, 2042–2071.

Iñigo, J.F., Laubach, S.E., Hooker, J.N., 2012. Fracture abundance and patterns in the Subandean fold and thrust belt, Devonian Huamampampa Formation petroleum reservoirs and outcrops, Argentina and Bolivia. Mar. Pet. Geol. 35, 201–218.

Institut Cartogràfic i Geològic de Catalunya, 2006. Regional geological map of Catalonia. https://www.icgc.cat/en/Public-Administration-and-Enterprises/Downloads/Geological-and-geothematic-cartography/Geological-cartography/Geological-map-1-50-000/Regional-geological-map-of-Catalonia-1-50-000 (accessed 2.1.21).

Instituto Geológico y Minero de España, 1995. Almacenamiento subterraneo de gas: previabilidad en formaciones detriticas y salinas. http://info.igme.es/ConsultaSID/r.asp?IdDESCRIPTOR=2681 (accessed 3.20.21).

Lai, J., Wang, G., Wang, S., Cao, J., Li, M., Pang, X., Zhou, Z., Fan, X., Dai, Q., Yang, L., He, Z., Qin, Z., 2018. Review of diagenetic facies in tight sandstones: Diagenesis, diagenetic minerals, and prediction via well logs. Earth-Science Rev. 185, 234 – 258.

Liu, C., Zhang, R., Zhang, H., Wang, J., Mo, T., Wang, K., Zhou, L., 2017. Genesis and reservoir significance of multi-scale natural fractures in Kuqa foreland thrust belt, Tarim Basin, NW China. Pet. Explor. Dev. 44, 495–504.

Luzón, A., 2001. Análisis tectosedimentario de los materiales terciarios continentales del sector central de la cuenca del Ebro (provincias de Huesca y Zaragoza) (Ph.D. thesis). Zaragoza University, Zaragoza.(in Spanish).

Luzón, A., 2005. Oligocene–Miocene alluvial sedimentation in the northern Ebro Basin, NE Spain: Tectonic control and palaeogeographical evolution. Sediment. Geol. 177, 19–39.

Mann, P., Gahagan, L., Gordon, M.B., 2003. Tectonic setting of the world's giant oil fields, in: Halbouty, M.. (Ed.), Giant Oil and Gas Fields of the Decade 1990–1999. AAPG Memoir, 78, pp. 15–105.

Martin, B., Owen, A., Nichols, G.J., Hartley, A.J., Williams, R.D., 2021. Quantifying downstream, vertical and lateral variation in fluvial deposits: Implications from the Huesca distributive fluvial system. Front. Earth Sci. 8, 564017. https://doi.org/10.3389/feart.2020.564017

Martínez-Martínez, J.M., Soto, J.I., Balanyá, J.C., 2002. Orthogonal folding of extensional detachments: Structure and origin of the Sierra Nevada elongated dome (Betics, SE Spain). Tectonics 21, 1–22.

Morad, S., Al-Ramadan, K., Ketzer, J.M., De Ros, L.F., 2010. The impact of diagenesis on the heterogeneity of sandstone reservoirs: A review of the role of depositional fades and sequence stratigraphy. Am. Assoc. Pet. Geol. Bull. 94, 1267–1309.

Moscariello, A., 2005. Exploration potential of the mature Southern North Sea basin margins: some unconventional plays based on alluvial and fluvial fan sedimentation models. Geol. Soc. London, Pet. Geol. Conf. Ser. 6, 595–605.

Moscariello, A., 2018. Alluvial fans and fluvial fans at the margins of continental sedimentary basins: geomorphic and sedimentological distinction for geo-energy exploration and development. Geol. Soc. London, Spec. Publ. 440, 215–243.

Muñoz, J.A., 1992. Evolution of a continental collision belt: ECORS-Pyrenees crustal balanced cross-section, in: McClay, K.R. (Ed.), Thrust Tectonics. Springer, Dordrecht, pp. 235–246.

Nichols, G., 2005. Tertiary alluvial fans at the northern margin of the Ebro Basin: a review. Geol. Soc. London, Spec. Publ. 251, 187–206.

Nichols, G.J., Hirst, J.P., 1998. Alluvial fans and fluvial distributary systems, Oligo-Miocene, northern Spain; contrasting processes and products. J. Sediment. Res. 68, 879–889.

Puigdefàbregas, C., Munñz, J.A., Marzo, M., 1986. Thrust belt development in the eastern Pyrenees and related depositional sequences in the southern foreland basin., in: Allen, P.A., Homewood, P. (Eds.), Foreland Basins. International Association of Sedimentologists Special Publication, pp. 229–246.

Puigdefàbregas, C., Muñoz, J.A., Vergés, J., 1992. Thrusting and foreland basin evolution in the Southern Pyrenees, in: McClay, K.R. (Ed.), Thrust Tectonics. Springer, Dordrecht, pp. 247–254.

Riba, O., 1976. Syntectonic unconformities of the Alto Cardener, Spanish Pyrenees: a genetic interpretation. Sediment. Geol. 15, 213–233.

Roure, F., Choukroune, P., Berastegui, X., Munoz, J.A., Villien, A., Matheron, P., Bareyt, M., Seguret, M., Camara, P., Deramond, J., 1989. Ecors deep seismic data and balanced cross sections: Geometric constraints on the evolution of the Pyrenees. Tectonics 8, 41–50.

Sáez, A., 1987. Estratigrafía y sedimentología de las formaciones lacustres del tránsito Eoceno-Oligoceno del NE de la Cuenca del Ebro (Ph.D. thesis). University of Barcelona, Barcelona.(in Spanish).

Sáez, A., Anadón, P., Herrero, M.J., Moscariello, A., 2007. Variable style of transition between Palaeogene fluvial fan and lacustrine systems, southern Pyrenean foreland, NE Spain. Sedimentology 54, 367–390.

Scherer, M., 1987. Parameters influencing porosity in sandstones: A model for sandstone porosity prediction. Am. Assoc. Pet. Geol. Bull. 71, 485–491.

Schneider, C.A., Rasband, W.S., Eliceiri, K.W., 2012. NIH Image to ImageJ: 25 years of image analysis. Nat. Methods 9, 671–675.

Serra-Kiel, J., Mató, E., Saula, E., Travé, A., Ferràndez-Canadell, C., Busquets, P., Samsó, J.M., Tosquella, J., Barnolas, A., Àlvarez-Pérez, G., Franquès, J., Romero, J., 2003a. An inventory of the marine and transitional Middle/Upper Eocene deposits of the Southeastern Pyrenean Foreland Basin (NE Spain). Geol. Acta 1, 201–229.

Serra-Kiel, J., Travé, A., Mató, E., Saula, E., Ferràndez-Canadell, C., Busquets, P., Tosquella, J., Vergés, J., 2003b. Marine and transitional Middle/Upper Eocene units of the southeastern pyrenean foreland basin (NE Spain). Geol. Acta 1, 177–200.

Sun, X., 2018. Pore structure characterization of low permeability and tight sandstone reservoirs of Huagang Formation in Xihu Depression (Ph.D. thesis). China University of Petroleum (East China), Qingdao.(in Chinese with English abstract).

Sun, X., Alcalde, J., Gomez-Rivas, E., Struth, L., Johnson, G., Travé, A., 2020. Appraisal of CO2 storage potential in compressional hydrocarbon-bearing basins: Global assessment and case study in the Sichuan Basin (China). Geosci. Front. 11, 2309–2321.

Sun, X., Gomez-Rivas, E., Alcalde, J., Martín-Martín, J.D., Ma, C., Muñoz-López, D., Cruset, D., Cantarero, I., Griera, A., Travé, A., 2021. Fracture distribution in a folded fluvial succession: the Puig-reig anticline (South-eastern Pyrenees). EarthArXiv. doi.org/10.31223/X5J31S

Suppe, J., Sàbat, F., Anton Muñoz, J., Poblet, J., Roca, E., Vergés, J., 1997. Bed-by-bed fold growth by kink-band migration: Sant llorenç de Morunys, eastern Pyrenees. J. Struct. Geol. 19, 443–461.

Taylor, K.G., Machent, P.G., 2011. Extensive carbonate cementation of fluvial sandstones: An integrated outcrop and petrographic analysis from the Upper Cretaceous, Book Cliffs, Utah. Mar. Pet. Geol. 28, 1461–1474.

Taylor, T.R., Giles, M.R., Hathon, L.A., Diggs, T.N., Braunsdorf, N.R., Birbiglia, G. V., Kittridge, M.G., MacAulay, C.I., Espejo, I.S., 2010. Sandstone diagenesis and reservoir quality prediction: Models, myths, and reality. Am. Assoc. Pet. Geol. Bull. 94, 1093–1132.

Travé, A., Calvet, F., Sans, M., Vergés, J., Thirlwall, M., 2000. Fluid history related to the Alpine compression at the margin of the south-Pyrenean Foreland basin: The El Guix anticline. Tectonophysics 321, 73–102.

Travé, A., Labaume, P., Calvet, F., Soler, A., 1997. Sediment dewatering and pore fluid migration along thrust faults in a foreland basin inferred from isotopic and elemental geochemical analyses (Eocene southern Pyrenees, Spain). Tectonophysics 282, 375–398.

Travé, A., Labaume, P., Vergés, J., 2007. Fluid systems in foreland fold-and-thrust belts: An overview from the southern Pyrenees, in: Lacombe, O., Lavé, J., Roure, F., Vergés, J. (Eds.), Thrust Belts and Foreland Basins. Springer, Berlin, Heidelberg, pp. 93–115.

Valloni, R., Zuffa, G.G., 1984. Provenance changes for arenaceous formations of the northern Apennines, Italy. Geol. Soc. Am. Bull. 95, 1035–1039.

Ventra, D., Clarke, L.E., 2018. Geology and geomorphology of alluvial and fluvial fans: current progress and research perspectives. Geol. Soc. London, Spec. Publ. 440, 1–21.

Vergés, J., 1993. Estudi geològic del vessant sud del Pirineu oriental i central. Evolució cinemàtica en 3D (Ph.D. thesis). University of Barcelona, Barcelona.(in Spanish).

Vergés, J., 2007. Drainage Responses to Oblique and Lateral Thrust Ramps: A Review, in: Nichols, G., Paola, C., Williams, E.A. (Eds.), Sedimentary Processes, Environments and Basins: A Tribute to Peter Friend. International Association of Sedimentologists Special Publication, pp. 29–47.

Vergés, J., Marzo, M., Muñoz, J.A., 2002. Growth strata in foreland settings. Sediment. Geol. 146, 1–9.

Vergés, J., Marzo, M., Santaeulària, T., Serra-Kiel, J., Burbank, D.W., Muñoz, J.A., Giménez-Montsant, J., 1998. Quantified vertical motions and tectonic evolution of the SE Pyrenean foreland basin. Geol. Soc. London, Spec. Publ. 134, 107–134.

Vergés, J., Muñoz, J.A., Martínez, A., 1992. South Pyrenean fold and thrust belt: The role of foreland evaporitic levels in thrust geometry, in: K.R., M. (Ed.), Thrust Tectonics. Springer, Dordrecht, pp. 255–264.

Vincent, S.J., 2002. The Sis palaeovalley: a record of proximal fluvial sedimentation and drainage basin development in response to Pyrenean mountain building. Sedimentology 48, 1235–1276.

Wang, H., Ma, F., Tong, X., Liu, Z., Zhang, X., Wu, Z., Li, D., Wang, B., Xie, Y., Yang, L., 2016. Assessment of global unconventional oil and gas resources. Pet. Explor. Dev. 43, 925–940.

Wang, Z., Lü, X., Wang, S., Li, Y., Zhou, X., Quan, H., Li, R., 2020. Fracture systems and petrophysical properties of tight sandstone undergoing regional folding: A case study of the Cretaceous reservoirs in the Kuqa foreland thrust belt, Tarim Basin. Mar. Pet. Geol. 111, 104055. https://doi.org/10.1016/j.marpetgeo.2019.104055

Watkins, H., Butler, R.W.H., Bond, C.E., Healy, D., 2015. Influence of structural position on fracture networks in the Torridon Group, Achnashellach fold and thrust belt, NW Scotland. J. Struct. Geol. 74, 64–80.

Watkins, H., Healy, D., Bond, C.E., Butler, R.W.H., 2018. Implications of heterogeneous fracture distribution on reservoir quality; an analogue from the Torridon Group sandstone, Moine Thrust Belt, NW Scotland. J. Struct. Geol. 108, 180–197.

Weissmann, G.S., Hartley, A.J., Scuderi, L.A., Nichols, G.J., Davidson, S.K., Owen, A., Atchley, S.C., Bhattacharyya, P., Chakraborty, T., Ghosh, P., Nordt, L.C., Michel, L., Tabor, N.J., 2013. Prograding distributive fluvial systems—geomorphic models and ancient examples, in: Driese, S.G., Nordt, Lee C. (Eds.), New Frontiers in Paleopedology and Terrestrial Paleoclimatology: Paleosols and Soil Surface Analog Systems. SEPM Special Publication, pp. 131–147.

Weissmann, G.S., Hartley, A.J., Scuderi, L.A., Nichols, G.J., Owen, A., Wright, S., Felicia, A.L., Holland, F., Anaya, F.M.L., 2015. Fluvial geomorphic elements in modern sedimentary basins and their potential preservation in the rock record: A review. Geomorphology 250, 187–219.

Wennberg, O.P., Azizzadeh, M., Aqrawi, A.A.M., Blanc, E., Brockbank, P., Lyslo, K.B., Pickard, N., Salem, L.D., Svånå, T., 2007. The Khaviz Anticline: an outcrop analogue to giant fractured Asmari Formation reservoirs in SW Iran. Geol. Soc. London, Spec. Publ. 270, 23–42.

Williams, E.A., Ford, M., Vergés, J., Artoni, A., 1998. Alluvial gravel sedimentation in a contractional growth fold setting, Sant Llorenç de Morunys, southeastern Pyrenees. Geol. Soc. London, Spec. Publ. 134, 69–106.

Yuste, A., Luzón, A., Bauluz, B., 2004. Provenance of Oligocene-Miocene alluvial and fluvial fans of the northern Ebro Basin (NE Spain): An XRD, petrographic and SEM study. Sediment. Geol. 172, 251–268.

Zhang, R., Yao, G., Shou, J., Zhang, H., Tian, J., 2011. An integration porosity forecast model of deposition, diagenesis and structure. Pet. Explor. Dev. 38, 145–151.

Zheng, H., Huang, X., Butcher, K., 2006. Lithostratigraphy, petrography and facies analysis of the Late Cenozoic sediments in the foreland basin of the West Kunlun. Palaeogeogr. Palaeoclimatol. Palaeoecol. 241, 61–78.

Zuffa, G.G., 1980. Hybrid arenites: their composition and classification. J. Sediment. Petrol. 50, 21–29.

Zuffa, G.G., 1985. Optical analyses of arenites: Influence of methodology on compositional results, in: Zuffa, G.G. (Ed.), Provenance of Arenites: NATO-Advanced Study Institute Series C. Reidel Publishing Company, Dordrecht, pp. 165–189.

Appendix 4 Fracture distribution in a folded fluvial succession: the Puig-reig anticline (South-eastern Pyrenees)

Sun, X., Gomez-Rivas, E., Alcalde, J., Martín-Martín, J.D., Ma, C., Muñoz-López, D., Cruset, D., Cantarero, I., Griera, A., Travé, A., 2021. Fracture distribution in a folded fluvial succession: the Puig-reig anticline (South-eastern Pyrenees). Marine and Petroleum Geology, 132, 105169. doi.org/10.1016/j.marpetgeo.2021.105169.

Marine and Petroleum Geology 132 (2021) 105169

Contents lists available at ScienceDirect

Marine and Petroleum Geology

journal homepage: www.elsevier.com/locate/marpetgeo

Fracture distribution in a folded fluvial succession: The Puig-reig anticline (south-eastern Pyrenees)

Xiaolong Sun [a], Enrique Gomez-Rivas [a,*], Juan Alcalde [b], Juan Diego Martín-Martín [a], Cunfei Ma [c], Daniel Muñoz-López [a], David Cruset [b], Irene Cantarero [a], Albert Griera [d], Anna Travé [a]

[a] Departament de Mineralogia, Petrologia I Geologia Aplicada, Facultat de Ciències de La Terra, Universitat de Barcelona (UB), C/ Martí I Franquès S/n, Barcelona, 08028, Spain
[b] Geosciences Barcelona (GEO3BCN-CSIC), Lluís Solé I Sabarís S/n, Barcelona, 08028, Spain
[c] School of Geosciences, China University of Petroleum (East China), Qingdao, 266580, China
[d] Departament de Geologia, Universitat Autònoma de Barcelona, Cerdanyola Del Vallès, 08193, Spain

ARTICLE INFO

Keywords:
Fractures
Fluvial fan
Structural position
Fold
Pyrenees

ABSTRACT

Sedimentary rocks of foreland fold-and-thrust belts typically undergo intensive fracturing as folds grow. The resulting fracture networks can present significant variations depending on the distribution of sedimentary facies and the complex structural characteristics of fold-and-thrust belts. The Puig-reig anticline, located in the south-eastern Pyrenees, mainly exposes proximal fluvial deposits in the north limb and medial fluvial deposits in the rest of the anticline. Thus, this anticline constitutes an excellent case study to investigate the main controls on the distribution of fracture networks in folded fluvial deposits, in terms of structural position and lithofacies variations. Outcrops were selected to be representative of different structural positions, from the fold hinge to its limbs, and of a variety of the main lithofacies, from proximal to medial fluvial deposits. Fracture data were acquired using the linear scanline method. The results indicate that the anticline rocks have been affected by four sets of fractures. The north limb is dominated by thick conglomerate bodies with interlayered sandstones deposited from unconfined flash floods and wide-shallow channel streams in the proximal fluvial fan, and presents large fracture spacing and low fracture intensity but relatively large fracture length and aperture. The crest and the crest-limb transition zones are mainly characterised by interlayered conglomerates, sandstones, siltstones and clays, deposited from braided channel streams and overbanks in the medial fluvial fan, and present fractures with relatively high fracture intensity and variable fracture length and aperture. The south limb, composed of channel filling sandstone layers and stable overbank fine deposits in the medial fluvial fan, is characterised by low fracture intensity and small fracture length and aperture. Based on multiple linear regression analysis, fracture intensity is mainly controlled by the structural position, bedding thickness and lithological associations, with relatively more intense fracturing in thin sandstone layers with multiple interlayers of fine deposits in the anticline crest. The fracture length mainly depends on bedding thickness and is affected lithological associations. The fracture apertures are mainly controlled by lithofacies, with relatively higher apertures affecting conglomerate bodies. The results of this study are relevant for characterising similar systems in the subsurface, where data is scarce.

1. Introduction

Fracture networks in rocks of gently deformed foreland basins and intensively deformed fold-and-thrust belts promote the formation of vertical and/or lateral fluid migration pathways within different hydrostratigraphic units (Travé et al., 2007; Fischer et al., 2009; Evans and Fischer, 2012; Evans et al., 2012; Ogata et al., 2014; Muñoz-López et al., 2020a). Many studies have analysed factors controlling the distribution of fracture networks, particularly how the structural position and the characteristics of sedimentary rocks impact the resulting fracture networks (Underwood et al., 2003; Florez-Niño et al., 2005; Lorenz et al., 2006; Wennberg et al., 2006; Ortega et al., 2010; Ogata et al.,

* Corresponding author.
E-mail address: e.gomez-rivas@ub.edu (E. Gomez-Rivas).

https://doi.org/10.1016/j.marpetgeo.2021.105169
Received 12 May 2021; Accepted 31 May 2021
Available online 4 June 2021

2017). Here we use the term 'fracture' in a wide sense to refer to discrete mechanical discontinuities in the rock mass formed under the action of stress, including low- or zero-offset fractures, joints, microfractures and veins (*i.e.*, sealed fractures) (Peacock et al., 2016), and leave out high-offset faults within large fault zones.

Fracture network attributes, including fracture intensity, orientation, length, aperture and connectivity have been described to be closely related to the structural position of a rock volume within a fold (Peacock, 2001; Bellahsen et al., 2006; Ghosh and Mitra, 2009; Watkins et al., 2015a). In asymmetric folds, fracture networks in fold hinges or forelimbs tend to have high intensity, with fractures presenting wider apertures and better connectivity than those located in fold backlimbs, due to the greater curvature and finite strain (Nelson and Serra, 1995; Watkins et al., 2015a). Besides, fracture intensity tends to increase in the proximity of large faults (Cooper et al., 2006). Other studies show that the intensity of certain fracture sets can vary with the structural position and finite strain, while in other sets it may show less variation across fold sections. Some examples are the Oil Mountain anticline in Wyoming (Hennings et al., 2000) and the Teton anticline in Montana (Ghosh and Mitra, 2009). Additionally, fractures formed prior to folding can contribute to the mechanical anisotropy of stratified units and thus significantly impact the resulting fracture networks formed during fold growth. For example, the Emigrant Gap anticline in Wyoming features constant fracture characteristics owing to the influence of pre-folding fractures (Bergbauer and Pollard, 2004). All these previous studies point out that the position with respect to a structural feature can be a key factor controlling fracture attributes, but there is great variability in their relationship.

Apart from the structural position, the characteristics of the hosting sedimentary rocks have also been reported to be key controls on the distribution of fracture networks. The depositional and diagenetic characteristics of a rock unit, including the lithofacies architecture, lithological assemblages, bedding thickness, depositional components, textures, grain size and presence of cements and other diagenetic products determine the rock mechanical properties, including stiffness, cohesion and angle of internal friction (Shackleton et al., 2005; Olson et al., 2007; Ferrill and Morris, 2008; Laubach et al., 2009). Some studies reported a clear negative correlation between fracture intensity and bedding thickness (Huang and Angelier, 1989; Florez-Niño et al., 2005; Wennberg et al., 2007), while others did not reveal systematic relationships (Guiton et al., 2003; Wennberg et al., 2006; Ortega et al., 2010; Awdal et al., 2013). Competent rocks, such as clay-poor carbonates, are typically associated with much higher fracture intensity than clay-rich rocks (Ferrill and Morris, 2008). Grain size has a significant effect on fracture propagation, in a way that increasing grain size has been found to reduce crack coalescence and crack damage thresholds (Eberhardt et al., 1999). The rock mechanical properties can also greatly evolve with progressive diagenetic events, thus affecting the evolution of fracture networks (Di Naccio et al., 2005; Laubach et al., 2009; Barbier et al., 2012).

Foreland basins and their adjacent fold-and-thrust belts contain significant hydrocarbon resources (Mann et al., 2003), and also show high potential for CO_2 storage (Sun et al., 2020). As important fluid migration pathways and potential reservoir space, fracture networks have been widely studied in thrust belts composed of carbonate deposits due to their abundant hydrocarbon resources, *e.g.*, in the Zagros fold-and-thrust belt (Stephenson et al., 2007), the Bighorn Basin (Bellahsen et al., 2006), the Apennines (Van Dijk et al., 2000) and the Oman Mountains (Gomez-Rivas et al., 2014), among other areas. However, studies of fracturing of thrust belts composed of sandstone deposits are significantly less well documented (Watkins et al., 2015a). An example of understudied systems is alluvial-fluvial fans, which are the main deposits in non-marine foreland basins at their active margins (Horton and Decelles, 2001).

The southern Pyrenees presents multiple fold and thrust related alluvial-fluvial fans, which are buried as subsurface reservoirs or exposed as outcrops (*e.g.*, Arenas et al., 2001; Jones, 2004; Sáez et al., 2007; Yuste et al., 2004). Such alluvial-fluvial strata in the subsurface show high potential to become effective reservoirs. For example, the eastern part of the Puig-reig anticline in the south-eastern Pyrenees was assessed as a potential site for gas storage (Instituto Geológico y Minero de España, 1995). Besides, the well-exposed outcrops can provide excellent reservoir analogues to investigate fracture distributions in folded alluvial-fluvial successions at basin margins. However, most studies of the southern Pyrenees focused on unravelling the different tectonic events and/or analysing the fingerprints of fluids to decipher the evolution of fluid flow (Travé et al., 2000; Beaudoin et al., 2015; Taillefer et al., 2017; Cruset et al., 2018, 2020, 2020; Lacroix et al., 2018; Nardini et al., 2019; Muñoz-López et al., 2020b), while only a few studies focused on the formation or distribution of fractures (*e.g.*, Tavani et al., 2011, 2020; Gutmanis et al., 2018). Here we present a systematic analysis of the fracture network of a folded fluvial succession exposed in the Puig-reig anticline. Fracture attributes from different structural positions and sedimentary facies were collected and analysed, with the overarching aim of determining what are the main depositional and structural controls on fracture distributions.

2. Geological setting

The Pyrenees is a doubly verging orogenic belt that formed during the continental collision between the Iberian and European plates from the Late Cretaceous to the Miocene (Muñoz, 1992; Vergés et al., 2002). This orogenic belt is characterised by an antiformal stack of basement-involved thrusts (the Axial Zone) surrounded by two fold-and-thrust belts that were transported to the north and south over the Aquitanian (France) and Ebro (Spain) foreland basins, respectively (Choukroune, 1989; Roure et al., 1989; Muñoz, 1992). The eastern part of the Ebro Basin displays an irregular shape bounded by the Pyrenees to the north and the Catalan Coastal Range to the southeast (Fig. 1A and B) (Vergés, 1993; Vergés et al., 1998). The Vallfogona thrust represents the major frontal thrust between the SE Pyrenean thrust sheets and the Ebro Basin. The Busa syncline and the Puig-reig anticline developed along the footwall of the Vallfogona thrust during the Late Eocene and Oligocene (Vergés, 1993).

Based on the available seismic profiles across the Puig-reig anticline (Fig. 1C), the anticline was interpreted to have been formed as a consequence of a duplex stack in depth (Vergés, 1993). In the lower part, the Banyoles and Igualada Formations (Middle-to-Upper Eocene) consist of marine marls. They were duplicated by thrusting and detached above the Beuda evaporitic formation (Middle Eocene) (Vergés et al., 1992; Serra-Kiel et al., 2003a, 2003b). In the upper part, the Berga Group and the Solsona Formation (Upper Eocene to Oligocene) were deposited during the endorheic stage of the Ebro Basin (Puigdefàbregas et al., 1986, 1992), after a rapid transition from marine to continental environments of deposition at around 36 Ma during the Priabonian (Costa et al., 2010). During the Oligocene, the Vallfogona footwall was folded forming the km-scale south-verging gentle anticline of Puig-reig. The fold-trend is ESE/WNW, slightly oblique to the main Pyrenean structures (Vergés, 1993).

To the north, at the footwall of the Vallfogona thrust, the Berga Group consists of more than 2000 m-thick alluvial and proximal fluvial conglomerates interbedded with minor sandstones and claystones, which display growth strata geometries (Ford et al., 1997; Suppe et al., 1997). To the south, the Berga deposits became progressively finer-grained and thinner-bedded fluvial conglomerates, sandstones and claystones of the Solsona Formation (Williams et al., 1998; Barrier et al., 2010). Finally, the Solsona deposits evolved downstream to terminal deposits of a distal fluvial system, which graded into evaporites and calcareous lacustrine sediments towards the centre of the Ebro Basin (Del Santo et al., 2000; Sáez et al., 2007; Barrier et al., 2010).

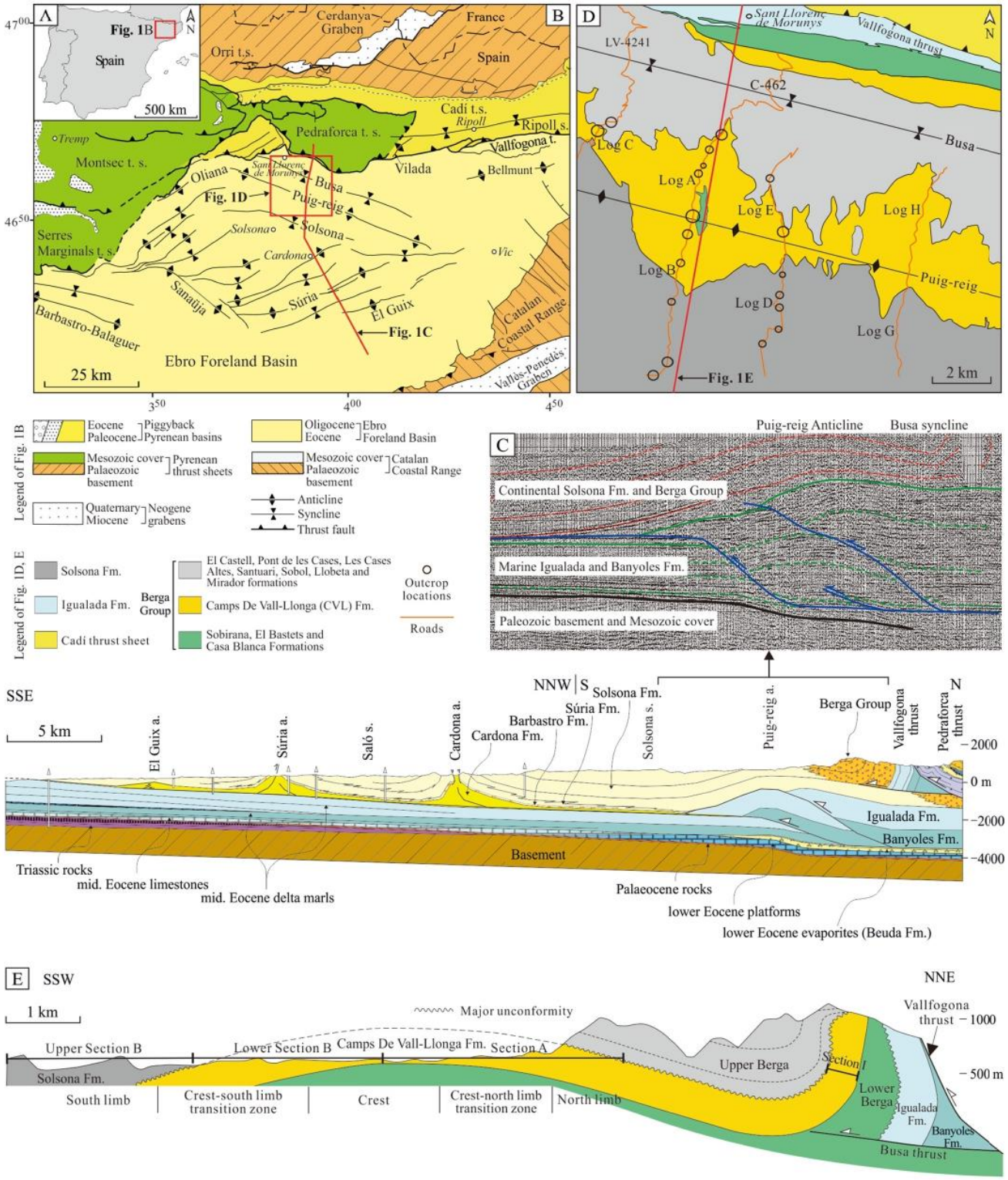

Fig. 1. (A–B) Geographical location and main structural units of the SE Pyrenean fold-and-thrust belt (Vergés, 1993). (C) Geological cross section of the frontal part of the SE Pyrenean fold-and-thrust belt and the Ebro Basin (Vergés, 1993). The seismic profile (Line S-2) is from the Spanish Geophysical Information System (SIGEOF) (Instituto Geológico y Minero de España, 1977). (D–E) Distribution of the Berga Group and the Solsona Formation and location of outcrops. The strata distribution in D is based on the regional geological map of Catalonia (Institut Cartogràfic i Geològic de Catalunya, 2006). The formation subdivision of the Berga Group follows the scheme of Williams et al. (1998). Fig. 1E is modified from Williams et al. (1998) and Barrier et al. (2010).

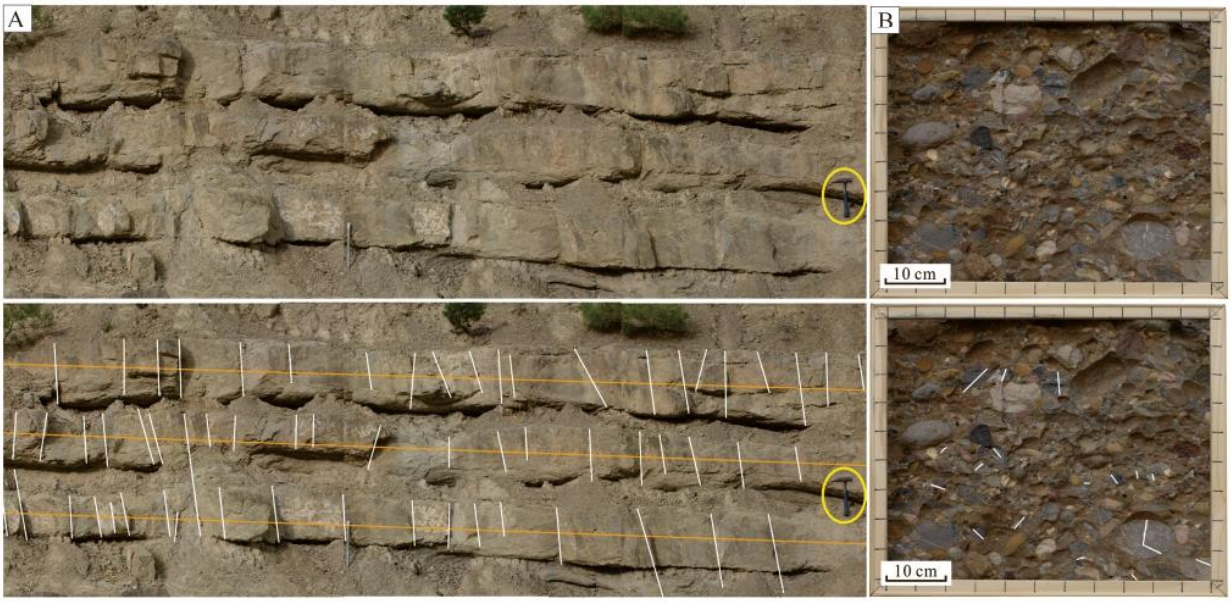

Fig. 2. Examples of outcrop photographs highlighting the different fracture collecting methods: (A) linear scanline method for large and intermediate fractures; (B) window sampling method for small fractures in conglomerates. Orange and white lines represent linear scanlines and identified fractures, respectively. (For interpretation of the references to colour in this figure legend, the reader is referred to the Web version of this article.)

3. Data and methods

The Puig-reig anticline exposes excellent outcrops along four roads perpendicular to the axial direction of the structure, roughly in a north-south direction, between the villages of Sant Llorenç de Morunys in the north and Solsona in the south (Fig. 1B and D). Seven high-resolution stratigraphic logs with a total length of over 3000 m were built based on the data collected from outcrops along these roads (Fig. 1D). Our study mainly focuses on the Camps de Vall-Llonga (a sub-formation of the Berga formation) and Solsona formations (Upper Eocene to Lower Oligocene; Carrigan et al., 2016), which cover most areas of the anticline. The ca. 9 km-long geological cross-section of the Puig-reig anticline (sections A and B, Fig. 1E) lies roughly parallel to the thrust direction of the south-eastern Pyrenees and displays the transition from proximal to medial fluvial deposits.

Three main sampling methods for collecting fracture data are widely used and discussed in the literature, namely the linear scanline, window sampling and circular scanline methods (*e.g.*, Zeeb et al., 2013a, 2013b; Watkins et al., 2015b; Healy et al., 2017 and references thereof). The linear scanline method was adopted in this study because of the nearly vertical outcrops present in the Puig-reig anticline (Fig. 2A), which prevented the use of other fracture sampling methods. The linear scanline method is a fast technique for recording a wide range of fracture attributes (listed in Table 1), including fracture orientation, length, spacing, intensity, aperture and fracture filling. The scanline locations were chosen to be representative of different structural positions as well as of different sedimentary facies and stratigraphic arrangements (*e.g.*, variable bed thickness, lithological associations, etc.). We acquired data from 53 scanlines that add up to around 1600 m in total scanline length (Table 2), along the three western-most roads (Fig. 1C). The fracture data was acquired in groups of at least two people, with the aim of reducing subjective acquisition biases (Andrews et al., 2019). Around 1800 fractures with lengths greater than 20 cm intersecting the scanlines were measured. We did not include large faults with high offsets and obvious fault zones. Small-scale fractures (with length smaller than 20 cm) were difficult to collect using the linear scanline method, especially in conglomerate layers containing abundant fractures confined to only one or a few clasts. To overcome this limitation, the window sampling method was used in zones with abundant small-scale fractures. Conglomerate layers from different structural positions were photographed using a rectangle frame with size dimensions of 45 × 55 cm (Fig. 2B). Cracked clasts located inside the frame were identified and such fracture data manually collected. The intensity of fractured clasts in conglomerates was defined as the ratio of the number of fractured clasts with respect to the number of identifiable clasts. Although we could not quantitatively distinguish fold-related fractured clasts from clasts in other times, such as those with fractures inherited from the source rocks or formed during clast transport, we assume a similar proportion of non-fold-related fractured clasts in different areas. Thus, we only used the intensity of fractured clasts in conglomerates as an indicator to show the relative fracture intensity in different structural positions.

To study fracture-filling cements, vein samples were collected from different structural positions. 60 polished thin sections of calcite veins were

Table 1
Definition of the fracture attributes collected and used in this study based on Zeeb et al. (2013a).

Attribute	Definition
Orientation	Orientation of a fracture on a sampling plane, including strike, dip direction and dip
Length	Length of the fracture trace on a sampling plane (m)
Spacing	Distance between two adjacent fractures (m)
Intensity(scanline)	Number of fractures per unit length (m^{-1})
Intensity(window)	Ratio of the number of fractured clasts to the number of identifiable clasts in a conglomerate sampling window
Aperture	Distance between the two walls of a fracture (mm)
Filling	Mineral precipitate filling fracture porosity to form a vein. This determines whether a fracture acts as a conduit or barrier for fluid flow

Table 2
Location, structural position and sedimentary characteristics of the selected linear scanlines.

Structural position	Sedimentary facies	Typical lithofacies	Thickness (m)	Number of scanline	Length of scanline (m)	Number of fracture	Location
North limb	Proximal fluvial fan	Tabular conglomerate bodies	>3	6	281	98	Log C
		Conglomerate bodies with interlayers	1–4	8	302	271	Logs A, C, E
		Tabular sandstone interlayers	1–2.7	3	58	62	Log E
Crest-North limb transition zone	Medial fluvial fan	Channelised conglomerate bodies	1–4	2	42	83	Log A
		Tabular massive medium to coarse sandstones	0.5–1	2	26	42	Log A
		Tabular bedding fine to very fine sandstones	0.7–1.7	2	28	36	Log A
Crest		Channelised conglomerate bodies	1–3	5	162	257	Logs A, B, E
		Tabular massive medium to coarse sandstones	0.7–1.6	6	147	315	Logs A, B, E
		Tabular bedding fine to very fine sandstones	0.35–2	4	101	195	Logs A, E
Crest-South limb transition zone		Channelised conglomerate bodies	1.3–3	4	127	127	Logs B, D
		Tabular massive medium to coarse sandstones	0.5–0.8	1	7	10	Log D
		Tabular bedding fine to very fine sandstones	1.2–1.8	2	41	74	Log B
South limb		Channelised (pebbly) sandstone bodies	0.5–2	4	186	120	Logs B, D
		Tabular bedding fine to very fine sandstones	0.6–2	4	125	145	Logs B, D

made for petrographic analysis, which was carried out using a Zeiss Axiophot optical microscope and a Technosyn Cold Cathodoluminescence microscope, model 8200 Mk5-1 operating 16–17 kV and 270–290 μA gun current. Furthermore, the geochemical results reported in Cruset et al. (2016) were incorporated into this study. The petrographic analysis in this study together with the geochemical analysis of Cruset et al. (2016) have allowed recognizing different generations of veins, which were combined with the field observations to explain the characteristics of veins in different lithofacies.

4. Results

4.1. Anticline structure

The Puig-reig anticline trends ESE/WNW and has a wavelength of more than 10 km. The ca. 9 km-long geological cross-section (sections A and B in Fig. 1E) exposes continuous outcrops in different structural positions. In this study, the anticline was divided into five structural positions from north to south, namely north limb, crest-north limb transition zone (NTZ), crest, crest-south limb transition zone (STZ) and south limb (Fig. 1E). We did not use the terms proximal and distal to refer to structural positions, as other previous studies did (*e.g.*, Ge et al., 1997; Martínez-Martínez et al., 2002), to avoid the potential confusions with common terms to divide environments of deposition in sedimentary systems (i.e., proximal, medial and distal).

Bedding dip mainly ranges from 5° to 15° in the anticline crest, towards the north in sections A, C, E and H and towards the south in sections B, D and G. The orientation of the fold hinge was estimated based on the distribution of bedding attitudes in the anticline crest, with a resulting strike of 105°. In the anticline crest a system of fractures was observed, including abundant joints and some strike-slip and normal faults with displacements smaller than 20 m and a few small low-angle reverse faults with displacements lower than 2 m, and previously observed also in other studies (Cruset et al., 2016). In the NTZ and north limb of the anticline, the strata mainly dip between 10° to 25° and between 10° to 20°, respectively, towards the north. In the STZ and south limb of the anticline, the strata mainly dip between 15° to 35° and between 10° to 15°, respectively, towards the south. These structural positions are characterised by joints and occasional strike-slip faults.

4.2. Sedimentology

The Camps de Vall-Llonga and Solsona Formations in the Puig-reig anticline were deposited as part of proximal to medial deposits of a fluvial fan system. The north limb is dominated by proximal fluvial deposits characterised by unconfined flash floods and wide-shallow channel streams. Clast- or reddish matrix-supported pebble to cobble conglomerates are the prevailing deposits, especially in the northwest of the anticline. The conglomerate bodies tend to present a massive structure, thick sheet geometries, unscoured or scoured basal surfaces, and broad distributions ranging from a few hundred meters up to 3 km. Fine to coarse sandstone interlayers display stable tabular geometries or pinch out laterally as sandstone lenses. The NTZ, crest and STZ of the anticline are dominated by medial fluvial deposits characterised by braided channel streams and overbanks. These deposits are composed of interlayers of conglomerates, sandstones, siltstones and clays. Channel lag deposits are dominated by clast-supported pebble to small cobble conglomerates with grey sand matrix. The conglomerates commonly present a massive structure, scoured basal surfaces, and channelised geometries. The interlayers of massive and laminated sandstones and overbank fine deposits tend to have tabular geometries. The south limb is also dominated by medial fluvial sediments. However, the conglomerate channel lags are replaced by (pebbly) sandstone channel lags, and the south limb is composed of more fine deposits from overbanks than the NTZ, crest and STZ. The distal fluvial fan is located southward of our study area, and is composed of terminal lobes representing low lake-level stages and fluvial-dominated deltas and interdistributary bays representing high lake level stages (Sáez et al., 2007).

4.3. Fracture attributes

4.3.1. Fracture orientation

Four fracture sets (F1, F2, F3 and F4) were identified in the Puig-reig anticline (from a total 1778 fractures measured) based on fracture orientation and their relationships with the fold hinge (Fig. 3 A). The F1 and F2 sets are oriented NNW-SSE and ENE-WSW, respectively. They are the predominant fracture sets observed at the target structure, accounting for 44% and 28% of the total fractures analysed, respectively. The F3 set is characterised by a WNW-ESE orientation and strikes roughly parallel to the anticline hinge. This set is less frequent and accounts for 17% of the total fractures. The F4 set with a NNE-SSW orientation is very limited along the selected scanlines, because they are sub-parallel to the directions of most scanlines. The lack of outcrops located parallel to bedding planes prevents the identification of systematic termination relations between the different fracture sets, thus making it very difficult to establish their relative ages. The predominance of fracture sets varies depending on the structural position of the outcrop within the anticline (Fig. 3A and B). The F1 set predominates in the north limb and NTZ, which also host a small amount of the other sets. Compared to other structural positions, the fold crest is dominated

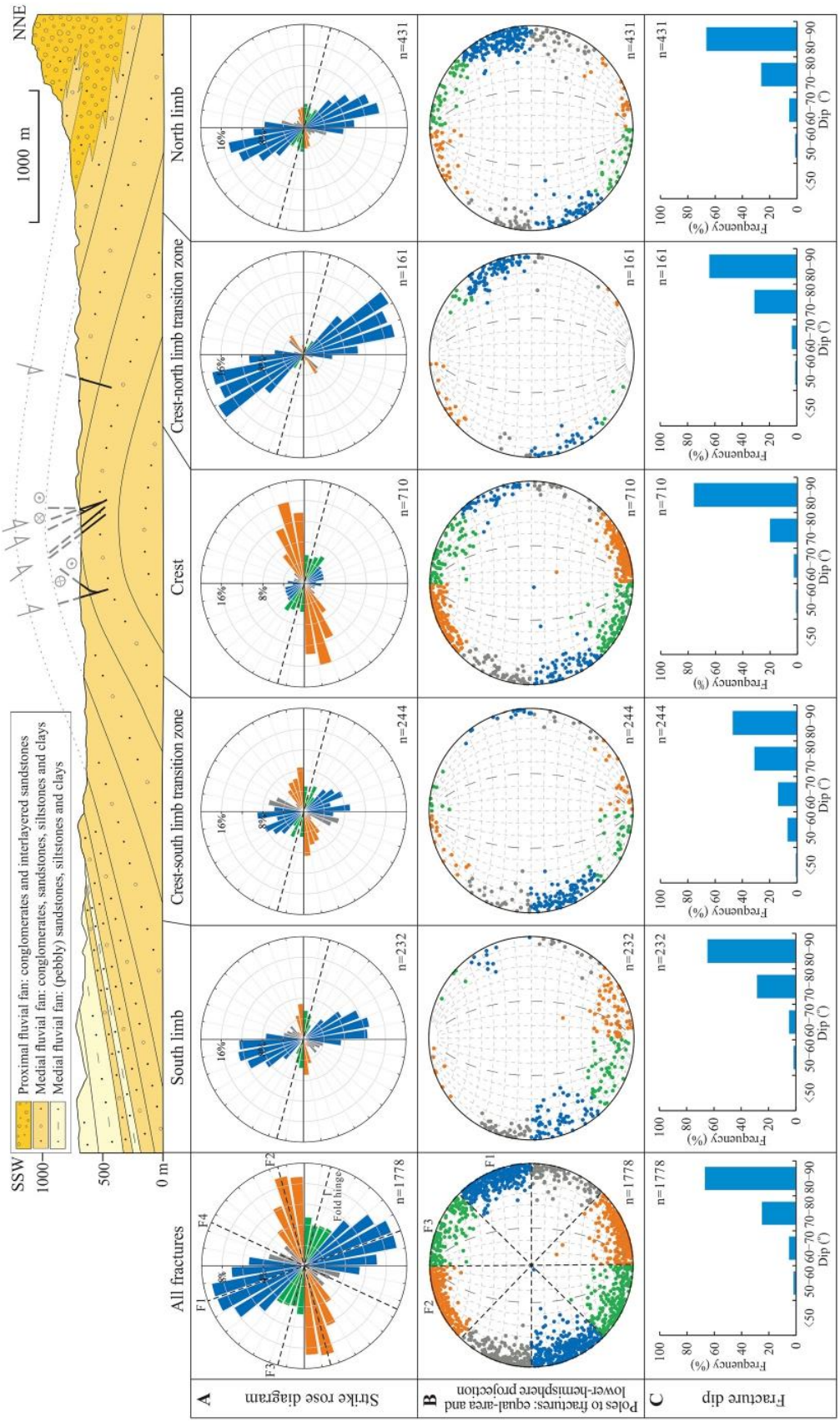

Fig. 3. (A) Rose diagrams displaying fracture strike, (B) stereograms showing fracture 3D orientation and (C) histograms showing fracture dip distribution for different structural positions. The cross section of the Puig-reig anticline is modified from Cruset et al. (2016).

by the F2 set although F1 and F3 sets are also present. From the fold crest to the south limb, the proportion of the F1 set increases significantly while the proportion of the F2 set decreases accordingly. All fractures present high dips, mostly ranging from 70° to 90° (92% of the fractures) (Fig. 3C) and tend to be sub-perpendicular to the bedding surfaces.

4.3.2. Fracture spacing, intensity and length

We consider the apparent fracture spacing as the distance between two adjacent fractures independently of their orientations. The apparent fracture spacing shows variation across the different structural positions (Fig. 4A). The crest and NTZ feature smaller fracture spacing than other zones of the anticline (0.55 m on average *vs.* 1.19 m on average for the other zones). The STZ presents similar spacing distribution but slightly larger overall spacing (0.88 m on average) than the crest and NTZ. In contrast, the north and south limbs conspicuously present larger fracture spacing than the other structural positions (1.55 m and 1.23 m on average, respectively). Fracture spacing also varies significantly depending on the sedimentary lithofacies. The proximal fluvial fan presents larger fracture spacing distributions compared to the medial fluvial fan, mainly ranging between 0.4 m and 3 m, with the largest fracture spacing developing in tabular conglomerate bodies. The medial fluvial fan in the NTZ, crest and STZ presents smaller fracture spacing, especially in tabular massive or bedding sandstone layers, generally smaller than 1 m. The medial fluvial fan in the south limb has larger fracture spacing, mainly between 0.4 m and 2 m, with larger values within the channelised (pebbly) sandstone bodies compared to tabular bedding sandstone layers (Fig. 5A). The cumulative distribution of fracture spacing fits a log-normal distribution (Fig. 6A). Although fracture spacing has a wide range from nearly 0 up to 10 m, it presents a narrow predominant range with 65% of the fracture spacings ranging from 0.2 to 1.2 m.

The apparent fracture intensity is the reciprocal of the apparent fracture spacing, showing the same distribution pattern. The crest presents the highest average fracture intensity (2 m^{-1}) followed by the NTZ (1.66 m^{-1}) and STZ (1.32 m^{-1}), while the south and north limbs present lower fracture intensity (0.94 m^{-1} and 0.70 m^{-1}, respectively) (Fig. 7A). The intensity of fractured clasts of conglomerate layers presents a similar distribution pattern as that of the apparent fracture intensity, with relatively higher values in the crest and NTZ (13.9% and 13.5%, respectively). The apparent fracture intensity also varies significantly in different sedimentary facies and lithofacies (Fig. 7B). The medial fluvial fan in the NTZ, crest and STZ presents the highest average fracture intensity, especially in massive or well-bedded sandstone layers (1.94 m^{-1}), while the proximal fluvial fan in the north limb and the medial fluvial fan in the south limb have lower intensity, especially for tabular conglomerate bodies and channelised (pebbly) sandstone bodies (0.33 m^{-1} and 0.63 m^{-1}, respectively). There can be an underestimation of the intensity of fracture sets intersecting scanlines at oblique angles because the apparent fracture spacing in these cases is higher than the true spacing (Zeeb et al., 2013a; Watkins et al., 2015b). This can be corrected with respect to the angle formed by the fracture and the scanline (Terzaghi, 1965):

$$I = \frac{1}{S_t} = \frac{1}{S_a \times \cos\theta} \quad (1)$$

where I is the true intensity of different fracture sets, S_t is the true fracture spacing, S_a is the apparent fracture spacing, and θ is the acute angle of fracture and scanline. The F4 set is sub-parallel to the directions of most scanlines, resulting in limited fractures intersecting scanlines and very small acute angles between fractures and scanlines. The corrected intensity is too sensitive to the number of fractures and the acute angles, leading to high uncertainty to the results. Thus, we only corrected the fracture intensity of the F1, F2 and F3 sets using this method. The F1 set presents high intensity in all structural positions, while the F2 and F3 sets mainly present high intensity in the crest and STZ of the anticline (Fig. 8A). Similar to the distribution of the apparent fracture intensity, the sum of the true fracture intensity of the three sets results in the highest intensity in the crest (2.38 m^{-1}) followed by the NTZ (1.68 m^{-1}) and STZ (1.56 m^{-1}), while the south limb and north limb correspond to the lowest intensity (1.02 m^{-1} and 0.85 m^{-1}, respectively) (Fig. 8A). Besides, the sum of the true fracture intensity varies significantly in different sedimentary facies and lithofacies (Fig. 8B). The massive or bedded sandstone layers of the medial fluvial fan in the NTZ, crest and STZ have the highest true fracture intensity, with 2.49 m^{-1} and 1.92 m^{-1} on average, respectively. The tabular conglomerate bodies in the north limb and the channelised (pebbly) sandstone bodies in the south limb show the lowest values, with 0.31 m^{-1} and 0.69 m^{-1} on average, respectively.

Fracture length varies from several decimetres to up to 10 m, but mainly ranges between 0.5 m and 2.5 m (for 74% of the fractures) (Fig. 4C). Although there is no clear relationship between the fracture length and the structural position in which fractures are located, the north limb presents larger fracture length (1.52 m on average) compared to the other structural positions within the anticline, while the south limb features the smallest fracture length (1.27 m on average) (Fig. 4C). The proximal fluvial fan in the north limb and the medial fluvial fan in the south limb present the largest and smallest fracture length, respectively. The fracture length of the medial fluvial fan in the NTZ, crest and STZ has values in between those of the other two facies (1.39 m on average). Furthermore, channelised conglomerate bodies tend to present longer fractures than sandstone layers (1.52 m and 1.30 m on average, respectively) (Fig. 5B). Fracture length distributions should normally be corrected for size bias, because the probability of small fractures to cut the scanline is significantly lower than that of large fractures, causing an underestimation of short fractures on the statistical distribution of the whole network (Zeeb et al., 2013a). The probability of collecting fractures greater than or equal to a certain length can be corrected according to the longest fracture length (Zeeb et al., 2013a). The corrected dataset does not fit to an exponential or a power-law distribution, and only a log-normal one presents a reasonable good fit (Fig. 6B).

4.3.3. Fracture aperture and filling

Fracture apertures resulting from stress related to the anticline growth could have potentially been affected by the subsequent stress release during the uplift and exhumation of the anticline. To avoid this uncertainty, in this study we only focus on fractures (now veins) filled with calcite cement precipitated during the anticline growth, where vein widths can represent fracture apertures not affected by the subsequent rock uplift and exhumation. Fracture apertures mainly range from 1 to 5 mm and present significant variation across the different structural positions (Fig. 4C). The north limb presents the largest fracture aperture, which mainly ranges between 1 mm and 5 mm but sometimes reaches up to several centimetres. The crest, NTZ and STZ present similar fracture aperture distributions that mainly range from 1 to 3 mm. The south limb has the smallest fracture aperture with all aperture values below 2 mm. Moreover, fracture aperture also varies significantly across the different sedimentary facies and lithofacies. Fractures in the proximal fluvial fan, especially within the conglomerate bodies with interlayered sandstones, present distinctively large apertures, mainly ranging from a few millimetres to a few centimetres. In the crest, NTZ and STZ, channelised conglomerate bodies present wider fractures (1.99 mm on average) than sandstone layers (1.41 mm on average). In the south limb, fracture apertures of the medial fluvial fan rocks are lower than 2 mm (Fig. 5C). Fracture apertures present a good fit to a power-law in a cumulative distribution plot (Fig. 6C). This fit becomes very clear if the highest fracture apertures (≥3 cm) are not included, which are locally developed in the upper part of log C and filled with large calcite veins, i.e., Cc3 defined below.

Four generations of veins have been identified based on their petrographic characteristics. The first generation of calcite cement (Cc1)

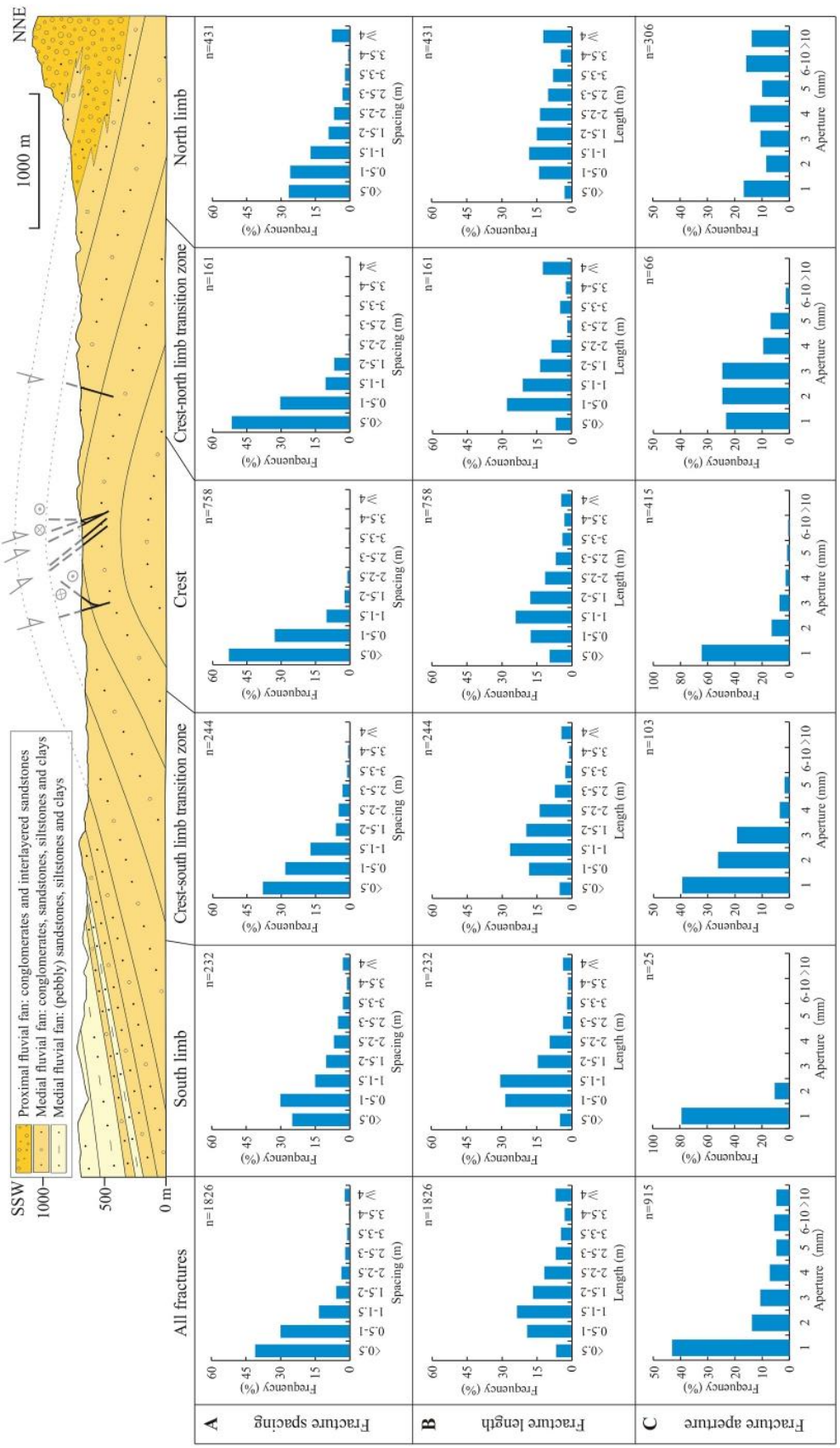

Fig. 4. Distribution of (A) fracture spacing, (B) length and (C) aperture in different structural positions. The cross section of the Puig-reig anticline is modified from Cruset et al. (2016).

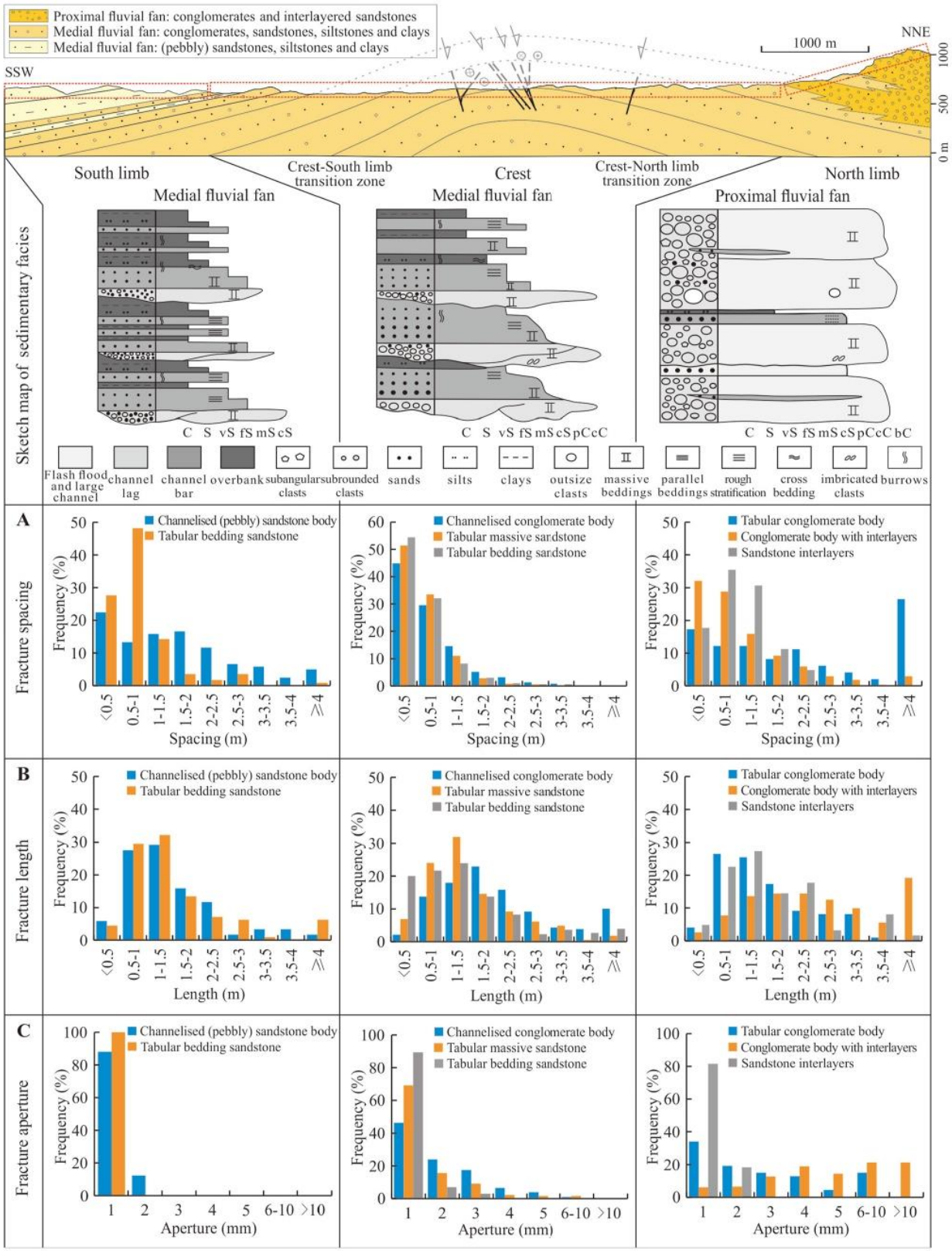

Fig. 5. Distribution of fracture (A) spacing, (B) length and (C) aperture for typical lithofacies in different sedimentary facies (proximal to medial fluvial fan). The cross section of the Puig-reig anticline is modified from Cruset et al. (2016).

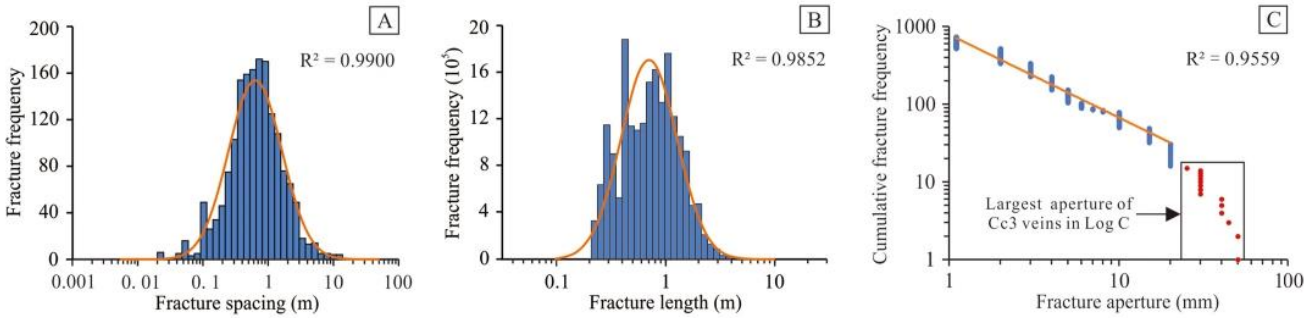

Fig. 6. Distributions of fracture attributes: (A) log-normal distribution of fracture spacing; (B) log-normal distribution of fracture length including correction for size bias with respect to the longest fracture; (C) power law distribution of fracture aperture. Note the logarithmic scales of the *X* axes in (A) and (B) and of both axes in (C).

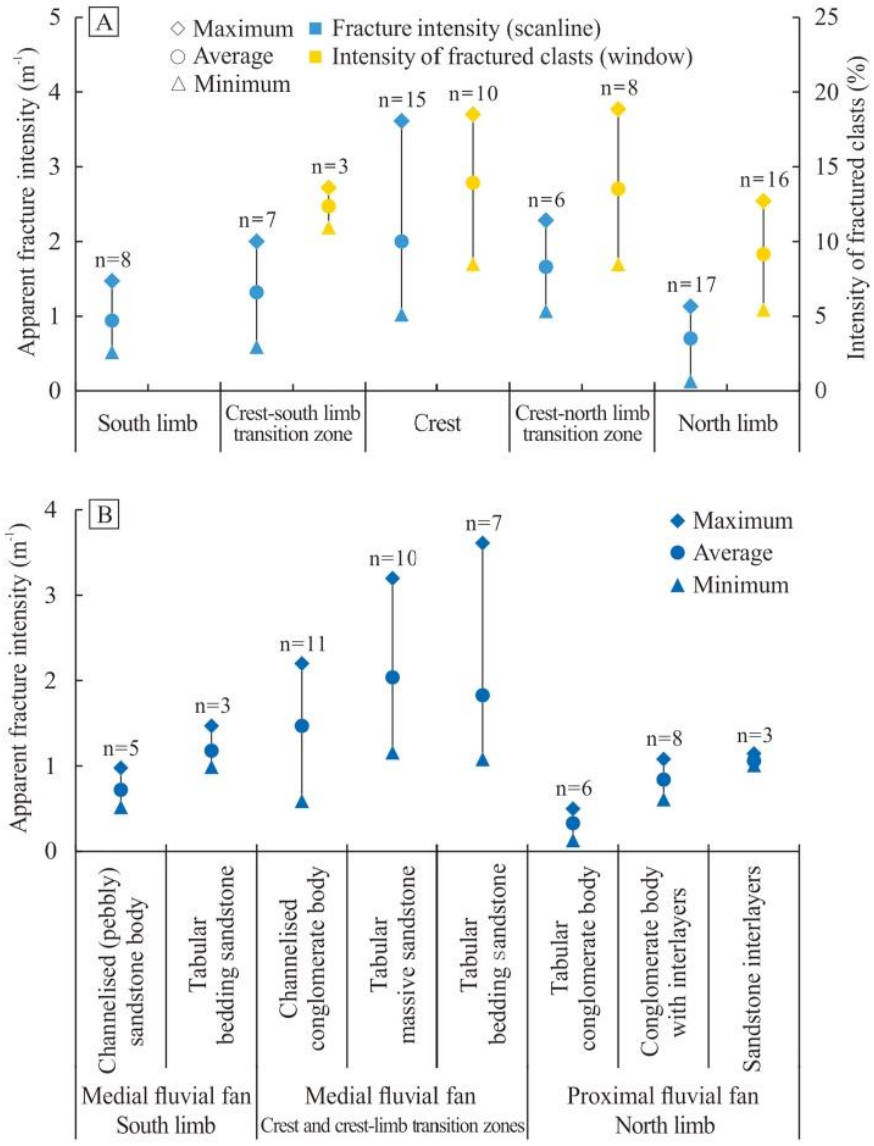

Fig. 7. (A) Apparent fracture intensity and intensity of fractured clasts of conglomerates in different structural positions, using the scanline and window fracture sampling methods, respectively. The window sampling was not used in the south limb due to the lack of conglomerate layers. (B) Apparent fracture intensity of typical lithofacies of different sedimentary facies (proximal to medial fluvial fan) in different structural positions. (*n* is the number of scanlines and windows).

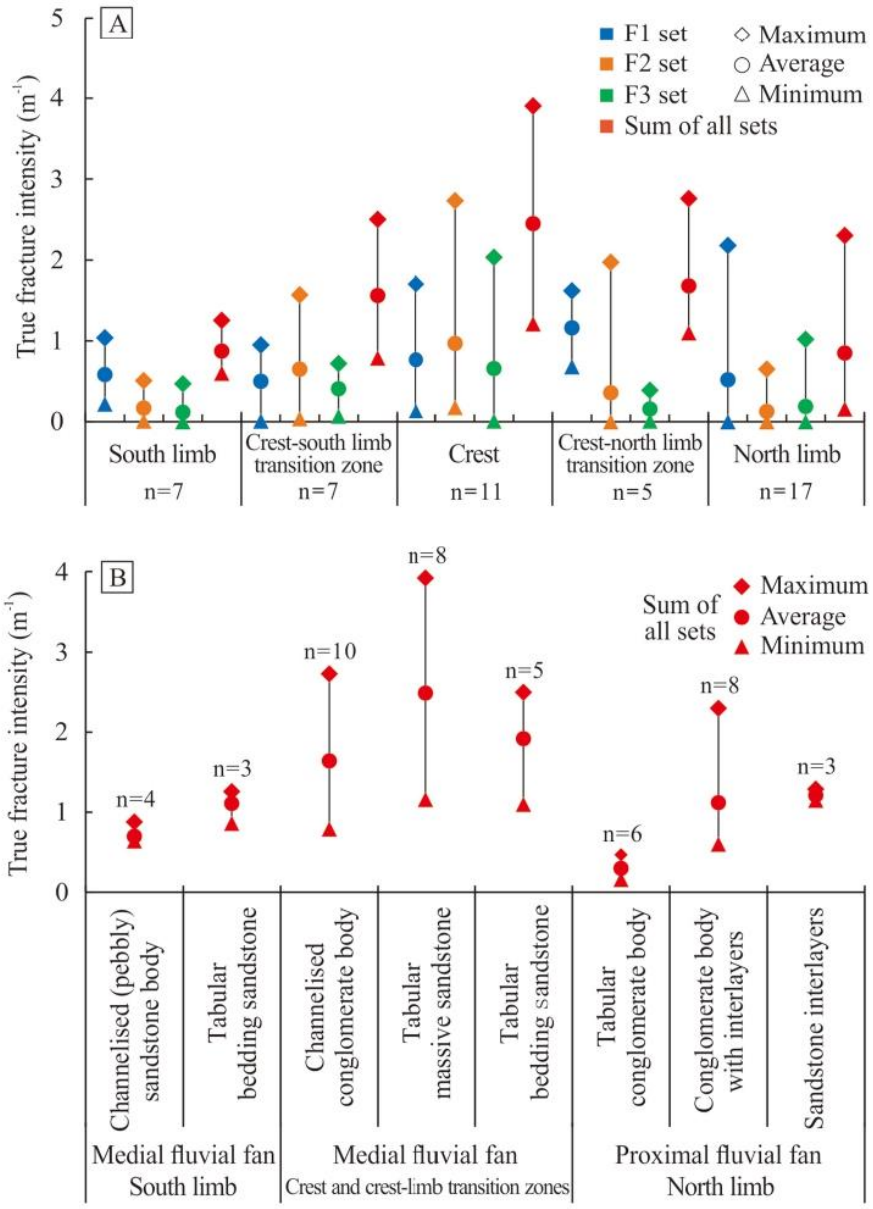

Fig. 8. (A) True fracture intensity of the F1, F2, F3 fracture sets in different structural positions, using the scanline sampling method. (B) True fracture intensity of typical lithofacies of different sedimentary facies (proximal to medial fluvial fan) in different structural positions. (*n* is the number of scanlines).

is the dominant one and is equivalent to the first generation of calcite cement identified by Cruset et al. (2016). Cc1 is the predominant cement filling fractures and interparticle pores throughout the Puig-reig anticline. Cc1 has bright orange cathodoluminescence and blocky or elongated crystal morphology with crystal size mainly ranging from 0.1 to 3 mm (Fig. 9A and B). Veins formed by multi-episodic crack-seal events are also occasionally observed (Fig. 9A and B). The second generation (Cc2) precipitated mainly in fractures and rarely in interparticle pores. Cc2 presents dull orange luminescence and blocky or elongated crystal morphology with slightly larger crystal sizes than Cc1, mainly ranging from 0.2 to 5 mm (Fig. 9C and D). The third (Cc3) and fourth (Cc4) cement generations only precipitated in fractures. Cc3 presents dull luminescence and euhedral blocky crystal morphology ranging in size from a few millimetres up to several centimetres (Fig. 9E and F). Cc4 is not luminescent and presents elongated crystal morphology or palisade structure made of bladed crystals with sizes generally smaller than 1 mm (Fig. 9G and H). This cement occasionally fills space originated by the reopening of veins hosting older cements (Fig. 9G and H).

5. Discussion

5.1. Controlling factors of fracture attributes

The fracture sets identified in the Puig-reig anticline present significant variation of their constituent attributes depending on their structural position within the anticline and the host facies (from the proximal to the medial fluvial fan). This section discusses how fracture network attributes vary across the different structural positions and sedimentary facies and thus identifies the controlling factors of fracture distribution in the Puig-reig anticline. Due to the lack of outcrops parallel to bedding, it is difficult to identify the terminations and relative cross-cutting relationships between the different fracture sets. Thus, systematically

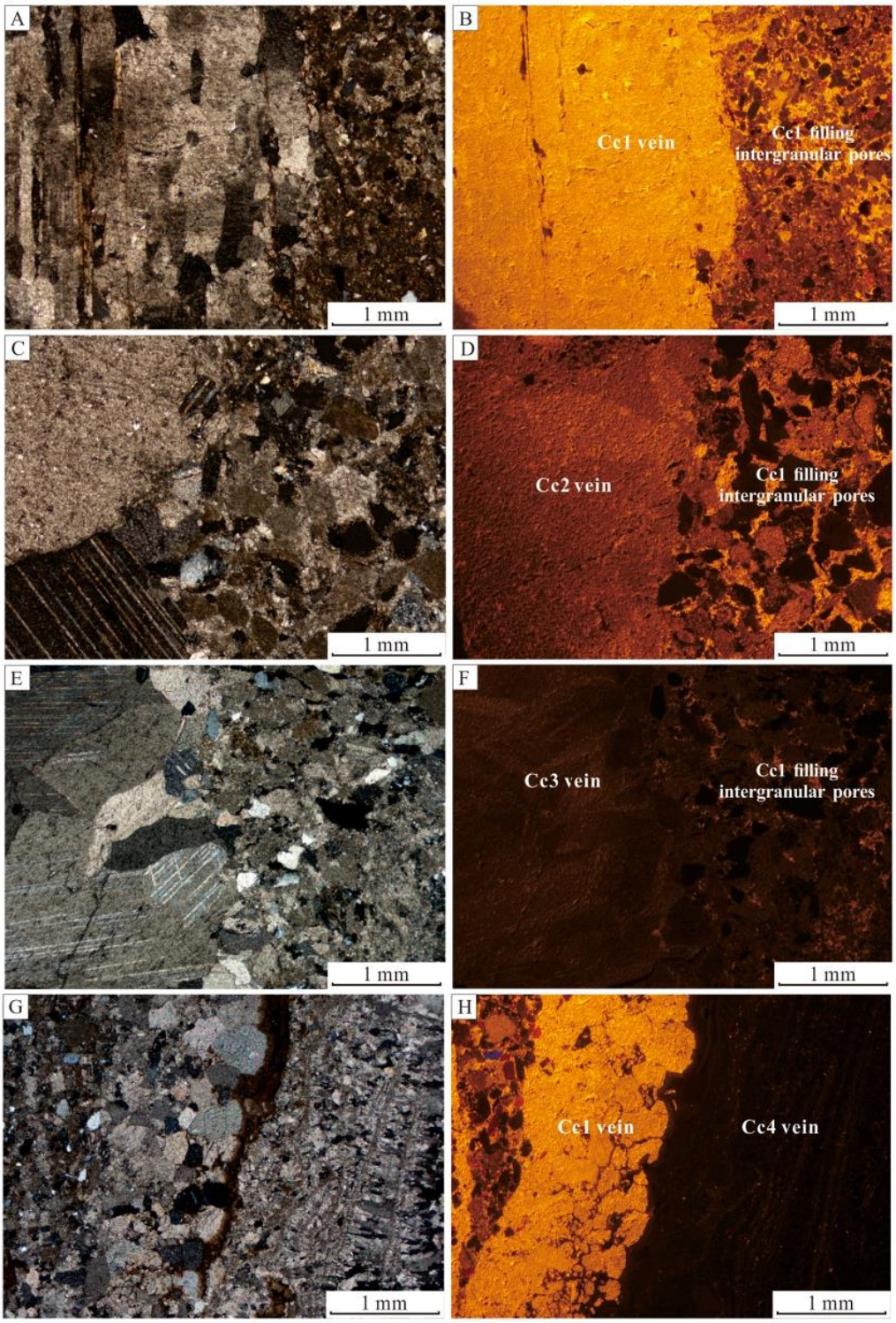

Fig. 9. Images of polarizing optical microscope (left) and cathodoluminescence (right) of calcite cements. (A–B) Cc1 calcite vein with homogeneous bright orange luminescence. (C–D) Cc2 calcite vein with duller luminescence than intergranular Cc1. (E–F) Cc3 calcite vein with duller luminescence than intergranular Cc1. (G–H) Fracture filled by Cc1 calcite vein was reopened and cemented by Cc4 calcite vein with black luminescence. (For interpretation of the references to colour in this figure legend, the reader is referred to the Web version of this article.)

establishing the chronology of the fracture sets and explaining the variation of fracture sets across the different structural positions are challenging tasks. Accordingly, we focus on the exploration of the distribution of fracture spacing, intensity, length and aperture, and the related controlling factors.

5.1.1. Controlling factors of fracture spacing and intensity

Fracture spacing presents a log-normal distribution, mainly ranging between 0.2 m and 1.2 m (Fig. 6A). However, the fracture spacing and intensity still vary significantly across the different structural positions (Figs. 4A, 7A and 8), with relatively smaller spacing and higher intensity in the crest, NTZ and STZ, and conversely, with relatively larger spacing and lower intensity in the south and north limbs. To determine the real relationship between fracture intensity and structural position, the effects of other potential controlling factors should be mitigated as much as possible. Thus, layers with same lithology and similar bedding thickness were chosen for comparison. Fig. 10A1-A2 show a clear negative correlation between fracture intensity and distance to the anticline hinge for conglomerate layers and sandstone layers, respectively, with fracture intensity decreasing significantly far from the anticline hinge. For folds developed according to the Tangential Longitudinal Strain model (TLS) (*e.g.*, Hudleston and Treagus, 2010), the fold hinge and nearby structural positions tend to experience more intensive fracturing due to their greater curvature and finite strain with respect to the limbs (Bellahsen et al., 2006; Iñigo et al., 2012; Awdal et al., 2013). If flexural slip was the dominant folding mechanism, then the thin and soft layers in limbs would be ones subjected to the highest strain. However, our field data better matches the first option because the anticline crest features more intensive fracturing than the limbs. Besides, a neutral line can divide a fold into an outer-arc extensional area and an inner-arc shortening area. Sets of layer-perpendicular extensional fractures are typical outer-arc extensional structures (Frehner, 2011). However, only a few normal faults developed in the crest of the Puig-reig anticline, which lacks systematic extensional fractures. Moreover, the analysis of Frehner (2011) reveals that when the fold is gentle (as in the case of the Puig-reig anticline) only a small area at the outer arc would undergo extension. These observations suggest that the anticline probably did not experience intensive outer arc extension.

Fracture intensity has been described to be closely related to the bedding thickness (Ladeira and Price, 1981). Some studies reported a

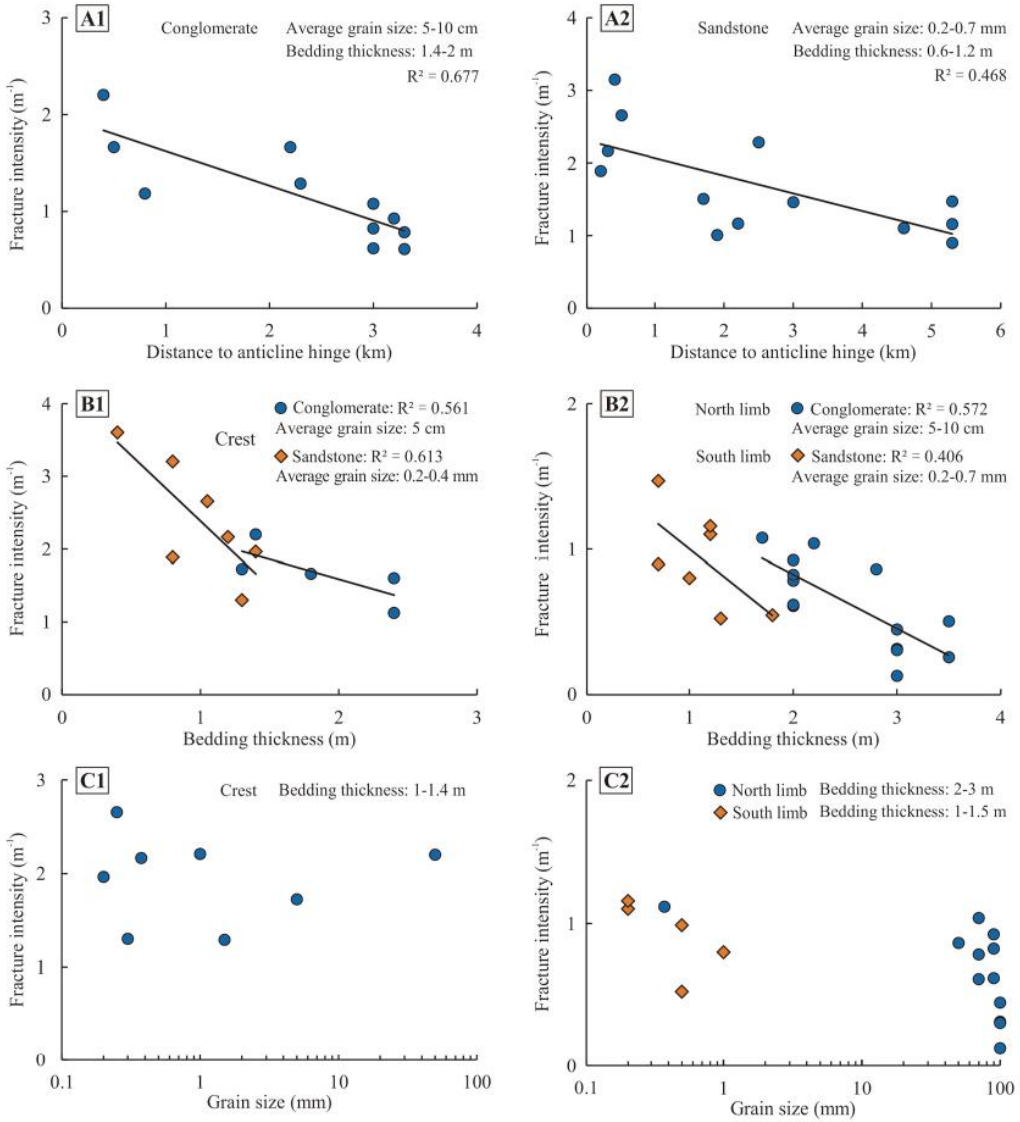

Fig. 10. Cross plots between fracture intensity and structural position and sedimentary characteristics. (A) Fracture intensity *vs.* distance to anticline hinge. (B) Fracture intensity *vs.* bedding thickness. (C) Fracture intensity *vs.* grain size.

clear negative correlation between fracture intensity and bedding thickness (Huang and Angelier, 1989; Florez-Niño et al., 2005; Wennberg et al., 2007). However, others did not reveal systematic relationships (Guiton et al., 2003; Ortega et al., 2010; Awdal et al., 2013). In this study layers with same lithology and located in the same structural position were chosen for comparison to determine the real relationship between fracture intensity and bedding thickness. Fig. 10B1 reveals a clear negative correlation between fracture intensity and bedding thickness for both conglomerate and sandstone layers in the anticline crest. Fig. 10 B2 shows a similar negative correlation for sandstone layers in the south limb and conglomerate layers in the north limb. Furthermore, conglomerate layers generally tend to be thicker than sandstone layers, thus resulting in lower fracture intensity for the same structural position, *e.g.*, in the anticline crest (Fig. 10B1). Moreover, fracture intensity decreases more significantly in sandstone layers compared to conglomerate layers. This can be observed from differences on the slope of the trend lines in Fig. 10B1 and B2.

The grain size of host rocks has been frequently considered as a critical factor controlling rock strength (Přikryl, 2001; Suorineni et al., 2009). Both physical experiments and numerical simulations have revealed that the strength of brittle rocks decreases with increasing grain size (Fredrich et al., 1990; Yu et al., 2018). Fracture intensity is generally related to the rock strength or brittleness, and is higher within the stronger and more brittle rocks (Nelson, 2001). Thus, coarse-grained rocks tend to present higher fracture intensity than fine-grained rocks, especially in carbonates (Hugman and Friedman, 1979; Hanks et al., 1997). However, a negative correlation between fracture intensity and grain size has also been reported in sandstones (Watkins et al., 2015a). In the present case, there also seems to be a subtle negative correlation between fracture intensity and grain size with relatively higher intensity in sandstone layers and lower intensity in coarse conglomerate layers. However, the variation of fracture intensity can be caused by other factors. There is not a clear relationship between fracture intensity and grain size when other factors, i.e., structural position and bedding thickness, are well controlled (Fig. 10C1 and C2). This indicates that grain size is not a significant factor controlling fracture intensity in the Puig-reig anticline, compared to the structural position or the bedding thickness.

In addition to the structural position, bedding thickness and grain size, here we explore the effect of lithological associations on fracture intensity. To mitigate the influence of other factors, the scanlines selected for comparison are those that correspond to layers with the same lithology, similar bedding thickness and that are located in same structural position. Fig. 11A presents three typical lithological associations in the anticline crest, where sandstone layers with multiple thin interlayers of fine sediments (Layer C-1) show relatively smaller fracture spacing than sandstone layers in between thick overbank fine deposits (Layer C-2) and those in between thick channel lag conglomerate bodies (Layer C-3). Similarly, Fig. 11B shows that sandstone layers with multiple interlayers of fine deposits (Layer S-1) present relatively smaller fracture spacing than those in between thick fine deposits (Layer S-2) in the south limb. In the north limb, Fig. 11C shows that conglomerate bodies with sandstone interlayers (Layer N-1) have smaller fracture spacing than other conglomerate bodies with a limited amount of sandstone lenses (Layer N-2). The high competence contrast at distinct mechanical stratigraphic positions (*e.g.*, at the interfaces between carbonate or sandstone layers and fine deposits) favours the development of joints or faults (Sibson, 1996; Wilkins et al., 2014). In this study, the interlayering between competent sandstone layers and thin incompetent fine deposits results in a high competence contrast, which favours the formation of fractures in the competent sandstone layers (*i.e.*, Layer C-1 and Layer S-1 in Fig. 11A and B). However, sandstone layers developed between thick incompetent fine deposits present relatively larger fracture spacing (Layer C-2 and Layer S-2 in Fig. 11A and B), compared to those with thin interlayers of fine deposits. This is probably because thick incompetent lithologies are capable of accommodating higher amount of pre-failure strain, *e.g.*, by means of inter-granular sliding, pressure solution, pore collapse and associated dewatering (Ferrill and Morris, 2008). Sandstone layers developed between thick conglomerate bodies (Layer C-3 in Fig. 11A) also present relatively larger fracture spacing. This is mainly because the competence contrast between competent sandstones and conglomerates is lower than that between competent sandstones and incompetent fine deposits. The competence contrast of interlayered conglomerate and sandstone layers in the north limb is higher than that of conglomerate layers with limited sandstone lens.

Based on the above analysis, we can conclude that fracture intensity is controlled by the structural position, bedding thickness and lithological associations, while the host rock's grain size only has a limited effect on fracture intensity. To quantitatively compare the relative importance of each factor for controlling fracture intensity, multiple linear regression analysis using SPSS software (IBM Corp, 2017) was employed in this study. First, lithological associations were classified and digitalised based on their effects on fracture intensity. The lithological association of competent layers with multiple thin incompetent layers (*e.g.*, Layer C-1 and Layer S-1 in Fig. 10) is assigned a value of 1 because it is conducive to the development of fractures. The lithological association of competent layers between thick incompetent layers (*e.g.*, Layer C-2 and Layer S-2 in Fig. 10) and the lithological association of interlayered competent conglomerate and sandstone layers (*e.g.*, Layer C-3 and Layer N-1 in Fig. 10) are assigned a value of 2. The lithological association of competent conglomerate layers with limited sandstone lens is assigned a value of 3, because it is not favourable for the development of fractures. Then, a multiple linear regression equation for fracture intensity can be used:

$$X_n = \frac{X - \overline{X}}{X_{max} - X_{min}} \tag{1a}$$

$$I_n = c_1 \times P_1 + c_2 \times P_2 + c_3 \times P_3 + c_4 \times P_4 \tag{2}$$

where, X, X_n, $\overline{X}$, $X_{\max}$ and $X_{\min}$ are the actual, normalised, average, maximum and minimum values for each parameter, respectively, I_n is the normalised fracture intensity, P_1 to P_4 are the normalised influence factors on fracture intensity, of structural position (distance to the anticline hinge), bedding thickness, lithological association, and lithology (grain size), respectively, and c_1 to c_4 are the standardised regression coefficients of the four influence factors, respectively. Finally, the relative importance of each factor for controlling fracture intensity can be determined based on the standardised regression coefficient of each factor. The data of 53 scanlines reached the following multiple linear regression equation:

$$I_n = -0.509 \times P_1 - 0.325 \times P_2 - 0.252 \times P_3 + 0.07 \times P_4 \quad (R^2 = 0.636) \tag{3}$$

Thus, this analysis confirms the qualitative observations that fracture intensity is mainly controlled by the structural position and is also moderately affected by bedding thickness and lithological associations, while the host rock's grain size has a very limited effect on fracture intensity.

5.1.2. Controlling factors of fracture length and aperture

Data displayed on Fig. 12A1 and A2 show positive correlations between fracture length and bedding thickness, for conglomerate and sandstone layers in the anticline crest and sandstone layers in the south limb of the anticline. Furthermore, fracture length is approximately equal to the bedding thickness in these cases. On the other hand, the fracture length of many conglomerate layers is larger than the bedding thickness in the north limb, while some thick conglomerate layers present anomalous small fracture lengths (Fig. 12A2). These anomalous values correspond to the tabular conglomerate bodies in the northwest zone of the anticline. The limited outcrop size in this area can exert an

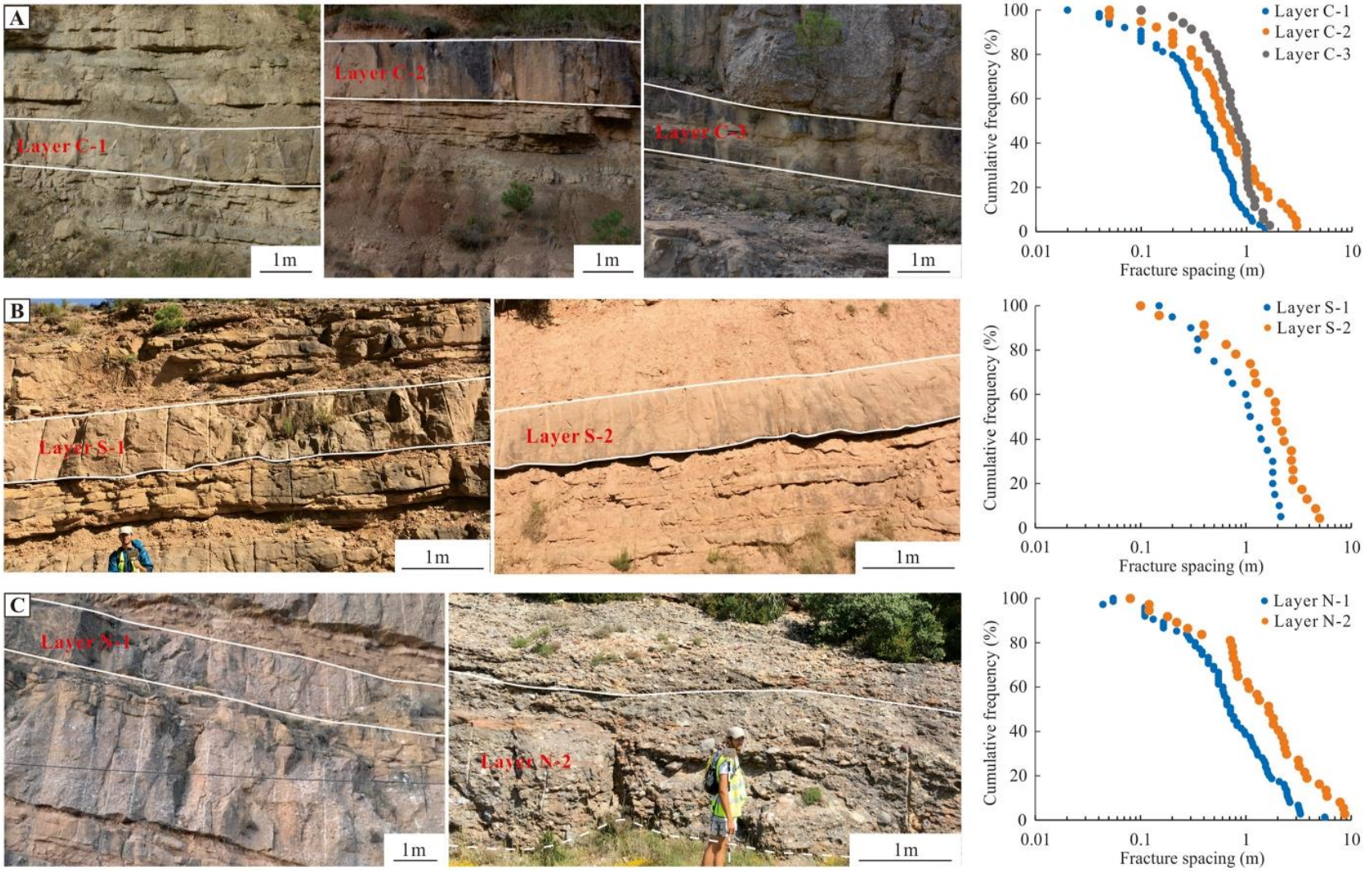

Fig. 11. Typical lithological associations in different sedimentary facies and their cumulative distributions of fracture spacing. (A) Massive sandstones with multiple interlayers of fine deposits (Layer C-1), massive sandstones between thick fine deposits (Layer C-2), and massive sandstones between thick conglomerate bodies (Layer C-3) in the anticline crest. (B) Massive sandstones with multiple interlayers of fine deposits (Layer S-1) and massive sandstones between thick fine deposits (Layer S-2) in the south limb. (B) Conglomerate bodies with stable sandstone interlayers (Layer N-1) and conglomerate bodies with limited sandstone lens (Layer N-2) in the north limb.

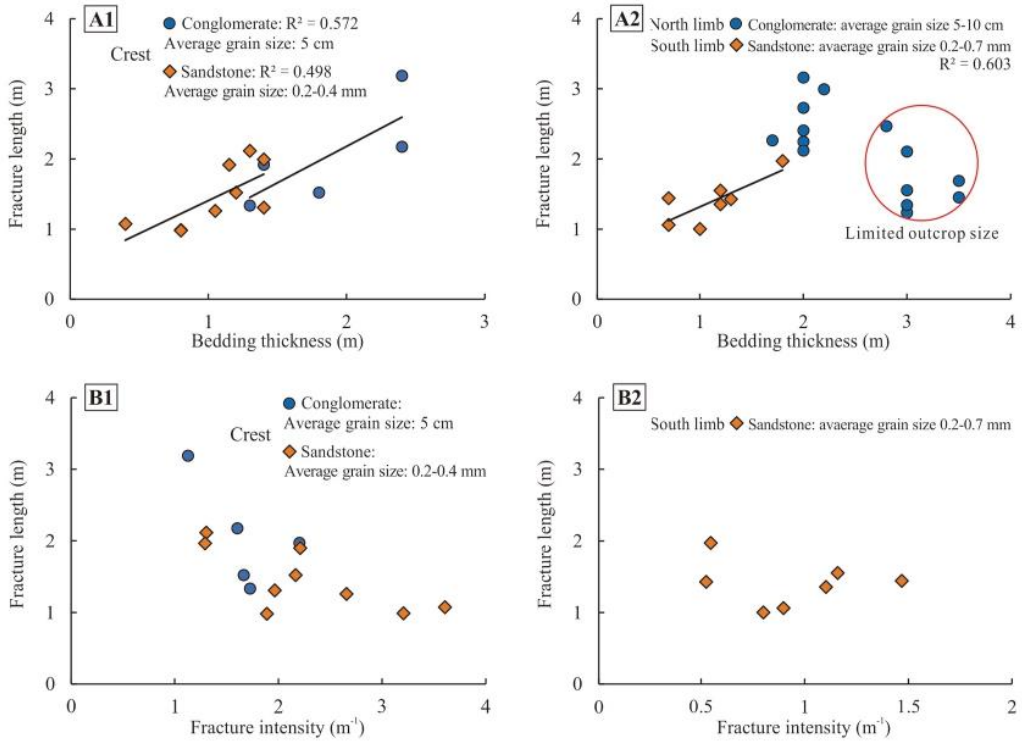

Fig. 12. (A1-A2) Cross plots between fracture length and bedding thickness. (B1–B2) Cross plots between fracture length and fracture intensity.

important effect on the collected data of fracture length due to the so-called 'censoring bias' (Zeeb et al., 2013a).

The types of fracture intersections with bedding interfaces are significantly affected by their strength. Fracture terminations are more likely to occur at very weak bedding interfaces between competent and incompetent layers, such as at interfaces between sandstone and clay, whereas strong bedding interfaces that put in contact competent layers favour fracture propagation across the interfaces (Cooke and Underwood, 2001). In the crest, crest-limb transition zones and south limb, where interbedding of conglomerates or sandstones and clays are common in the medial fluvial fan, more fractures tend to abut at the weak bedding interfaces. In this case, the fracture length is limited by the bedding thickness when fractures are stratabound (Wennberg et al., 2006). The fine deposits f the north limb are very sparse in the proximal fluvial fan, commonly resulting in strong contacts between adjacent conglomerate bodies or between conglomerates and sandstones. These relatively strong bedding interfaces in the proximal fluvial fan may promote the propagation of some long fractures but fewer facture population.

In addition, the fracture length may be structurally controlled and tend to be larger in higher strained zones to accommodate deformation during folding. For instance, Ghosh and Mitra (2009) calculated greater average fracture lengths in hinge zones compared to fold limbs. However, in the present case, the relatively higher strained crest corresponds to relatively higher fracture intensity but not larger fracture lengths. Besides, there is no clear correlation between the fracture length and intensity when other factors, *i.e.*, structural position and lithology, are well constrained (Fig. 12B1 and B2). Therefore, for the case study, the fracture length is not significantly affected by the structural position.

In the Puig-reig anticline, fracture apertures are generally smaller than 2 mm, while relatively larger values are mainly concentrated in conglomerate layers (Fig. 5C). This indicates that the sedimentary and diagenetic characteristics of the host rocks are the main controlling factor in terms of apertures rather than their structural position. This observation differs from some previous studies that suggested that wide apertures may be expected in high-strain zones (Jamison, 1997), *e.g.*, fracture apertures widen from the low-strain backlimb to the high-strain hinge (Iñigo et al., 2012). However, there is no clear correlation between fracture aperture and fracture intensity in this study (Fig. 13A), but we observe a subtle positive correlation between fracture aperture and length (Fig. 13B). This is consistent with other studies that reported that longer fractures tend to present wider apertures (Vermilye and Scholz, 1995; Olson, 2003; Ellis et al., 2012). We interpret this as an indication that these thick and massive conglomerate layers are not easily fractured, and thus strain tends to be accommodated by lengthening, widening and reopening of existing fractures rather than by developing new ones, thus resulting in larger fracture length and aperture but lower fracture intensity. The large aperture and prevalent calcite veins in conglomerate bodies are discussed in section 5.2.

5.1.3. *Fracture patterns in the Puig-reig anticline*

Based on the above analysis, Fig. 14 shows a schematic diagram that summarises the main fracture patterns of the Puig-reig anticline. The crest of the anticline, which is dominated by medial fluvial deposits (conglomerates, sandstones and clays), presents relatively high fracture intensity and variable fracture length and aperture. The north limb, which is dominated by proximal fluvial deposits (conglomerates and sandstones), presents relatively low fracture intensity but large fracture length and aperture. The south limb, dominated by medial fluvial deposits (sandstones and clays), presents relatively low fracture intensity and small length and aperture. The NTZ and STZ of the anticline feature variable fracture length and aperture and intermediate fracture intensity between the anticline crest and limbs. Fracture intensity is mainly controlled by the structural position, bedding thickness and lithological associations. Fracture length and aperture are mainly controlled by the host rock's sedimentary characteristics, while the structural position has a limited effect on them. Fracture length is mainly controlled by bedding thickness and affected by lithological associations. Fracture aperture is mainly controlled by lithology, with relatively larger values developed in conglomerate layers.

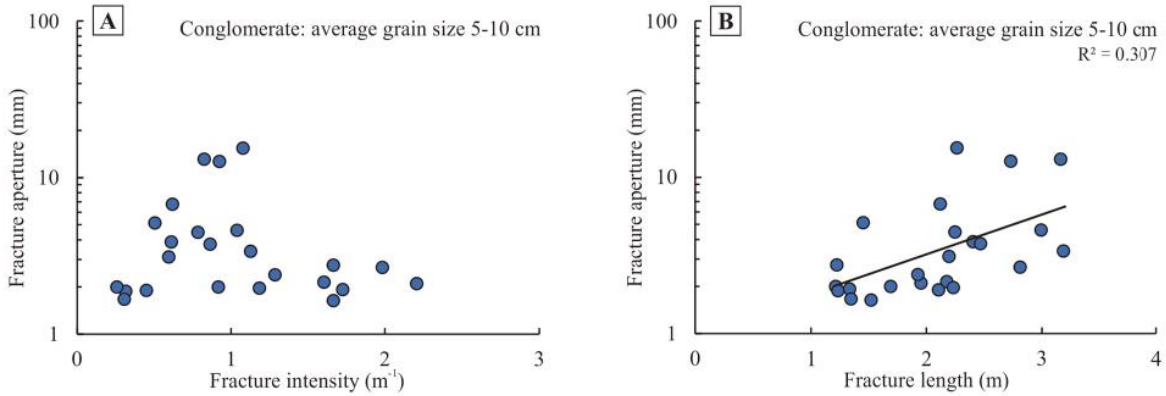

Fig. 13. (A) Cross plot between fracture aperture and fracture intensity. (B) Cross plots between fracture aperture and fracture length.

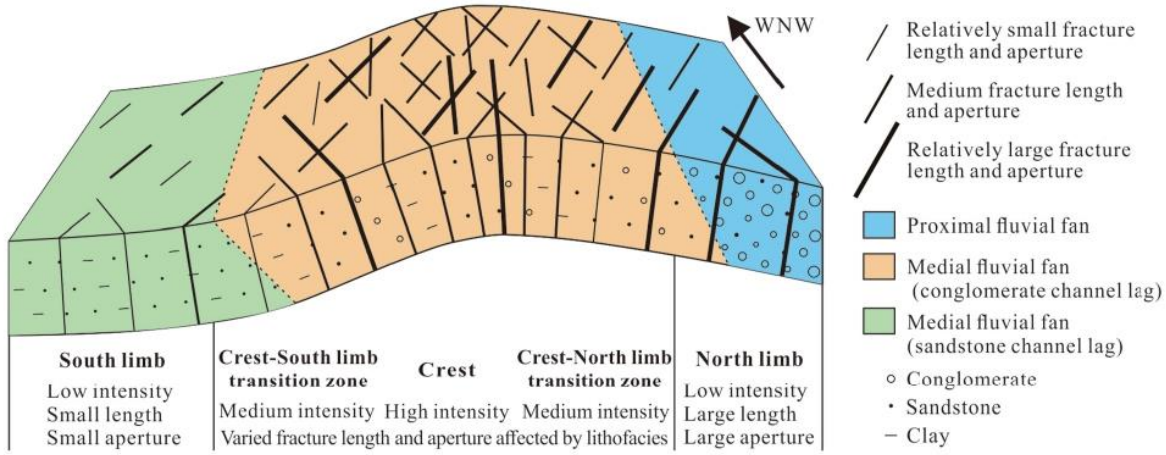

Fig. 14. Schematic diagram of fracture distribution across different structural positions and sedimentary facies. Note: the diagram does not show the termination relations between different fracture sets due to the lack of outcrops parallel to bedding planes to determine them.

5.2. Rock fracturing and vein formation

Fractures can potentially act as conduits for fluid flow and as depositional sites for cement precipitation. Therefore, fracture-filling cements are very useful to understand the conditions in which precipitation took place, including stress, strain, pressure, temperature, fluid composition and fluid origin during vein growth (Bons et al., 2012, and references therein). Structures and microstructures of calcite veins can be used to reveal fracture spatial and temporal distributions and also the fracturing and filling process in different structural positions and rock units (Gomez-Rivas et al., 2014). In the Puig-reig anticline, fractures are filled by four generations of calcite (Cc1 to Cc4) that formed veins (Fig. 8). Among these, Cc1 is the dominant generation, and is related to fluid flow during the anticline growth (Cruset et al., 2016). The clumped isotope thermometry data presented by these authors indicate that Cc1 precipitated from fluids at 92 °C to 129 °C. These temperatures are greater than the maximum temperatures reached by the Berga and Solsona strata during burial according to the maximum burial of 1.7 km and a geothermal gradient of 25 °C/km, indicating the input of external hydrothermal fluids. Besides, most Cc1 veins present a syntaxial microstructure with blocky calcite growing from the vein wall to the centre. Syntaxial veins with strong growth competition, formed by crystal growth into fracture porosity, are compatible with advective transport of fluid along fractures and fracture networks (Bons et al., 2012). Thus, fractures acted both as conduits for fluid flow and as depositional sites for calcite precipitation in the Puig-reig anticline during fold growth. More samples and geochemical data are required in order to carry out a more systematic study to reveal the origin of calcite cement and the temporal and spatial relationships between calcite cementation, fluid flow and fracture development. However, this is beyond the scope of the present study.

As discussed in section 5.1, the lower fracture intensity in the north limb is likely caused by its larger bedding thickness and lower strain compared to the crest, NTZ and STZ. When strain is high enough to cause brittle failure, fewer fractures develop in thick conglomerate bodies compared to sandstone layers. Besides, strain can also be accommodated by the cracking of clasts in conglomerates. Progressive stretching caused by folding can be accommodated by the propagation and/or re-opening and widening of previous fractures or by the formation of new ones (Watkins et al., 2015a). Strain accommodation by fracture propagation versus new fracture nucleation depends on the rock strength in a way that propagation rates decrease with increasing ductility (*e.g.*, Gomez-Rivas et al., 2015). Moreover, layer rotation (*e.g.*, due to folding), as well as mechanical anisotropy, can also reduce the fracture propagation rate (Gomez-Rivas and Griera, 2012). Eberhardt et al. (1999) found that longer grain boundaries and larger intergranular cracks, resulting from increasing grain size, provide longer paths of weakness for growing cracks to propagate along. This in turn promotes a reduction of the rock strength once the longer cracks begin to coalesce and interact. The propagation, re-opening and widening of existing fractures and the formation of new ones can operate at the same time in all structural positions and lithofacies. However, we observe that it is difficult to form

many new fractures to accommodate strain in the north limb due to the relatively lower strain in this structural position and the higher strength of these thick conglomerate bodies. Moreover, the existing fractures and veins in these thick conglomerate bodies act as weak parts compared to the host rock with high strength. Thus, the propagation, re-opening and widening of the existing fractures can accommodate strain when it is not high enough to form many new fractures. As a result, the conglomerate bodies in the north limb present relatively larger fracture length and aperture but lower intensity (Fig. 5). Besides, the re-opening or widening of existing fractures can also be proved by the observed multi-episodic crack-seal structure (Fig. 9A and B). Similarly, in the medial fluvial fan in the crest, NTZ and STZ, the channelised conglomerate bodies also present longer fractures with wider veins than those of sandstone layers.

5.3. Implications for reservoir potential

Fracture networks have a significant impact on reservoir performance. They can play a fundamental role in both controlling fluid migration and reservoir quality, especially in low-permeability and tight reservoirs in foreland fold-and-thrust belts (Casini et al., 2011; Wang et al., 2020). However, systematic fracture assessment in subsurface rocks is limited by the difficulty of sampling subseismic-scale fractures and because large fractures have much larger dimensions than that of the accessible rock volumes in boreholes (Ortega et al., 2006; Iñigo et al., 2012). Thus, a common strategy is to use outcrop analogues to understand the controlling factors of fracture networks and reduce uncertainty of subsurface predictions (Sanderson, 2016; Miranda et al., 2018). In the Pug-reig anticline, the distribution of fracture networks is significantly affected by the structural position and the host rock sedimentary characteristics, including bedding thickness, lithology and lithological associations. Although many fractures are sealed by calcite cement, this anticline can still be used as a reservoir analogue to explore the fracture distribution pattern and reservoir potential in folded clastic sediments, especially in the research context that fracturing in siliciclastic thrust belts is much less well documented than that in carbonate ones. The fluvial deposits present very low matrix porosity due to prevailing calcite cements, generally ranging from 0 to 4%. Among conglomerate and sandstone layers, only medium to coarse sandstones in the medial fluvial fan tend to present relatively high porosity (2.8% on average). Fracture intensity is mainly affected by structural position and sedimentary characteristics, with the relatively high values developing in the sandstone layers of the medial fluvial fan in the crest, NTZ and STZ of the anticline. The results indicate that the channel filling sandstone deposits, especially in the high strain zones, present relatively higher potential to be effective reservoirs.

6. Conclusions

The Puig-reig anticline, located in the south-eastern Pyrenean fold-and-thrust belt, is an excellent example of a folded fluvial depositional system, which exposes deposits of different sedimentary facies from the north limb to the south limb. A linear scanline method has been used to systematically collect fracture data, allowing the investigation of fracture distributions and their depositional and structural controlling factors. We reach the following conclusions:

(1) Four main sets of fractures have been identified, i.e., the NNW-SSE, ENE-WSW, WNW-ESE and NNE-SSW sets.
(2) Fracture attributes are strongly influenced both by their position within the fold and by the depositional characteristics of the sediments. Based on multiple linear regression analysis, fracture intensity is mainly controlled by the structural position, the bedding thickness and lithological associations, while grain size has a very limited effect on fracture intensity. Fracture length is mainly controlled by the bedding thickness and is affected by lithological associations. Fracture aperture is mainly controlled by lithology, with relatively larger values developed in conglomerate layers.
(3) Thick and massive conglomerate bodies can accommodate strain by the propagation and re-opening of existing fractures rather than by the formation of new fractures during fold growth, especially in the proximal fluvial fan in the north limb where strain was not high enough to promote the formation of a significant number of new fractures. Thus, compared to thin sandstone layers, conglomerate bodies tend to present relatively low fracture intensity but large fracture length and aperture.
(4) The study of the Puig-reig anticline reveals the fracture pattern in a folded fluvial succession, and provides an analogue case study for the prediction of subsurface fractured reservoirs with low matrix quality in fold-and-thrust belts.

Declaration of competing interest

The authors declare that they have no known competing financial interests or personal relationships that could have appeared to influence the work reported in this paper.

Acknowledgements

Funding was provided by the Catalan Council to the Grup Consolidat de Recerca "Geologia Sedimentària" (2017SGR-824) and the DGICYT Spanish Project PGC 2018-093903-B-C22 (Ministerio de Ciencia, Innovación y Universidades/Agencia Estatal de Investigación/Fondo Europeo de Desarrollo Regional, Unión Europea). XS acknowledges funding by the China Scholarship Council for a PhD scholarship (201806450043). EGR acknowledges funding provided by the Spanish Ministry of Science, Innovation and Universities ("Ramón y Cajal" fellowship RYC 2018-026335-I). JA is funded by MICINN (Juan de la Cierva fellowship - IJC 2018-036074-I). We thank associate editor Nicolas E. Beaudoin and two anonymous reviewers for their valuable suggestions, which have significantly improved this article.

References

Andrews, B.J., Roberts, J.J., Shipton, Z.K., Bigi, S., Tartarello, M.C., Johnson, G., 2019. How do we see fractures? Quantifying subjective bias in fracture data collection. Solid Earth 10, 487–516.
Arenas, C., Millán, H., Pardo, G., Pocoví, A., 2001. Ebro Basin continetal sedimentation associated with late compressional Pyrenean tectonics (North-Eastern Iberia): controls on basin margin fans and fluvial systems. Basin Res. 13, 65–89.
Awdal, A.H., Braathen, A., Wennberg, O.P., Sherwani, G.H., 2013. The characteristics of fracture networks in the shiranish formation of the bina bawi anticline; comparison with the Taq Taq field, Zagros, Kurdistan, NE Iraq. Petrol. Geosci. 19, 139–155.
Barbier, M., Hamon, Y., Callot, J.P., Floquet, M., Daniel, J.M., 2012. Sedimentary and diagenetic controls on the multiscale fracturing pattern of a carbonate reservoir: the Madison Formation (Sheep Mountain, Wyoming, USA). Mar. Petrol. Geol. 29, 50–67.
Barrier, L., Proust, J.N., Nalpas, T., Robin, C., Guillocheau, F., 2010. Control of alluvial sedimentation at foreland-basin active margins: a case study from the northeastern Ebro Basin (southeastern Pyrenees, Spain). J. Sediment. Res. 80, 728–749.
Beaudoin, N., Huyghe, D., Bellahsen, N., Lacombe, O., Emmanuel, L., Mouthereau, F., Ouanhnon, L., 2015. Fluid systems and fracture development during syn-depositional fold growth: an example from the Pico del Aguila anticline, Sierras Exteriores, southern Pyrenees, Spain. J. Struct. Geol. 70, 23–38.
Bellahsen, N., Fiore, P., Pollard, D.D., 2006. From spatial variation of fracture patterns to fold kinematics: a geomechanical approach. Geophys. Res. Lett. 33, 1–4.
Bergbauer, S., Pollard, D.D., 2004. A new conceptual fold-fracture model including prefolding joints, based on the Emigrant Gap anticline, Wyoming. Bull. Geol. Soc. Am. 116, 294–307.
Bons, P.D., Elburg, M.A., Gomez-Rivas, E., 2012. A review of the formation of tectonic veins and their microstructures. J. Struct. Geol. 43, 33–62.
Carrigan, J.H., Anastasio, D.J., Kodama, K.P., Parés, J.M., 2016. Fault-related fold kinematics recorded by terrestrial growth strata, Sant Llorenç de Morunys, Pyrenees Mountains, NE Spain. J. Struct. Geol. 91, 161–176.
Casini, G., Gillespie, P.A., Vergés, J., Romaire, I., Fernández, N., Casciello, E., Saura, E., Mehl, C., Homke, S., Embry, J.C., Aghajari, L., Hunt, D.W., 2011. Sub-seismic fractures in foreland fold and thrust belts: insight from the Lurestan Province, Zagros mountains, Iran. Petrol. Geosci. 17, 363–282.
Choukroune, P., 1989. The Ecors Pyrenean deep seismic profile reflection data and the overall structure of an orogenic belt. Tectonics 8, 23–39.

Cooke, M.L., Underwood, C.A., 2001. Fracture termination and step-over at bedding interfaces due to frictional slip and interface opening. J. Struct. Geol. 23, 223–238.
Cooper, S.P., Goodwin, L.B., Lorenz, J.C., 2006. Fracture and fault patterns associated with basement-cored anticlines: the example of Teapot Dome, Wyoming. Am. Assoc. Petrol. Geol. Bull. 90, 1903–1920.
Costa, E., Garcés, M., López-Blanco, M., Beamud, E., Gómez-Paccard, M., Larrasoaña, J. C., 2010. Closing and continentalization of the South Pyrenean foreland basin (NE Spain): magnetochronological constraints. Basin Res. 22, 904–917.
Cruset, D., Cantarero, I., Benedicto, A., John, C.M., Vergés, J., Albert, R., Gerdes, A., Travé, A., 2020. From hydroplastic to brittle deformation: controls on fluid flow in fold and thrust belts. Insights from the Lower Pedraforca thrust sheet (SE Pyrenees). Mar. Petrol. Geol. 120, 104517. https://doi.org/10.1016/j.marpetgeo.2020.104517.
Cruset, D., Cantarero, I., Travé, A., Vergés, J., John, C.M., 2016. Crestal graben fluid evolution during growth of the Puig-reig anticline (South Pyrenean fold and thrust belt). J. Geodyn. 101, 30–50.
Cruset, D., Cantarero, I., Vergés, J., John, C.M., Muñoz-López, D., Travé, A., 2018. Changes in fluid regime in syn-orogenic sediments during the growth of the south Pyrenean fold and thrust belt. Global Planet. Change 171, 207–224.
Del Santo, G., Garcia-Sansegundo, J., Sarasa, L., Torrebadella, J., 2000. Estratigrafía y estructura del Terciario en el sector oriental de la cuenca del Ebro entre Solsona y Manresa (NE de España). Rev. la Soc. Geológica España 13, 265–278 (in Spanish with English abstract).
Di Naccio, D., Boncio, P., Cirilli, S., Casaglia, F., Morettini, E., Lavecchia, G., Brozzetti, F., 2005. Role of mechanical stratigraphy on fracture development in carbonate reservoirs: insights from outcropping shallow water carbonates in the Umbria-Marche Apennines, Italy. J. Volcanol. Geoth. Res. 148, 98–115.
Eberhardt, E., Stimpson, B., Stead, D., 1999. Effects of grain size on the initiation and propagation thresholds of stress-induced brittle fractures. Rock Mech. Rock Eng. 32, 81–99.
Ellis, M.A., Laubach, S.E., Eichhubl, P., Olson, J.E., Hargrove, P., 2012. Fracture development and diagenesis of Torridon Group Applecross Formation, near an Teallach, NW Scotland: millennia of brittle deformation resilience? J. Geol. Soc. London. 169, 297–310.
Evans, M.A., Bebout, G.E., Brown, C.H., 2012. Changing fluid conditions during folding: an example from the central Appalachians. Tectonophysics 576–577, 99–115.
Evans, M.A., Fischer, M.P., 2012. On the distribution of fluids in folds: a review of controlling factors and processes. J. Struct. Geol. 44, 2–24.
Ferrill, D.A., Morris, A.P., 2008. Fault zone deformation controlled by carbonate mechanical stratigraphy , Balcones fault system , Texas. Am. Assoc. Petrol. Geol. Bull. 92, 359–380.
Fischer, M.P., Higuera-Díaz, I.C., Evans, M.A., Perry, E.C., Lefticariu, L., 2009. Fracture-controlled paleohydrology in a map-scale detachment fold: insights from the analysis of fluid inclusions in calcite and quartz veins. J. Struct. Geol. 31, 1490–1510.
Florez-Niño, J.M., Aydin, A., Mavko, G., Antonellini, M., Ayaviri, A., 2005. Fault and fracture systems in a fold and thrust belt: an example from Bolivia. Am. Assoc. Petrol. Geol. Bull. 89, 471–493.
Ford, M., Williams, E.A., Artoni, A., Vergés, J., Hardy, S., 1997. Progressive evolution of a fault-related fold pair from growth strata geometries, Sant Llorenç de Morunys, SE Pyrenees. J. Struct. Geol. 19, 413–441.
Fredrich, J.T., Evans, B., Wong, Teng-Fong, 1990. Effect of grain size on brittle and semibrittle strength: implications for micromechanical modelling of failure in compression. J. Geophys. Res. 95, 10907–10920.
Frehner, M., 2011. The neutral lines in buckle folds. J. Struct. Geol. 33, 1501–1508.
Ge, H., Jackson, M.P.A., Vendeville, B.C., 1997. Kinematics and dynamics of salt tectonics driven by progradation. Am. Assoc. Petrol. Geol. Bull. 81, 398–423.
Ghosh, K., Mitra, S., 2009. Structural controls of fracture orientations, intensity, and connectivity, Teton anticline, Sawtooth Range, Montana. Am. Assoc. Petrol. Geol. Bull. 93, 995–1014.
Gomez-Rivas, E., Bons, P.D., Koehn, D., Urai, J.L., Arndt, M., Virgo, S., Laurich, B., Zeeb, C., Stark, L., Blum, P., 2014. The Jabal Akhdar Dome in the Oman mountains: evolution of a dynamic fracture system. Am. J. Sci. 314, 1104–1139.
Gomez-Rivas, E., Griera, A., 2012. Shear fractures in anisotropic ductile materials: an experimental approach. J. Struct. Geol. 34, 61–76.
Gomez-Rivas, E., Griera, A., Llorens, M.G., 2015. Fracturing of ductile anisotropic multilayers: influence of material strength. Solid Earth 6, 497–514.
Guiton, M.L.E., Sassi, W., Leroy, Y.M., Gauthier, B.D.M., 2003. Mechanical constraints on the chronology of fracture activation in folded Devonian sandstone of the western Moroccan Anti-Atlas. J. Struct. Geol. 25, 1317–1330.
Gutmanis, J., Ardèvol i Oró, L., Díez-Canseco, D., Chebbihi, L., Awdal, A., Cook, A., 2018. Fracture analysis of outcrop analogues to support modelling of the subseismic domain in carbonate reservoirs, south-central Pyrenees. Geol. Soc. London, Spec. Publ. 459, 139–156.
Hanks, C.L., Lorenz, J., Teufel, L., Krumhardt, A.P., 1997. Lithologic and structural controls on natural fracture distribution and behavior within the Lisburne Group, northeastern Brooks Range and North Slope subsurface, Alaska. Am. Assoc. Petrol. Geol. Bull. 81, 1700–1720.
Healy, D., Rizzo, R.E., Cornwell, D.G., Farrell, N.J.C., Watkins, H., Timms, N.E., Gomez-Rivas, E., Smith, M., 2017. FracPaQ: a MATLAB™ toolbox for the quantification of fracture patterns. J. Struct. Geol. 95, 1–16.
Hennings, P.H., Olson, J.E., Thompson, L.B., 2000. Combining outcrop data and three-dimensional structural models to characterize fractured reservoirs: an example from Wyoming. Am. Assoc. Petrol. Geol. Bull. 84, 1–20.
Horton, B.K., Decelles, P.G., 2001. Modern and ancient fluvial megafans in the foreland basin system of the Central Andes, Southern Bolivia: implications for drainage network evolution if foldthrust belts. Basin Res. 13, 43–63.
Huang, Q., Angelier, J., 1989. Fracture spacing and its relation to bed thickness. Geol. Mag. 126, 355–362.
Hudleston, P.J., Treagus, S.H., 2010. Information from folds: a review. J. Struct. Geol. 32, 2042–2071.
Hugman, R.H.H., Friedman, M., 1979. Effects of texture and composition on mechanical behavior of experimentally deformed carbonate rocks. Am. Assoc. Petrol. Geol. Bull. 63, 1478–1489.
IBM Corp, 2017. IBM SPSS Statistics for Windows, Version 25.0. https://www.ibm.com/support/pages/downloading-ibm-spss-statistics-25.
Iñigo, J.F., Laubach, S.E., Hooker, J.N., 2012. Fracture abundance and patterns in the Subandean fold and thrust belt, Devonian Huamampampa Formation petroleum reservoirs and outcrops, Argentina and Bolivia. Mar. Petrol. Geol. 35, 201–218.
Institut Cartogràfic i Geològic de Catalunya, 2006. Regional Geological Map of Catalonia accessed 2.1.21). https://www.icgc.cat/en/Public-Administration-and-Enterprises/Downloads/Geological-and-geothematic-cartography/Geological-cartography/Geological-map-1-50-000/Regional-geological-map-of-Catalonia-1-50-000.
Instituto Geológico y Minero de España, 1977. Geophysical Information System accessed 10.1.20). http://info.igme.es/SIGEOF/#.
Instituto Geológico y Minero de España, 1995. Almacenamiento subterraneo de gas: previabilidad en formaciones detriticas y salinas accessed 3.20.21. http://info.igme.es/ConsultaSID/r.asp?IdDESCRIPTOR=2681.
Jamison, W.R., 1997. Quantitative evaluation of fractures on Monkshood anticline, a detachment fold in the foothills of western Canada. Am. Assoc. Petrol. Geol. Bull. 81, 1110–1132.
Jones, S.J., 2004. Tectonic controls on drainage evolution and development of terminal alluvial fans, southern Pyrenees, Spain. Terra. Nova 16, 121–127.
Lacroix, B., Baumgartner, L.P., Bouvier, A.S., Kempton, P.D., Vennemann, T., 2018. Multi fluid-flow record during episodic mode I opening: a microstructural and SIMS study (Cotiella Thrust Fault, Pyrenees). Earth Planet Sci. Lett. 503, 37–46.
Ladeira, F.L., Price, N.J., 1981. Relationship between fracture spacing and bed thickness. J. Struct. Geol. 3, 179–183.
Laubach, S.E., Olson, J.E., Cross, M.R., 2009. Mechanical and fracture stratigraphy. Am. Assoc. Petrol. Geol. Bull. 93, 1413–1426.
Lorenz, J.C., Cooper, S.P., Olsson, W.A., 2006. Natural fracture distributions in sinuous, channel-fill sandstones of the Cedar Mountain Formation, Utah. Am. Assoc. Petrol. Geol. Bull. 90, 1293–1308.
Mann, P., Gahagan, L., Gordon, M.B., 2003. Tectonic setting of the world's giant oil fields. In: Halbouty, M. (Ed.), Giant Oil and Gas Fields of the Decade 1990–1999, vol. 78. AAPG Memoir, pp. 15–105.
Martínez-Martínez, J.M., Soto, J.I., Balanyá, J.C., 2002. Orthogonal folding of extensional detachments: structure and origin of the Sierra Nevada elongated dome (Betics, SE Spain). Tectonics 21, 1–22.
Miranda, T.S., Santos, R.F., Barbosa, J.A., Gomes, I.F., Alencar, M.L., Correia, O.J., Falcão, T.C., Gale, J.F.W., Neumann, V.H., 2018. Quantifying aperture, spacing and fracture intensity in a carbonate reservoir analogue: crato Formation, NE Brazil. Mar. Petrol. Geol. 97, 556–567.
Muñoz-López, D., Alías, G., Cruset, D., Cantarero, I., John, C.M., Travé, A., 2020a. Influence of basement rocks on fluid evolution during multiphase deformation: the example of the Estamariu thrust in the Pyrenean Axial Zone. Solid Earth 11, 2257–2281.
Muñoz-López, D., Cruset, D., Cantarero, I., Benedicto, A., John, C.M., Travé, A., 2020b. Fluid dynamics in a thrust fault inferred from petrology and geochemistry of calcite veins: an example from the southern Pyrenees. Geofluids 2020 1–25.
Muñoz, J.A., 1992. Evolution of a continental collision belt: ECORS-Pyrenees crustal balanced cross-section. In: McClay, K.R. (Ed.), Thrust Tectonics. Springer, Dordrecht, pp. 235–246.
Nardini, N., Muñoz-López, D., Cruset, D., Cantarero, I., Martín-Martín, J., Benedicto, A., Gomez-Rivas, E., John, C., Travé, A., 2019. From early contraction to post-folding fluid evolution in the frontal part of the Bóixols thrust sheet (southern Pyrenees) as revealed by the texture and geochemistry of calcite cements. Minerals 9, 117.
Nelson, R.A., 2001. Geologic Analysis of Naturally Fractured Reservoirs. Gulf Professional Publishing, Houston.
Nelson, R.A., Serra, S., 1995. Vertical and lateral variations in fracture spacing in folded carbonate sections and its relation to locating horizontal wells. J. Can. Pet. Technol. 34, 51–56.
Ogata, K., Senger, K., Braathen, A., Tveranger, J., 2014. Fracture corridors as seal-bypass systems in siliciclastic reservoir-cap rock successions: field-based insights from the Jurassic Entrada Formation (SE Utah, USA). J. Struct. Geol. 66, 162–187.
Ogata, K., Storti, F., Balsamo, F., Tinterri, R., Bedogni, E., Fetter, M., Gomes, L., Hatushika, R., 2017. Sedimentary facies control on mechanical and fracture stratigraphy in turbidites. Bull. Geol. Soc. Am. 129, 76–92.
Olson, J.E., 2003. Sublinear scaling of fracture aperture versus length: an exception or the rule? J. Geophys. Res. Solid Earth 108, 2413.
Olson, J.E., Laubach, S.E., Lander, R.H., 2007. Combining diagenesis and mechanics to quantity fracture aperture distributions an fracture pattern permeability. Geol. Soc. Spec. Publ. 270, 101–116.
Ortega, O.J., Gale, J.F.W., Marrett, R., 2010. Quantifying diagenetic and stratigraphic controls on fracture intensity in platform carbonates: an example from the Sierra Madre Oriental, northeast Mexico. J. Struct. Geol. 32, 1943–1959.
Ortega, O.J., Marrett, R.A., Laubach, S.E., 2006. A scale-independent approach to fracture intensity and average spacing measurement. Am. Assoc. Petrol. Geol. Bull. 90, 193–208.
Peacock, D.C.P., 2001. The temporal relationship between joints and faults. J. Struct. Geol. 23, 329–341.
Peacock, D.C.P., Nixon, C.W., Rotevatn, A., Sanderson, D.J., Zuluaga, L.F., 2016. Glossary of fault and other fracture networks. J. Struct. Geol. 92, 12–29.

Přikryl, R., 2001. Some microstructural aspects of strength variation in rocks. Int. J. Rock Mech. Min. Sci. 38, 671–682.
Puigdefàbregas, C., Muñnz, J.A., Marzo, M., 1986. Thrust belt development in the eastern Pyrenees and related depositional sequences in the southern foreland basin. In: Allen, P.A., Homewood, P. (Eds.), Foreland Basins. International Association of Sedimentologists Special Publication, pp. 229–246.
Puigdefabregas, C., Muñoz, J.A., Vergés, J., 1992. Thrusting and foreland basin evolution in the Southern Pyrenees. In: McClay, K.R. (Ed.), Thrust Tectonics. Springer, Dordrecht, pp. 247–254.
Roure, F., Choukroune, P., Berastegui, X., Munoz, J.A., Villien, A., Matheron, P., Bareyt, M., Seguret, M., Camara, P., Deramond, J., 1989. Ecors deep seismic data and balanced cross sections: geometric constraints on the evolution of the Pyrenees. Tectonics 8, 41–50.
Sáez, A., Anadón, P., Herrero, M.J., Moscariello, A., 2007. Variable style of transition between Palaeogene fluvial fan and lacustrine systems, southern Pyrenean foreland, NE Spain. Sedimentology 54, 367–390.
Sanderson, D.J., 2016. Field-based structural studies as analogues to sub-surface reservoirs. Geol. Soc. Spec. Publ. 431, 207–217.
Serra-Kiel, J., Mató, E., Saula, E., Travé, A., Ferràndez-Canadell, C., Busquets, P., Samsó, J.M., Tosquella, J., Barnolas, A., Àlvarez-Pérez, G., Franquès, J., Romero, J., 2003a. An inventory of the marine and transitional middle/upper Eocene deposits of the southeastern pyrenean foreland basin (NE Spain). Geol. Acta 1, 201–229.
Serra-Kiel, J., Travé, A., Mató, E., Saula, E., Ferràndez-Canadell, C., Busquets, P., Tosquella, J., Vergés, J., 2003b. Marine and transitional Middle/Upper Eocene units of the southeastern pyrenean foreland basin (NE Spain). Geol. Acta 1, 177–200.
Shackleton, J.R., Cooke, M.L., Sussman, A.J., 2005. Evidence for temporally changing mechanical stratigraphy and effects on joint-network architecture. Geology 33, 101–104.
Sibson, R.H., 1996. Structural permeability of fluid-driven fault-fracture meshes. J. Struct. Geol. 18, 1031–1042.
Stephenson, B.J., Koopman, A., Hillgartner, H., McQuillan, H., Bourne, S., Noad, J.J., Rawnsley, K., 2007. Structural and stratigraphic controls on fold-related fracturing in the Zagros Mountain, Iran: implications for reservoir development. Geol. Soc. Spec. Publ. 270, 1–21.
Sun, X., Alcalde, J., Gomez-Rivas, E., Struth, L., Johnson, G., Travé, A., 2020. Appraisal of CO2 storage potential in compressional hydrocarbon-bearing basins: global assessment and case study in the Sichuan Basin (China). Geosci. Front. 11, 2309–2321.
Suorineni, F.T., Chinnasane, D.R., Kaiser, P.K., 2009. A procedure for determining rock-type specific hoek-brown brittle parameter s. Rock Mech. Rock Eng. 42, 849–881.
Suppe, J., Sàbat, F., Anton Muñoz, J., Poblet, J., Roca, E., Vergés, J., 1997. Bed-by-bed fold growth by kink-band migration: Sant llorenç de Morunys, eastern Pyrenees. J. Struct. Geol. 19, 443–461.
Taillefer, A., Soliva, R., Guillou-Frottier, L., Le Goff, E., Martin, G., Seranne, M., 2017. Fault-related controls on upward hydrothermal flow: an integrated geological study of the Têt fault system, eastern Pyrénées (France). Geofluids 2017 1–19.
Tavani, S., Granado, P., Corradetti, A., Seers, T., Casas, J.M., Muñoz, J.A., 2020. Transverse jointing in foreland fold-and-thrust belts: a remote sensing analysis in the eastern Pyrenees. Solid Earth 11, 1643–1651.
Tavani, S., Mencos, J., Bausà, J., Muñoz, J.A., 2011. The fracture pattern of the Sant Corneli Bóixols oblique inversion anticline (Spanish Pyrenees). J. Struct. Geol. 33, 1662–1680.
Terzaghi, R.D., 1965. Sources of error in joint surveys. Geotechnique 15, 287–304.
Travé, A., Calvet, F., Sans, M., Vergés, J., Thirlwall, M., 2000. Fluid history related to the Alpine compression at the margin of the south-Pyrenean Foreland basin: the El Guix anticline. Tectonophysics 321, 73–102.
Travé, A., Labaume, P., Vergés, J., 2007. Fluid systems in foreland fold-and-thrust belts: an overview from the southern Pyrenees. In: Lacombe, O., Lavé, J., Roure, F., Vergés, J. (Eds.), Thrust Belts and Foreland Basins. Springer, Berlin, Heidelberg, pp. 93–115.
Underwood, C.A., Cooke, M.L., Simo, J.A., Muldoon, M.A., 2003. Stratigraphic controls on vertical fracture patterns in Silurian dolomite, northeastern Wisconsin. Am. Assoc. Petrol. Geol. Bull. 87, 121–142.
Van Dijk, J.P., Bello, M., Toscano, C., Bersani, A., Nardon, S., 2000. Tectonic model and three-dimensional fracture network analysis of Monte Alpi (southern Apennines). Tectonophysics 324, 203–237.
Vergés, J., 1993. Estudi geològic del vessant sud del Pirineu oriental i central. Evolució cinemàtica en 3D. Ph.D. thesis. University of Barcelona, Barcelona (in Spanish).
Vergés, J., Marzo, M., Muñoz, J.A., 2002. Growth strata in foreland settings. Sediment. Geol. 146, 1–9.
Vergés, J., Marzo, M., Santaeulària, T., Serra-Kiel, J., Burbank, D.W., Muñoz, J.A., Giménez-Montsant, J., 1998. Quantified vertical motions and tectonic evolution of the SE Pyrenean foreland basin. Geol. Soc. London, Spec. Publ. 134, 107–134.
Vergés, J., Muñoz, J.A., Martínez, A., 1992. South Pyrenean fold and thrust belt: the role of foreland evaporitic levels in thrust geometry. In: K R, M. (Ed.), Thrust Tectonics. Springer, Dordrecht, pp. 255–264.
Vermilye, J.M., Scholz, C.H., 1995. Relation between vein length and aperture. J. Struct. Geol. 17, 423–434.
Wang, Z., Lü, X., Wang, S., Li, Y., Zhou, X., Quan, H., Li, R., 2020. Fracture systems and petrophysical properties of tight sandstone undergoing regional folding: a case study of the Cretaceous reservoirs in the Kuqa foreland thrust belt, Tarim Basin. Mar. Petrol. Geol. 111, 104055. https://doi.org/10.1016/j.marpetgeo.2019.104055.
Watkins, H., Butler, R.W.H., Bond, C.E., Healy, D., 2015a. Influence of structural position on fracture networks in the Torridon Group, Achnashellach fold and thrust belt, NW Scotland. J. Struct. Geol. 74, 64–80.
Watkins, H., Bond, C.E., Healy, D., Butler, R.W.H., 2015b. Appraisal of fracture sampling methods and a new workflow tocharacterise heterogeneous fracture networks at outcrop. J. Struct. Geol. 72, 67–82.
Wennberg, O.P., Azizzadeh, M., Aqrawi, A.A.M., Blanc, E., Brockbank, P., Lyslo, K.B., Pickard, N., Salem, L.D., Svånå, T., 2007. The Khaviz Anticline: an outcrop analogue to giant fractured Asmari Formation reservoirs in SW Iran. Geol. Soc. London, Spec. Publ. 270, 23–42.
Wennberg, O.P., Svånå, T., Azizzadeh, M., Aqrawi, A.M.M., Brockbank, P., Lyslo, K.B., Ogilvie, S., 2006. Fracture intensity vs. mechanical stratigraphy in platform top carbonates: the aquitanian of the asmari formation, Khaviz anticline, Zagros, SW Iran. Petrol. Geosci. 12, 235–246.
Wilkins, S., Mount, V., Mahon, K., Perry, A., Koenig, J., 2014. Characterization and development of subsurface fractures observed in the Marcellus Formation, Appalachian Plateau, north-central Pennsylvania. Am. Assoc. Petrol. Geol. Bull.
Williams, E.A., Ford, M., Vergés, J., Artoni, A., 1998. Alluvial gravel sedimentation in a contractional growth fold setting, Sant Llorenç de Morunys, southeastern Pyrenees. Geol. Soc. London, Spec. Publ. 134, 69–106.
Yu, Q., Zhu, W., Ranjith, P.G., Shao, S., 2018. Numerical simulation and interpretation of the grain size effect on rock strength. Geomech. Geophys. Geo-Energy Geo-Resour. 4, 157–173.
Yuste, A., Luzón, A., Bauluz, B., 2004. Provenance of Oligocene-Miocene alluvial and fluvial fans of the northern Ebro Basin (NE Spain): an XRD, petrographic and SEM study. Sediment. Geol. 172, 251–268.
Zeeb, C., Gomez-Rivas, E., Bons, P.D., Blum, P., 2013a. Evaluation of Sampling methods for fracture network characterization using Outcrops. Am. Assoc. Petrol. Geol. Bull. 97, 1545–1566.
Zeeb, C., Gomez-Rivas, E., Bons, P.D., Virgo, S., Blum, P., 2013b. Fracture network evaluation program (FraNEP): a software for analyzing 2D fracture trace-line maps. Comput. Geosci. 60, 11–22.

Appendix 5 Origin and distribution of calcite cements and their effects on reservoir potential in a folded fluvial succession: the Puig-reig anticline (SE Pyrenees)

Sun, X., Gomez-Rivas, E., Cruset, D., Alcalde, J., Muñoz-López, D., Cantarero, I., Martín-Martín, J.D., Travé, A., 2021. Fluid evolution and calcite cementation in a folded fluvial succession at an active basin margin: the Puig-reig anticline example (SE Pyrenees). In preparation.

Origin and distribution of calcite cements and their effects on reservoir potential in a folded fluvial succession: the Puig-reig anticline (SE Pyrenees)

Xiaolong Sun[a], Enrique Gomez-Rivas[a], David Cruset[b], Juan Alcalde[b], Daniel Muñoz-López[a], Irene Cantarero[a], Juan Diego Martín-Martín[a], Cédric M. John[c], Anna Travé[a]

[a] Departament de Mineralogia, Petrologia i Geologia Aplicada, Facultat de Ciències de la Terra, Universitat de Barcelona (UB), c/ Martí i Franquès s/n, Barcelona, 08028, Spain

[b] Geosciences Barcelona (GEO3BCN-CSIC), Lluís Solé i Sabarís s/n, Barcelona, 08028, Spain

[c] Department of Earth Science and Engineering, Imperial College London, Prince Consort Road, London, SW7 2AZ, UK

Abstract: As one of the predominant diagenetic products in clastic rocks, calcite cements are typical fingerprints of cement-forming fluids and are key controls on reservoir quality. The Puig-reig anticline, in the south-eastern Pyrenees, exposes excellent fluvial outcrops that underwent folding, fracturing and cementation. This anticline constitutes an excellent case study to investigate the origin and distribution of calcite cements during folding evolution and how they affect reservoir quality. Based on structural, petrological and geochemical analyses (carbon, oxygen, strontium and clumped isotopes and elemental composition), five generations of calcite cements (Cc0 to Cc4) have been identified, filling intergranular porosity of host rocks, faults and four fracture sets (F1 to F4). Cc0 precipitated in intergranular porosity from meteoric fluids in the phreatic zone during the early diagenetic stage. During the most intense phase of thrusting and folding, Cc1 precipitated in intergranular porosity, faults and F1 to F4 fracture sets from hydrothermal fluids that migrated from deeper areas of the Pyrenean chain. During the late stage of fold growth, Cc2 mainly precipitated in faults in the anticline crest. Cc2 could have resulted from the mixing between asynchronous hydrothermal and meteoric fluids or from hydrothermal fluids but at a shallower burial depth and with a greater admixture of meteoric waters than that of Cc1. Cc3 mainly precipitated in faults and F1 and F4 fracture sets in the north-western part of the anticline. Its parent fluids were dominated by formation fluids that probably migrated through the frontal thrust of the SE Pyrenees. During continuous fold denudation, Cc4 precipitated from meteoric fluids in F1 to F4 fracture sets across the anticline. At foreland basin margins, external fluids coeval with compressional deformation and/or substantial detrital carbonates of clastic rocks contribute to intensive calcite cementation. This can result in an overall occlusion of porosity and significantly damaged reservoir quality.

Keywords: calcite cementation; fluid regime; fluvial reservoir; anticline; Pyrenees

1 Introduction

Calcite in the form of cement is one of the predominant authigenic minerals in clastic rocks (Morad, 1998; Walderhaug & Bjørkum, 1998). The presence and distribution of calcite cement can exert significant effects on reservoir quality and heterogeneity (Dutton et al., 2002; Davis et al., 2006; Van den Bril et al., 2007; Xiong et al., 2016; Cui et al., 2017; Wang et al., 2017). In clastic rock settings, different phases of calcite cements can successively precipitate from local or external fluids during the evolution of sedimentary basins and orogens. On the macro scale, calcite cement distribution within clastic rocks is mainly controlled by the depositional environments and the stacking patterns of sequence stratigraphy (Morad, 1998; Taylor et al., 2000; El-ghali et al., 2006; Morad et al., 2010), and has been widely studied in shallow marine (Bjørkum & Walderhaug, 1990b; Walderhaug & Bjørkum, 1998; Taylor et al., 2000; Nyman et al., 2014), deep-water turbidite (Carvalho et al., 1995; Dos Anjos et al., 2000; Dutton, 2008; Mansurbeg et al., 2009; Yang et al., 2018) and alluvial-fluvial settings (Hall et al., 2004; Wanas, 2008; Taylor & Machent, 2011; Cruset et al., 2016; Olanipekun & Azmy, 2021). Another factor that controls cement distribution in rocks at multiple scales is the development of faults and fractures, which control fluid migration across different hydrostratigraphic units (Evans & Fischer, 2012; Evans et al., 2012). On the small scale, cement distribution is controlled by lithofacies and reservoir porosity and permeability, in a way that cementation tends to affect the more permeable deposits (Dutton et al., 2002; Hall et al., 2004; Van Den Bril & Swennen, 2009). Thus, calcite cement tends to be heterogeneously distributed and can exert key effects on reservoir quality, such as the partial or total reduction of permeability (Dutton et al., 2002).

Fracture networks tend to form in fold-and-thrust belts and their adjacent foreland basin margins due to intensive deformation. Calcite cementation of these fractures and their host rocks can be used to unravel the history and timing of fluid migration events (Hansman et al., 2018; Cruset et al., 2020b), the evolution of fluid regimes, the degree of fluid-rock interaction, and the deformation history of related structures (Travé et al., 1997, 1998; Bons et al., 2012; Beaudoin et al., 2014). The interplay between rock deformation, fluid flow and diagenesis in compressive settings has been analysed in many case studies, including examples from the Apennines (Smeraglia et al., 2018; Beaudoin et al., 2020), the Bighorn Basin in the Sevier fold-and-thrust belt (Beaudoin et al., 2011, 2013, 2014), the Oman Mountains (Breesch et al., 2009; Gomez-Rivas et al., 2014; Balsamo et al., 2016), the Sicilian fold-and-thrust belt (Dewever et al., 2010, 2013), and the Zagros fold-and-thrust belt (Ceriani et al., 2011; Shariatinia et al., 2013), among many others. The South Pyrenees is also an ideal natural laboratory due to its well-preserved and well-exposed outcrops. However, previous studies mainly focused on unravelling the relationships between fluid flow and deformation in the cover thrust sheets (Travé et al., 1997; Lacroix et al., 2011, 2014, 2018; Beaudoin et al., 2015; Crognier et al., 2018; Cruset et al., 2018, 2020a; Nardini et al., 2019; Muñoz-López et al., 2020a; b), whereas only a few studies focused on the

Ebro Foreland Basin (e.g., Travé et al., 2000, 2007; Cruset et al., 2016). On the other hand, compressional settings have high potential for carbon capture and storage (CCS) (Sun et al., 2020). The Ebro Foreland Basin has been assessed as one of the priority regions for CCS development in Spain (Sun et al., 2021a). However, there is significant uncertainty on the suitability assessment of storage sites in this hydrocarbon-limited basin due to the very limited geological and geophysical exploration data available. Thus, well-exposed structures of this area can be used as analogues to explore cement distribution, fluid evolution, and their effects on reservoir potential of such reservoir structures at depth.

The Puig-reig anticline, at the north-eastern margin of the Ebro Foreland Basin, exposes excellent outcrops of proximal to medial fluvial deposits. These outcrops are composed of interlayered conglomerates, sandstones and claystones and mainly belong to the Camps de Vall-Llonga and Solsona Formations. The sedimentary characteristics and fracture networks of these folded deposits from the Puig-reig anticline have been studied previously by Sun et al. (2021b, 2021c). Previously, Cruset et al. (2016) carried out a study of the geochemistry of calcite cements restricted to the anticline crest to unravel the composition of the fluids from which these cements precipitated. They described two cementation phases, the first of them related to the early fold growth and the second one associated with the crestal collapse. Based on previous studies, here we identify the complete sequence of calcite cementation filling both intergranular porosity and fractures in the whole anticline and during the complete fold evolution. We also unravel the conditions under which these cements precipitated and relate them to the sedimentological and structural evolution of the Puig-reig anticline. For this purpose, we use a multidisciplinary approach that integrates structural, petrographic and geochemical analyses of fracture-filling and intergranular porosity-filling calcite cements. Contrary to previous studies, special emphasis is put on understanding the distribution of calcite cement across different lithofacies and structural positions of the anticline. Based on the comprehensive analysis of cement distribution in the Puig-reig anticline, the results are compared with those reported from other areas worldwide in order to discuss universal rules for the distribution of calcite cement and the effects on reservoir potential in different settings.

2 Geological setting

The Pyrenees constitute an asymmetrical and doubly verging orogenic belt that generated during the collision between the Iberian and Eurasian plates from the Late Cretaceous to the Miocene (Muñoz, 1992; Vergés et al., 2002). This orogen comprises an antiformal stack of basement-involved thrusts (the Axial Zone), southward sided to the South Pyrenean fold-and-thrust belt and finally propagated to the Ebro Foreland Basin (Choukroune, 1989; Roure et al., 1989; Muñoz, 1992). The Vallfogona thrust acts as the major frontal thrust between the South Pyrenean fold-and-thrust belt and the eastern Ebro Foreland Basin (Fig. 1A, B, C). Vergés (1993) interpreted the Puig-reig anticline as a growth anticline

at the footwall of the Vallfogona thrust due to a duplex stack at depth, which can be observed in the seismic profiles across this anticline (Fig. 1C). In the deeper part, the Banyoles and Igualada Formations are composed of marine marls and deltaic sandstones deposited during the Middle and Late Eocene. These marine deposits were duplicated by thrusting and detached above the Lutetian Beuda gypsums and the late Priabonian Cardona salts (Vergés et al., 1992; Serra-Kiel et al., 2003a; b). In the upper and outcropping part of the Puig-reig anticline, the Berga Group and the Solsona Formation were deposited from alluvial to fluvial systems from the Late Eocene to the Oligocene, after the transition from marine to continental depositional environments (Costa et al., 2010). The Puig-reig anticline trends ESE/WNW and is slightly oblique to the main Pyrenean structures (Vergés, 1993). This gentle anticline has a wavelength of more than 10 km.

At the proximal area of the footwall of the Vallfogona thrust ramp, the Berga Group consists of coarse alluvial and proximal fluvial deposits and presents growth strata geometries (Ford et al., 1997; Suppe et al., 1997), which are dated between around 34 and 31 Ma (Carrigan et al., 2016). These coarse deposits become progressively finer-grained and thinner bedded towards the Ebro Foreland Basin and wedge out into the fluvial Solsona Formation (Williams et al., 1998; Barrier et al., 2010). Focusing on the outcrops of the Camps de Vall-Llonga (a sub-unit of the Berga Group) and Solsona Formations in the Puig-reig anticline (Fig. 1D), Sun et al. (2021b) interpreted these formations as deposited from a proximal to medial fluvial system. This anticline can be divided into five structural positions from north to south, i.e., north limb, crest-north limb transition zone (NTZ), crest, crest-south limb transition zone (STZ) and south limb (Fig. 1E). The proximal fluvial deposits, which concentrate in the north limb of the anticline and especially in the northwest part, are characterised by conglomerates with minor interbedded sandstones. These deposits represent sedimentary environments of unconfined flash floods or wide-shallow channel streams. The proximal-medial fluvial deposits, covering the NTZ, crest and STZ zones of the anticline, consist of interbedded beds of conglomerates, sandstones and claystones. The medial-distal fluvial deposits dominate the south limb of the anticline and consist of interbedded beds of sandstones and claystones. These medial fluvial deposits represent sedimentary environments of braided channel streams and overbanks. The distal fluvial deposits are located southward of our study area, and are composed of terminal lobes representing low lake-level stages and fluvial-dominated deltas and interdistributary bays representing high lake-level stages (Sáez et al., 2007).

Based on a previous study on fracture networks (Sun et al., 2021c), the anticline crest features abundant fractures and a system of faults, including strike-slip and normal faults characterised by displacements lower than 20 m. Other scarce small-scale low-angle reverse faults with displacements lower than 2 m are also present, which were previously observed in other studies (Cruset et al., 2016). Other structural positions are characterised by abundant fractures and a few strike-slip faults. Based on the fracture orientations and their relationships with the fold hinge, Sun et al. (2021c) identified four

fracture sets (not including faults) in the Puig-reig anticline with the following strikes: F1 (NNW-SSE), F2 (ENE-WSW), F3 (WNW-ESE) and F4 (NNE-SSW) (Fig. 2A). Fractures of the F4 set are difficult to identify because they are sub-parallel to most outcrop sections. The anticline crest features relatively high fracture intensity and variable fracture orientations including F1 to F3 sets (Fig. 2B). The NTZ shows a predominant F1 set and moderate fracture intensity. The STZ shows variable fracture sets like the anticline crest and moderate fracture intensity. The north and south limbs feature a predominant F1 set and relatively low fracture intensity.

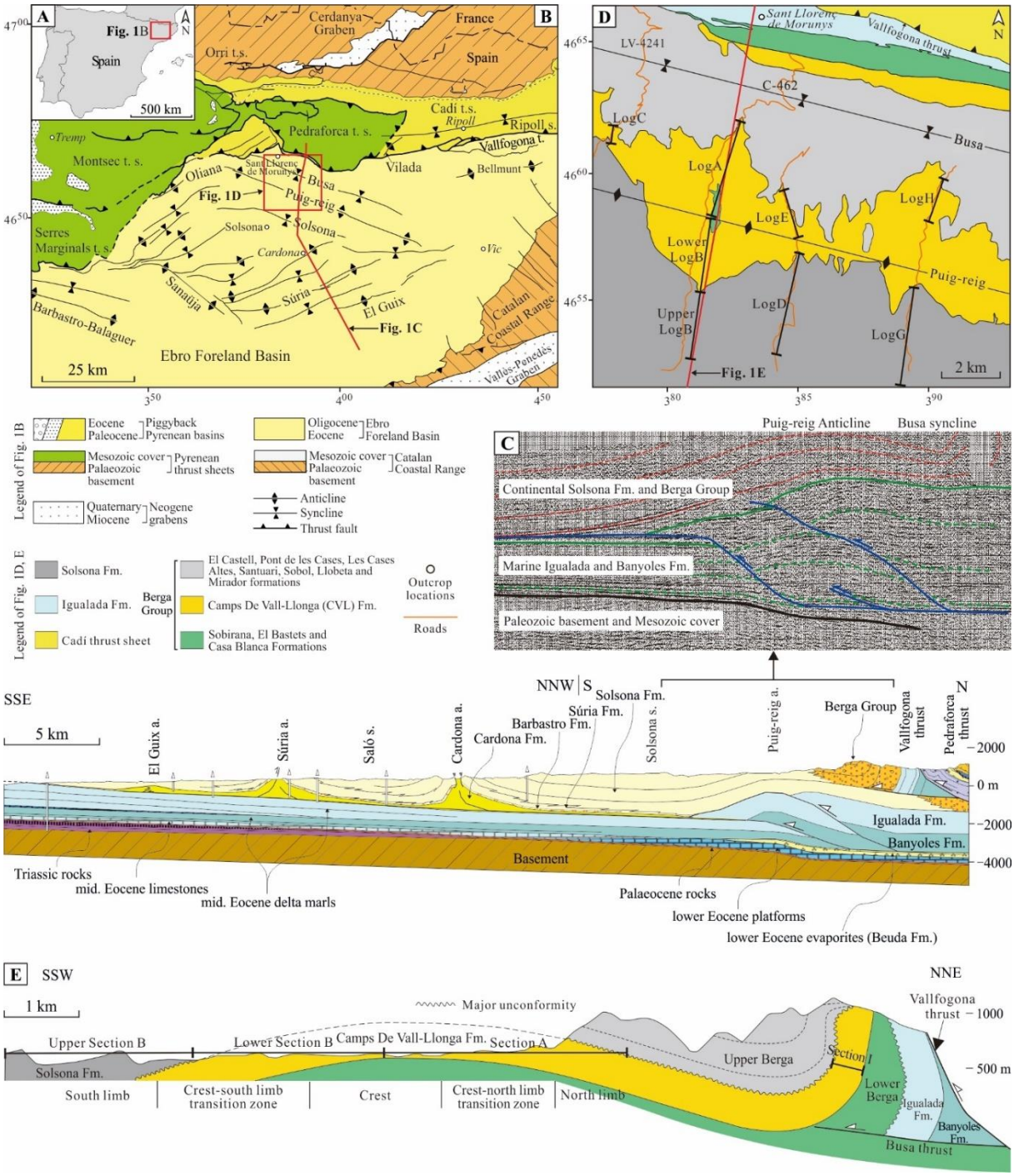

Figure 1. (A) Geographical location and (B) main structural units of the South Pyrenean fold-and-thrust belt and

the Ebro Foreland Basin (Vergés, 1993). (C) Geological cross-section of the frontal part of the SE Pyrenean fold-and-thrust belt and the Ebro Foreland Basin (Vergés, 1993). The seismic profile (Line S-2) is from the Spanish Geophysical Information System (Instituto Geológico y Minero de España, 1977). (D) Distribution of the Berga Group and the Solsona Formation and location of the studied outcrops. The strata distribution is based on the regional geological map of Catalonia (Institut Cartogràfic i Geològic de Catalunya, 2006). The subdivision of the Berga Group follows the scheme of Williams et al. (1998). (E) Geological cross-section of the north-eastern margin of the Ebro Foreland Basin, modified from Williams et al. (1998) and Barrier et al. (2010).

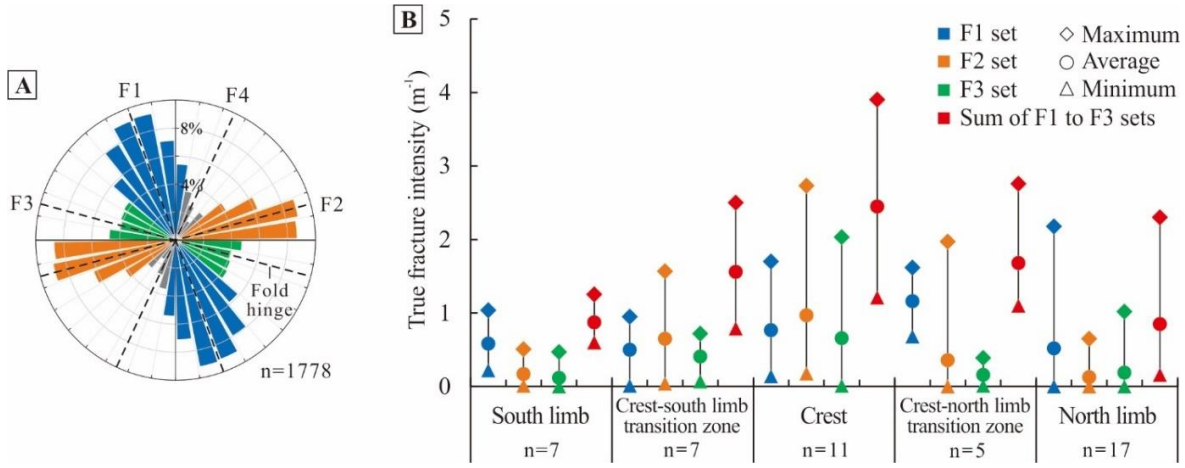

Figure 2. Distribution of fracture attributes in the Puig-reig anticline (modified from Sun et al., 2021c): (A) Rose diagram displaying fracture strike distribution ('n' is the number of fractures) and (B) fracture intensity in different structural positions ('n' is the number of linear scanlines).

3 Methods

3.1 Outcrops and samples

The Puig-reig anticline exposes excellent outcrops that mainly consist of deposits of the Camps de Vall-Llonga and Solsona Formations. These outcrops are distributed in the cross-sections along roads that cut through the structure in a roughly north-south direction (i.e., almost perpendicular to the fold trace), between the towns of Sant Llorenç de Morunys in the north and Solsona in the south (Fig 1B and D). In this study, fractures hosting calcite veins were plotted in equal-area lower-hemisphere stereograms. Samples of host rocks and fracture-filling veins, representing different structural positions of the anticline and different lithofacies, were selected for petrographic and geochemical analyses.

3.2 Petrography

A total of 108 polished thin sections of host rocks and fracture-filling calcite veins were made for petrographic observations. These were analysed to determine host rock compositions and to distinguish different generations of calcite cements using a Zeiss Axiophot optical microscope and a Technosyn Cold Cathodoluminescence microscope, model 8200 Mk5-1 operating 16 to 17 kV and 270 to 290 μA

gun current. Among these, 30 sandstone thin sections were selected to determine rock composition using the point-counting method. In addition, 60 thin sections from different lithofacies were selected to determine porosity and cement content of host rocks using NIS Elements and ImageJ software (Schneider et al., 2012). Based on the colour differences between different components, porosity was determined using microphotographs in parallel nicols, while cement content was determined using microphotographs in cathodoluminescence.

3.3 Carbon and oxygen isotopes

A total of 27 samples of fracture-filling veins and intergranular porosity-filling cements were selected for carbon- and oxygen-isotope analysis for different generations of calcite cements. Using a 500 μm-diameter dental drill, 50-70 μg of calcite powders were reacted with 100% phosphoric acid for five minutes at 70°C. The resultant CO_2 was analysed using an automated Kiel Carbonate Device coupled to an isotope ratio mass spectrometer Thermo Finnigan MAT-252 following a modified McCrea's method (1950). The results were calibrated with secondary standards (RC-1 and CECC), traceable to NBS-18 and NBS-19 international standards. The standard deviation is ±0.01‰ for $\delta^{13}C$ and ±0.03‰ for $\delta^{18}O$ with respect to the VPDB standard (Vienna Pee Dee Belemnite)

3.4 Clumped isotope thermometry

Clumped isotope thermometry was applied to four samples of calcite cements to calculate the temperatures and $\delta^{18}O$ values of the fluids from which these calcite cements precipitated. Measurements were carried out in the Qatar Stable Isotope Laboratory at Imperial College London using a fully automated system, Imperial Batch Extraction (IBEX), and following the method of Adlan et al. (2020). Around 4 mg aliquots of calcite powders for each sample were individually dropped into 105% phosphoric acid at 90°C and reacted for 10 min on an automated IBEX device. The resultant CO_2 was separated with a Porapak-Q trap and transferred into the bellows of a Thermo MAT 253 isotope ratio mass spectrometer (Thermo Instrument, Bremen, Germany). The characterisation of a replicate consisted of 8 acquisitions in dual inlet mode with 7 cycles per acquisition. The post-acquisition processing was completed using the free software Easotope (John & Bowen, 2016). We used the new Intercarb (I-CDES) approach to correcting our clumped isotope samples (Bernasconi et al., 2021) which relies on normalisation using 4 carbonate standards: ETH1 (0.205 ± 0016‰), ETH2 (0.209 ± 0.0015‰), ETH3 (0.613 ± 0.0014‰) and ETH4 (0.451 ± 0.0018‰). Values in the I-CDES are reported without acid correction factor at 90˚C. The raw Δ47 data were corrected for non-linearity using the pressure baseline correction (Bernasconi et al., 2013). Samples were measured three times (three replicate) and the average results were converted to temperatures using the interlaboratory calibration of Anderson et al. (2021). The calibration includes data from the Qatar Stable Isotope Laboratory, extends from 0-350˚C, and is measured using the new I-CDES scale: it is thus an ideal calibration for our study. Carbonate $\delta^{18}O$

values were corrected with the acid fractionation factors of Kim et al. (2015). The $\delta^{18}O_{fluid}$ was calculated using the equation of Kim et al. (2007) with the clumped isotope temperatures and the carbonate $\delta^{18}O$ values, and are expressed in ‰ with respect to the Vienna Standard Mean Ocean Water (VSMOW).

3.5 Strontium isotopes

Strontium isotopes ($^{87}Sr/^{86}Sr$) were measured for four samples of calcite cements. 10 to 20 mg of calcite powders for each sample were rinsed in ultrasonic MilliQ water to remove detrital contaminants. Each sample was treated individually to ensure that sufficient rinsing steps were applied. Cleaned fragments were dissolved in dilute nitric acid, and the resulting solution was centrifuged at medium speed for 20 minutes, and the supernatant was transferred to clean PFA beakers. Sr was separated from matrix and Rb using an extraction resin type Eichrom Sr-Spec in the ultra-clean laboratory LIRA (UB). Sr isotope ratios were determined by multicollector inductively coupled mass spectrometry on a Nu Instruments (Wrexham, UK) Plasma 3 MC-ICPMS at the University of Barcelona (CCiT-UB). $^{87}Sr/^{86}Sr$ ratios were normalized for instrumental mass bias with respect to the reference value of $^{86}Sr/^{88}Sr$ = 0.1194. Instrumental drift was corrected by sample-standard bracketing (SSB) using NBS987 = 0.710230 as the primary standard with matching standard and sample Sr concentrations. External analytical reproducibility during the session is $^{87}Sr/^{86}Sr = 0.710339 \pm 0.000012$ (2σ, n=14).

3.6 Elemental composition

Nine carbon-coated polished thin sections were selected to analyse major, minor and trace element concentrations on a CAMECA SX-50 electron microprobe. The microprobe was operated using 20 kV of excitation potential, 6 nA of current intensity and a beam diameter of 10 μm. In total, more than 400 probe points were selected, covering all generations of calcite cements recognized by petrographic observations. Detection limits are 107 ppm for Ca, 112 ppm for Mg, 119 ppm for Mn, 254 ppm for Sr, 77 ppm for Fe and 139 ppm for Na. Precision on major element analyses averages 1.03% standard error at 3σ confidence levels.

4 Results

4.1 Petrology of host rocks

Based on Folk's (1980) sandstone classification, all fluvial sandstone samples of the study area plot within the litharenite field (Fig. 3A). Framework grains are mainly composed of lithic fragments (60% to 90%) with minor quartz (5% to 30%) and very limited feldspar. Based on Zuffa's (1980) classification of hybrid arenites, these samples mainly plot in the carbonate extrarenite field with a minor number in the non-carbonate extrarenite field (Fig. 3B). The contents of carbonate extrabasinal grains range from 40% to 70%, mainly sourced from the Mesozoic-Cenozoic successions of the South Pyrenean cover thrust sheets and the Pyrenean Axial Zone (Devonian carbonates). The contents of non-carbonate

extrabasinal grains, including non-carbonate lithic, quartz and feldspar grains, range from 30% to 60%, mainly sourced from the Pyrenean Axial Zone (Riba, 1976; Williams et al., 1998; Barrier et al., 2010). The proximal fluvial fan has a slightly higher content in carbonate extrabasinal grains, compared to the medial fluvial fan. As shown in Fig. 3C, most samples present very low porosity, mainly ranging from 0% to 3%, with an average value of 1.2%. All samples have high contents of intergranular porosity-filling calcite cements, mainly ranging from 5% to 15%, with an average value of 11.6%. Most porosity has been destroyed by compaction and occluded by cementation.

4.2 Petrology of calcite cements

Field and microscope observations allow characterising the distribution and petrographic characteristics of fracture-filling and intergranular porosity-filling calcite cements (Fig. 4). Five calcite cement generations (Cc0 to Cc4) have been recognized in the Puig-reig anticline. Among these, Cc1 and Cc2 correspond to the two cementation phases identified by Cruset et al. (2016).

Cc0 calcite cement precipitated in intergranular pores but not in fractures. Although Cc0 only filled a small fraction of intergranular porosity, it can be found in different structural positions across the anticline and in different lithofacies from sandstones to conglomerates. Cc0 generally precipitated along clast edges, which is more frequently observed in conglomerate and coarse sandstone lithofacies due to their larger size of intergranular pores. Cc0 consists of subhedral to euhedral blocky to slightly bladed crystals, with crystal sizes smaller than 0.5 mm. Mechanical twins are rarely observed in this cement generation. Under cathodoluminescence, Cc0 crystals are non-luminescent with bright orange zonation (Fig. 4A1 and A2).

Cc1 calcite cement precipitated in both intergranular pores and fractures. Cc1 filled most intergranular porosity in all structural positions and lithofacies. This cement presents anhedral to subhedral blocky crystal morphology with crystal sizes mainly ranging from 5 to 500 μm and with some mechanical twins. In terms of veins, Cc1 filled fractures in different structural positions across the anticline and precipitated in reverse and strike-slip faults and F1 to F4 fracture sets (Fig. 4B1). This cement is characterised by subhedral to euhedral blocky to slightly elongated crystals with long axes generally perpendicular to fracture walls, and sometimes presents increasing crystal sizes from fracture walls to their centres. Besides, this cement occasionally presents subhedral elongated crystal textures arranged parallel to fracture walls, where multi-episodic veins are bounded by shear planes and have single vein widths generally smaller than 1 mm (Fig. 4B2 to B4). Crystal sizes of Cc1 veins can be up to 3 mm, but mainly range between 0.1 and 1 mm. Cc1 shows mechanical twins and homogeneously bright orange luminescence in both intergranular porosity and fractures. Cc1 filled the residual intergranular pores where Cc0 precipitated along clast edges (Fig. 4A1 and A2), indicating that Cc1 developed after Cc0.

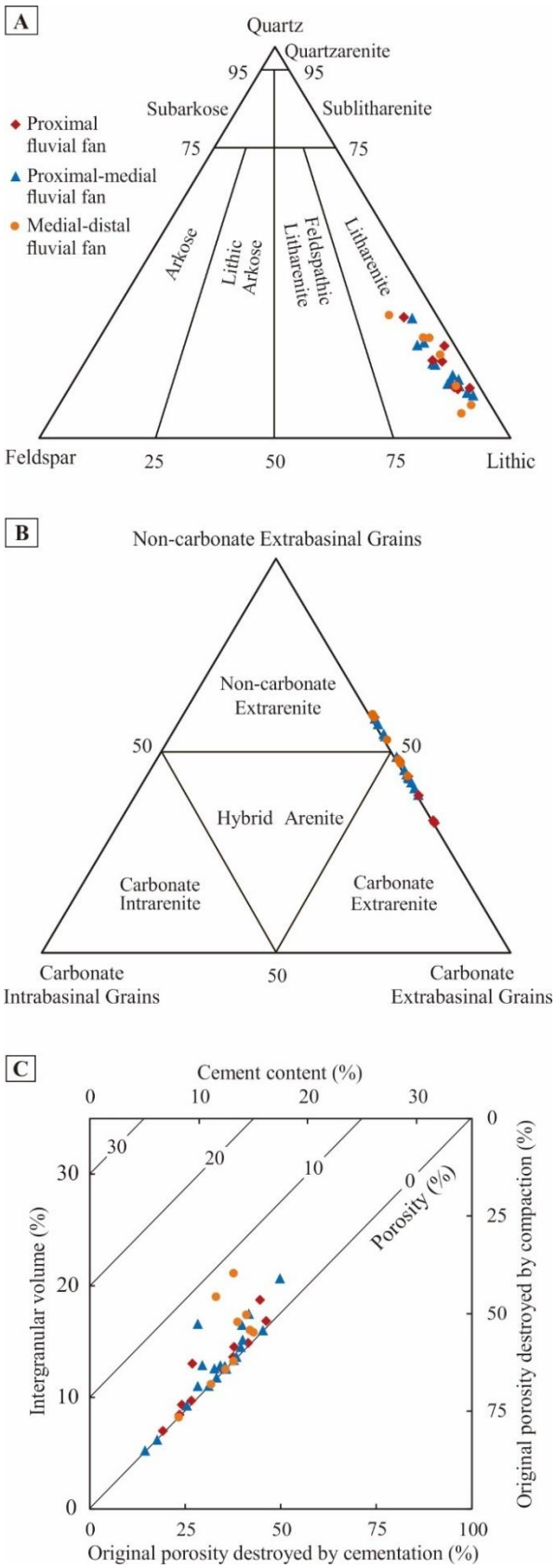

Figure 3. Classification of sandstones based on framework grain composition after (A) Folk's (1980) and (B) Zuffa's (1980) classification schemes. (C) Cross-plot of intergranular volume vs. cement content and porosity loss by compaction vs. cementation of sandstones after Houseknecht's (1987) method.

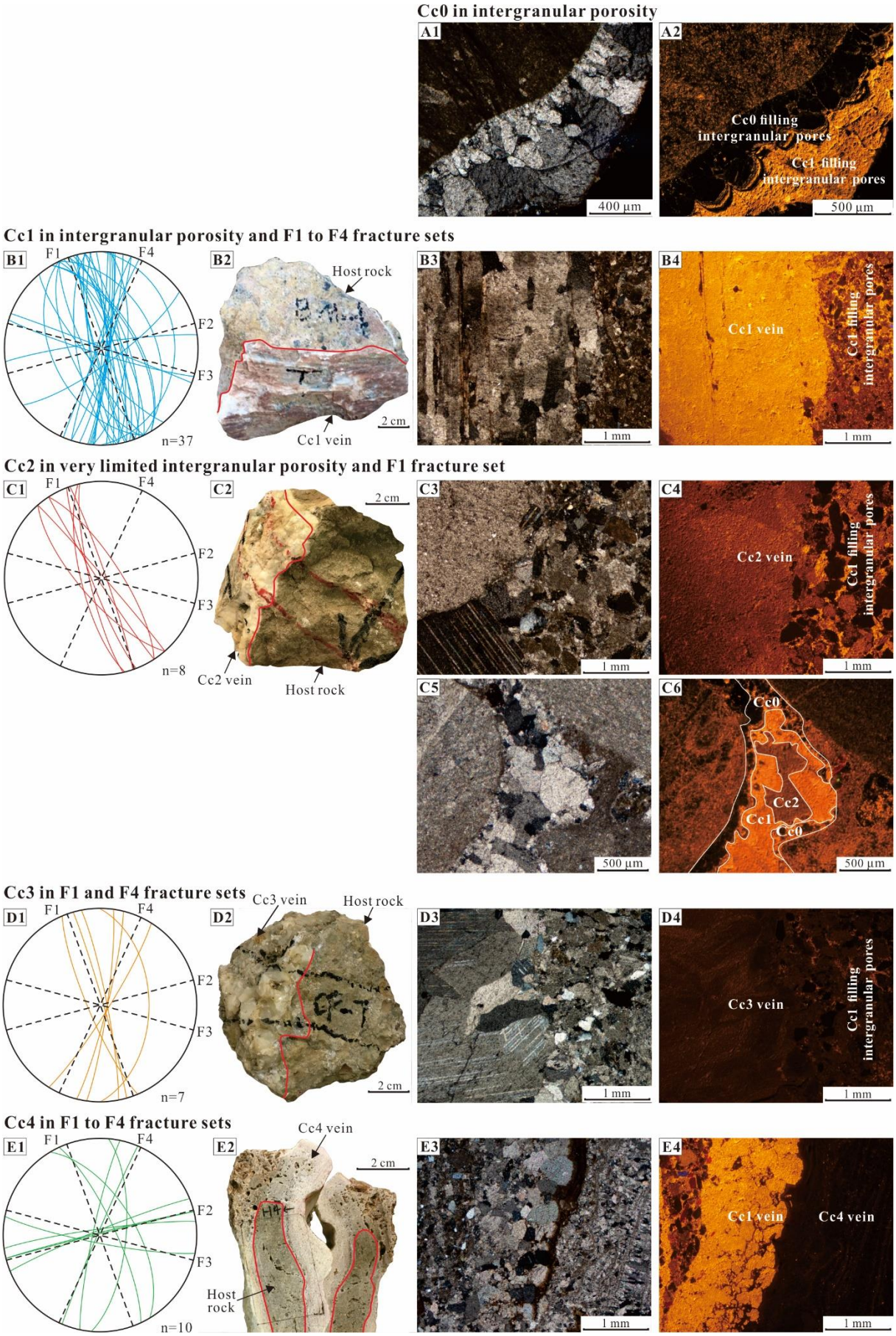
Cc0 in intergranular porosity
A1
A2
Cc0 filling intergranular pores
Cc1 filling intergranular pores
400 µm
500 µm
Cc1 in intergranular porosity and F1 to F4 fracture sets
B1
F1
F4
F2
F3
n=37
B2
Host rock
Cc1 vein
2 cm
B3
B4
Cc1 vein
Cc1 filling intergranular pores
1 mm
Cc2 in very limited intergranular porosity and F1 fracture set
C1
F1
F4
F2
F3
n=8
C2
2 cm
Cc2 vein
Host rock
C3
C4
Cc2 vein
Cc1 filling intergranular pores
1 mm
C5
C6
Cc0
Cc2
Cc1
Cc0
500 µm
Cc3 in F1 and F4 fracture sets
D1
F1
F4
F2
F3
n=7
D2
Cc3 vein
Host rock
2 cm
D3
D4
Cc3 vein
Cc1 filling intergranular pores
1 mm
Cc4 in F1 to F4 fracture sets
E1
F1
F4
F2
F3
n=10
E2
Cc4 vein
2 cm
Host rock
E3
E4
Cc1 vein
Cc4 vein
1 mm

Figure 4. Lower hemisphere Schmidt stereoplots of fractures hosting calcite veins, as well as hand specimens and paired optical and CL microphotographs for different generations of calcite cements. '*n*' represents the number of samples. (A1-A2) Cc0 calcite cement filled the intergranular porosity of host rocks and presents CL zonation characteristic; (B1-B4) Cc1 filled F1 to F4 fracture sets and intergranular porosity and presents homogeneous bright orange luminescence; (C1-C4) Cc2 veins developed in F1 fracture set and present duller luminescence than Cc1 filling intergranular porosity; (C5-C6) limited Cc2 cement filled residual pores after Cc0 and Cc1; (D1-D4) Cc3 veins precipitated in F1 and F4 fracture sets and present duller luminescence than Cc1 filling intergranular porosity; (E1-E4) Cc4 veins precipitated in F1 to F4 fracture sets and present non non-luminescent characteristic.

Cc2 calcite cement mainly precipitated in normal and strike-slip faults and fractures of the F1 set (Fig. 4C1). This cement concentrates in the anticline crest and occasionally in the NTZ and north limb of the anticline. It is formed by euhedral blocky to slightly elongated crystals with sizes up to 10 mm, but generally between 0.2 and 5 mm (Fig. 4C2 to C4). Cc2 presents mechanical twins and relatively dull orange luminescence compared to Cc1. It is inferred that Cc2 developed after Cc1 based on the following observations: in all samples hosting Cc2 veins, intergranular porosity was cemented by Cc1 (Fig. 4C3 and C4); and in one sample where intergranular pores were mainly filled by Cc1, limited Cc2 precipitated in the residual pores (Fig. 4C5 and C6). Besides, Cruset et al. (2016) recognised the sharp or gradual evolution from Cc1 to Cc2 within shear veins.

Cc3 calcite cement occasionally precipitated in F1 and F4 fracture sets (Fig. 4D1) in section C (Fig. 1D), i.e., at the western zone of the north limb of the anticline. This cement consists of euhedral blocky crystals, with large crystal sizes generally ranging from 1 to 20 mm (Fig. 4D2 to D4). Cc3 presents abundant mechanical twins and very dull luminescence. Occasionally, this cement shows a subtle zonation under cathodoluminescence (Fig. D4). Intergranular porosity was cemented by Cc1 in all samples hosting Cc3 veins, indicating that Cc3 developed after Cc1 (Fig. 4D3 and D4). However, the relative timing between Cc2 and Cc3 is not clear due to the lack of direct contacts between these two veins observed in this study.

Cc4 calcite cement precipitated in F1 to F4 fracture sets (Fig. 4E1), and can be identified in all the structural positions of the anticline. Cc4 is commonly found in fracture coatings as small as 1 mm-thick, but occasionally occurs as up to 10 mm-thick veins (Fig. 4E2). This cement is mainly characterised by anhedral to subhedral blocky crystals and a palisade structure of anhedral to subhedral bladed crystals (Fig. 4E2 to E4). Crystal sizes of Cc4 are up to 1 mm, but generally vary between 0.1 and 0.5 mm. This cement is generally non-luminescent under cathodoluminescence. Cc4 precipitated in some reopened fractures filled by previous cements (Fig. 4E3 and E4) and does not present crystals with clear mechanical twins (Fig. 4E2), indicating that Cc4 probably precipitated in relatively recent times after intensive compression.

4.4 Geochemistry of calcite cements

4.4.1 Carbon and oxygen isotopes

Due to the small size of intergranular porosity-filling Cc0, it was difficult to sample this cement and thus it was left out of various isotope analyses, including carbon, oxygen, strontium and clumped isotopes. The carbon and oxygen isotopic composition of conglomerate carbonate clasts and Cc1 to Cc4 generations of calcite cements is summarised in Table 1 and presented in Fig. 5A. The data of carbonate clasts are from Cruset et al. (2016). The carbonate clasts present a wide range of carbon and oxygen isotopic composition with $\delta^{13}C$ values ranging from -3.2 to +3.1‰ VPDB and $\delta^{18}O$ values from -8.9 to -3.1‰ VPDB. Cc1 shows $\delta^{13}C$ values between -3.3 and +0.8‰ VPDB and $\delta^{18}O$ values between -8.0 and -4.9‰ VPDB. Cc2 shows $\delta^{13}C$ values between -1.6 and +0.1‰ VPDB and $\delta^{18}O$ values between -10.2 and -8.4‰ VPDB. Cc3 presents $\delta^{13}C$ values between -0.1 and +0.8‰ VPDB and $\delta^{18}O$ values between -4.6 and -3.4‰ VPDB. Cc4 has $\delta^{13}C$ values ranging from -10.2 to -4.2‰ VPDB and $\delta^{18}O$ values from -8.0 and -5.1‰ VPDB. The $\delta^{13}C$ values of Cc1 to Cc3 are within the $\delta^{13}C$ range of carbonate clasts of host rocks, whereas Cc4 displays depleted $\delta^{13}C$ values with respect to carbonate clasts. Cc3 shows slightly higher $\delta^{13}C$ values than Cc1 and Cc2. The $\delta^{18}O$ values of Cc1, Cc3 and Cc4 are within the $\delta^{18}O$ range of carbonate clasts, whereas Cc2 presents slightly depleted $\delta^{18}O$ values with respect to carbonate clasts. Cc3 presents higher $\delta^{18}O$ values than Cc1 and Cc4, while Cc1 and Cc4 present higher $\delta^{18}O$ values than Cc2.

4.4.2 Clumped isotope thermometry

The Δ_{47} and estimated temperatures in °C and $\delta^{18}O_{fluid}$ in ‰ VSMOW of Cc1 to Cc4 generations of calcite cements are listed in Table 1 and presented in Fig. 5B. The data of Cc1 and Cc2 are from Cruset et al. (2016). The Δ_{47} values of Cc1 and Cc2 are modified from Cruset et al. (2016) by removing the acid correction factor (0.069‰ at 90˚C) to be able to compare to the values of Cc3 and Cc4 in the I-CDES that is expressed without correction factor at 90˚C. For Cc1, Δ_{47} values are 0.479 ± 0.009‰ and 0.425 ± 0.010‰, which translate to temperatures of 92 ± 5°C and 129 ± 8°C and $\delta^{18}O_{fluid}$ values of +4.7 ± 0.6‰ and +9.2 ± 0.7‰ VSMOW. For Cc2, Δ_{47} values are 0.505 ± 0.010‰ and 0.482 ± 0.004‰, which translate to temperatures of 77 ± 5°C and 90 ± 3°C and $\delta^{18}O_{fluid}$ values of −1.7 ± 0.7‰ and −0.7 ± 0.3‰ VSMOW. For Cc3, Δ_{47} values are 0.527 ± 0.001‰ and 0.501 ± 0.007‰, which are converted to temperatures of 49°C to 50°C and 59°C to 65°C and $\delta^{18}O_{fluid}$ values of 3.9 to 4.3‰ VSMOW and 5.2 to 6.4‰ VSMOW. For Cc4, Δ_{47} values are 0.619 ± 0.014‰ and 0.609 ± 0.012‰, which are converted to temperatures of 12°C to 21°C and 16°C to 23°C and $\delta^{18}O_{fluid}$ values of -5.7 to -3.6‰ VSMOW and -5 to -3.4‰ VSMOW.

Table 1. $\delta^{18}O$ and $\delta^{13}C$ values of conglomerate carbonate clasts and Cc1 to Cc4 generations of calcite cements. Δ_{47}, temperatures and $\delta^{18}O_{fluid}$ obtained from clumped isotope thermometry for Cc1 to Cc4. $^{87}Sr/^{86}Sr$ ratios of host

rocks and Cc1 to Cc4. $\delta^{18}O$ and $\delta^{13}C$ values of carbonate clasts, clumped isotope data of Cc1 and Cc2, and $^{87}Sr/^{86}Sr$ ratios of host rocks, Cc1 and Cc2 are from Cruset et al. (2016). Δ_{47} values of Cc1 and Cc2 are modified from Cruset et al. (2016) by removing the acid correction factor (0.069‰ at 90˚C) to be able to compare to the values of Cc3 and Cc4 in the I-CDES that is expressed without correction factor at 90˚C.

Sample	Cement / host rock	$\delta^{13}C$ VPDB	$\delta^{18}O$ VPDB	Δ_{47}	T °C	$\delta^{18}O_{fluid}$ VSMOW	$^{87}Sr/^{86}Sr$
AF2-10	Cc1	+0.8	-7.4				
AF2-11	Cc1	0	-8				
AF2-8	Cc1	-2.8	-7.7				
AF-3	Cc1	+0.7	-7.9				
AF-6	Cc1	-0.7	-7.9				
B-1	Cc1	-1.5	-8				
BM-1	Cc1	-1.7	-6.8				
BM-3	Cc1	-3.3	-6.7				
CF-1	Cc1	+0.8	-5				
CF-4	Cc1	+0.5	-6.7				
DS-2	Cc1	-1.2	-7.4				
DS-5	Cc1	+0.6	-7.4				
309B1	Cc1			0.479 ± 0.009	92 ± 5	+4.7 ± 0.6	
317	Cc1			0.425 ± 0.010	129 ± 8	+9.2 ± 0.7	
309A	Cc1						0.709246
314C	Cc1						0.709138
A3-1	Intergranular Cc1	+0.6	-7.4				
C3-2	Intergranular Cc1	+0.3	-4.9				
H5-1	Intergranular Cc1	0	-7.8				
AF2-5	Cc2	-1.6	-8.6				
AF-4	Cc2	+0.1	-8.4				
CF2-1	Cc2	0	-9.6				
CF-6	Cc2	-0.5	-10.2				
311A	Cc2			0.505 ± 0.010	77 ± 5	−1.7 ± 0.7	0.708947
311D	Cc2			0.482 ± 0.004	90 ± 3	−0.7 ± 0.3	0.709002
C3-3	Cc3	+0.6	-4.6				
CF2-4	Cc3	+0.8	-3.4	0.527 ± 0.001	50 (49 to 50)	+4.2 (+3.9 to +4.3)	0.708747
CF-3	Cc3	-0.1	-3.8	0.501 ± 0.007	62 (59 to 65)	+5.8 (+5.2 to +6.4)	0.708813
B-3	Cc4	-4.2	-8				
BD-2	Cc4	-10	-5.8	0.619 ± 0.014	16 (12 to 21)	-4.8 (-5.7 to -3.6)	0.710208
G-1	Cc4	-10.2	-5.1				
H-4	Cc4	-8.5	-5.5	0.609 ± 0.012	19 (16 to 23)	-4.3 (-5 to -3.4)	0.708757
H-5	Cc4	-9.4	-7.8				
302	Carbonate clast	-3.2	-4.7				
303	Carbonate clast	+3.1	-3.1				
311F	Carbonate clast	+1.2	-7.2				
311G	Carbonate clast	-0.8	-8.9				
312A	Carbonate clast	+0.6	-3.4				
GP-R4	Mudstone host rock						0.708865
IP-R	Host-marly limestone						0.708967

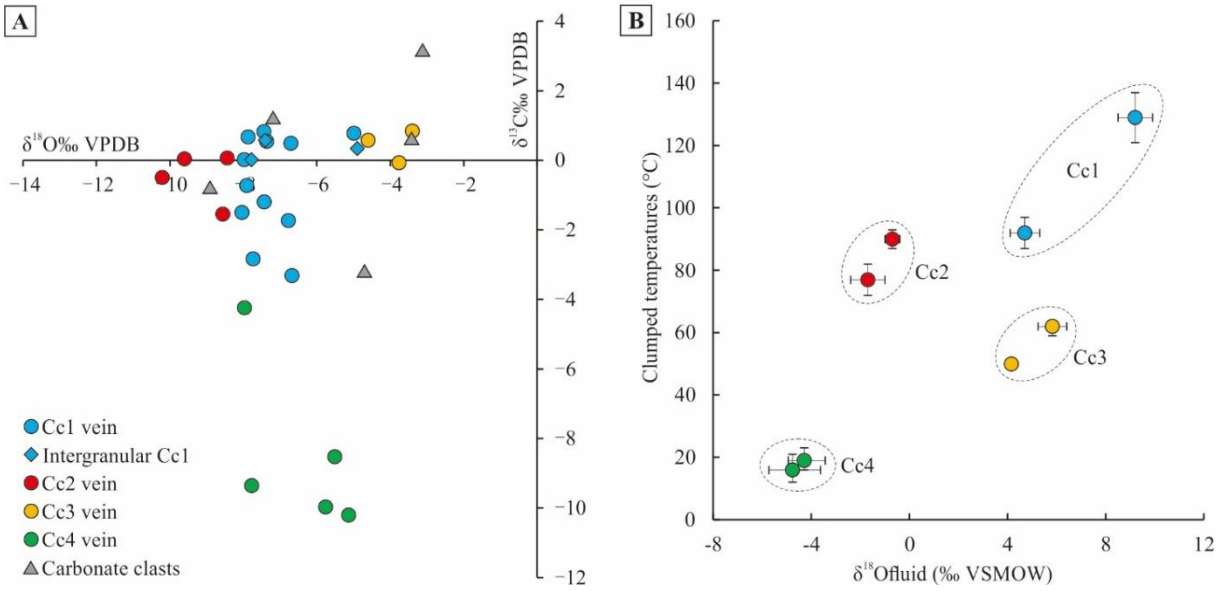

Figure 5. (A) $\delta^{18}O$ vs. $\delta^{13}C$ cross-plot of conglomerate carbonate clasts and Cc1 to Cc4 generations of calcite cements. $\delta^{18}O$ and $\delta^{13}C$ values of carbonate clasts are from Cruset et al. (2016). (B) Temperatures of precipitation in °C vs. $\delta^{18}O_{fluid}$ in ‰ VSMOW calculated from clumped isotope thermometry for Cc1 to Cc4 generations of calcite cements. Clumped isotope data of Cc1 and Cc2 are from Cruset et al. (2016).

4.4.3 Strontium isotopes

The strontium isotopic ratios of host rocks and Cc1 to Cc4 generations of calcite cements are listed in Table 1 and presented in Fig. 6. The data corresponding to host rocks, Cc1 and Cc2 are from Cruset et al. (2016). Host rocks have $^{87}Sr/^{86}Sr$ ratios of 0.708865 and 0.708967 for mudstone and marly limestone, respectively. Cc1 shows higher $^{87}Sr/^{86}Sr$ ratios of 0.709138 and 0.709246. Cc2 has $^{87}Sr/^{86}Sr$ ratios of 0.708947 and 0.709002. Cc3 shows lower $^{87}Sr/^{86}Sr$ ratios of 0.708747 and 0.708813. Cc4 presents variable $^{87}Sr/^{86}Sr$ ratios ranging from 0.708757 to 0.710208.

4.4.4 Elemental composition

The elemental composition, including Ca, Mg, Mn, Sr and Fe of Cc0 to Cc4 generations of calcite cements, is summarised in Table 2 and presented in Fig. 7. The elemental composition data of Cc1 and Cc2 calcite cements from Cruset et al. (2016) were integrated into these results. Cc0 has elemental composition values ranging from 546 to 2950 ppm in Mg and from below the detection limits to 1024, 221 and 178 ppm in Sr, Fe and Mn, respectively. Cc1 shows values ranging from 248 to 4500 ppm in Mg and from 158 to 4199 ppm in Mn, while values range from below the detection limits to 3100 and 1221 ppm in Fe and Sr, respectively. Cc2 has values ranging from 458 to 2846 ppm in Mg and from 202 to 2300 ppm in Mn, while values range from below the detection limits to 3200 and 3000 ppm in Fe and Sr, respectively. For Cc3, the Fe, Mg and Mn contents range from 483 to 2827 ppm, from 148 to 1062 ppm and from 545 to 1050 ppm, respectively, while the Sr content ranges from below the detection limit to 312 ppm. For Cc4, the Mg content ranges from 319 to 22340 ppm, while the Sr, Mn and Fe contents

range from below the detection limits to 1601, 604 and 459 ppm respectively. Besides, Cc4 has a Ca content ranging from 368470 to 398507 ppm, which is lower than that of Cc1 to Cc3 ranging from 381100 to 399540 ppm.

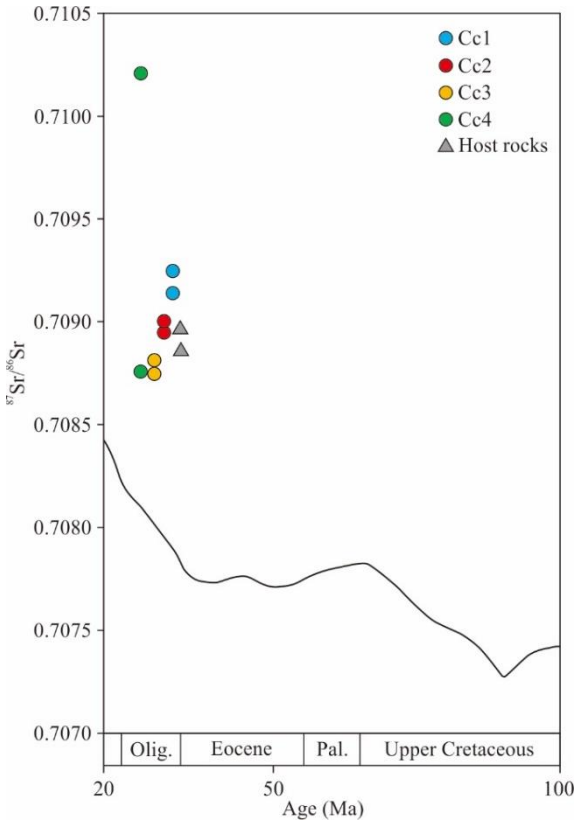

Figure 6. $^{87}Sr/^{86}Sr$ ratios of host rocks and Cc1 to Cc4 generations of calcite cements. The black line represents the $^{87}Sr/^{86}Sr$ ratios of seawater through time from the LOWESS curve (McArthur et al., 2012). Strontium isotope data of host rocks, Cc1 and Cc2 are from Cruset et al. (2016).

Table 2. Elemental composition of Cc0 to Cc4 generations of calcite cements. '*n*' represents the number of probe points. 'L.D.' represents detection limit. Elemental composition data of Cc1 and Cc2 calcite cements from Cruset et al. (2016) were integrated into these results.

Cement	n	Mg (ppm)			Mn (ppm)			Fe (ppm)			Sr (ppm)			Ca (ppm)		
		Max.	Min.	Av.	Max.	Min.	Av.	Max.	Min.	Av.	Max.	Min.	Av.	Max.	Min.	Av.
Cc0	47	2950	546	1716	178	<L.D.	153	221	<L.D.	145	1024	<L.D.	635	399540	395916	397879
Cc1	242	4500	248	1797	4199	158	1244	3100	<L.D.	412	1221	<L.D.	532	399508	381100	395855
Cc2	137	2846	485	1650	2300	202	986	3200	<L.D.	945	3000	<L.D.	745	399153	385000	394998
Cc3	22	1062	148	539	1050	545	790	2827	483	1794	312	<L.D.	273	399064	396320	397598
Cc4	48	22340	319	7449	604	<L.D.	250	459	<L.D.	211	1601	<L.D.	856	398507	368470	389674

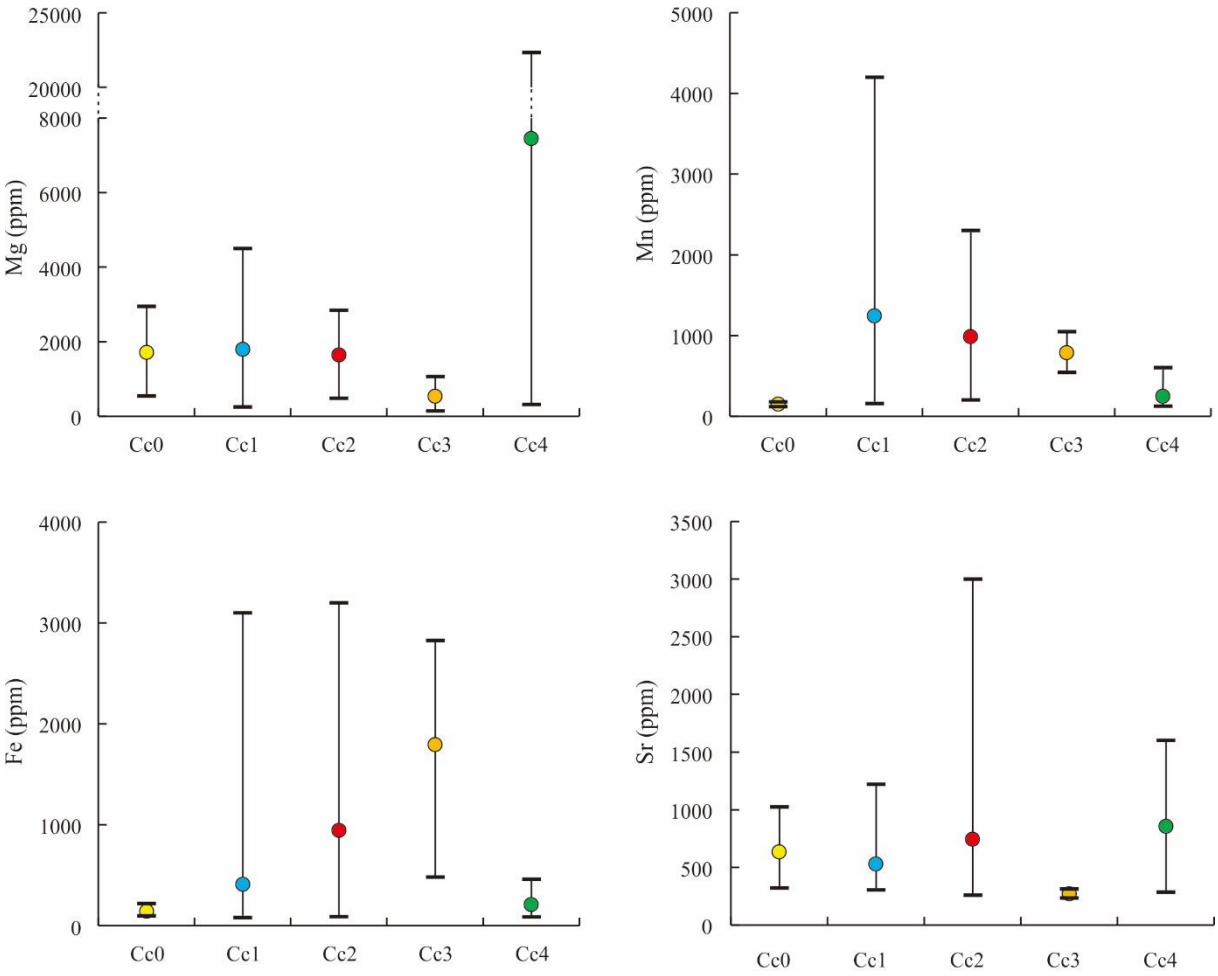

Figure 7. Mg, Mn, Fe and Sr composition of Cc0 to Cc4 generations of calcite cements. Elemental composition data of Cc1 and Cc2 calcite cements from Cruset et al. (2016) were integrated into these results.

5 Discussion

5.1 Fluid origin of calcite cements

The petrographic and geochemical characteristics of host rocks and calcite cements can be used to unravel the origin of the fluids from which Cc0 to Cc4 precipitated in the Puig-reig anticline. Despite the lack of isotope data for Cc0, its petrologic characteristics and elemental composition hint at the fluid source. The concentric zonation of Cc0, varying from non-luminescent to bright luminescent zones (Fig. 4A1 and A2), indicates fluctuations of the redox conditions probably in the meteoric phreatic environment (Muchez et al., 1998; Machel, 2000; Boggs & Krinsley, 2006; Vandeginste et al., 2012). The major non-luminescent zones represent oxidizing conditions during precipitation, whereas the minor bright luminescent zones are characteristic of more reducing conditions (Grover & Read, 1983; Parcerisa et al., 2006). Cc0 has much lower Mn and Fe contents than the other cements (Fig. 7), generally below the detection limits, which also supports the meteoric fluid origin. As the earliest cement, Cc0 precipitated in intergranular pores along the edges of the proximal to medial fluvial clasts (Fig. 4A1 and

A2). From the available data, it is inferred that Cc0 precipitated from meteoric fluids at the early diagenetic stage.

Cc1 was previously interpreted as precipitated from hydrothermal fluids from the Palaeozoic basement (Cruset et al., 2016). The clumped isotope data reveal that Cc1 precipitated at temperatures between 92°C to 129°C (Fig. 5B). However, previous studies involving cross-sections (Vergés, 1993) and vitrinite reflectance data (Clavell, 1992; Vergés et al., 1998), indicate a maximum burial depth of 1.7 km for the Berga Group and the Solsona Formation in the Puig-reig anticline. Assuming the current mean geothermal gradient of 26.7°C/km in the Ebro Foreland Basin (Fernàndez et al., 1998) and a general surface temperature of 20°C, the maximum temperatures reached by these formations should be much lower (around 65°C) than the temperatures at which Cc1 precipitated. This indicates an external hydrothermal fluid source from a depth of around 4 km, or even deeper if we consider cooling processes of the ascending fluids. The $\delta^{18}O_{fluid}$ of Cc1 ranges from +4.7 to +9.2‰ VSMOW (Fig. 5B), located within the range of formation, metamorphic and magmatic fluids (Taylor, 1987). Magmatic fluids are excluded because magmatism did not develop during the Pyrenean orogeny. The high $^{87}Sr/^{86}Sr$ ratios of Cc1, ranging from 0.709138 to 0.709246 (Fig. 6), indicate that hydrothermal fluids interacted with highly radiogenic sources, such as the Palaeozoic basement at depth and/or the silicic clasts of the Berga and Solsona fluvial deposits sourced from the Pyrenean Axial Zone (Riba, 1976; Williams et al., 1998; Barrier et al., 2010). Thus, the clumped isotope and strontium isotope data together indicate that fluids released from the Palaeozoic basement at depth could have been the high-temperature fluids responsible for the precipitation of Cc1 (Cruset et al., 2016).

Cc2 was previously interpreted as precipitated from mixed fluids by Cruset et al. (2016). Clumped isotope data presented by these authors indicate that Cc2 precipitated at temperatures ranging between 77°C and 90°C (Fig 5B). These precipitation temperatures are lower than those of the precipitation of Cc1 but still higher than the maximum burial temperatures reached by the Berga Group and the Solsona Formation. Cc2 presents lighter $\delta^{18}O$ values than Cc1 and host rocks (Fig. 5A). Cc2 has lower $^{87}Sr/^{86}Sr$ ratios than Cc1 (Fig. 6), indicating that the cement-forming fluids interacted with less radiogenic sources or mixed with fluids with lower $^{87}Sr/^{86}Sr$ ratios. The $\delta^{18}O_{fluid}$ composition of Cc2 ranges from -1.7 to -0.7‰ VSMOW (Fig. 5B), which is lower than that of Cc1 cement but higher than -6.4 to -4.6‰ VSMOW of modern rainwater (Travé & Calvet, 2001). Based on the available data, Cruset et al. (2016) interpreted that Cc2 precipitated in fractures from the mixing of meteoric waters with the hydrothermal fluids from which Cc1 precipitated. In addition, the Fe and Sr contents of Cc2 are slightly higher than those of Cc1 (Fig. 7), which was interpreted as the expulsion of formation fluids relatively rich in Fe and Sr from shale layers due to progressive compaction during burial (Hanshaw & Coplen, 1973; Travé et al., 1997; Cruset et al., 2016). In this study, we propose an alternative model in which Cc2 could have precipitated from hydrothermal fluids but at shallower burial depths and lower temperatures compared

to the parent fluids of Cc1. The interaction between the hydrothermal fluids and the shallower basement must have been relatively weak and retained the signatures of meteoric fluids to some extent, which resulted in the relatively lower temperatures, $\delta^{18}O_{fluid}$, $\delta^{18}O$ and $^{87}Sr/^{86}Sr$ ratios of the Cc2 cement and the cement-forming fluids. A more detailed discussion of the fluid flow and precipitation processes is provided in Section 5.2.

Cc3 was only identified in the north-western part of the study area (section C in Fig. 1D). This area is dominated by proximal fluvial deposits, which have higher contents of carbonate clasts than medial and distal fluvial deposits (Sun et al., 2021b). These clasts were mainly sourced from the marine carbonates of the Mesozoic-Cenozoic series of the South Pyrenean cover thrust sheets (Riba, 1976; Williams et al., 1998; Barrier et al., 2010) and the Pyrenean Axial Zone. Compared to the other cements, Cc3 has heavier $\delta^{18}O$ and $\delta^{13}C$ values (Fig. 5A), which are closer to the isotopic compositional range of marine carbonates (Veizer et al., 1999). This probably suggests interaction between the cement-forming fluids and marine carbonate clasts. Based on the LOWESS curve (McArthur et al., 2012), the $^{87}Sr/^{86}Sr$ ratios of Cc3 between 0.708813 and 0.708747 are higher than those of seawater when the Mesozoic marine carbonates were deposited, but slightly lower than those of the host rocks of the Berga Group and Solsona Formation (Fig. 6). This would suggest fluid-rock interaction between the cement-forming fluids and the radiogenic silicic clasts of the host rocks sourced from the Palaeozoic basement in the Axial Zone. Muñoz-López et al. (2020a) studied the influence of basement rocks on fluid chemistry in other outcrops elsewhere in the Pyrenees, and concluded that calcite cements precipitated from fluids that strongly interacted with basement rocks could have significantly higher $^{87}Sr/^{86}Sr$ (>0.710) in nearby areas. The $^{87}Sr/^{86}Sr$ ratios of Cc3 in our study area are lower than this value probably because carbonate clasts dominate over silicic clasts in the zone where Cc3 precipitated. The $\delta^{18}O_{fluid}$ of Cc3 ranges from +4.1 to +5.8‰ VSMOW (Fig. 5B), which corresponds to the range of formation fluids (Taylor, 1987). Compared to Cc1 and Cc2, Cc3 precipitated at significantly lower temperatures, ranging between 50°C and 62°C (Fig. 5B). According to the current mean geothermal gradient of 26.7°C/km in the Ebro Foreland Basin (Fernàndez et al., 1998) and assuming a general surface temperature of 20°C, strata with burial depths around 1.5 km can reach the temperatures at which Cc3 precipitated. However, the depth could be slightly higher if we consider that fluids cool down while ascending. Compared to other generations of calcite cements, Cc3 presents high Fe and low Mg and Sr concentrations (Fig. 7). The high Fe concentration could result from the interaction between the cement-forming fluids and host rocks or be sourced from external fluids. Based on the available data, it is inferred that Cc3 precipitated from formation fluids that strongly interacted with the host rocks.

Cc4 occurs as thin coatings covering fracture surfaces or presents palisade structures of bladed crystals (Fig. 4E3 and E4). This cement is non-luminescent and has low Mn and Fe concentrations (Fig. 7). Based on clumped isotope data, Cc4 precipitated from a fluid with temperatures ranging between

16°C and 19°C and with $\delta^{18}O_{fluid}$ ranging from -4.8 to -4.3‰ VSMOW (Fig. 5B). All these characteristics indicate a low-temperature meteoric fluid. In addition, Cc4 is characterised by highly depleted values of $\delta^{13}C$ with respect to host rocks, ranging from -10.2 to -4.2‰ VPDB (Fig. 5A), indicating a strong influence of organic-derived carbon (Irwin et al., 1977; Cerling, 1984; Vilasi et al., 2006). In the Puig-reig anticline, the exposed fine sediments, deposited from fluvial overbanks, have experienced intensive pedogenesis and can provide soil-derived carbon for calcite cement (Cerling & Quade, 1993). Other studies documented that similar calcite cements with palisade structure and depleted $\delta^{13}C$ precipitated from meteoric fluids with a strong influence of soil-derived carbon related to pedogenic processes (e.g., Travé and Calvet, 2001; Cantarero et al., 2010, 2014). The significantly variable $^{87}Sr/^{86}Sr$ ratios of Cc4, with a low value of 0.708757 and a very high value of 0.710208 (Fig. 6), could be related to variable interactions between fluids and the different compositions of host rocks. The high $^{87}Sr/^{86}Sr$ ratio probably indicates strong interaction between the fluid and the highly radiogenic silicic clasts in host rocks sourced from the Palaeozoic basement of the Axial Zone. Besides, this high ratio could also be affected by the clayey or siliceous impurities existing between the multi-layer palisades of Cc4 (Fig. 4E3 and E4). During the stages of no calcite cementation, clayey or siliceous impurities resulted from pedogenic processes could be transported by meteoric fluids. The presence of small percentages of clay minerals can significantly increase the measured $^{87}Sr/^{86}Sr$ ratios due to the decay of ^{87}Rb to ^{87}Sr (Banner, 1995).

5.2 Changes in fluid regime during fold evolution

This section discusses the changes in fluid regimes during the complete fold evolution, combining the fluid origin of calcite cement and the tectonic evolution of the Puig-reig anticline. As the earliest cement, Cc0 developed in all structural positions and lithofacies, indicating that the meteoric fluid from which Cc0 precipitated affected the whole anticline (Fig. 8A). This cement only precipitated in intergranular pores along clast edges and before the predominant Cc1 cement (Fig. 4A1 and A2). Therefore, we interpret that Cc0 precipitated during early diagenetic stages before systematic fracturing and significant burial. At this stage, deposits had not undergone intensive compaction and still had high intergranular porosity. Meteoric fluids in the phreatic zone filled the intergranular pores of these unconsolidated sediments deposited from the proximal to medial fluvial system and dominated the fluid regime from which Cc0 precipitated. Other studies documented similar calcite cements precipitated from meteoric fluids in a phreatic environment during early diagenetic stages (e.g., Emery & Dickson, 1989; Parcerisa et al., 2005; Cantarero et al., 2014b; Li et al., 2017).

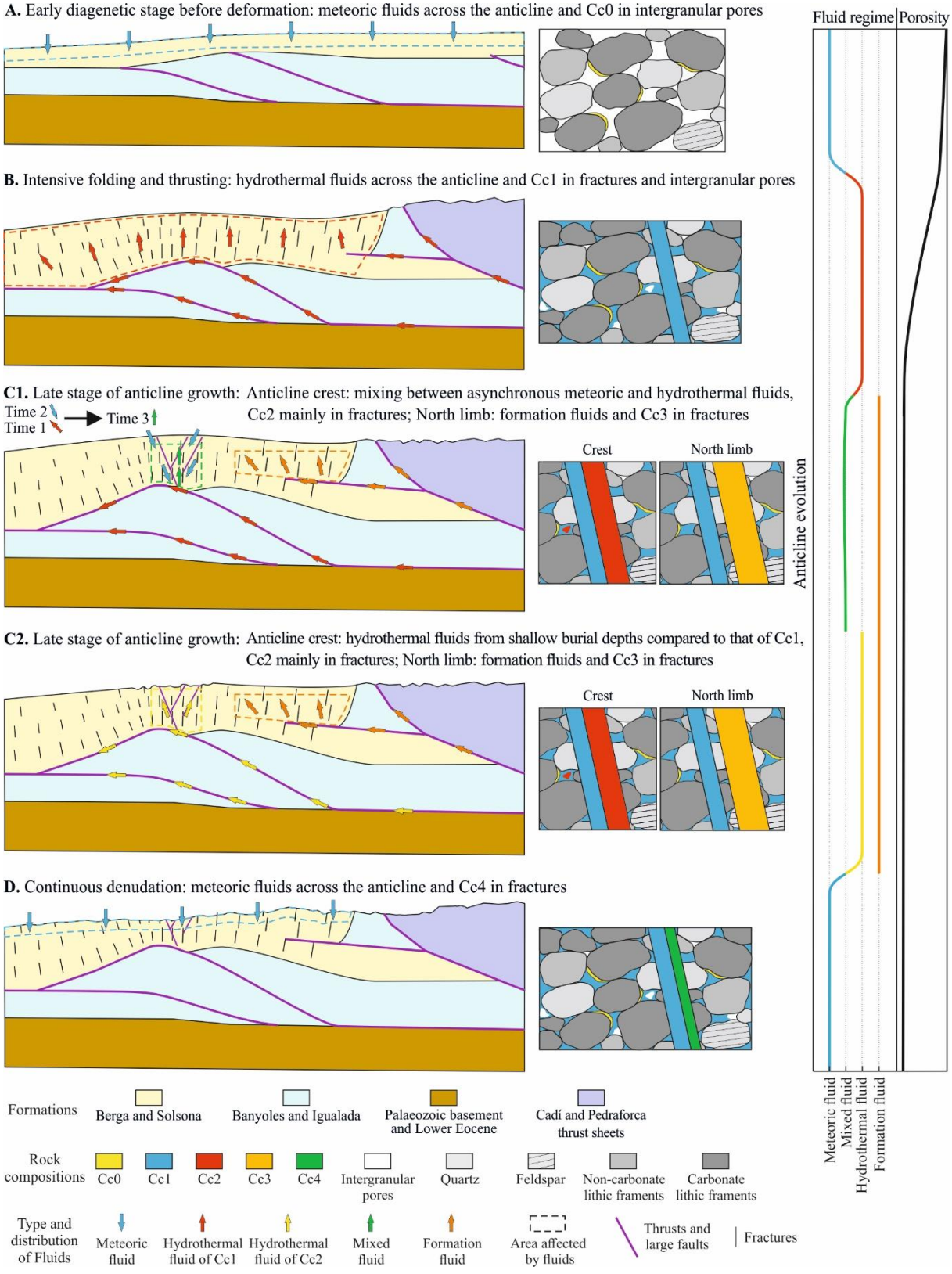

Figure 8. Schematic diagram of fluid regime evolution and related calcite cementation during the tectonic evolution of the Puig-reig anticline. (A) During early diagenetic stage before deformation, Cc0 precipitated in intergranular pores from meteoric fluids across the anticline. (B) During intensive folding and thrusting, Cc1 precipitated in intergranular pores and variable fractures from hydrothermal fluids across the anticline. (C) During

the late stage of anticline growth, Cc2 precipitated in fractures in the anticline crest from (C1) the mixing between asynchronous meteoric and hydrothermal fluids, as suggested by Cruset et al. (2016), or from (C2) hydrothermal fluids with meteoric signatures from shallower burial depth compared to that of Cc1, while Cc3 precipitated in fractures from formation fluids in the west zone of the north limb. (D) During the continuing denudation of the anticline, Cc4 precipitated in fractures from meteoric fluids across the anticline.

Due to progressive burial and compressional tectonics, abundant fractures were formed in the Puig-reig anticline during thrusting and folding. The damage zones of the blind thrust system at depth, responsible for the development of the Puig-reig anticline (Fig. 1C), could have provided the paths for the hydrothermal fluids from the Palaeozoic basement to migrate upwards and reach the Berga Group and the Solsona Formation (Cruset et al., 2016). The connected fracture network and intergranular porosity of these alluvial-fluvial deposits would have allowed vertical and lateral migration of the hydrothermal fluids across different stratigraphic units. Cc1 filled most intergranular pores in different lithofacies and variable faults and fracture sets in different structural positions, indicating that the hydrothermal fluid from which Cc1 precipitated would have migrated along the whole anticline (Fig. 8B). Fluid flow would have been triggered by horizontal or sub-horizontal compressive principal stress (e.g., when the least principal stress is vertical), rather than by fluid pressure increase associated with decompression or fluid heating (Staude et al., 2009).

Cruset et al. (2016) proposed that normal and strike-slip faults formed in the crest of the Puig-reig anticline during the crestal collapse, which provided connected paths for the percolation of low-temperature meteoric fluids from the surface to the bottom of the Berga and Solsona strata based on the fault-valve model (Sibson, 1981; Henderson & McCaig, 1996). These downward meteoric fluids would have then mixed with the upward hydrothermal fluids from the deeper basement from which Cc1 precipitated (Fig. 8C1). Then the mixed fluids would have migrated upwards through these connected faults due to the increasing fluid pressure related to the build-up stresses during compression (Henderson & McCaig, 1996) and finally would result in the precipitation of Cc2. Such hydrological models need to involve asynchronous downward flow of meteoric fluids and upward flow of hydrothermal fluids to be hydrodynamically plausible. Because simultaneous downward and upward flow, such as that invoked in other conceptual models of mixing of surface- and deep-derived fluids, would necessitate a geologically implausible fluid sink (Bons et al., 2012). Alternatively, as discussed in Section 5.1, Cc2 could have precipitated from hydrothermal fluids from the basement but at shallower burial depths and at lower fluid temperatures compared to that of Cc1 (Fig. 8C2). Meteoric fluids could have migrated downwards from the erosional surface of the Pyrenees to the shallower basement through thrusts of the Pyrenees driven by topography differences, but not through the faults in the Puig-reig anticline crest. The relatively low burial temperatures in such basement level would have resulted in a low degree of fluid-rock interaction, thus preserving part of the meteoric signatures of the parent fluids of Cc2 (Bons

et al., 2014). In contrast, the Cc1 cement-forming fluids would have been sourced from deeper parts of the basement according to their geochemical signature and higher clumped isotope temperature. Such hydrological model was proposed by Bons et al. (2014) to explain the hydrothermal ore deposits of the Schwarzwald district in SW Germany. Bons and Gomez-Rivas (2020) pointed out that meteoric fluids can infiltrate down from an erosional surface to be buried and then remobilised later, partly preserving their meteoric signatures. Such signatures can be preserved for long periods of time if temperatures are relatively low. In the late stage of the fold growth of the Puig-reig anticline, the underneath thrusting could have mobilised the shallower hydrothermal fluids to the bottom of the anticline. In addition, the anticline crest could have raised and undergone partial exhumation, which could have caused an instantaneous decrease in the overburden pressure of underneath rocks and thus resulted in an overpressure of the trapped pore fluids. To maintain the original relative fluid pressure underneath, fluids need to be expelled upwards, which could have resulted in the precipitation of Cc2 in the anticline crest. Such hydrological model was proposed by Staude et al. (2009) and was tested on the Schwarzwald hydrothermal ore district in SW Germany.

After Cc1 precipitation, external formation waters also characterized the fluid system of the Puig-reig anticline, resulting in Cc3 cement with different petrographic and geochemical characteristics compared to the other cements. Cc3 concentrates in the western zone of the north limb, indicating that the formation fluids locally migrated within the Berga Group (Fig. 8D). Based on the cross-sections (Fig. 1C and E), the frontal thrusts (such as the Vallfogona thrust) could have acted as the migration pathways for the formation fluids. For example, the blind branch of the Vallfogona thrust propagated into the lower and middle Berga Group in the north limb of the Puig-reig anticline, which could have facilitated the local input of the formation waters into the Berga Group.

Owing to continuous denudation after the fold growth of the whole Puig-reig anticline, the burial depths of the Berga and Solsona strata became shallower. Besides, some of the fractures sealed by previous calcite veins could have been reactivated during exhumation while new ones formed. Thus, some faults and fractures could have been reopened and allowed the input of meteoric fluids from which Cc4 precipitated. Cc4 developed in different fracture sets and different structural positions of the anticline, indicating that the meteoric fluid affected the whole study area (Fig. 8E).

5.3 Distribution patterns of calcite cements in different settings

Based on the comparison between the calcite cement distribution in the Puig-reig anticline and other areas worldwide, this section discusses the distribution patterns of calcite cements in detrital reservoirs in different settings. In the Puig-reig anticline, abundant fractures were filled by Cc1 to Cc4 calcite veins. Cc1 and Cc4 veins precipitated across the whole anticline, whereas Cc2 and Cc3 precipitated locally in the anticline crest and north limb, respectively. The intergranular porosity of host rocks corresponding to proximal and medial fluvial deposits was cemented by Cc0 and Cc1 calcite cements. As the

predominant calcite cement in both intergranular porosity and fractures, Cc1 precipitated from external hydrothermal fluids. These fluids are from relatively more internal and deeper parts of the SE Pyrenees, which migrated along connected thrusts and their damage zones to the Ebro Foreland Basin. Such fluids flowed coevally with the anticline growth during horizontal compression.

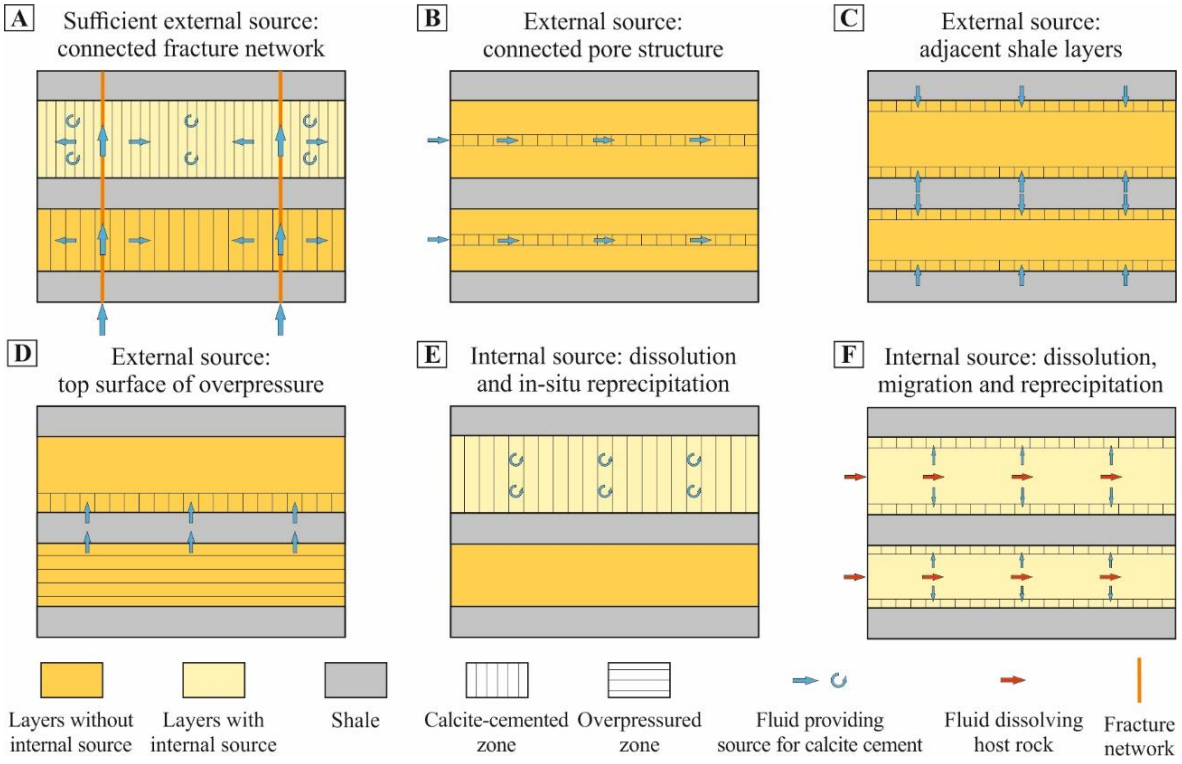

Figure 9. Schematic diagram of calcite cementation and distribution in detrital rocks in different settings. (A) Sufficient external sources migrate through connected fracture network; (B) External sources migrate through connected pore structure; (C) External sources migrate from adjacent shale layers; (D) External sources migrate from the top surface of an overpressured compartment; (E) Internal sources from host rocks: in-situ dissolution-reprecipitation; (F) Internal sources from host rocks: dissolution-migration-reprecipitation.

At foreland basin margins or fold-and-thrust belts, fracturing, thrusting and folding are generally accompanied by fluid flow of various external fluids. Connected fracture networks allow fluid migration across different hydrostratigraphic units (Evans & Fischer, 2012; Evans et al., 2012). The intensive deformation and sufficient external fluids result in changes of fluid conditions in host rocks and fractures, including temperature, pressure, pH, Eh, solute concentration, and thus provide the material sources and physical-chemical conditions for cementation (Bons et al., 2012). Thus, prevalent calcite cement can develop in detrital rocks and their hosting fracture networks at basin margins (Fig. 9A), such as the Berga Group and the Solsona Formation at the north-eastern margin of the Ebro Basin (Cruset et al., 2016), the Peraltilla and Sariñena Formations at the northern margin of the central Ebro Basin (Yuste et al., 2004), or the Siwalik Group near the frontal thrusts in the Himalayan Basin (Guilbaud et al., 2012), among many other examples. Apart from the external sources, detrital carbonates can provide the

internal sources for calcite cementation in detrital rocks by dissolution-reprecipitation (Morad, 1998). Carbonate grains are relatively rare in sandstones due to strong chemical weathering during sediment transport (Morad et al., 2010). However, tectonically active settings, such as those in foreland basin margins and fold-and-thrust belts, provide short time and distance for sediment exposure and transportation, thus resulting in relatively weak chemical weathering of these detrital carbonates (Zuffa, 1985). Extrabasinal carbonate grains can become an important component of sandstones in these settings, such as in the northern Ebro Basin (Yuste et al., 2004), the northern Apennines (Valloni & Zuffa, 1984), and the Laramide Foreland of southwestern Montana (Ingersoll et al., 1987). These detrital carbonates, such as biogenic carbonates, can provide the material sources for calcite cement by dissolution and favour the growth of cement by providing favourable nucleation substrates (Walderhaug & Bjørkum, 1998; Mansurbeg et al., 2009).

In other settings not featuring intensive deformation and sufficient external fluids, calcite cement tends to show heterogeneous distributions in sandstones, including continuously cemented layers, stratabound or scattered concretions, and patchy cements (Walderhaug & Bjørkum, 1998). In settings relying on external sources migrated from their adjacent layers through connected pore structures of host rocks, reservoir quality and lithofacies assemblages may exert a significant effect on cement distribution. Some studies documented that calcite tends to precipitate in more permeable reservoirs because these reservoirs favour fluid flow from which calcite cement can precipitate (Fig. 9B) (McBride et al., 1995; Dutton et al., 2002; Hall et al., 2004; Van Den Bril & Swennen, 2009). Other studies revealed that more intense calcite precipitation tends to occur along reservoir margins where sandstone reservoirs pinch out into fine deposits or are in contact with fine deposits (Fig. 9C), e.g., the Lower Cretaceous Pendência Formation in the Potiguar basin (Dos Anjos et al., 2000) and the Upper Permian Bell Canyon Formation in the Delaware Basin (Dutton, 2008). Organic acids generated during the maturation of organic matter in these fine deposits could result in the dissolution of carbonate elements, which could be transported to adjacent sandstone reservoirs and provide external fluids for calcite cement (Dos Anjos et al., 2000; Dutton, 2008). In addition, other studies documented that calcite cementation also occurs at the top of overpressured reservoirs, where periodic changes of fluid pressure and formation hydrochemical conditions resulted in calcite cement (Fig. 9D), e.g., the overpressured sandstone reservoirs in the central Junggar Basin (He et al., 2009; Yang et al., 2010) and in the Dongying Depression of the Bohai Bay Basin (Han et al., 2012; Zhang et al., 2019). In settings containing internal sources for carbonate cement, such as biogenic carbonates and carbonate rock fragments (Walderhaug & Bjørkum, 1998), cement distribution tends to be controlled by the distribution of these internal sources through in-situ dissolution and reprecipitation (Fig. 9E), e.g., the Fensfjord Formation (Walderhaug et al., 1989) and the Rannoch Formation (Bjørkum & Walderhaug, 1990a) in the North Sea. In addition, Liu et al. (2019) concluded a different fluid-rock interaction model of dissolution, migration and re-

precipitation in the Xujiahe Formation of the Sichuan Basin. Hydrocarbon-related acidic fluids tend to flow along the more permeable reservoirs, resulting in intensive dissolution in coarse reservoirs, whereas intensive re-precipitation occurs in the marginal impermeable fine reservoirs (Fig. 9F).

5.4 Effects of calcite cements on reservoir potential

Calcite cement distribution can be controlled by one of the aforementioned patterns or be affected by several patterns at the same time, depending on the specific geological backgrounds. Likewise, there are variable relationships between calcite cementation and reservoir quality in different settings. Calcite cementation is widely considered an important factor controlling reservoir quality because of its ability to reduce porosity and permeability (Davis et al., 2006; Dutton, 2008; Xiong et al., 2016). As an example of this control, the predominant calcite cement (Cc1) filled most fractures and resulted in the overall low porosity of host rocks in the Puig-reig anticline, which is currently lower than 2% on average (Figs. 3C and 10). On the other hand, calcite cement tends to precipitate in more permeable reservoirs (McBride et al., 1995; Dutton et al., 2002; Hall et al., 2004; Van Den Bril & Swennen, 2009). For example, in the Puig-reig anticline, medium-coarse sandstones in medial fluvial fan with relatively high porosity show higher calcite content. The values of porosity and cement content vary across different lithofacies (Fig. 10), and these two parameters do not present a clear negative correlation. Limited high porosity, mainly ranging from 2% to 8%, concentrates in channelised or massive medium to coarse sandstones in the medial fluvial fan. However, these lithofacies also feature almost the highest cement content. These sandstone lithofacies have better grain sorting than conglomerate ones and lower contents of ductile clayey matrix than fine lithofacies. Thus, they had a more appropriate pore structure for fluid flow from which calcite cement precipitated and thus contained a higher number of intergranular pores for cement growth and residual porosity. This resulted in the coexistence of relatively high values of cement content and porosity for these lithofacies. Similar cement and porosity distribution patterns controlled by lithofacies have been documented in other studies. For example, in the Huagang Formation in the Xihu Depression of the East China Sea Basin, coarse sandstone reservoirs have higher porosity but also relatively high content of quartz cement than other reservoirs (Sun et al., 2017).

Apart from reducing reservoir porosity and permeability, early calcite cement can affect the later evolution of reservoir quality (Hosa & Wood, 2017). For example, early cement can preserve intergranular space and improve reservoir quality by providing secondary porosity under the specific circumstance of intensive dissolution during later diagenetic stages, e.g., the Lower Devonian Jauf Formation in Saudi Arabia (Al-Ramadan et al., 2004), the Biyadh Formation in the western central Masila Basin (Hakimi et al., 2012), and the Upper Jurassic Ti-3 sandstones in the Flemish Pass Basin (Xiong et al., 2016). Besides, mechanical contrasts between layers could be affected by the distribution of early calcite cement, which could have a significant effect on fracture development and thus reservoir potential, an effect observed for example in the Madison Formation in the Sheep Mountain of the

Bighorn Basin (Barbier et al., 2012) and the Calcare Massiccio unit in the Umbria–Marche Apennines (Di Naccio et al., 2005). Thus, to determine the distribution of calcite cement and their real effects on reservoir potential, the specific geological backgrounds of host rocks should be fully considered.

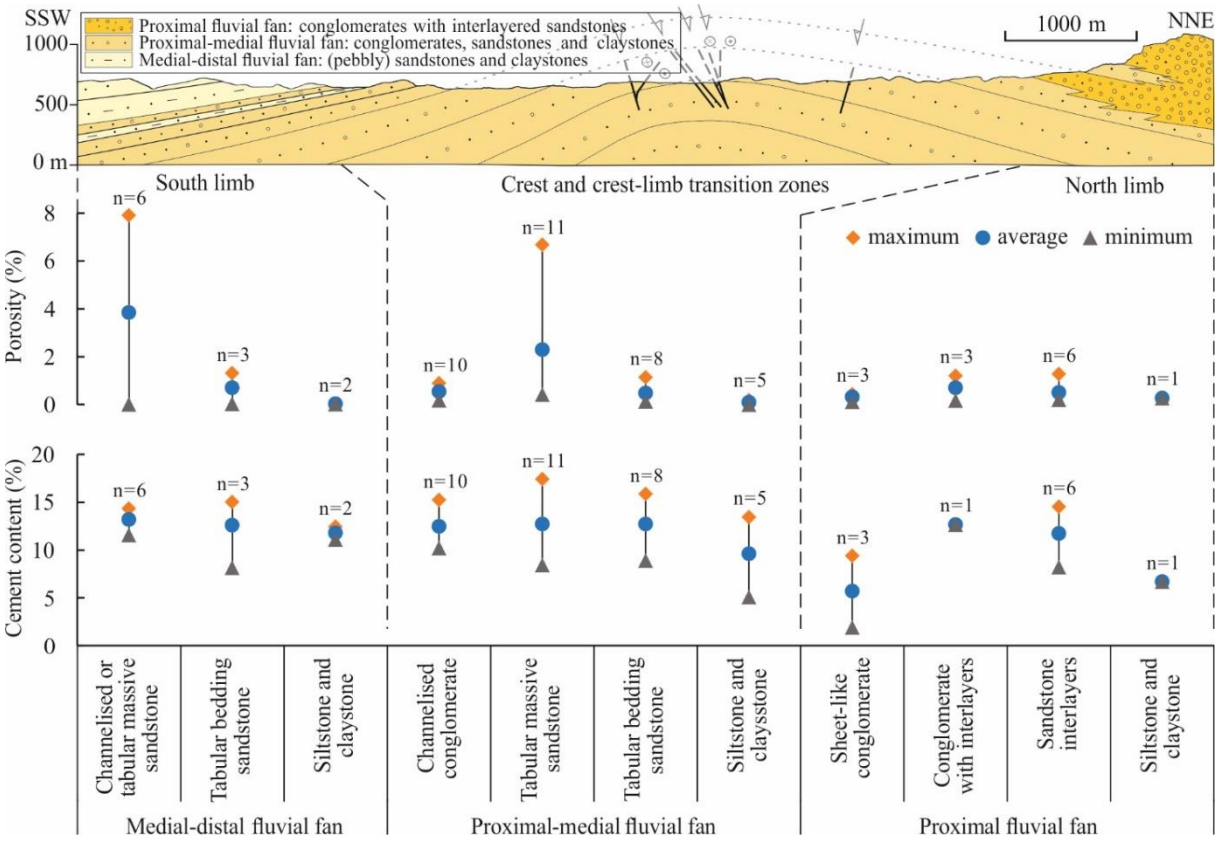

Figure 10. Distribution of porosity and calcite cement contents in different lithofacies, sedimentary facies and structural positions. '*n*' is the number of thin sections. The cross-section is modified from Cruset et al. (2016).

6 Conclusions

The Puig-reig anticline, in the south-eastern Pyrenees, exposes excellent outcrops of detrital rocks deposited from a proximal to medial fluvial system and cemented by calcite. The integration of structural, petrological and geochemical analyses allows unravelling the calcite cementation history and the related fluid regime changes during the anticline evolution. The comparison between this study and others worldwide in different settings allows the exploration of the distribution of calcite cement and its effects on reservoir quality. We reach the following conclusions:

(1) Five generations of calcite cements (Cc0 to Cc4) and five phases of fluid regimes have been identified. Cc0 precipitated in intergranular pores from meteoric fluids. As the predominant cement, Cc1 precipitated in intergranular pores, faults and F1 to F4 fracture sets from hydrothermal fluids. Cc2 mainly developed in normal and strike-slip faults in the anticline crest from the mixing between hydrothermal and meteoric fluids or from hydrothermal fluids with more meteoric signatures than Cc1.

Cc3 developed in F1 and F4 fracture sets in the western area of the north limb from formation fluids with temperatures between 50°C and 62°C. Cc4 precipitated in F1 to F4 fracture sets from meteoric fluids with temperatures between 16°C and 19°C.

(2) Calcite cementation and fluid regime changes occurred as the anticline evolved. In the early diagenetic stage, before intensive deformation, the fluid regime was dominated by meteoric fluids (Cc0). During the most intense phase of thrusting and folding, hydrothermal fluids from the internal and deeper parts of the SE Pyrenees migrated upwards through connected thrust systems and fracture networks and dominated the fluid regime (Cc1). In the later stage of the anticline growth, the mixed fluids between hydrothermal and meteoric fluids dominated the fluid regime in the anticline crest during the crest collapse (Cc2). Alternatively, the anticline crest could be dominated by the hydrothermal fluids at shallower burial depths than that of Cc1. Besides, formation fluids migrated through the frontal thrusts and dominated the western part of the north limb (Cc3). During the continuous denudation, the anticline was dominated by meteoric fluids due to the exhumation of strata, migrated through reopened and newly formed fractures (Cc4).

(3) In the Puig-reig anticline, the predominant calcite cement (Cc1) resulted from external fluids coeval with the compressional deformation of the anticline and the substantial detrital carbonates of host rocks. Calcite cements filled abundant fractures and reduced the overall intergranular porosity of host rocks. Contrarily, in other settings not featuring intensive deformation and sufficient external fluids, calcite cement tends to show heterogeneous distributions. Carbonate cement exerts significant but variable effects on reservoir quality, which largely depend on the specific geological backgrounds.

Acknowledgements

Funding was provided by the Catalan Council to the Grup Consolidat de Recerca “Geologia Sedimentària” (2017SGR-824) and the DGICYT Spanish Project PGC2018-093903-B-C22 (Ministerio de Ciencia, Innovación y Universidades/Agencia Estatal de Investigación/Fondo Europeo de Desarrollo Regional, Unión Europea). XS acknowledges funding by the China Scholarship Council for a PhD scholarship (201806450043). EGR acknowledges funding provided by the Spanish Ministry of Science, Innovation and Universities (“Ramón y Cajal” fellowship RYC2018-026335-I). JA is funded by MICINN (Juan de la Cierva fellowship - IJC2018-036074-I).

References

Adlan, Q., **Davies, A.J.** and **John, C.M.** (2020) Effects of oxygen plasma ashing treatment on carbonate clumped isotopes. *Rapid Commun. mass Spectrom.*, **34**, e8802.

Al-Ramadan, K.A., **Hussain, M.**, **Imam, B.** and **Saner, S.** (2004) Lithologic characteristics and diagenesis of the Devonian Jauf sandstone at Ghawar Field, Eastern Saudi Arabia. *Mar. Pet.*

Geol., **21**, 1221–1234.

Anderson, N.T., **Kelson, J.R.**, **Kele, S.**, **Daëron, M.**, **Bonifacie, M.**, **Horita, J.**, **Mackey, T.J.**, **John, C.M.**, **Kluge, T.**, **Petschnig, P.**, **Jost, A.B.**, **Huntington, K.W.**, **Bernasconi, S.M.** and **Bergmann, K.D.** (2021) A unified clumped isotope thermometer calibration (0.5–1,100°C) using carbonate-based standardization. *Geophys. Res. Lett.*, **48**, e2020GL092069.

Balsamo, F., **Clemenzi, L.**, **Storti, F.**, **Mozafari, M.**, **Solum, J.**, **Swennen, R.**, **Taberner, C.** and **Tueckmantel, C.** (2016) Anatomy and paleofluid evolution of laterally restricted extensional fault zones in the Jabal Qusaybah anticline, Salakh arch, Oman. *Geol. Soc. Am. Bull.*, **128**, 957–972.

Banner, J.L. (1995) Application of the trace element and isotope geochemistry of strontium to studies of carbonate diagenesis. *Sedimentology*, **42**, 805–824.

Barbier, M., **Hamon, Y.**, **Callot, J.P.**, **Floquet, M.** and **Daniel, J.M.** (2012) Sedimentary and diagenetic controls on the multiscale fracturing pattern of a carbonate reservoir: The Madison Formation (Sheep Mountain, Wyoming, USA). *Mar. Pet. Geol.*, **29**, 50–67.

Barrier, L., **Proust, J.N.**, **Nalpas, T.**, **Robin, C.** and **Guillocheau, F.** (2010) Control of alluvial sedimentation at foreland-basin active margins: A case study from the northeastern Ebro Basin (southeastern Pyrenees, Spain). *J. Sediment. Res.*, **80**, 728–749.

Beaudoin, N., **Bellahsen, N.**, **Lacombe, O.** and **Emmanuel, L.** (2011) Fracture-controlled paleohydrogeology in a basement-cored, fault-related fold: Sheep Mountain Anticline, Wyoming, United States. *Geochemistry, Geophys. Geosystems*, **12**, Q06011.

Beaudoin, N., **Bellahsen, N.**, **Lacombe, O.**, **Emmanuel, L.** and **Pironon, J.** (2014) Crustal-scale fluid flow during the tectonic evolution of the Bighorn Basin (Wyoming, USA). *Basin Res.*, **26**, 403–435.

Beaudoin, N., **Huyghe, D.**, **Bellahsen, N.**, **Lacombe, O.**, **Emmanuel, L.**, **Mouthereau, F.** and **Ouanhnon, L.** (2015) Fluid systems and fracture development during syn-depositional fold growth: An example from the Pico del Aguila anticline, Sierras Exteriores, southern Pyrenees, Spain. *J. Struct. Geol.*, **70**, 23–38.

Beaudoin, N., **Lacombe, O.**, **Bellahsen, N.** and **Emmanuel, L.** (2013) Contribution of studies of sub-seismic fracture populations to paleo-hydrological reconstructions (Bighorn Basin, USA). *Procedia Earth Planet. Sci.*, **7**, 57–60.

Beaudoin, N.E., **Labeur, A.**, **Lacombe, O.**, **Koehn, D.**, **Billi, A.**, **Hoareau, G.**, **Boyce, A.**, **John, C.M.**, **Marchegiano, M.**, **Roberts, N.M.**, **Millar, I.L.**, **Claverie, F.**, **Pecheyran, C.** and **Callot, J.-P.** (2020) Regional-scale paleofluid system across the Tuscan Nappe–Umbria–Marche Apennine Ridge (northern Apennines) as revealed by mesostructural and isotopic analyses of stylolite–vein networks. *Solid Earth*, **11**, 1617–1641.

Bernasconi, S.M., **Daëron, M.**, **Bergmann, K.D.**, **Bonifacie, M.**, **Meckler, A.N.**, **Affek, H.P.**, **Anderson, N.**, **Bajnai, D.**, **Barkan, E.**, **Beverly, E.**, **Blamart, D.**, **Burgener, L.**, **Calmels, D.**, **Chaduteau, C.**, **Clog, M.**, **Davidheiser-Kroll, B.**, **Davies, A.**, **Dux, F.**, **Eiler, J.**, **Elliott, B.**, **Fetrow, A.C.**, **Fiebig, J.**, **Goldberg, S.**, **Hermoso, M.**, **Huntington, K.W.**, **Hyland, E.**, **Ingalls, M.**, **Jaggi, M.**, **John, C.M.**, **Jost, A.B.**, **Katz, S.**, **Kelson, J.**, **Kluge, T.**, **Kocken, I.J.**, **Laskar, A.**, **Leutert, T.J.**, **Liang, D.**, **Lucarelli, J.**, **Mackey, T.J.**, **Mangenot, X.**, **Meinicke, N.**, **Modestou, S.E.**, **Müller, I.A.**, **Murray, S.**, **Neary, A.**, **Packard, N.**, **Passey, B.H.**, **Pelletier, E.**, **Petersen, S.**, **Piasecki, A.**, **Schauer, A.**, **Snell, K.E.**, **Swart, P.K.**, **Tripati, A.**, **Upadhyay, D.**, **Vennemann, T.**, **Winkelstern, I.**, **Yarian, D.**, **Yoshida, N.**, **Zhang, N.** and **Ziegler, M.** (2021) InterCarb: A community effort to improve interlaboratory standardization of the carbonate clumped isotope thermometer using carbonate standards. *Geochemistry, Geophys. Geosystems*, **22**, e2020GC009588.

Bernasconi, S.M., **Hu, B.**, **Wacker, U.**, **Fiebig, J.**, **Breitenbach, S.F.M.** and **Rutz, T.** (2013) Background effects on Faraday collectors in gas-source mass spectrometry and implications for clumped isotope measurements. *Rapid Commun. Mass Spectrom.*, **27**, 603–612.

Bjørkum, P.A. and **Walderhaug, O.** (1990a) Lateral extent of calcite-cemented zones in shallow marine sandstones. In: *North Sea Oil and Gas Reservoirs—II* (Ed. A.T. Buller, E. Berg, O. Hjelmeland, J. Kleppe, O. Torsæter, and J.O. Aasen), *Springer*, Dordrecht, 331–336.

Bjørkum, P.A. and **Walderhaug, O.** (1990b) Geometrical arrangement of calcite cementation within shallow marine sandstones. *Earth-Science Rev.*, **29**, 145–161.

Boggs, S. and **Krinsley, D.** (2006) Application of Cathodoluminescence Imaging to the Study of Sedimentary Rocks. *Cambridge University Press*, Cambridge.

Bons, P.D., **Elburg, M.A.** and **Gomez-Rivas, E.** (2012) A review of the formation of tectonic veins and their microstructures. *J. Struct. Geol.*, **43**, 33–62.

Bons, P.D., **Fusswinkel, T.**, **Gomez-Rivas, E.**, **Markl, G.**, **Wagner, T.** and **Walter, B.** (2014) Fluid mixing from below in unconformity-related hydrothermal ore deposits. *Geology*, **42**, 1035–1038.

Bons, P.D. and **Gomez-Rivas, E.** (2020) Origin of meteoric fluids in extensional detachments. *Geofluids*, **2020**, 1–8.

Breesch, L., **Swennen, R.** and **Vincent, B.** (2009) Fluid flow reconstruction in hanging and footwall carbonates: Compartmentalization by Cenozoic reverse faulting in the Northern Oman Mountains (UAE). *Mar. Pet. Geol.*, **26**, 113–128.

Cantarero, I., **Travé, A.**, **Alías, G.** and **Baqués, V.** (2010) Pedogenic products sealing normal faults (Barcelona Plain, NE Spain). *J. Geochemical Explor.*, **106**, 44–52.

Cantarero, I., **Travé, A.**, **Alías, G.** and **Baqués, V.** (2014a) Polyphasic hydrothermal and meteoric fluid regimes during the growth of a segmented fault involving crystalline and carbonate rocks

(Barcelona Plain, NE Spain). *Geofluids*, **14**, 20–44.

Cantarero, I., **Zafra, C.J.**, **Travé, A.**, **Martín-Martín, J.D.**, **Baqués, V.** and **Playà, E.** (2014b) Fracturing and cementation of shallow buried Miocene proximal alluvial fan deposits. *Mar. Pet. Geol.*, **55**, 87–99.

Carrigan, J.H., **Anastasio, D.J.**, **Kodama, K.P.** and **Parés, J.M.** (2016) Fault-related fold kinematics recorded by terrestrial growth strata, Sant Llorenç de Morunys, Pyrenees Mountains, NE Spain. *J. Struct. Geol.*, **91**, 161–176.

Carvalho, M.V.F., **De Ros, L.F.** and **Gomes, N.S.** (1995) Carbonate cementation patterns and diagenetic reservoir facies in the Campos Basin cretaceous turbidites, offshore eastern Brazil. *Mar. Pet. Geol.*, **12**, 741–758.

Ceriani, A., **Calabrò, R.**, **Di Giulio, A.** and **Buonaguro, R.** (2011) Diagenetic and thermal history of the Jurassic-Tertiary succession of the Zagros Mountains in the Dezful Embayment (SW Iran): constraints from fluid inclusions. *Int. J. Earth Sci.*, **100**, 1265–1281.

Cerling, T.E. (1984) The stable isotopic composition of modern soil carbonate and its relationship to climate. *Earth Planet. Sci. Lett.*, **71**, 229–240.

Cerling, T.E. and **Quade, J.** (1993) Stable carbon and oxygen isotopes in soil carbonates. In: *Climate Change in Continental Isotopic Records. Geophysical Monograph* (Ed. P.K. Swart, K.C. Lohmann, J. McKenzie, and S. Savin), *American Geophysical Union*, Washington, DC, 217–231.

Choukroune, P. (1989) The Ecors Pyrenean deep seismic profile reflection data and the overall structure of an orogenic belt. *Tectonics*, **8**, 23–39.

Clavell, E. (1992) Geologia del petroli de les conques terciàries de Catalunya. University of Barcelona

Costa, E., **Garcés, M.**, **López-Blanco, M.**, **Beamud, E.**, **Gómez-Paccard, M.** and **Larrasoaña, J.C.** (2010) Closing and continentalization of the South Pyrenean foreland basin (NE Spain): Magnetochronological constraints. *Basin Res.*, **22**, 904–917.

Crognier, N., **Hoareau, G.**, **Aubourg, C.**, **Dubois, M.**, **Lacroix, B.**, **Branellec, M.**, **Callot, J.P.** and **Vennemann, T.** (2018) Syn-orogenic fluid flow in the Jaca basin (south Pyrenean fold and thrust belt) from fracture and vein analyses. *Basin Res.*, **30**, 187–216.

Cruset, D., **Cantarero, I.**, **Benedicto, A.**, **John, C.M.**, **Vergés, J.**, **Albert, R.**, **Gerdes, A.** and **Travé, A.** (2020a) From hydroplastic to brittle deformation: Controls on fluid flow in fold and thrust belts. Insights from the Lower Pedraforca thrust sheet (SE Pyrenees). Mar. Pet. Geol. 120:104517.

Cruset, D., **Cantarero, I.**, **Travé, A.**, **Vergés, J.** and **John, C.M.** (2016) Crestal graben fluid evolution during growth of the Puig-reig anticline (South Pyrenean fold and thrust belt). *J. Geodyn.*, **101**, 30–50.

Cruset, D., **Cantarero, I.**, **Vergés, J.**, **John, C.M.**, **Muñoz-López, D.** and **Travé, A.** (2018) Changes

in fluid regime in syn-orogenic sediments during the growth of the south Pyrenean fold and thrust belt. *Glob. Planet. Change*, **171**, 207–224.

Cruset, D., **Vergés, J.**, **Albert, R.**, **Gerdes, A.**, **Benedicto, A.**, **Cantarero, I.** and **Travé, A.** (2020b) Quantifying deformation processes in the SE Pyrenees using U–Pb dating of fracture-filling calcites. *J. Geol. Soc. London.*, **177**, 1186–1196.

Cui, Y., **Jones, S.J.**, **Saville, C.**, **Stricker, S.**, **Wang, G.**, **Tang, L.**, **Fan, X.** and **Chen, J.** (2017) The role played by carbonate cementation in controlling reservoir quality of the Triassic Skagerrak Formation, Norway. *Mar. Pet. Geol.*, **85**, 316–331.

Davis, J.M., **Roy, N.D.**, **Mozley, P.S.** and **Hall, J.S.** (2006) The effect of carbonate cementation on permeability heterogeneity in fluvial aquifers: An outcrop analog study. *Sediment. Geol.*, **184**, 267–280.

Dewever, B., **Berwouts, I.**, **Swennen, R.**, **Breesch, L.** and **Ellam, R.M.** (2010) Fluid flow reconstruction in karstified Panormide platform limestones (north-central Sicily): Implications for hydrocarbon prospectivity in the Sicilian fold and thrust belt. *Mar. Pet. Geol.*, **27**, 939–958.

Dewever, B., **Swennen, R.** and **Breesch, L.** (2013) Fluid flow compartmentalization in the Sicilian fold and thrust belt: Implications for the regional aqueous fluid flow and oil migration history. *Tectonophysics*, **591**, 194–209.

Di Naccio, D., **Boncio, P.**, **Cirilli, S.**, **Casaglia, F.**, **Morettini, E.**, **Lavecchia, G.** and **Brozzetti, F.** (2005) Role of mechanical stratigraphy on fracture development in carbonate reservoirs: Insights from outcropping shallow water carbonates in the Umbria-Marche Apennines, Italy. *J. Volcanol. Geotherm. Res.*, **148**, 98–115.

Dos Anjos, S.M.C., **De Ros, L.F.**, **De Souza, R.S.**, **De Assis Silva, C.M.** and **Sombra, C.L.** (2000) Depositional and diagenetic controls on the reservoir quality of Lower Cretaceous Pendencia sandstones, Potiguar rift basin, Brazil. *Am. Assoc. Pet. Geol. Bull.*, **84**, 1719–1742.

Dutton, S.P. (2008) Calcite cement in Permian deep-water sandstones, Delaware Basin, west Texas: Origin, distribution, and effect on reservoir properties. *Am. Assoc. Pet. Geol. Bull.*, **92**, 765–787.

Dutton, S.P., **White, C.D.**, **Willis, B.J.** and **Novakovic, D.** (2002) Calcite cement distribution and its effect on fluid flow in a deltaic sandstone, Frontier Formation, Wyoming. *Am. Assoc. Pet. Geol. Bull.*, **86**, 2007–2021.

El-ghali, M.A.K., **Mansurbeg, H.**, **Morad, S.**, **Al-Aasm, I.** and **Ajdanlisky, G.** (2006) Distribution of diagenetic alterations in fluvial and paralic deposits within sequence stratigraphic framework: Evidence from the Petrohan Terrigenous Group and the Svidol Formation, Lower Triassic, NW Bulgaria. *Sediment. Geol.*, **190**, 299–321.

Emery, D. and **Dickson, J.A.D.** (1989) A syndepositional meteoric phreatic lens in the Middle Jurassic Lincolnshire Limestone, England, U.K. *Sediment. Geol.*, **65**, 273–284.

Evans, M.A., **Bebout, G.E.** and **Brown, C.H.** (2012) Changing fluid conditions during folding: An example from the central Appalachians. *Tectonophysics*, **576**–**577**, 99–115.

Evans, M.A. and **Fischer, M.P.** (2012) On the distribution of fluids in folds: A review of controlling factors and processes. *J. Struct. Geol.*, **44**, 2–24.

Fernàndez, M., **Marzán, I.**, **Correia, A.** and **Ramalho, E.** (1998) Heat flow, heat production, and lithospheric thermal regime in the Iberian Peninsula. *Tectonophysics*, **291**, 29–53.

Folk, R.L. (1980) Petrology of Sedimentary Rocks. *Hemphill Publishing Company*, Austin, 182 pp.

Ford, M., **Williams, E.A.**, **Artoni, A.**, **Vergés, J.** and **Hardy, S.** (1997) Progressive evolution of a fault-related fold pair from growth strata geometries, Sant Llorenç de Morunys, SE Pyrenees. *J. Struct. Geol.*, **19**, 413–441.

Gomez-Rivas, E., **Bons, P.D.**, **Koehn, D.**, **Urai, J.L.**, **Arndt, M.**, **Virgo, S.**, **Laurich, B.**, **Zeeb, C.**, **Stark, L.** and **Blum, P.** (2014) The Jabal Akhdar Dome in the Oman mountains: Evolution of a dynamic fracture system. *Am. J. Sci.*, **314**, 1104–1139.

Grover, G. and **Read, J.F.** (1983) Paleoaquifer and deep burial related cements defined by regional cathodoluminescent patterns, Middle Ordovician Carbonates, Virginia. *Am. Assoc. Pet. Geol. Bull.*, **67**, 1275–1303.

Guilbaud, R., **Bernet, M.**, **Huyghe, P.**, **Erens, V.**, **Chirouze, F.** and **Dupont-Nivet, G.** (2012) On the influence of diagenesis on the original petrographic composition of Miocene–Pliocene fluvial sandstone in the Himalayan foreland basin of western-central Nepal. *J. Asian Earth Sci.*, **44**, 107–116.

Hakimi, M.H., **Shalaby, M.R.** and **Abdullah, W.H.** (2012) Diagenetic characteristics and reservoir quality of the Lower Cretaceous Biyadh sandstones at Kharir oilfield in the western central Masila Basin, Yemen. *J. Asian Earth Sci.*, **51**, 109–120.

Hall, J.S., **Mozley, P.**, **Davis, J.M.** and **Roy, N.D.** (2004) Environments of formation and controls on spatial distribution of calcite cementation in Plio-Pleistocene fluvial deposits, New Mexico, U.S.A. *J. Sediment. Res.*, **74**, 643–653.

Han, Y., **He, S.**, **Song, G.**, **Wang, Y.**, **Hao, X.**, **Wang, B.** and **Luo, S.** (2012) Origin of carbonate cements in the overpressured top seal and adjacent sandstones in Dongying depression. *Acta Pet. Sin.*, **33**, 385.

Hanshaw, B.B. and **Coplen, T.B.** (1973) Ultrafiltration by a compacted clay membrane—II. Sodium ion exclusion at various ionic strengths. *Geochim. Cosmochim. Acta*, **37**, 2311–2327.

Hansman, R.J., **Albert, R.**, **Gerdes, A.** and **Ring, U.** (2018) Absolute ages of multiple generations of brittle structures by U-Pb dating of calcite. *Geology*, **46**, 207–210.

He, S., **Yang, Z.**, **He, Z.**, **Wu, H.**, **Wang, F.** and **Meng, X.** (2009) Mechanism of carbonate cementation and secondary dissolution porosity formation in deep-burial sandstones near the top

overpressured surface in central part of Junggar basin. *Earth Sci. - J. China Univ. Geosci.*, **34**, 759–768.

Henderson, I.H.C. and **McCaig, A.M.** (1996) Fluid pressure and salinity variations in shear zone-related veins, central Pyrenees, France: Implications for the fault-valve model. *Tectonophysics*, **262**, 321–348.

Hosa, A. and **Wood, R.** (2017) Quantifying the impact of early calcite cementation on the reservoir quality of carbonate rocks: A 3D process-based model. *Adv. Water Resour.*, **104**, 89–104.

Houseknecht, D.W. (1987) Assessing the relative importance of compaction processes and cementation to reduction of porosity in sandstones. *Am. Assoc. Pet. Geol. Bull.*, **71**, 633–642.

Ingersoll, R. V., **Cavazza, W.** and **Graham, S.A.** (1987) Provenance of impure calclithites in the Laramide foreland of southwestern Montana. *J. Sediment. Res.*, **57**, 995–1003.

Institut Cartogràfic i Geològic de Catalunya (2006) Regional geological map of Catalonia. https://www.icgc.cat/en/Public-Administration-and-Enterprises/Downloads/Geological-and-geothematic-cartography/Geological-cartography/Geological-map-1-50-000/Regional-geological-map-of-Catalonia-1-50-000. Accessed 1 Feb 2021

Instituto Geológico y Minero de España (1977) Geophysical Information System. http://info.igme.es/SIGEOF/#. Accessed 1 Feb 2021

Irwin, H., **Curtis, C.** and **Coleman, M.** (1977) Isotopic evidence for source of diagenetic carbonates formed during burial of organic-rich sediments. *Nature*, **269**, 209–213.

John, C.M. and **Bowen, D.** (2016) Community software for challenging isotope analysis: First applications of 'Easotope' to clumped isotopes. *Rapid Commun. Mass Spectrom.*, **30**, 2285–2300.

Kim, S.-T., **Coplen, T.B.** and **Horita, J.** (2015) Normalization of stable isotope data for carbonate minerals: Implementation of IUPAC guidelines. *Geochim. Cosmochim. Acta*, **158**, 276–289.

Kim, S.-T., **Mucci, A.** and **Taylor, B.E.** (2007) Phosphoric acid fractionation factors for calcite and aragonite between 25 and 75 °C: Revisited. *Chem. Geol.*, **246**, 135–146.

Lacroix, B., **Baumgartner, L.P.**, **Bouvier, A.S.**, **Kempton, P.D.** and **Vennemann, T.** (2018) Multi fluid-flow record during episodic mode I opening: A microstructural and SIMS study (Cotiella Thrust Fault, Pyrenees). *Earth Planet. Sci. Lett.*, **503**, 37–46.

Lacroix, B., **Buatier, M.**, **Labaume, P.**, **Travé, A.**, **Dubois, M.**, **Charpentier, D.**, **Ventalon, S.** and **Convert-Gaubier, D.** (2011) Microtectonic and geochemical characterization of thrusting in a foreland basin: Example of the South-Pyrenean orogenic wedge (Spain). *J. Struct. Geol.*, **33**, 1359–1377.

Lacroix, B., **Travé, A.**, **Buatier, M.**, **Labaume, P.**, **Vennemann, T.** and **Dubois, M.** (2014) Syntectonic fluid-flow along thrust faults: Example of the South-Pyrenean fold-and-thrust belt. *Mar. Pet. Geol.*, **49**, 84–98.

Li, Z., **Goldstein, R.H.** and **Franseen, E.K.** (2017) Meteoric calcite cementation: diagenetic response to relative fall in sea-level and effect on porosity and permeability, Las Negras area, southeastern Spain. *Sediment. Geol.*, **348**, 1–18.

Liu, Y., **Hu, W.**, **Cao, J.**, **Wang, X.**, **Zhu, F.**, **Tang, Q.** and **Gao, W.** (2019) Fluid–rock interaction and its effects on the Upper Triassic tight sandstones in the Sichuan Basin, China: Insights from petrographic and geochemical study of carbonate cements. *Sediment. Geol.*, **383**, 121–135.

Machel, H.G. (2000) Application of cathodoluminescence to carbonate diagenesis. In: *Cathodoluminescence in Geosciences* (Ed. M. Page, V. Barbin, P. Blanc, and D. Ohnenstetter), *Springer Berlin Heidelberg*, Berlin, Heidelberg, 271–301.

Mansurbeg, H., **Caja, M.A.**, **Marfil, R.**, **Morad, S.**, **Remacha, E.**, **Garcia, D.**, **Martin-Crespo, T.**, **El-Ghali, M.A.K.** and **Nystuen, J.P.** (2009) Diagenetic evolution and porosity destruction of turbiditic hybrid arenites and siliciclastic sandstones of foreland basins: Evidence from the Eocene Hecho Group, Pyrenees, Spain. *J. Sediment. Res.*, **79**, 711–735.

McArthur, J.M., **Howarth, R.J.** and **Shields, G.A.** (2012) Strontium Isotope Stratigraphy. In: *The Geologic Time Scale* (Ed. F.M. Gradstein, J.G. Ogg, M.D. Schmotz, and G.M. Ogg), *Elsevier*, 211–238.

McBride, E.F., **Milliken, K.L.**, **Cavazza, W.**, **Cibin, U.**, **Fontana, D.**, **Picard, M.D.** and **Zuffa, G.G.** (1995) Heterogeneous distribution of calcite cement at the outcrop scale in Tertiary sandstones, Northern Apennines, Italy. *Am. Assoc. Pet. Geol. Bull.*, **79**, 1044–1062.

Mccrea, J.M. (1950) On the isotopic chemistry of carbonates and a paleotemperature scale. *J. Chem. Phys.*, **18**, 849–857.

Morad, S. (1998) Carbonate Cementation in Sandstones: Distribution Patterns and Geochemical Evolution. In: *Carbonate Cementation in Sandstones* (Ed. S. Morad), *Blackwell Publishing Ltd.*, Oxford, 1–26.

Morad, S., **Al-Ramadan, K.**, **Ketzer, J.M.** and **De Ros, L.F.** (2010) The impact of diagenesis on the heterogeneity of sandstone reservoirs: A review of the role of depositional fades and sequence stratigraphy. *Am. Assoc. Pet. Geol. Bull.*, **94**, 1267–1309.

Muchez, P., **Nielsen, P.**, **Sintubin, M.** and **Lagrou, D.** (1998) Conditions of meteoric calcite formation along a Variscan fault and their possible relation to climatic evolution during the Jurassic–Cretaceous. *Sedimentology*, **45**, 845–854.

Muñoz-López, D., **Alías, G.**, **Cruset, D.**, **Cantarero, I.**, **John, C.M.** and **Travé, A.** (2020a) Influence of basement rocks on fluid evolution during multiphase deformation: the example of the Estamariu thrust in the Pyrenean Axial Zone. *Solid Earth*, **11**, 2257–2281.

Muñoz-López, D., **Cruset, D.**, **Cantarero, I.**, **Benedicto, A.**, **John, C.M.** and **Travé, A.** (2020b) Fluid dynamics in a thrust fault inferred from petrology and geochemistry of calcite veins: An

example from the southern Pyrenees. *Geofluids*, **2020**, 1–25.

Muñoz, J.A. (1992) Evolution of a continental collision belt: ECORS-Pyrenees crustal balanced cross-section. In: *Thrust Tectonics* (Ed. K.R. McClay), *Springer*, Dordrecht, 235–246.

Nardini, N., **Muñoz-López, D.**, **Cruset, D.**, **Cantarero, I.**, **Martín-Martín, J.**, **Benedicto, A.**, **Gomez-Rivas, E.**, **John, C.** and **Travé, A.** (2019) From early contraction to post-folding fluid evolution in the frontal part of the Bóixols Thrust Sheet (Southern Pyrenees) as revealed by the texture and geochemistry of calcite cements. *Minerals*, **9**, 117.

Nyman, S.L., **Gani, R.M.**, **Bhattacharya, J.P.** and **Lee, K.** (2014) Origin and distribution of calcite concretions in Cretaceous Wall Creek Member, Wyoming: Reservoir-quality implication for shallow-marine deltaic strata. *Cretac. Res.*, **48**, 139–152.

Olanipekun, B. and **Azmy, K.** (2021) Carbonate cementation in the Tithonian Jeanne d'Arc sandstone, Terra Nova Field, Newfoundland: Implications for reservoir quality evolution. *Sedimentology*, sed.12912.

Parcerisa, D., **Gómez-Gras, D.** and **Travé, A.** (2005) A model of early calcite cementation in alluvial fans: Evidence from the Burdigalian sandstones and limestones of the Vallès-Penedès half-graben (NE Spain). *Sediment. Geol.*, **178**, 197–217.

Parcerisa, D., **Gómez-Gras, D.**, **Travé, A.**, **Martín-Martín, J.D.** and **Maestro, E.** (2006) Fe and Mn in calcites cementing red beds: A record of oxidation–reduction conditions: Examples from the Catalan Coastal Ranges (NE Spain). *J. Geochemical Explor.*, **89**, 318–321.

Riba, O. (1976) Syntectonic unconformities of the Alto Cardener, Spanish Pyrenees: a genetic interpretation. *Sediment. Geol.*, **15**, 213–233.

Roure, F., **Choukroune, P.**, **Berastegui, X.**, **Munoz, J.A.**, **Villien, A.**, **Matheron, P.**, **Bareyt, M.**, **Seguret, M.**, **Camara, P.** and **Deramond, J.** (1989) Ecors deep seismic data and balanced cross sections: Geometric constraints on the evolution of the Pyrenees. *Tectonics*, **8**, 41–50.

Sáez, A., **Anadón, P.**, **Herrero, M.J.** and **Moscariello, A.** (2007) Variable style of transition between Palaeogene fluvial fan and lacustrine systems, southern Pyrenean foreland, NE Spain. *Sedimentology*, **54**, 367–390.

Schneider, C.A., **Rasband, W.S.** and **Eliceiri, K.W.** (2012) NIH Image to ImageJ: 25 years of image analysis. *Nat. Methods*, **9**, 671–675.

Serra-Kiel, J., **Mató, E.**, **Saula, E.**, **Travé, A.**, **Ferràndez-Canadell, C.**, **Busquets, P.**, **Samsó, J.M.**, **Tosquella, J.**, **Barnolas, A.**, **Àlvarez-Pérez, G.**, **Franquès, J.** and **Romero, J.** (2003a) An inventory of the marine and transitional Middle/Upper Eocene deposits of the Southeastern Pyrenean Foreland Basin (NE Spain). *Geol. Acta*, **1**, 201–229.

Serra-Kiel, J., **Travé, A.**, **Mató, E.**, **Saula, E.**, **Ferràndez-Canadell, C.**, **Busquets, P.**, **Tosquella, J.** and **Vergés, J.** (2003b) Marine and transitional Middle/Upper Eocene units of the southeastern

pyrenean foreland basin (NE Spain). *Geol. Acta*, **1**, 177–200.

Shariatinia, Z., **Haghighi, M.**, **Feiznia, S.**, **Hall, D.**, **Levresse, G.**, **Dehghani, A.M.** and **Rashidi, M.** (2013) Paleofluid analysis from fracture-fill cements in the Asmari limestones of the Kuh-I-Mond field, SW Zagros, Iran. *Arab. J. Geosci.*, **6**, 2539–2556.

Sibson, R.H. (1981) Fluid flow accompanying faulting: field evidence and models. In: *Earthquake prediction: an international review* (Ed. D.W. Simpson and P.G. Richards), *American Geophysical Union*, 593–603.

Smeraglia, L., **Bernasconi, S.M.**, **Berra, F.**, **Billi, A.**, **Boschi, C.**, **Caracausi, A.**, **Carminati, E.**, **Castorina, F.**, **Doglioni, C.**, **Italiano, F.**, **Rizzo, A.L.**, **Uysal, I.T.** and **Zhao, J.** (2018) Crustal-scale fluid circulation and co-seismic shallow comb-veining along the longest normal fault of the central Apennines, Italy. *Earth Planet. Sci. Lett.*, **498**, 152–168.

Staude, S., **Bons, P.D.** and **Markl, G.** (2009) Hydrothermal vein formation by extension-driven dewatering of the middle crust: An example from SW Germany. *Earth Planet. Sci. Lett.*, **286**, 387–395.

Sun, X., **Alcalde, J.**, **Bakhtbidar, M.**, **Elío, J.**, **Vilarrasa, V.**, **Canal, J.**, **Ballesterosg, J.**, **Heinemann, N.**, **Haszeldine, S.**, **Cavanagh, A.**, **Vega-Maza, D.**, **Rubiera, F.**, **Martínez-Orio, R.**, **Johnson, G.**, **Carbonell, R.**, **Marzan, I.**, **Travé, A.** and **Gomez-Rivas, E.** (2021a) Hubs and clusters approach to unlock the development of Carbon Capture and Storage – case study in Spain.

Sun, X., **Alcalde, J.**, **Gomez-Riva, E.**, **Owen, A.**, **Griera, A.**, **Martín-Martín, J.D.**, **Cruset, D.** and **Travé, A.** (2021b) Fluvial sedimentation of the Puig-reig anticline (South-eastern Pyrenees) and its reservoir potential.

Sun, X., **Alcalde, J.**, **Gomez-Rivas, E.**, **Struth, L.**, **Johnson, G.** and **Travé, A.** (2020) Appraisal of CO2 storage potential in compressional hydrocarbon-bearing basins: Global assessment and case study in the Sichuan Basin (China). *Geosci. Front.*, **11**, 2309–2321.

Sun, X., **Gomez-Rivas, E.**, **Alcalde, J.**, **Martín-Martín, J.D.**, **Ma, C.**, **Muñoz-López, D.**, **Cruset, D.**, **Cantarero, I.**, **Griera, A.** and **Travé, A.** (2021c) Fracture distribution in a folded fluvial succession: the Puig-reig anticline (South-eastern Pyrenees). *Mar. Pet. Geol.*, 105169.

Sun, X., **Lin, C.**, **Dong, C.**, **Zhang, X.**, **Ma, C.**, **Lin, J.** and **Xie, J.** (2017) Influence of chlorite on siliceous cement under control of reservoir lithology. *Earth Sci. - J. China Univ. Geosci.*, **42**, 1599–1607.

Suppe, J., **Sàbat, F.**, **Anton Muñoz, J.**, **Poblet, J.**, **Roca, E.** and **Vergés, J.** (1997) Bed-by-bed fold growth by kink-band migration: Sant llorenç de Morunys, eastern Pyrenees. *J. Struct. Geol.*, **19**, 443–461.

Taylor, B.E. (1987) Stable isotope geochemistry of ore-forming fluids. In: *Short Course in Stable*

Isotope Geochemistry of Low Temperature Fluids (Ed. T.K. Kyser), *Mineralogical Association of Canada*, 337–445.

Taylor, K.G., **Gawthorpe, R.L.**, **Curtis, C.D.**, **Marshall, J.D.** and **Awwiller, D.N.** (2000) Carbonate cementation in a sequence-stratigraphic framework: Upper Cretaceous sandstones, Book Cliffs, Utah-Colorado. *J. Sediment. Res.*, **70**, 360–372.

Taylor, K.G. and **Machent, P.G.** (2011) Extensive carbonate cementation of fluvial sandstones: An integrated outcrop and petrographic analysis from the Upper Cretaceous, Book Cliffs, Utah. *Mar. Pet. Geol.*, **28**, 1461–1474.

Travé, A. and **Calvet, F.** (2001) Syn-rift geofluids in fractures related to the early-middle Miocene evolution of the Vallès-Penedès half-graben (NE Spain). *Tectonophysics*, **336**, 101–120.

Travé, A., **Calvet, F.**, **Sans, M.**, **Vergés, J.** and **Thirlwall, M.** (2000) Fluid history related to the Alpine compression at the margin of the south-Pyrenean Foreland basin: The El Guix anticline. *Tectonophysics*, **321**, 73–102.

Travé, A., **Calvet, F.**, **Soler, A.** and **Labaume, P.** (1998) Fracturing and fluid migration during Palaeogene compression and Neogene extension in the Catalan Coastal Ranges, Spain. *Sedimentology*, **45**, 1063–1082.

Travé, A., **Labaume, P.**, **Calvet, F.** and **Soler, A.** (1997) Sediment dewatering and pore fluid migration along thrust faults in a foreland basin inferred from isotopic and elemental geochemical analyses (Eocene southern Pyrenees, Spain). *Tectonophysics*, **282**, 375–398.

Travé, A., **Labaume, P.** and **Vergés, J.** (2007) Fluid systems in foreland fold-and-thrust belts: An overview from the southern Pyrenees. In: *Thrust Belts and Foreland Basins* (Ed. O. Lacombe, J. Lavé, F. Roure, and J. Vergés), *Springer*, Berlin, Heidelberg, 93–115.

Valloni, R. and **Zuffa, G.G.** (1984) Provenance changes for arenaceous formations of the northern Apennines, Italy. *Geol. Soc. Am. Bull.*, **95**, 1035–1039.

Van den Bril, K., **Gregoire, C.**, **Swennen, R.** and **Lambot, S.** (2007) Ground-penetrating radar as a tool to detect rock heterogeneities (channels, cemented layers and fractures) in the Luxembourg Sandstone Formation (Grand-Duchy of Luxembourg). *Sedimentology*, **54**, 949–967.

Van Den Bril, K. and **Swennen, R.** (2009) Sedimentological control on carbonate cementation in the Luxembourg Sandstone Formation. *Geol. Belgica*, **12**, 3–23.

Vandeginste, V., **Swennen, R.**, **Allaeys, M.**, **Ellam, R.M.**, **Osadetz, K.** and **Roure, F.** (2012) Challenges of structural diagenesis in foreland fold-and-thrust belts: A case study on paleofluid flow in the Canadian Rocky Mountains West of Calgary. *Mar. Pet. Geol.*, **35**, 235–251.

Veizer, J., **Ala, D.**, **Azmy, K.**, **Bruckschen, P.**, **Buhl, D.**, **Bruhn, F.**, **Carden, G.A.F.**, **Diener, A.**, **Ebneth, S.**, **Godderis, Y.**, **Jasper, T.**, **Korte, C.**, **Pawellek, F.**, **Podlaha, O.G.** and **Strauss, H.** (1999) 87Sr/86Sr, δ13C and δ18O evolution of Phanerozoic seawater. *Chem. Geol.*, **161**, 59–88.

Vergés, J. (1993) Estudi geològic del vessant sud del Pirineu oriental i central. Evolució cinemàtica en 3D. University of Barcelona

Vergés, J., **Marzo, M.** and **Muñoz, J.A.** (2002) Growth strata in foreland settings. *Sediment. Geol.*, **146**, 1–9.

Vergés, J., **Marzo, M.**, **Santaeulària, T.**, **Serra-Kiel, J.**, **Burbank, D.W.**, **Muñoz, J.A.** and **Giménez-Montsant, J.** (1998) Quantified vertical motions and tectonic evolution of the SE Pyrenean foreland basin. *Geol. Soc. London, Spec. Publ.*, **134**, 107–134.

Vergés, J., **Muñoz, J.A.** and **Martínez, A.** (1992) South Pyrenean fold and thrust belt: The role of foreland evaporitic levels in thrust geometry. In: *Thrust Tectonics* (Ed. K.R. McClay), *Springer*, Dordrecht, 255–264.

Vilasi, N., **Swennen, R.** and **Roure, F.** (2006) Diagenesis and fracturing of Paleocene–Eocene carbonate turbidite systems in the Ionian Basin: The example of the Kelçyra area (Albania). *J. Geochemical Explor.*, **89**, 409–413.

Walderhaug, O. and **Bjørkum, P.A.** (1998) Calcite Cement in Shallow Marine Sandstones: Growth Mechanisms and Geometry. In: *Carbonate Cementation in Sandstones* (Ed. S. Morad), *International Association of Sedimentologists Special Publication*, 179–192.

Walderhaug, O., **Bjørkum, P.A.** and **Bolås, H.M.N.** (1989) Correlation of calcite-cemented layers in shallow-marine sandstones of the Fensfjord Formation in the Brage Field. In: *Correlation in Hydrocarbon Exploration* (Ed. J.D. Collinson), *Springer*, Dordrecht, 367–375.

Wanas, H.A. (2008) Calcite-cemented concretions in shallow marine and fluvial sandstones of the Birket Qarun Formation (Late Eocene), El-Faiyum depression, Egypt: Field, petrographic and geochemical studies: Implications for formation conditions. *Sediment. Geol.*, **212**, 40–48.

Wang, A., **Liang, T.**, **Li, L.**, **Wang, Z.**, **Fan, C.**, **Wang, Y.**, **Zhang, Y.** and **Kong, H.** (2017) Origin of diagenetic calcite cements in the continental Qaidam Basin, NW China: Implication for fluid flow and hydrocarbon migration. *J. Geochemical Explor.*, **182**, 94–109.

Williams, E.A., **Ford, M.**, **Vergés, J.** and **Artoni, A.** (1998) Alluvial gravel sedimentation in a contractional growth fold setting, Sant Llorenç de Morunys, southeastern Pyrenees. *Geol. Soc. London, Spec. Publ.*, **134**, 69–106.

Xiong, D., **Azmy, K.** and **Blamey, N.J.F.** (2016) Diagenesis and origin of calcite cement in the Flemish Pass Basin sandstone reservoir (Upper Jurassic): Implications for porosity development. *Mar. Pet. Geol.*, **70**, 93–118.

Yang, T., **Cao, Y.**, **Friis, H.**, **Liu, K.**, **Wang, Y.**, **Zhou, L.**, **Zhang, S.** and **Zhang, H.** (2018) Genesis and distribution pattern of carbonate cements in lacustrine deep-water gravity-flow sandstone reservoirs in the third member of the Shahejie Formation in the Dongying Sag, Jiyang Depression, Eastern China. *Mar. Pet. Geol.*, **92**, 547–564.

Yang, Z., **Zou, C.**, **He, S.**, **Li, Q.**, **He, Z.**, **Wu, H.**, **Cao, F.**, **Meng, X.**, **Wang, F.** and **Xiao, Q.** (2010) Formation mechanism of carbonate cemented zones adjacent to the top overpressured surface in the central Junggar Basin, NW China. *Sci. China Earth Sci.*, **53**, 529–540.

Yuste, A., **Luzón, A.** and **Bauluz, B.** (2004) Provenance of Oligocene-Miocene alluvial and fluvial fans of the northern Ebro Basin (NE Spain): An XRD, petrographic and SEM study. *Sediment. Geol.*, **172**, 251–268.

Zhang, T., **Zhang, S.**, **Meng, W.**, **Feng, Y.** and **An, T.** (2019) Characteristics and genetic mechanism of carbonate cements in sandstones near the overpressure top surface: A case study of the Niuzhuang Depression in Bohai Bay Basin. *J. Pet. Sci. Eng.*, **181**, 106172.

Zuffa, G.G. (1985) Optical analyses of arenites: Influence of methodology on compositional results. In: *Provenance of Arenites: NATO-Advanced Study Institute Series C* (Ed. G.G. Zuffa), *Reidel Publishing Company*, Dordrecht, 165–189.

Zuffa, G.G. (1980) Hybrid arenites: their composition and classification. *J. Sediment. Petrol.*, **50**, 21–29.

Appendix 6 Other conference publications

35th IAS Meeting of Sedimentology, June 21-25, 2021, Prague, Czech Republic:

Fracture distribution in a folded fluvial succession: the Puig-reig anticline (south-eastern Pyrenees)

Xiaolong Sun[a], Enrique Gomez-Rivas[a], Juan Alcalde[b], Juan Diego Martín-Martín[a], Daniel Muñoz-López[a], David Cruset[b], Irene Cantarero[a], Albert Griera[c], Anna Travé[a]

[a] Departament de Mineralogia, Petrologia i Geologia Aplicada, Facultat de Ciències de la Terra, Universitat de Barcelona (UB), C/ Martí i Franquès s/n, Barcelona, 08028, Spain

[b] Geosciences Barcelona (GEO3BCN-CSIC), Lluís Solé i Sabarís s/n, Barcelona, 08028, Spain

[c] Departament de Geologia, Universitat Autònoma de Barcelona, Cerdanyola del Vallès, 08193, Spain

Abstract: Fractures play a fundamental role in controlling both fluid migration and reservoir quality, especially in low-permeability and tight reservoirs, including those in foreland fold-and-thrust belts. However, systematic fracture assessment in subsurface rocks is limited by the inability of sampling subseismic-scale fractures and large fractures that exceed the dimensions of boreholes. A common strategy is to use outcrop analogues to understand the controlling factors of 3D fracture distributions and thus reduce uncertainties in their subsurface prediction. The Puig-reig anticline, located in the SE Pyrenees, exposes fluvial sedimentary deposits that host fracture networks. The linear scanline method has been used to systematically collect fracture data, allowing the investigation of fracture distributions and their depositional and structural controlling factors. The results indicate that fracture attributes are strongly influenced both by their position within the anticline and by the depositional characteristics of their host sedimentary rocks. Relatively high-strain zones, such as the anticline crest and nearby areas, feature relatively small fracture spacing and high intensity. Besides, channel filling sandstone layers present higher fracture intensity than channel lag conglomerate bodies due to smaller bedding thickness. In the two fold limbs, where strain was lower, fracture intensity is overall lower. In the anticline, conglomerate bodies tend to present relatively large fracture length and aperture compared to thin sandstone layers, especially in the proximal fluvial fan in the north limb. This is mainly because the thick and massive conglomerate bodies can accommodate strain by the propagation and re-opening of existing fractures apart from the formation of new fractures during fold growth. The Puig-reig anticline case study can be used as a reservoir analogue to explore the fracture distribution pattern and reservoir potential in folded fluvial clastic sediments.

Keywords: fractures; fluvial fan; structural position; fold; Pyrenees.

35th IAS Meeting of Sedimentology, June 21-25, 2021, Prague, Czech Republic:

Calcite cementation in a folded and fractured fluvial succession: the Puig-reig anticline (South-eastern Pyrenees)

Xiaolong Sun[a], Enrique Gomez-Rivas[a], Juan Alcalde[b], David Cruset[b], Daniel Muñoz-López[a], Juan Diego Martín-Martín[a], Irene Cantarero[a], Anna Travé[a]

[a] Departament de Mineralogia, Petrologia i Geologia Aplicada, Facultat de Ciències de la Terra, Universitat de Barcelona (UB), c/ Martí i Franquès s/n, Barcelona, 08028, Spain

[b] Geosciences Barcelona (GEO3BCN-CSIC), Lluís Solé i Sabarís s/n, Barcelona, 08028, Spain

Abstract: Cementation in clastic rocks exerts significant effects on fluid flow and reservoir properties. The Puig-reig anticline, located in the south-eastern Pyrenees, exposes fluvial sedimentary deposits hosting fracture networks, which are mainly filled with calcite cement. This anticline constitutes an excellent case study to investigate the origin and distribution of calcite cement within fracture networks and variable host rocks in fluvial facies. Five generations of calcite cement have been identified. The first generation (Cc0) precipitated in interparticle pores, featuring growth zonation with the alternation of non-luminescent and luminescent zones. It precipitated before intense folding and fracturing during the anticline growth. The second generation (Cc1) precipitated in both fractures and interparticle pores, with bright yellow luminescence and blocky crystal morphology. The third generation (Cc2) precipitated mainly in fractures and rarely in interparticle pores, with dull orange luminescence and blocky crystal morphology. The fourth generation (Cc3) only precipitated in fractures, presenting very dull luminescence and large euhedral and blocky crystals. Cc1 to Cc3 formed during folding or thrusting. The fifth generation (Cc4) precipitated in fractures, and it is non-luminescent and presents elongated crystal morphology and a palisade structure of bladed crystals. It formed after the anticline growth. As the predominant calcite cement, Cc1 filled interparticle pores and fractures throughout the anticline, resulting in the overall low matrix porosity and sealed fractures, whose distribution is affected by the host sedimentary facies and lithofacies. Channel filling sandstones in the medial fluvial fan present higher contents of calcite cement than overbank deposits and proximal fluvial deposits. Large and thick conglomerate bodies and coarse sandstones host larger calcite veins compared to fine sandstones and clay deposits. The study of outcrop analogues like the Puig-reig case is key for establishing predictive models of calcite cementation in the subsurface.

Keywords: calcite cement; fluid flow; fluvial fan; fold; Pyrenees.

Calcite cementation in a folded and fractured fluvial succession: the Puig-reig anticline (South-eastern Pyrenees)

Xiaolong Sun[a], Enrique Gomez-Rivas[a], Juan Alcalde[b], David Cruset[b], Daniel Muñoz-López[a], Juan Diego Martín-Martín[a], Irene Cantarero[a], Cédric M. John[c], Anna Travé[a]

[a] Departament de Mineralogia, Petrologia i Geologia Aplicada, Facultat de Ciències de la Terra, Universitat de Barcelona (UB), Barcelona, Spain

[b] Geosciences Barcelona (GEO3BCN-CSIC), Barcelona, Spain

[c] Department of Earth Science and Engineering, Imperial College London, UK

Geological setting

The Puig-reig anticline is in the South-eastern Pyrenees and developed along the footwall of the Vallfogona thrust (Fig. 1A and B). In the lower part, the Banyoles and Igualada Formations (middle to upper Eocene) consist of marine marls, which were duplicated by thrusting (Fig. 1C) (Vergés, 1993). In the upper part, the Berga Group and the Solsona Formation (upper Eocene to Oligocene) consist of continental alluvial-fluvial conglomerate, sandstone and mudstone deposits. Vallfogona footwall was folded forming km-scale south-verging gentle anticline.

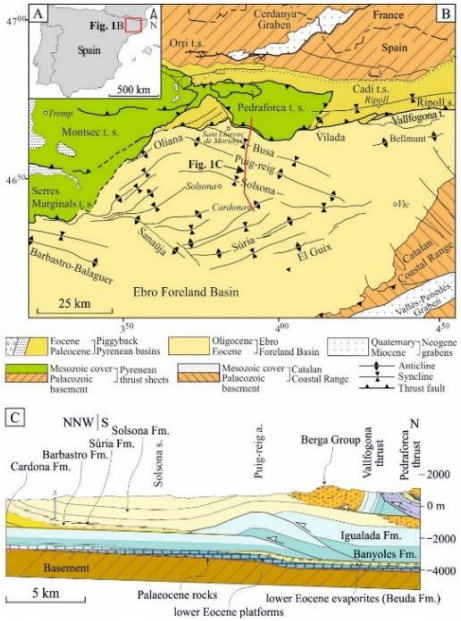

Figure 1. (A) Location and (B) main structural units of the South Pyrenean fold-and-thrust belt and the Ebro Basin; (C) Geological cross-section of the frontal part of the SE Pyrenean fold-and-thrust belt and the Ebro Basin (Vergés, 1993).

Petrology of calcite cements

Five generations of calcite cements (Cc0 to Cc4):

Cc0 precipitated in intergranular pores of host rocks and presents concentric zonation under cathodoluminescence (Fig. 2A1, A2);

Cc1 developed in intergranular pores, reverse and strike-slip faults, F1 to F4 joint sets and presents bright orange luminescence (Fig. 2B1 to B4);

Cc2 mainly developed in normal and strike-slip faults and F1 joint set in the fold crest, and shows dull orange luminescence (Fig. 2C1 to C4);

Cc3 mainly developed in F1 and F4 joint sets in the north limb and shows very dull orange luminescence (Fig. 2D1 to D4);

Cc4 developed in F1 to F4 joint sets across the anticline and is non-luminescent (Fig. 2E1 to E4).

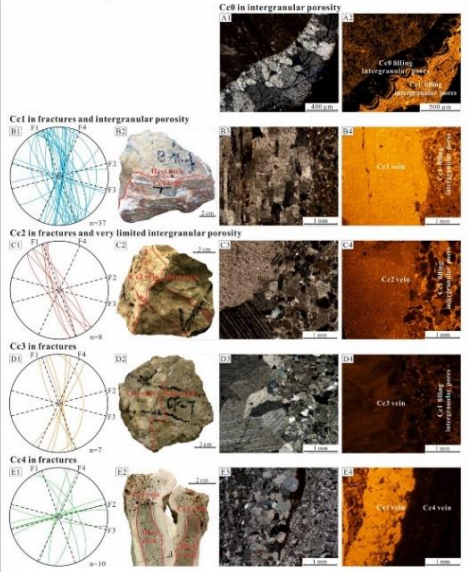

Figure 2. Lower hemisphere Schmidt stereoplots, hand specimens and microphotographs (polarizing optical microscope and cathodoluminescence (CL) microscope) for different generations of calcite cements.

Geochemistry and fluid origin of calcite cements

Cc0 presents luminescent zonation and very low Mn and Fe. It precipitated from meteoric fluids in fluctuating redox conditions.

Cc1 has variable $\delta^{13}C$ (-3.3 to +0.8‰ VPDB) and $\delta^{18}O$ (-8.0 to -4.9‰ VPDB) and high $\delta^{18}O_{fluid}$ (+4.7 to +9.2‰ VSMOW), fluid temperatures (92 to 129ºC) (Figs. 3, 4) and $^{87}Sr/^{86}Sr$ ratios (0.7091 to 0.7092). It precipitated from hydrothermal fluids.

Cc2 presents lower $\delta^{18}O$ (-8.4 to -10.2 ‰ VPDB), $\delta^{18}O_{fluid}$ (-1.7 to -0.7 ‰ VSMOW), fluid temperatures (77 to 90ºC) and $^{87}Sr/^{86}Sr$ ratios (0.7089 to 0.7090) than Cc1. It precipitated from the mixed fluids between hydrothermal and meteoric fluids.

Cc3 has higher $\delta^{13}C$ (-0.1 to +0.8‰ VPDB) and $\delta^{18}O$ (-4.6 to -3.4 ‰ VPDB) and lower fluid temperatures (50 to 62ºC) and $^{87}Sr/^{86}Sr$ ratios (0.7087 to 0.7088) than Cc1 and Cc2. It precipitated from formation fluids.

Cc4 has low Mn and Fe, $\delta^{13}C$ (-10.2 to -4.2‰ VPDB), $\delta^{18}O_{fluid}$ (-4.8 to -4.3 ‰ VSMOW) and fluid temperatures (16 to 19ºC) and variable $^{87}Sr/^{86}Sr$ ratios (0.7088 to 0.7102). It precipitated from meteoric fluids.

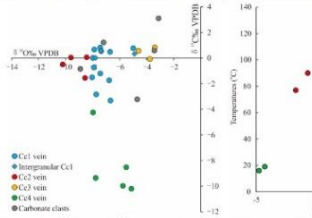

Figure 3. $\delta^{18}O$ vs. $\delta^{13}C$ cross-plot of conglomerate carbonate clasts and Cc1 to Cc4. Data of carbonate clasts are from (Cruset et al., 2016).

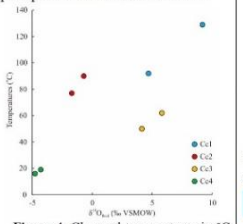

Figure 4. Clumped temperatures in °C vs. $\delta^{18}O_{fluid}$ in ‰ VSMOW for Cc1 to Cc4. Data of Cc1 and Cc2 are from (Cruset et al., 2016).

Changes in fluid regime during fold evolution

During early diagenetic stage before deformation: meteoric fluids in the phreatic zone dominated the whole anticline (Fig. 5).

During intensive folding and thrusting: hydrothermal fluids migrated from the Palaeozoic basement through connected blind thrust system and fracture network, which dominated the whole anticline.

During the late stage of fold growth and the early stage of fold uplift: meteoric fluids percolated from surface through fracture network in the fold crest and mixed with hydrothermal fluids, whereas formation fluids migrated from the frontal thrusts (*i.e.*, the Vallfogona thrust) and dominated the western zone of the north limb.

During the continuing fold uplift and denudation: meteoric fluids percolated from surface through reopened fractures and dominated the whole anticline.

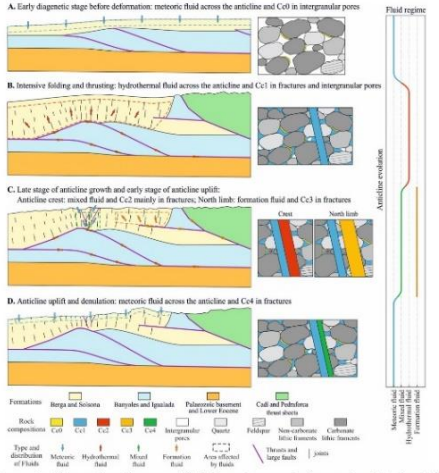

Figure 5. Schematic diagram of fluid regime evolution and related calcite cementation during the tectonic evolution of the Puig-reig anticline.

Conclusions

In the Puig-reig anticline, calcite cementation and fluid evolution were accompanied by fold evolution. Before intensive deformation, this anticline was dominated by meteoric fluids, from which Cc0 precipitated. During fold growth, it was affected by hydrothermal, mixed and formation fluids, from which Cc1 to Cc3 precipitated, respectively. During intensive fold uplift and denudation, it was again dominated by meteoric fluids, from which Cc4 precipitated.

Acknowledgements

Funding was provided by the Catalan Council to the Grup Consolidat de Recerca "Geologia Sedimentària" (2017SGR-824) and the DGICYT Spanish Project PGC2018-093903-B-C22. XS is funded by the China Scholarship Council for a PhD scholarship (201806450043). EGR is funded provided by the Spanish Ministry of Science, Innovation and Universities ("Ramón y Cajal" fellowship RYC2018-026335-I). JA is funded by MICINN (Juan de la Cierva fellowship - IJC2018-036074-I).

References

Vergés, J., 1993. Estudi geològic del vessant sud del Pirineu oriental i central. Evolució cinemàtica en 3D (Ph.D. thesis). University of Barcelona, Barcelona. pp. 47-78.

Cruset, D., et al., 2016. Crestal graben fluid evolution during growth of the Puig-reig anticline (South Pyrenean fold and thrust belt). Journal of Geodynamics. 101, 30–50.

X Congreso Geológico de España, July 5-7, 2021, Vitoria-Gasteiz, Spain:

Distribution of calcite cements in a folded fluvial succession: the Puig-reig anticline (South-eastern Pyrenees)

Distribución de cementos de calcita en un sistema fluvial: el anticlinal de Puig-reig (Pirineos Surorientales)

X. Sun[1], E. Gomez-Rivas[1,] J. Alcalde[2], D. Cruset[1], D. Muñoz-López[1], I. Cantarero[1], J.D. Martín-Martín[1] y A. Travé[1]

1 Departament de Mineralogia, Petrologia i Geologia Aplicada, Universitat de Barcelona (UB), 08028 Barcelona. xiaolong.sun@ub.edu e.gomez-rivas@ub.edu munoz-lopez@ub.edu i_cantarero@ub.edu juandiegomartin@ub.edu atrave@ub.edu

2 Geosciences Barcelona (GEO3BCN-CSIC), 08028 Barcelona. jalcalde@geo3bcn.csic.es dcruset@geo3bcn.csic.es

Resumen: *El cemento de calcita, como mineral autigénico predominante, tiene un efecto muy significativo en la potencial calidad como reservorio del anticlinal de Puig-Reig, que constituye un excelente análogo para el estudio de la distribución de cementos en diferentes facies sedimentarias gracias a la cantidad y calidad de los afloramientos. Tras un exhaustivo estudio estratigráfico y de recogida muestras, se han realizado análisis petrográficos de facies y sus cementos con microscopio óptico y de cátodo-luminiscencia. Se han identificado dos generaciones principales de cementación calcítica que se desarrollaron durante y después del crecimiento del anticlinal, aunque la mayor parte del cemento cristalizó de manera simultánea a su formación. La distribución del cemento está controlada por la posición estructural dentro del pliegue y por las facies y litofacies de la roca encajante. Los depósitos de canales fluviales en la cresta del anticlinal, de grano especialmente grueso, tienden a desarrollar más cementación. Es necesario profundizar en el estudio de las características de la cementación de calcita para obtener mejores estimaciones sobre la calidad de los reservorios y para guiar las actividades de exploración de hidrocarburos o el almacenamiento geológico de CO_2 en estructuras subterráneas similares.*
Palabras clave: *cementación de calcita, depósitos fluviales, fluidos, Pirineos*.

Abstract: *As the most prevalent authigenic mineral, calcite cement exerts a significant effect on reservoir quality of the Puig-reig anticline, which is an excellent outcrop analogue to study calcite cement distribution due to good and continuous exposure. After stratigraphic logging and rock sampling, two major generations of calcite cementation have been identified using petrographic observations under optical and cathodoluminescence microscopes. They formed during and after anticline growth, respectively. Most calcite cement formed simultaneously with the anticline. Calcite cement distribution is controlled by the structural position of sediments in the fold and also by host sedimentary facies and lithofacies. Fluvial channel deposits of the anticline crest, especially relatively coarse deposits, tend to host more calcite cement. A more detailed study on calcite cementation is required to predict high-quality reservoirs and further guide petroleum exploration or carbon storage in similar subsurface structures.*
Key words: *calcite cementation, fluvial fan deposits, fluids, Pyrenees.*

INTRODUCTION

Calcite is one of the most predominant authigenic minerals cementing clastic rocks and thus exerts significant effects on reservoir properties, fluid flow and solute transport (Dutton et al., 2002; Davis et al., 2006), thus becoming a key concern in hydrocarbon exploration and carbon sequestration. However, calcite cementation tends be heterogeneously distributed and be controlled by many factors, such as the tectonic settings, stratigraphic framework, sedimentary facies and lithofacies and fluid flow (Morad, 1998; Taylor et al., 2000; Cruest et al., 2016). Therefore, a comprehensive study of calcite distribution is a fundamental requirement for reservoir prediction.

GEOLOGICAL SETTING

The Puig-reig anticline is located in the south-eastern Pyrenean fold-and-thrust belt and the north-eastern part of the Ebro Basin. It formed above a thrust ramp consisting of middle and upper Eocene deltaic sandstones and marine marls, which changed into the alluvial-fluvial sediments of the Berga Group and the Solsona Formation after a rapid transition from marine to continental sedimentation (Williams et al., 1998; Sáez et al., 2007; Barrier et al., 2010). In this study, we focus on the Camps de Vall-Llonga Formation, a sub-unit of the Berga Group, and the Solsona Formation. These formations were deposited from a proximal to medial fluvial system. The proximal fluvial deposits, concentrating in the north limb of the anticline, represent sedimentary environments of unconfined flash floods or wide-shallow channel streams. The medial fluvial deposits, covering the rest of the anticline, represent sedimentary environments of braided channel streams and overbanks. The distal fluvial deposits are composed of terminal lobes and deltas, which are located southward of this anticline (Sáez et al., 2007).

METHODS

The study area presents excellent outcrops along roads that cut through the Puig-reig anticline. Seven high-resolution (decimeter-scale) stratigraphic logs with a total length exceeding 3000 m were analysed in detail. We recorded the thickness, grain size, sedimentary structures and bioturbations, which collectively allowed the identification of sedimentary facies and stratigraphic correlations. Petrographic observations were made using optical and cathodoluminescence microscopy to distinguish carbonate cement generations and determine their relative content in host rocks and veins. Forty polished thin sections from different structural positions of the anticline, and representing different sedimentary facies and lithofacies were analysed using a Zeiss Axiophot optical microscope and a Technosyn Cold Cathodoluminescence microscope, model 8200 Mk5-1 operating 16 to 17 kV and 270 to 290 μA gun current.

RESULTS AND DISCUSSION

Calcite is the most prevalent diagenetic mineral in the Puig-reig anticline. Two major generations of calcite cementation have been recognized from petrographic observations. The dominant calcite cement, which appears filling pores, replacing clasts and forming vein and micro-vein fillings (Fig. 1a-d), is closely related to fluid flow during the structural evolution of the Puig-reig anticline. This cement presents blocky crystal morphology and luminescence ranging from dull or bright orange colour. The second generation calcite is non-luminiscent and presents euhedral blocky structure. It is only found in veins filling the first vein generation (Fig. 1e and f), revealing that it formed in more recent periods, probably due to rock exposure after tectonic uplift.

In host rocks, the content of calcite cements mainly ranges from 5% to 15% of the total rock

volume, which resulted in the overall low matrix porosity. The distribution of calcite cements is controlled by several factors, such as the structural position in the fold and the host sedimentary facies and lithofacies. The anticline crest tends to have more calcite cements than the rocks of the limbs because the crest experienced more intense tectonic fracturing and associated fluid flow. On the other hand, medial fluvial channel deposits contain more calcite cements than overbank deposits and proximal fluvial deposits. Meanwhile, calcite veins appear preferentially developed in conglomerates and coarse sandstones rather than in fine and clay deposits. This reveals that sedimentary facies and primary lithofacies probably affected the pore structure, the degree of fracturing and fluid flow, thus controlling calcite cementation. A comprehensive study of calcite distribution on this kind of outcrop analogue is conducive to identify high-quality reservoirs for petroleum exploration or carbon storage in similar subsurface structures.

ACKNOWLEDGEMENTS

Funding was provided by the Grup Consolidat de Recerca "Geologia Sedimentària" (2017SGR-824) and the DGICYT Spanish Project PGC2018-093903-B-C22. XS acknowledges funding by the China Scholarship Council for a PhD scholarship (201806450043). EGR acknowledges funding provided by the Spanish Ministry of Science, Innovation and Universities ("Ramón y Cajal" fellowship RYC2018-026335-I). JA is funded by MICINN (Juan de la Cierva fellowship - IJC2018-036074-I)

REFERENCES

Barrier, L., Proust, J.N., Nalpas, T., Robin, C. y Guillocheau, F. (2010): Control of Alluvial Sedimentation at Foreland-Basin Active Margins: A Case Study from the Northeastern Ebro Basin (Southeastern Pyrenees, Spain). *Journal of Sedimentary Research*, 80: 728-749.

Cruset, D., Cantarero, I., Travé, A., Vergés, J. y John C.M. (2016): Crestal graben fluid evolution during growth of the Puig-reig anticline (South Pyrenean fold and thrust belt). *Journal of Geodynamics*, 101: 30-50.

Davis, J.M., Roy, N.D., Mozley, P.S. and Hall, J.S. (2006): The effect of carbonate cementation on permeability heterogeneity in fluvial aquifers: An outcrop analog study. *Sedimentary Geology*, 184: 267-280.

Dutton, S.P., White, C.D., Willis, B.J. and Novakovic, D. (2002): Calcite cement distribution and its effect on fluid flow in a deltaic sandstone, Frontier Formation, Wyoming. *AAPG Bulletin*, 86: 2007-2021.

Morad, S. (1998): Carbonate cementation in sandstones: Distribution patterns and geochemical evolution. IAS Special Publication. Oxford, UK: Blackwell Scientific, 1-26.

Sáez, A., Anadón, P., Herrero, M.J. y Moscariello, A. (2007): Variable style of transition between Palaeogene fluvial fan and lacustrine systems, southern Pyrenean foreland, NE Spain. *Sedimentology*, 54: 367-390.

Taylor, K.G., Gawthorpe, R.L., Curtis, C.D., Marshall, J.D. and Awwiller, D.N. (2000): Carbonate cementation in a sequence-stratigraphic framework: Upper Cretaceous sandstones, Book Cliffs, Utah-Colorado. Journal of Sedimentary Research, 70: 360-372.

Williams, E.A., Ford, M., Vergés, J. and Artoni, A. (1998): Alluvial gravel sedimentation in a contractional growth fold setting, Sant Llorenc de Morunys, southeastern Pyrenees. *Geological Society Special Publication*, 134: 69-106.

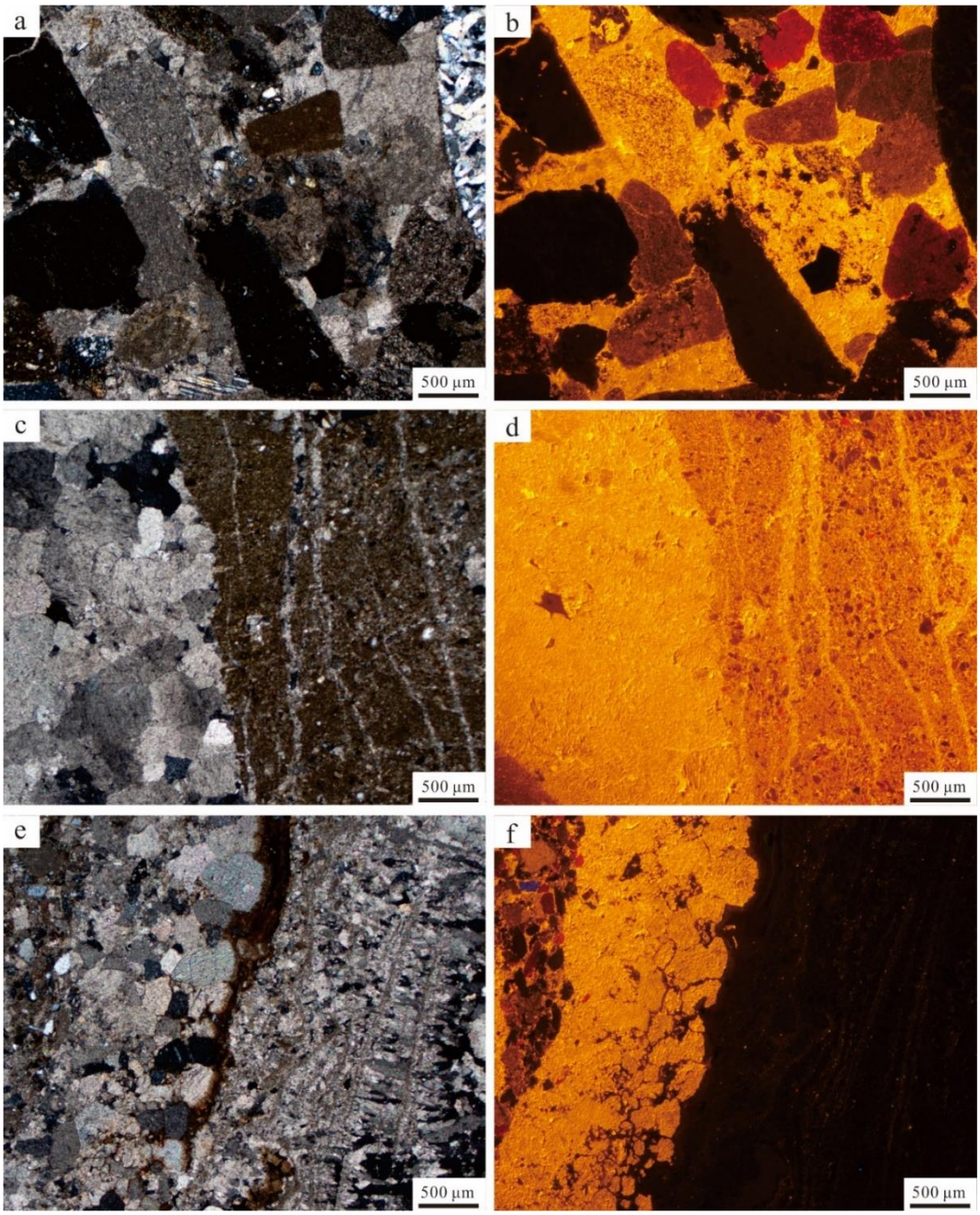

FIGURE 1. *Images of polarizing optical microscope and cathodoluminescence of calcite cements from the Puig-reig anticline: (a-b) prevalent pore filling calcite cements; (c-d) similar luminescence of calcite cement in vein, micro vein and pore filling; (e-f) non-luminous vein covering previous vein with bright orange luminescence.*